FERMI @elettra

Conceptual Design Report


FERMI
@elettra

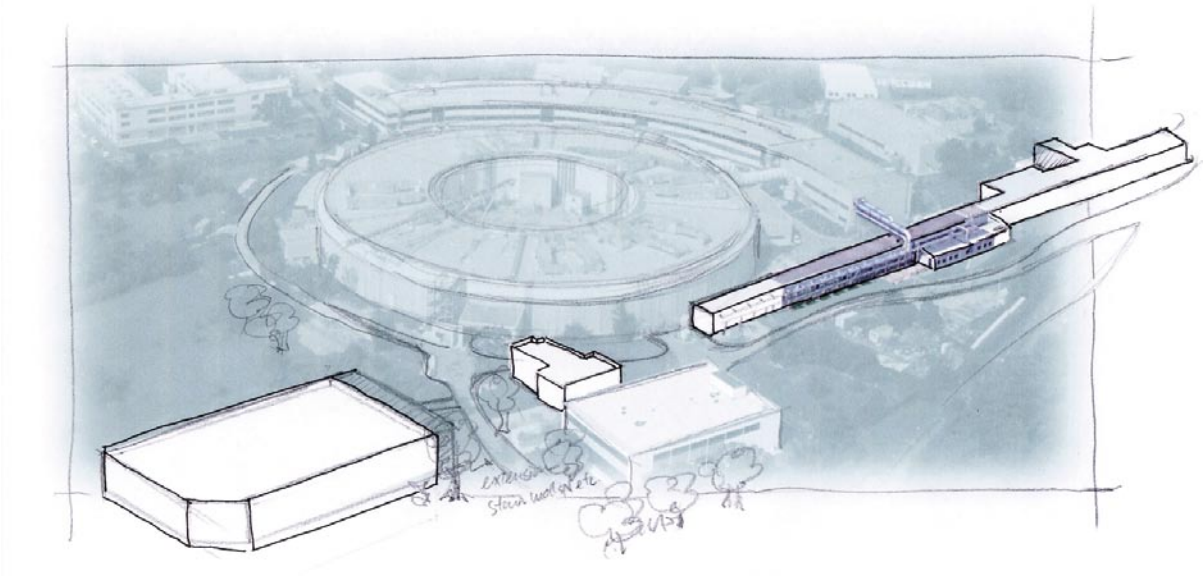

FERMI@Elettra
Conceptual Design Report

Foreword

The Conceptual Design Report of the FERMI@Elettra Project is the result of several years of incubation, development and international collaboration.

The concept started with a first proposal presented by the Trieste team in the beginning of 2002, reinforcing an already strong interaction between EU and USA synchrotron radiation laboratories, in response to a call for proposals by the Italian Ministry of Research. The proposal has evolved into the present Report that has been written in parallel with preliminary development activities. In particular, we strongly acknowledge contributions from the design study activities of the sixth framework EU program EUROFEL and the detailed physics and technological studies carried out together with Lawrence Berkeley National Laboratory, the Massachusetts Institute of Technology and the Linac Coherent Light Source (SLAC). The gratefully acknowledged help from many other expert teams, listed in this report, also contributed to make the report a solid conceptual base for the construction of the FERMI@Elettra facility.

The Free Electron Laser (FEL) activity at Sincrotrone Trieste has always been an important research and development topic; a strong international community has in fact grown around the EU storage-ring-FEL project, EUFELE, in operation at the ELETTRA storage ring, considered to a be the precursor to FERMI.

FERMI@Elettra has always been intended as a "User Facility" and as such it has involved, from the very beginning, the user community in defining the project physics goals and therefore the fundamental machine parameters and configurations. As a result, the facility design has been based on complex and still evolving techniques, such as "seeding", in order to ensure the high beam stability and synchronization needed for fine spectroscopy measurements.

FERMI will be an "International Open Access" Facility to serve the most advanced experiments proposed by the international user Communities. To further improve the overall service, and to ensure the best use of resources available in Europe, we have proposed, at the EU level, to develop our facility in coordination with other similar projects now in operation (FLASH, in Hamburg) or in the design and development stage (4GLS in Daresbury, BESSY-FEL in Berlin, MAX-IV in Lund, SPARX in Frascati and PSI-FEL in Villigen) and with previously existing facilities such as FELIX in Holland. The proposal is now evolving into an integrated EU facility-Consortium, IRUVX, that has been selected as one of the Facilities in the Roadmap of Research Infrastructures for Europe. The integration will, among others, offer the advantage of possibly making the various facilities cover different parameter ranges, thus helping extend the use of FEL generated Light over a much wider range of scientific fields.

The construction of FERMI has started thanks to the financial support of the Italian National and Regional Governments as well as of a project-financing supported loan from the European Investment Bank.
The first light is planned to be delivered to the users in 2009, thus translating the concepts of this CDR into practice!

Carlo Rizzuto

Contributors

The FERMI@Elettra Design Team

C.J. Bocchetta *(Project Director)*, A. Abrami, E. Allaria, I. Andrian, D. Bacescu, L. Badano, L. Banchi, D. Bulfone, C. Bontoiu, R. Bracco, F. Cargnello, K. Casarin, M. Cornacchia, P. Craievich, D. Cocco, M. Danailov, G. D'Auria, A. Demidovich, G. De Ninno, S. Di Mitri, B. Diviacco, M. Ferianis, A. Galimberti, A. Gambitta, M. Giannini, F. Iazzourene, E. Karantzoulis, D. La Civita, G. Loda, M. Lonza, C. Masciovecchio, F. Mazzolini, D. Morelli, M. Musardo, S. Noé, C. Pappas, G. Penco, K. Prince, L. Rumiz, S. Spampinati, M. Stefanutti, L. Tosi, G. Tromba, M. Trovò, A. Vascotto, M. Veronese, D. Wang, M.A. Weeks, D. Zangrando
Sincrotrone Trieste S.C.p.A., S.S. 14 Km 163,5 in Area Science Park, 34012 Trieste, Italy

F. Parmigiani
Dipartimento di Fisica, Università degli Studi di Trieste, Via A.Valerio, 2, 34127 Trieste, Italy

M. Zangrando
Laboratorio TASC INFM-CNR, S.S. 14 Km 163,5 in Area Science Park, 34012 Trieste, Italy

J.N. Corlett, L.R. Doolittle, W.M. Fawley, S.M. Lidia, G.E. Penn, A. Ratti, J.W. Staples, R.B. Wilcox, A.A. Zholents
Lawrence Berkeley National Laboratory, 1 Cyclotron Road, Berkeley, CA 94720, USA

C.M. LeCocq, P.J. Emma, Z. Huang, J. Wu
SLAC, Stanford Linear Accelerator Center, CA, USA

S. Tazzari
Dipartimento di Fisica, Università di Roma "Tor Vergata", Viale Ricerca Scientifica 1, 00133 Roma, Italy

W.A. Barletta
Fermilab and Department of Physics, MIT, USA

W.S. Graves, F.O. Ilday, F.X. Kaertner, T. Zwart
Massachusetts Institute of Technology, Cambridge, MA, USA

Machine Advisory Committee

A. Wrulich, *Chairman*
P.J. Emma
M. Eriksson
J. Hastings
C. Pagani
C. Pellegrini
M. Poole
R.W. Schoenlein
R.P. Walker
H. Weise

Scientific Advisory Council

I. Lindau, *Chairman*
D. Attwood
G. Chiari
G. Brown
C.S. Fadley
R. Huber
S. Larsen
D. Menzel
C.V. Shank
F. van der Veen

International Collaboration

EUROFEL, the European FEL Design Study, Partner Institutions:

BESSY, Germany
CCLRC, UK
CEA-SPAM, France
CNRS, France
DESY, Germany
ENEA, Italy
FZR, Germany
INFN, Italy
MAX-lab, Sweden
MBI, Germany
Sincrotrone Trieste, Italy
SOLEIL, France
TEMF, Germany
University of Hamburg, Germany
University of Rome "Tor Vergata", Italy
University of Strathclyde, UK

Acknowledgements

The conceptual design of FERMI@Elettra is the result of collaboration between the team at Sincrotrone Trieste and many scientists and institutions worldwide. In particular, accelerator scientists together with the user community worked to define the project concepts and facility parameters. We gratefully acknowledge the contributions from all people listed above.

Special thanks for the editing and publication of this report go to Massimo Cornacchia, Miltcho Danailov, Giovanni De Ninno, Simone Di Mitri, Bruno Diviacco, Mario Ferianis, Mario Giannini, Catherine LeCocq, Marco Lonza, Marina Nadalin, Fulvio Parmigiani, Giuseppe Penco, Giulia Quondam, Giuliana Tromba, Mauro Trovò, Carol Yen, Marco Zangrando.

Finally, the donation of seven accelerating linac section by CERN is also gratefully acknowledged.

Table of Contents

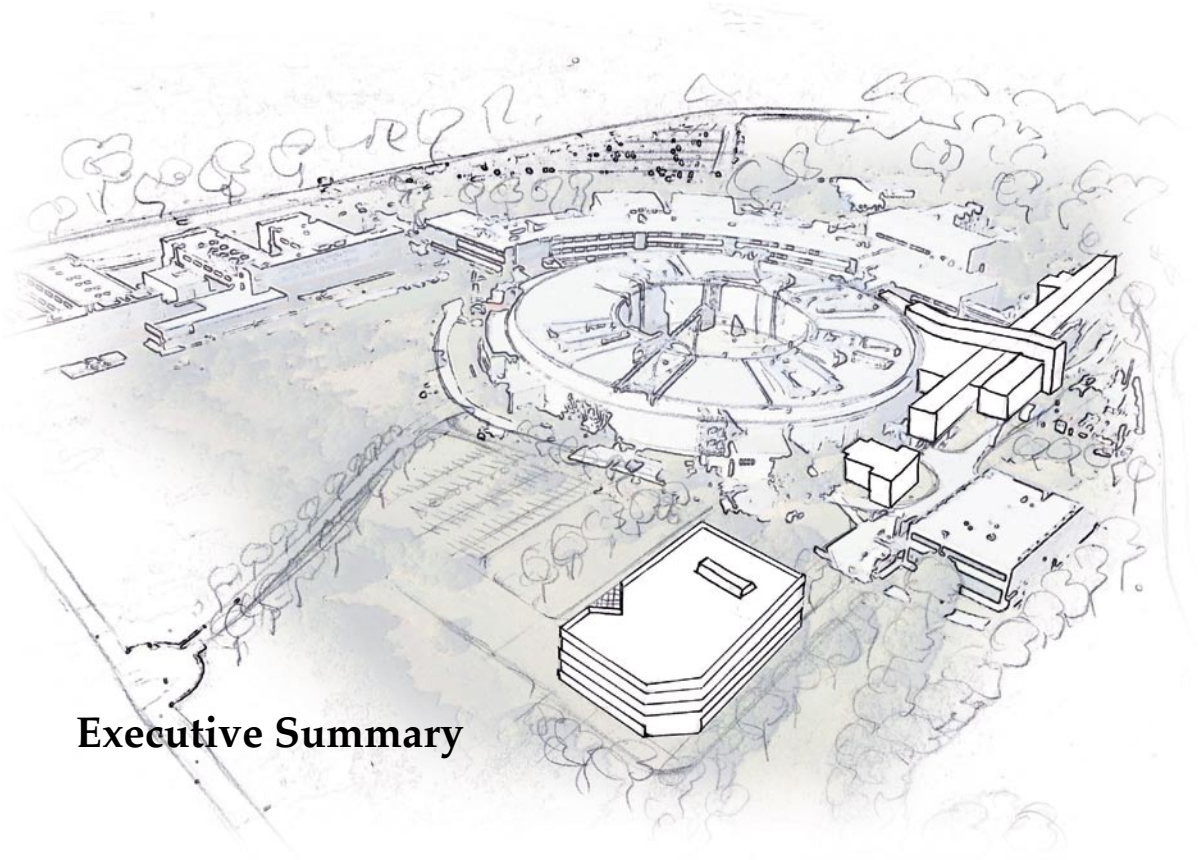

1 Executive Summary

1.1 Introduction

Synchrotron radiation is a fundamental and indispensable tool for the study of materials which encompasses a wide spectrum of sciences, technologies and applications, from life sciences to nano-technologies, from environmental sciences and geochemistry to archaeology.

Synchrotron radiation has seen an explosive growth in its application to research and development and in the number of facilities built to serve its users, covering a large range of radiation wavelengths, extending from the infrared down to hard X-rays, in the form of radiation pulses with time duration down to the few picoseconds range. The number of facilities in operation worldwide is close to eighty, serving tens of thousands of users per year.

The main figure of merit of radiation sources is brilliance, which defines the intensity of radiation, within a given bandwidth around the desired wavelength, that can be focused unto a sample of given area. Typical brilliance values for the highest performance "third generation" light sources are around 10^{19} to 10^{21} photons/s/mm^2/mrad^2/0.1% bandwidth. Another important characteristic is the pulse duration: ultra short, sub-picosecond radiation pulses are needed to open up the new investigation field covering not only the structure of a sample but also its dynamics during irradiation.

A strong need has emerged over the last few years, for a source of radiation with extremely high brilliance, close to full coherence, a bandwidth approaching the Fourier limit and with a stable and

well characterized temporal structure in the femtosecond and picosecond time domain. Such a source is the single-pass Free Electron Laser (FEL) that has the potential for producing light pulses with peak brilliance many orders of magnitude higher than that generated in present third generation sources and with sub-picosecond pulse lengths, as shown in Figure 1.1.1 [see also Chapter 3] in which the peak brightness (brilliance) and pulse duration performance of different types of X-ray sources is compared (see Table 1.1.1).

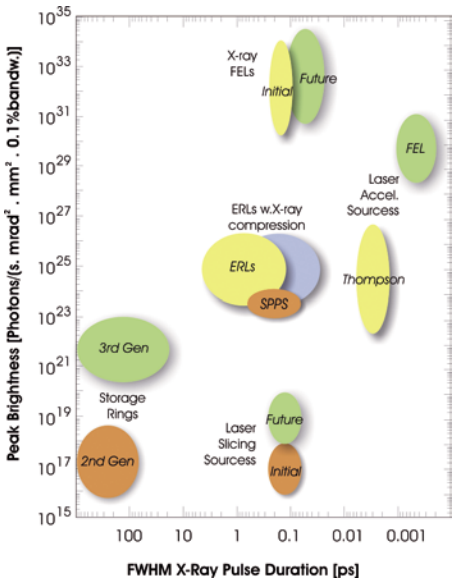

Figure 1.1.1:
Peak brightness (brilliance) versus pulse duration of various types of radiation sources.

The investigation domain opened by the new sources cover essentially all basic science fields giving access to explorations of matter in practically unexplored regimes. The scientific opportunities will in fact impact studies of a large number of disciplines ranging from materials and biomaterials sciences, nanosciences, plasma physics, molecular and cluster femto- and nano- physics and chemistry, as well as having various connections to life, environmental, astrophysical and earth sciences. As important as the immediate applications is the promise of new discoveries, studies and techniques that will emerge as this new tool is fully exploited. The potential is there to further develop technologies ranging from micro-electronics to energy. A more extensive presentation of the science case is given in Chapter 3.

The FERMI single pass FEL project at the ELETTRA Laboratory of Sincrotrone Trieste (ST) is one of the FEL based European projects, designed to become the international user facility in Italy for scientific investigations, with ultra high brilliance X-ray pulses, of ultra-fast and ultra-high resolution processes in material science and physical biosciences.

1.2 The Fermi FEL Facility

1.2.1 General Layout

The FERMI single-pass FEL facility will be driven by the present ELETTRA injector S-band linac, upgraded by the addition of seven accelerating sections[1] to bring its top energy to 1.2 GeV and of a new photoinjector, low emittance electron source. The Linac repetition rate will also be ramped up to from 10 Hz to 50 Hz. Injection into ELETTRA will be taken up by a new full energy booster synchrotron scheduled to become operational at the end of 2007 [1].

The upgraded Linac 1.2 GeV electron beam energy plus a complex of state-of-the-art undulators will allow FERMI to cover the 100-40 nm wavelength region in a first phase (FEL-1) and to reach down to 10 nm in a second, later phase (FEL-2). User experiments will be housed in the new experimental hall shown in Figure 1.2.1, located next to the ELETTRA light source [2], thus allowing for the possibility of eventually bringing ELETTRA photon beams into it to perform multi-beam experiments.

A general layout of the facility is shown in Figure 1.2.1. The accelerator and FEL complex comprises the following parts: a photoinjector and two short linac sections generating a bright, ~ 100 MeV electron beam, the main linear accelerator in which the beam is time-compressed and accelerated to ~ 1.2 GeV, the system to transport the beam to the undulators, the undulator complex generating the FEL radiation, the photon beamlines taking the radiation from the undulator to the experimental area and the experimental area itself. After leaving the undulators, while the FEL radiation is transported to the experimental areas, the electron beam is brought to a beam dump by a sequence of bending magnets. The FEL radiation transport system, designed to handle the high peak power of up to 10 GW in the sub-ps long pulse, includes a differentially pumped windowless vacuum system and low-Z material beam-line components operating at grazing incidence angles. The photon beam transport system incorporates all provisions and equipment necessary to ensure pulse length and energy resolution preservation, monochromatization, source shift compensation, beam splitting and focusing into the experimental chamber.

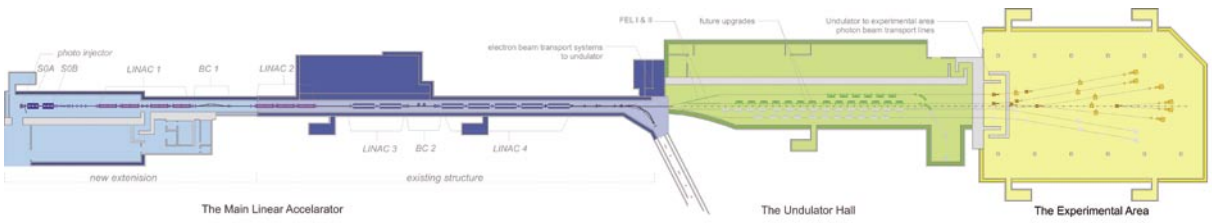

Figure 1.2.1:
FERMI General layout.

As above mentioned, the FEL facility operates two different free electron laser radiation sources, FEL-1 and FEL-2, to be realized in two phases. FEL-1, to be implemented first, is designed to operate in the time domain (short pulses) with two complementary modes: a high stability and a high intensity one.

[1]Courtesy of CERN

FEL-2, to be implemented in the second phase, is designed to operate with relatively long photon pulses, in the frequency domain to provide the highest energy resolution, i.e. the narrowest bandwidth.

The initial FERMI science program, by which the design choices have been guided, is structured to reach its final performance from the very start with diverse experiments and increasingly more demanding photon beam parameters (see Tables 3.1.2 through 3.1.7, Chapter 3), thus allowing high quality experiments to be performed from the very beginning of commissioning of both FEL-1 and FEL-2.

The classes of planned experiments, temporally ordered, are: single shot, high peak brightness experiments, pump-probe experiments and non-linear spectroscopy high-energy resolution experiments in both the time and the frequency domain.

The "roadmap" showing in more detail how the various stages of facility performance optimization will open up diverse experimental opportunities is shown in Figure 1.2.2.

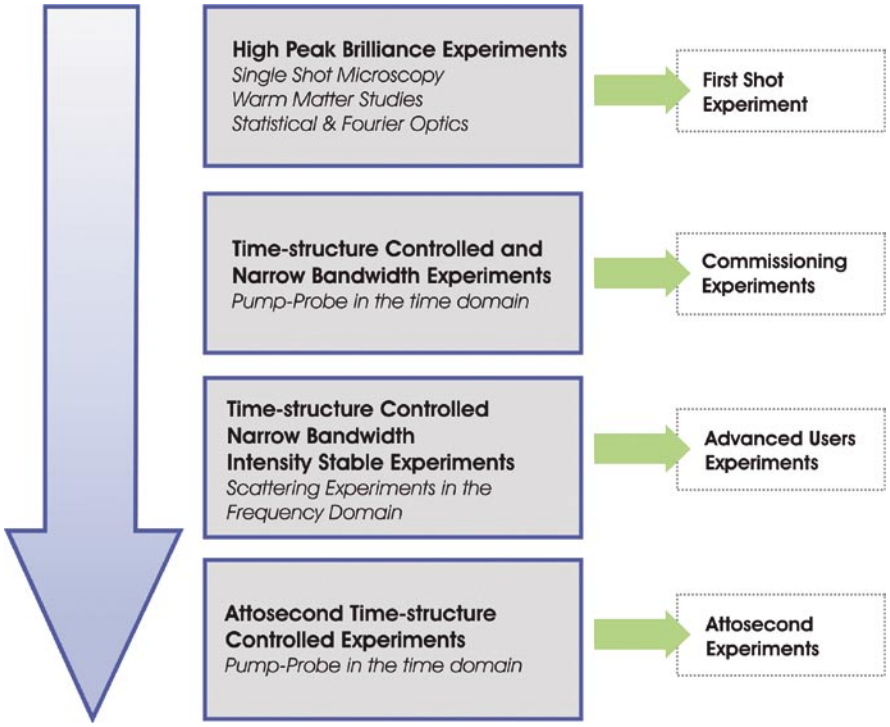

Figure 1.2.2:
Accessible experiments as the Fermi performance is gradually improved.

1.2.2 FEL Operation: Seeding Mechanism and Main FEL Parameters

The quite novel "seeding" scheme by which FEL-1 is designed to produce radiation down to 40 *nm* wavelength, is the following. An initial "seed" signal, provided by a conventional, high peak power

pulsed laser operating at wavelengths in the region 240-300 nm at the electron bunches repetition frequency, is made to overlap the electron beam in a first undulator magnet called the modulator. The laser field modulates the electron bunch energy at its own frequency and the modulation is converted to bunch charge spatial modulation by passing the electrons through a dispersive section.

The frequency spectrum of the so obtained charge modulated electron bunch contains higher harmonics of the seed laser wavelength so that intense coherent FEL radiation at the frequency of one of these harmonics can be finally obtained by passing the modulated bunch through a second set of undulators (the "radiator") tuned to select and amplify the desired harmonic.

For the FEL-2 beamline to reach the shortest foreseen design wavelength of 10 nm, a second undulator stage must be added to a first stage similar to FEL-1, consisting of a modulator plus a dispersive section plus a radiator, tuned to and seeded by the first stage output radiation.

One should note that the nature of the mechanism, with an external laser driving the FEL process, is particularly suitable for pump/probe synchronization at time scales well below 1 picosecond.

FERMI's resulting main parameters, collected in Table 1.2.1, were defined based on theoretical studies and simulations. A cornerstone has been provided by "start-to-end" simulations, in which the electron beam is tracked from the photocathode, through the linac and all the way through the FEL process. Exhaustive studies have also been carried out to estimate the effect of foreseen random perturbations and jitters of the accelerator and of the FEL parameters.

Table 1.2.1: Nominal electron beam and FEL parameters.

Parameters	*Value at 40 nm*	*Value at 10 nm*	*Units*
Electron beam energy	1.2	1.2	GeV
Peak current	800	500	A
Emittance (slice)	1.5	1.5	μm, rms
Energy spread (slice)	150	150	keV
Bunch duration	700	1400	fs, FWHM
Repetition rate	10	10	Hz
FEL peak power	2.5	0.6	GW
FEL pulse duration	200	400	fs, FWHM
# of photons/pulse	10^{14}	10^{12}	
Bandwidth	17	4	meV
Brilliance	~10^{31}	~10^{31}	ph/s/mm^2/mrad^2/0.1%BW

Another novel paramount feature of FERMI is that both FEL-1 and FEL-2 are designed to provide, at all design wavelengths, beam polarization ranging from linear-horizontal to circular to linear-vertical, continuously tunable by changing the undulator gap at constant electron beam energy.

The FEL-1 radiator and the final radiator section in FEL-2 have therefore been chosen to be of the APPLE-II, pure permanent magnet type. For the modulator a mechanically simpler configuration can be used because the input radiation seed can be linearly polarized.

The radiators for both FEL-1 and FEL-2 consist of a sequence of 6 and 10 undulator magnets respectively. Electromagnetic quadrupoles, high quality beam position monitors and quadrupole movers are installed in between magnets to correct the electron trajectory. More details on the undulators can be found in Chapter 7.

In summary, with a peak brightness in the lower energy region of the XUV spectrum that can reach values 10 orders of magnitude greater than that of third generation sources, with full transverse coherence, close to transform limited bandwidth, pulse lengths of hundreds of femtoseconds, variable polarization and tunability, the FERMI source is a powerful tool for scientific exploration.

Its coherence properties are expected to open up new perspectives for single shot imaging, allowing to study the dynamics of chemical reactions and of other time dependent phenomena. The high peak power will allow studying non-linear multi-photon processes in a regime so far never explored and enable studying dilute samples of paramount importance in atmospheric, astrophysical and environmental physics as well as in the characterization of nano-size materials. The short pulse duration will open the door to visualizing ultra-fast nuclear and electronic dynamics.

1.3 References

[1] C.J. Bocchetta et al., "*Elettra Present and Future Upgrades*", Proc PAC 2005, Knoxville, USA, cern.ch/AccelConf/p05/PAPERS/RPAE085.PDF

[2] M. Svandrlik et al., *"Elettra New Full Energy Injector Status Report Status*", Proc. EPAC 2006, Edimburgh, UK, accelconf.web.cern.ch/AccelConf/e06/papers/thpls033.pdf

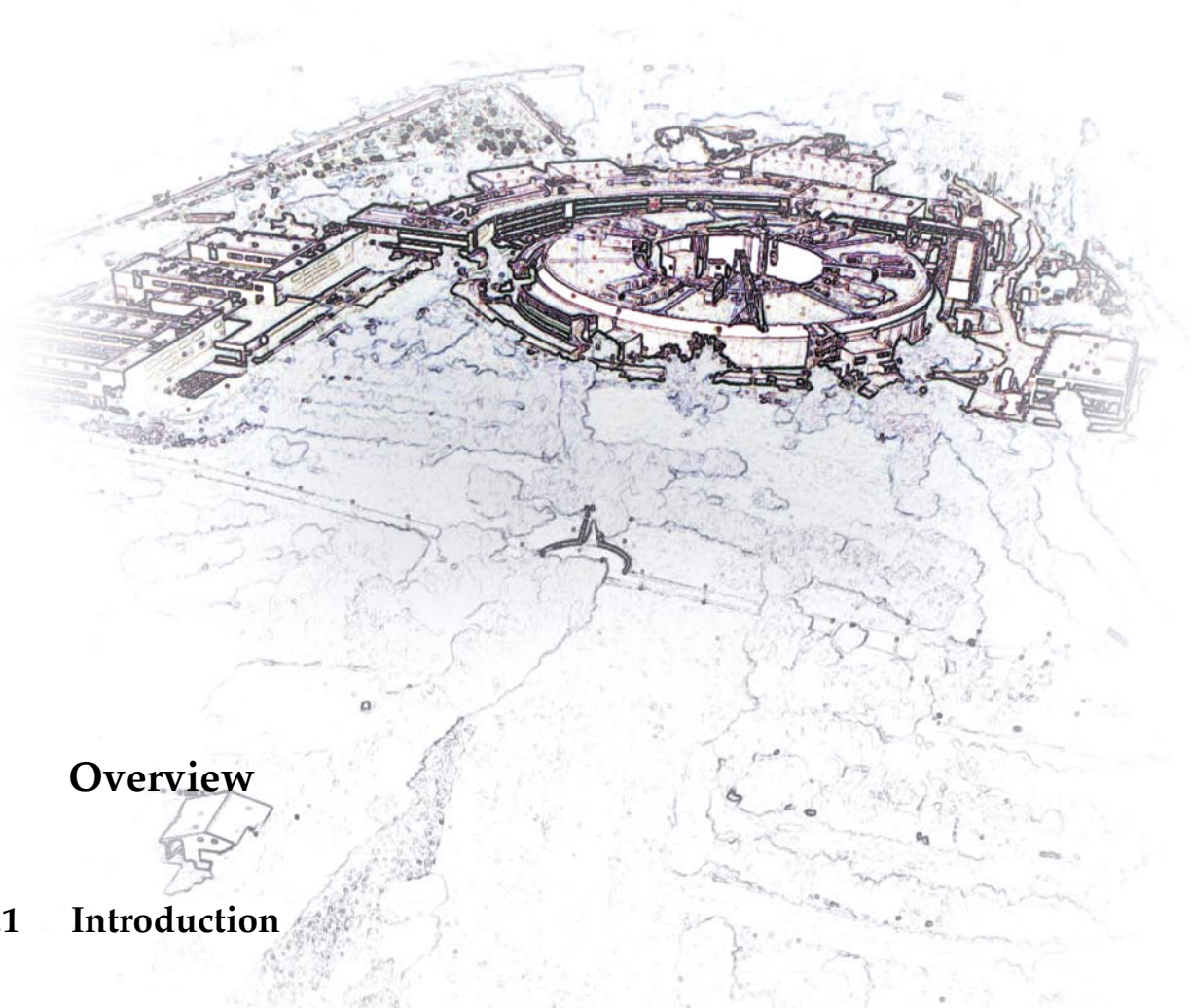

2 Overview

2.1 Introduction

The FERMI project at the ELETTRA Laboratory of Sincrotrone Trieste (ST) will be a national and international user facility for scientific investigations with high brilliance X-ray pulses of ultra-fast and ultra-high resolution processes in material science and physical biosciences. The underlying technology of the new facility is the Free-Electron-Laser (FEL) employing a master-oscillator-power-amplifier configuration with high gain harmonic cascades of wigglers. The full FERMI facility will consist of a linear accelerator plus two principal FEL beamlines in a new experimental hall in the complex environment of a multi-beamline user facility provided by the ELETTRA synchrotron light source.

The FERMI Project utilizes a 1.2 GeV linear accelerator, part of which is the current injector of the ELETTRA storage ring, and a new electron source based on photoinjector technology. In the near future, with the start of operation of the booster ring as the new ELETTRA injector, the existing linac will become available as part of a dedicated driver of the free-electron-laser. The addition of seven accelerating sections brings the linac energy to ~ 1.2 GeV. At this energy, and with state-of-the-art undulator technology, the free-electron-laser described in this report can operate in the 100-40 nm energy region in the initial phase (FEL-1) and down to 10 nm in a subsequent phase (FEL-2).

This chapter gives a broad overview of the facility and of the issues relevant to achieving the design objectives.

2.2 Principle of Operation

The FERMI project is based on the principle of high gain, harmonic generation FEL amplifier employing multiple undulators, up-shifting an initial "seed" signal in a single-pass [1,2,3]. The initial (master oscillator or seed) signal is provided by a conventional pulsed laser operating at wavelengths in the region 240-300 nm. The energy modulation induced by the interaction of the laser with the electron beam in the first undulator (the "modulator") is converted to spatial modulation by passing the beam through the magnetic field of a dispersive section. The bunching further increases the initial bunch modulation at harmonics of the seed wavelength. Thus re-bunched, the electrons emit coherent radiation in a second undulator (the "radiator") tuned at a higher harmonic corresponding to the desired FEL output. This scheme broadly describes the FEL-1 layout, down to 40 nm. To reach the shortest design wavelength of 10 nm, a second stage (modulator + dispersive section +radiator) is added to produce the FEL-2 configuration.

The choice of harmonic generation by an external seed laser is dictated by the scientific applications and the flexibility that such choice entails. As the seed laser determines the duration, bandwidth, and wavelength of the output radiation, all are tunable and controllable, covering a wide spectral range. The choice of design parameters, in fact, allows FERMI to generate FEL radiation with a wide range of characteristics tailored to match a diversity of experimental requirements, ranging from single shot, short (~100 fs), high brilliance, time-resolved experiments to ultra-fast pump-probe experiments, to high resolution (1 – 5 meV) experiments with close to transform-limited radiation on the *ps* time scale. The seed laser furthermore provides a reference signal throughout the FERMI facility (including the experimental beamlines) to facilitate the femtosecond level precision timing and synchronization of all systems.

Delivering such flexibility to serve a broad range of potential applications imposes severe requirements on the quality of the electron beam. To meet these requirements the FERMI FEL design is based on extensive studies of possible perturbations that may affect the electron beam dynamics, of means to correct them, and of parameter optimization. These studies show that the most important determinants of the quality of the FEL radiation are the quality and uniformity of the electron beam properties along the bunch (energy, energy spread, transverse emittance, electron optics, peak current, etc.), as well as the pulse-to-pulse stability of such properties.

2.3 Performance Characteristics

Table 2.3.1 lists some of the basic parameters of the electron beam and of the FEL radiation at 40 nm (FEL-1) and 10 nm (FEL-2).

Table 2.3.1: Nominal electron beam and FEL parameters.

Parameters	*Value at 40 nm*	*Value at 10 nm (fresh bunch)*	*Units*
Electron beam energy	1.2	1.2	GeV
Peak current	800	500	A
Emittance (slice)	1.5	1.5	μm, rms
Energy spread (slice)	150	150	keV
Bunch duration	700	1400	fs, FWHM
Repetition rate	10	10	Hz
FEL peak power	1 ÷ 5	0.5 ÷ 1	GW
FEL pulse duration	50 ÷ 100	100 ÷ 200	fs, FWHM
# of photons/pulse	10^{14}	10^{12}	
Bandwidth	~ 20	5	meV

2.4 Overall Layout

Figure 2.4.1 shows the layout of the facility. The accelerator and Free-Electron-Laser (FEL) complex comprise the following parts:

- A photoinjector and two short linac sections (SØA and SØB), generating a bright electron beam and accelerating it to ~ 100 MeV.
- The main linear accelerator, where the electron beam is time-compressed and accelerated to ~ 1.2 GeV.
- The electron beam transport system to the undulators.
- The undulators complex, in which the FEL radiation is generated.
- The photon beam transport lines from the undulator to the experimental area.
- The experimental area.

The new constructions include extending back the linac tunnel by ~ 80 m to make room for the photoinjector, new accelerating sections and the first bunch compressor. At its downstream end, the tunnel is extended by ~ 30 m to accommodate additional accelerating sections and the electron beam transfer line up to the Undulator Area. While only two lines (FEL-1 and 2) are envisaged initially, the transverse dimension of the Undulator Area allows installation of up to four undulators side-by-side. Finally, an experimental hall will house the FEL radiation beamline optics and the experimental hutches.

The following sections offer a brief overview of each major component. The reader is directed to the appropriate chapters for more detailed information and references.

2.5 The Photoinjector

The photoinjector is based on the proven 1.6 cell electron gun developed at BNL/SLAC/UCLA [4]. Given the similarities between the LCLS and FERMI photoinjector requirements, this design draws heavily on the LCLS concept to produce a 10 ps long pulse with 0.8-1 nC charge and a rms normalized transverse emittance of 1.2 mm-mrad at 100 MeV. The repetition rate is 10 Hz during the initial stage of operation, but the design allows for upgrading the photoinjector to 50 Hz. Following standard layout schemes, the design includes a solenoid for emittance compensation and acceleration to 100 MeV with two S-band rf sections. These sections, named SØA and SØB, are part of the present ELETTRA injection system.

A laser pulse provides temporal and spatial bunch shaping. The FERMI design calls for a novel temporal bunch profile in which the bunch current increases approximately linearly with time (linear ramp). Such profile at the start of acceleration produces a more uniform energy and current profile at the entrance to the undulators.

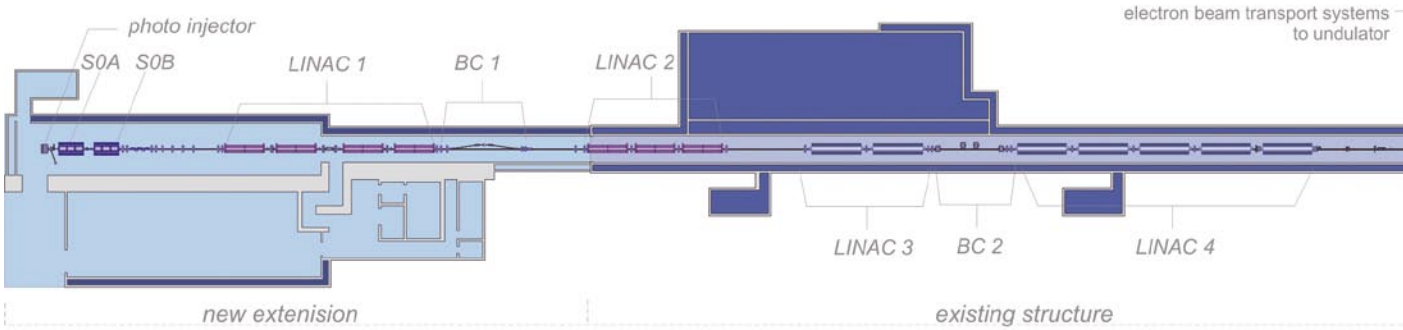

The Main Linear Accelarator

Simulations using the GPT and Astra codes indicate that the electron beam performance objectives for injection into the main linac at ~ 100 MeV are attainable. The timing and charge stability, – 0.5 ps and 1% respectively, are challenging but within present state of the art.

2.6 Acceleration, Compression and Transport to the Undulators

The function of the system is to accelerate the ~10 ps long electron bunch exiting the photoinjector to ~1.2 GeV and to compress the beam to its final duration and peak current. Two FEL layouts are envisaged in FERMI.

FEL-1 will cover the 100-40 nm energy wavelength range. Depending on the user experiments, an electron bunch length of 200 fs and a peak current of 800 A or higher can be provided ("short bunch"). For those experiments for which the timing jitter is critical, and to account for a predicted e-beam timing jitter of ~ 400 fs, the "medium bunch" design aims at a duration of 700 fs. Including the inevitable inefficiency of the compression system, the obtainable peak current is ~800 A with 0.8 nC of charge from the photoinjector.

FEL-2 covers the 40-10 nm wavelength range. This line will be developed to produce a narrow bandwidth (10 meV), close-to Fourier-transform limited radiation pulse.

Alternatively, ~200 fs long, high brightness FEL radiation pulses can be produced using the "fresh-bunch" technique. In both cases, a ~1.4 ps "long bunch" of electrons ~ is required from the electron accelerator. With a 1 nC bunch charge from the injector the attainable peak current is ~ 500 A.

In both the above cases, the energy and charge distributions correlated with the distance along the electron bunch should be as flat as possible in order not to broaden the FEL bandwidth. The design values of energy and peak current variations along the useable part of the bunch are specified to be less

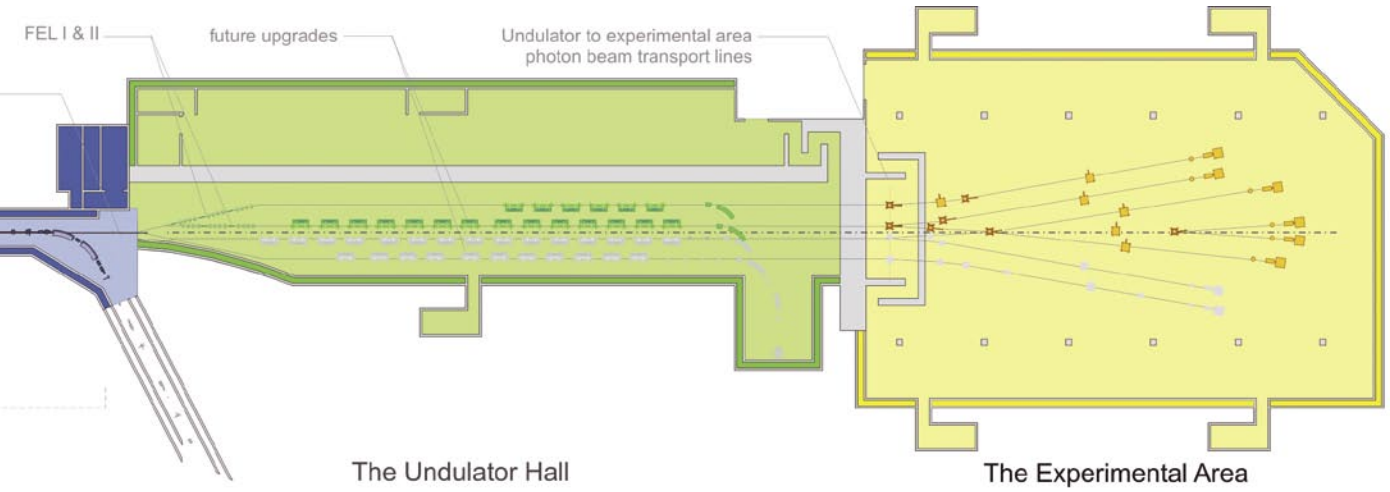

Figure 2.4.1: *Overall FERMI layout.*

than $2x10^{-4}$ and ~ 100 A respectively. The horizontal and vertical normalized emittances at the end of the linac (1.2 GeV) should not exceed 1.5 mm-mrad to meet the desired photon throughput. This value, ~ 30% higher than predicted by photoinjector simulations, includes a safety margin against emittance dilution effects. As an emittance of 1.5 mm-mrad is demanded at the shortest output wavelength, the accelerator performance is designed to satisfy this most stringent requirement. The specification could be relaxed during longer wavelength operation.

At the exit of the photoinjector, the ~ 100 MeV electrons enter the L1 linac (four C-type sections) where they are accelerated to ~ 250 MeV. Acceleration off-crest creates the correlated energy spread along the bunch needed to compress it in the first compressor, BC1. An X-band rf structure tuned at the 4th harmonic of the main (3 GHz) linac frequency is placed half-way between the four C-type sections of L1. The function of the structure is to provide the non-linear quadratic and, when operated off-crest, cubic corrections of the correlated momentum distribution along the bunch in presence of the photoinjector and the magnetic compressors non-linearities and of longitudinal wakefields.

The L2 and L3 linac structures, located between the first and second bunch compressors, accelerate the beam from ~ 250 MeV to ~ 650 MeV. They also provide the residual momentum chirp needed for the second compressor, BC2. After BC2 the beam is accelerated to its final ~1.2 GeV energy in the L4 structure. The rf phases of the linac sections following BC1 are chosen to provide the necessary momentum spread for compression and also to cancel the linear part of the longitudinal wakes. The non-linear correlated momentum spread at the end of the linac is fine-tuned by acting on the amplitude and phase of the x-band structure.

The linac focusing system is designed to minimize transverse emittance dilution due to transverse wakefields, momentum dispersion and coherent synchrotron radiation in bends.

Two transfer lines, one assigned to FEL-1 and the other to FEL-2, transport the electron beam from the linac end to the undulators. This system, called the “Spreader”, starts with two, three degree bending magnets that deflect the beam away from the linac. In the line that leads to the FEL-2 undulator, two more, three degree bend dipoles of opposite polarity bring the beam back parallel to the linac at a distance from it of 1 m. When operating the FEL-1 line, one of the afore-mentioned dipoles is switched off and the beam proceeds to a second pair of dipoles that again bend the beam parallel to the linac and displaced from it by 3 m. The two undulator lines are thus parallel and separated by 2 m. The electron optics is designed to cancel any emittance blow up due to the emission of coherent synchrotron radiation in the bends by a suitable choice of the (small) bending angles and of the phase advances between dipoles. The lattice of the spreader is flexible, and allows to switch from the configuration for photon delivery to a configuration less suitable for operation but optimized for electron beam diagnostics purposes.

2.7 The Undulators and the FEL Process

FEL-1 and FEL-2 are required to provide, at all wavelengths, continuously tunable beam polarization ranging from linear-horizontal to circular to linear-vertical. The FEL-1 radiator and the final radiator in FEL-2 have therefore been chosen to be of the APPLE-II [5], pure permanent magnets type. For the modulator a simple, linearly-polarized configuration is best, due to both its simplicity and because the input radiation seed can be linearly polarized. The wavelength will be tuned by changing the undulator gap at constant electron beam energy. The FEL-1 and FEL-2 radiators consist of 6 and 10 undulator magnets. The magnetic lengths of the individual magnets are 2.34 m (containing 36 periods) for the

FEL-1 and first FEL-2 radiators and 2.40 m (48 periods) for the second FEL-2 radiator, respectively. Electromagnetic quadrupoles, high quality beam position monitors, and quadrupole movers are installed in between magnets to correct the electron trajectory.

The accelerator and FEL parameters were defined based on theoretical studies and simulations. A cornerstone has been provided by "start-to-end" simulations, in which the electron beam is tracked from the photocathode, through the linac and all the way through the FEL process. The exhaustive studies carried out included foreseeable consequences random perturbations and jitters of accelerator and FEL parameters.

The consequences of orbit displacements from the ideal trajectory in the undulators were simulated. At the shortest design wavelength of 10 nm, the FEL process requires the straightness of the electron trajectory in the undulators to stay within 10 μm (rms value over the undulators length). While this requirement is beyond the state-of-the-art of present surveying techniques, realistic simulations show that a combination of the latter and of beam-based-alignment procedures [6] (tested at the Stanford Linear Collider and proposed for the LCLS) will achieve the desired performance.

2.8 The Photon Beam Transport and Experimental Areas

After leaving the undulators, the electron beam, carrying an average power of 75 W (at 50 Hz), will be dumped into a shielding block by a sequence of bending magnets, while the FEL radiation is transported to the experimental areas. Pulse length preservation, monochromatization, energy resolution, source shift compensation, focusing into the experimental chamber and beam splitting are all included in the design of the FEL radiation transport system. It is designed to handle the high power of up to 10 GW in a sub-ps long pulse. Its differentially pumped vacuum system is windowless, the low-Z material beam line components operate at grazing incidence angles, and the radiation intensity is controlled by a gas absorption cell.

2.9 Applications of FERMI

The FERMI FEL covers the lower energy region of the XUV spectrum. With a peak brightness of about 6 orders of magnitude greater than third generation sources, full transverse coherence, (close to) transform limited bandwidth, pulse lengths of the order of a picosecond or less, variable polarization and energy tunability, the FERMI source is a powerful tool for scientific exploration in a wide spectrum of disciplines. The coherence properties will open up new perspectives for single shot imaging, allowing to study the dynamics of chemical reactions and other phenomena. The high peak power will allow studying non-linear multi-photon processes in a regime never explored before. The short pulse duration will open the door to visualizing ultra-fast nuclear and electronic dynamics. The high peak power enables studying dilute samples that are of paramount importance in atmospheric, astrophysical and environmental physics as well as in the characterization of nano-size materials.

Applications of FERMI therefore extend from chemical reaction dynamics to biological systems, materials and surfaces, nano-structures and superconductors. The nature of HGHG, with an external laser driving the FEL process, is particularly suitable for pump/probe synchronization at time scales well below 1 picosecond.

2.10 Summary

This report describes the FERMI free-electron-laser, a source unique in its capability to produce intense, tunable coherent radiation of picosecond and sub-picosecond duration in the 100 to 10 *nm* wavelength region. The strength of the design concept relies on extensive studies on the optimization and control of the primary electron beam, as well as on well-tested theory and simulations of the FEL process.

The FERMI design uses the most up-to-date, normal conducting linac technologies developed primarily at SLAC and applied to the Linac Coherent Light Source, a free-electron-laser under construction there. The FERMI design also greatly profited from the advances in knowledge and technology made by the synchrotron radiation community, and in particular, from the experience gained at ELETTRA on the technology of insertion devices, on radiation transport and on the experimental utilization of XUV and soft X-ray radiation.

2.11 References

[1] R. Coisson and F. De Martini, Quantum Electronics **9** (1982) 939.

[2] R. Bonifacio et al., Nucl. Instrum. and Meth. A **296** (1990) 787.

[3] L.H. Yu, Phys. Rev. A **44** (1991) 5178.

[4] D. Palmer, "The next generation photoinjector", Stanford University dissertation, 1998.

[5] S. Sasaki, Nucl. Inst. And Meth. A **347** (1994) 83.

[6] P. Emma et al., Nucl. Inst. And Meth. A **429** (1999) 407.

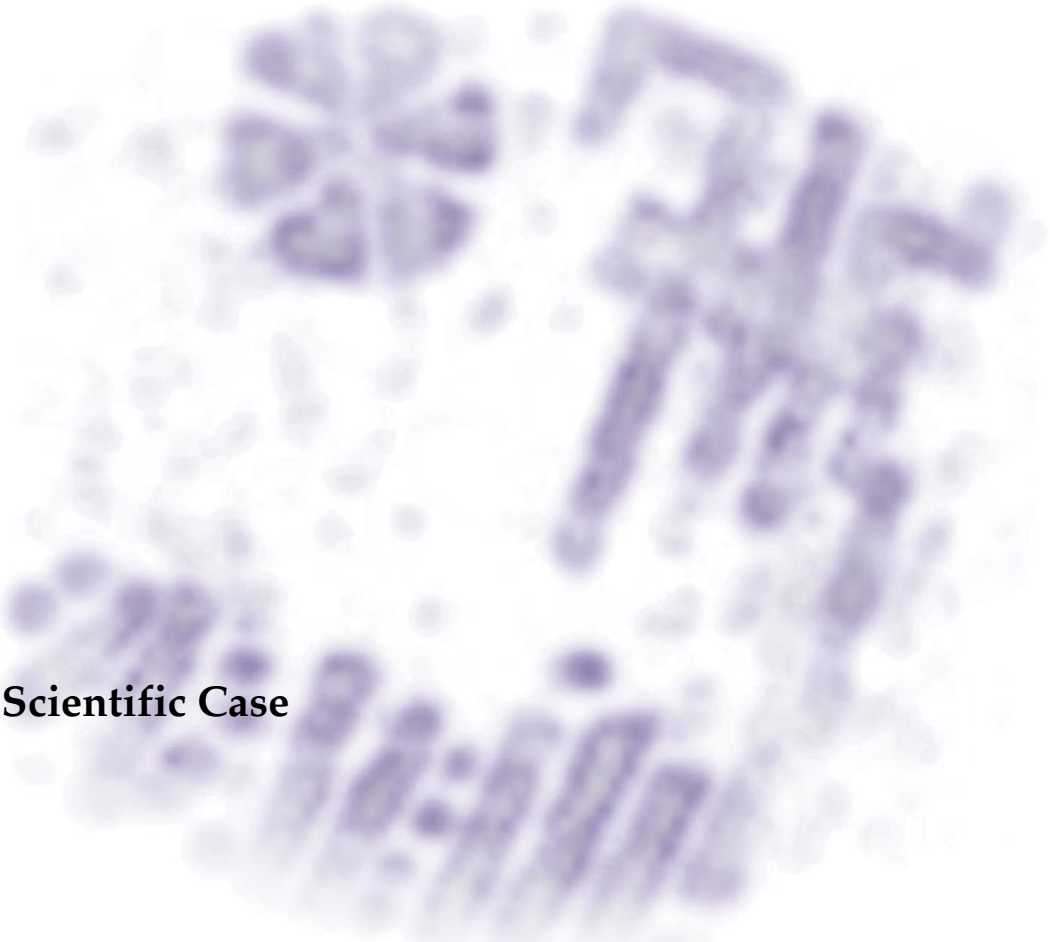

3 The Scientific Case

Synopsis

The FERMI FEL source at ELETTRA is designed to supply photons in a spectral range from 100 to 10 nm, covering the region from the VUV to the lower energy soft X-ray regime. FERMI will be much brighter than the existing third generation synchrotron sources with a temporal structure that meets the essential requirements of structural studies with ultra-short, variable polarization pulses of radiation.

FERMI will be realized in two phases: FEL-1, covering the 100 to 40 nm wavelength range, is designed to operate in the time domain in two complementary operating modes: a) high stability and b) high intensity. FEL-2, covering the 40 to 10 nm wavelength range, is designed to operate in the frequency domain (high energy resolution) and with relatively long photon pulses. The FERMI science program is structured to allow users to perform high quality experiments already under the specified FEL-1 initial operation parameters and to proceed to ever more demanding experiments and beam requirements as the source performance is improved.

The coherence properties of FERMI beams allow taking single shot images of complex molecules and performing nano-structures imaging. Samples can be probed in time resolved single shot experiments, of great significance to life sciences as well as to environmental, materials and chemical sciences.

The high peak power can trigger non-linear, multi-photon processes never explored before, unperturbed by any pondermotive effects.

The FERMI average beam power, comparable or slightly higher than that of the best synchrotron light sources, will enable first investigations of dilute samples crucial to the understanding of atmospheric, astrophysical and environmental physics as well as to the characterization of nano-sized materials.

The FERMI short pulse duration properties allow studying ultra-fast dynamic processes such as electronic relaxation, bond formation and breaking reactions or conformational molecular changes.

Teams of world-class scientists, leaders in their respective fields, have proposed a first series of experiments exploiting each of these features that are unique to free-electron-lasers, outlined below.

The extremely high brightness and short pulse duration provided by FERMI will open up a new regime of X-ray microscopy. With present synchrotron-based X-ray microscopes, radiation damage due to chemical changes, diffusion, and local heating, over timescales greater than microseconds, limits the resolution achievable in studying living systems to ~20 nm. This limitation can be circumvented by using intense pulses of duration shorter than that of any process that causes structural changes over time scales longer than the resolution of interest, such as delivered by FERMI. Indeed, flash imaging can be extended at FERMI to atomic resolution, for imaging of single molecules.

The high flux of the FERMI FEL will improve the lateral resolution and increase the data acquisition rate of the full-field X-ray microscope (FFXM). For instance, X-ray fluorescence microscopy may be extended to microscales by exciting high-lying electron levels In such experiments the typically low cross sections will be compensated by the several orders-of-magnitude higher flux available at FERMI. In conjunction with the FFXM, the coherence of the FERMI output radiation also allows using lensless imaging techniques such as phase contrast imaging, micro-tomography and holography.

Small particles, such as nanocrystals and clusters, are different from bulk matter; finite size effects influence effectively all properties of matter. The finite number of constituents and the discrete nature of of phonon, electron, or other quasi-particle densities of states alter the constituent interactions and lead to different geometric and electronic ground state configurations and different dynamical behavior. The results are strong changes in optical, magnetic, chemical and thermodynamic properties. The FERMI spectral range of 100 to 10 nm is one in which plasma absorption processes break down and new physical processes involving core levels become important. Clusters, as a form of matter intermediate between atoms and bulk solids, are ideal samples to study these processes. By varying their size, one can investigate the role of inner- and interatomic, i.e., collective, effects, thus contributing to our understanding of energy deposition, energy transfer, and radiation damage in matter.

3.1 Introduction

Chemical, physical and biological processes are intrinsically dynamic in nature since they are related to electronic and atomic structures that evolve with time. The characteristic time scales span from a few femtoseconds, in the case of electronic processes, to a few tens or hundreds of femtoseconds, in the case of atomic and molecular processes. Furthermore, other phenomena controlling the behavior of critical systems may occur over relatively longer time scales, ranging from a few picoseconds to a few hundreds of picoseconds or more. These phenomena include phase transitions, such as those related to magnetic ordering or to superconductivity. The capability of measuring such processes at the relevant time scales will open totally new perspectives in the way they can be studied. In particular, direct observation of electronic processes, of structural dynamics and of dynamic critical phenomena such as phase transitions, opens up an unexplored landscape in the study of condensed matter physics.

Such perspectives were already evident to the developers of the first coherent sources of femtosecond optical pulses. The availability of ultra-short coherent light pulses has in fact produced remarkable scientific results, recognized by the award of the 1999 the Nobel Prize for Chemistry to Ahmed Zewail for his pioneering work on the application of ultra-short laser infrared spectroscopy to the study of the dynamics of chemical bonds.

Currently available, coherent light sources cover only a limited wavelength range, so that their use is confined to optical and spectroscopic techniques in the infrared, visible and near-ultraviolet range, excluding all measurements needing photons of energy higher that a few eV. There is therefore a strong scientific need for a tunable light source covering the energy range from vacuum ultraviolet (VUV) to X-rays, with a stable and well-characterized temporal structure in the picosecond to femtosecond time domain. To develop such a source international research is moving in three main directions:

1) laser driven light sources using non-linear processes to create very high harmonics,

2) laser "bunch-slicing" techniques based on the interaction between an ultra-short laser pulse and an electron bunch in a storage ring and

3) free-electron-lasers (FEL).

The first two techniques can produce radiation pulses in the femtosecond time domain and in the soft X-ray region, but with low brilliance (i.e. a low useful photon flux on sample). In contrast FELs can produce light pulses with a peak brilliance as much as ten orders of magnitude higher than generated in present third generation synchrotron light sources but with photon energies reaching from the VUV to the hard X-ray region, i.e. from ~10 eV (120 nm) to ~10 keV (0.12 nm) and above.

FEL amplifiers can operate in several different regimes. The most studied ones are SASE (Self Amplification of Spontaneous Emission) and amplification of a coherent input signal generated by a traditional laser harmonic (Seeding). SASE operation can produce very high brilliance but with a pulse temporal structure which is the envelope of a series of micro-pulses with completely random intensity and duration. In contrast, FEL sources based on seeding, while also producing very high brilliance, can deliver coherent radiation pulses with a tailored time profile and intensity. In seeded systems utilizing helical field undulators, one can also fast-tune the polarization of the radiation from linear to circular. For performing reproducible measurements under controlled conditions, seeded FELs therefore represent a superior choice. SASE sources are most useful when the information that one wants to collect does not depend on the pulse temporal structure. They are even indispensable when the wavelength is beyond the range thought practical with seeded systems, due to the lack of suitable laser seeds.

The prospects for the blossoming of a new field of close to fully coherent, ultra-fast X-ray science in physics, chemistry and biology are indeed exciting.

One should nonetheless say that such performances are likely to concern a small minority of the experiments that rely on synchrotron radiation sources. Storage rings are likely to remain the workhorses of synchrotron radiation science for many years to come. By providing X-ray beams with high flux and brightness and outstanding stability, reproducibility and reliability, they will continue to serve the needs of a vast scientific community even as linac-based sources open up new scientific frontiers with their sub-picosecond pulse duration and extremely high peak brightness and coherence.

3.1.1 Required and Delivered Performance of Ultra-intense and Ultra-short Duration Radiation Sources

A common measure of the performance of synchrotron radiation sources are graphs of the time-averaged flux (photons/s/mrad/0.1%BW) and brightness (photons/mm^2/mrad^2/0.1%BW) available for experiments as functions of X-ray energy.

More recently other metrics have been proposed such as the flux density on a small sample. Another metric is the useful flux within the phase space acceptance of a small sample such as a 50-100 micron protein crystal with a mosaicity of several milliradians [1]. With increasing scientific interest in short pulses, the peak (or instantaneous) values of these metrics during the pulse have become important figures-of-merit to complement the generally used spectral curves of flux and brightness.

As far as user requirements are concerned, a contrasting, non-exhaustive list of desired beam properties is:

- as many as 10^{12} X-ray photons in a single ultra-fast pulse;
- pulse intensities not exceeding 10^8 photons with pulses spaced by the relaxation time of the process under investigation;
- auxiliary laser pulses synchronized to within ~20 fs of the X-ray pulse;
- asynchronous operation possible;
- high (~1%) of pulse-to-pulse reproducibility and stability;
- tunable polarization of the radiation;
- multi-colour X-rays on sample.

The performance data of several types of X-ray sources from the point of view of peak brightness and pulse duration are compared in Figure 3.1.1 [2] and Table 3.1.1.

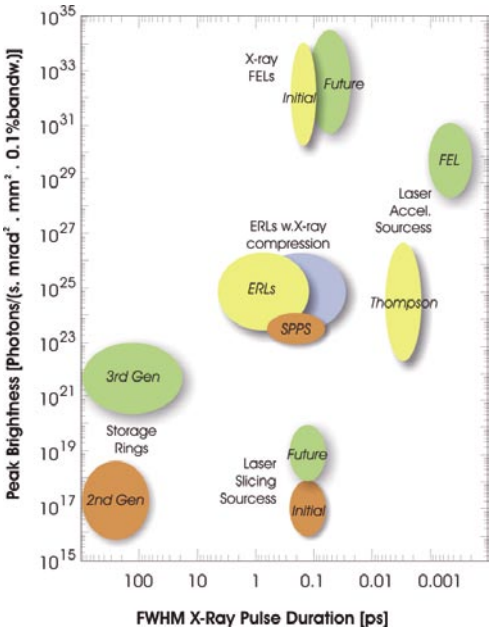

Figure 3.1.1:
Peak brightness and pulse duration ranges of next generation light sources. The time average brightness is the peak brightness times the duty factor [2].

Table 3.1.1: Additional characteristics of X-ray sources.

	Maximum Duty Factor	*Laser synchronization*	*Pulse repetition rate*
Storage rings	~10^{-3}	No	10 – 100 MHz
Slicing Sources	~10^{-9}	Limited	1 – 10 kHz
ERLs	~10^{-3}	No	10 – 100 MHz
ERLs w. X-ray pulse compression	~10^{-8}	Yes	10 kHz
SPPS beamline at SLAC	~10^{-11}	No	100 Hz
Warm linac driven X-ray FELs	~10^{-10}	Some	100 – 1000 Hz
Laser Accel. Sources	~10^{-12}	Yes	1 – 10 kHz

3.1.2 Short Review of the Scientific Motivations for Major FEL Projects

Four classes of information, depending on the photon energy, can be extracted from the study of the interaction of radiation with matter.

Electronic processes in the valence band and collective mode excitations in elastic and inelastic scattering processes can be studied using photons with energy between the UV and far VUV regions (wavelength between 200 nm and 40 nm)

Photons in the extremely soft X-ray range (λ~10 nm) allow to taking advantage of the specificity of shallow core levels of chemical elements to obtain phase contrast images, also by microscopy.

Photons with wavelength around 1 nm, comparable to the typical inter-atomic distances, are mainly used in materials science, in particular to study deeper core levels, such as the L2,3 edges of transition metals, and thus of many magnetic systems, superconductors and highly correlated electronic systems. They also allow the study of the K-edges of oxygen and carbon, which are the main constituents of organic and biological materials and are used in technological applications such as nano-fabrication.

From the above one can conclude that radiation sources with wavelength in the UV (200 nm) to soft X-ray (1 nm) range have great relevance for the very large and important fields concerning the study of chemical, physical and material properties suitable for technological applications.

If one adds to the high brilliance, typical of FEL radiation, polarization and control of the beam temporal structure, one sees that it becomes possible to study the mechanisms of structural dynamics of a wide range of materials and material states, covering both hard and soft matter.

To study ultra-fast dynamics (from picoseconds to femtoseconds) in matter, one can use the “pump-probe” (or stroboscopic) technique, based on exciting a sample with a suitable wavelength (pump) followed by probing the excited sample with a radiation pulse, in general of a different wavelength,

whose duration is shorter than the characteristic time of the process under observation. The delay time between the pulses is optically controlled so that the short pulse works as a probe of the temporal evolution is of the process under observation. The two wavelengths can be delivered by the same source or from two (appropriately correlated) different sources.

3.1.3 The FERMI@Elettra Project

The FERMI FEL will be built in two phases called FEL-1 and FEL-2.

FEL-1, covering the 100 to 40 nm wavelength range, is designed to operate in the time domain and in two complementary modes of operation: a) high stability mode and b) a high intensity mode.

FEL-2, covering the 40 to 10 nm wavelength range, is designed to operate in the frequency domain (high energy resolution) and with relatively long photon pulses (~ 1 ps).

These design choices will yield a source quite unique among the other FELs under construction or proposed for construction in Europe, USA and Japan.

3.1.4 FERMI@Elettra Photon Parameters

The initial FERMI science program is structured to allow performing experiments with different, and increasingly more demanding photon parameters.

Consequently, in order for high quality experiments to be performable from the very beginning of FEL-1 and FEL-2 operation, classes of experiments are expected to start taking data in the following order:

- Single shot, High Peak Brilliance Experiments;
- Pump-Probe Experiments in both the time and the frequency domains;
- High Energy Resolution Experiments in the frequency, time and non-linear spectroscopy domains.

The idea is illustrated in the following block diagram.

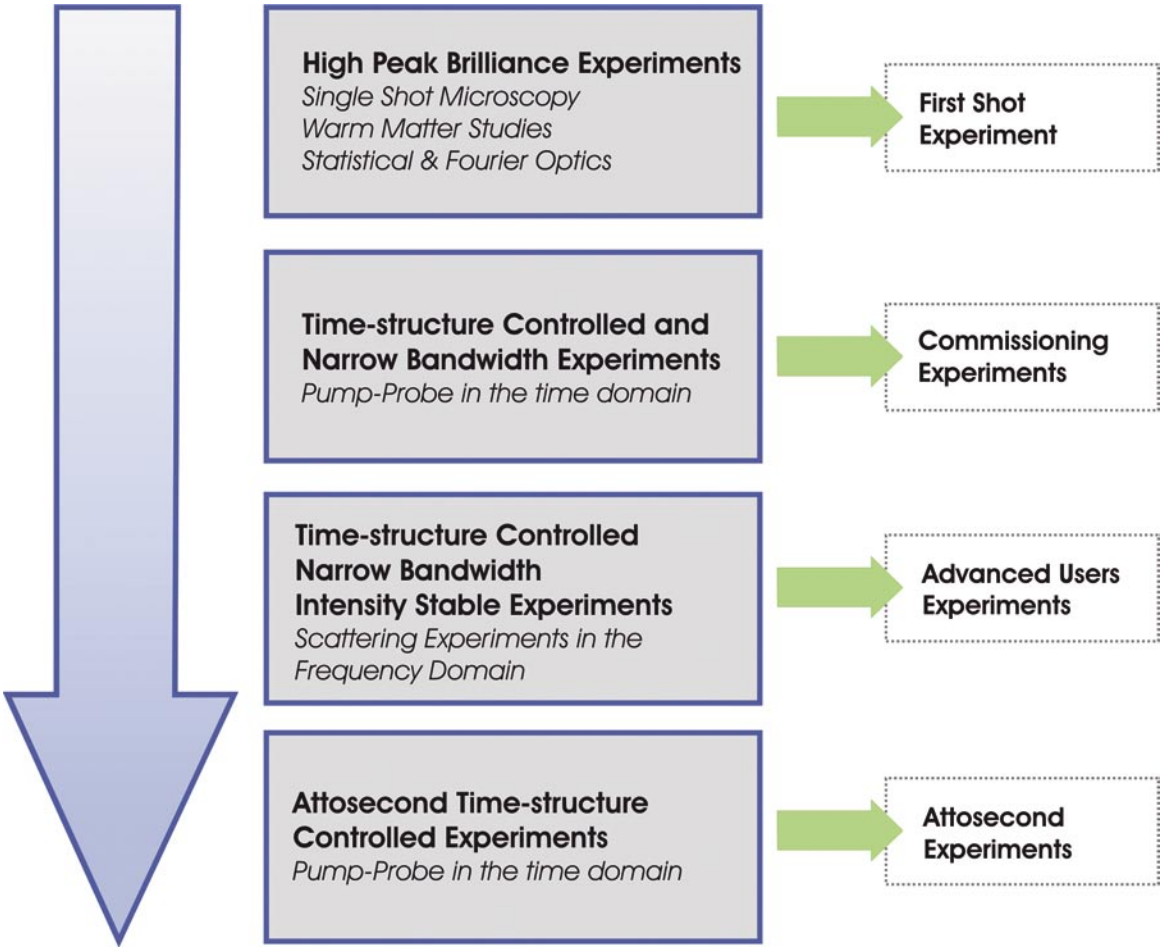

Figure 3.1.2:
Accessible experiments by increasing the FEL performances.

Three different stages of FEL operation have been defined on the basis of beam quality, described by the delivered set of beam parameters: the first, characterised by the "acceptance parameters", defines the end of commissioning, the second is characterised by a "standard parameters" set and the third by having the "advanced parameters" set. The parameter sets for each regime, defining the feasibility of the experiments and therefore driving the technical design of FEL-1 and FEL-2, are listed in Tables 3.1.2 through 3.1.7.

Table 3.1.2: Starting parameters for FEL-1.

Parameter	*Value*	*Comments*
Photon energy range	100 ÷ 40 nm	
Pulse length	50 ÷ 100 fs	
Bandwidth		Incoherent light
Polarization		Not Required
Repetiton rate	10 (50) Hz	Single shot experiments
Peak power (*)	> 2.5 GW	Full Power Requested
Harmonic peak power	Not requested	
Photons per pulse (*)	$> 10^{14}$	
Peak brightness (*)	$> 10^{31}$	Ph/s/mm^2/mrad^2/0.1%bw
Pulse-to-pulse stability		
Pointing stability	< 20 μrad	
Spot size (intensity)	280 μm	
Divergence (intensity)	50 (at 31 eV) μrad	
Beam Properties	Gaussian	
Time jitter	150 fs	

(*) 200 fs pulse length.

Table 3.1.3: Starting parameters for FEL-2.

Parameter	*Value*	*Comments*
Photon energy range	40 ÷ 10 nm	
Pulse length	100 ÷ 200 fs	
Bandwidth		Incoherent light
Polarization		Not Required
Repetiton rate	10 (50) Hz	Single shot experiments
Peak power	1 GW	Full Power Requested
Harmonic peak power	Not requested	
Photons per pulse	$> 10^{13}$	
Peak brightness	$> 10^{31}$	Ph/s/mm^2/mrad^2/0.1%bw
Pulse-to-pulse stability		
Pointing stability	< 20 μrad	
Spot size (intensity)	200 μm	
Divergence (intensity)	15 μrad	
Beam Properties	Gaussian	
Time jitter	150 fs	

Table 3.1.4: Standard parameters FEL-1.

Parameter	*Value*	*Comments*
Photon energy range	100 ÷ 40 nm	
Pulse length	50 ÷ 100 fs	Any value in between is acceptable
Bandwidth	20 meV	Close to TL
Polarization	Linear / Circular	Variable
Repetiton rate	10 (50) Hz	
Peak power	1 ÷ 5 GW	
Harmonic peak power	Few %	
Photons per pulse	$> 10^{14}$	
Peak brightness	$> 10^{31}$ Ph/s/mm^2/mrad^2/0.1%bw	
Pulse-to-pulse stability	20-30%	rms
Pointing stability	< 20 μrad	
Spot size (intensity)	280 μm	
Divergence (intensity)	50 μrad	
Transverse Stability	About 10% spot dimension	
Wavelength Stability	$5\ 10^{-4}$	
Beam Properties	Gaussian	
Waist location variation	2 m	
Tuneability	10 ÷ 20%	Around given photon energy
Time jitter	150 fs	

Table 3.1.5: Standard parameters FEL-2.

Parameter	*Value*	*Comments*
Photon energy range	40 ÷ 10 nm	
Pulse length	100 ÷ 200 fs	Any value in between is acceptable
Bandwidth	5 meV	Closed to TL
Polarization	Linear / Circular	Variable
Repetiton rate	10 (50) Hz	
Peak power	0.5 ÷ 1 GW	
Harmonic peak power	Few %	
Photons per pulse	$> 10^{12}$ in 1 meV BW	
Peak brightness	$> 10^{31}$ Ph/s/mm^2/mrad^2/0.1%bw	
Pulse-to-pulse stability	About 50 %	rms
Pointing stability	< 20 μrad	
Spot size (intensity)	About 200 μm	
Divergence (intensity)	15 μrad	Not restrictive
Transverse Stability	About 10% spot dimension	
Wavelength Stability	10^{-5}	rms
Beam Properties	Gaussian	
Tuneability	10-20%	Around given photon energy
Time jitter	150 fs	

Table 3.1.6: Advanced Parameters FEL-1.

Parameter	*Value*	*Comments*
Photon energy range	100 ÷ 40 nm	
Pulse length	50 ÷ 100 fs	Any value in between is acceptable
Bandwidth	About 20 meV (FWHM)	Close to TL
Polarization	Linear / Circular	Variable
Repetiton rate	50 Hz	
Peak power	1 ÷ 5 GW	
Harmonic peak power	Few %	
Photons per pulse	$> 10^{13}$	
Peak brightness	$> 10^{31}$ Ph/s/mm^2/mrad^2/0.1%bw	
Pulse-to-pulse stability	5 %	rms
Pointing stability	< 20 μrad	
Spot size (intensity)	280 μm	
Divergence (intensity)	50 μrad	
Transverse Stability	About 10% spot dimension	
Wavelength Stability	$5\ 10^{-4}$	rms
Beam Properties	Gaussian	
Waist location variation	2 m	
Tuneability	10 ÷ 20%	Around given photon energy
Time jitter	150 fs	

Table 3.1.7: Advanced Parameters FEL-2.

Parameter	*Value*	*Comments*
Photon energy range	40 ÷ 10 nm	
Pulse length	100 ÷ 1000 fs	Any value in between is acceptable
Bandwidth	> 5 meV	Closed to TL
Polarization	Linear / Circular	Variable
Repetiton rate	50 Hz	
Peak power	0.3 - 1 GW	
Harmonic peak power	Few %	
Photons per pulse	$> 10^{13}$ in 1 meV BW	
Peak brightness	$> 10^{31}$ Ph/s/mm^2/mrad^2/0.1%bw	
Pulse-to-pulse stability	About 20 %	rms
Pointing stability	< 20 μrad	
Spot size (intensity)	About 200 μm	
Divergence (intensity)	15 μrad	Not restrictive
Transverse Stability	About 10% spot dimension	
Wavelength Stability	10^{-5}	rms
Beam Properties	Gaussian	
Tuneability	10 ÷ 20%	Around given photon energy
Time jitter	150 fs	

3.1.5 Scope of the Science with FERMI@Elettra

The FERMI FEL source will cover the range wavelength range from VUV to the lower energy portion of the soft X-ray region. Therefore, in order to provide new scientific opportunities, it must be much brighter than the existing third generation synchrotron sources and have the temporal structure needed for studies requiring ultra-short pulses with variable polarization. In addition, experimentalist will have a further variety of operational options provided by the possibility of bringing into the FEL experimental hall, photon beams extracted from the adjacent ELETTRA synchrotron radiation source.

The available range of scientific applications covers several fields of hard and soft matter science:

- chemical reaction dynamics;
- study of the electronic structure of atoms, molecules and clusters;
- biological systems;
- inhomogeneous materials on a microscopic scale;
- geophysics and study of extra-terrestrial materials;
- material properties under extreme conditions (pressure, temperature, etc.);
- surfaces and interfaces;
- nano-structures and semiconductors;
- polymers and organic materials;
- magnetism and magnetic materials;
- superconductors and highly correlated electronic materials.

3.2 Science Case

3.2.1 Exploiting the Main Photon Parameters

The laser-like properties of the FERMI FEL output radiation, coherence, high peak and average power and ultra-short pulse, will unlock the gates to new scientific frontiers, allowing one to perform new classes of experiments, not feasible using incoherent synchrotron radiation sources.

Coherence will open up a new era for imaging, where samples can be probed in time resolved single shot experiments. Coherent imaging has great potential in life sciences as well as in environmental, materials and chemical sciences.

High peak power at soft X-ray photon energies triggers non-linear, multi-photon processes in a regime never explored before, unperturbed by any pondermotive effects, which scale with the square of the inverse frequency and thus complicate tremendously the understanding of such reactions when using optical lasers.

High average power, comparable or slightly higher than that of present synchrotron sources, in pulses far shorter than available from synchrotrons, enables studying for the first time dilute samples of paramount importance in atmospheric, astrophysical, environmental physics as well as in the characterization of nano-size materials. Moreover, it allows access to fundamental reactions governed by small cross sections.

Ultra-short time properties will open the door to visualize ultra-fast nuclear and electronic dynamics such as in electronic relaxation, bond formation and breaking reactions or in conformational molecular changes.

The interest in the science described above is confirmed by the first and second call for proposals, for the initial round of experiments at FERMI, having been responded to by world-class teams of scientists – leaders in their respective fields of study. The letters of intent from these teams are presented in the accompanying appendix.

In the following sections the scientific goals to be pursued in this first round of experiments is briefly described.

3.2.2 Ultra-fast Coherent Imaging and Nano-spectroscopies

The extremely high brightness and short pulse duration of VUV- and X-FELs allow one to explore a new regime of X-ray microscopy. With current synchrotron-based X-ray microscopes, the optics for which have steadily been improving, the highest resolution achieved on living systems has reached a limit of ~20 nm, imposed by radiation damage. The damage is caused mainly by chemical changes, diffusion, and local heating over timescales greater than microseconds [3,4]. This resolution barrier can be overcome by using intense pulses of duration shorter than that of any process causing structural damage. [5]. Indeed, the concept of flash imaging can be extended to achieve atomic size resolution [6] for the imaging of single molecules.

The experimental method of choice to perform imaging with resolution of ~20 nm to <0.2 nm, is single-particle diffraction [7,8]. While, for given resolution, other methods require less dose (and hence induce less damage) [9], diffractive imaging does not require any optics and hence does not impose any technological limit to the resolution.

At FERMI, the long-term research program in ultra-fast, time-resolved, coherent diffraction imaging has three main aims:

a) determine the ultimate limits of imaging with FEL radiation,
b) study the interactions of matter with X-ray pulses,
c) develop a program of high-resolution, biological imaging.

Extending diffraction imaging to the ultimate goal of atomic resolution with future X-ray FELs will require much learning and the development of new experimental techniques. This extension demands an ultra-fast, bright, coherent source leading to new science in its own right, capable of high-resolution single-shot imaging beyond the radiation damage limit, time-resolved high-resolution imaging of the interaction of FEL pulses with matter, and high-resolution time-resolved soft-X-ray imaging of the interaction of particles with optical laser pulses, for example, to study alignment of particles with high-field lasers.

To achieve these goals the FERMI science program has approved the proposal of a team that will bring to Sincrotrone Trieste new technologies it has been developing over the last several years, including:

(i) high-efficiency multilayer, submicron focusing optics,
(ii) a unique diffraction camera based on a multilayer mirror filter,
(iii) beam-splitting and pump-probe imaging methods,
(iv) injection techniques to guide particles, under vacuum, into the FEL beam,
(v) robust image reconstruction methods, and
(vi) diagnostics and alignment aids.

The multilayer systems were developed for high-power operation and are extremely stable at temperatures as high as 500 °C. They have been tested under high peak power conditions at the FLASH soft-X-ray FEL. The team is tooled-up to fabricate multilayer optics operating at near-theoretical efficiency with atomic spacing dimensional control across large areas. The group novel diffraction camera uses one such multilayer mirror with a change in d spacing by a factor of two over a transverse distance of 25 mm. The multilayer optics operates at normal incidence for wavelengths from 3 nm to 32 nm.

The team will carry out high-resolution, two-dimensional imaging of biological materials beyond the radiation damage limit by flash imaging in a single shot, which is expected to produce the highest achieved resolution images of cells and sub-cellular structures in an unmodified state. Another major field of investigation will be the study of the interaction of FEL pulses with atomic clusters and particles, for the validation of molecular dynamics and hydrodynamics models [6,10,11,12,13].

The team is also developing particle injection systems based on electrospray to be integrated into the FERMI end-station. Such systems will deliver particles from solution or atomic clusters of noble gases into the interaction region of the focused FEL beam, allowing to study the interaction of clusters and particles with the radiation pulse, to explore the dynamics of Coulomb explosions and the resolution limits that can ultimately be achieved. Three-dimensional imaging of reproducible samples injected into the beam will exploit algorithms specially developed to produce imaging of molecules with atomic size resolution.

3.2.3 Full Field X-ray Microscopy and Lensless Imaging

The Full-field X-ray Microscope (FFXM) will benefit from the high flux of the FERMI FEL, allowing a gain in achieving higher lateral resolution, as well as a faster acquisition rate. A challenging possibility for x-ray fluorescence microscopy can be explored, at micro-scales, exciting the high-lying electron levels. The typically low cross sections will be compensated by the several orders-of-magnitude higher FERMI flux.

In conjunction with the FFXM, the coherence of FEL radiation is fundamental to lensless imaging techniques such as phase contrast imaging, micro-tomography and holography. Recent coherent light scattering experiments have shown that phase information can be retrieved by iterative algorithms applied to an over-sampled diffraction pattern [14,15], or through a mask-based, holographically formed interference pattern [16]. In addition, extension of oversampling methods to three-dimensional imaging has been experimentally demonstrated on micron-sized, nanostructured, Ni arrays at a resolution of 50 nm (see Figure 3.2.1).

Since lensless imaging does not require focusing systems, affected by inherent technological constraints that limit the resolution, the coherence and intensity of the FERMI FEL open up unprecedented

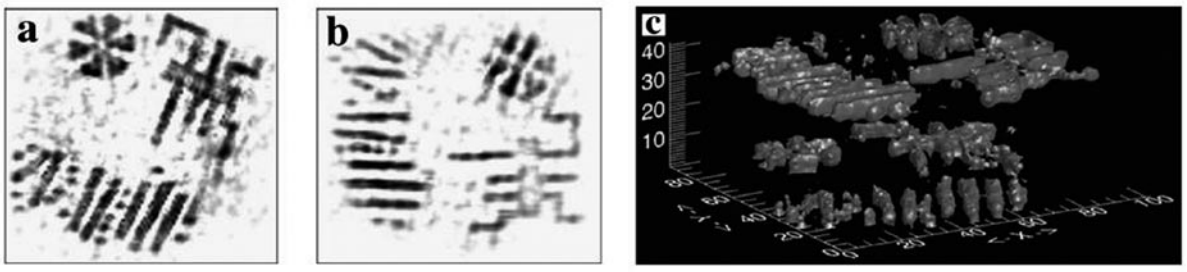

Figure 3.2.1:
The reconstruction of a 3D nanostructured material at 50 nm resolution. (a), (b) The reconstructed top and bottom layered pattern. (c) The reconstructed 3D structure displayed in iso-surface rendering [17].

opportunities. First pilot experiments using a 32 nm beam at DESY have demonstrated a lateral resolution of 60 nm. For FEL-2 at FERMI, imaging samples at the diffraction limit of 10 nm can be envisaged.

A team led by Sincrotrone Trieste researchers is proposing to design and implement on one of the two FEL beamlines a "beam-tailoring" optical approach to lensless microscopy to explore new regimes of FFXM and lensless imaging. The planned research includes implementation of non-conventional optics, along with the development of next generation detectors tailored to the demands of 'one-shot' microscopy.

The beam tailoring requirement for this line of research is simply demagnification of the beam spot delivered by the source to the FFXM. Technical challenges for the experimenter are

a) source displacement as a function of beam energy,
b) shot-to-shot, longitudinal bunch position jitter compatible with spot sizes of <10 μm,
c) preservation of the spatial coherence of the FEL beam.

The experimental station can easily accomodate the optical elements for FFXM and the same detector can be used also for lensless imaging. The main experiment components are: (i) transport system for samples, sample holder and precise manipulation stage, (ii) stage for the optical elements, (iii) fast detector to monitor the diffraction pattern and (iv) long working distance optical microscope for pre-alignment of the sample with the FEL beam, placed behind the focusing optics to ensure optimal illumination of thin samples (e.g., cell-type structures). The detector must have a central hole or be otherwise shielded from the direct FEL beam. The sample stage is particularly critical, because it must allow reproducible feeding of identical samples after each shot.

The source characteristics required for the microscopy branch of the FEL microscopy beamline, including the FFXM, are as follows:

Parameters considered for the first harmonic:

Bunch length 200 fs

Energy bandwidth ≈ 3 meV

Peak Power 0.4 GW (2 10^{13} ph/s) down to 40 nm (10-30 eV) FEL-1 (80 mJ)

Peak Power 0.15 GW (2 10^{12} ph/s) up to 10 nm (30-120 eV) FEL-2 (30 mJ)

Source geometry

FEL-1:

Source waist 280 μm (FWHM≈160 μm)

Divergence* (σ): 140μrad @ 10 eV; 70μrad @20 eV; 50μrad @30 eV

FEL-2:

Source waist 210 μm (FWHM≈120 μm)

Divergence* (σ): 65μrad @ 30 eV; 33μrad @ 60 eV; 22μrad @ 90 eV; 15μrad @ 120 eV

* (Divergences are diffraction limited).

3.3 Low Density Matter - Atomic, Molecular and Cluster Physics

3.3.1 Cluster and Nanoparticle Spectroscopy

Small particles are different from bulk matter; finite size effects influence all properties of matter. In particular, the finite number of constituents and the discrete nature of phonon, electron, or other quasi-particle densities of states alter the constituent interactions and leads to different geometric and electronic ground state configurations as well as influencing the dynamical behavior of nanoscale matter. This results in strong changes of optical, magnetic, chemical and thermodynamic properties [18].

Although a large variety of such effects has been studied in recent years, in many cases a deeper insight was hampered by the lack of adequate light sources for spectroscopy of gas phase nanoparticles. The FERMI FEL will allow performing much broader, in-depth studies in the several areas discussed here below.

Electronic structures of nanoparticles

Examples of important quantum size effects in small particles are the highly discrete electronic density of states in metal clusters [19], the metal/nonmetal transition in divalent metals [20], the indirect/direct band-gap transition in silicon clusters [21], the general increase of the band-gap in semiconductor clusters [22], or the increase of the magnetic moment of ferromagnetic clusters [23]. For other properties like superconductivity only some evidence for related effects have been found in small particles [24]; the question of down to what size "classical" superconductivity exists is completely open.

Even a seemingly easy problem such as the total valence bandwidth in nanoparticles, is not yet solved. The calculated and measured bandwidths of simple structures such as sodium clusters differ significantly [25]. The situation is even worse in the case of d-bands of transition metals that determine important properties such as magnetism or chemical reactivity. In that case, bandwidths and positions are often unknown. The same applies to dynamic properties such as ultra-fast electronic relaxation processes after d-band or shallow core state excitation. The related spectroscopic features such as line shapes (with phonon and low energy electronic contributions) or satellite structures (strong correlations as for the "6 eV satellite" in nickel) constitute an entirely unexplored, yet interesting and important, field of research - no gas phase experiments on size-selected clusters exist at all.

The reason for this lack of knowledge, despite the wealth of existing photoelectron spectroscopy results concerning free clusters and nanoparticles, is that the limited photon energy of standard laser systems allows studying electronic states only down to ~5 eV below the Fermi energy. This limitation prevents measuring the full valence electron structure as well as, for example, performing photon energy dependent spectroscopy across shallow core edges (resonance photoemission [26]), data that would greatly contribute to the understanding of the evolution of the electronic structure as a function of cluster size.

The beam intensities available at 3rd generation synchrotron radiation facilities are still far below what is required for meaningful gas phase experiments. Size-selective spectroscopy at the FEL light source will therefore allow measurements of unprecedented significance and will undoubtedly lead to a deeper understanding of the electronic structure of nanoscale metals and semiconductors, as well as of electron correlation effects in solids in general.

Femtosecond dynamics and pump-probe spectroscopy

To follow the temporal evolution of intra-molecular, photo-induced processes, femtosecond pump-probe techniques are the only means of resolving, in real time, relaxation processes and nuclear motion. To date such measurements cover the range of conventional femtosecond lasers. Higher harmonic generation has been used to form ultra-short pulses, even in the attosecond time range, at VUV wavelengths [27]. Since the Nobel awarded work of Zewail and others [28], femtosecond real-time spectroscopy has been applied in many fields of chemistry and physics. The group of Stienkemeier has successfully combined femtosecond lasers with helium nano-droplet isolation experiments, and pump-probe techniques are routinely performed using standard lasers in the IR, VIS and UV range. The multiple aspects of this work are summarized in a recent review article in J. Phys. B [29]. Elementary excitations of superfluids, desorption and energy relaxation in nano-clusters, wave packet propagation in small molecules, bond formation processes, as well as quantum interference oscillations requiring resolution down to the attosecond range have been carried out. The group of v.Issendorff has also applied fs pump-probe spectroscopy to study electron emission and electron-phonon coupling in highly excited sodium clusters [30].

However, the number of photons per pulse, as much as a factor of 108 smaller than that available from an FEL, prevented carrying out sophisticated experiments in dilute systems. FEL high intensity femtosecond pulses will therefore be the first useful tool for studying time resolved ESCA (usually associated with high binding energies) photoelectrons, photo-absorption and photoemission.

Studies at ultra-low temperatures

HElium NanoDroplet Isolation (HENDI) has become a standard technique to form neutral and charged molecules, clusters and nanostructured complexes at ultracold temperatures. Here a beam of superfluid helium droplets (HeN, $102 < N < 108$) is produced and doped with molecules and clusters, or with the respective charged entities of interest. The droplets cool the embedded species to 380 mK at which temperature, even for larger species, only vibrational ground states are populated. Because atoms or molecules can be picked-up from different sources sequentially, otherwise unfeasible experiments can be done under ultra-low temperature conditions. The nano-droplets act as an ultra-cold trap in which the weak interaction with the superfluid helium environment guarantees minimal matrix perturbations. The well-collimated beam trapped particles traveling in ultra high vacuum provides a stable regenerating target even for complex, radiation-damage-sensitive molecular structures. FERMI XUV radiation will extend optical techniques with these dilute targets to desired higher excitation energies.

Thermodynamics of nanoparticles

Caloric curves describe the relation between the internal energy and the temperature of a thermodynamic system. Knowledge of the caloric curve provides an exhaustive insight into the thermodynamics of the system, by revealing the different thermodynamic potentials as well as phase transitions such as boiling, melting and structural transitions.

Note that the thermodynamics of small systems strongly differs from that of the bulk. On one hand they involve surface effects that typically lower melting points and latent heats [31-33] while in small clusters with specific crystalline structures such effects are reversed [34]. On the other hand, there are substantial differences between the textbook thermodynamics of infinite systems and that of clusters, due to the limited number of degrees of freedom of the latter. In particular, in infinite systems the singularities that indicate phase transitions are broadened, and specific effects such as negative heat capacities can

be observed [35]. The experimental method to access caloric curves of small clusters uses the laser fragmentation pattern of mass selected and thermalized clusters [31]. The temperature influence is visible in the fragmentation pattern and can be compared to a controlled variation of the energy using a laser. The fragmentation spectra relate energy and temperature and therefore serve as caloric curves of mass selected clusters. Strongly bound systems like group 3 metals or noble metals, that are of high general interest, cannot be studied yet due to the lack of high intensity lasers with photon energies of 3 to 4 times the atomic binding energies.

Chemistry of molecular clusters and nanocrystal interfaces

Reactions at interfaces, such as aerosols or nanocrystal surfaces, have emerged in recent years as an important issue in fundamental and applied molecular science. Aside from the intrinsic interest in surface reactions, gas phase reactions cannot explain all measured data. A case that has received considerable attention originated from the measurement of large amounts of Cl2 produced by the reaction of radicals with solvated NaCl molecules, in the laboratory [36] and in the marine troposphere. The results could only be explained by the reaction of the radicals with chloride ions accumulated at the surface of the water droplets. A recent "perspective" article in Science highlights the importance of understanding these processes at the water interface [37].

3.3.2 Ultra-fast Cluster Interactions

The understanding of the interaction of high intensity, short-wavelength, short-pulse radiation with matter is essential for virtually all future FEL experiments and even more important for flash imaging of nanosized particles. The FERMI FEL will supply photons in the very interesting spectral regime ranging from 100 to 10 nm in which plasma absorption processes break down and new physical processes involving core levels become important. Clusters as a form of matter intermediate between atoms and bulk solids are ideal samples to study these processes. By varying their size the role of inner- and inter-atomic collective effects can be investigated. These studies will contribute to our understanding of energy deposition, energy transfer, and radiation damage in matter that is essential to plan future experiments. Furthermore, clusters and nanoparticles irradiated by intense FEL pulses exhibit a wealth of interesting non-linear physics covering atomic and cluster physics, biochemistry and plasma physics.

Initial experiments at the FLASH facility at DESY provide an insight into the absorption processes and the ionization dynamics with ultra-fast, intense VUV-pulses in rare gas clusters. The results for single shot imaging of gas phase nanoparticles hold great promise for various types of time-resolved structure determination. These studies are the first steps into a new interdisciplinary field with many fundamental open questions.

The FERMI FEL with its seeding scheme will provide unique possibilities for these studies, such as reproducible and well-controlled pulse shapes (which are extremely helpful for all non-linear studies) and stable synchronization to external lasers.

To make these studies possible experimenters and ELETTRA beamline scientists will work together to develop and build tools for investigating ultra-fast processes in gas phase particles, in particular

- gas phase, molecular beam apparatus with pulsed sources of rare gases and metal clusters,
- time-of-flight based electron and ion spectrometers for the kinematics and momentum analysis of ionization products,

- angle-resolving XUV spectrograph with a 2D position sensitive detector,
- a 2D-scattering detector for high repetition rate experiments on gas phase samples,
- specialized optics for pump–probe experiments with high power density beams.

The experimental team also plans to address, among others, the following topics of interest for FERMI:

1. Time resolved ionization dynamics – Multiple ionization of clusters is expected to proceed on at least two different time scales. The electrons leave the cluster within a few fs, while the Coulomb explosion, i.e., ion motion, takes place on a time scale in the range of several hundred fs to ps, depending on the cluster size. Experiments with optical lasers give strong evidence that the ionization dynamics is sensitive to pulse length and shape [38, 39]. Cluster dynamics will be studied with pump-probe techniques by measuring the intensity of scattered light as a function of the time delay. The measurement can be done by splitting the FEL beam into a low intensity pump pulse (2-5% of the total intensity) and a high intensity probe pulse. In this way the pump pulse inducing the initial non-linear processes will be only a minor contribution to the total scattered signal. Assuming tight focusing into a 5 μm spot, a power density of more than 1014 W/cm^2 can be achieved even in the pump pulse. In addition, two-colour pump-probe experiments, making use of the first and third harmonics of the FEL, are ideally suited for this application because they are automatically synchronized. Furthermore, pump-probe studies with a femtosecond-IR laser as pump and the FEL as a probe yields the angular distribution of the scattered light on a 2D-detector to provide information on the time evolution of electron density with nanometer spatial resolution.
2. The role of inner-shell electrons – Theoretical studies predict that the photo-absorption of atoms in clusters can be substantially smaller than that of isolated atoms, if inner shell electrons are involved [39]. The reduced absorption is due to bleaching, as the Auger decay rates of delocalized valence electrons in clusters are reduced.
3. Slowing down the Coulomb explosion – According to theory [40], the positive charges accumulate preferentially in the outer part of the clusters while the inner part stays almost neutral. This effect can possibly be used to slow down the Coulomb explosion when clusters or macromolecules are embedded in a large He droplet. The ionization dynamics can be investigated with time resolved scattering and with time of flight mass spectroscopy.
4. Production of high harmonics of VUV radiation.

According to recent theoretical work, processes involving the vibration of inner-shell electrons [41] might allow to efficiently generate high harmonics by VUV radiation.

3.3.3 Spectroscopic Studies of Atoms, Ions, Neutral Molecules and Reaction Intermediates

Non-linear optics in absorption and ionization; double ionization – FERMI will allow exploring non-linear optical systems that were hitherto inaccessible with lasers, particularly shallow core levels. Noble gases atoms are the simplest ones to investigate in such experiments. Much work has been done with conventional lasers on Ne, Ar, Kr and Xe [42]. Fewer experiments have been done on He for two

reasons: the energies required are higher due to the higher ionization potential of He, and He is less easily polarized than the other noble gases, resulting in lower cross-sections. Several key experiments are planned for FERMI, namely:

- Two-photon resonant absorption at the doubly excited states of He, to access even states. Comparing rates from estimated cross-sections with the FERMI parameters indicates that the flux density is sufficient.

- Multi-photon, double ionization of He and of the other rare gases is an experiment of considerable interest [43]. Double ionization is a basic process in atomic and molecular physics, in which a single energetic photon injects two coherent electrons into the continuum. The origin of the process lies in the electron–electron correlation in the initial state. Since the first observation of of high ion yields by double and multiple ionization using intense, linearly polarized photon pulses, only a few experiments have been performed to elucidate the mechanism behind these processes. At intensities such as provided by FEL sources, Parker et al. [44] have predicted interesting phenomena to occur, including single-photon-induced double ionization. They show, for example, that the electron pair in the continuum behaves as a single correlated wave-packet that absorbs and shares energy in units of the energy of the exciting field, like in the ATI process.

- Basic non-linear interaction between atoms and strong electromagnetic fields can be studied in a clean way for the first time because the pondermotive potential will be negligible when using high photon frequencies. Many-electron processes become increasingly important at higher frequency, an with ultra-short photon pulses. Two-photon, inner-shell ionization is another interesting test case for which theoretical predictions are already at hand.

- Pump-probe, two-colour experiments will use the FEL beam in combination with a beamline laser. Important processes include auto-ionization, fragmentation, and conformational changes. The main differences between the two approaches are the amount of internal energy in the excited state, and the spectroscopic methods applicable in the probe step.

- Dilute species: neutral cluster beam spectroscopy – Using the source developed by the Milani group [45], refractory metal clusters and their oxides will be characterized to elucidate the relationship between size and electronic structure. The interaction of free clusters with atomic and molecular species such as oxygen, hydrogen, water and hydrocarbons will be characterized as a function of mass and production conditions. The most used techniques will be time-of-flight mass spectrometry and fluorescence spectroscopy; test runs have been carried out at ELETTRA, and more are planned on free clusters and condensed samples.

- Dilute species: macromolecules – The proposal is aimed at studying the secondary structure of biomolecules using circular dichroism (CD). Circular dichroism in optical absorption is a standard method of determining protein folding for the wavelength range down to about 180 nm. The intensity changes are small, about 10^{-3} to 10^{-4}, and the amount of detailed information is limited (the spectra typically show a few wiggles over a 60-70 nm wavelength range). Nevertheless the basic structures of helix, coil and sheet can be distinguished. Experiments with FERMI will provide structural information about free macromolecules, potentially more detailed than with UV/visible absorption circular dichroism, because the spectral range is much broader. The technique can also be used for general ion spectroscopy.

3.3.4 Spectroscopic Studies of Reaction Intermediates

Most information available to date on excited states of ions has been obtained by the application of conventional photo-electron spectroscopy. States accessible by this technique are only a fraction of the total, and most of the literature is concentrated on the spectroscopy of stable species. Information about reactive intermediates is much more limited as the species need to be prepared in situ, and therefore generally a high sensitivity method is required. High sensitivity laser techniques - even via multi-photon processes - offer access only to the lowest states of cations. High resolution data are available for stable molecules and some reactive intermediates. [46] Variable photon energy studies using conventional photo-electron spectroscopy are few in number and the data are fragmentary [47]. Information comes also from discharges by emission, an environment in which states excited by collisions are important; the method is limited to states that fluoresce. A route, which leads to highly excited states or to states not accessible through conventional photo-electron spectroscopy is, for example, resonant Auger spectroscopy, for which the selection rules are different [48]. Such studies on radicals are virtually nonexistent. In natural environments excited states are produced and play important roles, as they can be formed by collisions. The concentrations are necessarily small since, because of the high internal energy content, such states are very reactive. In case of dissociation, excited states can be a source of fast neutral or ionic fragments (in their ground or excited state), also very reactive.

FERMI will allow accessing higher lying states of reactive intermediates through the application of well-developed and highly sensitive techniques. The relevant intensities are often increased by near-resonant, auto-ionization of highly excited states [46] in which case states not accessible by direct ionization from the ground state or levels outside of the Frank-Condon region become observable. The experimental arrangement (section 3.4) will be designed to detect all particles produced in the absorption event, so both fragmentation and (auto) ionization dynamics will be studied. The addition of a synchronized, tunable laser allows further extending such studies by either preparing the initial state of the radical using a visible, UV or VUV photon – i.e., above or below the first ionization potential – or by directly measuring the auto-ionization lifetimes by varying the delay between the two lasers.

The use of the laser-FEL combination provides other possibilities. For example, photo-dissociation of state-selected ions can be studied. Pulsed-field ionization of long-lived high-n Rydberg states of neutral radicals is a convenient route to prepare molecular ions from radicals in one or more selected rovibronic states. After initial excitation, the Rydberg electron is removed by a weak pulsed field to leave the pre-selected quantum state of the ionic core unchanged. FERMI FEL radiation in the 12.0-18.0 eV range can produce a Rydberg state of a radical or complex, which upon pulsed field ionization yields an ion in the selected quantum state. A synchronous pulsed UV laser can then be used to photo-dissociate the state-selected ions. The cation fragment can be detected by velocity-map imaging which allows determining the relative quantum yields of the various product channels, and their spatial anisotropies, each as a function of the initial parent quantum state and the photolysis wavelength.

As a first study, the double ionization of ozone by two-photon absorption (FEL-1 photons) will be studied as a function of the photon energy. Two- and three-body dissociation processes of O_3^{++} will be investigated for the first time including the detection of the neutral fragment. The 3D electron-ion-neutral velocity image will then be measured as a function of the field power density. A similar detailed study of the double photo-ionization of O_3 by single-photon absorption (using FEL-2) will be done for comparative purposes.

Recently the application of short pulse, high intensity, visible-IR lasers has stimulated strong experimental

and theoretical interest in the multiple ionization process [49]. FERMI allows examining strong field effects at shorter wavelengths. By varying the pulse length, intensity and photon energy (also beyond the single photon multiple ionization limit), the importance of these effects can be examined in detail. The excitation region of particular interest is the range accessible by FEL-1. At higher energies many-electron atomic/molecular processes are predicted to dominate [49]. The capability of tailoring the electronic structure of small molecules (by using selected radicals or other reactive intermediates) offers the unique possibility of studying the role of molecular structure in high-field multiple ionization.

3.4 Scattering Spectroscopies

Time-resolved resonant scattering with coherent radiation can be applied to the study of complex dynamics in disordered systems by means of the "speckle" technique. This technique analyzes the temporal correlations among the scattered photons from incident, spatially coherent radiation. Due to the characteristics of the FERMI radiation it will be possible to access as yet unexplored space-time scales. Interesting examples include the study of critical fluctuations under equilibrium conditions of polymers, colloidal suspensions and liquid crystals [50], the non-equilibrium dynamics during phase separation and the spinodal decomposition of liquid systems, including magnetic and glass systems, magnetic domain dynamics in thin films and multi-layers [51], the study of stripes in high-Tc superconductors and phase separation in manganites [52].

3.4.1 Time-resolved Resonant Scattering of Disordered Systems

One of the current goals of condensed matter physics is the measurement of collective dynamical properties that are due to atomic, electronic and magnetic-density fluctuations. These fluctuations are responsible for specific vibrational, electronic and magnetic elementary excitations, which are often related to many macroscopic properties in condensed matter systems. The experimental challenge is to measure the dynamical structure factor S(Q,E) (or, in time resolved experiment, its Fourier transform F(Q,t)) in the largest region of energy (E) (or time t) and momentum transfer (Q) spaces. The specific research interest is the study of S(Q,E) associated with the collective dynamics in systems without translational invariance: glasses, liquids, and dense fluids. This aim, of great interest for basic and applied research, has been pursued using visible light, x-ray and neutron scattering.

Operating the FERMI photon source between 40 nm and 10 nm will probe regions of (E,Q) space not otherwise accessible for kinematic reasons, with the sufficient intensity to meet the energy and angular resolution requirements. The ultra-short and polarized nature of the FEL radiation pulse opens a completely new field of investigations that will extend and complement the research activity that will start at the IUVS beamline under construction at ELETTRA and at other similar experimental stations.

3.4.2 Resonant Inelastic X-ray Scattering

The FERMI project aims to achieve transform-limited, mJ, soft x-ray pulses for the first time. An enormous advantage of using a transform-limited source is that the x-ray pulse produced can be highly monochromatic. For example, a 1 pico-second long pulse has a bandwidth of only 2 meV. With such a source, an instrument for resonant inelastic x-ray scattering (RIXS) in the photon energy range from 30-120 eV is possible that will dramatically outperform counterparts on third-generation synchrotron sources.

Inelastic x-ray scattering is a photon-in/photon-out method with compelling fundamental advantages over methods such as angle-resolved photoemission, which measure the out-going electron. These advantages are:

(1) an energy resolution which is not limited by the core-hole lifetime;

(2) the considerably greater sampling depth of the out-going photon compared to an electron;

(3) the ability to exploit high incident photon number that would cause space charge blowup of the electron emission, limited only by considerations of radiation damage to the sample;

(4) the ability to work in biologically important solutions or in applied fields.

With the capability to tune to the resonant energy of the L and M absorption edges of many important constituent atoms, the technique is the soft x-ray equivalent of the well-known and powerful Raman technique.

The resonant method allows access to excitations otherwise forbidden by selection rules; it provides element and site-specific information; and it can significantly increase cross-sections to permit measurement of weak collective electric and magnetic excitations. The FERMI photon range encompasses the M-edges of transition metals, allowing the experimenter to study the physics of electron dynamics in highly correlated electron systems – a major frontier of condensed matter physics today. In such systems, the traditional description using single electron-like quasi-particles breaks down, and fundamentally new states of matter occur. A new instrument at FERMI can measure the dynamics of spin-charge separation and the excitation spectrum of high-Tc superconductors or colossal magneto-resistive materials to test theoretical models.

In the most complex systems there are poorly understood interplays between the fluctuations associated with spin, charge, orbital, and lattice degrees of freedom that can be separated and studied with the resolution and high flux of this instrument.

3.5 Non-linear Spectroscopies

The second round of experiments with the FERMI FELs, using the advanced parameter set, will exploit photon intensities that will give access to novel, in-depth studies of non-linear phenomena.

3.5.1 VUV Non-linear Optics in Condensed Matter

The theoretical description of nonlinear effects in solids is a formidable task, and important difficulties have delayed any accurate calculations for many years. Even at the simplest level of approximation – treating electrons as independent particles interacting with the electromagnetic field in the long wavelength limit and neglecting local field effects – the calculation of nonlinear coefficients is cumbersome. Moreover, many-body effects might be important; in fact, note only recently is theory able to reproduce ab initio the systematics of the linear response in solids, including these effects, using either many-body perturbation theory [54] or, even more recently, time-dependent density functional theory [55].

One important nonlinear process is second harmonic generation. Although several calculations of the corresponding susceptibility have been performed for various semiconductors in the visible range, a consistent picture has not emerged from these calculations [56]. For instance, the question of the importance of excitonic or local field effects is not yet settled. Attempts have been made in the low energy range only [57, 58]. Ab initio calculation of nonlinear properties must now be extended to the XUV region.

The unique properties of FERMI@Elettra extend into the XUV region the techniques for nonlinear optics in condensed matter already developed in the visible. The investigations of non-linear optics in condensed matter will develop from a FERMI end-station dedicated to this task and will benefit from the collaboration of an international group of partners of complementary experience, expertise and interests. Continuous, close theoretical support to the experimenters will be provided via a novel approach to the use of numerical simulation as a design tool for optimization of experiments. The first experiments will be in the fields of two-photon absorption (TPA) in solid targets, second harmonic generation (SHG) in condensed media and transient phenomena.

In general, nonlinear optical effects can be readily observed by using coherent sources of radiation. In the XUV region of the spectrum such sources were not directly available until recently. At present two kinds of coherent UV sources are available, namely soft X-ray lasers [50] and multiple harmonic generation in gaseous targets from visible laser pulses [51]. The intensity delivered by these systems is generally not suitable for performing nonlinear optical experiments. Only very recently FEL radiation has been used in the EUV [52]. To date, in fact, very few experiments are reported using such sources, the nonlinear medium being in general a gas jet expanding into vacuum. Experiments on two-photon absorption in He gas have been reported as a tool for autocorrelation of high-harmonic coherent pulses [53].

From the point of view of nonlinear optics, gas systems suffer from several limitations. a) the center-symmetry of the medium allows only nonzero odd nonlinear susceptibility terms, b) albeit variable, the matter density of gaseous nonlinear media is always low, and this fact may reduce the efficiency of the nonlinear process, c) gaseous targets are intrinsically unstructured, therefore no effects related to the presence of medium discontinuities can be observed.

No experiments, to our knowledge, have been so far attempted in the XUV range on nonlinear optical effects in condensed matter. The reason for this is mainly due to the lack of sufficiently intense short pulses of coherent laser radiation in the XUV region. The high brilliance, coherent FERMI source will remove this limitation.

Despite absorption, there are various reasons for attempting nonlinear optical experiments on solids in the XUV region. First, non center-symmetric material systems may be selected which have a nonzero, second order susceptibility £q(2) that drives more intense, non-linear effects. Then, the presence of well-defined material-vacuum and/or material-material buried interfaces allows surface and bulk effects to be discriminated and may also switch on interaction with collective material excitations.

3.5.2 The UNUS Project

The UNUS Project is conceived around a single end station for FERMI to be designed and built specifically for nonlinear optical experiments, with aim of extending and testing for the first time our knowledge of nonlinear properties of condensed matter in the XUV region. For this challenging task experiments must be modeled theoretically and simulated numerically to guide and optimize the experiments.

Beam intensity, polarization, short duration, monochromaticity and temporal coherence of FERMI radiation offer exciting possibilities for nonlinear optical experiments. In particular, nonlinear optical phenomena are effective when the optical fields become comparable with the atomic field strength (≈ 108 V/m) associated with the relevant electronic levels. This condition imposes a minimum value for the brilliance on sample of the order of 1015 W/m^2 for FEL operation at 31 eV. Short duration of the FEL pulses, besides helping in obtaining high intensities, is per se an attractive feature that allows time resolved measurements in so far unexplored temporal domains with x-ray pulses. The most promising time duration for coherent pulses is in the tens of fs where a sufficient resolution is achievable on most electronic collective excitations in condensed matter.

Operationally, the first set of experiments will proceed along the three lines: two photon absorption, harmonic generation in condensed matter and transient phenomena

- Two photon absorption: This technique makes use of "virtual" intermediate electronic states to reach the final state. It will be used within the VUV and XUV range of FERMI as applied for instance to 3p shells of 3d metals, to 4f shells of some noble metals and also to K shell excitation of selective light elements. The latter possibility has particular relevance to the analysis of electronic bonds. By continuously tuning the FEL radiation, one could develop a two-photon NEXAFS [59] for dipole-forbidden final states, thus offering an original perspective in the simulation and solution of local structure around an absorbing site.

- Harmonic generation in condensed matter: Higher harmonic generation (HHG) has been explored for more than two decades, and coherent radiation has been generated in the VUV and XUV from gaseous samples starting from visible laser pulses [60-63]. UNUS will study the nature of the intrinsic nonlinearities in optical response in condensed matter in the VUV to XUV photon energy range by measuring the nonlinear susceptibilities in condensed matter.

- Transient phenomena – XUV or VUV photo-excitation of materials can be readily obtained in a conventional synchrotron beamline provided that a) time separation between pulses is consistently larger than the lifetime of the transition being measured and b) the intensity of the (monochromatized) exciting pulse is sufficiently high. This last condition is very seldom true in practice and very few fluorescence photons per bunch are generally obtained [64]. This implies the use of photon counting techniques with sophisticated timing systems to obtain the decay parameters of the fluorescent signal. The pulsed excitation provided by FERMI can be exploited in transient studies by probing unexplored ranges of characteristic de-excitation times of systems under high intensity VUV excitation. In this respect the investigation of temporal properties of the radiative (e.g. fluorescence, phosphorescence and luminescence) and non-radiative (e.g. Auger and photoelectric emission) de-excitation channels could become a natural topic to be studied.

3.6 Exploiting the Schemes to Produce Intense EUV and Soft X-ray in the Attosecond Time-domain

Zholents and Fawley have proposed [65] producing isolated soft x-ray pulses pulses of ~100 attosecond duration using electrons selected by their previous interaction with a few-cycle, intense laser pulse. They call this process "seeded attosecond x-ray radiation (SAXR)." In principle, SAXR allows excellent

temporal synchronization between the attosecond x-ray probe pulse and a pump source that can be the same few-cycle pulse or another signal derived from it. Thus, it is conceivable to track the temporal evolution of atomic or molecular states during a single optical cycle in the process of laser-assisted photoionization.

As a specific example they choose 2 nm as the x-ray source wavelength to eventually produce 1-nm wavelength attosecond radiation. However, as long as an intense, coherent source is available, attosecond pulse generation at both longer and shorter wavelengths is also possible with the same scheme. In particular the harmonic cascade of FEL-2 of FERMI is well suited to performing the first experimental verification of this scheme. A sample layout is in Figure 3.6.1.

Figure 3.6.1:
A schematic of the components involved in attosecond x-ray pulse production.

SAXR requires an ultra-relativistic electron beam, a few-cycle, intense optical laser pulse and an intense pulse of coherent x-ray radiation, together with a number of magnetic undulators and transport elements.

3.7 Instrumentation R&D

FERMI, like more conventional synchrotron light sources, is planning an R&D campaign focused on developing instrumentation specially dedicated to the exploration of ultra-fast processes. The main instrumentation items are briefly discussed in the following paragraph.

3.7.1 Sub-picosecond Streak Camera

The sub-picosecond resolution Streak Camera (SPSC) FERMI project calls for a system with 500 fs temporal resolution, 10-100 nm photon wavelength range, with an efficiency of $> 10^{-6}$. The 500 fs temporal resolution for x-rays, is challenging. The resolution of streak cameras has slowly improved over the years from around 2 ps in 1990 [66] to the best achieved so far 800 fs [67]. This improvement mainly resulted from the reduction of jitter in triggering of the camera by use of an improved design of photoconductive switch and from improved laser stability. The temporal range is also challenging; however, it can be achieved by use of a variable sweep rate. The SPSC would have a wide temporal window and a narrow temporal window mode. These modes would be used respectively for finding the beam in time, and for high temporal resolution measurements.

The camera will be designed to be read at up to the FERMI-FEL, 50 Hz repetition rate. The requisite dynamic range of the camera depends on whether the system is used in single shot or in the accumulation mode; the R&D goal is to develop the more challenging, single shot capable device.

Applications of such a camera range from measuring the separation of pulses created by an X-ray beam splitter, to measuring the decay of x-ray fluorescence from a plasma. The baseline dynamic range design value is 103. This sets the required number of electrons per temporal resolution element and thus determines the space charge broadening of the beam.

The streak camera is shown schematically in Figure 3.7.1. X-rays hitting the transmission photocathode produce the electron beam, consisting mainly of low energy secondaries. The width of the electron energy distribution and its mean energy mainly depend on the work function of the material, the best being CsI or KBr, with an energy spread of around 1 eV. However, because these materials are easily radiation damaged, gold, having a higher work function and consequently higher energy spread but being radiation hard, will also be considered for the application. The emitted electrons are accelerated in a field of up to 25 KV/mm, established between the photocathode and a mesh or a slit. The accelerated electrons are then deflected by a time varying electric field, and focused unto a detector plane by a magnetic lens.

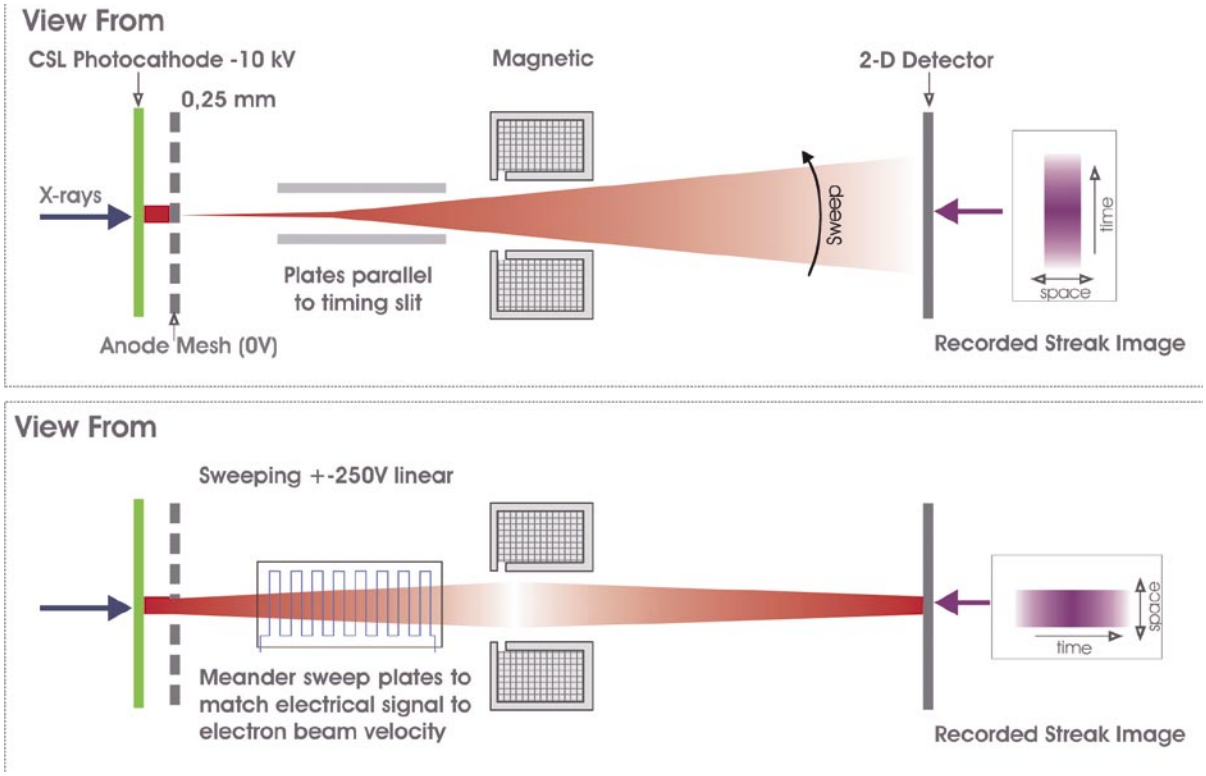

Figure 3.7.1: *General arrangement of the streak camera components.*

3.7.2 Detection and Diagnostic of Ultra-short EUV and Soft-X-ray Photon Pulses

There are currently two interesting methods for the temporal characterization of XUV pulses. The first one is the extension of the auto-correlation technique, developed for measuring visible pulses, into the X-ray region. Auto-correlation requires splitting the pulse into two replicas which are then recombined in a suitable nonlinear medium, where the nonlinear process is sensitive to their temporal overlap. Examples of such nonlinear processes are second-harmonic generation in a nonlinear crystal (for visible pulses), two-photon ionization, or index variation in a Kerr medium. A serious drawback of this method is that the efficiency of nonlinear processes depends on pulse intensity, and if the intensity is too low the method is not applicable. The generalized cross-section for two-photon ionization decreases rapidly with wavelength; for example, for argon at 53 nm, it is only 2.1×10^{-52} $W^{-2}cm^6$. To measure a statistically significant auto-correlation over reasonable number of pulses, a few nJ of focused X-UV radiation are sufficient. Single-shot measurements instead require a thousand-fold increase in pulse energy. The auto-correlation method does not give complete information about the pulse temporal shape, the auto-correlation trace being symmetric by definition.

A second class of measurement techniques, also suited for pump-probe measurements, is based on the cross-correlation of the X-ray pulse with a longer wavelength (visible or infrared) probe pulse. In this case the single-photon XUV process becomes the limiting factor. Again for argon at 53 nm the corresponding ionization cross section is 8×10^{-20} cm^2, and ~ 5 fJ of XUV energy per pulse would provide a detectable signal, while single-shot capability requires pulse energies greater than 5 nJ.

This second method will be first tested using femtosecond X-ray pulses obtained by high-order harmonic generation (HHG) in noble gases. The technique will then be used to measure the duration of the most energetic FEL X-ray pulses.

3.7.3 Optical Component Development

The experimental program at FERMI will require the development of a new generation of optical components tailored to the ultra-brilliant, ultra-fast FEL output radiation. The main areas and items of interest to be developed, possibly on different time scales, are the following:

Spectral analysis of EUV FEL radiation

The information about the FEL spectrum is essential both during the development and characterization of the source, and for defining the experimental conditions for the users. Since the FEL is operated at low repetition rate, the spectrum must be obtained on-line, using a single shot.

A single-shot online EUV and soft X-ray spectrometer is an essential instrument for the FEL facility.

Time-compensated broad-band monochromators.

A filter tunable over the whole spectral region covered by both FEL-1 and FEL-2 may be required to suppress background radiation outside the FEL spectral band and high-order harmonics. The filter can be a broad-band grating monochromator. The design must preserve the FEL pulse time duration and produce an output beam with the smallest possible dispersion. As in the previous case, a tunable EUV and soft X-ray filter will be needed by many users and should therefore be part of the FERMI FEL beamlines.

Optical systems for focusing the FEL beam

Focusing of the FEL beam on sample is required by almost all experiments. The development of focusing for all kinds of FEL operating modes is therefore essential.

Beam-splitters for EUV ultra-short pulses

Beam-splitters for ultra-short intense EUV pulses are crucial items for many experiments and need developing. A short-term goal is to build a prototype of such a time-compensated beam splitter for visible-UV, ultra-short pulses, using grazing-incidence gratings in a time-compensated configuration. The task will be performed in close collaboration with ULTRAS-Politecnico Milano. The prototype will be tested and operated with visible-UV radiation, in air, to demonstrate its feasibility. The same configuration, with the appropriate choice of gratings, can be used for all wavelengths in the 3-100 nm range, covering the whole spectral range of both FEL-1 and FEL-2.

Time-compensated high-resolution monochromators

Although the FEL intrinsic spectral resolution is high, some proposed experiments require even higher resolution. High-resolution monochromators to respond to this asks for the study and design of time-compensated configurations.

3.7.3.1 Time-compensated Instruments for Handling FEL Radiation

The use of grazing-incidence optics for the EUV intense FEL radiation is chosen to ensure safe operation of the optics and high efficiency of the instrument.

In particular, the use of reflective grazing-incidence gratings as beam handling devices for EUV ultra-short pulses offers many advantages but also raises design issues related to the preservation of the pulse time duration. Only the zero-order beam has the original ultra-short pulse duration, since the grating acts like a mirror, while the duration of the diffracted orders is altered. The total difference in optical paths of rays diffracted by N grooves at wavelength l is DOP=Nml, where m is the diffracted order.

The effect becomes dramatic in the femtosecond time scale: considering a 200 grooves/mm grating illuminated over a 30 mm length, the total number of grooves involved is 6000, corresponding to a maximum delay in the first diffracted order of 240 mm, i.e. 800 fs at l=40 nm.

The effect therefore reduces both the time resolution capability and the peak intensity of ultra-short pulses. In addition, the grating introduces also spectral broadening, since the different spectral components of the pulse are diffracted in different directions.

It is nevertheless possible to design time-compensated configurations by using two gratings in a subtractive and compensated dispersion configuration. In such a configuration, the second grating compensates both the time difference and the spectral broadening introduced by the first one [68].

3.7.3.2 Focusing of the FEL Beam

The FEL beam must be focused on the sample resting in the experimental chamber. Since different power densities and/or different illuminated areas are required, different spot sizes on sample are required. Focusing in the 4-100 nm wavelength range is efficiently done by grazing-incidence mirrors.

Several solutions can be proposed. One example is the use of a pair of deformable cylindrical mirrors in the Kirkpatrick-Baez configuration, whose radius of curvature can be varied between infinite (plane mirrors, no focusing) and a given value. A different choice calls for several (2 to 4) ellipsoidal mirrors with different radius of curvature.

The proposed solutions take into account that the minimum focal spot size is limited by diffraction to $\approx 2.44 \cdot \lambda \cdot f/\#$ where λ is the wavelength and $f/\#$ the numerical aperture of the beam. For example, a 20 μm spot at 40 nm requires $f/\# \approx 200$, i.e. an angular aperture of 5 mrad. Taking into account the intrinsic divergence of the FEL beam and the actual distance between the FEL source and the mirror, the exit arm of the mirror must be quite short (~ 0.5-1 m). The mechanical mounting of the optics has therefore to be carefully studied to avoid interference between the focusing optics and the diagnostic instruments around the sample.

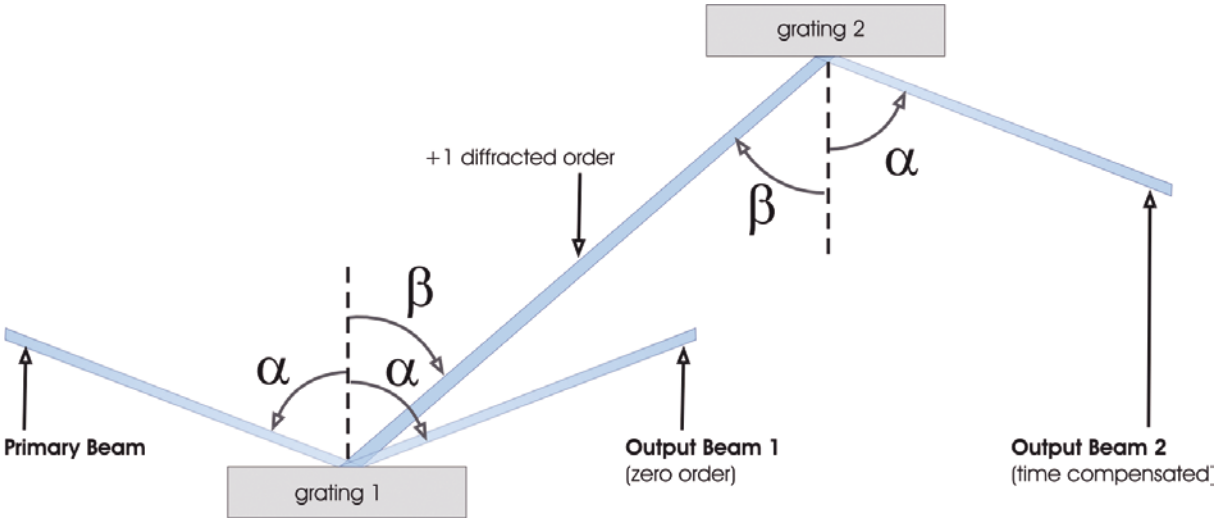

Figure 3.7.2:
Layout of a time-compensated beamsplitter.

3.7.3.3 Beam Splitter in the Visible-to-UV Range Using Grazing-incidence Plane Gratings

A simple beam-splitter consists of a diffraction grating: the incident beam is diffracted into several output beams, corresponding to the zero order and the other, diffracted orders. To preserve the temporal structure of the incoming radiation a time-compensated configuration using two gratings in subtractive and compensated dispersion must be used [69]. The layout is shown in Figure 3.7.2. The gratings are mounted in the so-called Z-configuration, with the incidence angle on the second grating equal to the diffraction angle from the first one; consequently, the diffraction angle from the second grating is equal to the incidence angle on the first one, so that the output beam is parallel to the input one. In such an arrangement, the rays with a longer optical path from the first grating have a shorter optical path from

the second grating, and vice versa. Furthermore, also the spectral dispersion of the non-monochromatic radiation is almost compensated by the Z-configuration, since the second grating has a subtractive spectral dispersion with respect to the first one.

A schematic of the prototype to be realized is shown in Figure 3.7.3. The optics will be mounted on a breadboard of approximately 1 m × 0.4 m. The optical system consists of two gratings and three plane mirrors. All optics are operated at grazing incidence, with incidence angle in the range 80°-86°. The two gratings are rotated along with the input wavelength in order to work at constant subtended angle $\alpha+\beta$ and maintain the direction of output beam 2 fixed, parallel to the input beam. Mirror M1 must also reflect the zero order in a fixed direction and is therefore also is rotated and translated along with the wavelength. To select the delay between output beam 1 and 2, Mirrors M2 and M3 can be rotated and translated.

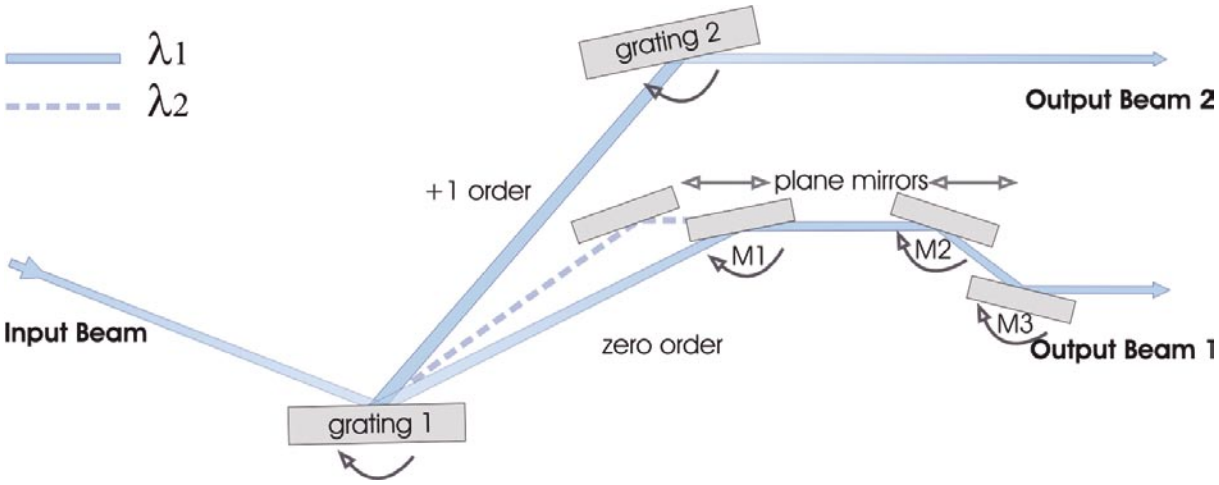

Figure 3.7.3:
Schematic of the beam-splitter to be realized.

3.8 References

[1] "Synchronization of X-ray Pulses to the Pump Laser in an Ultrafast X-ray Facility", J. N. Corlett, W. Barry, J. M. Byrd, R. Schoenlein, and A. Zholents, Proceedings of EPAC 2002, Paris, France.

[2] "Introduction to special section on future light sources," W. A. Barletta and H. Winick, Nuc. Inst. and Meth., A500, pp. 1 – 10, (March 2003).

[3] Schneider, G., Cryo X-ray microscopy with high spatial resolution in amplitude and phase contrast, Ultramicros. 75, 85 (1998).

[4] Howells, M., T. Beetz, H. N. Chapman, C. Cui, J. M. Holton, C. J. Jacobsen, J. Kirz, E. Lima, Marchesini, H. Miao, D. Sayre, D. A. Shapiro, and J. C. H. Spence. An assessment of the resolution limitation due to radiation-damage in x-ray diffraction microscopy. J. Electron Spectrosc. Rel. Phenom. (in press, 2005). http://arxiv.org/pdf/physics/0502059.

[5] Da Silva, L. B., J. E. Trebes, R. Balhorn, S. Mrowka, E. Anderson, D. T. Attwood, T. W. Barbee, J. Brase, Corzett, J. Gray, J. A. Koch, C. Lee, D. Kern, R. A. London, B. J. MacGowan, D. L. Matthews, and G. Stone, X-ray laser microscopy of rat sperm nuclei. Science 258, 269–271 (1992).

[6] Neutze, R., R. Wouts, D. van der Spoel, E. Weckert and J. Hajdu, Potential for biomolecular imaging with femtosecond x-ray pulses, Nature 406, 757 (2000).

[7] Sayre, D. Prospects for long-wavelength x-ray microscopy and diffraction, in Springer Lecture Notes in Physics 112, M. Schlenker et al Eds. p. 229 (1980).

[8] Miao, J., J. Kirz, D. Sayre, The oversampling phasing method Acta Cryst D 56 1312 (2000).

[9] Sayre, D. and H. N. Chapman, X-ray microscopy, Acta Cryst. A 51, 237 (1995).

[10] Jurek, Z., G. Faigel, and M. Tegze, Dynamics in a cluster under the influence of intense femtosecond hard x-ray pulses, Euro. Phys. J. D 29, 217-229 (2004a).

[11] Jurek, Z., G. Oszlanyi and G. Faigel, Imaging atom-clusters by hard x-ray free-electron-lasers, Europhys Lett. 65, 491-497 (2004b).

[12] Hau-Riege, S.P., London R.A., Szöke, A. Dynamics of X-Ray Irradiated Biological Molecules, Phys. Rev. 69, 051906 (2004).

[13] Bergh, M., Timneanu, N., van der Spoel, D.: A Model for the Dynamics of a Water Cluster in an X-ray Free Electron Laser Beam. Phys. Rev. E 70 051904 (2004).

[14] J. Miao, P. Charalambous, J. Kirz, D. Sayre, Nature 400, (1999) 342.

[15] K. A. Nugent et al, Phys. Rev. Lett. 77, (1996) 2961.

[16] S. Eisebitt et al, Nature, 432, (2004) 885.

[17] J. Miao et al, Phys. Rev. Lett. 89, (2002) 088303.

[18] H. Haberland (ed.), Clusters of Atoms and Molecules, Vol. I + II, Springer Series of Chemical Physics, Vol. 52 and 56, (Berlin 1995).

[19] G. Wrigge, M. Astruc Hoffmann, and B.v. Issendorff, Phys.Rev. A 65, 063201 (2002).

[20] B. v.Issendorff, and O. Cheshnovsky, Annu. Rev. Phys. Chem. 56, 549–580 (2005).

[21] L. Canham, Nature 408, 411 (2000).

[22] A.D. Yoffe, Advances in Physics 42, 173 (1993).

[23] Billas, Isabelle M. L.; Chatelain, A.; de Heer, Walt A., Science, 265, 1682 (1994).

[24] Ramiro Moro, Shuangye Yin, Xiaoshan Xu, and Walt A. de Heer, Phys. Rev. Lett. 93, 086803 (2004); Science 300, 1265 (2003).

[25] M. Moseler, B. Huber, H. Häkkinen, U. Landman, G. Wrigge, M. Astruc Hoffmann, and B. v. Issendorff, Phys. Rev. B 68, 165413 (2003).

[26] C. Guillot et al., Phys. Rev. Lett. 39, 1632 (1977).

[27] M. Schnürer, Ch. Spielmann, P. Wobrauschek, C. Streli, N.H. Burnett, C. Kan, K. Ferenc, R. Koppitsch, Z. Cheng, T. Brabec and F. Krausz, Phys. Rev. Lett. 80, 3236 (1998).

[28] Femtochemistry, Ultrafast Dynamics of the Chemical Bond, World Scientific Series in 20th Century Chemistry, edited by A. H. Zewail (World Scientific, Singapur, 1994).

[29] F. Stienkemeier and K.K. Lehmann, (invited Topical Review) J. Phys. B 39 R127–R166 (2006).

[30] M. Maier, G. Wrigge, M. Astruc Hoffmann, P. Didier, and B. v. Issendorff, Phys. Rev. Lett. 96, 117405 (2006).

[31] M. Schmidt, R. Kusche, W. Kronmüller, B.v. Issendorff and H.Haberland, Phys. Rev. Lett. 79, 99 (1997).

[32] M. Schmidt, R. Kusche, B.v. Issendorff, and H. Haberland, Nature 393, 238 (1998).

[33] M. Schmidt, R. Kusche, T. Hippler, J. Donges, W. Kronmüller, B.v. Issendorff and H. Haberland, Phys. Rev.Lett. 87, 203402 (2001).

[34] G. A. Breaux, R. C. Benirschke, T. Sugai, B. S. Kinnear, and M. F. Jarrold, Phys. Rev. Lett., 91, 215508. (2003).

[35] M. Schmidt, Th. Hippler, J. Donges, B.v. Issendorff and H. Haberland, Phys. Rev. Lett. 86, 1191 (2001).

[36] E.M. Knipping, M.J. Lakin, K.L. Foster, P. Jungwirth, D.J. Tobias, R.B. Gerber, D. Dabdub and B. Finlayson-Pitts, Science 288, 301 (2000).

[37] B.C. Garrett, Science 303, 1146 (2004).

[38] T. Döppner, T. Fennel, T. Diederich, et al., Phys. Rev. Lett. 94, 13401 (2005).

[39] U. Saalmann and J. M. Rost, Phys. Rev. Lett. 89, 143401 (2002).

[40] C. Siedschlag and J. M. Rost, Phys. Rev. Lett. 93, 43402 (2004).

[41] M. Brewczyk and K. Rzazewski, J. Phys. B 34, L289 (2001).

[42] S.M. Koeckhoven et al, Phys. Rev. A 49 (1994) 3322.

[43] J. Colgan and M. S. Pindzola, Phys. Rev. Lett. 88 (2002) 173002.

[44] J. S. Parker, L. R. Moore, K. J. Meharg, D. Dundas and K. T. Taylor, J. Phys. B: At. Mol. Opt. Phys. 34 L69 (2001).

[45] E. Barborini, P. Piseri, and P. Milani, J. Phys. D 32 (1999) L105.

[46] E. W. Schlag, "ZEKE Spectroscopy", Cambridge University Press 1998 and refs. Therein.

[47] J. M. Dyke et al., J. Chem. Phys. 108 6258 (1998); J.D. Barr et al., J. Electron Spectrosc. Relat. Phenom. 108, 47 (2000); J. Chem. Phys. 110 345 (1999).

[48] S. L. Sorensen et al., Phys. Rev. A 64, 012719 (2001).

[49] Phay J. Ho et al., Phys. Rev. Lett. 94, 093002 (2005); A. S. Alnaser et al., Phys. Rev. Lett. 93 113003 (2004); S. A. Novikov and A.N. Hopersky, J. Phys. B 33 2287 (2000).

[50] Proceedings of the 5th International Conference on X-Ray Lasers to be held in Lund, Sweden, June 10-14 1996.

[51] A. McPherson, G. Gibson, H. Jara, U. Johann, T.S. Luk, I. A. McIntyre, I. A.; K. Boyer, C. K. Rhodes, JOSA B 4, 595(1987).

[52] T. Laarmann,, A. R. B. de Castro, P. Gürtler, W. Laasch, J. Schulz, H. Wabnitz, and T. Möller, Phys. Rev. A 72, 023409 (2005).

[53] T. Sekikawa, A. Kosuge, T. Kanai and S. Watanabe, Nature 432, 605 (2004). W. Hanke and I. J. Sham, Phys. Rev. B 21, 4656 (1980).

[54] S. Albrecht, L. Reining, R. Del Sole and G. Onida, Phys. Rev. Lett. 80, 4510 (1998).

[55] F. Sottile , V. Olevano and L. Reining, Phys. Rev. Lett. 91, 56402 (2003).

[56] S. Bergfeld and W. Daum, Phys. Rev. Lett. 90, 036801 (2003).

[57] E. K. Chang, E. L. Shirley, and Z. H. Levine, Phys. Rev. B 65, 035205 (2002).

[58] R. Leitsmann, W. G. Schmidt, P. H. Hahn and F. Bechstedt, Phys. Rev. B 71, 195209 (2005).

[59] J. Stohr "Nexafs Spectroscopy", Springer (Berlin) 1996.

[60] A. L'Huillier and Ph. Balcou, Phys. Rev. Letters 70, 774 (1993).

[61] P. Corkum, Phys. Rev. Lett. 71, 1994 (1993).

[62] M. Hentschel, R. Kienberger, Ch. Spielmann, G. A. Reider, N. Milosevic, T. Brabec, P. Corkum, U. Heinzmann, M. Drescher, and F. Krausz, Nature 414, 509 (2001).

[63] G. Sansone, E. Benedetti, J.-P. Caumes, S. Stagira, C. Vozzi, M. Pascolini, L. Poletto, P. Villoresi, S. De Silvestri, and M. Nisoli, Phys. Rev. Lett. 94, 193903 (2005).

[64] N. Mahne, S. Nannarone, A.M.Malvezzi, ELETTRA User Meeting, Trieste (2004).

[65] Alexander A. Zholents and William M. Fawley , "Proposal for Intense Attosecond Radiation from an X-Ray Free-Electron-Laser," Phys. Rev. Lett.., V. 92, Number 22, 4 June 2004.

[66] Murname M.M., Kapteyn H.C., Falcone R.W., Appl. Phys. Lett., vol 56,nr 20, pp. 1948-1950 (1990).

[67] C. Belzile, J.C. Kieffer, C.Y. Cote, T. Oksenhendler, D. Kaplan, Rev. Sci. Instr., vol. 62, iss. 3, pp. 1617-1620 (March 2002).

[68] P. Villoresi, Appl. Opt. 38, 6040 (1999).

[69] L. Poletto et al, Appl. Phys. B 78, 1009 (2004).

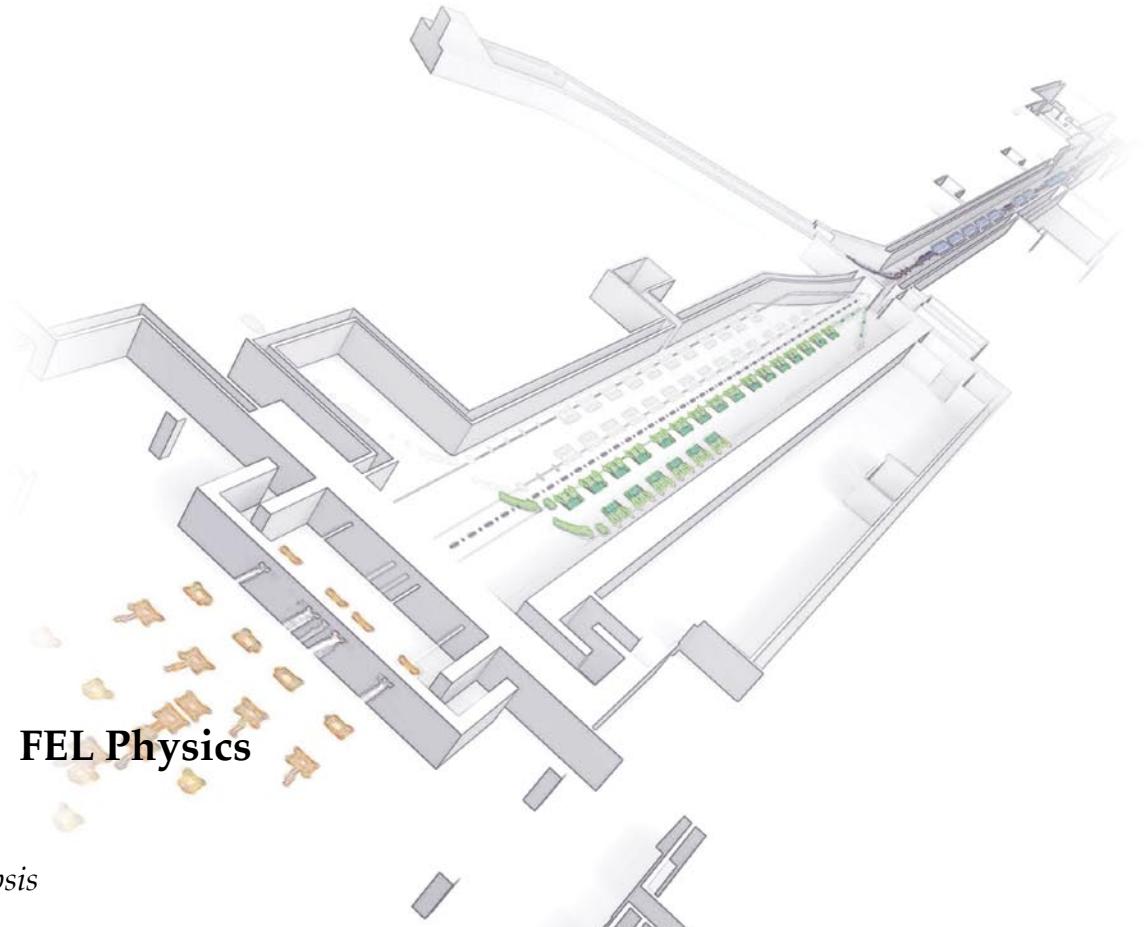

4 FEL Physics

Synopsis

The FERMI@Elettra project is based on the harmonic up-shifting of an initial "seed" signal in a single-pass FEL amplifier employing multiple undulators. The basic principles which underlie this approach are: the energy modulation of the electron beam via the resonant interaction with an external laser seed in a first undulator (modulator); the use of a chromatic dispersive section to then develop a strong density modulation with large harmonic overtones; the production of coherent radiation by the microbunched beam in a downstream undulator (radiator). The first stage of the project, FEL-1, will generate coherent output radiation in the 40-100 nm spectral range. For these wavelengths, users require short (<100 fs) pulses with adjustable polarization and high temporal and spatial reproducibility. FEL-1 relies upon a single-stage, harmonic generation scheme (i.e., modulator-dispersive section-radiator), like the one already operational at Brookhaven [1,2].

The project's second stage, FEL-2, extends the spectral range to 10 nm. Present user requirements include narrow-bandwidth pulses with high peak brilliance and adjustable polarization. For FEL-2, a two-stage harmonic cascade is needed to reach short wavelengths. The selected configuration is based on the so-called "fresh bunch" approach [3], in which the output from the first radiator energy modulates (in a subsequent modulator) a part of the electron beam that did not interact with the external seed. If at the time FEL-1 becomes operational a suitable seed laser source (using harmonic generation in gas) is available at ~ 40 nm, then FEL-2 could be operate with a single up-shift in frequency as in FEL-1 thus eliminating the harmonic cascade. Design choices for FEL-2 do not preclude this attractive possibility.

For the first modulator, which must satisfy FEL resonance over a nominal wavelength range of 240 to 360 nm, the undulator wavelength, λ_w, selected is 160 mm. For the second stage modulator of FEL-2, the adopted λ_w is 65 mm, matching that of the first stage radiator. The choice of λ_w for the radiators is driven by two principal requirements: (1) the FEL resonance be physically possible at the maximum output wavelength (*i.e.*, 100 nm for FEL-1 and 40 nm for FEL-2) for beam energies of 1.2 GeV; (2) there be sufficient gain (*i.e.*, $a_w \geq 1$, a_w being the normalized rms undulator magnetic strength) at the shortest desired output wavelength. To deliver output radiation with a polarization that is continuously tunable from linear to circular polarizations, the final radiators have an APPLE configuration. Wavelength tuning will be done by changing the undulator gap (and thus a_w) rather than by changing the electron beam energy. As the coupling between the radiation and the electron beam can depend strongly upon beam radius, the FERMI design includes external quadrupole focusing to produce an average value of 10 m for the Twiss beta function in each plane.

Of major concern are variations in beam characteristics affect the shot-to-shot repeatability of the FEL output. The most sensitive parameter is the initial electron beam energy. A critical quantity affecting the requisite electron beam duration is the timing jitter of the beam relative to that of the seed laser. An electron beam pulse of at least 600 fs is needed for 100 fs seed pulses. This timing jitter is one of the most demanding requirements on the injector and accelerator subsystems.

Adopting slightly off-optimum parameters (with respect to output power) lessens the sensitivity of the FEL performance. As the final design of FEL-2 will be modified based on FEL-1 performance, present calculations are representative rather than fully consistent design sets. For both FEL-1 and FEL-2, calculations based on time-steady input parameters and full start-to-end time-dependent simulations were performed using the 3D numerical codes Genesis [4] and Ginger [5]. Wakefields from surface roughness of the beam pipe in the undulator are seen to yield values that are much smaller than the fundamental FEL parameter and much smaller than the energy jitter from all sources (~0.09%). Consequently this phenomenon should have minimal effect on the output power or effective bandwidth of the FELs.

4.1 Introduction

The FERMI@Elettra project is based on the principle of harmonic up-conversion of an initial "seed" signal in a single pass, FEL amplifier employing multiple undulators. The basic principles which underlie this approach to obtaining short wavelength output are: the energy modulation of the electron beam via the resonant interaction with an external laser seed in a first undulator (called "modulator"); the use of a chromatic dispersive section to then develop a strong density modulation with large harmonic overtones; the production of coherent radiation by the micro-bunched beam in a downstream undulator (called "radiator"). In the following, each of these elements is discussed in turn.

An external laser provides an initial, wavelength-tunable seed signal. This signal, in conjunction with the magnetic field generated by the modulator, produces a relatively strong energy modulation $\Delta\gamma$ of the beam electrons via resonant interaction. The modulation has a sinusoidal variation in time identical to that of the seed's angular frequency, ω_0 ($=2\pi c/\lambda_0$, where λ_0 is the seed wavelength). When the modulator's length is comparable to or shorter than the exponential gain length for FEL radiation power *and* when the number of undulator periods obeys the relation $2N_u (\Delta\gamma/\gamma_0) < 1$, very little accompanying density modulation (*i.e.*, micro-bunching) is produced in the modulator.

Following its exit from the modulator, the electron beam then passes through a chromatic dispersion section in which a density modulation develops from path length differences associated with the energy modulation. So long as $\Delta\gamma >> \sigma_\gamma$, where σ_γ is the initial "incoherent" slice energy spread, a strong periodic density modulation is created at wavelength λ_0 containing large higher harmonic components (up to harmonic number $m \sim \Delta\gamma/\sigma_\gamma$). Note that at a given longitudinal position in the electron beam, the relative spread in the induced $\Delta\gamma$ must also be quite small or else the density modulation will be degraded, especially at higher harmonics. Consequently, the transverse extent of the seed laser (assumed to be characterized by a Gaussian-like transverse profile) should be significantly greater than that of the electron beam.

At this point the electron beam enters the radiator, whose wavelength and magnetic strength are tuned such that the FEL resonance occurs at an integral harmonic m of the original seed laser wavelength:

$$\lambda_R = \frac{\lambda_0}{m} = \frac{\lambda_u}{2\gamma^2}\left(1 + a_w^2\right) \qquad 4.1.1$$

where a_w is the normalized rms undulator magnetic strength. For FERMI, m varies between 3 and 6 for the first radiator. If, as in FEL-1, this radiator is the final undulator, it generally is made sufficiently long for the FEL radiation to grow to saturation (or even longer via tapering if greater output power is sought).

For a multistage harmonic cascade such as FEL-2, the first radiator is generally much shorter than that necessary for power saturation. In the so-called "fresh bunch" approach, the duration of the electron bunch is several times longer than the duration of the seed laser pulse. In that case radiation from the first radiator is used to energy-modulate part of the electron beam in a subsequent modulator, the first radiator is made only long enough that the radiation is sufficient to produce adequate downstream energy modulation. The emitted radiation is effectively coherent spontaneous emission, whose power scales as the square of the product of the current and the longitudinal distance inside the undulator (ignoring diffraction and debunching effects). Following the first radiator is a section (essentially a chicane) that temporally delays the electron beam in order to make the output radiation temporally coincident with a "fresh" section of the electron beam closer to the beam head. This fresh section of the bunch has not had its incoherent energy spread increased via FEL interaction in the first stage modulator and radiator. Thus, it can be far more easily energy- and density-modulated in the second stage undulators than the "used" electron beam section that interacted with the seed laser pulse in the first modulator and radiator.

The second stage for the fresh bunch approach consists of a modulator, a final radiator, and, in general, an intervening dispersive section. The modulator uses the radiation from the first stage radiator as its seed radiation; it must therefore have its undulator period and magnetic strength tuned to be resonant at that same wavelength. Since the radiation diffracts freely once it departs the first radiator, care must be taken 1) that the temporal delay section is not too long and 2) that the necessary second modulator length does not exceed the Rayleigh length. Otherwise, the coupling between the radiation and the electron beam may be too weak for sufficient energy modulation to develop. The second stage modulator, radiator, and intervening dispersive section are quite similar in concept to the first stage. In general, the harmonic upshift factor between the second stage modulator and radiator is 4 or less for the FERMI case. Moreover, the amount of microbunching at the new harmonic in the second radiator is also generally less than half that produced in the first stage because both the undulator parameter a_w and the initial radiation intensity are smaller.

This combination generally leads to a smaller energy modulation at the end of the second modulator. The second stage radiator is usually much longer than that of the first stage both because the initial bunching is normally smaller and because the FEL is normally run to saturation (which requires more distance because the corresponding exponential gain lengths are longer due to the smaller a_w). The process of light emission in the final radiator includes at first quadratic part (as in the first stage and in single-stage FEL-1 configuration) and then an exponential growth regime. This it is similar to the classic HGHG scheme of Yu.

4.2 Basic FEL Output Requirements and Related Issues

The baseline FEL output requirements for FEL-1 and FEL-2 are summarized in Table 4.2.1. At all wavelengths, both FEL-1 and FEL-2 are to have continuously tunable output polarization ranging from linear-horizontal to circular to linear-vertical. Consequently, the FEL-1 radiator and final radiator in FEL-2 have an APPLE configuration. Both FELs will operate at 10-50 Hz; this specification is constrained by the accelerator (see chapter 6) and not by the FEL subsystems.

Present scientific proposals for the application of FEL-1 involve time-domain experiments such as pump-probe interactions and possibly nonlinear phenomena. Consequently, the requirements for FEL-1 are more related to total photon number per pulse (*i.e.*, $0.4 - 2 \times 10^{14}$) and pulse duration (20-100 fs) than they are to spectral bandwidth. A critical parameter affecting the requisite electron beam duration is the timing jitter of the beam relative to that of the seed laser. In order to assure sufficient overlap between the seed and the electrons, the duration of the electron bunch must be longer than the duration of the seed pulse plus two times the rms timing jitter. If the expected rms timing jitter from the accelerator is of order 150 fs (see Chapter 6), an electron bunch duration of at least 600 fs is needed for 100 fs seed pulses. This timing jitter is one of the most demanding requirements on the injector and accelerator subsystems.

Another important parameter associated with FEL-1 time domain experiments is shot-to-shot repeatability. Ideally, for nonlinear phenomena experiments, the shot-to-shot rms jitter in normalized photon number should be 5% or less. As explained in Section 4.4, such a low value seems unlikely with the presently expected accelerator and injector parameters. A large class of FEL-1 experiments can tolerate values as high as 25% by recording the shot-by-shot photon number for post-processing. Other FEL-1 output specifications related to jitter parameters are: pointing, virtual waist location and angular divergence jitter, shot-to-shot transverse profile changes. Although none of these is likely on an individual basis to prevent FERMI from successfully reaching the goal of 5% (spatially) local intensity fluctuations at the experimental sample, taken together they will likely produce jitter exceeding this goal even in the absence of fluctuations in photon number. Notably, some experiments (*e.g.*, those using gaseous samples) may be insensitive to pointing or profile changes. In the operation of FEL-1, the wavelength jitter should be less than the individual shot bandwidth in order to not increase the effective time-averaged, output bandwidth as seen by the user.

In contrast to FEL-1, in which timing and photon number jitter are critical parameters, most FEL-2 users are (presently) interested in frequency domain experiments in which longitudinal coherence and narrow bandwidth are most important. The most important output goal for FEL-2 is $\geq 10^{12}$ photons/pulse/meV. Consequently, FEL-2 specifications favour long output pulses (≥ 1 ps) whose spectral properties (ΔE_ω < 10 meV) are as close as possible to the transform limit. Although the total photon jitter is not critical for most experiments in the frequency domain, shot-to-shot central wavelength jitter during

Table 4.2.1: FEL-1 and FEL-2 expected performance.

Parameter	*FEL-1*	*FEL-2*
Wavelength range [nm]	100 to 40	40 to 10
Output pulse length (rms) [fs]	≤ 100	> 200
Bandwidth (rms) [meV]	17 (at 40 nm)	5 (at 10 nm)
Polarization	Variable	Variable
Repetition rate [Hz]	50	50
Peak power [GW]	1 to >5	0.5 to 1
Harmonic peak power (% of fundamental)	~ 2	~ 0.2 (at 10 nm)
Photons per pulse	10^{14} (at 40 nm)	10^{12} (at 10 nm)
Pulse-to-pulse stability	≤ 30 %	~50 %
Pointing stability [μrad]	< 20	< 20
Virtual waist size [μm]	250 (at 40 nm)	120
Divergence (rms, intensity) [μrad]	50 (at 40 nm)	15 (at 10 nm)

narrow bandwidth operation may be of concern unless the bandwidth can be maintained at or below the required spectral resolution (~5 meV).

For some experiments (such as RIXS where one is examining a small inelastic scattering cross-section in the presence of a much larger elastic scattering cross-section), a spectral resolution of 10^5 requires that the integrated noise photon level (at the detector) be less than 1 part in 10^5 of the wanted signal. Without spectral filtering, this requirement could be more severe than that of rms bandwidth. For example, if the integrated noise power is 1 part in 10^4 but has a bandwidth 100 times greater than the main signal, the total (signal + noise) rms bandwidth increases by only ~40% from that of the signal, but the unfiltered spectral resolution would still miss the 10^5 criterion by a factor of ten.

A multi-stage harmonic cascade is more sensitive to energy spread than SASE because of the very non-linear process leading to harmonic micro-bunching at the seed frequency. A very sharp limit in fact exists on the tolerable bunch energy spread.

Furthermore, because in multi-stage operation the first stage output radiation power scales quadratically with bunch current, the end output power also drops sharply as the bunch current is lowered below design. Should one rely upon strong exponential gain in the final radiator the output power would also be very sensitive to the beam current.

4.3 Undulator and Transport Lattice Design

4.3.1 Choice of Undulator Type and Wavelength

Due to the requirement that the output radiation polarization be continuously tunable from linear to circular, the FERMI project has chosen the APPLE configuration for the final radiators (FEL-1 radiator and FEL-2 second stage radiator). For the initial modulator, a simple, linearly-polarized configuration is optimal both due to its simplicity and because the input radiation seed can be linearly polarized. As the short first modulator produces little if any gain, there is little cost or space advantage in using a circular polarization for which the electron beam/radiation coupling is somewhat better. For the case of the first stage radiator and second stage modulator (for the fresh bunch approach), FEL-2, will use linearly-polarized undulators, because of their simplicity and lower cost. If for whatever reasons (*e.g.*, suppression of higher harmonic emission) circular polarization is required, such a design change could be made without requiring greater undulator length.

Wavelength tuning in the undulators will be done by changing the gap (and thus a_w) rather than by changing the electron beam energy. Hence, the maximum wavelength reachable for a given fixed beam energy is set by the magnetic field at the undulator pole tips, the minimum gap obtainable, and the undulator wavelength. These considerations strongly constrain the available parameter space, especially for FEL-1.

For the first modulator, which must satisfy FEL resonance over a nominal wavelength range of 240 to 360 nm, the undulator wavelength selected is 160 mm. For the second stage modulator of FEL-2, the adopted undulator wavelength of 65 mm agrees with that chosen for the first stage radiator (see the discussion in the next paragraph). The choice of undulator wavelength for the radiators is driven by two principal requirements: (1) the FEL resonance be physically possible at the longest desired output wavelength (*i.e.*, 100 nm for FEL-1 and 40 nm for FEL-2) at an electron beam energy of 1.2 GeV; (2) there be reasonable gain (*i.e.*, $a_w \geq 1$) at the shortest desired output wavelength. The first requirement drives one to small gaps (for large a_w) and longer wavelengths. The second requirement pushes one to shorter wavelengths (but as λ_u decreases, the maximum possible a_w for a given gap opening begins to decrease exponentially making the first requirement becomes difficult to meet). The present design choice is a minimum gap opening of 10 mm; this value allows for an 8 mm "stay clear", a 1 mm pipe thickness, and 1 mm clearance. With all this in mind, a 65 mm wavelength was chosen for the FEL-1 radiator and first FEL-2 radiator and a 50 mm wavelength for the final FEL-2 radiator.

4.3.2 Undulator Segmentation and Focusing Issues

In order to produce high powers, the active radiator lengths for FEL-1 and FEL-2 are in the range 15-30 m – far too long to be practical as one continuous magnetic structure. Consequently, the radiators will be subdivided into modules, each consisting of an active segment of undulator and a drift section with containing elements such as quadrupoles, a longitudinal phase shifter, beam position monitors, dipole correctors, and diagnostics. Tentatively, ~1.0 m is allowed for the end drift sections; the exact distance will be determined on the basis of detailed engineering. In order to keep the fraction of space occupied by the active magnetic segment reasonable (i.e., ≥0.5), lengths of 2.34 m (= 36 periods) for the FEL-1 and first FEL-2 radiators, and 2.40 m (= 48 periods) for the second FEL-2 radiator have been chosen. These "active", full strength lengths do not include the 2-3 poles at the beginning and end of each segment of

undulator needed for adiabatic matching. While longer undulator segments are permitted by magnetic force considerations, the desire for a Twiss beta function of ~7-10 m limits the total module length to ~ 3.5 m.

The coupling between the radiation and the electron beam can depend strongly upon the beam radius. As the FEL radiation emissivity scales directly with the electron beam density, there is a premium for minimizing the beam radius. However, reducing the electron beam radius increases the spread of transverse velocities (due to emittance). Diffraction (which spreads the radiation) can reduce the coupling despite the larger current density. Consequently, for a given emittance and radiation wavelength, there is an optimum electron beam radius for maximizing energy extraction. For FERMI, this radius is generally in the vicinity of 100 microns. For normalized electron beam emittance of ~1.5 mm-mrad, this radius is much smaller than that obtainable with the natural focusing of the undulator. Consequently, our design includes external quadrupole focusing to produce an average value of 10 m for the Twiss beta function in each plane.

The external quadrupoles also compensate for changes in natural undulator focusing 1) since a_w is being changed when varying the output wavelength, and 2) at a fixed wavelength, whenever the undulator polarization is changed (*e.g.*, from vertical to circular). For APPLE-type undulators the focusing for circular and vertical polarization can be negative (i.e., defocusing) in the *x*-plane; for long undulators such as the final radiator in FEL-2, this defocusing must be compensated for by external focusing. Thus, the FERMI control system must actively modify the quadrupole strengths whenever non-negligible changes are made in the undulator gaps and/or polarizations.

The decision to tune output wavelengths by changing the undulator gaps (i.e., a_w values) implies active control of the longitudinal phase slip between the electron beam and radiation in the drifts between undulator sections. The phase advance in a simple drift section of length L_B, $\Delta\theta = k_w L_B / \left(1 + a_w^2\right)$, is not necessarily a multiple of 2π as one varies the FEL wavelength λ_s (and thus a_w). Consequently, a very weak magnetic chicane (strength $R_{56} \sim 2\lambda_s$) is needed to act as a "phase shifter" in the drift section. The initial estimate is that that ~200 mm of longitudinal space will be needed for this element.

4.3.3 Undulator Error Tolerance Calculation

Apart from electron beam errors such as offset, tilt, and mismatch, other errors are possible within the undulator. These include: 1) tilt and offsets of entire segments of undulator, 2) "global" segment mistuning errors such that the average a_w is offset by a constant amount within each segment (e.g. due to an incorrect gap setting), 3) "local" undulator errors due to individual pole strength errors. Local errors can lead both to longitudinal phase errors between the electron beam and the FEL radiation and to the electron beam wandering away from the central axis of undulator and radiation.

To lowest order, tilt and offset in the undulator are equivalent to errors (equal and opposite in value) in the initial electron beam position and tilt. Sensitivity to such errors is discussed in Section 4.4.2. In a multi-segment undulator, the effect of these errors could, in a statistical sense, grow as $\sqrt{N}$ where N is the number of segments. Hence, if the overall tolerable tilt and offset values are, say, Y, then the equivalent rms tolerances on individual segments might need to be reduced to $Y/\sqrt{N}$. However, with active dipole correctors between segments this estimate may be unduly pessimistic.

"Global" mistuning of segments will lead to a longitudinal phase error that grows with distance along the undulator. If this error becomes comparable to π/2 radians, there can be significant loss of FEL gain.

In contrast, smaller scale errors in some circumstances can lead to higher radiation power than obtainable from a constant a_w undulator. This effect appears due to a serendipitous tapering which extracts more power. A rough criterion for the rms accuracy of setting a_w (equivalently the gap opening) in the FEL-1 radiator and the final radiator of FEL-2, was obtained from a series of GINGER runs in which random mistunings with a given rms expectation value were applied to each individual radiator segment. For FEL-1 at 40-nm output wavelength, the results (see Figure 4.3.1 left) show that on average, the rms segment mistuning error in a_w must exceed 0.002 before the output power begins to drop more than a few percent. This constraint appears be relatively easy to meet for the FERMI undulators. For FEL-2, the results (see Figure 4.3.1 right) are quite similar with rms errors below 0.002 showing essentially no effect on the average output power at 10-nm with the standard deviation remaining less than 10%.

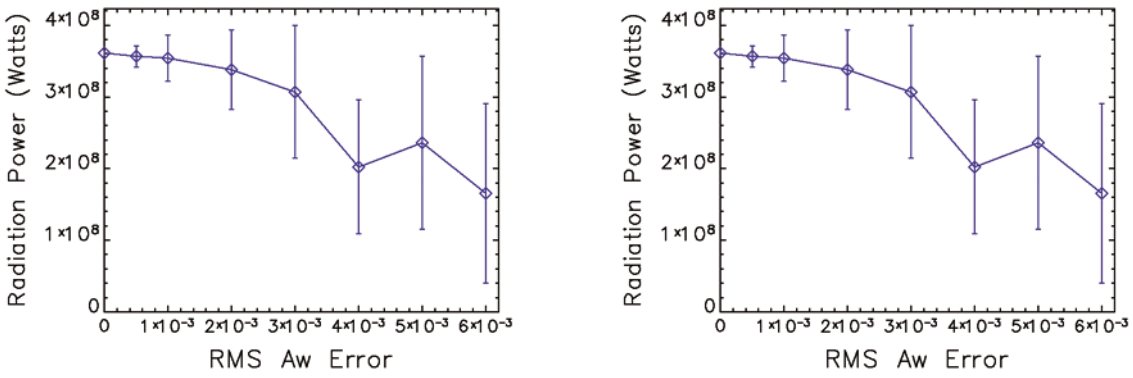

Figure 4.3.1:
Left: Output radiation power at 40-nm from FEL-1 in the presence of random segment of undulator mistuning as a function of rms error in aw. The diamond symbol and error bars refer to the mean and standard deviation over 64 independent mistunings. The distribution of errors at individual segments follows a one-dimensional Gaussian. Right: Output radiation power at 10-nm from FEL-2 (fresh bunch approach). The diamond symbol and error bars refer to the mean and standard deviation over 25 independent mistunings. The distribution of errors at individual segments follows a one-dimensional Gaussian.

Within each undulator period, the two individual pole errors of one undulator period are decomposed into an "even" component which leads to no net transverse kick but does induce a phase error through a net change in a_w, and an "odd" component that produces a net transverse kick on the beam. This odd component causes the electron beam both to wander off-axis and also to suffer a net phase error. In the absence of any correction, the beam-wander increases steadily with z, as does the longitudinal phase error.

In the actual physical situation, for a given sorting of the individual poles within a given segment of undulator, the strength errors are "frozen" (i.e., do not vary in time) and may therefore be corrected in an average sense in *z* by the insertion of dipole shims. With "virtual" shims implemented in the XWIGERR code, time independent GINGER calculations were performed to determine output power sensitivity to undulator pole strength errors for FEL-1 at 40-nm and FEL-2 at 10-nm (fresh bunch approach) [3].

Results show a relatively tight correlation between the residual phase error and the output power. For FEL-1, virtually no power is lost for residual phase errors below 0.2 radians; for FEL-2 at 10-nm the equivalent value is 0.15 radians. The correlations are less for tilt and offset residuals. For FEL-1, little power is lost for <20-micron offsets and 50-microradian tilts; for FEL-2 the equivalent numbers are ~10 microns and 25 microradians. These values constitute system requirements for the FEL undulator.

4.3.4 Post-Modulator Dispersive Section Design and Issues

Following each modulator a dispersive magnetic chicane produces a strong coherent micro-bunching from the energy modulation impressed upon the electron beam by the FEL interaction in the modulator. For reasonably large input seed powers (e.g. ≥ 10 MW) and short wavelengths ($\lambda_0 \leq 300$ nm), the necessary R_{56} dispersion parameter is ~100 μm or less in the first stage modulator. For the fresh bunch approach, the second stage dispersive element is typically 5 times smaller. Preliminary design of the dispersive sections reveals no significant engineering or space issues. Detailed analysis is still required to set limits for higher order optical terms, such as could be induced by fringe fields and/or geometric aberrations. However, no practical problems are expected given the allowed longitudinal space of ~30 m and the relatively large seed wavelength. The actual design of the dipole elements of this chicane could introduce a transverse focusing effect that will be properly modelled with the FEL simulation codes.

4.3.5 Delay Section Needs and Issues for FEL-2 Fresh-Bunch Approach

In the fresh bunch approach to FEL-2, the e-beam must be delayed by ~0.5 – 1.0 ps relative to the FEL radiation in order that a "fresh" section of the e-beam be energy-modulated in the second stage modulator. A 1-ps delay is equivalent to an R_{56} of 600 μm. Inasmuch as the radiation field carries the "imprinting" signal, the allowed longitudinal space of ~1.8 m is more than adequate to contain the needed chicane. The delay section must also contain various diagnostics and at least a quadrupole singlet (and possibly doublet) for matching the e-beam to the second stage optics. FEL simulations of this section include diffractive effects.

4.4 FEL-1 Design and Parameters Calculations

The nominal design parameters of FEL-1 are presented in Table 4.4.1.

Table 4.4.1: Nominal design value and presumed rms jitter for FEL-1 parameter.

Input Seed Laser	
Power [MW]	100
Wavelength [nm]	240 - 300
Waist size [microns]	300
Input Electron Beam	
Energy [GeV]	1.2
Current [A]	800
Rms energy spread [keV]	150
Rms emittance [mm-mrad]	1.5
Modulator Undulator	
Period [m]	0.16
Length [m]	3.04
Number of periods	19
Radiator Undulator	
Period [m]	0.065
Section length [m]	2.34
End drift length [m]	1.04
Number of sections	6
Total length [m]	20.28
FEL parameter ρ	2.9×10^{-3}

As most user proposals for FEL-1 concern ultra-fast, pump-probe and other time-domain phenomena, the relevant electron beam characteristics are those of the "medium bunch" option for which the main body current is ~800 A; the flat-top duration is ~700 fs (which allows for timing jitter); the total charge is ~0.7 nC, and the incoherent energy spread is 150 keV. For FEL-1, the output power is relatively insensitive to the actual value of the energy spread so long as the input laser power and modulator

length can produce a coherent energy modulation ΔE an order of magnitude greater than σ_E. A nominal laser power of 100 MW has been adopted; lower values would require increasing the modulator length beyond the ~3 m used here. The laser beam comes to a focus halfway in the modulator with a rms waist size of 300 μm. This value is significantly greater than the electron beam transverse size so as to minimize the induced incoherent energy spread.

Figure 4.4.1 shows the undulator layout for FEL-1 that includes a modulator, dispersive chicane, and the radiator sections consisting of active undulators and end drifts.

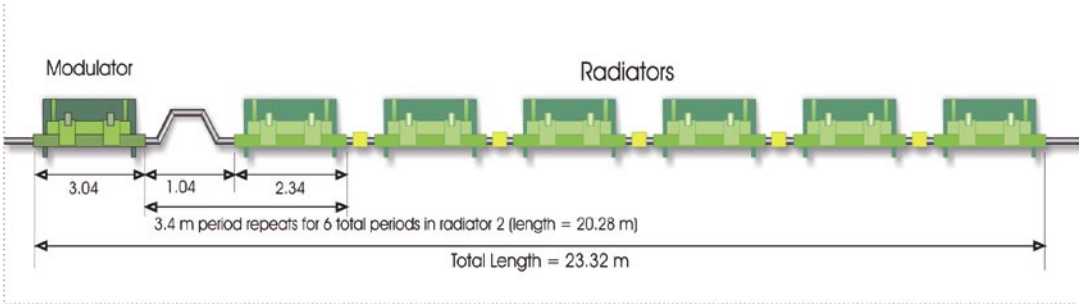

Figure 4.4.1:
Nominal undulator layout for FEL-1. The radiator consists of 6 sections, each 2.34 m long separated by 1.04 m drifts containing a focusing quadrupole, phase corrector, and diagnostics. Between the modulator and radiator is a dispersive section whose purpose is to convert energy modulation into strong microbunching.

The electron beam and seed laser enter from the left. The drift length between the modulator exit and radiator entrance, and between the individual radiator sections, is 1.04 m including the space associated with the partial strength poles at entrance and exit. At the modulator exit, the peak-to-peak energy modulation, 2ΔE, is ~4 MV and the rms energy spread is ~1 MV. A simple scaling argument ($R_{56} \times \Delta E/E = \lambda_{MOD}/4$) suggests that the necessary R_{56} is about 35 microns, close to the design value.

For purposes of FEL gain simulations, each radiator undulator section is 2.34-m long and is composed 16 full-strength 6.5 cm periods. Two periods or fewer are required for adiabatic transition to and from each end drift, resulting in a physically usable drift section length of 0.84 m. In the calculations, each drift section includes a "perfect" phase shifter that ensures the longitudinal phase slippage in the drift is an exact multiple of 2π. Since photon number is a critical parameter for FEL-1, the nominal layout includes sufficient sections (6) in the final radiator to ensure power saturation at the shortest design wavelength (40 nm), although as few as three sections are necessary for saturation at 100-nm wavelength.

The general procedure for optimizing the undulator parameters for each wavelength was as follows. The normalized modulator strength a_w (= $K/\sqrt{2}$ for a linearly-polarized undulator) was set to the nominal FEL resonance value. Then the radiator performance was optimized with respect to values of the dispersion parameter R_{56} and a_w. Figure 4.4.2 displays the growth of power and coherent micro-bunching at 40-, 60-, and 100-nm wavelengths as predicted by the GENESIS and GINGER codes for the parameters of Table 4.4.1.

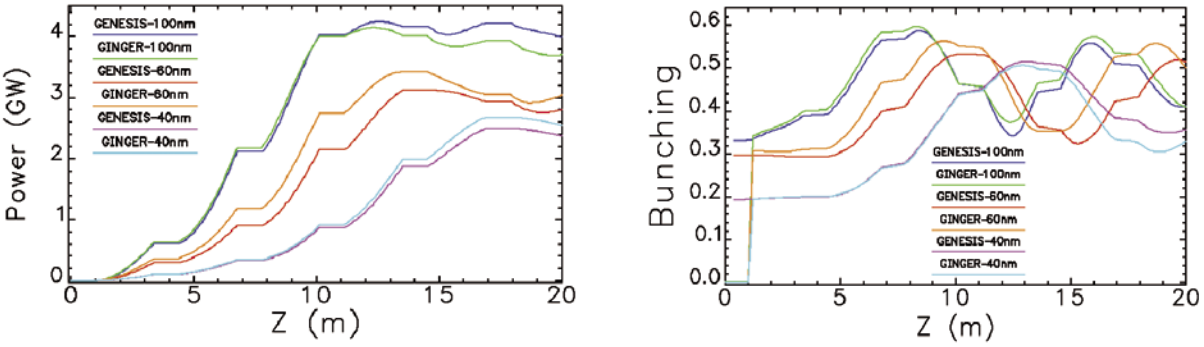

Figure 4.4.2:
GENESIS and GINGER results for radiation power and microbunching fraction for FEL-1 at 100-, 60-, and 40-nm wavelengths.

At the longer wavelengths power and bunching saturation was reached well before the end of the sixth section. The figure also shows good basic agreement between the GENESIS and GINGER predictions. The peak power of 2.5 GW at 40 nm corresponds to an extraction efficiency of 0.26%, quite close to the 3D FEL parameter of 2.9×10^{-3}. That parameter is likely to be an overestimate because the Ming Xie fitting formula [6] does not allow for the 1-m drift sections. The output power can be doubled by properly tapering the six radiator segments.

4.4.1 Sensitivity to Jitter of Input Parameters: Time-Independent Simulation Results

To estimate the sensitivity of output power to electron beam and laser parameters, extensive GENESIS and GINGER simulations were performed varying parameters one at a time. The studies described in this section are limited to axisymmetric effects for both the electron beam and input laser. Section 4.4.2 discusses sensitivity to non-axisymmetric effects such as an input transverse offset or tilt of the entering electron beam. Each individual beam or seed parameter was varied around a central value for the "medium bunch" case, as shown in Table 4.4.1. The calculations were done in the "time-independent" or "time-steady" limit in which all properties of a time-varying electron and laser pulse are replaced by a single, representative value. This approximation models performance with just a single longitudinal "slice," thus dramatically reducing computational time. To estimate the expected shot-to-shot jitter in the output power and photon number of FEL-1 at 40 nm (i.e., the wavelength with the greatest sensitivity), time-independent calculations were performed in which the input laser seed power and various electron beam quantities were varied independently around their individual design values following a tolerance budget summarized in Table 4.4.2.

Two sets of calculations were done for FEL-1. First, fluctuations of only a single parameter were considered. For each electron beam parameter (*e.g.*, energy, current, *etc.*), a Gaussian distribution of 50 parameter values was generated with the appropriate standard deviation (Table 4.4.2).

Table 4.4.2: Adopted Shot-to-Shot Variation Budget.

Parameter	*Normalized shot-to-shot variation*
Emittance	10%
Peak current	8%
Mean energy	0.10%
Energy spread	10%
Seed power	5%

Each value was used in different GINGER simulation runs to initialize the electron beam (or input seed laser). Then, a second set of calculations was done with simultaneous, multi-parameter jitters; a set of 400 parameter values were created in which each and every beam parameter was randomly varied following the appropriate Gaussian distribution. These runs produced the data for the curves of Figure 4.4.3, where, as an example, only sensitivity to energy and current fluctuations are reported.

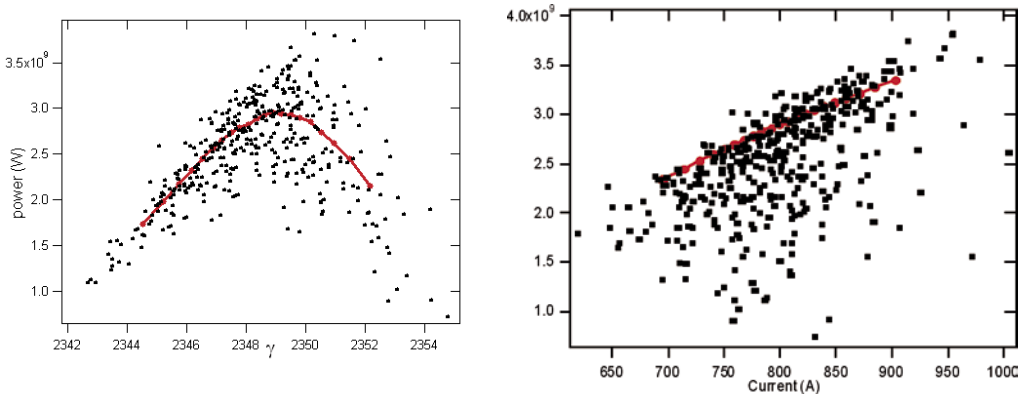

Figure 4.4.3:
Left: FEL output power as a function of electron beam energy in the case of a single parameter only (curve) and multiparameter (dots) variation. Right: FEL output power as a function of beam current in the case of a single parameter only (curve) and multiparameter (dots) variation.

First, the effect of a jitter only in the mean electron energy was considered based on a Gaussian distribution with a normalized rms of 0.1% – the design goal for beam energy at the end of the linac (see Chapter 6). The single parameter sensitivity scans show that energy plays a crucial role in the FEL performance of FERMI. The multiparameter results (see Figure 4.4.3 left) of output power vs. beam energy, although they show scatter due to the other parameters fluctuations, remain very well correlated to the electron energy variation.

For the case of current jitter (see Figure 4.4.3 right), the output power grows monotonically with increasing current. As was true for the electron beam energy, one sees a clear correlation between multi-parameter jitter output power and the input electron beam current. For the adopted central design point, FEL-1 shows little sensitivity to the electron beam incoherent energy spread, emittance and seed laser power (data not shown). The overall (multi-parameter) estimated fluctuation in output power is about 22%.

One possible way to reduce the sensitivity of the FEL-1 output power to the mean electron energy is to enlarge the effective energy bandwidth of the radiator by using different a_w values in different undulator sections of the radiator. With this approach, electron bunches with mean energies slightly different from the nominal value will still encounter some section whose a_w is close to FEL resonance. To reduce sensitivity to the mean electron energy without simultaneously increasing sensitivity to electron beam current, a simple tapering configuration was investigated. Section by section, a_w was alternatively set to higher and lower values relative to a constant tapering along z. To lowest order, this type of variation favors neither higher nor lower beam energies (relative to the nominal value). For this new configuration the normalized standard deviation of the output power for the adopted energy jitter is less than 5%, and, more importantly, the power fluctuations are also reduced in the multi-parameter jitter case down to about 10%.

4.4.2 Input Transverse Tilt and Offset Sensitivity

Control of displacements and tilts of the electron beam is important to insure the performance of the FERMI FEL. Electron beam offsets can occur due to upstream pointing errors, undulator misalignments, or internal structure in the electron bunch arising from time-dependent linac wakefields, in which case they will also be sensitive to timing jitter. FEL performance in the presence of such offsets was modeled with the GENESIS code, because a fully three-dimensional field solver is necessary to capture all non-axisymmetric effects. Simulation studies included initial offsets for the electron beam only; the laser seed and undulators were assumed to lie along a common axis.

"Global" sensitivity studies simulating various types of jitter simultaneously – including jitter arising from initial tilt or offset – were performed at various wavelengths. The most prominent effect of electron beam offsets is a large drop in output power when the transverse overlap in the first undulator between the electron beam and input radiation seed decreases significantly. In addition, the FEL radiation beam develops offsets comparable to those of the electron beam. Investigation of the behavior of the output phase revealed that phase variations with longitudinal position can significally affect the spectral width of the output radiation. As was true for the jitter studies without offsets or tilts, the most significant source of shot-to-shot fluctuations is predicted to be jitter in the electron beam energy. However, when using expected values for fluctuations in the electron beam and laser seed power, simulations suggest that the combined effect of the jitter on the other FEL parameters are comparable in some cases to the effect of energy jitter. For the standard deviations chosen, i.e., 100 microns in position and 10 microradians in tilt, the predicted fluctuations in output power for untapered undulators (normalized standard deviations) are 13% at 100 nm, 24% at 60 nm, and 28% at 40 nm. Results for the 40-nm case are shown in Figure 4.4.4.

The output power from tapered undulators shows less sensitivity to jitter in the electron beam energy. Our studies also reveal correlations between beam parameter errors and output power. In addition to mistuning of a_w such that the nominal energy does not quite yield the optimal power (easily corrected

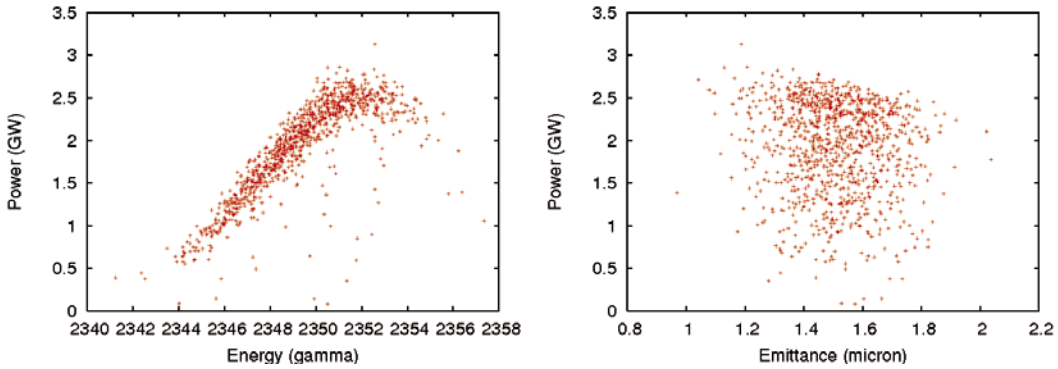

Figure 4.4.4:
Left: Output power versus energy at 40 nm with all input e-beam parameters and the laser seed power simultaneously varying as given in Table 4.4.2. Right: Output power versus emittance.

in practice), the only significant correlation is between the beam transverse emittance and the output power. Rather than reaching a local maximum at the nominal electron emittance, the performance improves significantly as emittance is decreased. The time-dependent jitter study discussed in Section 4.4.3.2 does include such correlations.

4.4.3 Time-Dependent Calculations

Complete "start-to-end" (S2E) simulations that begin at the emitting cathode and end at the undulator exit (for the electron beam) and/or the experimental sample (for the photons) are the most accurate means of estimating the performance sensitivity of an FEL. Extensive modelling of the injector and linac (see chapter 5) yielded so-called "golden" macroparticle files for input in the FEL simulations. Due to the relatively large temporal jitter (~350 fs) expected at the linac exit, a pulse shorter than 700 fs FWHM would lead to unacceptable (for use in pump-probe experiments) shot-to-shot fluctuations in output power as many seed pulses would fall temporally outside the electron beam pulse.

Both the GINGER and GENESIS FEL simulation codes were used to predict the full, time-dependent radiation output corresponding to these macroparticle "golden" files. In general, the FEL codes use a total number of macroparticles per time interval that is greater than that generally available from most ELEGANT output files. GENESIS solves this problem by using a special algorithm that creates, as needed, new macroparticles in the "empty" regions of 6D phase space between the ELEGANT macroparticles. GINGER uses a different algorithm with which to populate fully a given time slice; ELEGANT macroparticles from adjacent temporal regions are used with their 5D coordinates (x,x',y,y',γ) carefully interpolated in order to maintain their individual deviation from a coarse-grained average in time. In principle, both algorithms should maintain the local time-dependence of various higher order correlations (*e.g.*, $\langle xy' \rangle$, $\langle \gamma x' \rangle$, *etc.*).

For both codes, it was necessary to rematch the 4D phase space (x,x',y,y') to the FEL-1 undulator lattice. In FEL operation, rematching will be done by a series of dipoles and quadrupoles upstream of the

modulating undulator. Computationally the rematching was accomplished by determining the Twiss α and β in the central temporal regions of the ELEGANT files, computing the requisite transformation matrix to give the correct match, and then applying this matrix to all the macroparticles. This calculation uses only the temporally-central, "well-behaved" portion of the electron beam thereby neglecting any current spikes the head and/or tail regions with "abnormal" phase space properties.

Nearly all the FEL-1 time-dependent simulations were done at 40 nm for which FEL performance is most critical. The input radiation seed was taken to be either a Gaussian temporal profile pulse of 100 fs (FWHM) – appropriate for pump-probe experiments – or a constant intensity, flat-top pulse in which the laser fully covered the e-beam – appropriate for experiments in which maximum photon number but not timing synchronization is needed.

In all cases the seed beam has a Gaussian transverse intensity profile with a 210-micron waist occurring at the mid-point of the modulator. The simulations normally adopt a temporal slice spacing of either 0.8 fs (i.e., 240 nm) or 1.6 fs. After each modulator run, the particles arewritten out to disk. They are then read into the subsequent radiator run with the longitudinal phases (relative to a plane wave) multiplied by the harmonic upshift number, in this case 6 (= 240 nm/40 nm). However, the temporal spacing and resolution in the radiator runs remain the same (i.e., 0.8 fs). In other words, the macroparticles are not reorganized into independent 40-nm slices; rather, physical quantities such as current and microbunching fraction at 40-nm wavelength are effectively averaged over a 240-nm interval. So long as the normalized output spectral bandpass is small compared with 40 nm /240 nm = 1/6, this temporal resolution is more than adequate.

4.4.3.1 Expected Performance for the Nominal Working Point

A campaign of time-dependent start-to-end simulations was performed making use of various electron beam distributions provided appropriate to the gun and linac operation (see Chapter 6). Figure 4.4.5 shows the GENESIS-predicted output temporal and spectrum profiles at 40-nm wavelength for an optimized (i.e., flat in both energy and current) input electron beam distribution. The input seed was a 40-fs (rms) Gaussian at a peak power of 100 MW.

The output number of photons per pulse is about 1014 with ~80% in single transverse mode. The output pulse length is 54 fs rms and the relative spectral bandwidth 0.03%, about a factor of 2.2 above the transform limit

As reported in Chapter 6, wakefields arise from the interaction of the electromagnetic fields of the electron beam with the features of the vacuum chamber walls including breaks in the geometry of the

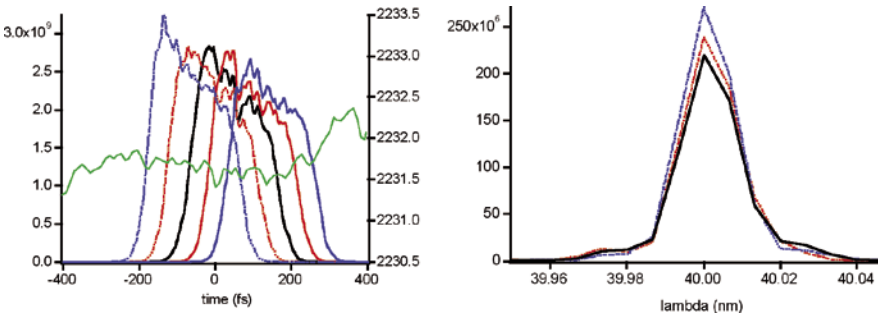

Figure 4.4.5:
Left: FEL-1 temporal profiles corresponding to different seed positions along the bunch (green trace, right vertical scale) resulting from a GINGER simulation in time-dependent mode (40 nm). Right: corresponding spectrum profiles.

beam pipe cross-section. Preliminary calculations were performed using a wakefield code based on a numerical physics package developed by H.-D. Nuhn at SLAC. This code currently includes effects from vacuum chamber resistivity, surface roughness, geometric breaks, and a "synchronous term." Calculations for FERMI assumed a high-aspect ratio, rectangular , Al vacuum pipe of 6.0-mm inner vertical height with a surface roughness of 100-nm amplitude with a longitudinal period of 25 microns. The geometric wake was calculated presuming a 10-cm break occurring every 3.4 meters. An "AC" conductivity model was used for the resistive wake.

With these choices, the resulting longitudinal wakefield is unlikely to degrade FEL-1 output. Apart from large spikes at the head and the tail of ~-60 kV/m amplitude, the wakes of the particle distribution (see Figure 4.4.6) have temporal variations of only 5 KV/m or less. As shown in Figure 4.4.6, a representative calculation of FEL output with and without wakefield effects included substantiates this assessment.

During the engineering design of the FERMI undulator and vacuum chamber, these wake calculations will be repeated to include more realistic roughness numbers and perhaps a non-circular geometry.

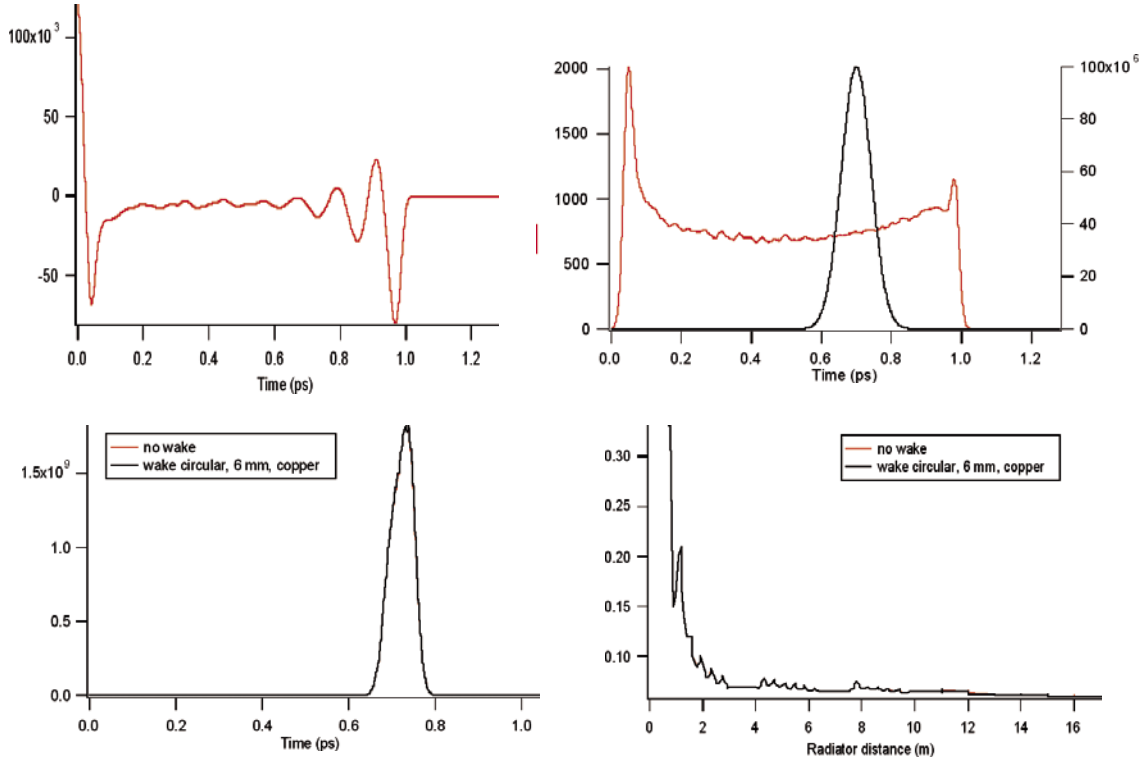

Figure 4.4.6:
Upper left: time-dependent longitudinal wake results for the "medium bunch" distribution (copper, circular cross section with diameter of 6 mm). Upper right: "medium bunch" current distribution (red curve) and temporal profile of superimposed seed pulse. Down left: temporal profile of the FEL-1 output power resulting from a Genesis simulation including (black curve) and neglecting (red curve) wake fields. Note that curves are practically overlapped. Down right: Bandwidth as a function of radiator distance (FEL-1) including (black curve) and neglecting (red curve) wake fields.

4.4.3.2 Sensitivity to Jitter of Input Parameters

To examine the effects of injector and accelerator jitters upon the shot-to-shot, time-resolved properties of the output FEL-1 radiation, 100 individual files of 1M macroparticles were propagated starting from the injector (GPT code) through the linac (Elegant code). Each file included the effects of random jitter in the individual injector and accelerator cell voltages. The jitter follows Gaussian distributions with variances set by the budget allowances allocated by the gun and linac groups. GINGER time-dependent simulations for the FEL-1 lattice tuned at 40 nm were performed over a large time window with high resolution. For each jittered file, simulations where done using artificial macroparticles created from the time-dependent envelope quantities previously determined by the *elegant2genesis* code and also using directly the ELEGANT particles. Note that only the effect of the jitter on the electron bunches has been considered without taking into account any jitter source in the seed laser.

The 100 jittered files have been produced starting from one hundred GPT files that consider the possible jitter sources in the gun. Those files have been propagated through the linac with ELEGANT. Output distributions have been pre-processed in order to evaluate the resulting jitter in bunch arrival times (Figure 4.4.7).

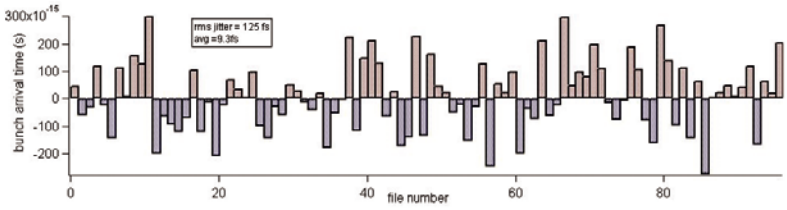

Figure 4.4.7:
Arrival time jitter of the 100 elegant files with respect to the arrival time of the nominal file.

The analysis shows a distribution with an rms jitter of about 130 fs, which is close to the value predicted by LiTrack simulations (see Chapter 6). These data can be fit with a Gaussian distribution (Figure 4.4.8).

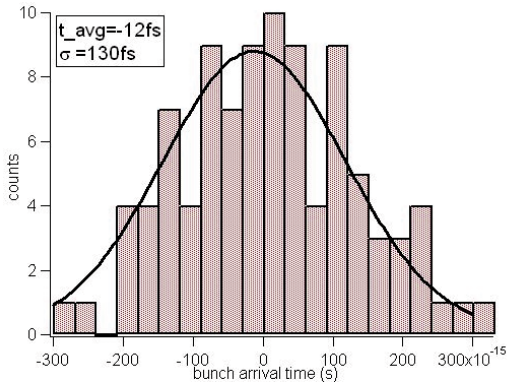

Figure 4.4.8:
Distribution of the arrival time jitter reported in Figure 4.4.7; data can be fitted with a Gaussian distribution, whose sigma is about 130 fs.

By plotting the electron energy and current profiles of the 100 bunches taking into account of the arrival time (Figures. 4.10-4.14) it is evident that a time window exists of the order of 400 fs in which the fluctuations of electron parameters due to the jitter arrival time are small. This window forms the "useful" part of the bunches for the FEL process. The analysis of the effect of variations in electron beam properties on that window is reported is reported in the following.

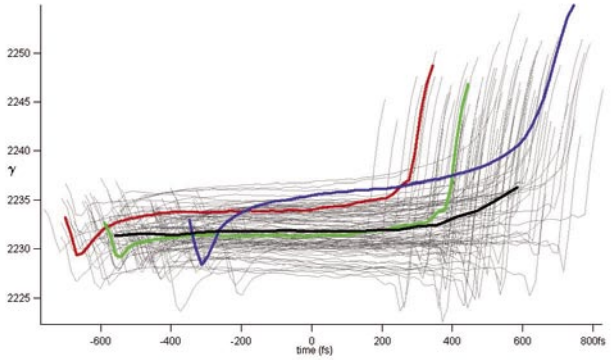

Figure 4.4.9:
Temporal profile of the electron beam mean energy of the one hundred jittered ELEGANT files.

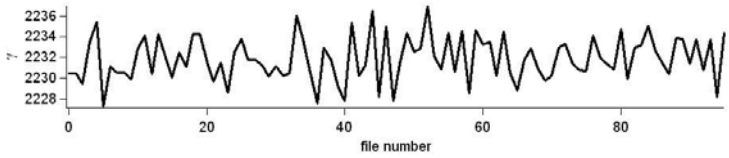

Figure 4.4.10:
Average of the electron mean energy of the jittered electron bunch calculated in the useful time window (-200 fs; 200 fs).

The electron mean energy, γ, in the useful part of the bunch (from -200 fs to 200 fs) presents a distribution with an rms of 0.09%, in agreement with the values of reported in Chapter 6.

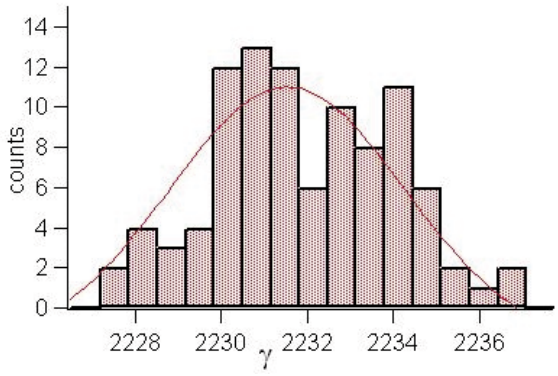

Figure 4.4.11:
Distribution of the average electron mean energy of the useful part of the jittered bunches; data can be fitted with a Gaussian distribution whose sigma is 0.09%.

The current distribution shows an rms value (6.6%) that is slightly lower than the one reported in Chapter 6 (8%). Similar analyses have been performed for other electron beam properties, (emittance, energy spread, etc.). With respect to beam emittance, data show a distribution with an rms value that is close to the one reported in chapter 6 (about 12%). The energy spread, instead, is slightly affected by the temporal jitter of bunches and the rms distribution shows a larger value (almost 20% instead of 10%). Calculated electron beam average values and corresponding standard deviations are reported in Table 4.4.3.

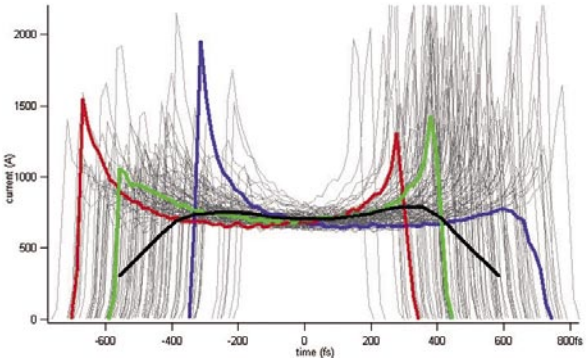

Figure 4.4.12:
Temporal profile for current of the one hundred jittered files.

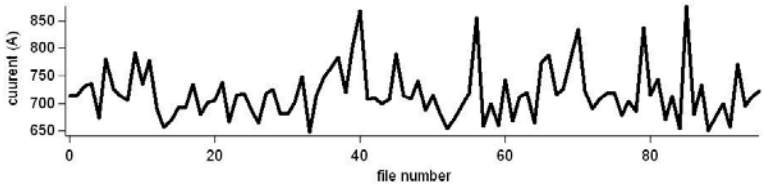

Figure 4.4.13:
Average of the electron bunch current calculated on the useful part of the jittered files (from -200 fs to 200 fs).

Table 4.4.3: Average values and corresponding standard deviations for the main electron beam parameters extracted from time-dependent simulations.

Quantity	*Mean Value*	*Std. Dev.*
Gamma	2231.9	0.09%
Current (A)	718	6.6%
Incoherent energy spread	0.33	19.5%
Normalized emittance	1.35	12.4%

The FEL simulations assume the nominal setup of FEL-1 (see Section 4.4) optimized in terms of a_w and R_{56} to maximize the output power extracted from an ideal bunch, whose parameters are equal to the average values reported in Table 4.4.3. Time-dependent simulations using this optimized setup for the jittered files show a high sensitivity to beam jitters (e.g., about 50% of fluctuation in the output power), far from the predictions of time-independent simulations.

Consequently, a new optimization procedure was needed to find baseline characteristics that minimize the effect of the beam jitters. To reduce the sensitivity of the FEL output power the tuning of the radiator was changed slightly to a setting with a smaller value of a_w. The setup utilized for simulations is the following: a seed laser of 100 MW with a Gaussian temporal profile (100 fs rms), the modulator tuned at 240 nm, the dispersive section set with a $R_{56}=19\cdot10^{-6}$ and the radiator tuned at 40 nm.

Figure 4.4.14 displays the output power profiles obtained from the 100 jitter bunches, while Figure 4.4.16 shows the corresponding output spectra. Red, Green and Blue traces in Figure 4.4.14 and Figure 4.4.16 correspond to the electron bunches reported in Red, Green, Blue in Figure 4.4.9 and Figure 4.4.12.

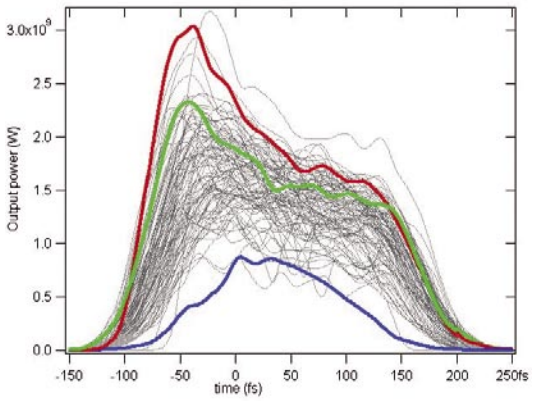

Figure 4.4.14:
Temporal profiles for the FEL output radiation at 40 nm obtained from GINGER simulations using the jittered ELEGANT files; Red, Green and Blue curve refer to bunches reported with the same colors in Figure 4.4.9 and Figure 4.4.12.

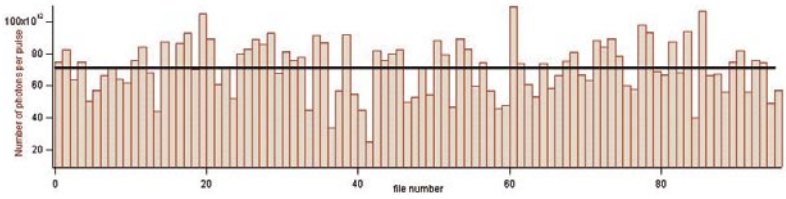

Figure 4.4.15:
Number of photons per pulse obtained from the FEL simulation at 40 nm. Data show an average number of photons of the order of $70\cdot10^{12}$ with an rms fluctuation of about 23%.

Integrating the pulse profile yields the number of photons of each FEL pulse. Figure 4.4.15 reports the number of photons of FEL output pulses for each of the one hundred jittered electron bunches. Statistical analysis of data shows a distribution that is close to a Gaussian centered at $70\cdot10^{12}$ photons per pulse with a standard deviation of about 23%.

The output spectra of the FEL pulses shown in Figure 4.4.16 demonstrate that the jitter of the input electron beam parameters induces a fluctuation of the central wavelength. However, such a fluctuation is about a factor 3 smaller than the average bandwidth and, as a consequence, does not affect substantially the FEL performance (see Table 4.4.4). Considering the equation for the undulator resonance $\lambda = L_w \cdot \frac{(1+a_w)}{2\gamma^2}$ one can derive that, if the emission wavelength is defined by the resonance wavelength of the radiator, the jitter in wavelength should be two times that associated to the jitter in electron mean energy. This estimate is not true for a seeded FEL in which the emission wavelength is defined by the seeding laser and only partially by the undulator resonance wavelength.

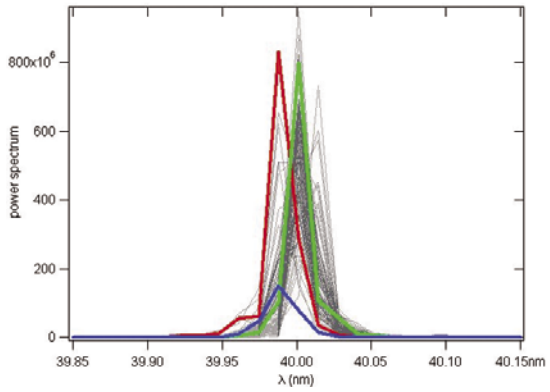

Figure 4.4.16:
Output power spectra obtained from the FEL simulations of the jittered files.

These results are in agreement with predictions and the calculated fluctuation for the wavelength is small compared to the fluctuation of the mean energy of the input jittered bunches.

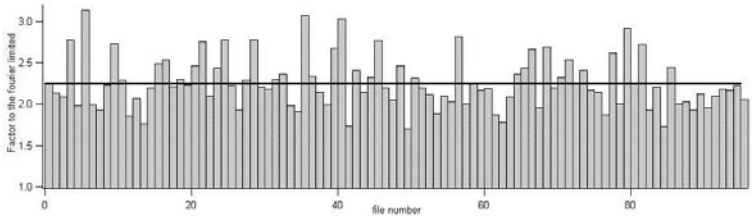

Figure 4.4.17:
Factor to the Fourier transform limit of the FEL output pulses for the jittered ELEGANT files.

The FEL output pulses were also characterized in terms of how close they are to the Fourier transform limit. Figure 4.4.17 shows the distance of each FEL output pulse to the Fourier limit for the one hundred simulated jittered files. The average Fourier factor for the simulated data is 2.2 and the standard deviation of the distribution is about 13%.

Table 4.4.4: Statistics of the one hundred FEL pulses.

Quantity	*Mean Value*	*Std. Dev.*
Average pulse width (fs)	73.2	
Average photon number	7.1e+13	23.3%
Average central wavelength (nm)	40.0019	0.013%
Average bandwidth	0.033%	
Fourier factor	2.2	13%

To verify the prediction of time independent simulations that indicate that the jitter in the mean electron energy is the strongest limiting factor for achieving a good output stability, one plots (in Figure 4.4.18) the number of photons per pulse v. the average electron beam energy. The clear correlation between the two quantities confirms the high sensitivity of the FEL output to the mean electron energy.

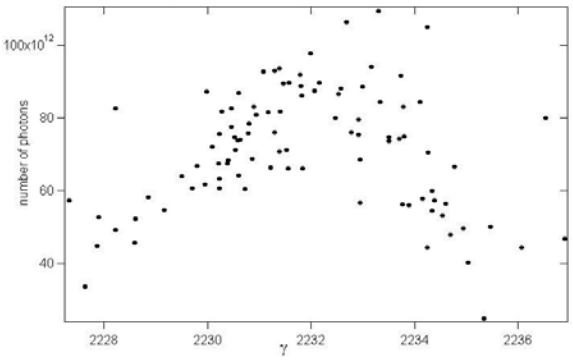

Figure 4.4.18:
Number of photons per pulse v. the average electron mean energy of the corresponding electron bunch.

4.4.4 Diagnostics Needs for FEL-1

Some routine measurements will guide the operators in maximizing the output from FEL-1. Within the different segments of undulator and other lattice elements, electron beam position monitors are needed to ensure that the beam orbit stays as close as possible to the magnetic axis. Following the chromatic dispersion element, the electron bunch will have both strong energy modulation and micro-bunching; the latter can be measured with coherent optical transition radiation (COTR) from an insertable foil. In the radiator, the build up of the coherent harmonic signal can be determined section-by-section by purposely mistuning the magnetic strength of the downstream undulator sections so as to eliminate any additional emission. COTR in the drift sections can also be used to measure the z-dependent evolution of the micro-bunching. The COTR signal should also be rich in harmonics of the initial seed laser. Ideally for comparison with simulations, measurements of the microbunching and FEL radiation should be done following each radiator undulator section. Finally, measurements of the final energy spread of the e-beam upon exit from the final undulator section should be commensurate with the FEL emission from the radiator.

4.5 FEL-2 Design and Parameters Calculations

As mentioned in the Section 4.1, most proposed experiments using FEL-2 will be in the frequency domain, in which case narrow spectral bandwidth is crucial. Consequently, the baseline design of FEL-2 utilizes a relatively long (~1.5 ps) electron beam pulse with a moderate (~500 A) current. Figure 4.5.1 shows the layout adopted for the fresh bunch approach.

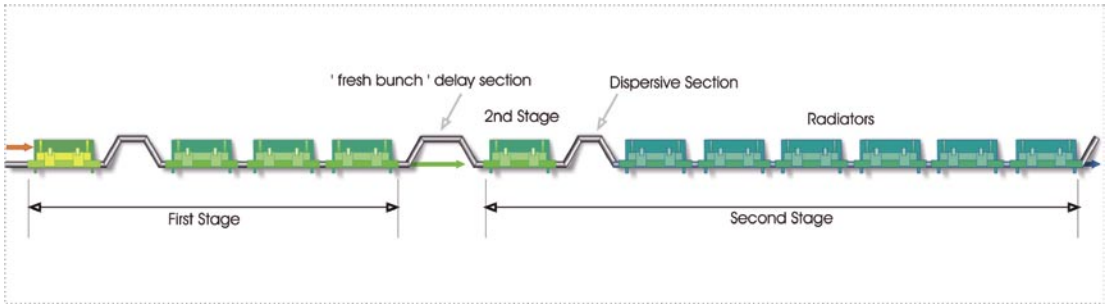

Figure 4.5.1:
Nominal undulator layout for FEL-2.

For the fresh bunch approach, such a long pulse is essential given the practicalities of temporal jitter and the accuracies of a temporal delay section. The core design for the first stage of the fresh-bunch FEL-2 is parallels that of FEL-1. Specifically, relatively strong, input seed power (~100 MW) energy-modulates a 500 A electron beam in a long period (~16-cm wavelength) undulator followed by a dispersive section with R_{56} ~ 25 μm. The dispersive section produces strong bunching at the fundamental ($b \geq 0.5$) and also at the second through sixth harmonics in the following radiator. Where the design for the FEL-2 fresh-bunch layout begins to differ significantly is that the first stage radiator is relatively short (*e.g.*, 2-3 segments) and only brings the radiation to a sufficient level (~200 MW) to provide adequate coherent energy modulation in the following undulator. This choice contrasts with the FEL-1 radiator that is long enough (*e.g.*, 5-6 segments) to reach FEL power saturation (~1-4 GW). The basic characteristics for the second stage modulator are the same as for the first stage radiator (*e.g.*, 65 mm period; 2.34 m segment length) so as to minimize costs. In general, the first stage should be as short as possible to minimize SASE that increases the incoherent energy spread of the "fresh" portion of the e-beam to be used in the second stage modulator and radiator. A secondary consideration is that the cost is also lowered. Provisionally the fresh bunch delay section is presumed to have a 1.8 m length (necessary in the numerical simulations to include proper diffraction effects).

The second stage (final) radiator has a somewhat shorter period (*i.e.*, 50 mm) and is subdivided into 2 m long active segments of undulator separated by 1 m drifts. These breaks contain a quadrupole singlet for focusing, a phase shifter, dipole correctors, and diagnostics. The length of the final radiator is somewhat arbitrary; in general for the fresh bunch approach one wants sufficient length for power saturation, ~6 segments at 10 nm wavelength. However, one could certainly increase the output power by adding more radiator segments with tapered magnetic strengths.

4.5.1 Fresh Bunch Time-Independent Results

Following similar strategies described in Section 4.4.1, a series of simulations were performed to optimize the output power of the second stage. As the final design of FEL-2 will be modified based on FEL-1 performance the calculations presented here are representative rather than fully consistent design sets. Assuming that most of the first stage of FEL-2 would be similar to that of FEL-1, the most sensitive quantities to vary are the number of radiator sections in the first stage and the strength of the dispersive section following the second stage modulator. A good design point was a three-section first radiator that would emit ~250 MW of power at 40 nm wavelength. With that choice, at the end of the second modulator, the peak-to-peak energy modulation is ~1.8 MeV, as compared with 2.5 MeV modulation in the first stage. The final radiator is 6 sections long and produces (see Figure 4.5.2) a peak power of 0.63 GW (1.4 GW) and a bunching of 0.44 (0.53) at 10 nm (20 nm) for 500 A beam current.

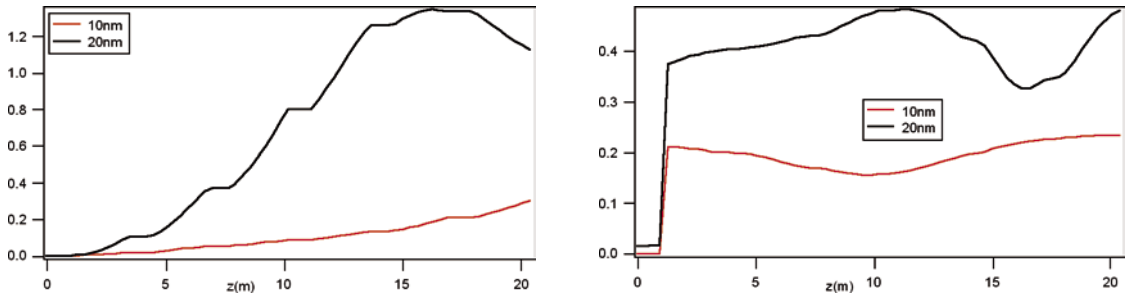

Figure 4.5.2:
Power and bunching for different FEL-2 configurations as a function of position within the radiator.

A small number of time-independent, single parameter variation scans were performed to determine the sensitivity of the final output. Not surprisingly given the much larger total number of undulator periods in FEL-2 as compared with FEL-1 plus the additional sensitivity connected with having a second stage of modulation, one observes a much greater dependence upon electron beam parameters, especially beam energy.

4.5.1.1 Fresh Bunch Time-Dependent Results

A number of full start-to-end simulations were done for the fresh bunch approach to FEL-2. Simulations concentrated upon 10 nm output cases as these were likely to be the most sensitive to imperfect electron beam parameters. The first stage radiator output was at 40 nm so the second stage had a 4:1 up-conversion ratio. An example of output temporal and spectrum profiles based on an optimized input electron beam is shown in Figure 4.5.3.

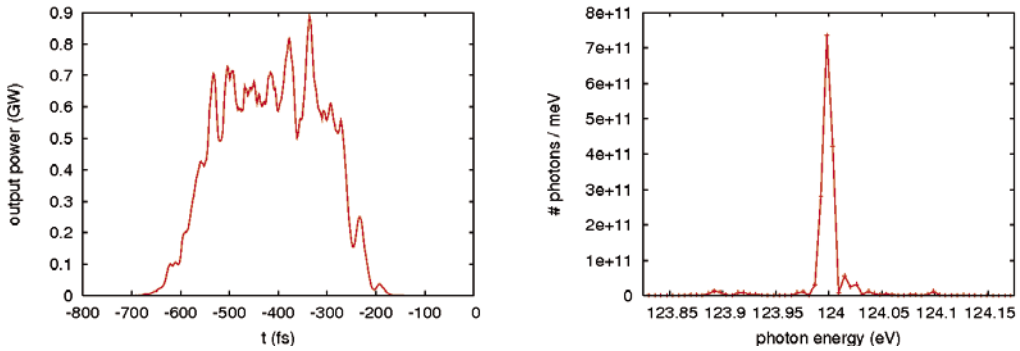

Figure 4.5.3:
FEL-2 temporal and spectrum profiles for fresh-bunch scheme resulting from a GENESIS simulation in time-dependent mode.

The number of photons obtained per pulse is about 10^{13} (93% in single transverse mode). The output pulse length is 110 fs (rms) and the bandwidth 5 meV, about a factor about 1.5 above the transform limit. The peak brightness is about 10^{32} photons /mm2/mrad2 /sec/ 0.1% bandwidth.

A concern for FEL-2 is whether jitter in beam parameters combined with wakefield effects in the accelerator (discussed at length in Section 6.8.3) will significantly degrade the narrow spectral profile typified by Figure 4.5.3. As displayed in Figure 4.4.16, the fluctuations in beam energy can jitter the position of the peak of the spectrum of FEL-1 by ~10^{-3} with little noticeable increase in bandwidth. FEL-2 is more sensitive to jitter in beam parameters than FEL-1 due to the reduced value of rho in the second radiator. In addition, the amount of bunching produced by the second dispersion section is sensitive to lower input radiation at the beginning of the second stage due to energy mismatches in the first stage of the cascade. Although a detailed quantitative answer to this question would require many hundreds of simulation runs, the analysis the time-variation of energy during the beam pulse given in Section 6.8.3 permits a semi-quantitative answer. These considerations do not include the effect of wakefields in the undulator, discussed in the following section.

For that sub-set of users who require narrow bandwidth radiation, special care will have to be taken to minimize the fluctuations in the non-linear chirp (σ_{a2} in Eq. 6.8.2) that is induced by wakefields throughout the accelerator and wiggler. As the non-linear (quadratic) component directly influences the radiation bandwidth at the FEL design point, fluctuations in this component could lead to uncertainties in the output bandwidth beyond the few meV level desired by users studying RIXS phenomena. The analysis of Section 6.8.3 indicates that even in the long bunch case the fluctuation in a_2 is ~60%, producing a commensurate increase in the effective (average) bandwidth. In the medium bunch case the fluctuation in a_2 is two times smaller, an amount that would not significantly reduce the effective bandwidth. Therefore, in the final design of FEL-2 the pulse length will be selected to optimize the average photon number within the desired 5 meV bandwidth.

The second concern for FEL-2 is whether the fluctuations in the central frequency (which in FEL-2 can be much larger than the bandwidth) are tolerable in RIXS experiments. As RIXS measures only

frequency differences, the jittering of the central value does not matter as long as 1) the output frequency is measured, and 2) the linewidth is sufficiently small.

Even if the quadratic chirp could not be sufficiently well controlled (unlikely in light of the analysis of Section 6.8.3), an alternative approach would be to control the magnitude of the linear component of chirp. Then, unlike the behaviour seen in Figure 4.4.16, the central value of the spectrum would remain fixed by the central value of the spectrum of the seed laser with the bandwidth varying from pulse-to pulse. One could then use a monochromter upstream of the experimental sample. Options for the placement of this monochrometer are presently being studied.

4.5.2 Wakefield Calculations

As was done for the FEL-1 "medium bunch" in Section 4.4.3.1, the expected longitudinal wakes were also calculated in the FEL-2 "long bunch" case. As before, the rectangular Al vacuum chamber characteristics were 6.0 mm vertical inner height, a surface roughness of 100 nm amplitude with a longitudinal period of 25 microns, and a presumed 10 cm break occurring every 3.4 meters. The resistive wake calculation was based upon an AC conductivity model. Figure 4.5.4 shows the calculated wakes versus distance back from the beam head.

Once again, with the exceptions of possible spikes in the head and tail regions, over an interval exceeding 1.0 ps there is a nearly constant wake of ~ 4.4 kV/m with temporal fluctuations of ± 2.5 kV/m or so.

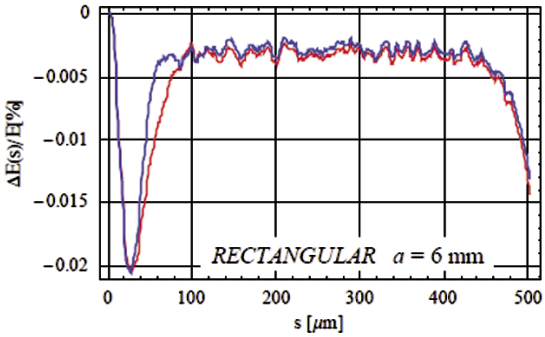

Figure 4.5.4:
Time-dependent longitudinal wake results for the "long bunch" distribution. Red corresponds to the aluminum and blue to the copper chamber respectively.

Over a 50 m total vacuum chamber length, a fluctuation of ± 150 kV corresponds to less than 0.01% of total energy – much less than the FEL parameter. Consequently this variation is unlikely to cause any significant degradation of emitted power. Moreover, as the wake function from the wiggler has very little curvature, the wakefield in the wiggler will have minimal effect on the line width of FEL-2.

Fluctuations in power are equivalent to a slight line broadening, but do not shift the output wavelength. In contrast, if the surface roughness were to grow to ~500 nm amplitude, the fluctuations from this wake component increase by a factor about 25 to approximately 15 kV/m. Over 40 m of vacuum chamber, this wake would lead to a normalized beam energy fluctuation of 0.05% which could prove quite troublesome both in output level and in bandwidth. Therefore, further studies are needed to set specifications and tolerances for the FEL-2 vacuum chamber as a compromise between ease and cost of fabrication and FEL performance. In any case the conclusions presented at the end of the preceding section remain valid.

4.5.3 Diagnostics Needs for FEL-2

For most items, the diagnostic needs of FEL-1 and FEL-2 are quite similar. The first stage of FEL-2 can be considered a somewhat shorter version of FEL-1 and the various diagnostics proposed for FEL-1 could be replicated here. For the fresh bunch approach, the output radiation of the first stage will be used to modulate a portion of the electron bunch; therefore, detailed radiation diagnostics would prove extremely useful. In order to tune the delay section between the first and second stages, a cross-correlator between the first stage coherent signal and the spontaneous emission from the second stage might be useful. In addition a diagnostic of micro-bunching after the second stage modulator is likely to be essential. A diagnostic to resolve in z the build up of coherent radiation in the second stage radiator would also provide valuable information. Since the undulator gaps can be opened, a gross mistuning downstream of the desired diagnostic point might be sufficient.

4.5.4 Results for the "Alternative" Whole Bunch Configuration and Comparison with Fresh Bunch Approach

An alternative scheme that was considered for FEL-2 is based on the so-called "whole-bunch" approach. Here, the entire electron beam pulse is energy-modulated by the external laser seed and, following the first radiator, there is neither a temporal delay section nor a second modulator. Instead, the electron beam immediately enters a weak dispersive section followed by a second radiator whose FEL resonant wavelength is tuned to an integer harmonic of the first radiator. Due to the relatively small harmonic micro- bunching at this new wavelength, this second radiator must operate deep in the exponential gain regime. Thus, to keep the exponential gain length and power saturation lengths acceptably small, the energy modulation produced by the first (and only) modulator must be relatively small compared to $\rho\gamma_2$ where ρ_2 is the FEL parameter for the second radiator (generally ~ 1×10^{-3}).

This small energy modulation means that at entrance to the first radiator the e-beam will have a smaller micro-bunching level relative to that of the fresh bunch scheme. Consequently, the whole bunch approach can fail (in terms of the needed second radiator undulator length for saturation) if the initial energy spread becomes too large. Moreover, because the micro-bunching level is small at the beginnings of both the first and second radiator, the relative strength of the shot noise micro-bunching is much higher and the final SASE strength can be two or more orders of magnitude greater in the whole bunch approach than in the fresh bunch approach. The main potential advantage of the whole bunch scheme is that it is less sensitive to shot-to-shot fluctuations of the relative timing between the e-beam and external seed laser. This advantage comes with the price of great difficulty in producing an electron bunch with minimal non-linear energy chirp.

A representative output temporal profile and spectrum obtained at 10 nm using the whole bunch configuration are shown in Figure 4.5.5. The initial electron beam distribution used is the same as for the fresh-bunch calculation shown in Figure 4.5.3.

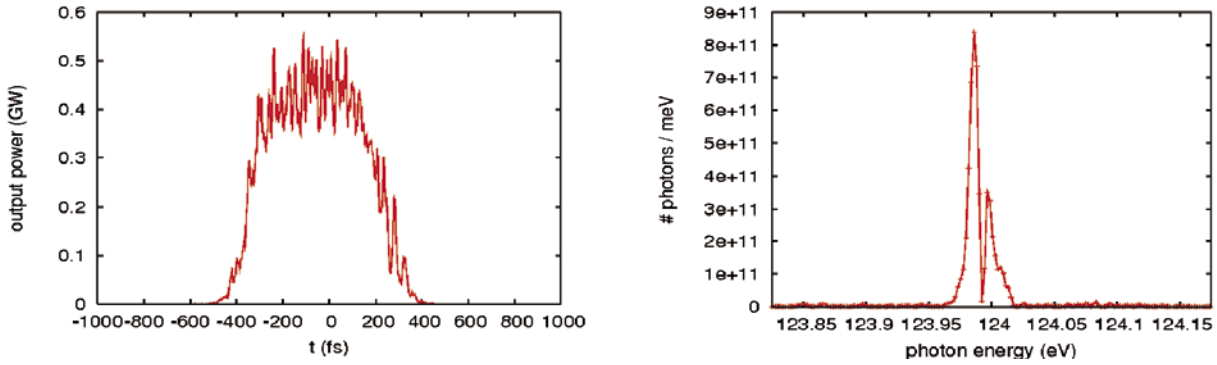

Figure 4.5.5:
FEL-2 temporal and spectrum profiles for whole-bunch scheme resulting from a GENESIS simulation in time-dependent mode.

In this whole-bunch example, the number of photons obtained per pulse is about 10^{13} (93% in single transverse mode). The output pulse length is 200 fs (rms) and the bandwidth 4 meV. This gives a result which is a factor about 2.5 above the transform limit.

4.7 References

[1] L.H. Yu et al., Phys. Rev. Lett. 86 (2001) 5902.

[2] A. Doyuran et al., Phys. Rev. Lett. 91 (2003) 07480.

[3] I. Ben-Zvi, K. M. Yang, and L. H. Yu, Nucl. Inst. Meth. A, 318, (1992) 726.

[4] S. Reiche, Nucl. Instrum. Meth. A 429 (1999) 243.

[5] W. Fawley, Report LBNl-49625, 2001.

[6] Ming Xie, Nucl. Instrum. Meth. A 445, (2000) 59.

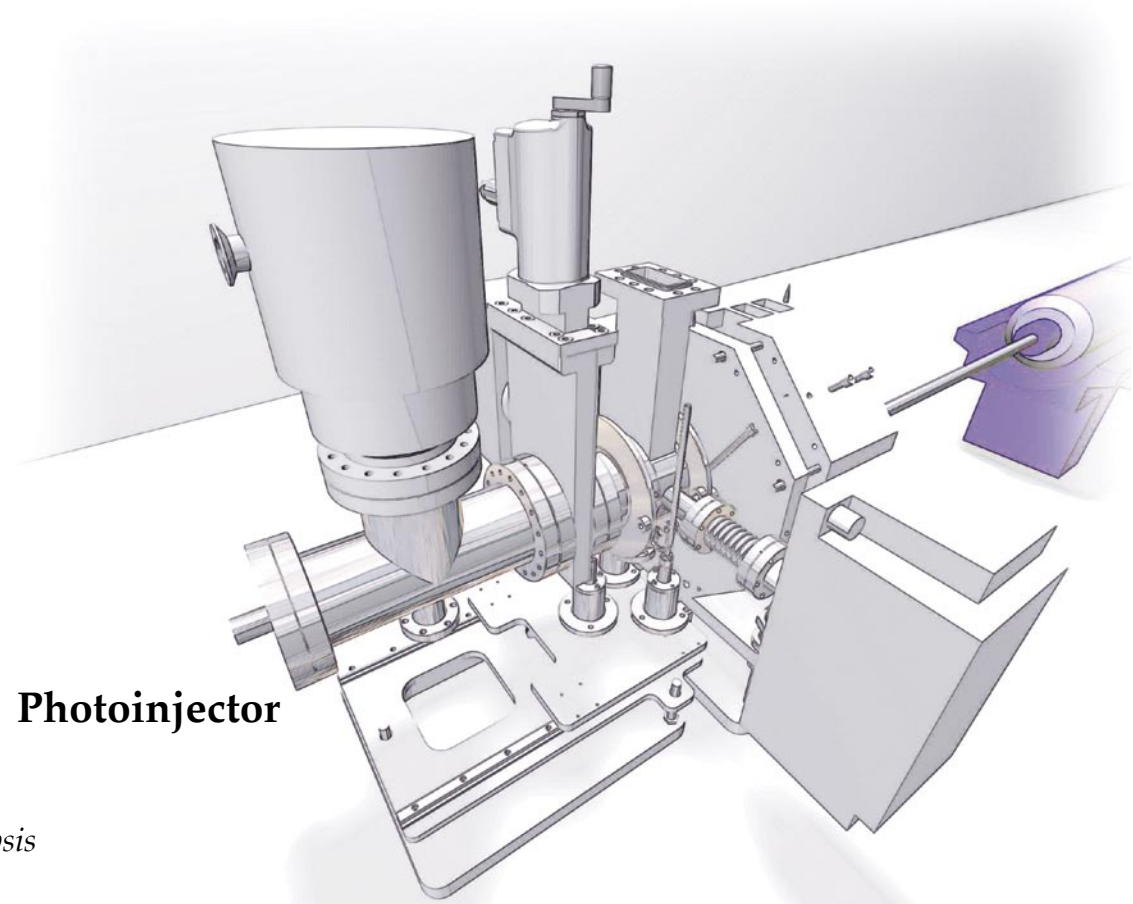

5 Photoinjector

Synopsis

The front-end injection systems of the FERMI@Elettra linac produce the high brightness electron beams that define the performance of the FEL and the quality of the x-ray beams delivered to the users. The injector mainly consists of the RF gun, based on the BNL/UCLA 1.6 cell design [1] and scaled to European S-band frequency, its compensation solenoid and two traveling wave S-band rf sections (called SØA and SØB) which accelerate the beam up to 100 MeV. The slice emittance at the end of the injector is specified to be less than 1.5 mm mrad. The injector must provide a linearly current ramped bunch in order to linearize wakefield effects in the linac sections [2]. This requirement translates into finding the best laser pulse shape at the cathode that produces an electron bunch evolving into the desired current profile along the drift between the gun and the first booster section. Two main bunch configuration have been studied: a 0.8 nC/9 ps long "medium length bunch (MLB)" configuration and a 1 nC/11 ps "long bunch (LB)". It is shown that the optimum laser temporal profile for both the MLB and the LB regimes is a quadratic ramp, which is transformed to a linear ramp by space charge forces in the injector. As the charge density varies from head-to-tail in the bunch, a best compromise has to be found for the emittance compensation process. As a consequence it is shown that slice emittance as well as charge distribution must be ramped along the bunch (see Paragraph 5.6.1): slice emittance values range from 0.7 to 1.1 mm mrad for the MLB regime and from 0.8 to 1.2 mm mrad for the LB regime while the current increases from 40 A up to 80 A.

Furthermore, since a seeded harmonic cascade FEL is very sensitive to shot-by-shot variations in beam characteristics, the effects of jitters on the FEL performance have been studied in the ramped current scenario. In particular, time jitters are critical because they are translated into energy jitter in the two

chicanes, thus affecting the FEL output power stability. The main source of time jitter comes from jitter in the drive laser arrival time at the cathode with respect to the gun RF waveform, specified to be equal to or less than 200 fs and corresponding to a 0.1 deg jitter in the RF phase seen by the beam. Hundreds of simulation of the injector output beam quality (Section 5.6.2) with input parameters randomly picked, within tolerance values dictated by present technology and supported by measurements, have been performed; they show that the overall expected rms time jitter value at the injector exit is 350 fs. Sensitivity studies and tolerance budgets concerning injector output current, energy, emittance and injector optics parameters are included in the discussion.

5.1 Introduction

This chapter describes the critical technical components of the photo-injector system and the associated beam dynamics, optimized to deliver the high quality electron beams FERMI requires.

Section 5.2 provides an overview of the various injector systems and subsystems. Different injector operating modes are described corresponding to the different linac set-up's required by FEL beam characteristics tailored to meet user needs.

Sections 5.3 and 5.4 describe the main photoinjector components: electron source and RF gun. The photoinjector drive laser main specifications are given at the end of Section 5.3 and discussed in more detail in Chapter 10.

RF gun design considerations are presented in Section 5.4, where various cavity geometry options, studied in order to optimize the efficiency of energy transfer to the electron beam, are described. A study of power coupling into the various cavity modes falling within the bandwidth of the RF drive pulse is also presented, followed by a study of the transient cavity response and, finally, of the effects of the cavity design on the extracted beam quality.

Section 5.5 describes the low energy, off-axis diagnostics beamline. Beam dynamics simulation results using ASTRA, GPT, ELEGANT, and MAD are presented.

Section 5.6 beam dynamics optimization studies are discussed for the various operating modes. Optimized baseline beamline configurations and drive laser pulse shapes are presented, supported by space-charge tracking codes simulations. Optimization of the beam transport through the linac sections up to the FEL undulator entrance requires significant deviations from the canonical 'flat-top' temporal laser pulse shape at the photocathode. The physics of nonlinear electron current emission has been revisited in order to find the optimum temporal profile of the drive laser. It is shown that a linear current ramp at the injector output is required and that the laser pulse intensity should therefore follow a quadratic curve. Parametric sensitivity studies are performed around the baseline configurations and jitter studies are presented showing the stability degree of the found solutions. The conclusions of this chapter are summarized in Section 5.7.

5.2 Overview of Electron Source and Injection System

The front-end injection system of the FERMI linac is designed to produce the high brightness electron beams that determine the FEL performance and the quality of x-ray beams delivered to the users. The electron source and the injection system are specifically designed to minimize technical risk and

cost by utilizing existing accelerator components and by leveraging on the technical designs of other, contemporary x-ray FEL projects. The injector major components are shown in Figure 5.2.1.

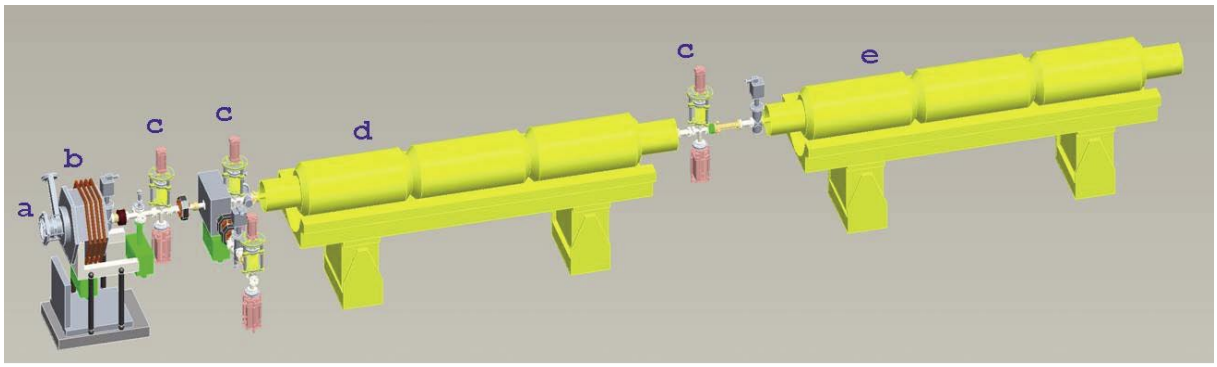

Figure 5.2.1:
The FERMI@Elettra FEL photoinjector. a) RF Gun, b) Solenoid, c) Pop-in screens, d), e) SØA and SØB booster accelerating sections.

5.2.1 Electron Source and RF Gun

The FERMI electron source is a metallic photocathode (polycrystalline copper) illuminated by an intense, 263 nm wavelength UV laser whose pulse shape is chosen to optimize the final beam quality. Because the best measured values of the quantum efficiency of copper at 263 nm are in the range 10^{-5}-10^{-4}, the laser must deliver ~500 μJ on the cathode in order to produce a ~1 nC bunch charge.

The photocathode also serves as the conducting back plane of a one and a half cell RF gun. A first stage gun is designed for a pulse repetition rate of up to 10 Hz. An upgraded version, not described here, reaching up to 50 Hz repetition rate, is foreseen as a second stage.

The first stage gun operates in the fundamental, TM010-π ('pi') mode of the two-cell cavity, resonant at 2997.9 MHz. Its design utilizes, with appropriate slight shape modifications, proven industrialized technologies, previously optimized for operation at 2856 MHz.

It is specified to provide a peak accelerating gradient of 110 MV/m, and an output beam energy of ~5 MeV at 10 Hz repetition frequency. It is powered by a fraction (~60%) of the power delivered by the first linac klystron. The cavity filling time to its nominal field value is ~2.8 μsec assuming a 10 MW peak input pulse.

External solenoid magnets are integral to the RF gun operation. A multiple pancake, emittance compensating solenoid provides focusing to help transport the beam from the gun exit to the entrance of the booster linac structures.

5.2.2 Gun-to-Linac Drift

The gun-to-linac (GTL) drift section encompasses the beamline from the gun exit to the entrance of the first booster accelerator (see Figure 5.2.2).

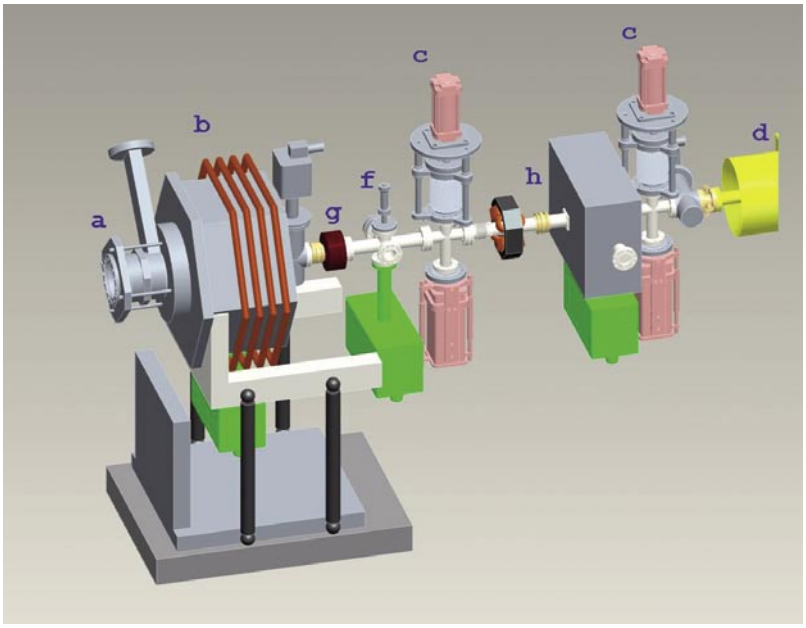

Figure 5.2.2:
Gun-to-linac beamline. See text for details.

The GTL beamline contains the instrumentation for the low energy beam diagnostics and trajectory correction, and the vacuum instrumentation for the entire front-end section. Two dipole trim magnets (h) allow correcting beam offset and angle. Two vacuum crosses (c) support retractable beam profile image screens, a charge-measuring Faraday cup and horizontal and/or vertical slits. An inductive toroid (g) is placed near the gun exit for non-destructive bunch charge measurements. A six-way cross (f) in the beamline allows for on-axis injection of the photocathode drive laser pulse, vacuum pumping and measurement.

Together with the low energy, off-axis diagnostic beamline, the GTL allows measuring transverse and longitudinal beam phase space properties.

5.2.3 Low Energy Diagnostic Beamline

The off-axis, low energy diagnostic beamline concept is shown in Figure 5.2.3. It is equipped with a magnetic spectrometer to measure beam energy and energy spread, an important tool for optimizing the gun performance.

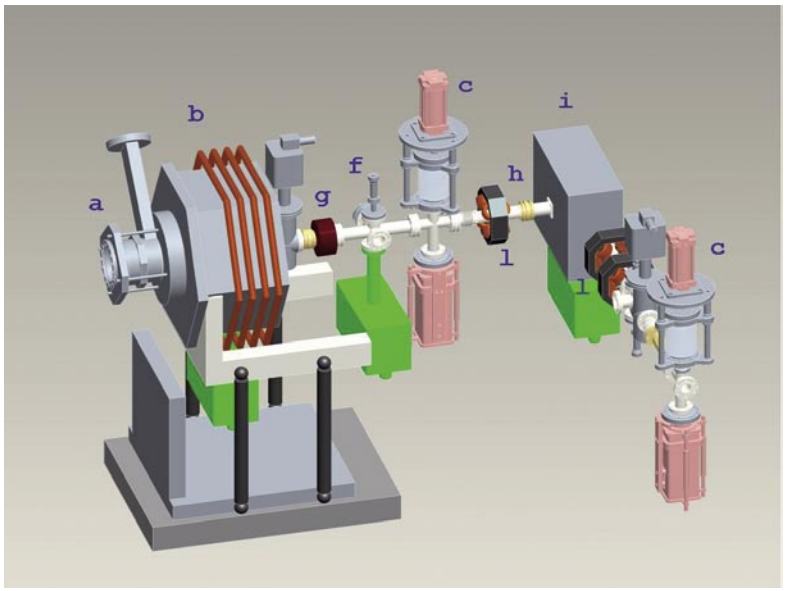

Figure 5.2.3:
Off-axis, diagnostic beamline. See text for details.

The beamline main components are: the 90-degree spectrometer magnet (i), three quadrupole magnets (l), two dipole trim magnets, a beam profile screen and a Faraday cup (c). The beamline dispersion is adjusted so as to maximize the spectrometer energy resolution.

5.2.4 Booster Accelerating Modules

The two booster traveling-wave accelerating structures SØA and SØB, are shown in Figure 5.2.1. Each section is composed of 93 identical on-axis, iris-coupled cells, resonating at 2.998 GHz. The two end cells are used to couple RF power into and out of the structure. The ~3.3 m active structure length requires ~3.5 m of beamline. It operates in the $2\pi/3$ mode, and provides peak accelerating gradients of ~19 MV/m, for a total maximum energy gain of ~45 MeV (including a 10% margin). The booster sections are equipped with solenoids to provide transverse focusing, to assist with emittance compensation, and to match the optical (lattice) functions at the input to the main linac.

5.2.5 Operating Modes

Several configurations of the electron bunch to be produced have been considered in the optimization study process, in order to make the machine design as flexible as possible so as to satisfy the various user requirements [3]. Eventually, two main bunch configurations have been selected: a "medium length bunch (MLB)" configuration and a "long bunch (LB)"one. At the linac output the bunch design specifications call for a 600 fs/1 kA peak in the MLB mode and a 1.5 ps /0.5 kA peak in the LB mode.

The simulations of e-beam dynamics have been separated into two parts: tracking through the low energy injector part, including SØA and SØB, in which the beam is space charge dominated (up ~100 MeV), and tracking through the rest of the linac. Injector simulations are performed using two space charge tracking codes: ASTRA [4] and GPT [5].

As discussed in Chapter 6, in order to compensate the wakefield effects in the linac sections and to provide a flat distribution in phase space at the linac output, the injector output electron bunch current distribution is designed to be linearly ramped in time [6], in both the MLB and the LB regimes. This unconventional specification originated in the Linac optimization studies, which showed that the nonlinearity of the linac accelerating field waveform and the nonlinear time-of-flights in the bunch compressors play an important role in beam dynamics [2,6] and are such that, with the commonly used flat top charge distribution, the longitudinal phase space footprint at the end of the linac would exhibit a quadratic chirp degrading the FEL performance [7].

5.3 Photocathode and Drive Laser Systems

The photoinjector system for FERMI requires a robust, pulsed UV laser system. The system requirements for the photoinjector laser are presented in Table 5.3.1.

Table 5.3.1: Temporal specifications for the UV laser pulse.

Wavelength	< 270 nm
Required pulse energy at the cathode (Cu)	~0.5 mJ
Pulse duration range (FWHM)	1 - 20 ps
Rise/fall time range (10-90 %)	0.5 – 5 ps
Instantaneous power flatness (rms)	< 5%
Synchronization (rms)	< 300 fs
Pulse repetition rate range	10 Hz - 50 Hz

Specifications for the beam transverse profile parameters at the cathode are listed in Table 5.3.2:

Table 5.3.2: Spatial specifications for the UV laser spot at the photocathode.

Beam diameter range (FWHM)	2-4 mm
Edge ramp width (10-90 %)	0.5 mm
Intensity flatness (rms)	< 5%

Beam shaping techniques based on refractive, reflective, diffractive, and absorptive optics are used to transform Gaussian-like spatial profiles into the desired longitudinal profile [8]. A more detailed description of the photoinjector drive laser is given in Chapter 10.

5.4 RF Gun Design and Optimization

Meeting the FERMI photoinjector electron beam brightness specifications requires studying all possible perturbation effects in the RF gun that may degrade the beam quality. The present generation of RF guns allows a coupled-cavity, resonant 'zero' order mode, at a frequency lower (typically by ~ 10 MHz) than that of the main accelerating mode (the 'pi' mode), and that can be excited by the drive klystron pulse. Its undesired field may rise to significant amplitude and thus interfere with the beam dynamics of the emitted electrons, eventually affecting the beam quality. To evaluate such effects, the frequency separation between the two resonant modes was studied for different cavity geometries. The coupling between the gun cavity and the power feed wave guide has also been also analyzed, together with the transient effects during cavity filling. After estimating the amplitude of the excited 'zero' mode, beam dynamics simulations were performed showing the beam quality behavior as a function of the zero mode amplitude and frequency separation.

5.4.1 RF Cavity Design

The first gun cavity design [9] was obtained by reducing the BNL/SLAC/UCLA 1.6 gun geometry by a factor $K = f_{BNL}/f_{FERMI} \approx 0.96$. Such simple scaling does raise the main resonant frequency from 2856 MHz to 2997.9 MHz, but disregards other issues involved in normal conducting RF cavity optimization [10]. In particular, to investigate ways of increasing the resonant frequency separation between the pi and the zero modes and to decrease the coupling of the zero mode to the klystron drive pulse, several RF cavity geometries have been examined, all resonating at the European frequency of 2997.9 MHz but differing in cell lengths and pi-to-zero mode frequency separation. A detailed study of the cavity

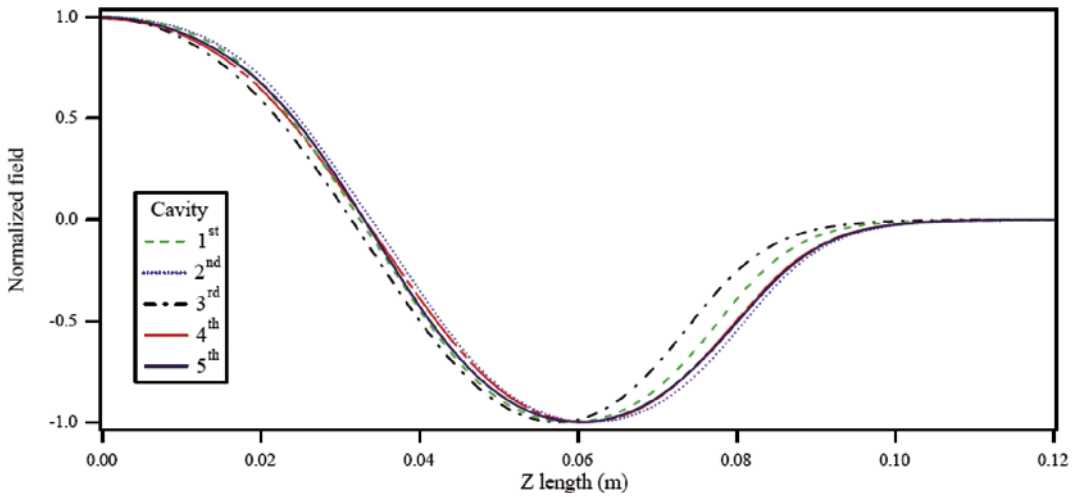

Figure 5.4.1:
Axial electric field of the five cavities (pi-mode).

modes was performed using both frequency-domain and time-domain electromagnetic models [3]. For the largest foreseeable separation, the cavity drive efficiency decreases by ~10%. Great care was taken, using SUPERFISH modeling, to re-scale and optimize each cavity geometry to produce a nearly 1:1 ratio between the pi-mode peak field in the full and in the half cells, as well as to control the frequency separation between the two resonant modes. Various geometries are described in detail in [3, 11].

Field profiles along the axis, for 5 such cases, whose parameters differ slightly while all falling within an acceptable range, are shown in Figure 5.4.1. The main difference between cases is the value of the launching phase that optimizes the beam energy gain and plays an important role in the beam dynamics.

Ref. [3] describes in detail the dependence of shunt impedance on the cavity geometry and the calculations of the effective R/Q for all design options.

5.4.2 Power Coupling

In order to estimate the power coupling between the gun and the waveguide, a three-dimensional model of the basic pillbox RF gun structure was created and implemented using Microwave Studio [12] (Figure 5.4.2). The results obtained are in good agreement with SUPERFISH models. The cavity is modeled with symmetric waveguides and ports. Full height WR-284 waveguides are used: they extend to within 3 mm from the outer cavity walls, in which a rectangular opening provides the waveguide-to-cavity coupling iris. The dimensions of the coupling aperture were varied until the time-domain response, at the smallest mode frequency separation, roughly corresponded to the values measured at the SLAC gun Test Facility (GTF) [13]. The coupling aperture dimensions were then kept fixed while adjusting the cells iris radius to vary the π and zero mode frequency separation. The frequency separation was also varied by varying cell geometries.

Time-domain calculations were also performed using Microwave Studio to obtain the waveguide coupling factors (β) for the pi and zero modes at their resonant frequencies. Results have shown that, in all cases studied, the pi mode is over-coupled (β>1) while the zero mode is under-coupled (β<1).

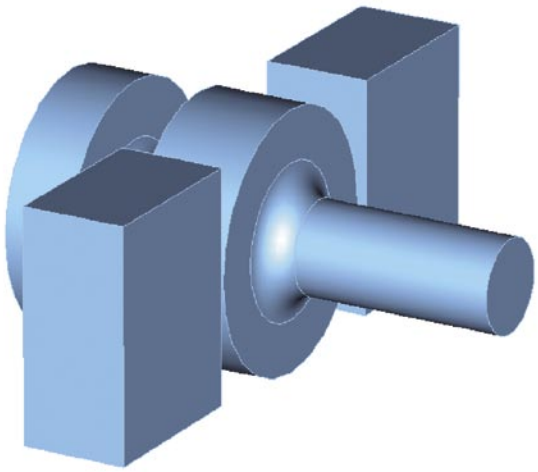

Figure 5.4.2:
Microwave Studio model for the RF gun with dual waveguide feeds.

5.4.3 Klystron Pulse Shape and Gun Cavity Transient Response

The transient response of the two-mode RF gun structure has been analyzed using a realistic excitation signals.

A model of the klystron pulse that drives the cavity modes, assumed to have a 3 μsec flat-top with linear, 100 ns, rise and fall times and a superimposed single carrier frequency modulation at 2998 MHz, has been analyzed. The amplitude and the relative phase of the klystron pulse frequency components, normalized to the 2998 MHz component are plotted in Figure 5.4.3 versus their frequency difference from the 2998 MHz. The drive pulse amplitude ratio and relative phase with respect to the 2998 MHz component are tabulated in Table 5.4.1.

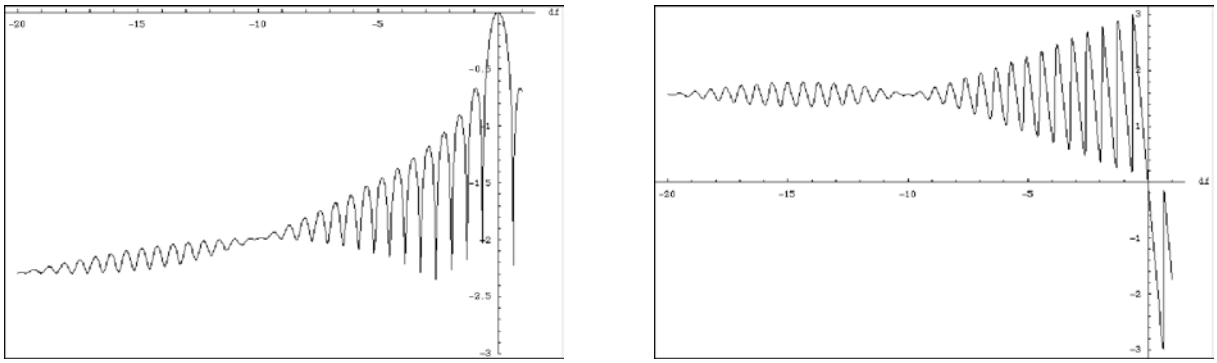

Figure 5.4.3:
Log-amplitude (left) and relative phase (right) of the klystron voltage pulse frequency components, normalized to the 2998 MHz component, versus frequency difference (in MHz).

At large offsets from the carrier frequency and at steady-state, the relative amplitude is seen to decrease exponentially, while the relative phase oscillates about $\pi/2$. Hence, one does expect that, at steady-state, while the π mode will track the phase and amplitude of the 2998 MHz component, the zero mode amplitude and phase will deviate from it as shown in Figure 5.4.3. This estimate does not account for differences in coupling to the klystron pulse for the two modes, nor for mode quality factor differences in coupling to the klystron pulse of the two modes, nor for mode quality factor differences. Those effects are discussed in the next sections.

Table 5.4.1: Relative amplitude and phase at several frequency offsets from the carrier frequency.

Δf (MHz)	0	-3.5	-5	-10	-15	-20
Relative amplitude	1.	0.052	0.024	0.010	0.007	0.005
Relative phase (°)	0.	77.94	122.5	90.	102.0	90.

5.4.4 Two-Mode Resonant Cavity Response under Ideal RF Drive

The behavior of the RF gun structure under non-trivial RF drive waveforms is determined from analysis of the equivalent circuit equation. The transient and steady state response of the cavity modes have been determined and related to measured values of the fields in the full- and the half-cells. In this section, the RF drive waveform is assumed to take an idealized, though nontrivial form, the phase of the RF drive signal was assumed to remain constant over the pulse.

Assuming that the two cavity modes (0 and π) present within the bandwidth of the RF drive, are independently coupled (frequency separation between the two modes larger than the width of each resonance), the time dependence of the voltage of each mode with the coupling to finite conductivity walls and an external waveguide can be expressed as [3]:

$$\left(\frac{d^2}{dt^2}+\frac{\omega_0}{Q_{L,0}}\frac{d}{dt}+\omega_0^2\right)V_0=\frac{2n_0\omega_0}{Q_{ext,0}}\frac{d}{dt}V_{+,0} \qquad 5.4.1$$

$$\left(\frac{d^2}{dt^2}+\frac{\omega_\pi}{Q_{L,\pi}}\frac{d}{dt}+\omega_\pi^2\right)V_\pi=\frac{2n_\pi\omega_\pi}{Q_{ext,\pi}}\frac{d}{dt}V_{+,\pi} \qquad 5.4.2$$

Under constant phase approximation, a time domain solution to equations 5.4-1 and 5.4-2 that allows an analytical formulation of both transient and steady-state behaviors has been derived [3]:

$$\begin{aligned}
&\tilde{V}_\pi(t)\Big/\left(V_{F0}n_\pi\frac{2\beta_\pi}{1+\beta_\pi}\right)=\cos\psi_\pi e^{-i\psi_\pi}\times\\
&\left(\left\{1-e^{-\left(\frac{1+i\tan\psi_\pi}{2Q_{L,\pi}}\right)\omega t}+(\omega\tau-i)\left[\frac{\omega\tau+2Q_{L,\pi}\cos\psi_\pi e^{i\psi_\pi}}{(\omega\tau)^2+(2Q_{L,\pi}\cos\psi_\pi)^2}\right]\left[e^{-\left(\frac{1+i\tan\psi_\pi}{2Q_{L,\pi}}\right)\omega t}-e^{-(\omega t)/(\omega\tau)}\right]\right\}-\right.\\
&\left.H(t-T)\left\{1-e^{-\left(\frac{1+i\tan\psi_\pi}{2Q_{L,\pi}}\right)\omega(t-T)}+(\omega\tau-i)\left[\frac{\omega\tau+2Q_{L,\pi}\cos\psi_\pi e^{i\psi_\pi}}{(\omega\tau)^2+(2Q_{L,\pi}\cos\psi_\pi)^2}\right]\left[e^{-\left(\frac{1+i\tan\psi_\pi}{2Q_{L,\pi}}\right)\omega(t-T)}-e^{-\omega(t-T)/(\omega\tau)}\right]\right\}\right)\\
&\tilde{V}_0(t)\Big/\left(V_{F0}n_0\frac{2\beta_0}{1+\beta_0}\right)=\cos\psi_0 e^{-i\psi_0}\times\\
&\left(\left\{1-e^{-\left(\frac{1+i\tan\psi_0}{2Q_{L,0}}\right)\omega t}+(\omega\tau-i)\left[\frac{\omega\tau+2Q_{L,0}\cos\psi_0 e^{i\psi_0}}{(\omega\tau)^2+(2Q_{L,0}\cos\psi_0)^2}\right]\left[e^{-\left(\frac{1+i\tan\psi_0}{2Q_{L,0}}\right)\omega t}-e^{-(\omega t)/(\omega\tau)}\right]\right\}-\right.\\
&\left.H(t-T)\left\{1-e^{-\left(\frac{1+i\tan\psi_0}{2Q_{L,0}}\right)\omega(t-T)}+(\omega\tau-i)\left[\frac{\omega\tau+2Q_{L,0}\cos\psi_0 e^{i\psi_0}}{(\omega\tau)^2+(2Q_{L,0}\cos\psi_0)^2}\right]\left[e^{-\left(\frac{1+i\tan\psi_0}{2Q_{L,0}}\right)\omega(t-T)}-e^{-\omega(t-T)/(\omega\tau)}\right]\right\}\right)
\end{aligned} \qquad 5.4.3$$

The equivalent circuit parameters are related to measured quantities: coupling, calibrations derived from numerical simulations, cavity shunt impedance and electric field at the cathode.

An ideal RF source waveform has been assumed, defined as:

$$V_F(t)/V_{F0} = H(t)\left(1 - e^{-t/\tau}\right) - H(t-T)\left(1 - e^{-(t-T)/\tau}\right) \qquad 5.4.4$$

The rise and fall times of the waveform (τ) are assumed to be 100 ns, for a 10%-90% pulse risetime of ~220 ns. The pulse is held for 3 μsec (T) before it begins to decay. The drive source central frequency is matched to that of the π mode in the cavity. The WR-284 waveguide cutoff frequency is 2.08 GHz for the dominant TE_{10} mode. The peak power of the forward wave is adjusted to produce ~110 MV/m at the cathode in the π mode.

A Python script was written to generate the time dependent complex mode voltages (Eq. 5.4-3) from the RF power source waveform (Eq. 5.4-4). For four different frequency separation cases (4.6 MHz, 7.12 MHz, 12.5 MHz, 17.6 MHz) the corresponding waveforms for the forward and reverse waves, the peak cathode electric field in the pi and zero modes, and the combined electric field in the half and full cavity cells have been calculated. The electric field was obtained from field measuring probes inserted in both cells and, in presence of a significant zero mode excitation they do differ significantly from the unperturbed pi mode values. Figure 5.4.4 displays, for the 12.5 MHz case, the forward and reverse wave amplitudes (a) and the peak pi and zero modes electric fields (b).

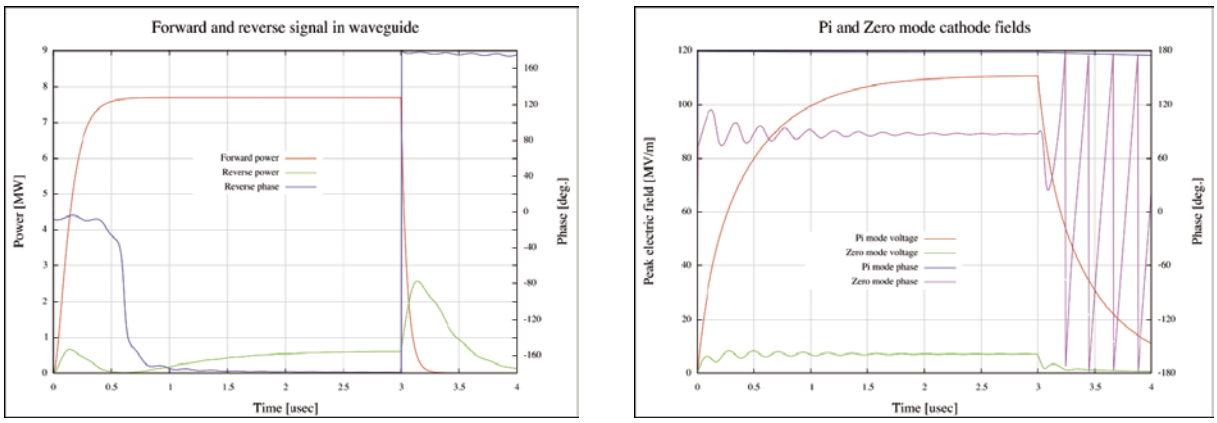

a) b)

Figure 5.4.4:
Incident and observed waveforms for 12.5 MHz frequency separation.

Even though this model makes several assumptions, such as constant phase of the drive pulse throughout the entire pulse length, it provides an analytical, closed-form expression useful to predict the state of the fields in the RF gun cavities at any time during the pulse, in order to pursue beam dynamics studies, and against which measured quantities may be benchmarked.

5.4.5 Two-Mode Resonant Cavity Response under Measured or Simulated RF Drive

The behavior of the RF gun structure under non-trivial RF drive waveforms is derived from numerical analysis of the equivalent circuit equations. In order to benchmark the technique, the computed transient and steady-state cavity responses are compared to measured values of the fields in the full and half cells of the GTF RF gun.

The circuit equations in the time domain are solved by integrating the differential equations from Section 5.4.4 in the slowly varying envelopes approximation [3].

The complex RF drive voltage waveform is obtained by measuring the forward klystron pulse amplitude and phase at a power divider upstream of the RF gun full cell. The forward phase is measured with respect to a low-level clock signal. The same power divider, which also functions as a directional coupler, is used to measure the reflected signal.

In order to benchmark the results of the method against FERMI Linac measured data, the SLAC GTF injector case was simulated first, using a particular GTF measured waveform [14] as the drive pulse.The resulting forward wave signals were used to derive the complex voltage waveform driving the pi and zero modes, which can be written

$$\tilde{V}_+ = \left|\tilde{V}_+\right| e^{-i\varphi_+}, \qquad 5.4.5$$

where amplitude and phase are both time dependent quantities. Under the slowly (with respect to the instantaneous phase of the drive signal) varying envelope approximation, the derivative of the complex waveform is expressible in terms of derivatives of the envelope amplitude and phase:

$$\tilde{V}'_+ = \left(\left|\tilde{V}_+\right|' - i\varphi'_+\left|\tilde{V}_+\right|\right)e^{-i\varphi_+} \qquad 5.4.6$$

Equations of motion 5.4-5 and 5.4-6 were numerically integrated using a Python script and the results of the fit are shown in Figure 5.4.5, displaying excellent agreement between the computed and measured waveforms. The mode frequency-beating in the cavity field amplitude is evident.

An analysis of the GTF injector case was first of all performed to benchmark the results of this method against the measured data. The results of the fit are shown in Figure 5.4.5, displaying excellent agreement between the calculated and measured waveforms. The mode frequency-beating in the cavity field amplitude is evident.

Applying this method to the FERMI FEL injector to four different frequency separation values yields the corresponding forward and reverse waveforms, the peak cathode electric fields in the pi and zero modes and the combined electric fields in both the half and the full cells. The latter quantities are measured by field probes in both cells. Input parameter values were computed using Superfish and the drive frequency was matched exactly to the pi mode resonance. In addition, only near-critical coupling of the waveguide to the RF gun, $\beta_\pi=\beta_0=1.05$, was assumed for both modes. For all four cases the results are

generally similar to the GTF ones quoted above and, as mentioned earlier, in presence of significant zero mode excitation the combined fields do differ significantly from the unperturbed pi mode values.

The peak forward power required to drive the peak pi mode amplitude to *~110 MV/m* is empirically determined and the time along the pulse at which the peak amplitude is reached in the full-cell, which is the time at which the electron beam should be launched by firing the photocathode drive laser, is recorded. Peak electric field values and phases relative to the forward wave phase are tabulated in Table 5.4.2.

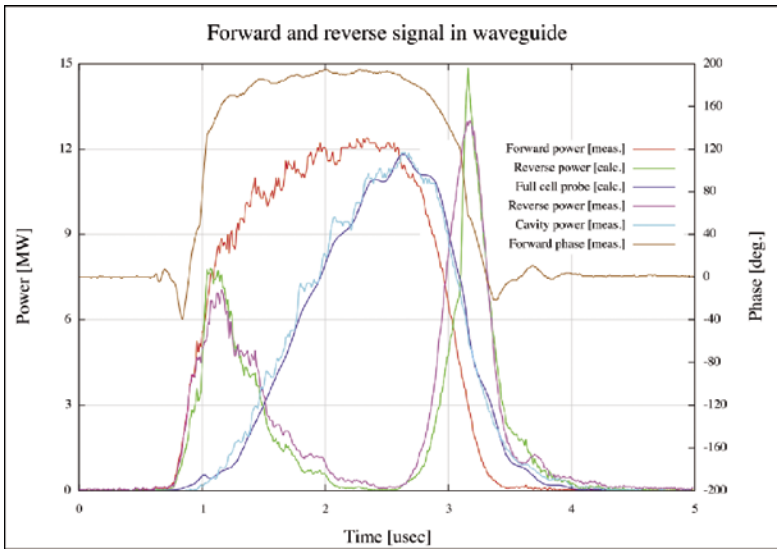

Figure 5.4.5:
Measured and calculated time dependence of the forward and reflected power from the RF gun, and full cell cavity probe signal.

Table 5.4.2: FERMI RF gun operational parameters.

Mode separation, Δf [MHz]	4.6	7.12	12.5	17.6
$P_{forward}$ [MW]	9.2	9.3	9.9	10.1
t_{peak} [μsec]	2.82	2.81	2.81	2.82
$\phi_{forward}$ [°]	174.3	175.2	175.2	174.3
P_{cav} [MW]	7.05	7.1	7.5	7.6
E_{π} [MV/m]	110.3	109.9	110.2	110.4
$\Delta\phi_{\pi}$ [°]	-6.7	-6.8	-6.8	-6.6
E_0 [MV/m]	9.07	5.86	3.1	2.4
$\Delta\phi_0$ [°]	-92.4	-83.6	-83.2	-86.1
$\Delta\phi_0 - \Delta\phi_{\pi}$ [°]	-85.7	-76.8	-76.4	-79.5
E_{half} [MV/m]	111.3	111.4	111.0	110.9
$\Delta\phi_{half}$ [°]	-11.3	-9.8	-8.4	-7.8
E_{full} [MV/m]	110.	108.8	109.6	110.0
$\Delta\phi_{full}$ [°]	178.1	176.2	174.8	174.6
$\Delta\phi_{full} - \Delta\phi_{half}$ [°]	189.4	186.0	183.2	182.4

5.4.6 Beam Dynamics Simulations

The analysis of the previous section yields a data set describing the optimized cavity parameters at the appropriate electron beam launching time. The analysis has been used to perform parametric sensitivity studies and to generate accurate relative field and phase values for beam dynamics calculations.

The effect of zero-mode excitation on the beam dynamics has been studied for the MLB bunch case, assuming for simplicity a flat-top bunch profile [15]. Similar analyses can be extended to the ramped-current bunches. The electron beam was generated from a 9 ps (FWHM) long, flat topped drive laser pulse with 0.5 ps linear rise and fall times. The (hard edge) spot size diameter at the cathode was 1 mm. The bunch charge was 800 pC and the initial (thermal) emittance is ~0.6 mm mrad [16]. The evolution of the transverse rms beam phase space and of the emittance is shown in Figure 5.4.6. Slice parameters were computed using 1 ps length slices, symmetric about the bunch center-of-charge. The bunch longitudinal blow-up decreases the slice peak current from an initial value of ~90 A at generation to ~75 A at the booster linac entrance and all the way down to the injector exit.

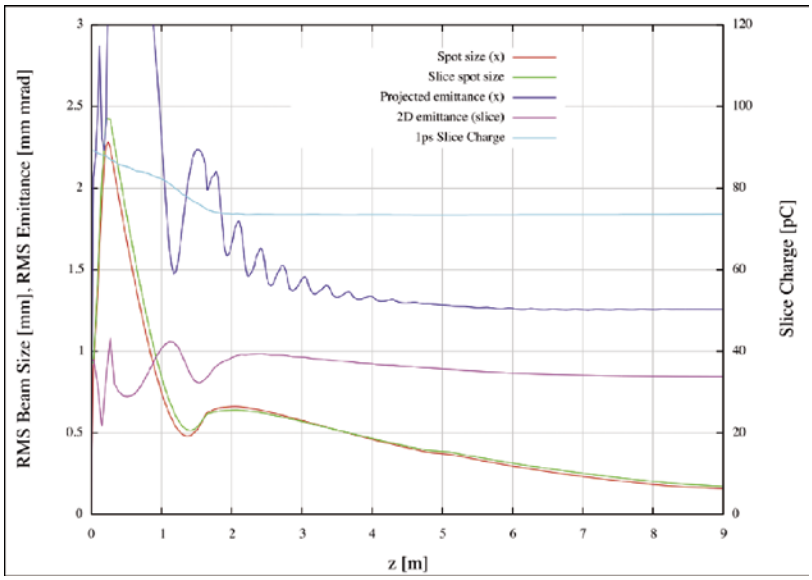

Figure 5.4.6:
Transverse beam evolution through the injector.

Figure 5.4.7 shows the beam energy and longitudinal emittance evolution in the injector. The average beam energy reaches ~95 MeV at the injector exit. The rms bunch length grows by ~30%, from ~0.8 mm to ~1.05 mm. The region of largest longitudinal blow-up rate is the gun-to-linac drift space, where the beam has relatively low kinetic energy and is decreasing in spot size under the effect of emittance compensation processes and of matching to the linac optics.

The longitudinal emittance is defined as

$$\varepsilon_z = \sqrt{\left\langle z^2 \right\rangle \left\langle \Delta E^2 \right\rangle - \left\langle z \cdot \Delta E \right\rangle^2} \quad , \qquad 5.4.7$$

where z and ΔE are the particle offset in longitudinal position and the energy offset with respect to the synchronous particle. Figure 5.4.7 displays the evolution of longitudinal emittance, total rms energy spread and linear correlation of the longitudinal phase space $\langle z\,(d\Delta E/dz)\rangle$.

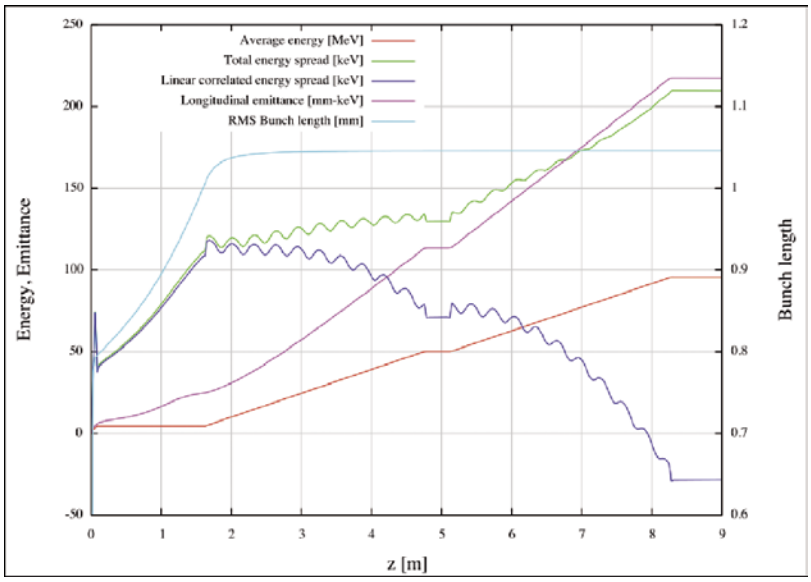

Figure 5.4.7:
Longitudinal beam evolution through the injector.

The linear correlation indicates the orientation of the phase space. It has greatest meaning in the region upstream of the booster linac sections. RF field curvature in the linac introduces significant quadratic and higher order polynomial nonlinearities. The resulting longitudinal phase space of the beam in the gun-to-linac and booster-to-linac regions is shown in Figure 5.4.8.

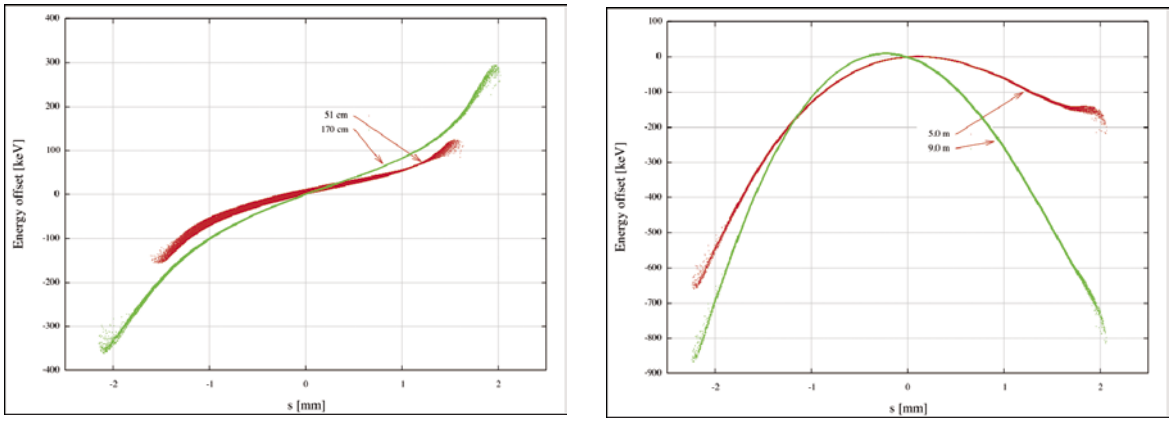

Figure 5.4.8:
Longitudinal phase space in the gun-to-linac region (respectively at 50 cm and at 170 cm from the cathode) (on the left), and at the exit of SØA (at 5 m from the cathode) and SØB (at 9 m from the cathode) (on the right).

In the gun-to-linac region, the overall energy spread is dominated by the correlated contribution. The longitudinal emittance blow-up in the gun-to-linac drift is due to the increase in bunch length and to increasing space charge force terms.

The baseline beam dynamics outlined above was used to generate a collection of nominal beamline parameters that led to optimized RF gun voltages and phases, solenoid magnet peak field settings, booster linac voltages and phases, etc. For each gun mode frequency separation value, a set of beam dynamics simulations was produced, both with and without the zero mode, as a function of the pi-mode phase with respect to the bunch launch time.

The modes are assumed to be excited by the GTF-like klystron pulse described previously, which introduces specific zero-mode amplitudes and phases relative to the pi mode. The zero mode, when present, lags behind in phase with respect to the pi mode according to the phase difference tabulated in Table 5.4.2. This effectively allows studying the beam dynamics sensitivity to the stability of the laser arrival time at the photocathode.

Analysis of the beam transverse phase space at the injector exit (~8.28 m) provides information on the degree to which the zero mode excitation interferes with the emittance compensation process. In general, for the relatively long and intense bunches considered here, one finds that the normalized emittance is more sensitive to offsets in the pi-mode phase than to the presence of a perturbing zero-mode. This because space charge forces and 'normal' RF field nonlinearities (due to the pi mode alone) are the dominant contributors to transverse emittance and energy spread. Nevertheless, quantitative understanding of the zero-mode influence will be essential during commissioning and whenever short and/or low charge bunches are used.

5.4.6.1 Transverse Phase Space

The transverse emittance variation with the pi-mode phase is shown in Figure 5.4.9. The quoted bunch emittances are averages over 100 longitudinal bunch slices.

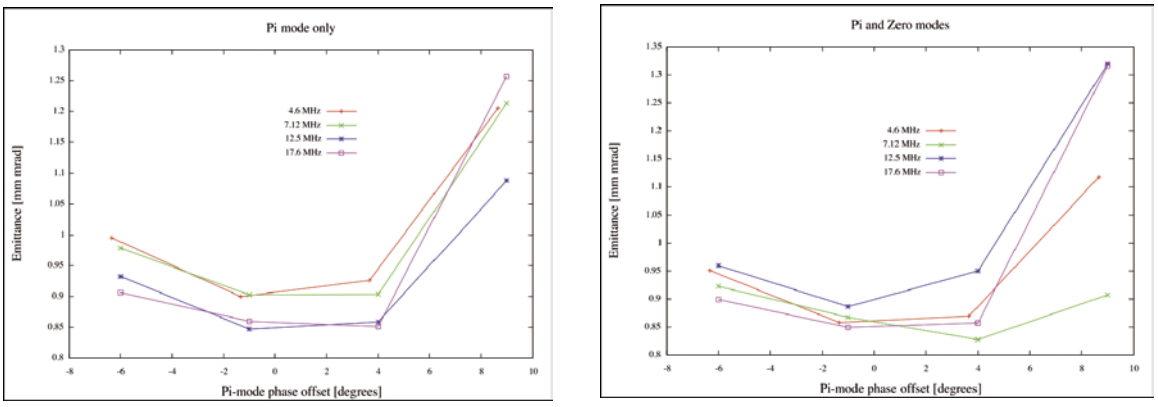

Figure 5.4.9:
Variation of normalized transverse emittance with respect to pi-mode phase offset, for the pi-mode only cases (on the left) and pi+zero-mode cases (on the right).

The emittance sensitivity to phase offsets decreases at negative detuning angles while it increases for positive detuning. When adding the zero mode excitation, the transverse emittance sensitivity to the pi mode phase remains more or less constant, an indication that the zero mode influences primarily the longitudinal phase space. The figure also shows that, as mentioned above, changing the cavity geometry (the beam transit RF phase) in the direction of increasing the mode separation improves the emittance only slightly.

5.4.6.2 Longitudinal Phase Space

The influence of the zero mode on the longitudinal phase space footprint was initially noticed studying the correlated energy spread of photoinjector-generated electron bunches [17]. Beating between the two modes introduces additional correlated energy spread that must be accounted for in following the beam through the accelerator.

Results of beam dynamics simulation runs are compared in the gun-to-linac drift region (~0.5 m), before the nonlinear RF curvature makes it difficult to extract the influence of the zero-mode. Differences in total energy spread, linear correlation, and longitudinal emittance between the pi+zero mode cases and the pi-mode only cases, computed as a function of the pi-mode phase offset, are shown in Figure 5.4.10, Figure 5.4.11 and Figure 5.4.12.

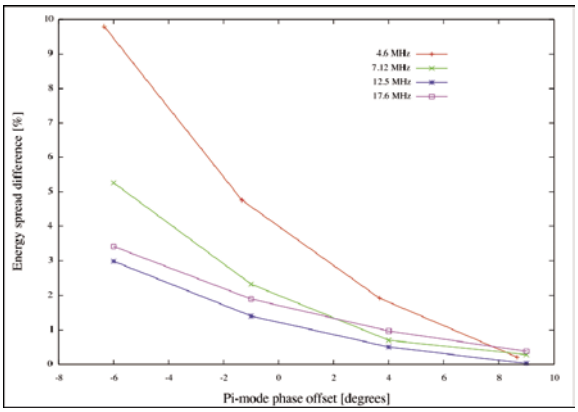

Figure 5.4.10:
Difference in total energy spread between pi+zero mode cases and pi-mode only cases.

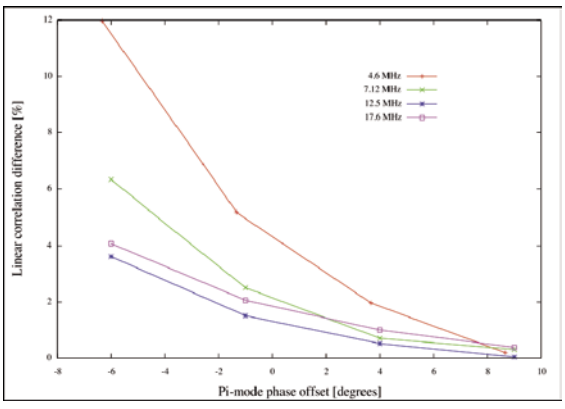

Figure 5.4.11:
Difference in linear correlation between pi+zero mode cases and pi-mode only cases.

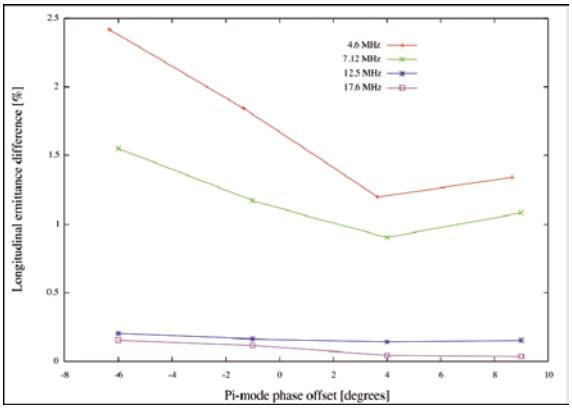

Figure 5.4.12:
Difference in longitudinal emittance between pi+zero mode cases and pi-mode only cases.

Comparing the results of Figure 5.4.10 and Figure 5.4.11, it is again evident from simulations that in the gun-to-linac drift region the total energy spread is dominated by the correlated one. Several interesting and relevant effects of the zero-mode excitation are observed. First, the difference in the amount of correlated energy spread generally decreases as the mode separation increases. Second, the sensitivity of the difference in the correlated energy spread with respect to the pi-mode phase offset significantly decreases as the mode separation increases. Last, the difference in longitudinal emittance (Figure 5.4.12) is largely removed by increasing the mode separation.

5.5 Diagnostic Beamline Design

Figure 5.5.1 shows the photoinjector and diagnostic beamline layouts. The diagnostics in this area monitors the gun performance and characterizes the electron bunch produced by the RF gun. The low

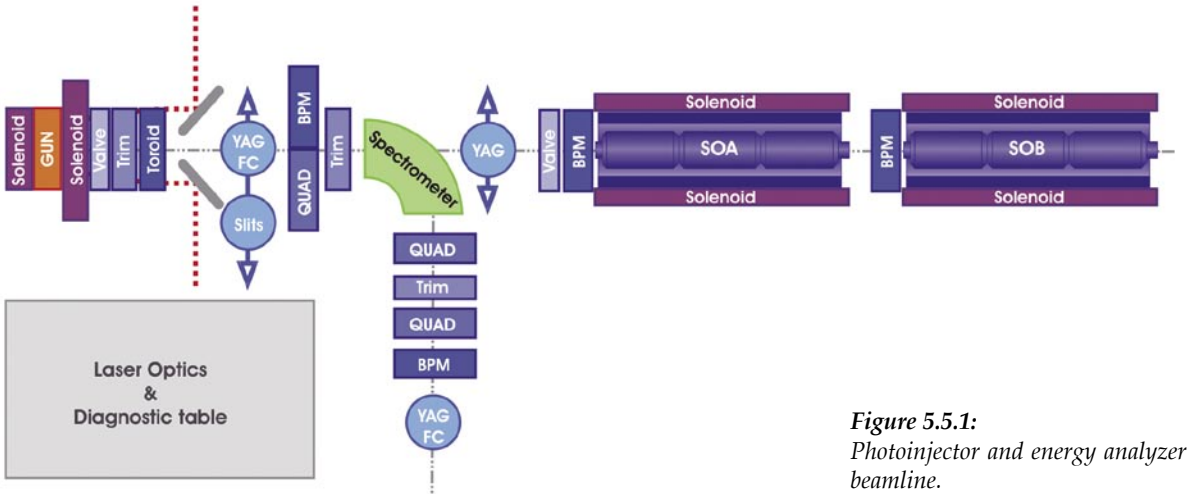

Figure 5.5.1:
Photoinjector and energy analyzer beamline.

energy transport line from the gun to the entrance of the first booster linac (SØA) allows for two modes of operation: direct transport ("in-line") and deflection to an energy analyzing branch beamline. Two horizontal and vertical dipole correctors (trim) and two BPMs allow for trajectory corrections. A single magnetic quadrupole is included in the direct transport beamline to compensate for any residual phase-induced quadrupole field components in the RF gun or in the linac coupling cells that may interfere with emittance compensation by breaking the cylindrical symmetry. Standard in-line and intercepting diagnostics measure the bunch current, transverse distribution and emittance. An energy analyzer comprised of a 90° bend and three quadrupoles will be used to measure the beam energy and energy spread. A streak camera deployed at the end of the energy analyzer beamline allows for detailed study of the beam longitudinal phase space profile. A complete description of the individual diagnostic components appears in Chapter 11.

5.5.1 RF Gun and In-line Transport Optics

The in-line beamline connects the RF gun output flange to the entrance to the booster accelerator (SØA/SØB) and to the following linac sections. The current physics model of the beamline assumes idealized field profiles of the beamline elements. The electron beam distribution, RF gun and linac cavity modes, solenoid magnet fields, and the resulting beam dynamics were assumed to be axisymmetric. In this approximation, no additional beamline elements are required to generate the high-brightness electron bunches and propagate them between the gun and booster linac.

The physics model uses a simplified, free space model of the solenoid magnets. The resulting field distribution has a fairly long longitudinal reach that may likely interfere with downstream diagnostic performance. A companion bucking solenoid will be included to cancel the on-axis magnetic field at the cathode plane.

5.5.2 Diagnostic Components and Measurements

5.5.2.1 Beam Properties to be Measured Directly

The photoinjector beamline requires diagnostics to accurately and adequately measure the electron beam produced by RF gun and photoinjector laser. Measurements on the electron beam include: (i) bunch charge and photocathode quantum efficiency (Q.E.), (ii) transverse beam position, (iii) beam energy and energy spread, (iv) transverse beam profile, and (v) thermal emittance. Only bunch charge and transverse beam position measurements may be performed with non-interceptive diagnostics. All other measurements will require beam interception and/or deflection. Additional measurements need to be performed on the photoinjector laser beam. Most important are the laser spot size, energy distribution and total energy deposited at the photocathode. They are provided by optical diagnostics (virtual cathode and camera, laser pulse joule-meter, etc.) located close to the RF gun. Information on the longitudinal laser pulse distribution will be obtained from the optical spectrum, and/or by direct measurement with a streak camera.

Beam current and bunch charge will be closely monitored during commissioning and operation to detect and correct any slow drift in the photocathode average quantum efficiency (Q.E.): charge variations will be fed-back to the photocathode drive laser in order to correct them by modulating the laser intensity. A map of the photocathode Q.E. over the region of interest can than be obtained by sweeping a small size laser spot over the cathode and measuring the emitted photo current.

Abnormally large charge variations that could indicate large changes in the average photocathode Q.E. will require more extensive corrective action.

5.5.2.2 Summary of Standard In-Line Diagnostic Elements

The in-line beamline is equipped with a standard complement of diagnostics. Bunch charge will be inferred from current measurements using an inductive toroid and an intercepting Faraday cup (FC). The difference signals from capacitive button-type beam position monitors (BPMs) will provide the bunch charge-centroid position, while the sum signals will be used to measure the bunch charge after calibration with the FC. To determine the photocathode quantum efficiency the drop-in Faraday cup will provide the most accurate bunch charge values.

YAG-coated scintillator screens generating optical transition radiation (OTR) when hit by the beam will be the primary diagnostic for transverse electron beam size and profile. Paired with an upstream quadrupole magnet, they will be used to measure the transverse beam emittance by the quadrupole-scan method. At low bunch charges, the photocathode thermal emittance may also be measured in the same way.

5.5.2.3 Standard Diagnostic Resolution and Sensitivity

The electron beam charge is specified to be in the 0.3-1.0 nC range, with a ~10 ps (FWHM) bunch length under normal operation conditions. The charge measurement nominal resolution is consequently specified to be in the ~10-50 pC range. A spot size diameter at the cathode of around 0.5 mm (rms) increases up to 2-3 mm before entering the solenoid at about 30 cm from the cathode. The solenoid focuses the bunch down to 0.4 mm (rms) at about 1.5 m from the cathode. Thus position resolution of ~10-100 μm is sufficient when measuring the transverse bunch size before it enters the solenoid.

During commissioning and for measuring the thermal emittance, the injector may be operated at reduced bunch charge levels, typically ~50 pC or less. To measure the charge, Faraday cups with less than 10 pC resolution will have to be deployed on both beamlines. At such low bunch charges the YAG-coated OTR screens have sufficient sensitivity to provide gross spot size and trajectory measurements.

5.5.3 Beam Properties Measured with an Energy Analyzer and Streak Camera

A dispersive beamline that deflects the beam by 90° is used to measure the average beam energy and energy spread. Single-shot streak-camera measurements of Cherenkov or OTR light radiated by the final screen may be used to probe the longitudinal beam distribution and determine the longitudinal phase space emittance.

5.5.3.1 Energy Analyzer Optics

A detailed description of the energy analyzer optics is given in Section 5.4 of Ref. [3]. Its optical functions have been designed to minimize the beam spot size at the image screen, while maintaining a given dispersion. The resulting optical functions are shown in Figure 5.5.2.

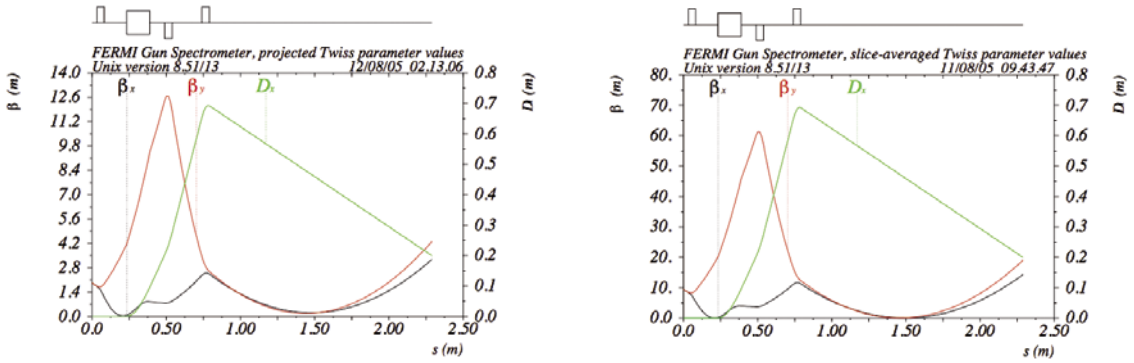

Figure 5.5.2:
MAD models of energy analyzer showing the evolution of projected (left) and slice-averaged (right) Twiss parameters.

The screen location at ~1.5 m coincides with the nominal beam waist position. At this point, for a beam energy of 5.3 MeV, or $\gamma \sim 10.4$ the optical functions and the emittance take the values:

$\beta_X \sim$ 0.25 m
$D_X \sim$ 0.45 m
$\varepsilon_X \sim$ (1.0 mm mrad) / (10.4) = 0.1 mm mrad

The minimum relative energy resolution is then $\delta_{min} \geq 3.6\ 10^{-4}$, or ~2 keV.

The beamline layout presented here is the result of a compromise between the requirements of producing a high brightness electron beam, which tends to require shorter drift lengths between the RF gun and the first booster linac for proper emittance compensation, and the needs of the diagnostics and other instrumentation required to diagnose and to preserve the high quality of the beam.

5.6 Injector Performance Studies

The beam dynamics in the injector system has been modeled extensively - from the photocathode to the exit of the booster accelerator modules - using 2D and 3D space-charge tracking codes (GPT and ASTRA). Some approximations have been made regarding the beamline and its components. Firstly, the entire beamline was assumed to possess perfect azimuthal symmetry about the beamline axis. Secondly, the RF gun model used in the simulations did assume the presence of the TM010-π ('pi') mode only. As shown in the previous sections, the lower-frequency mode response is a complicated function of the RF pulse history and gun geometry. The optimization studies presented here will therefore require some recalibration once the RF gun behavior has been more completely characterized. Lastly, longitudinal wakefield effects from the booster accelerator structures have been included in an approximate form: time-dependent longitudinal impulses are computed based on the published wakefield data [18] and the longitudinal bunch charge distribution.

Flexibility in the beamline design and tuning for optimum performance has required some compromise. Space allocation for the beamline instrumentation, including the special diagnostic-dedicated branch requires a minimum drift distance between the RF gun exit and the first booster structure entrance of about 1.6 m, still sufficiently close to the optimum matching point for emittance compensation located at ~ 1.4 m from the cathode.

To optimize the performance in the remainder of the linac, a new type of initial pulse current shape, namely a linear ramped current distribution, has been adopted. In particular, to produce a bunch with uniform current and energy at the entrance of the FEL undulators, accelerating structure wakefields and compression parameters effects lead to the choice of a bunch current in the shape of a quasi-linear head-to-tail ramp. This section describes the optimized beam dynamics for the ramped current distribution for two different bunch configurations: a 0.8 nC/9 ps long "medium length bunch (MLB)" and a 1 nC/11 ps "long bunch (LB)", and includes parametric sensitivity studies and parameter jitter analysis.

5.6.1 Optimum Baseline Configurations

Table 5.6.1 summarizes the main optimized bunch parameters at the exit of photoinjector, in both the MLB and the LB regimes.

Table 5.6.1: Main bunch parameters at the exit of the photoinjector.

Parameters at the exit of the photoinjector	*MLB*	*LB*
Electron beam energy [MeV]	95	95
Bunch charge [pC]	800	1000
Peak current [A]	From 40 to 80	From 40 to 100
Ramped Bunch length [ps]	8	9
Slice emittance [mm-mrad]	< 1	< 1
Projected emittance [mm mrad]	< 1.5	< 1.5
Energy spread (uncorrelated) [kev]	<2	<2

5.6.1.1 Medium Length Bunch Regime

In a seeded FEL, the temporal overlap of an ultra short (~100 fs) seed laser pulse with the electron beam at the undulator entrance is a critical issue. To relax jitter tolerances, a 'medium length' bunch case has been considered, consisting of a 600 fs electron bunch with a peak current around 1 kA. This translates to a required extracted charge of 800 pC and to a drive laser pulse at the cathode of about 9 ps FWHM, with 0.5 ps of rise/fall time. As mentioned earlier a conservative value of 110 MV/m for the gun accelerating gradient was considered, even if better performances could be obtained by increasing it to 140 MV/m.

As described in [19] a backward tracking simulation performed by LiTrack [20] revealed that a linearly ramped current distribution at the photoinjector exit is a very convenient method to linearize the

wakefields fields in the Linac accelerating sections. Figure 5.6.1 shows the longitudinal phase space (a) and the current profile (b) required by the linac optimization studies at the exit of the photoinjector for the MLB case.

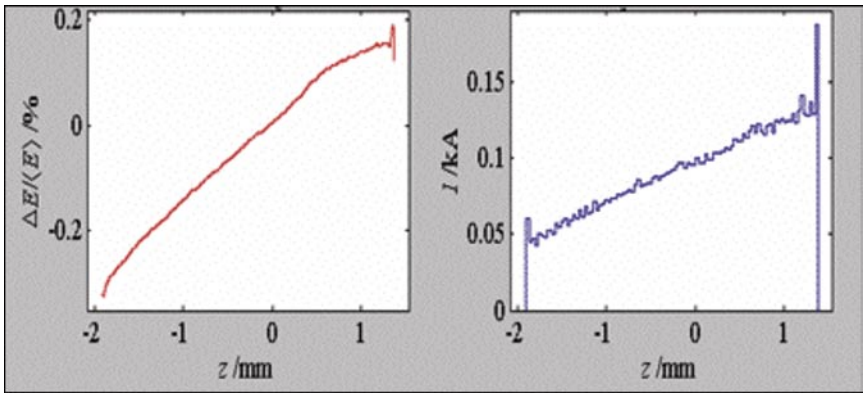

Figure 5.6.1:
On the left: Longitudinal phase space; on the right: current distribution at the exit of the photoinjector for the MLB case (peak slice current on the bunch tail, LiTrack notation).

In order to satisfy these requirements, and to provide an injector output beam with a tailored current profile, the evolution of the initial profile of an emitted bunch in the injector due to the strong non-linearity of the longitudinal space charge field has been studied: the redear is referred to [21, 22] for a more detailed description. Several initial current distributions were analyzed in order to find the one which best linearizes the space charge field. In order to avoid a strong compression along the linac, the linear current ramp bunch at the injector exit must be about 2.5 mm (~8 ps) long. Because the bunch length is blown-up during transport from the cathode to the first accelerating section, the above

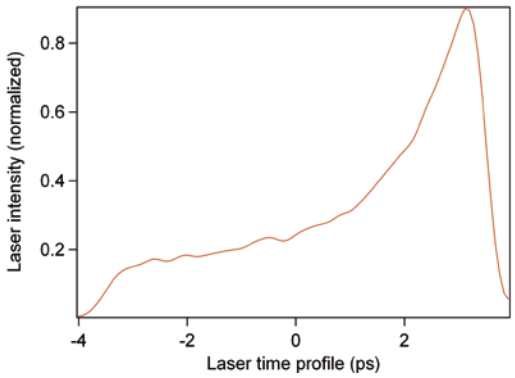

a)

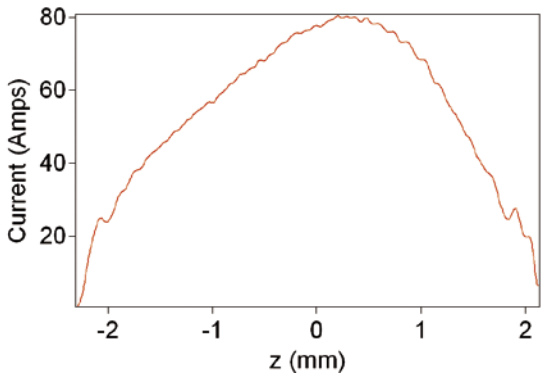

b)

Figure 5.6.2:
a) The optimized longitudinal laser shape is a fourth-degree polynomial;
b) Bunch current distribution at the end of the photoinjector, LiTrack notation.

requirement limits the allowed ramped fraction of the bunch. A fourth-degree polynomial distribution (see Figure 5.6.2) was found to be effective in compensating the high orders contributions of the space charge field (see Figure 5.6.3) while maximizing the bunch fraction that samples a linear space-charge field. The current distribution plotted in Figure 5.6.2a has been adopted as the baseline ramp for the MLB case, with the assumption that the laser pulse can be so shaped. However in a more conservative scenario even a quadratic distribution could be used without severe drawbacks.

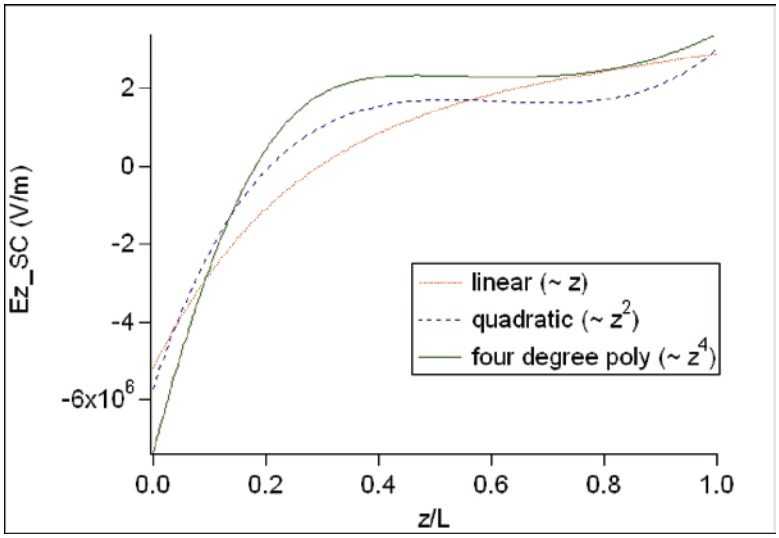

Figure 5.6.3:
Comparison between the longitudinal space charge fields sampled by a linear, a quadratic and a fourth-degree polynomial distribution at the cathode.

Because of the non-uniform charge distribution of the ramp, it is difficult to find an injector parameter set that completely satisfies the invariant envelope equation, performing perfect emittance compensation for all slices. Since each slice contains a different amount of charge for any given set of injector parameters, it evolves in a particular and unique way in the gun-to-SØA drift. An "average" setting has therefore been found that minimizes the projected emittance at the exit of the photoinjector (see Figure 5.6.4). The resulting emittance, including the thermal contribution, reaches ~1.39 mm mrad, and if one includes only 80% of the bunch particles, reduces to 1.21 mm mrad.

The thermal emittance contribution has been included following the empirical formula [16]:

$$\varepsilon_{th}(mm\ mrad) = 0.16 + 0.93 \cdot \sigma_X(mm) \qquad 5.6.1$$

where σ_X is the drive laser spot rms radius.

Thus, assuming a drive laser spot radius of 1mm, the thermal emittance is about 0.6 mm mrad.

Dividing now the longitudinal bunch profile at the end of SØB into 100 slices and calculating the emittance and the energy spread of each slice, one obtains the plot shown in Figure 5.6.5. As expected, the ramped current distribution also affects the slice emittance modulation along the bunch. The slice emittance of the minimum current slices (at the head) is around 0.7 mm mrad, while the highest current slice reaches 1.1 mm mrad. Figure 5.6.6 shows a top view of the bunch at the injector exit: the transverse dimension is quite constant along ~70% of the bunch length.

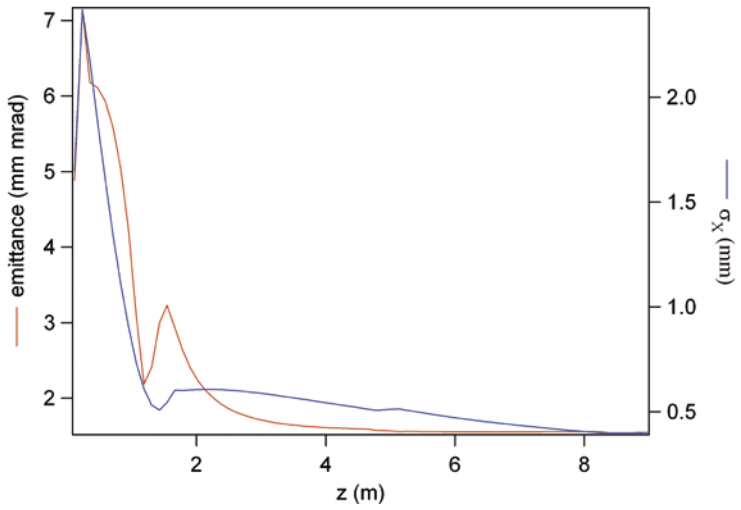

Figure 5.6.4:
Projected Emittance (red line) and RSM transversal spot (blue line) evolution through the injector in the ramped MBL regime.

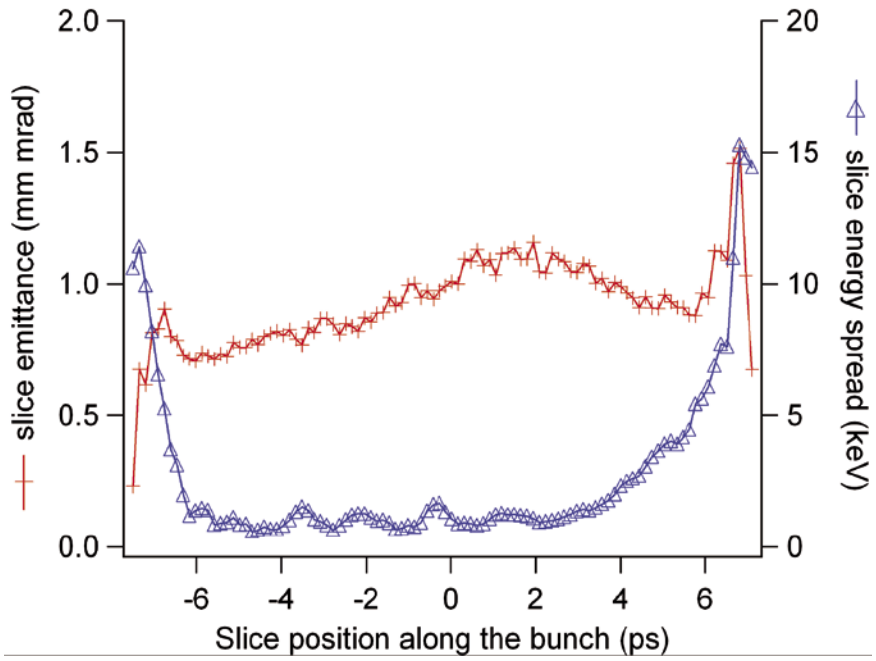

Figure 5.6.5:
Slice emittance (red line) and slice energy spread (blue line) along the ramped MBL bunch, at the exit of the photoinjector (~100 MeV). The head of the bunch is on the left.

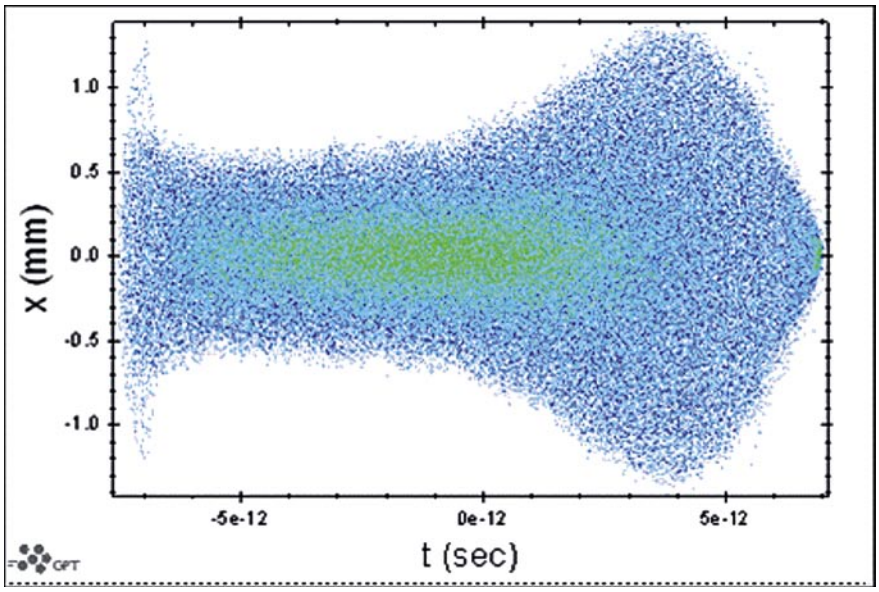

Figure 5.6.6:
Top view of the ramped MBL calculated at the exit of the photoinjector. The head of the bunch is on the left.

5.6.1.2 Long Bunch

The 'long' bunch case is the configuration selected for running at high bunch charge (1 nC) and a long drive laser pulse (~10 ps) at the cathode. An in-depth investigation of the best ramped current profile was carried out, starting from the backtracked results obtained with Litrack and plotted in Figure 5.6.7.

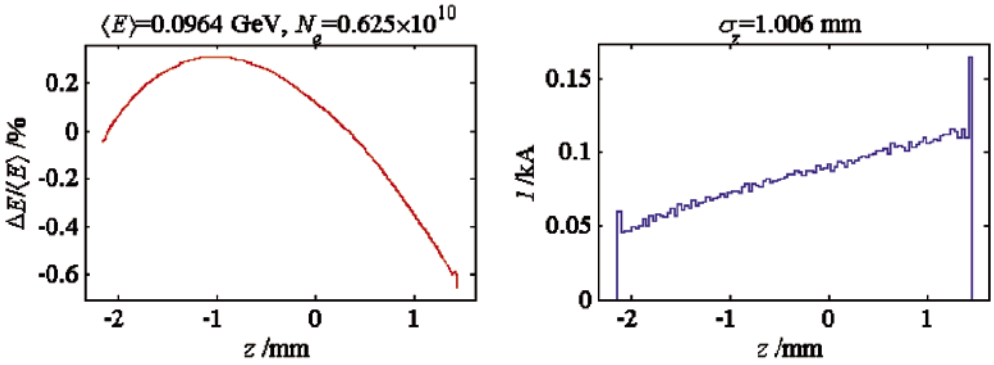

Figure 5.6.7:
(On the left) Longitudinal phase space and (on the right) current distribution at the exit of the photoinjector for the long bunch case (highest slice current in the bunch tail) obtained by the Litrack backtracking.

As in the MBL case, the electrons in the highest current region are pushed back by the space charge forces in the gun-to-SØA drift, so that only a fraction of the bunch has a ramped current profile. It was found that the length of the non-ramped fraction depends mainly on the highest (peak) slice current value, I-peak: for I-peak~100 Amps, the non-ramped fraction is about 1-1.5mm long. Since in the LB case the required ramp is longer than in the MBL case (~4 mm, i.e. ~13 ps) the ramped fraction of the bunch at the injector exit must also be longer.

Figure 5.6.8 shows the optimized laser pulse shape at the cathode and the electron bunch current profile at the exit of the photoinjector: the ramped fraction is about 66% of the total.

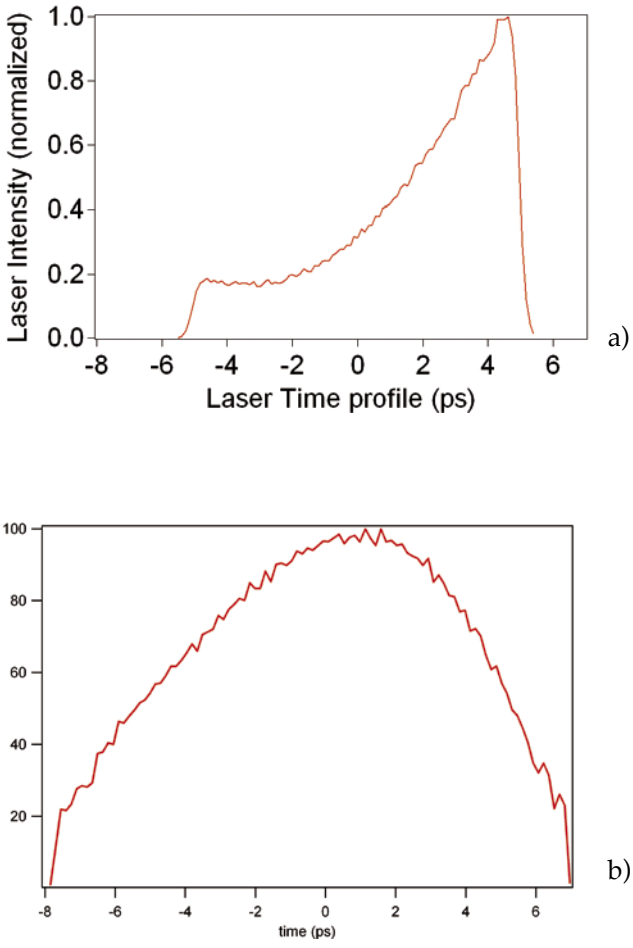

Figure 5.6.8:
a) The optimized longitudinal laser shape is a quadratic polynomial;
b) Bunch current distribution at the end of the photoinjector (I-peak~90 Amps).

Figure 5.6.9 shows the result of the emittance compensation process. Even in this case, because of the non uniformity of the slice charge density, obtaining good matching condition is an issue. At 100 MeV the projected emittance reaches 1.39 mm mrad.

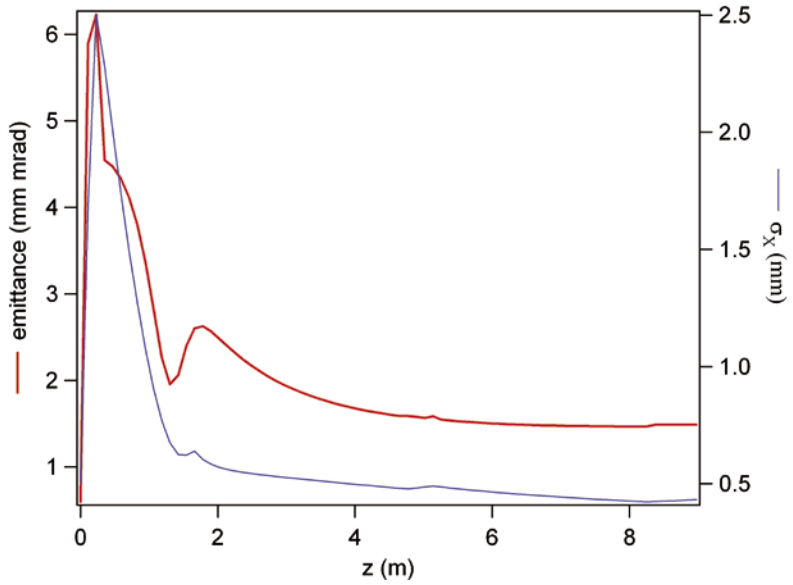

Figure 5.6.9:
Projected Emittance (red line) and rms transversal spot (blue line) evolution through the injector in the ramping long bunch regime.

As in the MBL case a slice analysis of the bunch at the exit of the photoinjector was performed and the results are shown in Figure 5.6.10. The slice emittance behavior (from 0.7 to 1.2 mm mrad) is consistent with the charge density ramp along the bunch and satisfies the specification (less than 1.5 mm mrad).

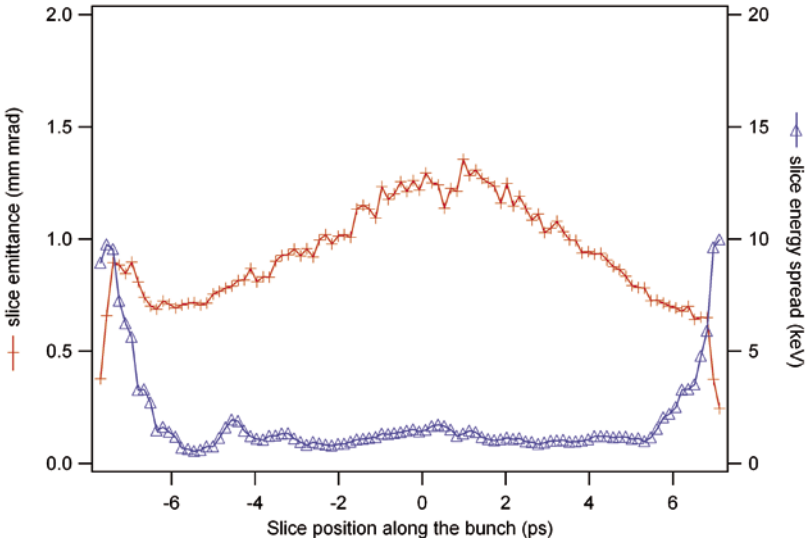

Figure 5.6.10:
Slice emittance and energy spread along the bunch for the LB case.

5.6.2 Parametric Sensitivity Studies

5.6.2.1 Parameter Choices, Tolerances and Jitter Studies

The stability and the robustness of the proposed baseline injector configuration has been investigated. The characteristic variations of the output bunch parameters as a function of the input parameters have to be carefully estimated, because a seed harmonic cascade FEL is very sensitive to shot-to-shot stability. The temporal stability of the electron bunch at the entrance of the undulator, for example, is an important operational requirement to guarantee a reliable synchronization with the seed laser. Moreover the energy stability of the electron bunch is a condition for the stability of the FEL radiation itself; it is therefore important to investigate the contribution to the energy jitter of the injector parameters jitters.

Time of flight, energy, energy spread, peak current and emittance at the end of the injector have been identified as the main output parameters whose shot by shot variation, as well as the corresponding effects on the bunch slice properties , should be quantified.

Moreover, the strong correlation introduced by space charge effects between the various injector parameters does not allow considering each of them separately, but requires performing complete tracking simulations that include all the jitters simultaneously. By randomly sampling each injector component parameter within a tolerance range dictated by present technology, a large number of injector cases have been tracked with GPT and ASTRA, thus obtaining a statistically significant evaluation of the expected jitter of relevant beam output parameters. The solenoid current jitter has been neglected because of the very high stability specified for its power supply. Table 5.6.2 shows the expected rms jitter of each of the considered injector parameters while the computed beam output jitters are collected in Table 5.6.3 and Table 5.6.4.

Table 5.6.2: Expected rms variations of the injector parameters.

InjectorParameter	*Expected rms variation*
RF injection phase	0.1 deg
Laser Arrival time	200 fs
Gun Eacc	0.25 %
Solenoid strength	0.005 %
SØA-SØB Eacc	0.25 %
SØA-SØB RF phase	0.1 deg
Charge (laser pulse energy)	4 %
Laser spot size	4 %
Laser pulse length	5 %

In order to estimate the current jitter an equivalent current $\hat{I}$, independent from the longitudinal bunch profile, has been defined as:

$$\hat{I} = \frac{Q}{\sqrt{12}\sigma_t} \qquad 5.6.2$$

where Q is the total bunch charge and σ_t is the rms bunch length. This figure of merit represents the peak current of a uniform distribution having σ_t as rms bunch length, but the treatment is general and any other distribution (gaussian, parabolic, quadratic, etc...) can be taken as reference, with $\hat{I}$ the corresponding peak current.

Random gaussian sampling of all the injector parameters according to the tolerances of Table 5.6.2 has been performed for the medium and for the long bunch case.

Figure 5.6.11, Figure 5.6.12 and Figure 5.6.13 show the simulated output parameters jitter and the corresponding histograms for the MLB case.

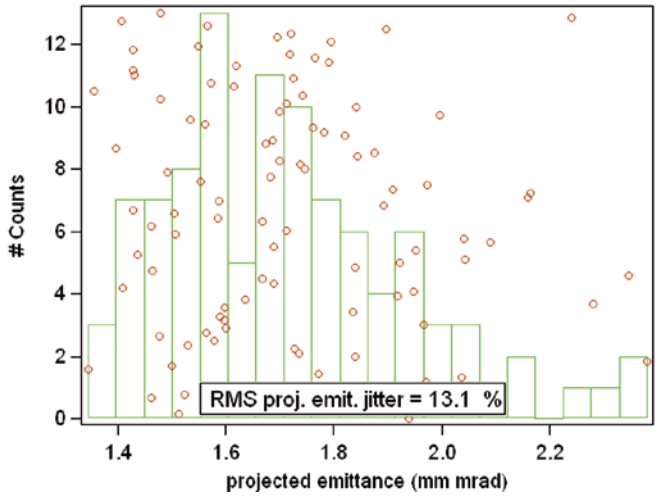

Figure 5.6.11:
Projected emittance jittered values obtained by randomly sampling input injector parameters.

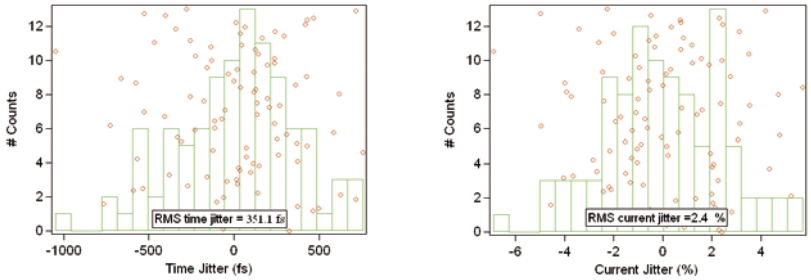

Figure 5.6.12:
Time (on the left) and current (on the right) jittered values obtained by randomly sampling input injector parameters.

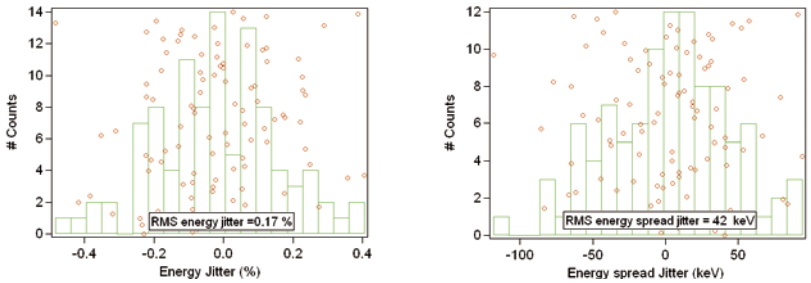

Figure 5.6.13:
Energy (on the left) and energy spread (on the right) jittered values obtained by randomly sampling input injector parameters.

Since the laser pulse shaping process could introduce additional jitter sources, a preliminary study has been made to identify the main parameters whose jitter could affect the shaping of the laser pulse, and their correlation to each other. As an example, a pulse length jitter produces jitter in the ramping current distribution.

Furthermore, regarding the optical matching between the injector and the linac, an analysis of the Twiss parameters jitter has been carried out using the above set of output jittered bunches. The results are given in Table 5.6.3. The average α_x and β_x are respectively -0.09 and 18 m, but the jittered outputs are spread out with a standard deviation of 0.15 and 2.1 m respectively. This should be taken into account for the finalization of the optics matching.

Table 5.6.3: Output parameters jitters for the ramped MLB.

Output parameters	*rms jitter*
Time (fs)	351
Current (%)	2.4
Energy (%)	0.17
Energy Spread (keV)	42
Emittance (%)	13.1
Alpha	0.15
Beta (m)	2.1

The above described issues concerning the emittance compensation of a ramped current distribution are reflected in a reduced stability of the optimized injector parameters setting, leading to a rms jitter of the projected emittance of about 13%.

As for the MBL case simulations using a set of randomly sampled injector parameters (following Table 5.6.2) were also run. The results are reported in Table 5.6.4.

Table 5.6.4: Output parameters jitters for the long ramped bunch.

Output parameters	*rms jitter*
Time (fs)	266
Current (%)	3.3
Energy (%)	0.17
Energy Spread (keV)	24
Emittance (%)	6.3
Alpha	0.26
Beta (m)	6.3

5.6.2.2 Sensitivity Studies

The sensitivity of each injector input parameter to time, energy, energy spread, current and emittance jitter has been studied for both the medium length and the long bunch case. In particular, the smallest change of each input parameter with respect to its optimum setting that produces a given change of one of the output parameters was evaluated using ASTRA and GPT. Table 5.6.5 and Table 5.6.6 show the results obtained for the medium length and the long bunch case respectively. As an example, in the medium length bunch case, a 1.5% variation of the gun solenoid field with respect to its optimum value produces a 1% variation of the peak current $\hat{I}$, while to produce a 100 fs change in the bunch arrival time a 10.7% field increase would be needed.

Table 5.6.5: MBL case. The minimum parameter value variation producing the output variation indicated in brackets in the first row. The range considered to compute the sensitivity is reported in brackets in the first column. (n/s = not sensitive; * = extrapolated).

Parameters (variation)	ΔI *(1%)*	ΔT *(100 fs)*	σ_E *(10 keV)*	$\Delta E/E$ *(0.1%)*	ε_{proj} *(10%)*	$<\varepsilon_{slice}>$ *10%*
Gun Solenoid (2%)	1.5%	10.7% *	1.1 %	n/s	0.2%	2%
Gun Eacc (1%)	0.47%	0.13%	0.12%	0.96%	0.33%	4.3%
RF phase gun (1°)	0.65° *	2.8°	0.8°	3.8°	0.5° *	4.8° *
SØA Eacc (5%)	20% *	2%	3.9%	0.21%	n/s	n/s
SØA RF phase (0.2°)	6.2° *	n/s	0.1°	1.9° *	n/s	n/s

Table 5.6.6: LB case. The minimum parameter value variation producing the output variation indicated in brackets in the first row. The range considered to compute the sensitivity is reported in brackets in the first column. (n/s = not sensitive; * = extrapolated).

Parameters (variation)	ΔI *(1%)*	ΔT *(100 fs)*	σ_E *(10 keV)*	$\Delta E/E$ *(0.1%)*	ε_{proj} *(10%)*	$<\varepsilon_{slice}>$ *10%*
Gun Solenoid (2%)	2.2%	10% *	5 % *	n/s	0.8%	1.2%
Gun Eacc (1%)	0.6%	0.15%	0.17%	1.6% *	0.5%	0.9%
RF phase gun (1°)	1.0°	0.3°	0.28°	1.8° *	2.9° *	4.6° *
SØA Eacc (5%)	20% *	2%	1.1%	0.2%	n/s	n/s
SØA RF phase (0.2°)	6.2° *	n/s	0.22° *	0.7° *	n/s	n/s

These results are useful to identify the main sources of output jitter. For example, concerning the time jitter, the main contributions come from the Gun (accelerating gradient and RF phase) and from the time jitter of the laser. The pulse to pulse stability of the ramped current distribution is the object of further studies.

5.6.2.3 Additional Statistical Studies of Bunch Parameters

A polynomial fitting of the longitudinal phase space, current bunch profile and slice emittance provided further insights into the reproducibility of the bunch parameters.

LB case: Figure 5.6.14 shows fourth order polynomial curve fits of the longitudinal phase spaces of twelve randomly selected bunch configurations, while Figure 5.6.15 shows fits of their current profiles. The curves fit the synchronous bunch core (3 mm) with the tails left out.

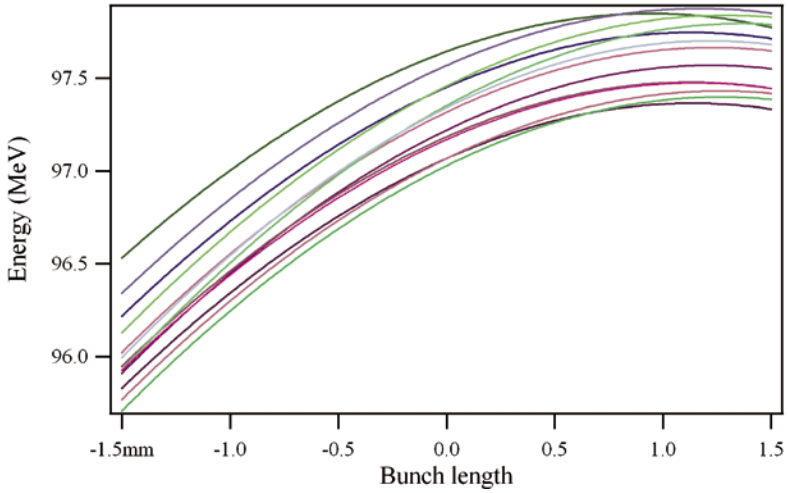

Figure 5.6.14:
12 polynomial curve fits (fourth order), randomly sampled among the thousands performed, of the longitudinal phase spaces of bunches simulated for the long ramped case. Bunch head is on the left.

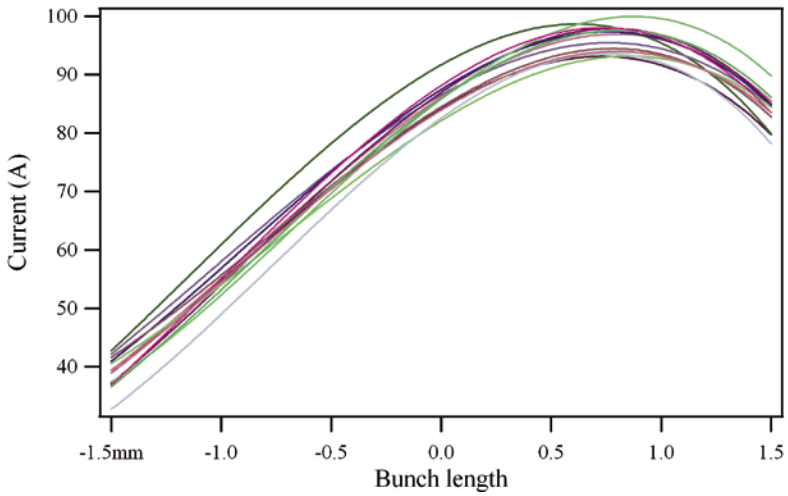

Figure 5.6.15:
12 polynomial curve fits (fourth order), randomly sampled among the thousands performed, of the current profile of bunches simulated for the long ramped case. Bunch head is on the left.

Each fit provides a set of polynomial coefficients for functions described by $f_i(z) = c0_i + c1_i \cdot z + c2_i \cdot z^2 + \ldots$ where *i* is the simulation index. The average coefficient values and their standard deviation (sdv) was computed. Table 5.6.7 reports the results for the longitudinal phase space, the current profile and the slice emittance. The average coefficients can be used to analytically reconstruct the injector output particle distribution including jitter. This knowledge is useful for tracking in longitudinal phase space (for instance using LiTrack).

Table 5.6.7: Statistical analysis of fitting coefficients. The curve function used is a polynomial as: $f_i(z) = c0_i + c1_i \cdot z + c2_i \cdot z^2 + \ldots$

Fit coefficient	*Longitudinal phase space*	*Current profile*	*Slice emittance*
<c0>	97.27	86.8	1.06
c0sdv	0.17	3	0.07
<c1>	513	$2.3\ 10^4$	308
c1sdv	50	$2\ 10^3$	45
<c2>	$-2.17\ 10^5$	$-1.14\ 10^7$	$-2.6\ 10^5$
c2sdv	2860	$1.0\ 10^6$	$4\ 10^4$
<c3>	$-6.6\ 10^6$	$-4.0\ 10^9$	$-1.1\ 10^8$
c3sdv	$4.3\ 10^5$	$3.7\ 10^8$	$2\ 10^7$
<c4>	-	-	$5.5\ 10^{10}$
c4sdv			$9\ 10^9$

5.7 Conclusions

An injector design based on proven technologies and techniques, suitable for producing the high-brightness electron beams required for successful operation of the FERMI@Elettra FELs is presented.

Photocathode performance specifications are well established and conservative. Laser systems are aggressive in average and peak power, but benefit from parallel developments ongoing at other laboratories and in industry. The laser profile tailoring is critical, and will require development to produce suitably reliable pulse shapes at the photocathode.

The design of the off-axis diagnostic beamline in its present stage guarantees that all basic information, such as beam energy, energy spread and position, is obtainable within specification, but still needs additional development and more detailed studies. Additional measurements to be provided for include longitudinal phase space correlations and thermal emittance in the low bunch charge regime.

The sensitivity of the baseline beam dynamics solution to zero mode excitation in the RF gun cavity has been analyzed for various cavity geometries, having different frequency separations between the pi and

the zero mode. An analysis of the transient behavior of the pi and zero modes of the RF gun has been presented. The length and intensity of the electron bunches have been found to affect the longitudinal phase space more than the transverse one. The analysis has also shown heightened sensitivity of the energy correlations present at the RF gun exit to amplitude perturbations resulting from small mode frequency separation.

Optimization of the beamline optics and the drive-laser profile has produced a flexible beamline design that can accommodate various linac operating modes and supply high brightness electron beams suitable for generating a variety of seeded-FEL pulses up to the soft X ray region.

The production and transport of bunches with large initial nonlinear variation of the instantaneous current have been demonstrated to undergo a redistribution of charge such that a linear current ramp is developed over much of the bunch at the injector exit. Such bunches have been shown to be amenable to standard emittance compensation techniques.

The sensitivity of the parameters to changes in some baseline design parameters has been analyzed. The most significant element of the jitter budget remains the timing jitter at the exit of the injector, most of which arises from the drive laser arrival time jitter. For the medium length bunch cases, a rms output timing jitter of ~350 fs or less is achievable for a drive-laser arrival time jitter of 200 fs (rms) or less. In the long bunch cases, the tolerances are more relaxed.

5.8 References

[1] D. Palmer, "The next generation photoinjector", Stanford University dissertation, 1998.

[2] A. Zholents et al., "Formation of Electron Bunches for Harmonic Cascade X-Ray Free-Electron-Lasers", Phys. Rev. Spec. Topics Accel. Beams, **9**, 120701 (2006).

[3] S. Lidia, G. Penco and M. Trovò, "Technical Design and Optimization Study for the FERMI@Elettra FEL Photoinjector", ST/F-TN-05/13, August 2005.

[4] K. Flöttman, https://www.desy.de/~mpyflo/Astra_dokumentation.

[5] S.B. Van der Geer, et. al., http://www.pulsar.nl/gpt/index.html.

[6] A. Zholents et. al., "Formation of electron bunches for harmonic cascade x-ray Free-Electron-Lasers", EPAC'06, Edinburgh, June 2006.

[7] W. Fawley and G. Penn, "Thoughts on Spectral Broadening Effects in FERMI and other FEL's Based upon Seeded Harmonic Generation", ST/F-TN-06/07, May 2006.

[8] F.M. Dickey and S.C. Holswade, eds. Laser Beam Shaping: Theory and Techniques, Marcel Dekker, Inc. (New York, 2000).

[9] P. Craievich and V. Verzilov, "Case Study for Modification and Use of the LCLS RF Photoinjector as an Electron Source for the ELETTRA Linac FEL", ST/M-03/02, May 2003.

[10] T.P. Wrangler, RF Linear Accelerators, John Wiley & Sons (1998).

[11] M. Trovò and P. Craievich, "RF Cavity Geometries for Fermi Gun", ST/F-TN-05/29, December 2005.

[12] Microwave Studio, CST.

[13] J. Schmerge (SLAC), private communication.

[14] J. Schmerge (SLAC), private communication.

[15] G. Penco, et. al., "Optimization studies of the FERMI@Elettra Photoinjector", Proceedings of the 10th European Particle Accelerator Conference, Edinburgh, 2006.

[16] W. Graves, et. al., Proceedings of the 2001 Particle Accelerator Conference, Chicago, 2001.

[17] J. Schmerge, et. al., Proceedings of the Physics and Applications of High Brightness Electron Beams, Erice, 2005.

[18] P. Craievich, T. Weiland and I. Zagorodnov, "The Short-Range Wakefields in the BTW Accelerating Structure of the ELETTRA Llinac", ST/M-04/02, June 2004.

[19] A. Zholents et. al., Technical Note, "FERMI@Elettra Accelerator Technical Optimization Final Report", ST/F-TN-06/15, July 2006.

[20] K. Bane and P. Emma, "LiTrack: a Fast Longitudinal Phase Space Tracking Code with Graphical Interface", PAC '05, Knoxville, Tennesse (2005), 4266.

[21] G. Penco, "Longitudinal Space Charge Field at the Cathode In Case of a Non Uniform Bunch", ST/F-TN-06/03, March 2006.

[22] G. Penco, M.Trovò, S.Lidia, "Ramping Longitudinal Distribution Studies for the FERMI@Elettra Injector", Proc. FEL conf. 2006.

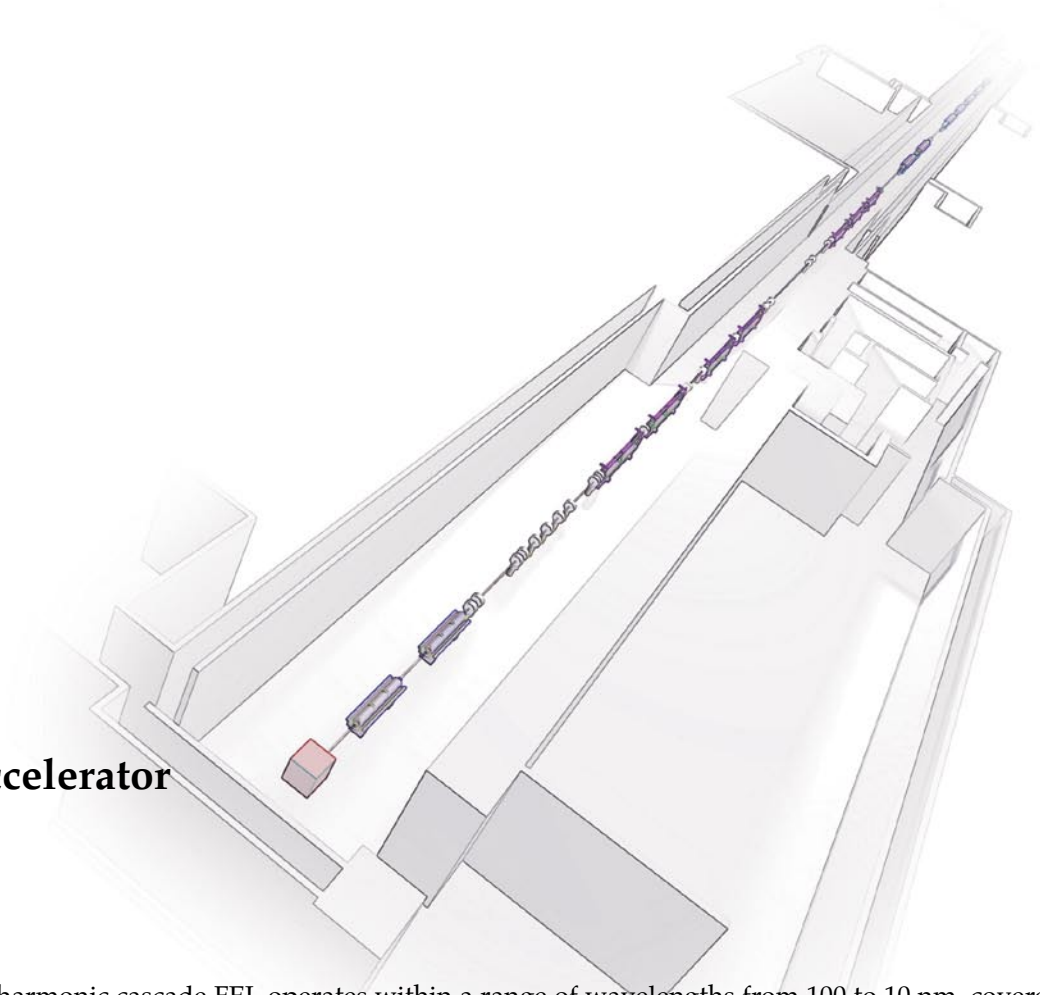

6 Accelerator

Synopsis

The FERMI harmonic cascade FEL operates within a range of wavelengths from 100 to 10 nm, covered by two distinct undulator chains at the fixed energy of ~1.2 GeV. Two electron beam scenarios have been developed: the medium length bunch (MLB) mode with a bunch length of ~ 700 fs and the long bunch (LB) mode with a bunch length of ~1.4 ps. The electron peak current is 800 or 500 A, respectively. The accelerator was designed with sufficient flexibility to accommodate such variations in bunch parameters. Other important electron beam parameters include the normalized slice electron beam emittance and the slice energy spread, which are about 1.5 μm rad and 150 keV, respectively. A challenging aspect was the demand to produce an electron beam with as uniform as possible peak current and energy distributions along the bunch. For this reason, a new parameter, the "flatness", defines the value of the quadratic component of energy variation along the bunch for which the increase in bandwidth of the x-ray signal due to this variation becomes equal to the Fourier transform limited bandwidth defined by the bunch length. Tracking results predict flatness of 0.8 MeV / ps^2 for the MLB mode and of 0.2 MeV / ps^2 for the LB mode.

Since the RF photocathode gun produces 0.8 nC and 1 nC for the two options distributed over bunch length of 9 ps and 11 ps respectively, the bunch has to be compressed by a total factor of about 9 before it enters the undulator. The acceleration and compression is done in the main S-band linac. The two bunch compressors (BCs) consist of symmetric magnetic chicanes, each 8.0 m long. They include trim quadrupoles for a fine tuning of the dispersion bump. The locations and compression

factor of the two chicanes were fixed in order to minimize the 6-dimensional emittance dilution of the electron bunch in presence of space charge forces and wake fields. The electron energy at BC1 is ~230 MeV in order to avoid space charge effects, while compressing the bunch early enough in the linac to reduce the effects of transverse wake fields. The energy of the second compressor is about 580 MeV, which balances the conflicting requirements of minimizing the transverse and longitudinal emittance dilution by coherent synchrotron radiation (CSR) and that of canceling the final correlated energy spread by means of the downstream longitudinal wake field. By using a weak chicane with a bending angle smaller than 0.07 rad per dipole and a large initial correlated energy spread within the range of 1.0% - 2.5%, the CSR effects can be reduced, but the chromatic aberrations make the tolerances on the magnets field quality tighter.

A short X-band RF structure is used prior to the first compressor in order to linearize the longitudinal phase space. It operates in the deceleration mode with a peak voltage of 18 MV; its contribution to the transverse and longitudinal wake fields is negligible compared to that of the main linac.

Since the whole beam delivery system acts like a huge amplifier of energy and density modulations, a laser heater is foreseen at 100 MeV just after the photoinjector to Landau damp the microbunching instability. The uncorrelated energy spread induced by this tool is able to suppress the modulation in the energy and density distributions at a scale small with respect to the bunch length; but, at the same time, the bunch compression brings the induced slice energy spread closer to the FEL threshold. It is important for the FEL process to provide slice energy spread not much larger than 150 keV (rms value). Simulations have been made which calculate the emittance dilution in the linac due to transverse wakefields and anomalous momentum dispersion, each of which arises with component misalignments. These simulations include realistic correction techniques and successfully demonstrate that the required level of transverse emittance preservation is achievable. Jitter studies implemented in full start-to-end simulations have been performed and a tolerance budget of the linac stability has been defined according to the FEL specifications.

The beam delivery system ends with a transfer line located between the end of the linac and the entrance of the FEL. This part includes the emittance diagnostic section, the electron beam switchyard for the two FELs, called “spreader”, and the matching sections. The design meets the constrains imposed by the existing and planned building boundaries, by the desire to utilize existing equipment and by the demands for various diagnostic instruments.

6.1 Introduction and Overview

This chapter describes the accelerator physics aspects, the engineering considerations and the choice of parameters that led to the design of the FERMI Free-Electron-Laser accelerator. The accelerator covers the region from the exit of the injector to the entrance of the first FEL undulator and its layout is described in paragraph 6.2. The tracking results of the electron beam dynamics from the photocathode to the linac end are shown in paragraph 6.3.

Paragraph 6.4 includes the technical aspects of the accelerating structures, modulators and low level RF (LLRF) system; it also contains some considerations about the upgrade needed to improve the linac stability.

When the intense electron bunch propagates down the accelerator, it is subject to various collective effects [1]. It was found that the longitudinal wakefields are responsible for the nonlinear variation of

the energy along the bunch. Paragraph 6.5 shows the geometric wakefields of the accelerating structures used in the tracking study. Paragraph 6.6 discusses the longitudinal dynamics during compression and acceleration. The emission of coherent synchrotron radiation (CSR) [3 and refs in 4] in the bunch compressors and the spreader is a relevant topic, since it may contribute to the emittance dilution. The microbunching instability is driven by a combination of longitudinal space charge (LSC) [5 and refs in 4], bunch compression and CSR; they continue to play a visible role in the formation of the microstructures on the electron bunch even at high energies and, if unaccounted for, can increase the energy spread in the electron beam beyond the tolerance for proper FEL operation. The design and the implementation of a laser heater [5] for energy Landau damping is presented, together with an estimate of its effect on the particles distribution. Nonlinear components in the RF waveform and in the time-of-flight characteristics of the bunch compressor are taken into account as they are often responsible for the appearance of high spikes in the peak current at the edges of the electron bunch [6]. The leading spike may induce resistive wall wakefields that modulate the energy of the electron bunch during its motion through the spreader and the undulator.

The transverse dynamics is studied in paragraph 6.7. Single particle dynamics considerations led to the evaluation of the magnets field quality needed in order to minimize aberrations. The collective effect of the beam break up (BBU) instability is also discussed. The impact of the transverse wakefields is enhanced by the trajectory distortion if the tolerance budget for field quality and accelerator alignment is not satisfied. Trajectory bumps were proposed to cancel the transverse-longitudinal position correlation created by the wakefields [2]. Finally, the transverse acceptance and tolerance budget required for a total emittance blow up smaller than 10% are listed.

The jitter studies of paragraph 6.8 focus mainly on the longitudinal dynamics, since the FEL process is more sensitive to the longitudinal than to the transverse planes. Both MLB and LB modes have been analyzed in time dependent, full start-to-end simulations that include errors within the specified tolerance budget. Jitter studies of the slice parameters have been also performed. Paragraph 6.9 describes the beam collimation to be located in the Spreader and the beam dump. It is followed by the last paragraph 6.10 which contains some general considerations about instrumentation, diagnostic and feedback, directing the reader to the specific chapter for more details of the hardware involved.

6.1.1 Overview of Design Specifications

The FERMI accelerator is schematically shown in Figure 6.1.1. It consists of four linacs L1 – L4, two bunch compressors (BC1 and BC2), a laser heater and a spreader. The latter switches the electron beam into one of the undulator lines (not shown). The laser heater is the first component of the accelerator. At its output the energy of the electron beam is ~100 MeV and the peak current is 60-70 A. At the end of acceleration the electron beam energy is approximately 1.2 GeV and the electron peak current is either 500 A or 800 A, depending on the bunch length needed for the FEL operating modes. The latter envisage two options for the electron bunch length: the medium length bunch (MLB) mode with a bunch length of the order of 700 fs and the long bunch (LB) mode with a bunch length of the order of 1.4 ps. The electron beam delivery system was designed with sufficient flexibility to accommodate both. Other important electron beam parameters include the normalized slice emittance and the slice energy spread, which are 1.5 μm rad and 150 keV respectively for both bunch lengths.

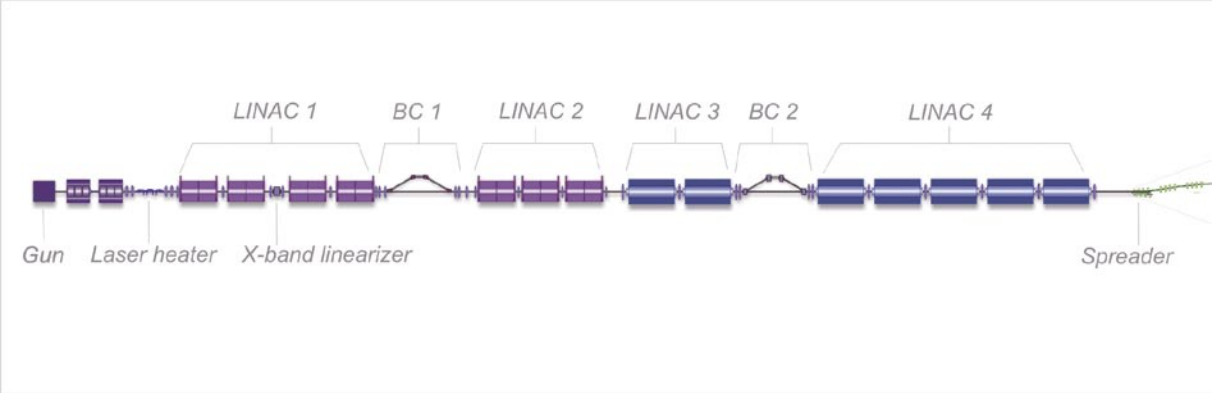

Figure 6.1.1:
A schematic of the FERMI accelerator.

The list of the beam specifications is shown in Table 6.1.1. A new parameter, the "flatness", is also quoted. It defines that value of the quadratic component of the average energy variation along the bunch for which the increase in bandwidth of the x-ray signal becomes equal to the Fourier transform limited bandwidth defined by the bunch length.

Table 6.1.1: Main electron beam specifications.

	MEDIUM	***LONG***	***Units***
Bunch Charge	0.80	1.00	nC
Bunch Length, FWHM	700	1400	fs
Peak Current	800	500	A
Slice Norm. Emittance	<1.5	<1.5	μm
Flatness, $\lvert d^2E/dt^2 \rvert$	<0.8	<0.2	MeV/ps^2

Table 6.1.2 lists the major machine parameters for the medium length and long bunches.

Table 6.1.2: Basic linac and compressors parameters.

Configuration		*MLB*	*LB*	*Units*
Charge		0.8	1	nC
Linac-1: voltage		47 x 4	47 x 4	MV
Linac-1: phase		54	62	deg
X-band: voltage		18	18	MV
X-band: phase		-90	-90	deg
Linac-2: voltage		47 x 3	47 x 3	MV
Linac-2: phase		70	72	deg
Linac-3: voltage		120 x 2	120 x 2	MV
Linac-3: phase		70	72	deg
Linac-4: voltage		120 x 5	120 x 5	MV
Linac-4: phase		109	105	deg
BC1	E	230	244	MeV
	R_{56}	-0.0280	-0.0280	m
	σ_δ	2.7	2.0	%
	C.F.	4.5	2.5	
BC2	E	584	602	MeV
	R_{56}	-0.0162	-0.0315	m
	σ_δ	1.1	1.2	%
	C.F.	2.5	3.5	

The compression factors are determined by the need to reduce the CSR instability and the CSR induced growth of the projected emittance. The energy of the first magnetic chicane (BC1) avoids a beam dynamics dominated by space charge forces, while that of the second (BC2) is limited by CSR that might arise with a high momentum compaction lattice

As for the linac, phases and voltages of the accelerating structures were chosen in order to achieve the desired compression and, at the same time, to manage the longitudinal wake for best cancellation of the final energy chirp.

The location of the different types of accelerating structures in the linac layout was mainly guided by the minimization of the transverse wake fields by putting the structures with the highest impedance at the linac end, where a shorter bunch is accelerated.

6.2 Accelerator Lattice and Components

Figure 6.2.1 shows the Twiss functions of the entire accelerator, together with a description of the locations of the major components. The parameters of each component are presented in the following sections.

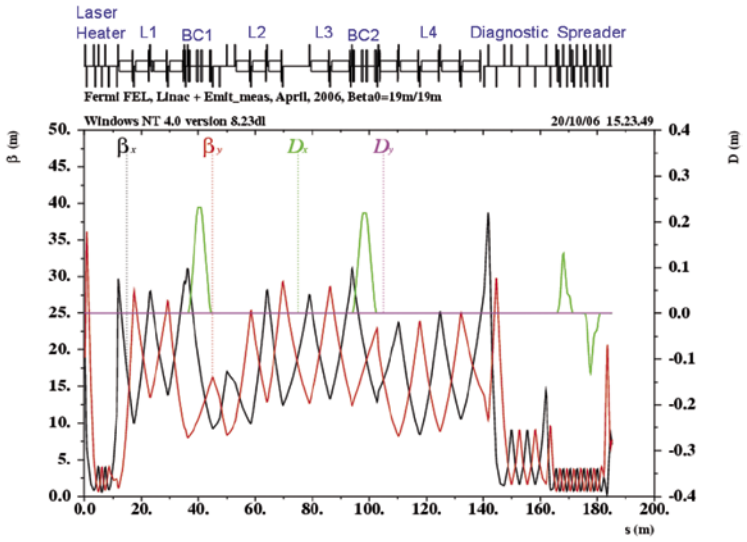

Figure 6.2.1:
Twiss functions of the accelerator.

6.2.1 Laser Heater

The plot of the Twiss functions in this area is shown in Figure 6.2.2. The lattice was designed to be flexible enough to accommodate variations in the input beta-functions in the range of 3 – 40 m.

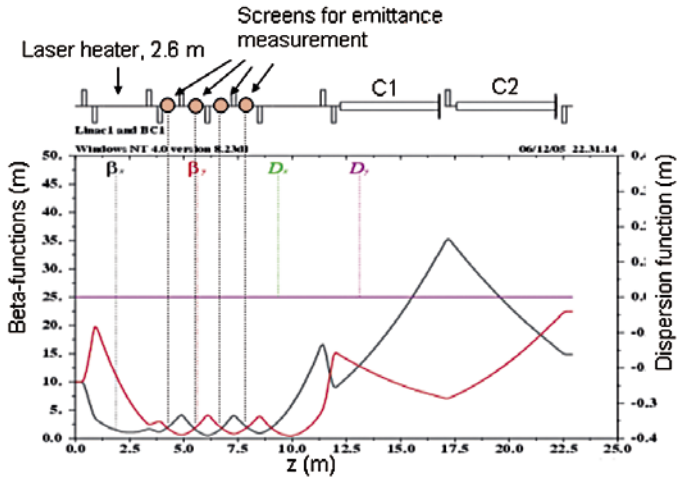

Figure 6.2.2:
Twiss functions of the laser heater and adjacent diagnostic section.

6.2.2 First Bunch Compressor

A schematic of the bunch compressor is shown in Figure 6.2.3. It consists of a chicane built from four rectangular bending magnets [7]. Because of its symmetry, this bunch compressor is a perfect achromat. Nevertheless, leakage of the dispersion function after the last bend may occur due to errors; for this reason, trim quadrupoles (shown in Figure 6.2.3 between the first and second bends and the third and fourth bends) are added for a fine tuning of the dispersion function.

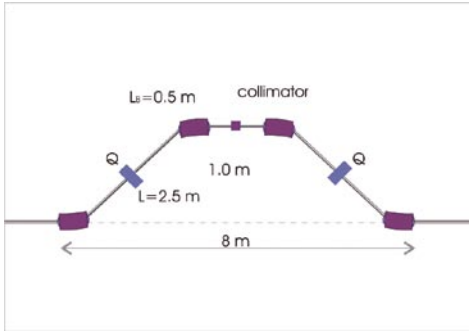

Figure 6.2.3:
A schematic of the bunch compressor.

It is important for the design of the bunch compressor to take CSR into account. Although transverse microbunching radiative fields affect the emittance directly, an indirect emittance excitation via longitudinal-to-transverse coupling:

$$\delta\varepsilon_x \approx H\left(\delta E / E\right)^2 \qquad 6.2.1$$

typically dominates. ΔE/E is the energy spread caused by CSR and H is the optical function defined in [8].

According to Eq. 6.2.1, the BC1 lattice was designed in such a way that the magnitude of H in the last bend of the chicane can be varied by up to a factor of four. This will give some flexibility to maneuver

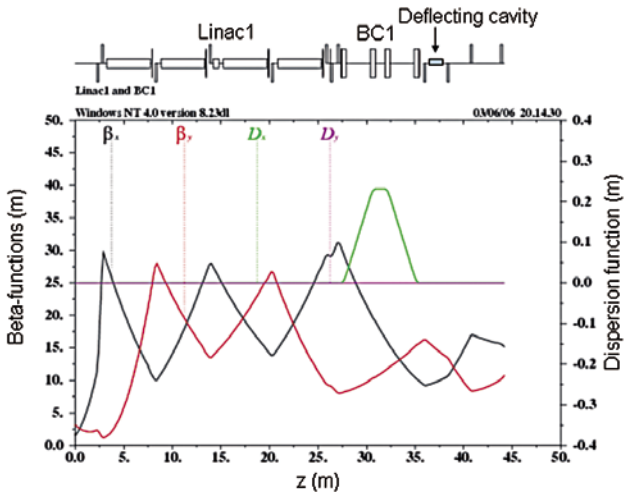

Figure 6.2.4:
Twiss functions of the first bunch compressor and adjacent L1.

between such tasks as containing the emittance excitation due to CSR, which benefits from a smaller H, and containing the energy spread growth due to the microbunching instability, which benefits from a larger H. Four quadrupole magnets after the chicane are used to match the Twiss functions into the downstream L2 (see, Figure 6.2.4). Between these magnets space has been reserved for a deflecting cavity to be used for emittance measurements and for a beam dump to be used during commissioning.

6.2.3 Second Bunch Compressor

The Twiss functions of this compressor are shown in Figure 6.2.5. The lattice of BC2 is exactly the same as that of BC1, shown in Figure 6.2.3, and designed so that the magnitude of H in the last bend of the chicane can vary by up to a factor of four. The physics considerations are also the same as those discussed for BC1.

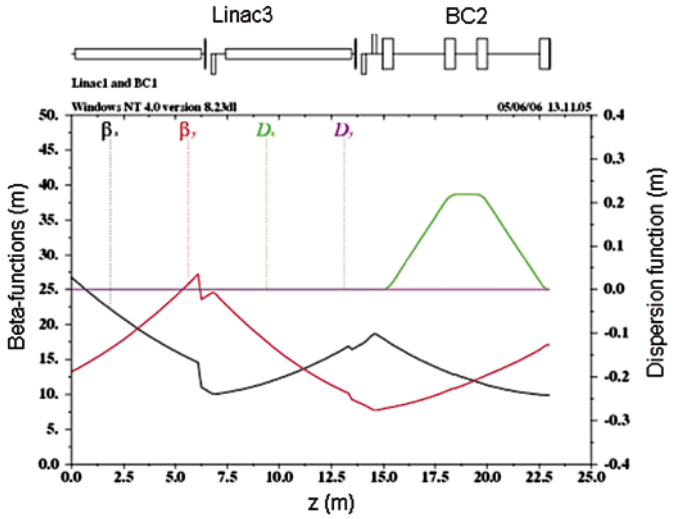

Figure 6.2.5:
Twiss functions of the first bunch compressor and adjacent L3.

6.2.4 Linac End Section and Spreader

6.2.4.1 Layout

A detailed description of the transfer line connecting the accelerator to the undulator chains may be found in [44]; this reference includes considerations on some technical aspects of the design.

A simplified schematic of the spreader is shown in Figure 6.2.6. One of the design goals is to minimize its length for two main reasons: the cost of the building housing the line and the fact that the position of the start of the experimental area is fixed and delimited by the existing building. For this reason, strong quadrupoles and short drifts are used. The bending angle of the spreader's bending magnets is also predetermined as a design requirement of the experimental area is to shift FEL-2 line by 1 m and FEL-1 line by 3 m from the linac line [45].

The spreader starts with two 3 degrees bending magnets of that deflect the electron beam away from the linac. Two more 3 degrees bending magnets with of opposite polarity turn the electron beam back into the straight line of FEL-2. Alternatively, the third magnet is switched off and the electron beam proceeds to the second pair of magnets that deflect electron beam back into the straight line of FEL-1 (see Figure 6.2.6).

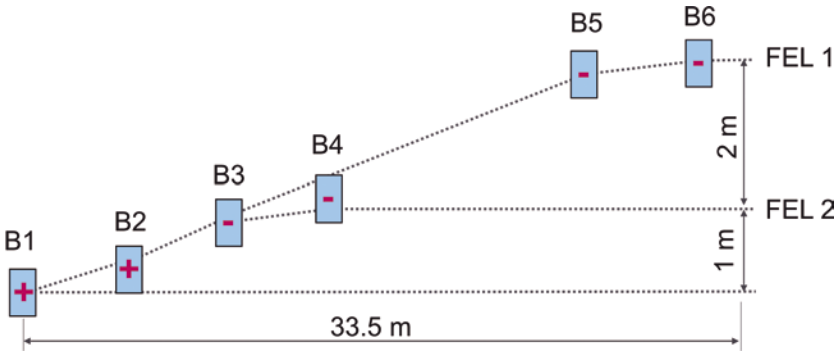

Figure 6.2.6:
A schematic of the spreader.

It is important that the spreader lattice preserves the electron beam emittance. This is done by two means: i) by using a lattice with small *H* function in the magnets; ii) by employing a scheme of emittance self-compensation. Besides four bending magnets, the lattice includes twelve quadrupoles that are arranged like a FODO lattice with $\pi/2$ betatron phase advance in x and y planes per unit cell. The latter is comprised of two quadrupoles and two drift lengths. Two cells are used between two adjacent bending magnets to produce $-I$ transfer matrix in each plane. This arrangement in the horizontal plane provides a basis for a compensation of the emittance excitation due to coherent synchrotron radiation (CSR) in the spreader's bending magnets.

6.2.4.2 Emittance Diagnostic Section

The emittance diagnostic section is located between the linac and the spreader and is designed for measuring the emittance using optical transition radiation from the screens that can be inserted into the electron beam path. Vertical and horizontal beam emittances will be derived from the measurements of the electron beam sizes at several locations with various betatron phase advances. Two variants of the lattice are proposed, corresponding to an invasive and a non-invasive modes of operation: i) a production lattice designed for normal operation during x-ray beam delivery and ii) a diagnostic lattice designed for emittance measurements when the photon beam is not delivered and the electron beam can be intercepted

In the latter case a periodic lattice is used with a betatron phase advancing from one screen to the next by approximately $\pi/4$ in both planes and with almost equal horizontal and vertical beta functions at all the screens' locations. A RF deflecting cavity is located upstream of the screens and is used for slice emittance measurements. A more detailed schematic of the part of the spreader leading to FEL-2 and the associated Twiss functions are shown in Figure 6.2.7.

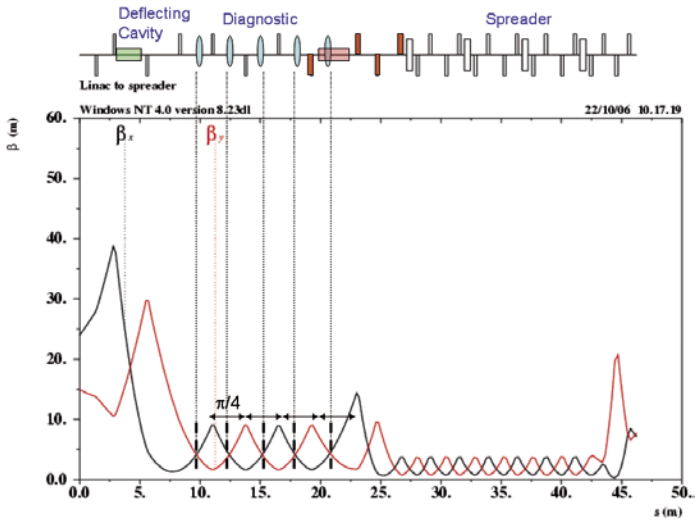

Figure 6.2.7:
Twiss functions of the transfer line for diagnostic purposes beginning from L4 and ending at the entrance of the FEL-2.

6.2.4.3 Production Lattice

The lattice configuration during photon beam delivery is shown in Figure 6.2.8. It is less favorable for emittance diagnostics because of the less periodic behaviour of the Twiss functions within the screen area and less regular advance of the betatron phases. In spite of this shortcoming, all the screens can still be used for quick beam characterization albeit less accurate than that of the dedicated line.

A distinctive feature of the production lattice is the presence of the two local peaks of the beta functions in the diagnostic section just upstream of the spreader. The lattice is tuned such as to have 3/2 π betatron phase advance between the local peaks of the beta functions where adjustable x and y collimators will be used. The energy collimator will be used near the peak of the dispersion function inside the spreader, as shown in Figure 6.2.9 for FEL-2.

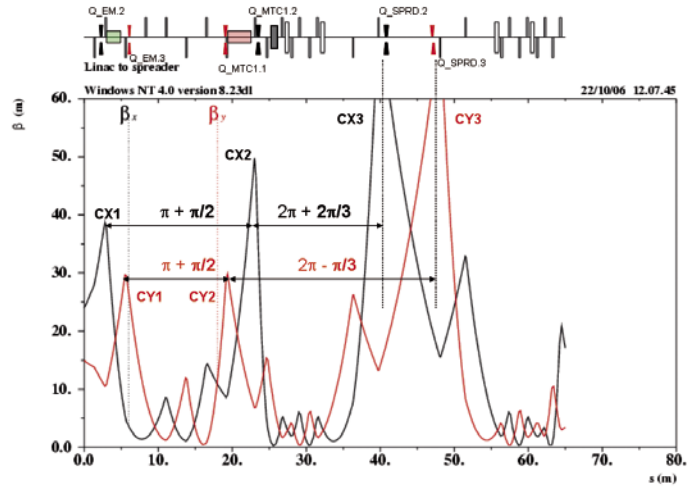

Figure 6.2.8:
Twiss functions of the transfer line in the configuration suitable FEL operation beginning from L4 and ending at the entrance of the FEL-1. The locations of the betatron collimators are shown.

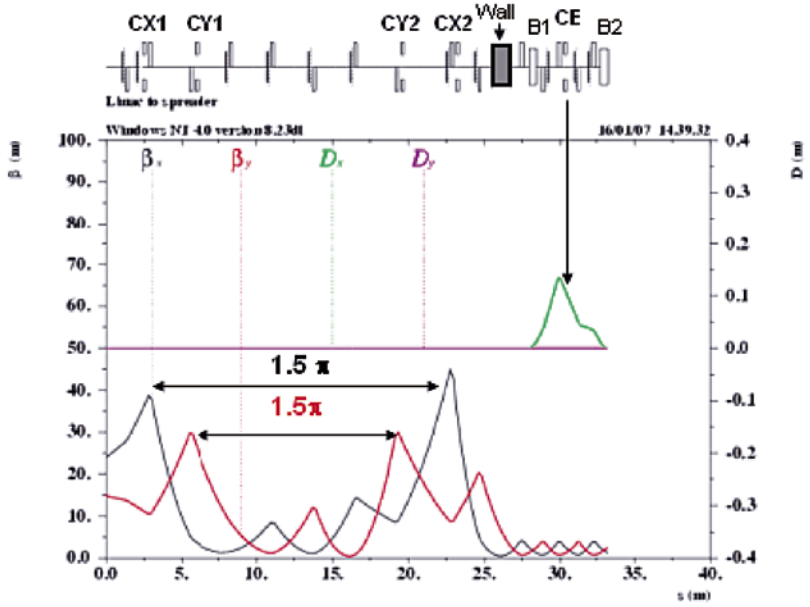

Figure 6.2.9:
Schematic and lattice functions of the FEL-2 production lattice from the end of the linac and through the first two bending magnets of the spreader. The top line indicates the location of the collimators.

Matching sections after the spreader are very similar for FEL-2 and FEL-1. Four matching quadrupoles provide enough flexibility to adjust the Twiss functions at the FEL input. A 5 m long drift is reserved after the last quadrupole and precision cavity BPMs will be placed on both sides of this drift. The electro-optical monitor for measuring the electron bunch arrival time will also be placed inside this drift.

6.2.4.4 Time-of-flight Adjustment

The two quadrupoles placed between each pair of dipoles are separated by a unit transfer matrix and located close to the positive and negative peaks of the dispersion function. Thus, one can simultaneously change their gradients and produce a dispersion bump localized between the quadrupoles. By controlling this bump one would be able to regulate the R_{56} of the spreader making it to be exactly zero or any other reasonable value. In fact, it is proposed to keep it slightly positive in some cases in order to disperse the electrons in the spikes of the peak current.

The time-of-flight parameter R_{56} of the spreader shown in Figure 6.2.8 can be adjusted within a relatively large range of values. In order to do this one needs to synchronously tune two quadrupoles, one of which is located near the peak of the dispersion function. With this arrangement the dispersion function gets a kick at the first quadrupole, oscillates between B2 and B3 magnets and gets a compensating kick at the second quadrupole.

Figure 6.2.10 shows the spreader part of FEL-2 when the strength of the Q2 and Q10 quadrupoles is lowered by 10% with the goal to increase R_{56} from 0.9 to 5.5 mm. Figure 6.2.10 shows that this adjustment causes some beating of the beta-functions at the end of the lattice that must be corrected in the matching lattice downstream. Tweaking the same quadrupoles in the opposite directions, i.*e.* reducing the gradient in one quadrupole and increasing in the another quadrupole by the same amount, allows a fine

adjustments of the dispersion function thus enabling the correction of any dispersion leak that might be caused by errors (magnetic or alignment) without affecting the beta-functions and R_{56}.

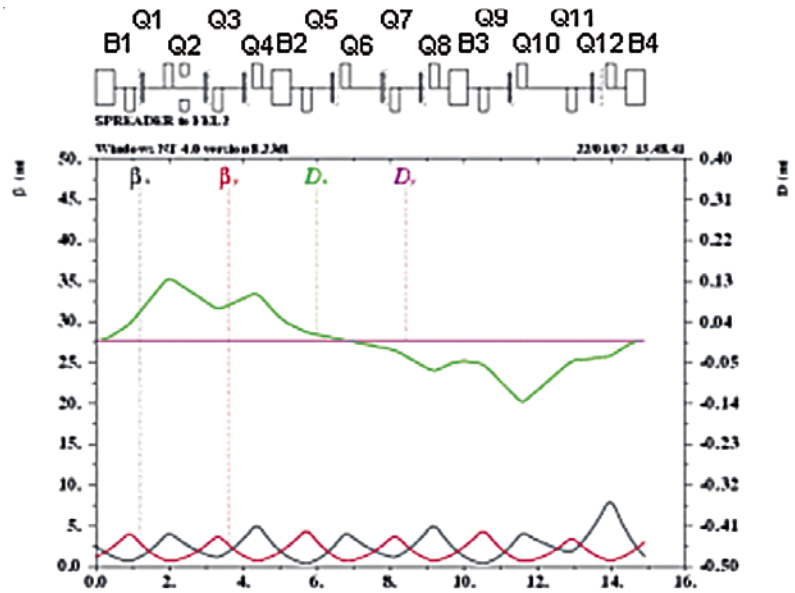

Figure 6.2.10: *Schematic and lattice functions for a spreader part leading to FEL-2. A reduction of the Q2 and Q10 quadrupole gradients by 10% changed R56 from 0.9 mm to 5.5 mm.*

6.2.4.5 Technical Aspects

This paragraph shows the solutions adopted for the hardware of two difficult areas of the spreader in terms of high congestion of components occupancy. Figure 6.2.11 shows the layout of the area downstream of the B3 bending magnet where two beam lines split.

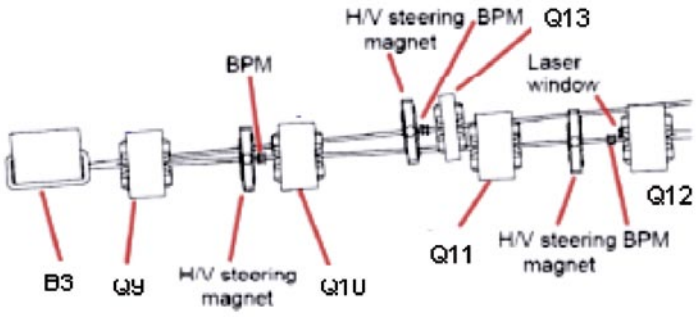

Figure 6.2.11: *The layout of the area downstream of the B3 bending magnet where two beam lines split.*

The electron beam following the FEL-2 line goes through the centers of the Q9, Q10, Q11 and Q12 quadrupoles, while the FEL-1 beam goes through the center of the Q13 quadrupole and in a chamber that penetrates the iron of Q10. In Q9 the beam trajectory is off-axis (see, Figure 6.2.12) which means that this quadrupole must accommodate the vacuum chamber for both beams. The location of this quadrupole is appropriately chosen; its conceptual design is shown in Figure 6.2.12.

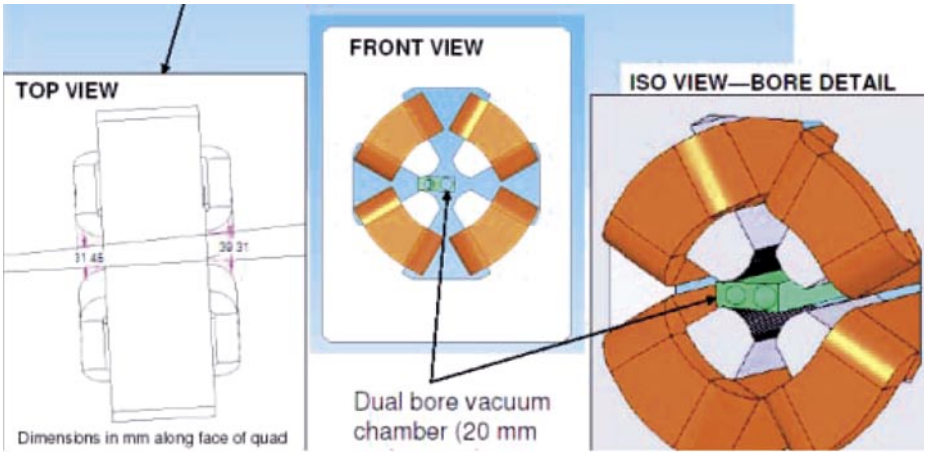

Figure 6.2.12:
Top, front and isometric view of the quadrupole Q9 showing also electron beam trajectories and a sketch of the vacuum chambers for the central and periphery beams.

Figure 6.2.13 shows the seed laser port and the surrounding apparatus. The location for this port just upstream of the last bending magnet B4 is the closest to FEL-2 and it is still more than 11 m away from it.

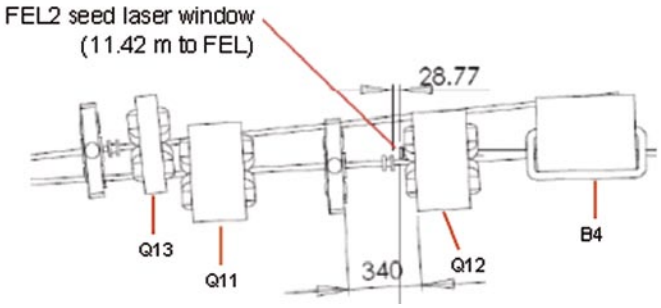

Figure 6.2.13:
Top view of the seed laser port for FEL-2 and surrounding apparatus.

Figure 6.2.14 shows the fine details of the laser port, such as flange, window sizes and window separation from the electron beam axis. Like for the quadrupole Q9, the quadrupole Q12 accommodates the vacuum chamber that allows two beams, the electron beam and the laser beam, both heading towards the FEL-2.

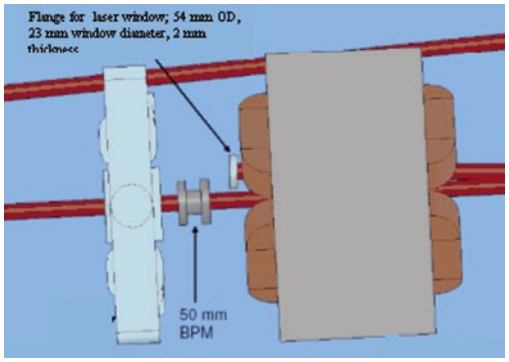

Figure 6.2.14:
Details of the seed laser port.

The design of the seed laser port for FEL-1 is exactly the same as the one just described for FEL-2. This port is located upstream of the bending magnet B6 and the quadrupole Q18 (not in figures).

6.3 Tracking Study

This paragraph shows the results of particle tracking for the nominal set of operation of the FERMI Linac. Simulations with several codes [30, 40] show rather an accurate agreement in their results. They confirm also the original estimate that CSR and LSC wake potentials contribute only weakly to the formation of the electron bunch on a scale large compared to the bunch length.

6.3.1 Medium Length Bunch Mode

The electron beam parameters of the medium length bunch mode (MLB) are given in the Table 6.3.1.

Table 6.3.1: Electron beam parameters for the MLB mode.

Bunch charge	0.8	nC
Beam energy	1.140	GeV
Peak current (beam core)	800	A
Bunch duration (full width, beam core)	700	fs
Slice energy spread (rms, beam core)	150	keV
Slice emittance (rms, beam core)	1.5	μm
Laser heater (energy spread rms)	12	keV
Compression factor in BC1 / BC2	4.5 / 2.5	
Flatness	0.8	MeV/ps^2

Figure 6.3.1 shows the electron distribution in the longitudinal phase space and a histogram of the peak current. Figure 6.3.2 shows the plot of the slice emittance and slice energy spread at the end of the accelerator for the MLB.

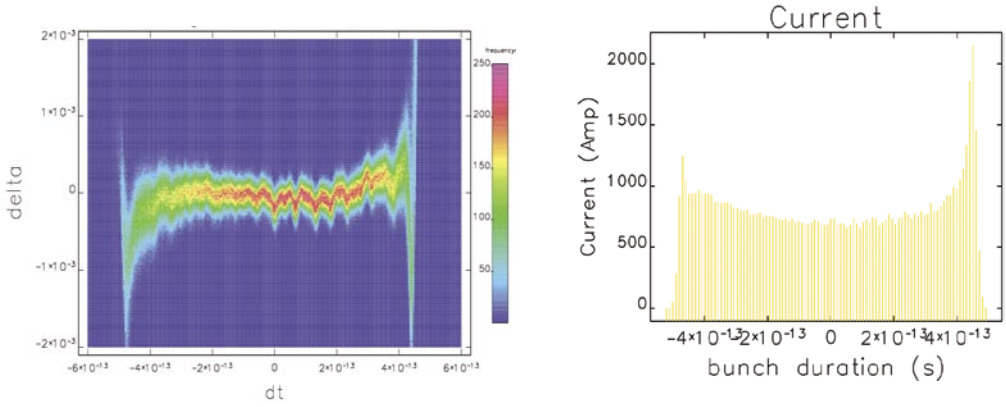

Figure 6.3.1:
MLB mode: density plot showing the distribution of the electron relative energy spread versus time and the histogram of the peak current.

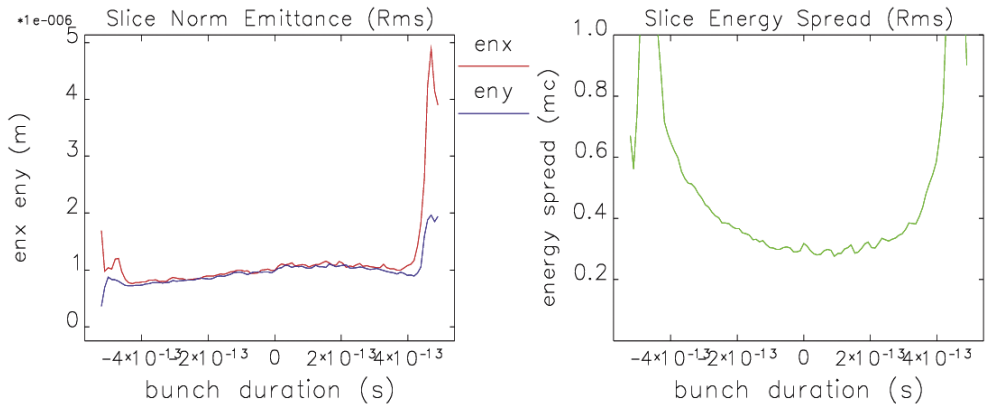

Figure 6.3.2:
MLB mode: slice normalized emittance (left) and slice energy spread (right) at the end of the accelerator.

According to this plot, there is no growth of slice emittance during acceleration and compression. The variation of the slice emittance seen in Figure 6.3.2 is due to the ramped peak current in the injector. We note that the smallest emittance is at the head of the electron bunch. This may have a useful implication because head-electrons radiate in the final stage of the harmonic cascade FEL with the most demanding specification for the electron beam emittance.

6.3.2 Long Bunch Mode

The electron beam parameters for the long bunch mode are given in the Table 6.3.2.

Table 6.3.2: Electron beam parameters for the LB mode.

Bunch charge	1.0	nC
Beam energy	1.170	GeV
Peak current (beam core)	500	A
Bunch duration (full width, beam core)	1400	fs
Slice energy spread (rms, beam core)	150	keV
Slice emittance (rms, beam core)	1.5	μm
Laser heater (energy spread rms)	15	keV
Compression factor in BC1 / BC2	2.5 / 3.5	
Flatness	0.2	MeV/ps^2

Figure 6.3.3 shows the electron distribution in the longitudinal phase space and a histogram of the peak current obtained with Elegant for the LB. Figure 6.3.4 shows the plot of the slice emittance and slice energy spread at the end of the accelerator.

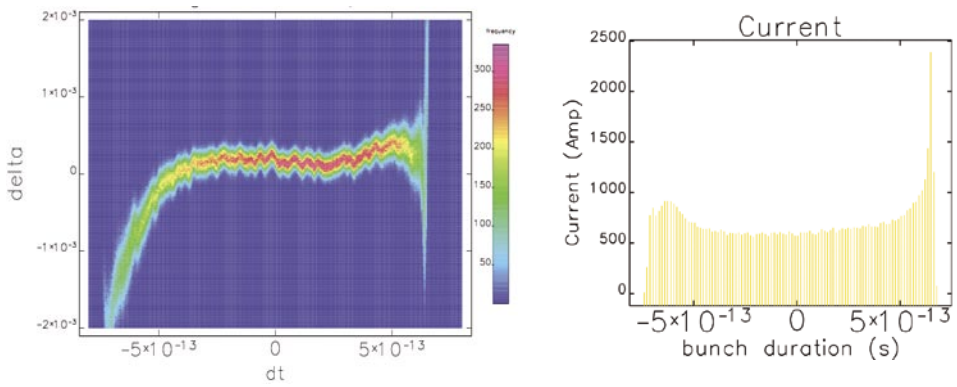

Figure 6.3.3:
LB mode: density plot showing the distribution of the electron relative energy spread versus time and the histogram of the peak current.

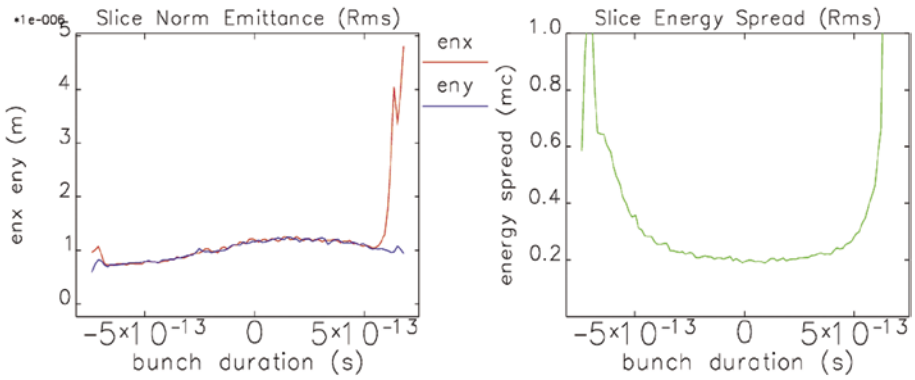

Figure 6.3.4:
LB mode: slice normalized emittance (left) and slice energy spread (right) at the end of the accelerator.

6.4 The Linear Accelerator

In order to raise the operating energy to 1.2 GeV, necessary to satisfy the specifications of the FERMI project, seven additional sections will be installed in addition to the present linac. These sections were obtained from CERN after the decommissioning of the LEP Injector Linac (LIL). These sections will also allow to maintain an adequate margin over the maximum operating energy, providing a more flexible and reliable operation, which is particularly important in a user facility such as FERMI. In addition to the energy upgrade, the linac will also be modified in several other ways:

- the installation of a new high brilliance source, made of a last generation photoinjector of the SLAC-UCLA-BNL type. This gun, operating like the rest of the linac at 2998 MHz, is described in mode details in Chapter 5 of this document;
- a laser heater section;
- the installation of an accelerating section in 4th harmonic (in the X-band region, 11.4 GHz) to linearize the longitudinal compression;
- the installation of two bunch compressors based upon magnetic chicanes, which allow to increase the peak power of the beam and to simultaneously reduce the pulse length;
- the performance improvement of the existing RF plants, and the optimization of such systems in terms of amplitude and phase stability, using advanced digital feedback techniques;
- the improvement of the beam diagnostic system along the entire linac, including the installation of new devices such as deflecting cavities to measure bunch length.

6.4.1 Existing Linac and Future Upgrade

The present Linac is composed of eight high power RF plants, each of them equipped with a 45 MW S-band klystron modulator Thales TH 2132A; two 3.2 m long accelerating sections (SØA, SØB), powered from the same klystron; seven 6.1 m long accelerating structures (S1 to S7), each one equipped with an RF compression system (SLED) and powered with its own 45 MW klystron. All these components are housed in two adjacent areas: the klystron gallery, at ground level, where all the RF generators are located and the accelerator tunnel (112 m long), situated 5 m below the ground level to ease the specifications of radiation safety.

The two areas are connected by means of a suitable number of apertures, placed near each RF plant, that allow the passage of waveguides, signal cables, piping, etc. In order to accommodate the energy upgrade and the conversion to injection into the FEL, the klystron building and injector tunnels will be expanded by about 85 m. The new building will house the new front end up to the first bunch compressor (see, Figure 6.4.1).

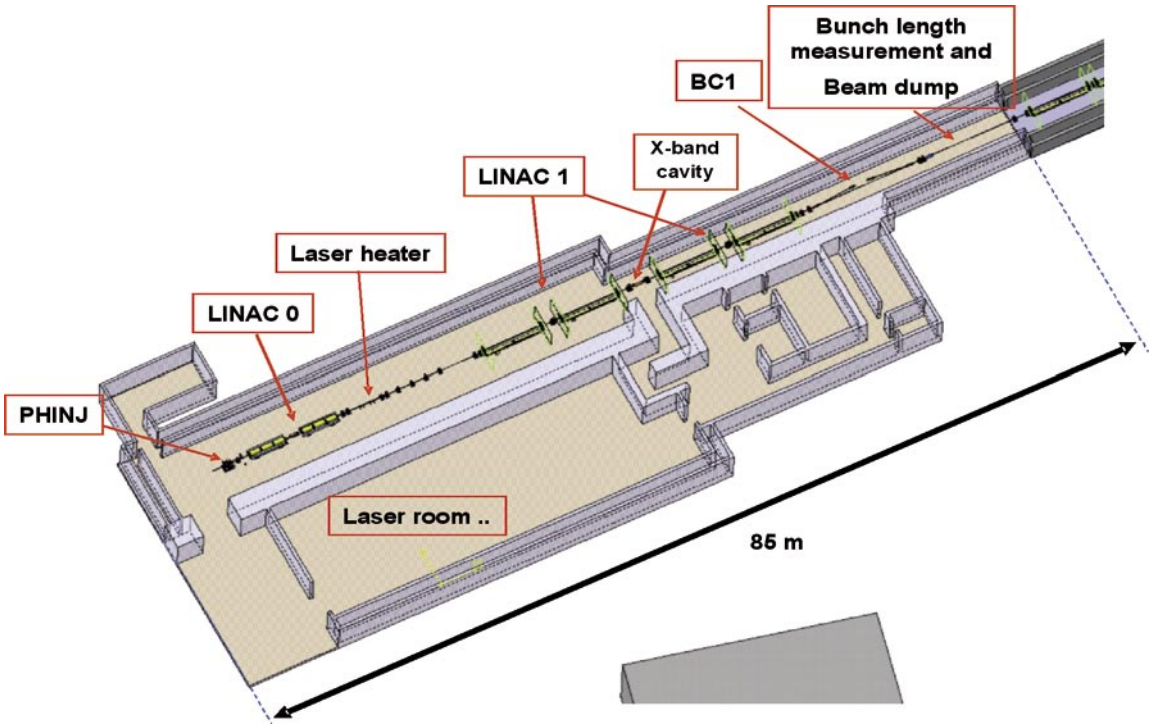

Figure 6.4.1:
The new machine Front-end.

6.4.2 Accelerating Structures

The accelerator uses three types of sections [10]. The S0A and S0B sections follow the electron gun and are used for the initial acceleration and the emittance compensation scheme. A detailed description of the injector and its parameters can be found in Chapter 5. Seven CERN-type sections (C1-C7) are divided

between L1 (four sections) and L2 (three sections) and are used upstream and downstream BC1. S0A, S0B and the CERN sections are traveling wave (TW) structures operating in the 2/3 π mode and coupled on axis. Seven ELETTRA-sections (S1-S7) make up L3 (two sections) and L4 (five sections) and are used upstream and downstream of BC2. They are backward traveling wave (BTW) structures operating in the 3/4 π mode and magnetically coupled. The inner geometries of the accelerating structures are shown schematically in Figure 6.4.2.

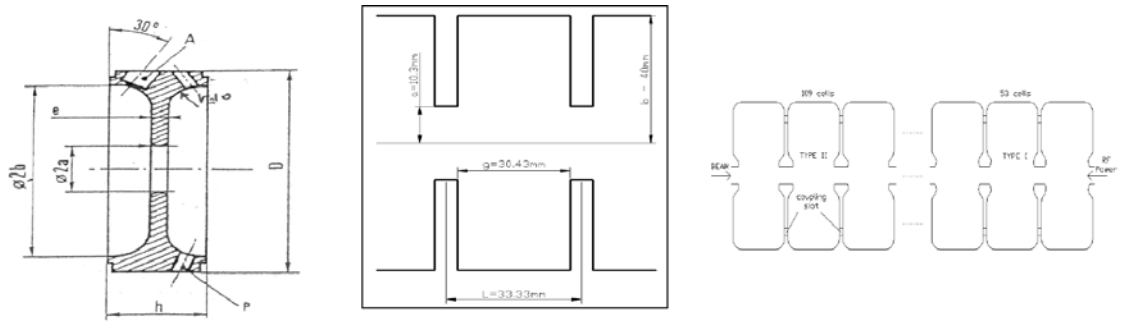

Figure 6.4.2:
FERMI accelerating structures. a) S0A-S0B geometry. b) C-type geometry (CERN). c) S-type geometry.

The first two geometries, shown in Figure 4a and 4b, are SLAC-type sections configured in traveling forward wave (TFW) mode with on-axis coupling and operated to a relatively modest gradient of 18 MV/m. The geometry shown in Figure 4c corresponds to a nose-cone type section with magnetic coupling; they operate in Backward Traveling Wave mode (BTW) and at high gradient (up to 25 MV/m). Unlike the previous two types, these have an iris radius of only 5 mm. The S-sections are supplied by an RF pulse compression system of the Sled type and by a TH 2132° klystron. The same type of klystron supplies two structures of the others.

Table 6.3.1 summarizes the main operational parameters of each of the three section types. An operating margin of up to 15% is available on top of the nominal energy gain.

Table 6.4.1: Linac energy budget.

Linac energy budget					
Type of structure	**Quantity**	**ΔE (MeV)**	**Maximum energy gain on crest (MeV)**	**Operating margin (%)**	**Operating energy gain on crest (MeV)**
Gun	1	5	5		5
S0A-S0B	2	50	100	10	90
C1-C7	7	55	385	15	329
S1-S7	7	140	980	14	840
X-band	1	-20	-20	0	-20
With X-band		**Total**	**1450**		**1244**
Without X-band		**Total**	**1414**		**1264**
FERMI energy 1200 MeV					

Figure 6.4.3 shows the new FERMI layout including the necessary building expansion, the planned distribution of the various section types in the new linac and the relative RF plants. For comparison, the existing buildings are shown below this drawing.

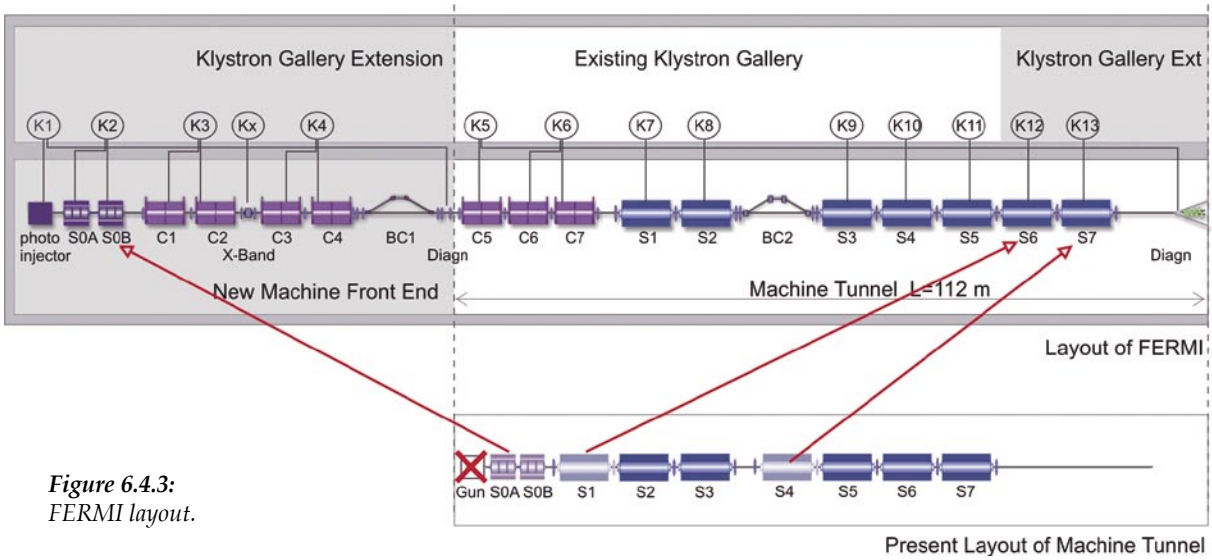

Figure 6.4.3:
FERMI layout.

The building expansion for the new front end is visible in the front of the existing structure. The figure also shows the RF systems and sections that will be relocated: S0A and S0B will be installed right after the photoinjector; S1 and S4 will be moved to the high energy end of the linac. A length of 10.5 m is kept available downstream of the S2 accelerating section. The proposed layout would leave the position of S2-S7 accelerating sections unchanged, thus reducing the impact of the machine upgrade.

6.4.3 HV Modulators

The present RF system is based on eight high power modulators, capable of 102 MW peak power and operating at 10 Hz, with their own klystrons (Thales TH 2132A, 3 GHz, 45 MW peak power, 4.5 μsec pulse width). The configuration adopted for each power station is based on an 18-cell PFN (Guillemin type E Pulse Forming Network), resonant charged with a constant current HV power supply (FUG-HCK 6750M-30000) and discharged with a double gap thyratron (EEV CX 1536X). The use of a coupled inductance PFN optimizes the rectangular pulse shape at the output compared to a conventional L-C network with the same number of elements.

The need to supply seven supplementary accelerating sections C1-C7 and the new Photocathode RF Gun will bring the total number of FERMI RF systems from eight to thirteen (MDK1-MDK13); the two deflecting structures that will be used for diagnostic purposes will keep the RF power from MDK1 and MDK6 respectively. Only the section S1-S7 will be fed through the existing SLED system.

In order to evaluate the energy gain of the linac, the plan is to operate each plant with a 10-15% margin on the maximum available klystron power, with an RF pulse width less than 3.5 μsec. Even if in the initial phase the system will be operated at 10 Hz, the upgrade of all system is planned to include the capability of operating at 50 Hz at a later phase. Particular care will be given to the stability of each station in terms of amplitude and phase of the fields with each section. This results in the very demanding tolerances required on the RF sections by the FERMI specifications. This challenging task starts from the optimization of the performance of the modulators. It is therefore planning to design and build new modulators for all of the stations in the system and to compare two prototypes: one based upon conventional technology, thyratron and an extremely low ripple PFN, in combination with a HV pulse transformer. A second based on a hybrid technology combining a solid state switch (an inductive adder) with a HV pulse transformer. Test both PFN and solid state allows the evaluation of performance, cost and risk. This R&D plan is intended to verify system performance especially in terms of stability and reliability, extremely important for a user facility like FERMI. This will lead the final design for the upgrade of the whole system.

6.4.3.1 Modulators Upgrade Plans

The klystron pulse specifications for the FERMI project are given in Table 6.4.2.

Table 6.4.2: Klystron modulator pulse specifications.

Parameter	*Value*	*Units*
Klystron	TH2132	Thales
Micro Perveance	1.9 to 2.1	$\mu A/V^{3/2}$
Peak Cathode Voltage	314	kV
Peak Cathode Current	350	A
Pulse Width	4.5	μs
Pulse Repetition Frequency	10-50	Hz
Rise/Fall Time	<2	μs

The present systems will meet all of the above specifications with the exception of the pulse repetition frequency. A prototype modulator based on the same technology, with an additional improvement on the pulse flatness ($\leq 0.1\%$) and capable of operating at 50 Hz is being assembled. It will be installed and tested on the photoinjector. At the same time, a solid state design is proposed which we expect should result in reduced capital cost, improved efficiency, reliability and maintainability. The solid state design should also eliminate most single point failures of the modulator by employing redundancy. A simplified schematic of the proposed modulator is shown in Figure 6.4.4.

The proposed solid state modulator is an inductive adder, similar to those proposed by SLAC for the NLC and operating at SLAC for ORION, and for the SPEAR III injection kickers. The design in Figure 6.4.4 uses a minimum of six steel cores, each driven by two 6.5 kV, 800 A IGBT switches. In this design the adder circuit would drive the existing ELETTRA pulse transformer in the existing high voltage tank for the klystron. The modulator would easily fit in the present electronics enclosures.

The operation of the modulator is as follows. Each core is driven by two parallel IGBT drivers. The IGBTs switch 4 kV through a single turn primary. A single turn is passed through the aperture of each of the cores, inductively adding the primary voltages in series. The output pulse is then feed to the primary of the existing pulse transformer to drive the klystron cathode. Pulse shaping will be required because of a resonant condition caused by the modulator stack leakage inductance and primary to secondary capacitance, the leakage inductance and winding capacitance of the pulse transformer, and the klystron capacitance. This will cause an overshoot and oscillations on the flat top if all the IGBTs are quickly switched on at the same time. A solution is to slow down the rise time from the inductive adder. This is best accomplished by delaying turn on of some of the cells, as has been demonstrated with the 8-pack modulator at SLAC. Further shaping of the output pulse is required because of voltage droop during the pulse flat top caused by a finite capacitance, and transformer magnetizing inductance. The droop can be corrected by a bouncer circuit composed of an SCR switch and a resonant RC circuit where a sinusoidal voltage is subtracted from the main output pulse. The modulator parameters for this circuit are given in Table 6.4.3.

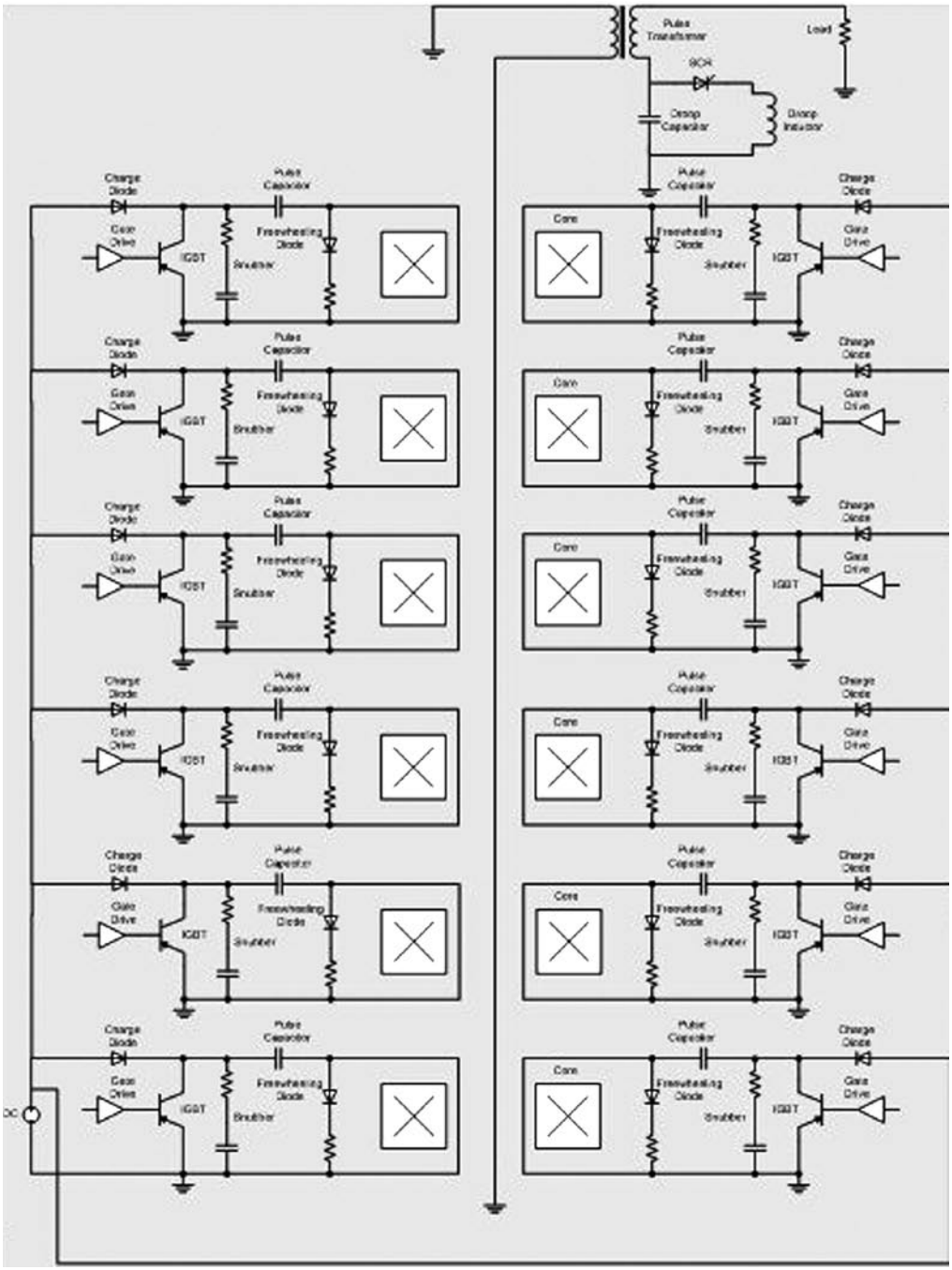

Figure 6.4.4:
Simplified schematic of a proposed solid state klystron modulator.

Table 6.4.3: List of modulator parameters.

Parameter	*Value*	*Units*
Number of Modulators	15	
Maximum Output Voltage	335	kV
Maximum Output Current	425	A
Maximum Repetition Frequency	60	Hz
Maximum Pulse Width	4.5	μs
Minimum Pulse Width	<100	ns
Rise Time	<2	μs
Fall Time	<1	μs
Pulse Flatness	<±1	%
Minimum # of Cells	6	
Minimum # of IGBTs	8	
Maximum IGBT Voltage	4000	V
Maximum IGBT Current	3000	A
Timing Jitter (rms)	<50	ns
Primary Power Supply	10	kW

6.4.4 LLRF System

The specifications of the RF control and timing systems are extremely demanding and require adopting state of the art technologies. One additional complication is the use of the X-band cavity, which is likely to be at an integer harmonic of the USA S-band frequency (2856 MHz) and therefore not an exact multiple of the existing linac operating at the European S-band frequency (2998 MHz). Local phase locked loops are planned to ensure the stability of each station.

The conceptual design of the LLRF system is made of three major components: the RF reference distribution system, the RF controller hardware, firmware, software and the interface with the timing and synchronization system. Each of these three components has been developed to a level of details sufficient to provide a reference design.

6.4.4.1 RF Reference Distribution System

This system was chosen to operate at 491 MHz, which is the frequency distributed throughout FERMI. It will be used locally to develop all the intermediate frequencies and in combination with local oscillators. This choice eliminates asynchronous events, since the same RF reference is used for the creation of all frequencies and phases.

The RF controller will make use of an FPGA-based digital processor [11] which takes advantage of the high dynamic range available in modern ADCs and DACs by down-converting the S and X bands to 48.2 and 47.6 MHz respectively. The RF and timing system distributes an RF reference signal at 491.64 MHz to all the RF stations. The digital controllers then process this frequency and synthesize the IF locally. The resulting IF is then used to lock each station to a phase reference provided by the synchronization system. This provides frequency references across the facility and eliminates asynchronous events.

Coherence between S and X bands is established by their common subharmonic of 15.779 MHz, which generates the S-band frequency when multiplied by 190, and the X-band driver when multiplied by 724. The reference signal of 491.64 MHz is 8 x 74/19 of the 15.779 MHz subharmonic. It is divided by 8 to get a 61.45 MHz digital clock for the ADC, DAC, and FPGA. A combination of DDS techniques and frequency multiplier chains are used to generate the S band (multiply by 6 + 87/111/8) and X band outputs (multiply by 24 - 2/3 - 86/111/8). Each station will be individually controlled by a single FPGA system that works off the 491 MHz reference frequency and the laser distributed timing pulses, as shown in Figure 6.4.5. In this approach the most critical components are the dividers and amplifier, as they can add noise to the system. These components are part of the proposed R&D plan for the RF controller upgrades.

6.4.4.2 Single Station Controllers

Each station requires a dedicated controller to ensure that the cavity fields are indeed synchronized to each individual bunch to the specified level of amplitude and phase. A block diagram of the system is shown in Figure 6.4.5. To accomplish this, each section will have a dedicated temperature stable reference, which will be used to calibrate each read-back point in between pulses. This will reset all errors in real time and will minimize the effects of slow drifts.

A Field Programmable Gate Array (FPGA) based digital controller will then take the reference phase provided by the laser distribution system and lock to it the local RF phase. After down conversion to the IF, the signals are digitized by 14 bit ADCs and all signal processing is then implemented in the FPGA. The firmware that programs the FPGA is the heart of the system and performs a multitude of tasks, from the actual feedback control, (although it is unlikely to have a closed feedback loop with such a short pulse due to the internal delay of the system), to adaptive feed forward compensation, to interlocks and protection. The firmware also contains the interface with local networks and the code to interact with the control system.

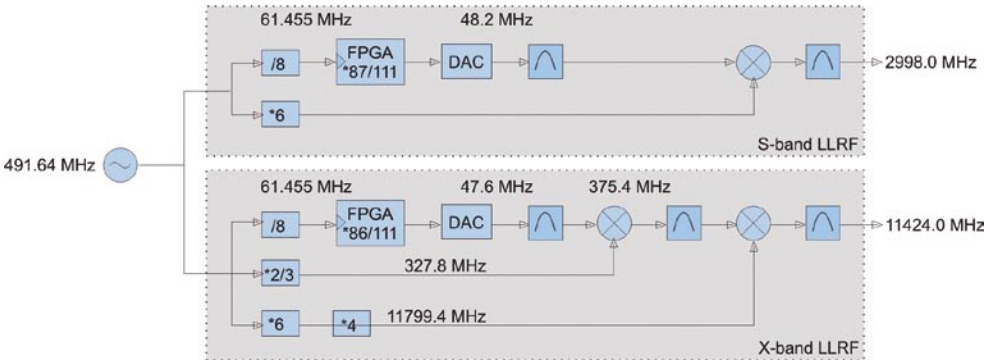

Figure 6.4.5:
Single station RF controller block diagram.

6.4.4.3 Synchronization System

The synchronization system will distribute phase references to each station. The specifications correspond to maintaining a sub 100 fs synchronicity across the 300 m of the facility. Integration of the synchronization system with the local RF controllers is essential. Such system is described in detail in Chapter 10. Figure 6.4.6 shows the block diagram of the system and its integration with the RF controllers.

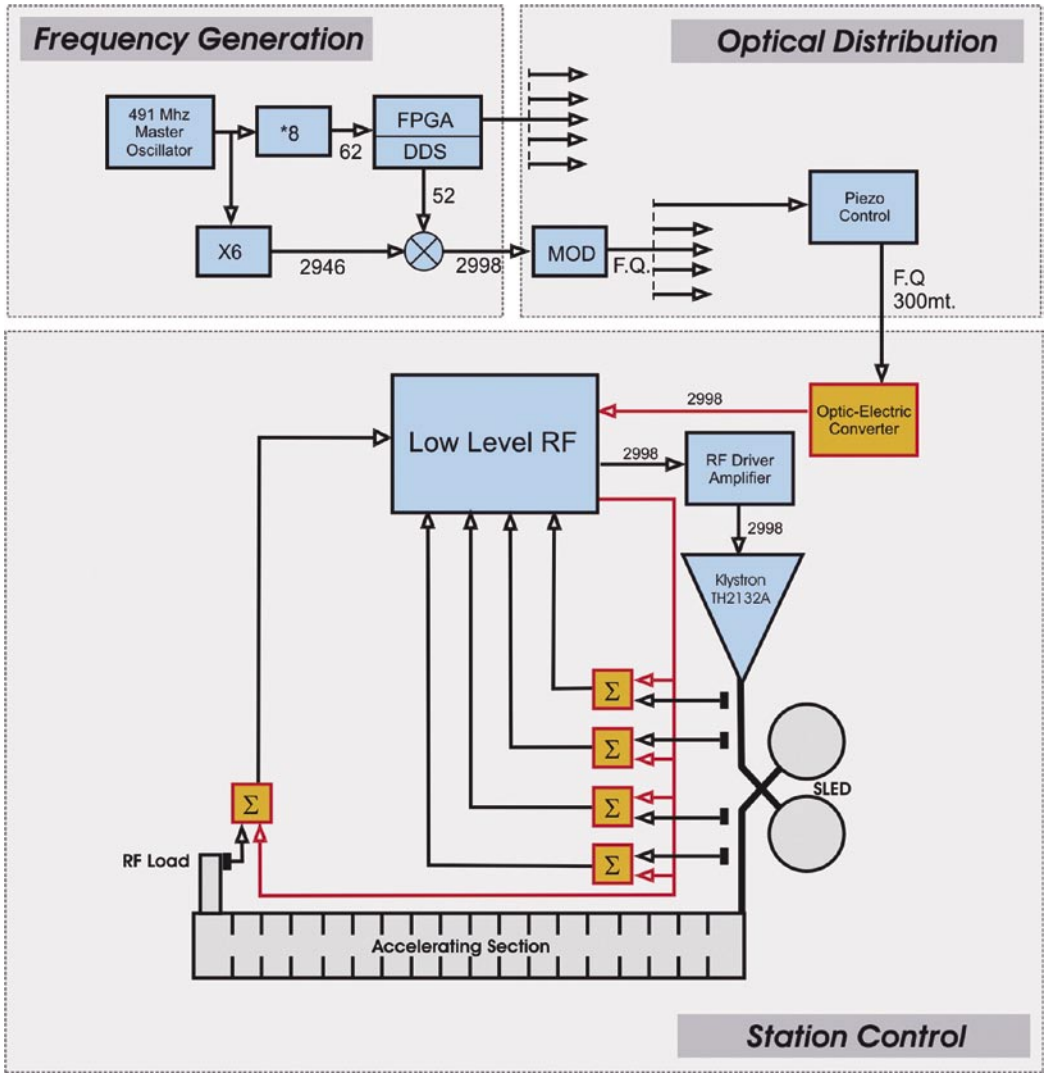

Figure 6.4.6:
Block diagram of the integration of synchronization and RF control systems.

6.4.4.4 Auxiliary Systems

The linac upgrade will require both the construction of new systems as well as the upgrade of several auxiliary systems that are part of the existing linac. In addition to the systems already described here, such systems include:

- Control system
- Feedback systems
- Vacuum system
- Beam instrumentation and feedback systems
- Conventional facilities (buildings, utilities)

In addition to the extension of the linac building and klystron gallery, the linac upgrade will require the installation of new AC power and water cooling capacity to be able to energize and cool the additional sections that will be installed. This corresponds to 1.5 MW of AC total power (whose 0.5 MW of the existing accelerator) at 50 Hz and to 300 kW of heat load on the existing systems, excluding the auxiliary systems.

Several of the existing systems will be upgraded. Some of them, like the controls and vacuum systems, benefit from the ongoing booster construction, where the new hardware is already being deployed and therefore the linac upgrade will be an extension of the existing construction. Others, like feedbacks and beam instrumentation, need significant upgrades to meet more demanding specifications.

6.4.5 Linac Stability

Sensitivity studies have been performed to determine the variation of the Linac output parameters with respect to the phase and amplitude jitters of the accelerating fields, electron bunch charge and electron emission time at the cathode (see, Chapter 5). The obtained sensitivities have been used to form a tolerance budget for each segment of the Linac (L1-L4 and the X-band structure). They provide a collection of tolerances that need to be met.

The results indicate that the most stringent phase specifications concern the first Linac segment (L1), while the tightest amplitude control is required on L4. In this process a tolerance budget among the various elements of the Linac was allocated, trading off amplitude and time jitter in the RF gun with those of each accelerating section. The corresponding specifications in amplitude and phase result in the tightest phase control in L1 (0.09 ^{o}S) and amplitude control in L4 (0.05%). While the present RF systems have not yet achieved these demanding goals, some preliminary measurements were performed on the existing systems. So far, stability of the order of 0.1% amplitude and 0.1 ^{o}S can be achieved, not including potential benefits from the noise correlation among different stations in the Linac [12]. With the above conditions, the error tracking analysis showed a satisfactory result in the final slice energy and peak current as a function of the time defined by the master clock. In order to be able to assess the stability of the existing systems, preliminary phase jitter measurements were performed on some of the present RF transmitter in operation at ELETTRA. While operating at 10 Hz, four of the existing systems (MK3, MK4, MK5 and MK7) were tested by observing the pulse to pulse variation of the mean (integrated) phase in the range from 1 sec. up to 10 min. (10 to 6000 pulses). The measurement setup is shown in Figure 6.4.7.

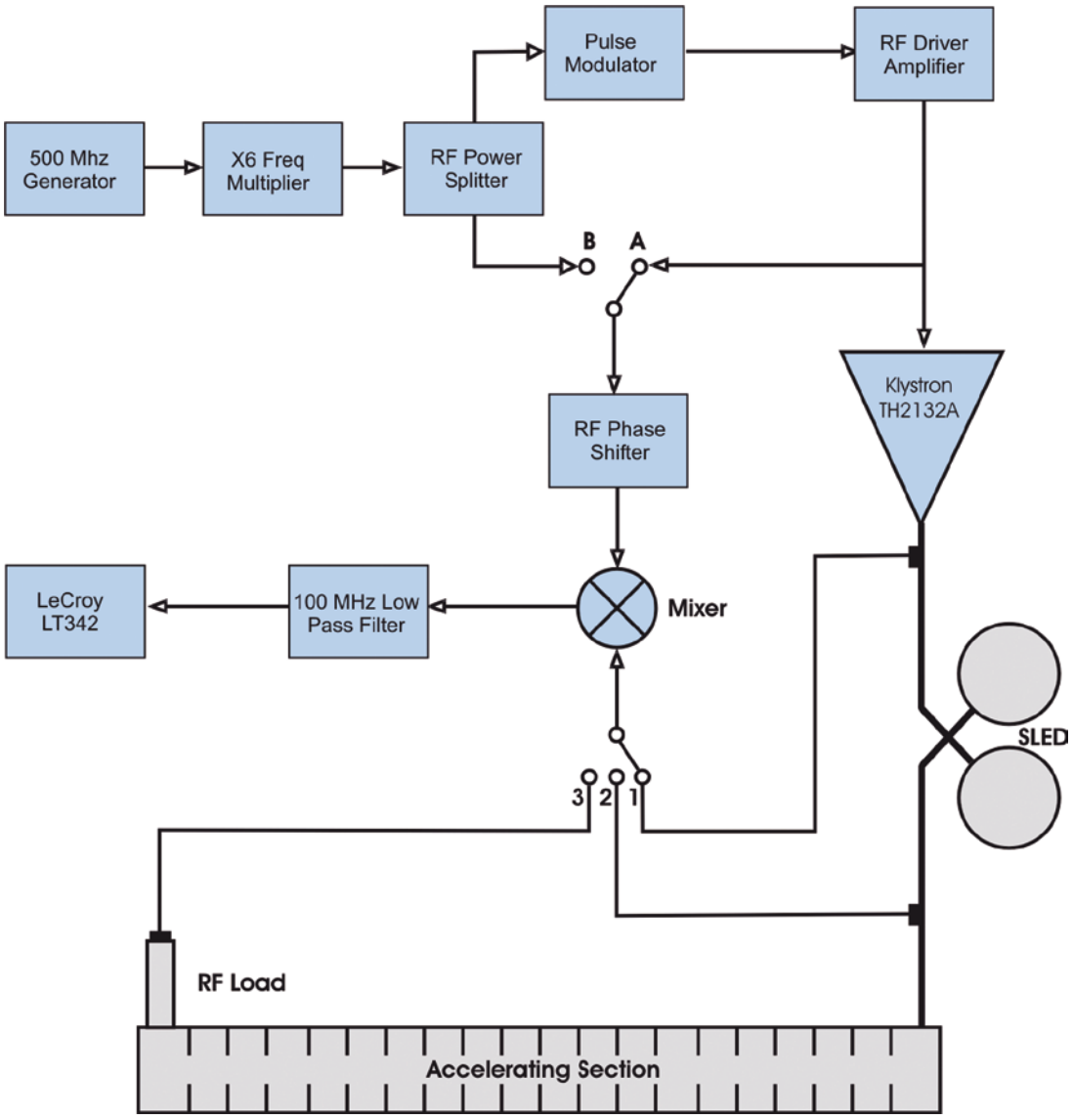

Figure 6.4.7:
Phase jitter measurement layout.

As one can see from the scheme, the measurements tried to characterize all the system's components, from the klystron up to the RF water load of the accelerating section. The phase noise was measured over 1 μsec of the 3.0 μsec total RF pulse length. Table 6.4.4 reports the results of the measurements.

Table 6.4.4: Pulse to pulse main phase variation (^{0}S rms).

	MK3	MK4	MK5	MK7	AVG
			Klystron (pos: A-1)		
1 sec	0.031	0.048	0.034	0.019	0.033
5 sec	0.036	0.048	0.034	0.030	0.037
10 sec	0.036	0.037	0.034	0.034	0.035
30 sec	0.036	0.070	0.038	0.030	0.043
1 min	0.041	0.092	0.041	0.030	0.051
5 min	0.056	0.088	0.038	0.049	0.058
10 min	-	-	-	-	-
			Driver-Klystron (pos: B-1)		
1 sec	0.056	0.038	0.049	0.034	0.044
5 sec	0.067	0.038	0.053	0.060	0.055
10 sec	0.056	0.042	0.057	0.053	0.052
30 sec	0.078	0.069	0.057	0.060	0.066
1 min	0.111	0.046	0.064	0.056	0.069
Time	0.108	0.080	0.200	0.060	0.112
10 min	0.130	0.096	0.230	0.120	0.144
			Driver-Klystron-SLED detuned (pos: B-2)		
1 sec	0.045	0.069	0.071	0.069	0.064
5 sec	0.068	0.061	0.056	0.084	0.067
10 sec	0.057	0.058	0.060	0.065	0.060
30 sec	0.079	0.061	0.060	0.084	0.071
1 min	0.090	0.088	0.056	0.126	0.090
5 min	0.188	0.104	0.075	0.168	0.134
10 min	0.354	0.561	0.188	0.172	0.319
			Driver-Klystron-SLED detuned-Section (pos: B-3)		
1 sec	0.153	0.169	0.177	0.098	0.149
5 sec	0.138	0.184	0.162	0.184	0.167
10 sec	0.181	0.157	0.181	0.162	0.170
30 sec	0.169	0.184	0.211	0.218	0.196
1 min	0.173	0.184	0.238	0.169	0.191
5 min	0.358	0.338	1.076	0.237	0.502
10 min	0.634	0.441	1.027	0.335	0.609

The last column shows the average values over the four stations. Acquisition problems resulted in the missing data klystron (A-1), 10 min. period. A preliminary analysis shows that the pulse to pulse variation of the mean phase remains within acceptable levels; for example, the klystron (A-1) stays within 0.04 ^{0}S over 1 sec. (10 pulses), reaching 0.06 ^{0}S in 5 min. (3000 pulses). The same parameters vary between 0.15 ^{0}S and 0.6 ^{0}S over the whole system, thus is required a feedback system capable of keeping the transmitters within the specifications.

Figure 6.4.8 shows the oscilloscope trace relative to the acquisition of 3000 pulses from the klystron in the MK5 section: over 5 min. of statistics, the pulse to pulse integrated phase variation is below 0.06 ^{0}S.

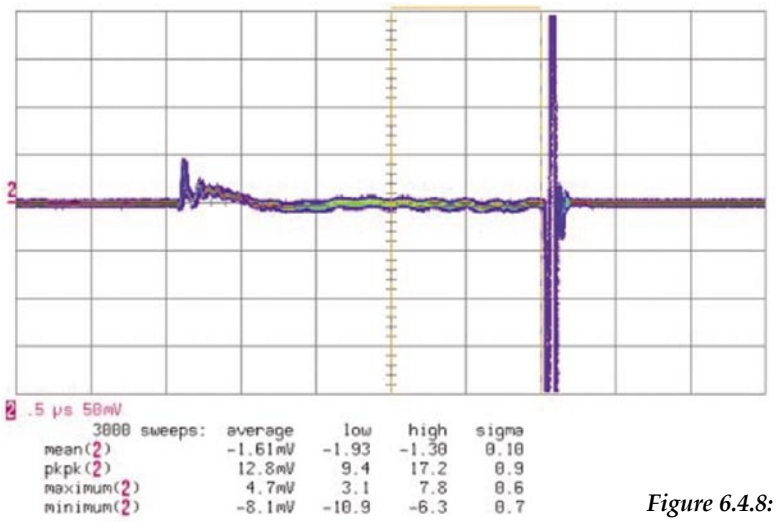

Figure 6.4.8:
MDK5 Klystron 1 µsec averaged phase noise (3000 pulses, 5 min).

6.5 The Geometric Wake Functions of the Accelerating Structures

The geometric wake functions of the accelerating structures in the FERMI Linac plays an important role in the formation of the final electron beam [13]. Particular care was taken in the management of the wakefields in the BTW structures, which have the highest impedances, as shown in Figure 6.5.1.

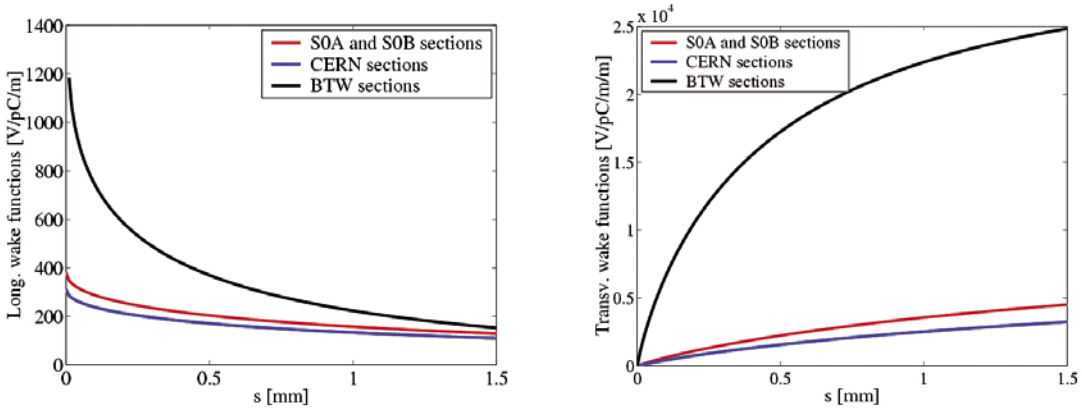

Figure 6.5.1:
Longitudinal (left) and transverse (right) wake functions of the accelerating structures used in the FERMI Linac.

The longitudinal wake field introduces second and third order energy chirps, thus reducing the compression efficiency and leading to current spikes at the bunch edges. The wake field in L4 increases the final correlated energy spread, with an impact on the HC FEL bandwidth [14]. The transverse wake field, driven by trajectory distortion caused by field errors and elements misalignment, induces the BBU instability, that is, a correlation in the transverse-longitudinal particle positions. The instability increases the projected emittance by causing a launching error and an optical mismatch of the bunch-trailing electrons. An in-depth study of the wake functions was performed and techniques are proposed to minimize the phase space dilutions. The wake functions of the three types of accelerating sections have been calculated in [15,16] using analytical approximation for the S0A, S0B and CERN sections and a time domain code for the BTW sections [17].

6.5.1 Longitudinal Wake Potentials

For a longitudinal charge distribution λ_z, the voltage gain of a test electron due to the electromagnetic wakes of the electrons behind of it is given by the wake potential [18]:

$$W(s) = -\int_{s}^{\infty} w(s-s')\lambda_z(s')ds' \qquad 6.5.1$$

It was found that by computing the short-range wake numerically and fitting it with a simple function, one can obtain a result that is valid over a large range of s (position along the bunch) and over a useful range of parameters [19]; this consideration applies to the steady state situation, which is reached in an approximate distance $a^2/2\sigma_z$ (where a is the section aperture and σ_z the rms bunch length) from the entrance of the accelerating section, by fitting generally short with respect to the section length (about 0.5 m for a 200 fs bunch and 5 mm aperture). In what follows, the steady state wake functions [18] will be used.

For S0A and S0B accelerating structures one obtains:

$$w(s) = 380\exp\left(-\sqrt{s(mm)/1.28}\right) \quad \left[\frac{V}{pC\,m}\right] \qquad 6.5.2$$

For the CERN accelerating structures:

$$w(s) = 311\exp\left(-\sqrt{s(mm)/1.38}\right) \quad \left[\frac{V}{pC\,m}\right] \qquad 6.5.3$$

For the ELETTRA accelerating structures:

$$w(s) = 1345\exp\left(-\sqrt{s(mm)/0.3}\right) \quad \left[\frac{V}{pC\,m}\right] \quad \text{for s<1 mm} \qquad 6.5.4$$

The wake potential in the BTW structures is stronger than in TW structures because of the magnetic coupling that requires a smaller iris radius. However, the former provides a higher energy gain.

It has been shown [13] that, for 1 nC charge distributed over 12 ps bunch length traveling through the S0A, S0B and L1 sections (for a total length of ~ 24 m), the cubic energy chirp is dominated by the longitudinal wake potential contribution.

The cubic energy chirp is responsible for the appearance of the bifurcation in phase space after the bunch compressors; this phase space distortion in turn leads to spikes in the peak current at the edges of the electron bunch [13]. It is therefore desirable to minimize it. One way to achieve this is to use a density distribution with the linearly ramped peak current shown with the bold line in Figure 6.5.2a. It gives a wake potential with a significantly reduced cubic chirp a_3=890 MV/nC (see also the bold line in Figure 6.5.2b). The part under the bold line in Figure 6.5.2 contains approximately 40% of the total charge.

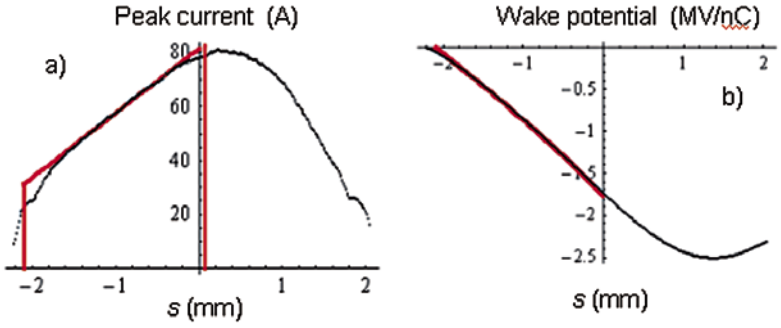

Figure 6.5.2:
Density distribution with a linear ramped peak current (a) and its corresponding wake potential (b). The bold line shows the ideal distribution and its associated wake potential, while the black line shows the actual distribution and wake potentials obtained in simulations.

6.5.2 Transverse Wake Potentials

As suggested in [15,16], an analytical approximation to the wake function for the TW structure (SØA, SØB and CERN sections) may be used for the transverse case. With the geometric parameters in [20] the transverse wake function up to 5 mm bunch length (s in meters) is:

$$w_{\perp}^{1}(s) = 9623 \cdot \left[1 - \left(1 + \sqrt{\frac{s}{0.60 \cdot 10^{-3}}}\right) \cdot e^{-\sqrt{s/0.60 \cdot 10^{-3}}}\right] \left[\frac{V}{pC \cdot m \cdot m}\right] \qquad 6.5.5$$

$$w_{\perp}^{1}(s) = 7524 \cdot \left[1 - \left(1 + \sqrt{\frac{s}{0.70 \cdot 10^{-3}}}\right) \cdot e^{-\sqrt{s/0.70 \cdot 10^{-3}}}\right] \left[\frac{V}{pC \cdot m \cdot m}\right] \quad 6.5.6$$

For the BTW accelerating structure an analytical model was chosen which is a combination of periodic and one-cell structure solutions. The transverse wake function up to 2 mm bunch length is (s in meters) [17]:

$$w_{\perp}^{1}(s) = 27984 \cdot \left[1 - \left(1 + \sqrt{\frac{s}{0.12 \cdot 10^{-3}}}\right) \cdot e^{-\sqrt{s/0.12 \cdot 10^{-3}}}\right] + 13992 \cdot \sqrt{s} \left[\frac{V}{pC \cdot m \cdot m}\right] \quad 6.5.7$$

The SØA, SØB and CERN sections are characterized by relatively weak wake fields compared with the S-sections.

6.6 Compression and Longitudinal Dynamics

In order to achieve high peak current and small energy spread the electron beam must be manipulated in longitudinal phase space. This is normally achieved by using a series of RF accelerating structures and magnetic chicanes (bunch compression system). It is desirable that this process remains linear in order to avoid bifurcation in longitudinal phase space and high peak current spikes at the edges of the electron bunch. A distribution as uniform as possible is also aimed for, as it provides the maximum peak current in the main body of the bunch and narrows the bandwidth of the FEL output.

6.6.1 Magnetic Compression

The rms bunch length after the BC1 is [21,22,23]:

$$\sigma_z = \left\langle s^2 - \langle s \rangle^2 \right\rangle = \sqrt{(1 + hR_{56})^2 \sigma_{z0}^2 + (R_{56}\sigma_{\delta 0})^2} \approx |1 + hR_{56}|\sigma_{z0} \quad 6.6.1$$

where σ_{z0} and σ_{d0} are the rms bunch length and uncorrelated energy spread before BC1. The compression factor is:

$$C = \frac{\sigma_{z0}}{\sigma_z} \approx \frac{1}{1 + hR_{56}} \quad 6.6.2$$

The uncorrelated energy spread after the compression is $C\sigma_{\delta 0}$.

A 4-th harmonic cavity, called the "linearizer" in Figure 6.1.1, helps to linearize the energy chirp before BC1 [21,22,23]. The quadratic energy chirp is zero if the following condition is imposed [8]:

$$U_4 = -\frac{U_0 + U_1 \cos(\phi_1)}{16 \cos(\phi_4)} \qquad 6.6.3$$

where U_0 is the acceleration amplitude of the two accelerating sections preceding the laser heater (see, Figure 6.1.1) where acceleration is on-crest; U_1 is the acceleration amplitude of the four accelerating sections placed between the laser heater and BC1, with off-crest acceleration at phase ϕ_1 (referred to the crest of the rf wave). U_4 and ϕ_4 are the amplitude and phase of the 4-th harmonic X-band cavity.

Similar considerations can be drawn for the second stage of bunch compression using L2, L3 and BC2.

6.6.2 Coherent Synchrotron Radiation

Coherent synchrotron radiation (CSR) in the bending magnets of the two bunch compressors plays a major role in the micro-fragmentation of the electron bunch. This CSR causes variation of the electron energy along the electron bunch. In the case of the long magnet with bending angle [24]:

$$\varphi_M \geq \left(24 \frac{\ell_b}{R}\right)^{1/3} \qquad 6.6.4$$

one can write for the rate of the electron bunch energy loss per unit length z of the magnet (see, refs in 4):

$$\frac{dE}{dz} = -\int_{-\infty}^{\infty} ds \lambda_z(s) F_{\parallel}(s) = -3^{2/3} \frac{N^2 e^2}{R^{2/3} \ell_b^{4/3}} \qquad 6.6.5$$

where N is the number of particles per bunch and λ_z the density distribution.

The electron bunch moves inside the vacuum chamber that acts as a waveguide for the radiation. Not all spectral components of the CSR propagate in the waveguide and therefore the actual radiated energy is smaller than in a free space environment (see, Figure 6.6.1).

Because of shielding [25 and refs in 4], CSR is suppressed in BC1 where the electron bunch length exceeds 2-3 ps and is only important in the 4-th magnet of BC2 where the bunch length shrinks below 1-1.5 ps. This magnet is 0.5 m long and has a 9.35 m bending radius. The calculated average energy loss per electron due to CSR in free space (i.e. without shielding) is 340 keV for a 0.7 ps long electron bunch but the steady state formula slightly overestimates the effect. Therefore, this study concludes that the CSR effects are less important than the wakefields perturbations of the linac discussed in the previous paragraphs.

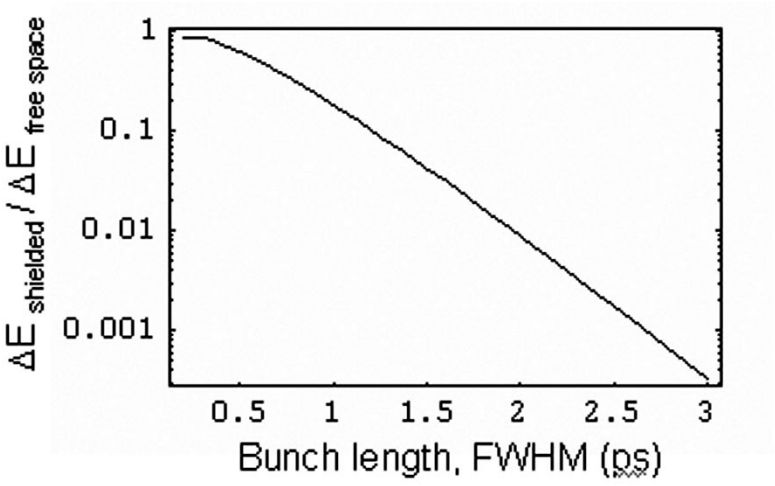

Figure 6.6.1:
Suppression of CSR by the vacuum chamber shielding.

6.6.3 Reverse Tracking

One of the problems faced by the accelerator optimization study was how to obtain, at the end of the accelerator, a distribution with as constant peak current and energy as possible along the electron bunch. Chapter 4 describes why this is a necessary performance aspect for the electron beam in order to optimize both the output power and bandwidth of the FEL radiation. This problem is considerably simplified by using the backward tracking technique justified and demonstrated in [13]. The technique consists in setting up a desirable "flat-flat" (in peak current and energy) distribution at the end of the linac. Starting with this distribution and tracking it backward, a nearly linear ramped peak current was obtained at the start of the linac. This is the reasoning that led to the ramped peak current distribution mentioned in paragraph 6.5.1 and used in start-to-end simulations.

6.6.4 Microbunching Instability

At a scale much smaller than the bunch length other additional effects gain significance. At this scale shielding is not effective and any microstructure in the charge distribution along the bunch will emit CSR as in free space. Such microstructures induce LSC forces which modulate the energy of electrons in the bunch. Together, the LSC and the CSR effects give rise to the so-called microbunching instability (μBI) that can be triggered even by the initial shot noise in the charge distribution [5 and refs in 4] at the cathode of the photoinjector. The end result of this perturbation is an increase of the slice momentum spread which, if it is too large, reduces the gain and increases the bandwidth of the FEL.

Simulations show that the entire machine acts as gigantic amplifier of the initial noise through a mechanism similar to self-amplification of spontaneous emission (SASE) in FELs. A reliable estimate of the growth of the momentum spread is at present fraught with uncertainty, as the simulations of the microbunching instability with particle tracking codes require a very large number of macroparticles; for example, a computation simulating the behaviour of a 6 ps long electron bunch (FWHM) using 10^6 macroparticles still generates a numerical noise approximately 50 times larger than the real shot

noise. The predictions are particularly uncertain in the second bunch compression where the instability gain is large, leading to a nonlinear evolution of its growth. Appendix A of this Chapter discusses the development of a Vlasov solver to overcome this problem.

The results presented in the next paragraph rely therefore on the linear theory [4 and refs. therein] and they assume an uncorrelated energy spread of the final beam of 150 keV rms.

6.6.4.1 Gain Function and Energy Landau Damping

The spectral dependence of the gain of the microbunching instability was calculated for the set of machine and electron bunch parameters listed in Table 6.6.1. The results are presented in Figure 6.6.2.

Table 6.6.1: Parameters relevant to the microbunching instability and used to calculate its gain.

Parameter	*Value*	*Units*
Uncorr. energy spread	2	keV
Beam energy	100	MeV
Compr. Factor BC1	4	
Beam energy BC1	220	MeV
Linac length up to BC1	30	m
Compr. Factor BC2	2.5	
Beam energy BC2	600	MeV
Linac length up to BC2	50	m
Linac length after BC2	70	m

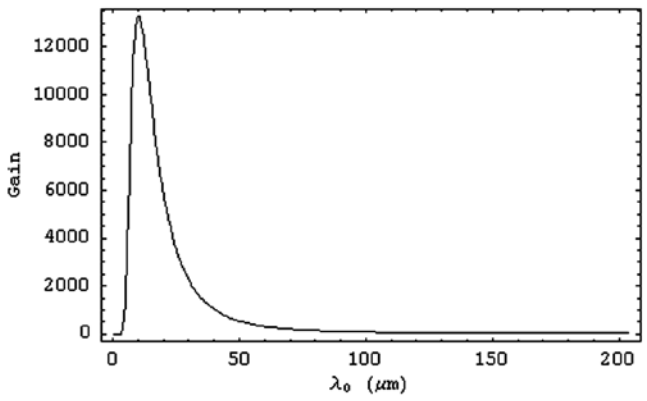

Figure 6.6.2:
Spectral gain function of the microbunching instability at the end of the linac in the linear approximation.

Because most of the microbunching instability gain occurs after BC2, one can effectively suppress it by using only BC1 for bunch compression [26]. Although this is a potentially attractive option, it is not yet sufficiently demonstrated because difficulties were encountered in obtaining "flat-flat" distribution at the end of the linac due to strong longitudinal wakefields in L3 and L4. This is an option that requires further studies and will be pursued in the future.

The slice energy spread in the electron bunch after the second bunch compressor was calculated by assuming that the energy spread induced by microbunching instability will eventually become incoherent energy spread. This approach results in an unacceptably large number for the momentum spread at the undulator entrance: σ_E= 4.3 MeV. To overcome this problem, a laser heater was proposed in [5]. It consists of a laser beam which, by interacting with the electron beam, increases its uncorrelated energy spread so that the μBI (see, Figure 6.6.2) is Landau damped.

At first, it is simply assumed that the laser heater provides additional energy spread which adds in quadrature to the existing, uncorrelated one generated by the photoinjector. Figure 6.6.3 shows the uncorrelated energy spread at the end of the linac as a function of the one induced by the laser heater alone for both the MLB and LB modes. The calculation is simplified by the fact that the interaction between the laser and the electron beam is weak because the required energy spread needed is small. In this case the changes in laser and electron dimensions along the interaction region can be neglected. Even the slippage effect is negligible because the slippage length is small with respect to the electron and to the laser pulse length. The heating process is therefore well described by the small gain theory with a single mode [27].

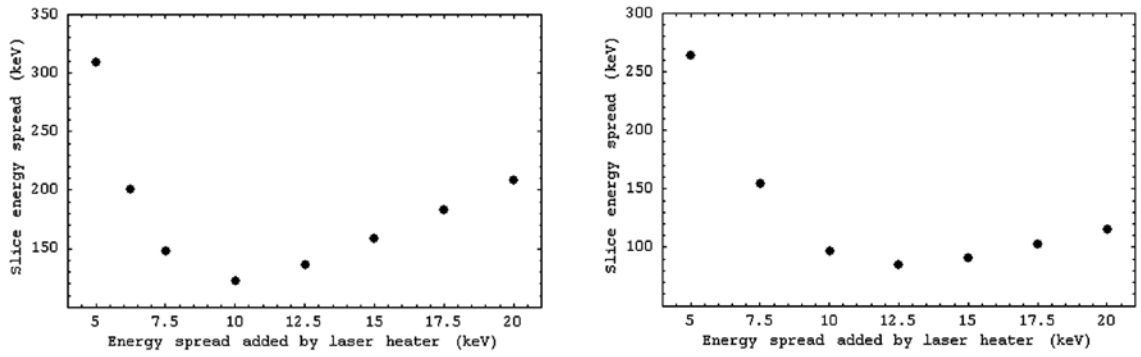

Figure 6.6.3:
Medium bunch (left) and long bunchs modes (right). Uncorrelated slice energy spread after the second bunch compressor as a function of the one added by the laser heater.

The gain in density modulation in a linear compressor due to an upstream energy modulation for a Gaussian energy distribution is [29]:

$$G(\lambda) = \left|\frac{b_f(\lambda_f)}{b_o(\lambda_0)}\right| = k_f R_{56} \frac{\Delta\gamma}{\gamma} e^{-\frac{1}{2}(R_{56} k_f \delta_0)^2} \qquad 6.6.6$$

where k_f is the compressed modulation wave number characterizing the instability, R_{56} is the momentum compaction of the magnetic chicane and δ_0 is average uncorrelated energy spread just before the compression. The Landau damping of the instability is proportional to the damping coefficient $e^{-\frac{1}{2}(R_{56} k_f \delta_0)^2}$.

Figure 6.6.4 shows the damping coefficient for a Gaussian energy distribution as function of the compressed modulation wavelength: the solid curve corresponds to 10 keV of rms uncorrelated energy spread boosted by the laser heater; the dashed curve reproduces the Landau damping provided at BC1 by the natural 2 keV rms energy spread of the beam without laser heater.

Eq. 6.6.7 describes the instability gain in 1-D approximation. If the transverse spatial distribution of the electron bunch is taken into account, then the energy distribution after heating is given by [28]:

$$v(\delta_0) = \frac{1}{\pi\sigma_x^2\sqrt{2\pi}\sigma_\gamma} \int r dr \cdot e^{-\left(\frac{r^2}{2\sigma_x^2}\right)} \int \frac{d\xi}{\sqrt{(\Delta\gamma_L(r))^2 - (\delta_0 - \xi)^2}} e^{-\frac{\xi^2}{2\sigma_I^2}} \qquad 6.6.7$$

where *r* is the coordinate running over the transverse profile of the beam, σ_x is the rms transverse electron beam size, σ_y is the standard deviation of the Gaussian electron energy distribution before the interaction, ξ is the particle energy coordinate, δ_0 the mean energy spread of the beam $\Delta\gamma_L(0)$, the maximum energy modulation amplitude induced by the heater. In such a case, the instability gain assumes the form [29]:

$$G(\lambda) = \left|\frac{b_f(\lambda_f)}{b_o(\lambda_0)}\right| = k_f R_{56} \frac{\Delta\gamma}{\gamma} \int v(\delta_o) e^{-\delta_0} d\delta_0 \qquad 6.6.8$$

Eq. 6.6.9 reduces to eq. 6.6.7 in the 1-D approximation and for a Gaussian energy distribution.

In Figure 6.6.5 the damping coefficient is plotted as a function of k_f for different values of the ratio between the transverse dimension of the laser and of the electron beam, $B=\sigma_r/\sigma_x$, and assuming a total energy spread of 10 keV rms. For comparison, the outer line refers to the damping coefficient in the 1-D approximation and for a Gaussian energy distribution, as in eq. 6.6.7.

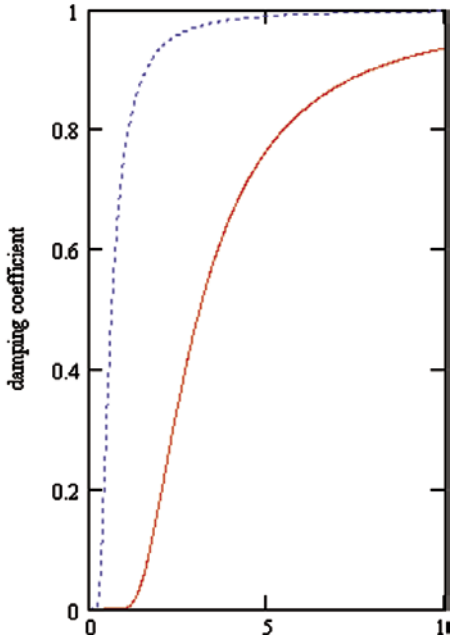

Figure 6.6.4:
Damping coefficient for 10 keV rms (solid line) and 2 keV rms (dotted line) of induced energy spread as function of the compressed modulation wavelength in microns.

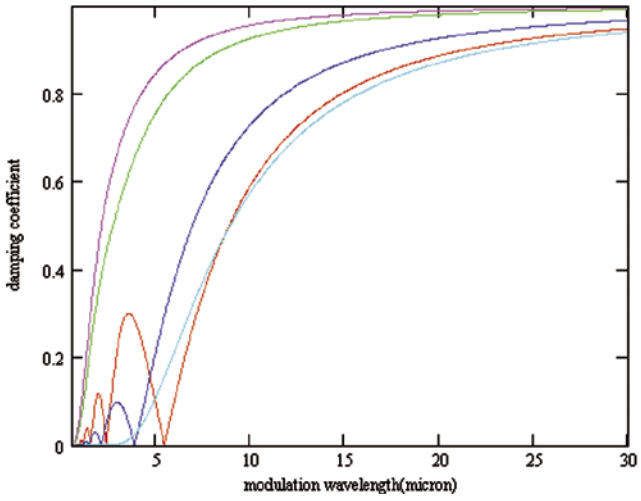

Figure 6.6.5:
Damping coefficient for different values of $B=\sigma_r/\sigma_x$ in the range 0.3 – 2.0. The modulation wavelengths are compressed.

The instability gain after BC1 was also calculated analytically including the energy modulation from the geometric wake field and from longitudinal space charge in L1 and including CSR in BC1. Figure 6.6.6 shows the instability gain as function of the compressed modulation wavelength, for three cases of the ratio $B=\sigma_r/\sigma_x$. An uncorrelated energy spread of 10 keV rms is assumed in the calculation.

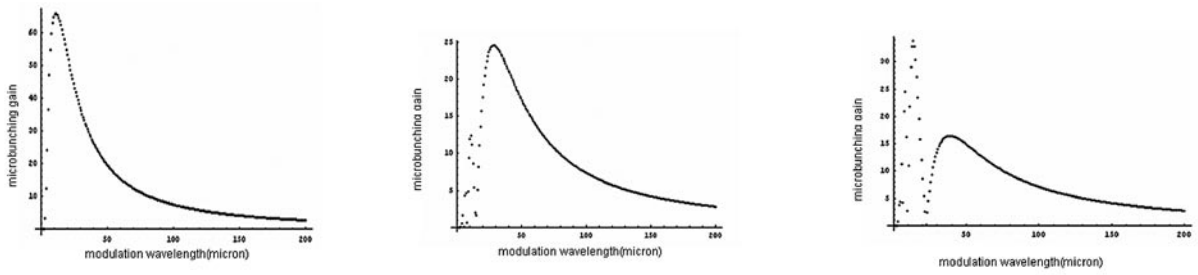

Figure 6.6.6:
From left to right, microbunching gain at BC1 for B=0.3, 1, 3. 10 keV rms uncorrelated energy spread. The modulation wavelengths are those of the compressed beam.

6.6.4.2 The Laser Heater

The laser heater consists of an undulator located in a magnetic chicane where a laser interacts with the electron beam, causing an energy modulation within the bunch on the scale of the optical wavelength (see, Figure 6.6.7). The corresponding density modulation is negligible and the coherent energy–position correlation is smeared by the chicane [8].

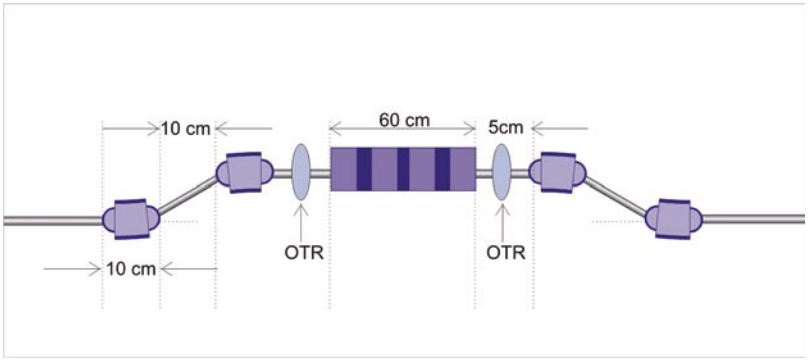

Figure 6.6.7:
Laser heater scheme.

According to [8], the induced energy spread should be in the range 10 – 17 keV. For a required energy spread, the needed laser power decreases quadratically with the electron beam transverse dimensions; at the same time, a too low a value of the transverse beam size makes the efficiency of the heating process more sensitive to the laser-beam transverse alignment. The specification for the accuracy of the alignment of both the external laser and the electron beam with the undulator axis is less then 0.1 mm.

A laser power of 1.6 MW is required to induce 10 keV rms energy spread for the MLB mode for a laser heater undulator with a Ti:Sa cathode laser operating at 780 nm. As for the LB mode, an uncorrelated energy spread of 12.5 keV asks for a laser power of 2.33 MW.

Since the slice parameters of the electron bunch, such as average energy, Twiss parameters, etc…, are not constant along the bunch, there is a different heating of the various longitudinal slices. In particular, a strong dependence of the induced energy spread has been found on the variation of the transverse beam size along the bunch (see, Figure 6.6.8). In order to achieve B>1 that is a bunch length at the laser heater longer than the transverse beam size, the laser is matched to the maximum slice transverse dimension.

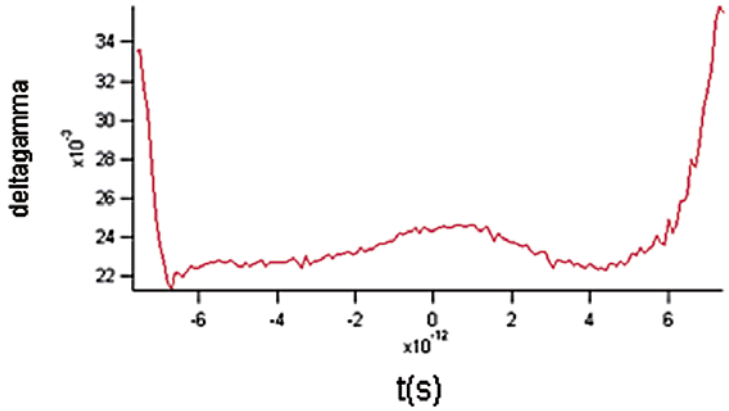

Figure 6.6.8:
Uncorrelated energy spread after heating.

The interaction of laser heater and electron bunch was studied through Elegant [30] for the MLB mode using the parameters reported in Table 6.6.2. The particle tracking includes an exact expression of the magnetic field of the undulator (without errors), a fundamental Gaussian mode laser and CSR in the chicane of the heater. The resulting slice energy spread is within 11.1 keV and 12.6 keV in the bunch core. The CSR effect on transverse emittance and energy spread is negligible.

Table 6.6.2: Parameters of laser heater for the MLB mode.

Number of undulator periods	12
Undulator periods	5 cm
Undulator k	0.487 (0.104 Tesla peak magnetic field)
Laser peak power	1.3 MW
Laser wavelength	780 nm
Laser waist	912.2 μm
Chicane bending angle	7.05 degrees
Chicane bending magnets length	10 cm
Chicane drift between bending magnets	10 cm
Chicane undulator's drift	80 cm
β_x before chicane	11.89 m
α_x before chicane	0.03
β_y before chicane	10.49 m
α_y before chicane	-3.332

As anticipated, the energy-position correlation induced by the heater decoheres by the small chicane because electrons with different divergences follow different paths independently of their longitudinal position if $\sigma_{x'} \times |R_{52}| > 780\ \text{nm}/2\pi$. For the MLB mode, where $\sigma_{x'} = 26 \times 10^{-6}$, $|R_{52}| = 25$ mm. the condition for decoherence is $\sigma_{x'} \times |R_{52}| = 650$ nm.

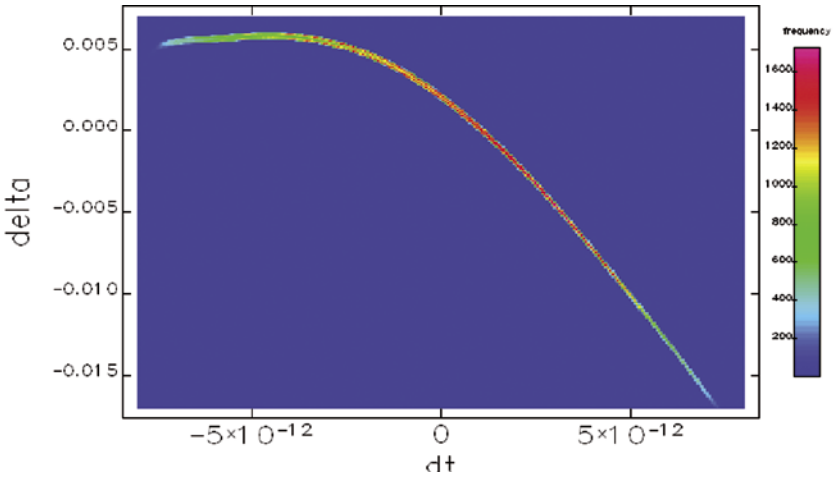

Figure 6.6.9:
Longitudinal phase space just after the laser heater. The interaction is described by the parameters listed in Table 6.6.2.

6.7 Transverse Dynamics

The main goal of the study of the transverse beam dynamics is the preservation of a small normalized emittance during acceleration and transport to the undulator. The factors contributing to emittance degradation may be caused by single particle dynamics and collective effects [4]. The single particle dynamics evaluates the consequences of geometric and chromatic aberrations of the lattice and of quantum fluctuations in the dispersive regions. The collective motion is described in terms of the beam break up (BBU) instability, since the CSR contribution has already discussed in Section 6.5. Trajectory distortions and their correction are also presented in this paragraph, together with specifications for the transverse acceptance.

6.7.1 Chromatic Aberrations

The emittance blow up caused by chromatic aberrations defines the tolerances on the dipoles and quadrupoles components of the field. The tolerances are evaluated below.

6.7.1.1 Dipoles

A quadrupolar and sextupolar field component in a dipole with horizontal dispersion D_x and horizontal beta function β_x dilutes the horizontal emittance through the generation of first and second order horizontal dispersion. The tolerances for the quadrupolar (b1) and the sextupolar (b2) components at a radius R from the magnetic axis with respect to the main field component (b0) are given by [31]:

$$\left|\frac{b_1}{b_0}\right| < \frac{1}{|\theta_b|}\frac{R}{\eta_x \sigma_\delta}\sqrt{\frac{2\varepsilon_{x0}}{\beta_x}\frac{\Delta\varepsilon_x}{\varepsilon_{x0}}} \qquad 6.7.1$$

$$\left|\frac{b_2}{b_0}\right| < \frac{1}{|\theta_b|}\left(\frac{R}{\eta_x \sigma_\delta}\right)^2\sqrt{\frac{\varepsilon_{x0}}{\beta_x}\frac{\Delta\varepsilon_x}{\varepsilon_{x0}}} \qquad 6.7.2$$

If the multipolar component is calculated at R = 20 mm, then an emittance growth of less than 1% is guaranteed by the following tolerances on all the dipoles: $|b_1/b_0| < 0.6\times10^{-4}$ at BC1 and $|b_1/b_0| < 1.5\times10^{-4}$ at BC2 for the quadrupolar component; $|b_2/b_0| < 1.2\times10^{-4}$ at BC1 and $|b_2/b_0| < 10\times10^{-4}$ at BC2 for the sextupolar component. Because of the very small energy spread at the Spreader ($\sigma_\delta < 0.1\%$), the tolerances about the multipolar components in those dipoles are more relaxed.

6.7.1.2 Quadrupoles

The chromatic aberration in a quadrupole is a 2nd order effect in the particle coordinates; it depends on the integrated quadrupole strength (*kl*), on the β-function at the quadrupole and on the relative energy spread of the particle (σ_δ):

$$\frac{\Delta\varepsilon}{\varepsilon} \cong \frac{1}{2}\beta^2\sigma_\delta^2(kl)^2 \qquad 6.7.3$$

The most critical point of the lattice from the point of view of chromatic aberrations is expected to be in proximity of BC1, where the rms correlated energy spread may reach a maximum value of about 3%.Eq. 6.6.3 has been evaluated and summed over all the linac sections, giving a total contribution to the emittance blow up of less than 6%.

6.7.2 Geometric Aberrations

The emittance blow up by geometric aberrations is evaluated for the sextupolar component in the dipoles only. The multipolar components in the quadrupole magnets have been found to be much smaller.

6.7.2.1 Dipoles

The second order geometric aberrations describe the quadratic dependence of the focusing strength on the transverse position of a particle. The systematic sextupolar component of the dipole field has been recognized to be the main source of geometric aberrations. Their effect on the emittance increase is [32]:

$$\frac{\Delta\varepsilon}{\varepsilon} \cong \frac{1}{2}(k_2 l)^2 x_0^4 \left(\beta + \alpha l + \frac{1}{4}\gamma l^2\right) \approx \frac{1}{2}(k_2 l)^2 \beta^3 \varepsilon \qquad 6.7.4$$

According to eq. 6.7.4, a sextupolar component of 4×10^{-4} at 20 mm leads to an emittance increase of less than 1%.

6.7.3 Quantum Fluctuations (ISR)

High energy electrons passing through a curved beam transport system emit Incoherent Synchrotron Radiation (ISR) and suffer from quantum excitations that increase the transverse emittance. The emittance blow up for a symmetric chicane of identical rectangular magnets is calculated with the following formula [32]:

$$\Delta\varepsilon_x \approx 8\cdot10^{-8}\cdot E^5[GeV]\cdot\frac{\theta^5}{l_b^2}\left[(L+l_b)+\left(\frac{\hat{\beta}+\check{\beta}}{3}\right)\right] \qquad 6.7.5$$

where E is the beam energy, L and θ are the dipole length and bending angle respectively, l_b the bunch length, β the Twiss function in the chicane.

This blow up becomes only significant for very high beam energies; thus, the largest effect is expected to be in BC2 at 600 MeV and in the Spreader at 1.2 GeV. The evaluation of eq. 6.7.5 for BC1, BC2 and the simulation result for the Spreader are summarized in Table 6.7.1.

Table 6.7.1: Emittance blow up due to the ISR emitted in the dipoles of BC1, of BC2 and of the Spreader (the unperturbed normalized emittance is 1.5 μm).

	$\Delta\varepsilon_x$ [μm]	$\Delta\varepsilon_x/\varepsilon\ [\%]_x$
BC1	4×10^{-4}	0.03
BC2	2×10^{-2}	1.33
SPREADER	4×10^{-2}	2.66

6.7.4 Trajectory Distortions

Alignment and field errors cause trajectory distortions which are corrected by means of a properly arranged scheme of steerers and Beam Position Monitors (BPMs). These errors are also sources of mismatch between the beam phase space ellipse and the Twiss ellipse of the transport line. The chromatic dependence of the betatron phase advance may cause filamentation of phase space with consequent emittance dilution. It may also diminish the effectiveness of the compensation of the transverse wakes by the orbit bump method described earlier (6.4.2). Misalignment studies have been performed under the assumption of independent mechanical supports of each of the magnetic elements and accelerating structures. Ground motion and vibrations have been assumed to be much smaller than the static errors.

6.7.4.1 Misalignment and Field Errors

Skew field components in dipoles and quadrupoles may lead to emittance blow up. The specifications for the elements alignment and field quality are listed below.

6.7.4.1.1 Dipoles

A roll angle ϕ_b of the dipoles generates a residual vertical dispersion which in turn leads to a vertical emittance dilution. The tolerance for the dipole roll angle is given by [31]:

$$\phi_b < \frac{1}{\theta_b \sigma_\delta}\sqrt{\frac{2\varepsilon_{y0}}{\beta_y}\frac{\Delta\varepsilon_y}{\varepsilon_{y0}}} \qquad 6.7.6$$

For a blow up $\frac{\Delta\varepsilon_y}{\varepsilon_{y,0}} \le 1\%$, the stronger constraint comes from the maximum bending angle at BC1 (θ_b = 0.085 rad) in presence of the maximum relative energy spread ($\sigma_\delta = 3\%$), giving a tolerance $\phi_b \le 830$ μm (rms value).

A dipole field error induces emittance blow up through parasitic dispersion according to [33]:

$$\frac{\Delta\varepsilon}{\varepsilon}(s) \cong \frac{1}{2} N_M \beta^2 \frac{\sigma'^2_{err}}{\sigma^2_\beta} \qquad 6.7.7$$

where N_M is the number of magnets affected by the error $\sigma'_{err} = \left(\frac{\Delta B \cdot l}{B\rho}\right)_{rms}$. A relative dipole field error of 5×10^{-5} contributes to an emittance blow up of less than 1%.

6.7.4.1.2 *Quadrupoles*

A roll angle $\phi_{q,1}$ of a quadrupole in a dispersion free region induces geometric coupling. The tolerance for the quadrupole roll angle is given by [31]:

$$\phi_{q,1} < \frac{1}{|kl|}\sqrt{\frac{2}{\beta_x\beta_y}\frac{\varepsilon_{y0}}{\varepsilon_{x0}}\frac{\Delta\varepsilon_y}{\varepsilon_{y0}}} \qquad 6.7.8$$

For $\frac{\Delta\varepsilon_y}{\varepsilon_{y,0}} \le 1\%$, one obtains a relaxed constraint of $\phi_{q,1} \le 20$ mrad (rms value) for an average focusing length $f = 1/kl = 5$ m and average betas of 20 m.

The skew field component in a dispersive region leads to a residual vertical dispersion and consequently to a vertical emittance dilution. In this case, the tolerance for the quadrupole roll angle becomes [31]:

$$\phi_{q,2} < \frac{1}{|kl|}\frac{1}{\eta_x\sigma_\delta}\sqrt{\frac{2\varepsilon_{y0}}{\beta_y}\frac{\Delta\varepsilon_y}{\varepsilon_{y0}}} \qquad 6.7.9$$

The condition $\frac{\Delta\varepsilon_y}{\varepsilon_{y,0}} \le 1\%$ is satisfied by $\phi_{q,2} \le 10$ mrad (rms value) for an uncorrected horizontal dispersion of 1 cm and an rms relative energy spread of 3%.

A lateral misalignment of the quadrupole also generates residual dispersion in both planes; for a given maximum allowed emittance growth the transverse alignment of the magnet should be [31]:

$$\Delta x, \Delta y < \frac{1}{|kl|}\frac{1}{\sigma_\delta}\sqrt{\frac{2\varepsilon_0}{\beta}\frac{\Delta\varepsilon}{\varepsilon_0}} \qquad 6.7.10$$

$\frac{\Delta\varepsilon}{\varepsilon_0} \le 1\%$ is obtained by $\Delta x, \Delta y \le 110$ μm (rms value) for the maximum conceivable energy spread $\sigma\delta = 3\%$.

Finally, field errors in both the normal and skew components of the quadrupole gradient generate emittance dilution according to [33]:

$$\frac{\Delta\varepsilon}{\varepsilon} \cong \frac{1}{2}N_M\beta^2k^2l^2\left(\sigma_\alpha^2 + \sigma_k^2\right) \qquad 6.7.11$$

where $\alpha = k\phi_{q,1}$ and N_M is the number of quadrupoles in the line. An rms gradient error $\sigma_k = 0.1\%$ and an rms roll angle $\phi_{q,1} = 300$ μm limit the emittance blow up to the order of 0.1%.

6.7.4.2 Launching Error

An optical mismatch of the beam phase space ellipse from the Injector into the start of the linac may cause emittance blow up through chromatic filamentation. In the pessimistic hypothesis of complete filamentation, a β-mismatch and a D-mismatch at the beginning lead to, respectively:

$$\alpha_i = 0 \Rightarrow \frac{\Delta\varepsilon}{\varepsilon} \cong \frac{1}{2}\left(\frac{\Delta\beta}{\beta}\right)^2 \qquad \frac{\Delta\varepsilon}{\varepsilon_\beta}(s) \cong \frac{1}{2}\sigma_\delta^2\left(\frac{\tilde{\eta}^2 + (\alpha\tilde{\eta} + \beta\tilde{\eta}')^2}{2\varepsilon_0\beta}\right) \qquad 6.7.12$$

A β-mismatch of 5% causes an emittance blow up of 13%, while a residual dispersion D = 5x10^{-3} m with divergence D′ = 5x10^{-4} generates a blow up of up to 15%.

6.7.4.3 Trajectory Correction

A satisfactory trajectory correction can be obtained in the 120 m long FERMI Linac by using 40 pairs of correctors and 40 BPMs, active on both transverse planes. Each drift between two consecutive accelerating structures includes one BPM and one steerer, separated by a quadrupole magnet. This scheme allows both local and global methods of correction.

Particle tracking simulations have been performed with Elegant in a realistic operational scenario that includes reading the beam position at the BPM locations and correcting the trajectory in presence of transverse wakes.

Figure 6.7.1 shows an ensemble of trajectories, including field errors, elements misalignment and trajectory correction consistent with the tolerance errors budget shown in Table 6.7.2, Table 6.7.3 and Table 6.7.4. The trajectory correction requires an average kick per steerer of 1.5 mrad.

Figure 6.7.1shows that the rms off axis-trajectory is within 700 μm peak-to-peak in both planes.

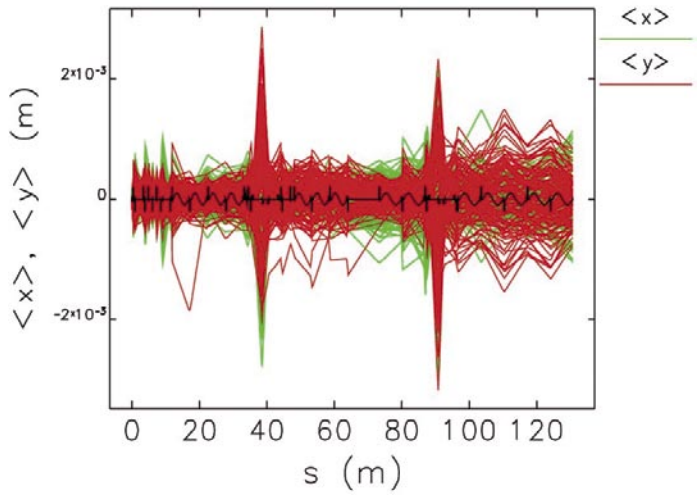

Figure 6.7.1:
Ensemble of 120 trajectories along the FERMI Linac after correction (Elegant simulations). It includes field errors and elements misalignment shown in the errors budget in Tables 6.6.2 - 6.6.4. The large excursion take place in the compression chicanes.

Table 6.7.2: Elements misalignment (rms values).

	Δx, Δy [μm]	*Δz [μm]*	*Δθ [μrad]*
Dipole	-	-	300
Quadrupole	150	200	300
BPM (30 μm RMS resolution)	150	200	-
Acc. Structure	300	-	-

Table 6.7.3: Field quality (rms values).

	Main field component [%]
Dipole	$\Delta B/B = 0.01$
Quadrupole	$\Delta K1/K1 = 0.1$

Table 6.7.4: Launching error.

	Nominal Set	*Jitter [p-t-p]*
$\|\Delta x\|, \|\Delta y\|$	100 μm	< 100 μm
$\|\Delta x'\|, \|\Delta y'\|$	100 μrad	-

6.7.5 The Beam Break-Up Instability

The wakefields in the S1-S7 Linac sections, with an impedance which is higher than of the rest of the linac, make this part of the layout particularly sensitive to the BBU instability. Possible solutions have been considered, inspired by the research of a similar effect in linear colliders. At the end, the local trajectory bump method was adopted. This method consists in an empirical search of a "golden" trajectory which makes the wake induced kicks compensating each other. By applying this scheme, the residual "banana shape" distortion of the transverse profile of the bunch corrected along its length can be reduced to be no greater than the nominal unperturbed rms beam size.

6.7.5.1 Theoretical Model

An analytical study based on a continuous model which describes the transverse motion of a single bunch in presence of transverse wake fields was performed in [37]. Such a study predicts the emittance growth under the combined influence of the short-range transverse wakefields, injection offsets, finite emittance and misaligned accelerating sections. It was found to be in good agreement with the numerical simulation results using Elegant, as Figure 6.7.2 shows. The comparison was repeated with different initial offsets and the results are listed in Table 6.7.5. The beam shape with the tailing particles traveling off-axis w.r.t. the head axis is here named "banana shape".

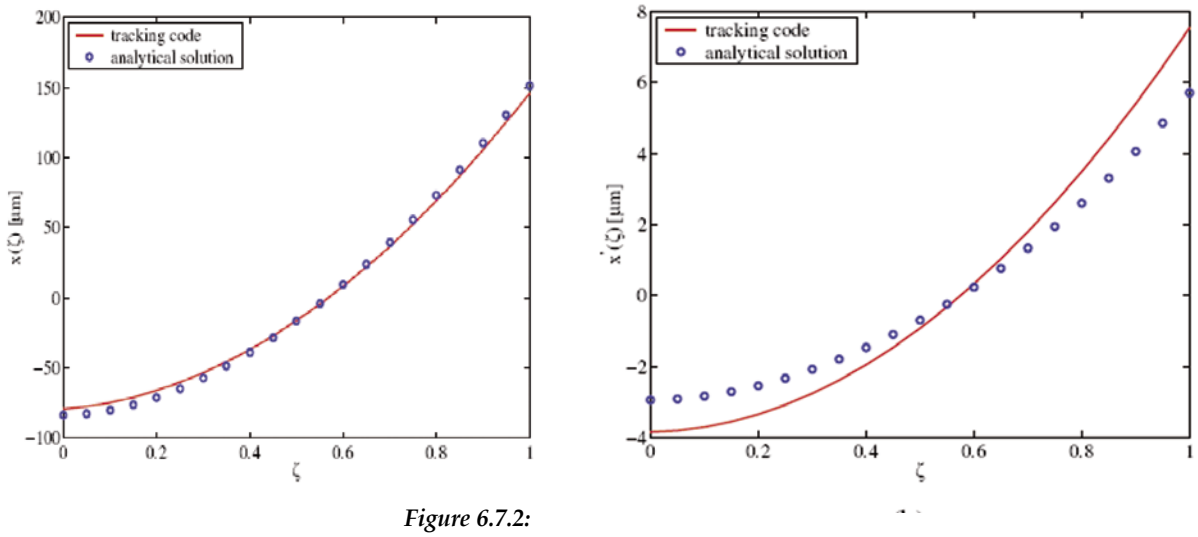

Figure 6.7.2:
Analytical (blue circles) and tracking (red line) results for the lateral displacement (a) and angular divergence (b) at the L4 end for an initial offset of 200 μm of a 0.33 nC, 200 fs long bunch.

Table 6.7.5: Analytical solution and ELEGANT tracking with FW bunch length of 200 μm and different initial offset X_0.

	ELEGANT	*Analytical*
X_0[μm]	$\varepsilon_{n,rms}$ [μm]	$\varepsilon_{n,rms}$ [μm]
50	0.08 × 10-2	0.08 × 10-2
100	0.33 × 10-2	0.34 × 10-2
150	0.75 × 10-2	0.76 × 10-2
200	1.32 × 10-2	1.34 × 10-2
250	2.07 × 10-2	2.10 × 10-2
300	2.97 × 10-2	3.02 × 10-2
500	8.24 × 10-2	8.40 × 10-2

6.7.5.2 Control of the Instability

The ensemble of trajectories subject to field errors, elements misalignment and steering corrections is plotted in

Figure 6.7.1. The corresponding banana shape distortions induced by the BBU instability at the Linac end are shown in Figure 6.7.3.

A parameter called Ratio was associated with each banana shape and is defined as the transverse deviation of the bunch tail with respect to the head in units of the beam size of a perfect, linear machine (nominal beam size). The banana shape obtained after a simple trajectory correction, hence without any particular attempt to preserve the emittance, increases the beam size by about 6.5 times over the 600 fs bunch duration; its maximum excursion is 2 mm with respect the bunch head. This numbers is unacceptable as it would compromise the FEL process [38].

For this reason a local bump was applied at the beginning of the Linac region where the transverse wakefields are strongest. Figure 6.7.3 shows that the change of sign of the horizontal trajectory after the bump reduces the final banana shape distortion to the level of one standard deviation of the nominal beam size. This is acceptable and gives confidence that this instability will not compromise the quality of the electron beam.

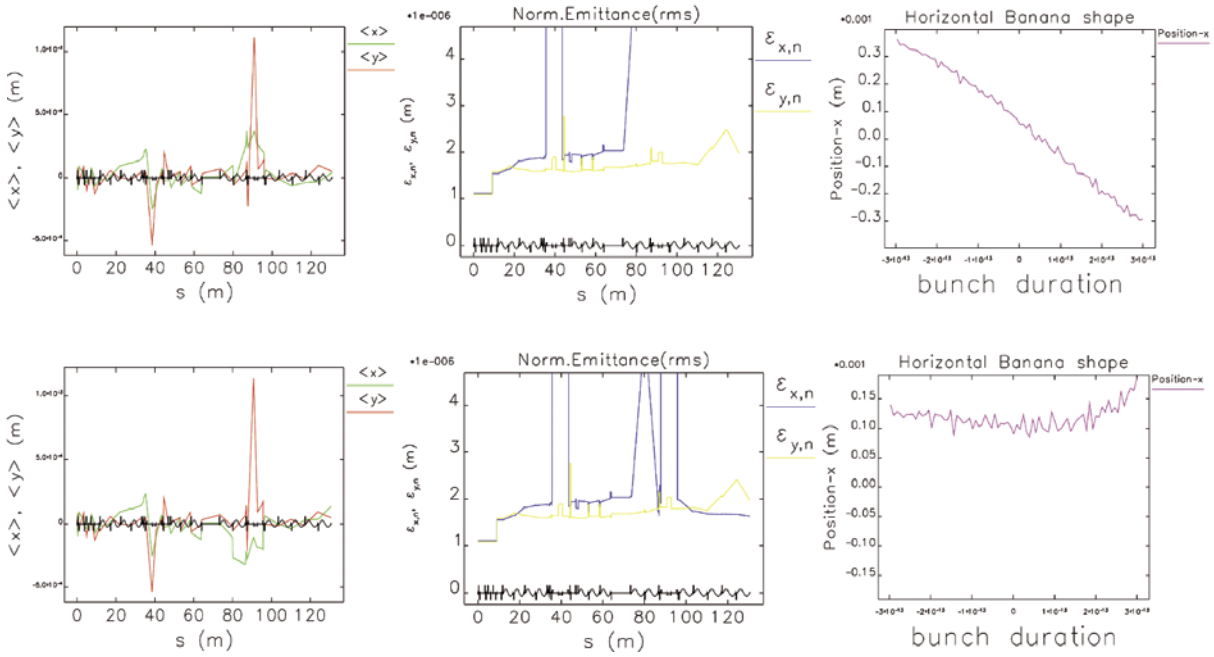

Figure 6.7.3:
Evidence of BBU instability in the horizontal plane, before the local trajectory bump (top plots) and after the bump (bottom plots). From left to right: electron bunch trajectory, evolution of the normalized transverse emittance along the Linac and banana shape in the horizontal plane at the Linac end.

6.7.5.3 Effect of Trajectory Jitter

Local methods of correction like the one used in the above example have the disadvantage of being dependent on the particular conditions of operation and jitters in some beam parameters. For this reason, a trajectory jitter – generated by varying the beam launching error – was simulated and the resulting in the banana shape was computed. Figure 6.7.4 demonstrates that a properly corrected banana shape is not appreciably affected by this jitter, since it remains below the 1-σ level.

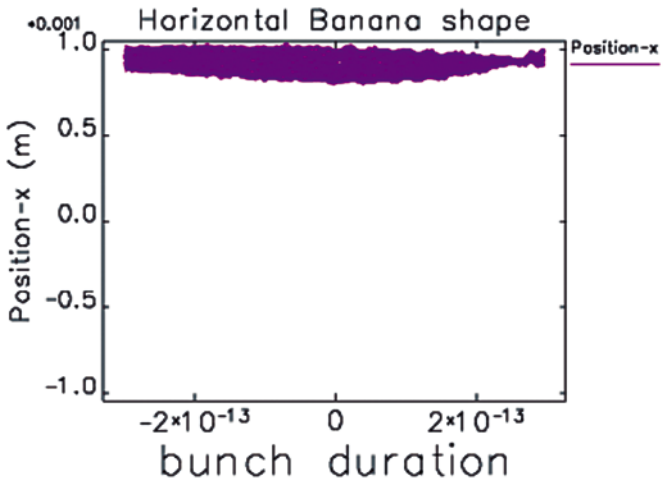

Figure 6.7.4:
Effect of the launching error jitter on the banana shape at the end of the Linac.

6.7.6 Transverse Acceptance and Error Tolerances

The "beam stay clear" region, i.e. the transverse aperture needed to comfortably accommodate the electron beam, including trajectory distortions, is calculated along the whole accelerator and spreader. The width of the vacuum chamber is also fixed according to the specification of the vacuum pressure in the linac.

6.7.6.1 Beam Size and Aperture

The optics from the Injector end to the Spreader end is shown in Figure 6.7.5. The horizontal dispersion in the two chicanes corresponds to the bending angles for the compression of the medium length bunch.

Table 6.7.6 shows that the chromatic contribution to the horizontal beam size is the only important difference between the different machine setups and it is always much bigger than the one due to betatron oscillations.

Table 6.7.6: Chromatic and geometric contributions to the horizontal emittance in the dispersive regions of the FERMI Linac.

Location	*Beam Size*	*SHORT*	*MEDIUM*	*LONG*
BC1	$\eta_x\sigma_\delta$ [mm]	3.1	5.7	4.0
	σ_β [mm]	0.20		
BC2	$\eta_x\sigma_\delta$ [mm]	0.7	1.9	2.6
	σ_β [mm]	0.150		
SPREADER	$\eta_x\sigma_\delta$ [mm]	0.130		
	σ_β [mm]	0.050		

The formula for the calculation of the "beam stay clear" includes the geometric ($\varepsilon_x\beta$) and the chromatic ($D_x\sigma_\delta$) contributions, as well as the off-axis displacement of the bunch centroid (after trajectory correction):

$$h.bsc = 1.2 \cdot \left(3\sqrt{\varepsilon_g \beta + (\eta_x \sigma_\delta)^2} + u_{oa}\right) \qquad 6.7.13$$

A margin of error of 20% is added to specify the minimum half -width of the vacuum chamber that is able to accommodate the beam along the Linac. Figure 6.7.6 and Figure 6.7.7 show, respectively, the behaviour along the Linac of the rms geometric emittances and of the rms correlated energy spread (MLB mode). In dispersion free regions, h.bsc (6.6.14) assumes its maximum value in the horizontal plane at the beginning of the Linac, where h.bsc = 3.1 mm. An rms normalized emittance ε_n = 1.5 μm and an off-trajectory error u_{oa} = 1 mm are assumed. Because of the symmetry of optics in the two planes and of the round beam injected into the Linac, the same upper limit also applies in the vertical plane.

For a detailed evaluation of the width of the vacuum chamber in the chicanes the reader is referred to [7].

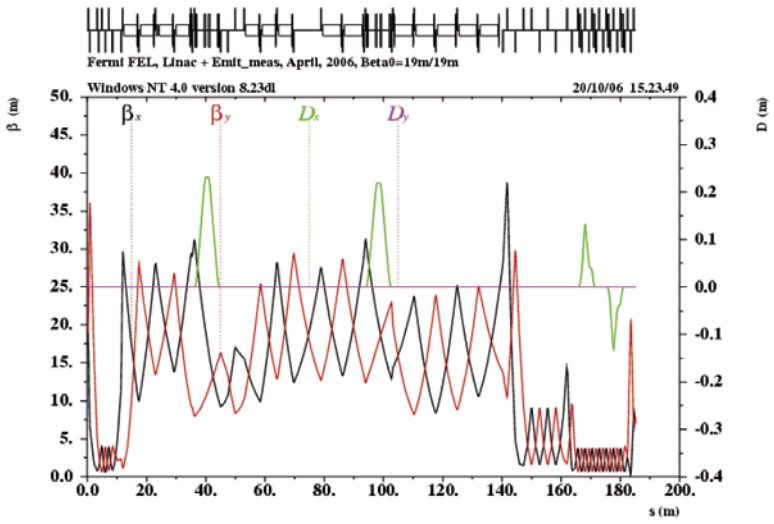

Figure 6.7.5:
FERMI Linac optics from the Injector end (where the beam average energy is 95 MeV) to the Spreader end (where the beam average energy is 1180 MeV).

The vacuum chamber aperture along the Linac and the Spreader is dictated by several constraints that include the vacuum pressure, the magnet design and the beam acceptance discussed above. Preliminary estimates indicate that a vacuum pressure lower than 10^{-7} mbar can be guaranteed in the Linac drifts with a vacuum chamber radius of 30 mm.

Table 6.7.7 summarizes some of the vacuum specifications in various regions of the electron beam.. The vacuum chamber apertures in the chicanes and in the Spreader are shown in Table 6.7.8.

Table 6.7.7: FERMI vacuum system. Main parameters.

Section	*Int. diameter [mm]*	*Material*	*Pressure [mbar]*	*Main pump [l/s]*	*# of pumps*
GUN	---	---	$<5x10^{-9}$	---	---
LINAC	30	Stainless steel	$<1x10^{-7}$	300	2 per module
UNDULATOR	30 (h) / 6 (v)	Aluminum	$<5x10^{-6}$	40	1 per module

Table 6.7.8: Total width of the vacuum chamber in regions including dipoles.

Location	*Total width*	*Units*
BC1	450	mm
BC2	240	mm
Spreader $D_x=0$	4.0	mm
Spreader $D_x\neq0$	4.4	mm

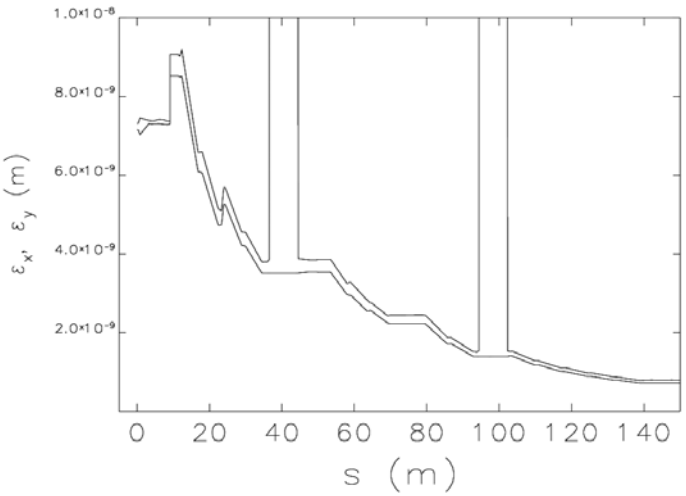

Figure 6.7.6:
Rms geometric emittances along the FERMI Linac for the MLB mode. The chromatic contribution to the emittance is included, as indicated by the fast reversible growth in the dispersive regions of the chicanes.

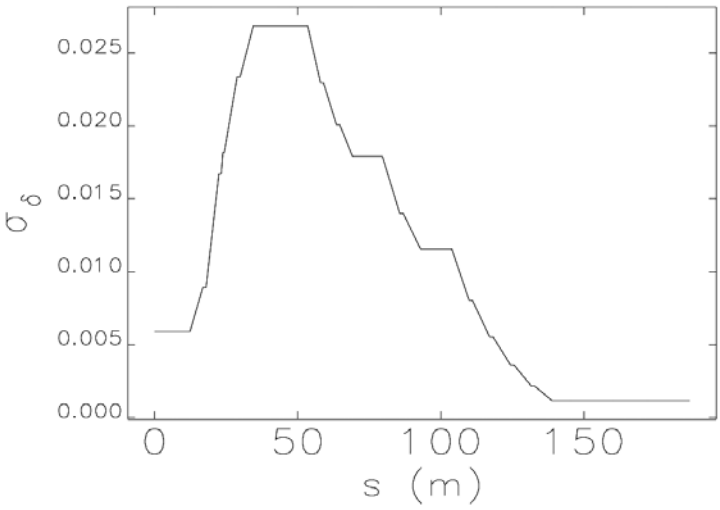

Figure 6.7.7:
Correlated rms energy spread along the FERMI Linac for the MLB mode.

6.7.6.2 Elements Misalignment

Analytical calculations and simulations are in agreement in predicting the tolerances on the alignment of the magnetic elements and of the accelerating structures required in order to avoid emittance blow up; they are summarized in Table 6.7.9. These tolerances are not sufficient to avoid the BBU instability, even though, in general, the suppression of BBU is made easier end more efficient as the misalignment of the elements in the lattice is reduced.

Table 6.7.9: Tolerances for elements misalignment, rms values. BPMs resolutions of 30 μm rms and maximum correction strength of 2 mrad have been assumed.

	Δx, Δy [μm]	*Δz [μm]*	*Δφ Roll [mrad]*
DIPOLE	-	-	0.8
QUADRUPOLE	100	150	1.0
BPM	100	150	-
ACC. STRUCT.	150	-	-

The tolerances on the launching error at the beginning of the Linac are given below; they include the following contributions from the jitter of the bunch centroid position and divergence:

$$|\Delta x|, |\Delta y| < 100\ \mu m$$

$$|\Delta x'|, |\Delta y'| < 100\ \mu rad \qquad 6.7.14$$

6.7.6.3 Field Quality

The tolerances listed in Table 6.7.10 – Table 6.7.13 have been chosen to reduce the emittance blow up due to filamentation below the 1% level. The definition of the multipolar components is in [39].

Table 6.7.10: Tolerances for the quadrupole magnets of the Main Linac (LS – L4). LS includes Q_L1.1 and Q_L1.2. L1 and L2 include the quadrupoles near bunch compressor BC1 and BC2, respectively.

	LS	*L1*	*L2*	*L3*	*L4*	*Units*
# of Quads	8	13	6	3	6	
Integrated Gradient Range	0.04 – 1.06	0.01 – 0.58	0.06 – 0.56	0.01 – 0.77	0.09 – 2.17	T
Gradient Homogeneity in ± 10 mm	0.09	0.17	0.26	0.24	0.11	%
Sext. comp.: $\lvert b_2/b_1 \rvert$ at R=20 mm	4.7	8.6	13.2	12.2	5.6	%
Expected Total Length	150					mm
PS Stability (rms)	0.01					%

Table 6.7.11: Tolerances for the dipole magnets of the first bunch compressor (BC1).

# of Dipoles	4			
Magnetic Length [mm]	500			
Curvature Angle [rad]	0.055 – 0.085			
B_0 Range [T]	0.068 – 0.169			
Total Gap [mm]	30			
Magnets Type	Rectangular			
Expected Total Length [mm]	550			
Magnet Name	**B11**	**B12**	**B13**	**B14**
Field Homogeneity: $\lvert \Delta b_0 / b_0 \rvert$ at x=±25 mm [%]	0.075	0.008	0.009	0.138
Quadrupolar component: $\lvert b_1 / b_0 \rvert$ at R=20 mm [%]	0.06	0.006	0.007	0.11
Sextupolar component: $\lvert b_2 / b_0 \rvert$ at R=20 mm [%]	1.5	0.012	0.014	2.8
Decupolar component: $\lvert b_4 / b_0 \rvert$ at R=20 mm [%]	100	0.05	0.06	100
PS Stability (rms)	0.01 %			

Table 6.7.12: Tolerances for the dipole magnets of the second bunch compressor (BC2).

# of Dipoles	4			
Magnetic Length [mm]	500			
Curvature Angle [rad]	0.052 – 0.080			
B_0 Range [T]	0.168 – 0.386			
Total Gap [mm]	30			
Magnets Type	Rectangular			
Expected Total Length [mm]	550			
Magnet Name	**B21**	**B22**	**B23**	**B24**
Field Homogeneity: $\lvert \Delta b_0 / b_0 \rvert$ at x=±25 mm [%]	0.188	0.019	0.023	0.250
Quadrupolar component: $\lvert b_1 / b_0 \rvert$ at R=20 mm [%]	0.15	0.015	0.018	0.20
Sextupolar component: $\lvert b_2 / b_0 \rvert$ at R=20 mm [%]	10.6	0.10	0.11	14.1
Decupolar component: $\lvert b_4 / b_0 \rvert$ at R=20 mm [%]	100	0.5	0.5	100
PS Stability (rms)	0.01 %			

Table 6.7.13: Tolerances for the quadrupole magnets of the Spreader. SPRD2 quadrupoles include also Q_SPRD.5, Q_SPRD.6 with g < 14.3 T/m and L_m=0.1 m.

	DIAGN.-COLL.	*MATCH*	*SPRD2**	*SP2 FEL-2*	*SPRD1*	*SP2 FEL-1*	*Units*
# of Quads	7	4	10 + 2	4	12	4	
Integrated Gradient Range	0.20 – 4.07	0.80 – 7.31	1.12 – 7.25	1.35 – 10.25	1.12 – 7.25	1.35 – 10.25	T/m
Gradient Homogen. in ± 10 mm	0.024		0.09	0.09	0.014	0.09	%
Sext. comp.: $\|b_2/b_1\|$ at R=20 mm	1.2		4.6	4.6	0.7	4.6	%
Expected Total Length	200	200	250	250	250	250	mm
PS Stability (rms)	0.01						%

Table 6.7.14: Tolerances for the dipole magnets of the Spreader.

	SPREADER FEL-1 + FEL-2
# of Dipoles	6
Magnetic Length [mm]	500
Curvature Angle [rad]	0.0523598
B_0 Range [T]	0 – 0.592
Total Gap [mm]	30
Magnets Type	Rectangular
Expected Total Length [mm]	550
Field Homogeneity: $\lvert \Delta b_0 / b_0 \rvert$ at x=±25 mm [%]	0.029
Quadrupolar component: $\lvert b_1 / b_0 \rvert$ at R=20 mm [%]	0.023
Sextupolar component: $\lvert b_2 / b_0 \rvert$ at R=20 mm [%]	2.16
Decupolar component: $\lvert b_4 / b_0 \rvert$ at R=20 mm [%]	10.0
PS Stability (rms)	0.01 %

6.7.6.4 Optical Mismatch at the Injection

Analytical calculations and preliminary results from jitter studies in time-dependent simulations provide indications on the tolerances of the optical mismatch of two electron beam Twiss parameters at the beginning of the Linac. They are listed below for an emittance dilution no larger than 10%

$$\begin{cases} D_i < 1 \ mm \\ D_i^{'} < 0.5 \ mrad \end{cases} \quad \text{and} \quad \left(\frac{\Delta\beta}{\beta_0} \right)_i < 3\% \qquad 6.7.15$$

6.8 Beam Jitters Sensitivities and Effects of Errors

This paragraph addresses the problem of the unwanted variation of the accelerator settings during operation. The FEL operation requires stringent specifications for the stability of the linac output parameters: electron bunch arrival time, relative peak current and relative mean energy. In order to understand the sensitivity of these parameters to jitters of various error sources along the linac, an elaborate study using the tracking codes LiTrack [40] and Elegant [30] was performed and is reported in this section.

In section 6.8.1 the effect of errors on the longitudinal dynamics are described; the results were used to create a tolerance budget for some linac parameters. A slice-by-slice jitter analysis of the flatness of the longitudinal phase space is also presented, since this is a critical parameter in the FEL process.

In paragraph 6.8.2 the results of tracking studies that include realistic errors in the relevant accelerator parameters are presented. The Elegant code was used to generate a set of beam coordinates at the end of the linac. These coordinates were then picked up as inputs for the FEL simulations described in Chapter 4.

6.8.1 Longitudinal Dynamics

The LiTrack code was used for the sensitivity studies [8] of the FERMI linac, sketched in Figure 6.8.1. The simulation technique is described in [8]. It is to be noted that the medium length and Long bunch configurations requires different particle distributions, both with ramped peak currents from the photoinjector.

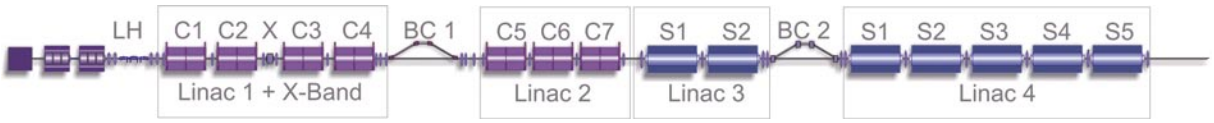

Figure 6.8.1:
Layout of the FERMI linac used in the sensitivities study with LiTrack.

The basic parameters of the linac and of the compressors used in the 1-D tracking simulations (LiTrack) and of the sensitivity studies can be found in Table 6.1.1, of Section 6.1.1.

6.8.1.1 Medium Length Bunch Mode

Table 6.8.1 lists the sensitivities of some electron beam parameters to RF phase, RF voltage and compressor chicane bend power supplies variations. Each sensitivity number quoted in the table independently causes a 10% peak current increase, a 0.1% relative mean energy increase and 150 fs final timing increase.

The sensitivities reported in Table 6.8.1 are used to generate a tolerance budget based on summing random, uncorrelated effects:

$$\sqrt{\sum_{i=1}^{14}\left(\frac{p_{tol}}{p_{sen}}\right)_i^2} < 1 \qquad 6.8.1$$

The sensitivities in Table 6.8.1 are weighting values for the summation in eq. 6.7.1. The overall tolerance budget is obtained by choosing the individual tolerances such that $p_{tol} < p_{sen}$ for all the indexes *i*. Table 6.8.1 lists the sensitivities for the MLB mode.

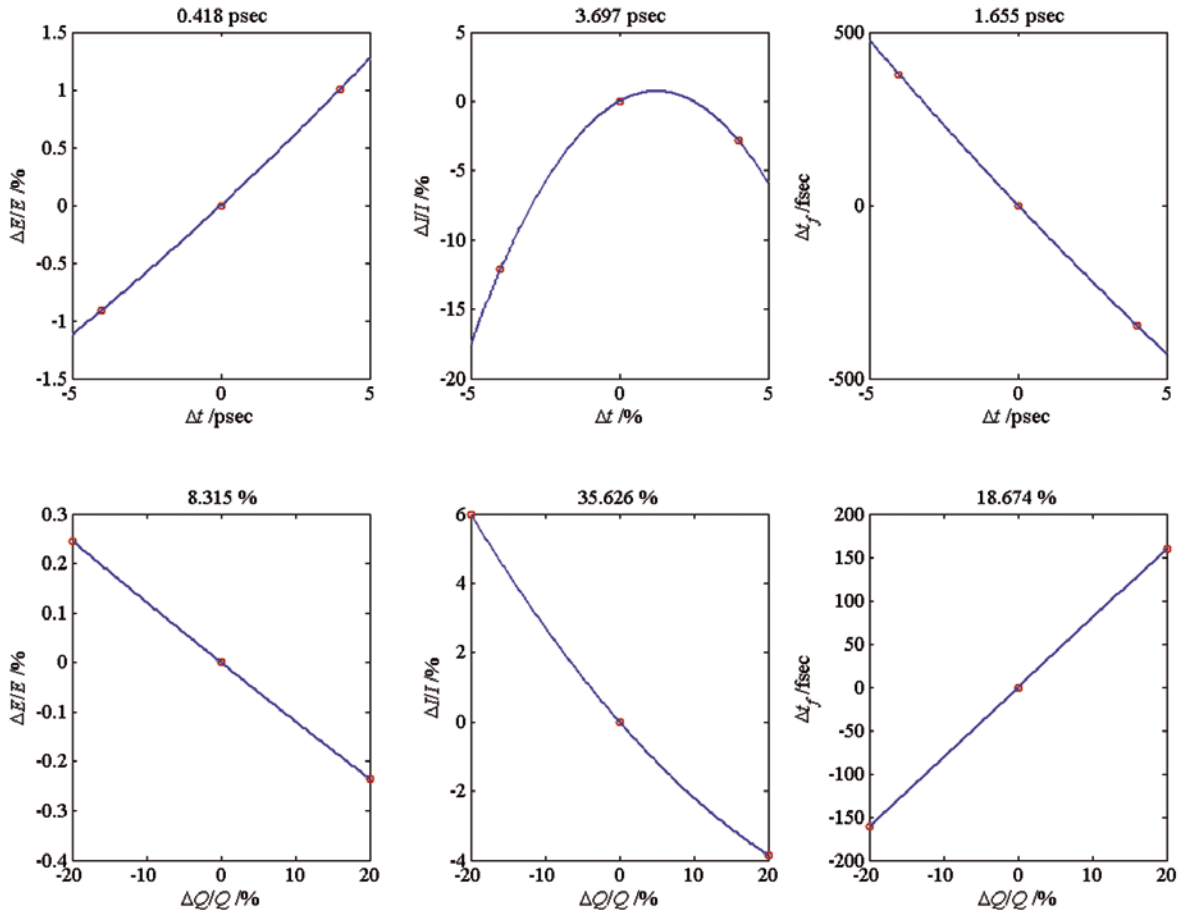

Figure 6.8.2:
Rms final relative mean energy ΔE/E, relative peak current ΔI/I and final timing jitter Δt_f as a function of gun timing jitter Δt_0 (upper plots) and relative initial bunch charge variations ΔQ/Q (lower plots).

Table 6.8.1: Individual rms sensitivities for the MLB mode. Each parameter variation causes a $\Delta I/I_0$=+10% peak current change or a $\Delta E/E_0$=+0.1% relative energy change and Δt = 150 fs timing change at the end of acceleration.

Parameters	S_{ee}.	*Unit*	*ΔI/I0=+10%*	*ΔE/E0=+0.1%*	Δt_f*=+150fsec*
L1 RF phase	ϕ1	S-band deg	-0.26	0.27	-0.18
LX RF phase	ϕx	X-band deg	0.85	-3.35	**9.81**
L2 RF phase	ϕ2	S-band deg	-4.24	0.96	-1.87
L3 RF phase	ϕ3	S-band deg	-2.48	0.56	-1.10
L4 RF phase	ϕ4	S-band deg	>10	-0.33	>10
L1 RF voltage	ΔV1/V1	%	**13.42**	0.48	-0.24
LXRF voltage	$\Delta V_x/V_x$	%	11.05	-3.85	2.06
L2 RF voltage	ΔV2/V2	%	-7.91	0.63	-1.19
L3 RF voltage	ΔV3/V3	%	-4.60	0.37	-0.70
L4 RF voltage	ΔV4/V4	%	>20	0.20	>20
Gun timing	Δt0	ps	**3.70**	0.42	-1.66
Initial charge	ΔQ/Q	%	-35.63	-8.32	18.67
BC1 chicane	ΔB1/B1	%	-1.56	1.59	-0.20
BC2 chicane	ΔB2/B2	%	-2.22	0.52	-0.27

Table 6.8.2 lists three possible tolerance budgets. If the first budget (fourth column in Table 6.7.3) is used, the relative peak current fluctuations at the linac end will be held to <10% rms. If the smaller tolerance from each column is applied (bold text), all three performance specifications ($|\Delta I/I|$<10%, $|\Delta E/E|$<0.1% and $|\Delta t_f|$<150 fsec) will simultaneously be met. We can see from Table 6.8.2 that the relative mean energy jitter is the leading output parameter that determines the tolerance on the photoinjector and linacs. It is worth pointing out that the tolerances on the voltage and phase of the accelerating section as well as of photoinjector parameters are exchangeable, i.e. the photoinjector parameters could be relaxed if the rf voltage is tightened and vice versa.

Table 6.8.2: MLB mode tolerance budget for <0.1% rms final relative mean energy, <10% rms peak current jitter or <150 fs final timing jitter. All the specifications are satisfied if the tighter tolerance is applied.

Parameters	S_y.	Unit	$\|\Delta I/I0\| < 10\%$	$\|\Delta E/E0\| < 0.1\%$	$\|\Delta t_f\| < 150$ *fsec*
L1 RF phase	ϕ1	S-band deg	0.20	**0.10**	**0.10**
LX RF phase	ϕx	X-band deg	0.50	**0.30**	0.70
L2 RF phase	ϕ2	S-band deg	0.50	**0.10**	0.40
L3 RF phase	ϕ3	S-band deg	0.20	**0.10**	0.20
L4 RF phase	ϕ4	S-band deg	0.70	**0.10**	1.00
L1 RF volt.	ΔV1/V1	%	1.00	**0.10**	0.15
LXRF volt.	$\Delta V_x/V_x$	%	0.80	**0.50**	**0.50**
L2 RF volt.	ΔV2/V2	%	0.80	**0.10**	0.20
L3 RF volt.	ΔV3/V3	%	0.50	**0.10**	0.15
L4 RF volt.	ΔV4/V4	%	1.50	**0.05**	1.00
Gun timing	Δt0	ps	0.35	**0.25**	0.35
Initial charge	ΔQ/Q	%	5.00	**3.00**	4.00
BC1 chicane	ΔB1/B1	%	0.15	0.10	**0.02**
BC2 chicane	ΔB2/B2	%	0.25	0.03	**0.02**

6.8.1.2 Long Bunch Mode

Table 6.8.3 shows the sensitivities in the LB mode.

Table 6.8.3: Individual rms sensitivities for the LB mode. Each causes ΔI/I0=+10% peak current change, ΔE/E0=+0.1% final relative energy change and Δt = 150 fs final timing change.

Parameters	S_y.	*Unit*	*ΔI/I0=+10%*	*ΔE/E0=+0.1%*	Δt_f*=+150 fsec*
L1 RF phase	ϕ1	S-band deg	-0.60	0.43	-0.23
LX RF phase	ϕx	X-band deg	1.53	-4.77	**10.05**
L2 RF phase	ϕ2	S-band deg	-2.66	0.92	-1.15
L3 RF phase	ϕ3	S-band deg	-1.55	0.54	-0.67
L4 RF phase	ϕ4	S-band deg	>10	-0.43	>10
L1 RF voltage	ΔV1/V1	%	1.81	0.55	-0.22
LXRF voltage	$\Delta V_x/V_x$	%	-45.95	-5.01	2.13
L2 RF voltage	ΔV2/V2	%	-8.14	0.57	-0.65
L3 RF voltage	ΔV3/V3	%	-4.74	0.33	-0.38
L4 RF voltage	ΔV4/V4	%	>20	0.20	>20
Gun timing	Δt0	ps	**8.01**	0.45	-3.16
Initial charge	ΔQ/Q	%	>40	-7.96	12.97
BC1 chicane	ΔB1/B1	%	1.67	-1.88	-0.26
BC2 chicane	ΔB2/B2	%	-1.93	0.36	-0.14

Table 6.8.4 shows that the relative mean energy jitter and the final timing jitter are the leading output parameter to influence the tolerance on photoinjector and linacs.

Table 6.8.4: LB mode tolerance budget required for <0.1% rms final relative mean energy, <10% rms peak current jitter and <150 fs final timing jitter.

Parameters	S_y.	*Unit*	$\|\Delta I/I0\|$=10%	$\|\Delta E/E0\|$=0.1%	$\|\Delta t_f\|$=150 fsec
L1 RF phase	ϕ1	S-band deg	0.30	**0.10**	**0.10**
LX RF phase	ϕx	X-band deg	0.70	**0.50**	0.90
L2 RF phase	ϕ2	S-band deg	0.60	**0.15**	0.25
L3 RF phase	ϕ3	S-band deg	0.50	**0.10**	0.15
L4 RF phase	ϕ4	S-band deg	1.50	**0.10**	1.00
L1 RF volt.	ΔV1/V1	%	0.50	**0.10**	**0.10**
LXRF volt.	$\Delta V_x/V_x$	%	5.00	**0.50**	0.60
L2 RF volt.	ΔV2/V2	%	2.00	**0.15**	**0.15**
L3 RF volt.	ΔV3/V3	%	1.10	**0.10**	**0.10**
L4 RF volt.	ΔV4/V4	%	2.00	**0.08**	1.50
Gun timing	Δt_0	ps	1.20	**0.25**	0.60
Initial charge	ΔQ/Q	%	7.00	**3.00**	6.00
BC1 chicane	$\Delta B_1/B_1$	%	0.20	0.04	**0.02**
BC2 chicane	$\Delta B_2/B_2$	%	0.20	0.02	**0.02**

6.8.2 Global Jitter Study

The tolerances derived in the previous section for the phases and voltages of the accelerators and for the R56 compression parameters of the chicanes were applied to a statistical study that uses the technique of Latin Hypercube Sampling (LHS) [41]. A number of configurations having randomly picked RF voltages, phases and compression parameter within the specified tolerances were the input to LiTrack. A statistical analysis of global output parameters like mean energy, peak current and timing confirmed the tolerance budget. Further statistical analyses were done on a number of slices inside the bunch with a fixed slice length of 10 fs. The results of the medium and long bunch are shown in the following sections.

6.8.2.1 Medium Length Bunch Mode

Figure 6.8.3 shows the statistical results over 400 different configurations of the accelerations, compressions and photoinjector parameters.

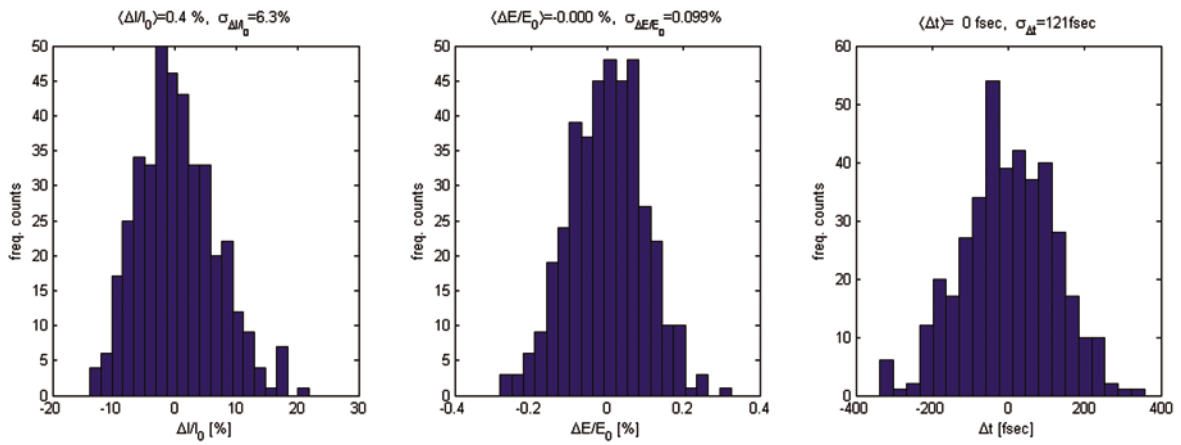

Figure 6.8.3:
Histograms for MLB mode of the relative peak current $\Delta I/I_0$ (left), final relative mean energy $\Delta E/E_0$ (center) and final timing jitter Δt_f (right). I_0 is the nominal peak current and E_0 is the nominal mean energy.

6.8.2.2 Long Bunch Mode

Figure 6.8.4 shows statistical results obtained in the same way as in the previous case (see, above)

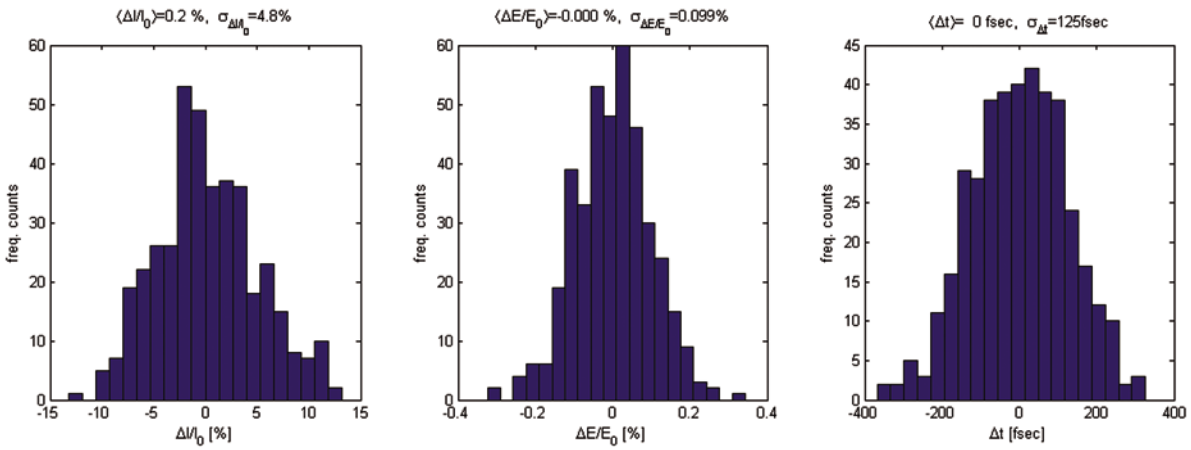

Figure 6.8.4:
Histograms for LB mode (lower plots) of the relative peak current $\Delta I/I_0$ (left), final relative mean energy $\Delta E/E_0$ (center) and final timing jitter Δt_f (right). I_0 is the nominal peak current and E_0 is the nominal mean energy.

6.8.3 Slice Jitter Analysis

An additional requirement is the need to have a longitudinal phase space as uniform as possible in the useful part of the bunch. Slice jitter studies have been conducted with 400 seeds for each linac configuration. For each seed the energy variation in the central part of the bunch is described by the following function:

$$E(t) = a_0\left(1 \pm \frac{\sigma_{a_0}}{a_0}\right) + a_1\left(1 \pm \frac{\sigma_{a_1}}{a_1}\right)\cdot t + a_2\left(1 \pm \frac{\sigma_{a_2}}{a_2}\right)\cdot t^2 \qquad 6.8.2$$

The flatness of the longitudinal phase space is defined as the average quadratic component in the energy chirp ($\hat{a}_2$) and its rms fluctuation (σ_{a_2}).

6.8.3.1 Medium Length Bunch Mode

Table 6.8.5 collects statistical parameters of the polynomial coefficients of eq. 6.7.2 that fit the E-t data in a least squares sense. The case reported here refers to the MLB mode.

Table 6.8.5: Statistical parameters of the polynomial coefficients for the MLB mode.

Medium bunch case M6				
	Unit	mean	rms	rms/mean %
a0	MeV	1140.86	1.140	0.10
a1	MeV/ps	0.0138	1.410	10220.94
a2	MeV/ps^2	3.570	1.030	28.95

Figure 6.8.5 shows a set of 10 randomly chosen seeds of the energy versus time along the bunch (left plots) together with the first derivative of the relative energy (central plots). The figure on the right shows the pattern of the first derivative when the quadratic chirp is removed.

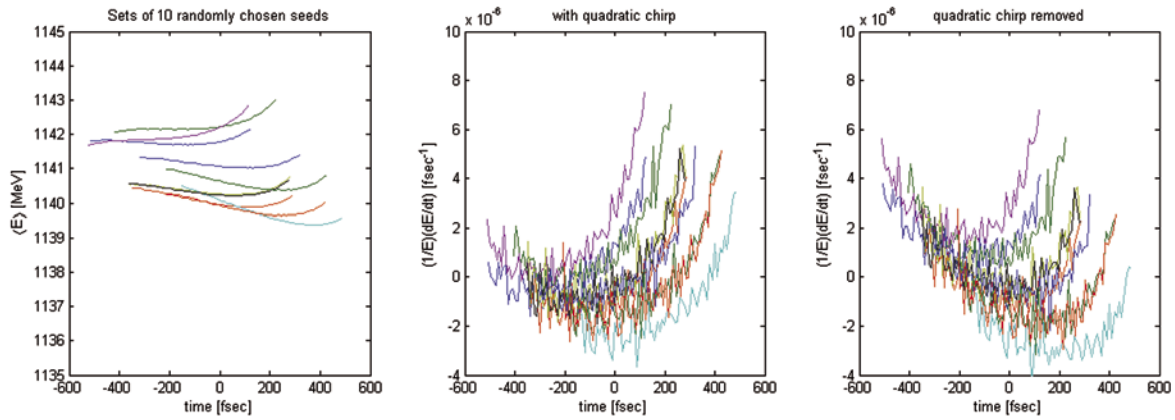

Figure 6.8.5:
Set of 10 randomly chosen seeds for MLB mode (b) (left plots) together with relative first derivative of the energy with respect to time inside the bunch with quadratic chirp (central plots) and with quadratic chirp removed (right plots).

6.8.3.2 Long Bunch Mode

The same statistical study applied to the long bunch gave the results shown in Table 6.8.6.

Table 6.8.6: Statistical parameters of the polynomial coefficients for the LB mode.

Long bunch case L4				
	Unit	mean	rms	rms/mean %
a0	MeV	1170.69	1.21	0.10
a1	MeV/ps	0.662	0.468	70.69
a2	MeV/ps^2	0.140	0.086	61.43

Figure 6.8.6 shows set of 10 randomly chosen seeds for the LB mode (left plots) together with first derivative of the energy deviation with respect to time inside the bunch with quadratic chirp (central plots) and with quadratic chirp removed (right plots).

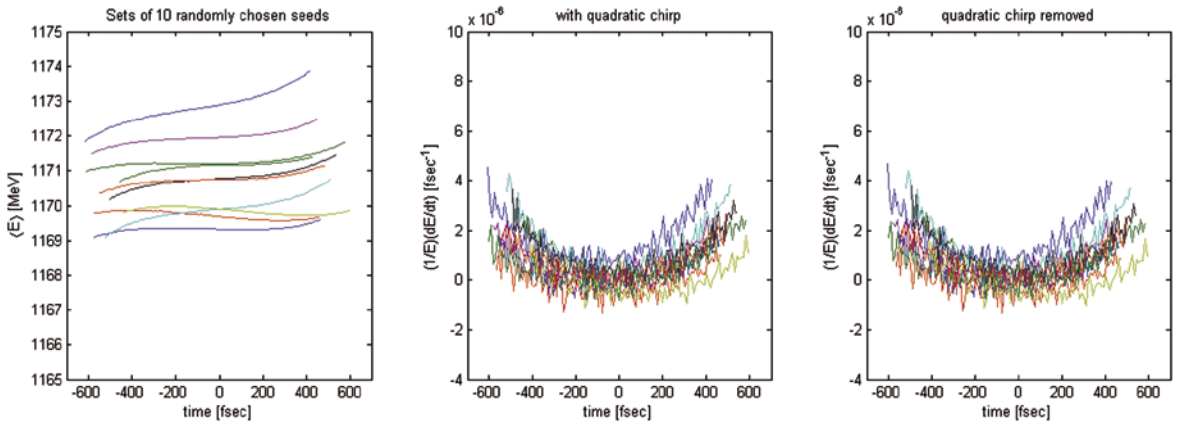

Figure 6.8.6:
Set of 10 randomly chosen seeds for long bunch case (b) (left plots) together with relative first derivative of the energy with respect to time inside the bunch with quadratic chirp (central plots) and with quadratic chirp removed (right plots).

6.8.4 Tracking Studies with Errors

A study was conducted to investigate the effect of a realistic acceleration environment that includes predicted errors in the photoinjector and in the linac. The simulation ("start-to-end") applied to the MLB configuration, follows the electron beam from the photo-cathode to the end of the acceleration.

Two codes were used for the tracking studies: GPT [42] for the photoinjector and Elegant for the linac. Eighty-four different particle distributions in the 6D phase space were randomly generated and converted into an Elegant input format. The particle distribution was tracked under the combined influences of the linac errors with rms values taken from Table 6.8.2. The 84 output particle distributions at the linac end were used as inputs for the FEL simulations. The statistical analysis on 84 different particle distributions obtained from Elegant gave jitters at the end of acceleration that are in good agreement with the 2-D LiTrack results:

$$\Delta I/I < 9.2\% \text{ rms}, \Delta E/E < 0.092\% \text{ and } \Delta t_f < 93\text{fs}$$

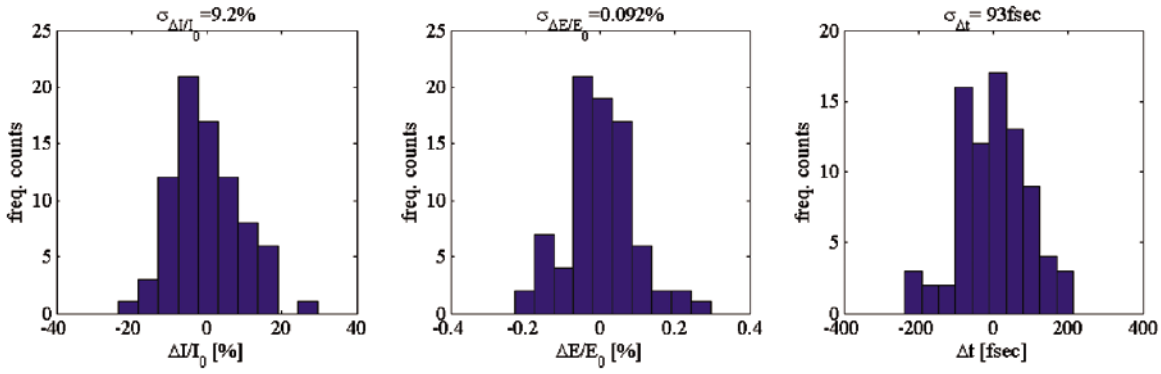

Figure 6.8.7:
Histograms for the MLB mode of the relative peak current $\Delta I/I_0$ (left), relative mean energy $\Delta E/E_0$ (center) and timing jitter Δt (right) obtained by means of Elegant simulations. I_0 is the nominal peak current and E0 is the nominal mean energy.

6.9 Collimation and Beam Dump

A 1.2 GeV electron beam loss can damage the permanent magnet modules of the insertion devices. To avoid this, beam collimation is essential for the protection of the undulator modules. In addition to collimators, beam stops and beam dump systems are needed for the machine and personnel protection systems. The specifications of these systems depend on the beam energy and power. These are estimated below.

6.9.1 Power Specifications

The following assumptions were made in the calculation of the electron beam power:

- maximum electron energy 1.5 GeV,
- maximum charge per pulse 1 nC,
- maximum repetition rate 50 Hz.

These assumptions are based on the projected operational specifications and possible future developments, like the energy upgrade to 1.5 GeV and the repetition rate of 50 Hz. The potential also exist for multi-bunch operation in a single pulse, with up to 100 bunches accelerated in a linac macropulses. This mode of operation is not part of the baseline design, but it cannot be excluded in a future development. A similar consideration applies to an upgrade of the linac repetition rate to 100 Hz.

Table 6.9.1: Average power and energy of the electron beam.

Mode	*Repetition rate [Hz]*	*Power [W]*	*Energy per pulse [J]*
Single pulse	50	75	1.5
100 macro pulses	50	7500	150
100 macro pulses	100	15000	150

The minimum possible geometric emittances are 0.5 nm in each plane, the energy spread is 0.1%, the average beta function is 10 m and the dispersion smaller than 0.001 m. Thus, under these conditions of maximum foreseeable electron beam density, the transverse beam dimension is 0.15 mm (rms value) and the beam transverse area, covering 4σ of the charge distribution, 0.4 mm^2.

The maximum peak power involved for a maximum peak current of 1.5 kA and a 0.6 ps long pulse is 1.5 TW. This peak power translated to peak energy density (with the previously found beam dimensions) is listed in Table 6.9.2.

Table 6.9.2: Peak energy density of the electron beam.

Single pulse density	0.42 kJ / cm^2 / pulse
Bunch train density	42 kJ / cm^2 / macro pulse

Only a small amount of the electron beam energy will be deposited to the chamber. In Figure 6.9.1 the electron energy loss for Steel and Al chambers is shown. For a 2 mm thick steel chamber the electrons will loose approximately 10% of their energy and 5% for Al. For the single pulse operation the maximum deposited energy will be 42 J / cm^2 and for the future macro-pulse mode it will be 4 kJ / cm^2. Note that metal damaging level starts at ~100 Joules / cm^2.

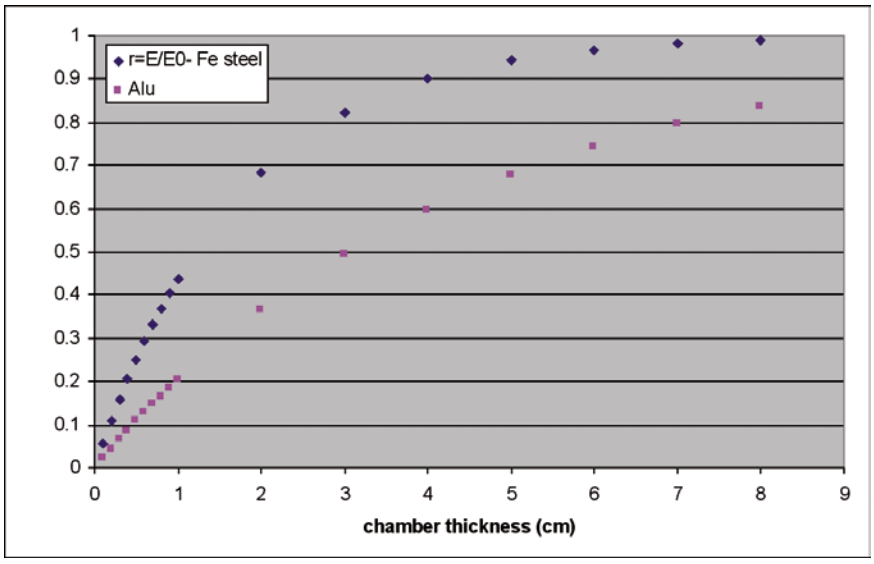

Figure 6.9.1:
Energy deposited vs. chamber thickness.

6.9.2 Beam Collimation

Beam collimation is essential in order to provide protection of the undulator modules from miss-steered beams. In addition, other undesirable effects like halo and dark current created in the gun and bunch compressors, wake field generated tails in the linac, mismatched and miss-steered beam, particles produced by Coulomb Scattering may damage and compromise the beam quality. The collimator section serves as transverse and longitudinal phase space filter. Particles outside this region are blocked and cannot be lost in the undulator modules. In the transverse plane this is achieved by a set of apertures limiting the transverse phase space volume. In the longitudinal plane similar pair of apertures at opposite dispersion regions limits the off-energy particles, dark current electrons and energy tails produced in the bunch compressors.

The collimator section is a key component of the FEL since it will be directly positioned in front of the undulators. Phase space parameters like emittance, length and energy spread can be measured there. The choice of the material and the shape and length of the collimators will be decided after a Monte-Carlo study on material and the secondary particle capturing efficiency. Both transverse and energy collimation are considered.

6.9.2.1 Betatron Collimation

In order to keep the collimation system as compact as possible a scheme with two single absorbers is adopted. This scheme has high efficiency with just two apertures working in parallel for both transverse dimensions. The two absorber blocks are separated by ~$\pi/2$ phase advance difference (see, Figure 6.2.8). Assuming a pipe radius of 8 mm a beam stay clear of 4 mm (26 σ of transverse beam dimensions) and betas at the undulators of the order of 10 m, the collimator acceptance is 0.8 μm. The aperture radius of the absorbers is about 3.5 mm for a 15 m distance between the absorber blocks.

6.9.2.2 Energy Collimation

Energy collimation will be achieved in a closed dispersive region using another pair of absorbers of about the same apertures as in the transverse case. The collimators will be installed at the point of maximum dispersion of the Spreader lattice (see, Figure 6.2.1).

6.9.3 Beam Dump

Beam stoppers, beam dump and the machine protection system are sketched here, together with some considerations on their implementation in the FERMI layout.

6.9.3.1 Linac Beam Stoppers and Beam Dumps

Four beam stoppers will be installed in the Linac for beam commissioning, tuning up and radiation safety. They will be situated after the gun, after each bunch compressor and at the end of the linac. Additionally at the end of the linac a beam dump will also be constructed for energy measurements. It consists of a DC electromagnet able to deflect the beam by 20 deg. followed by a simple short transfer line (in the already existing tunnel of the existing transfer line to the storage ring) at the end of which a small dump will be situated. A general view is shown in Figure 6.9.2.

6.9.3.2 Machine Protection System

Due to the low beam power of the baseline design with single pulse operation no fast beam abort system is needed. In case of problems (e.g. miss-steering, bad transmission, etc…) the linac gun will be inhibited. In a future upgrade a fast beam abort system might be needed.

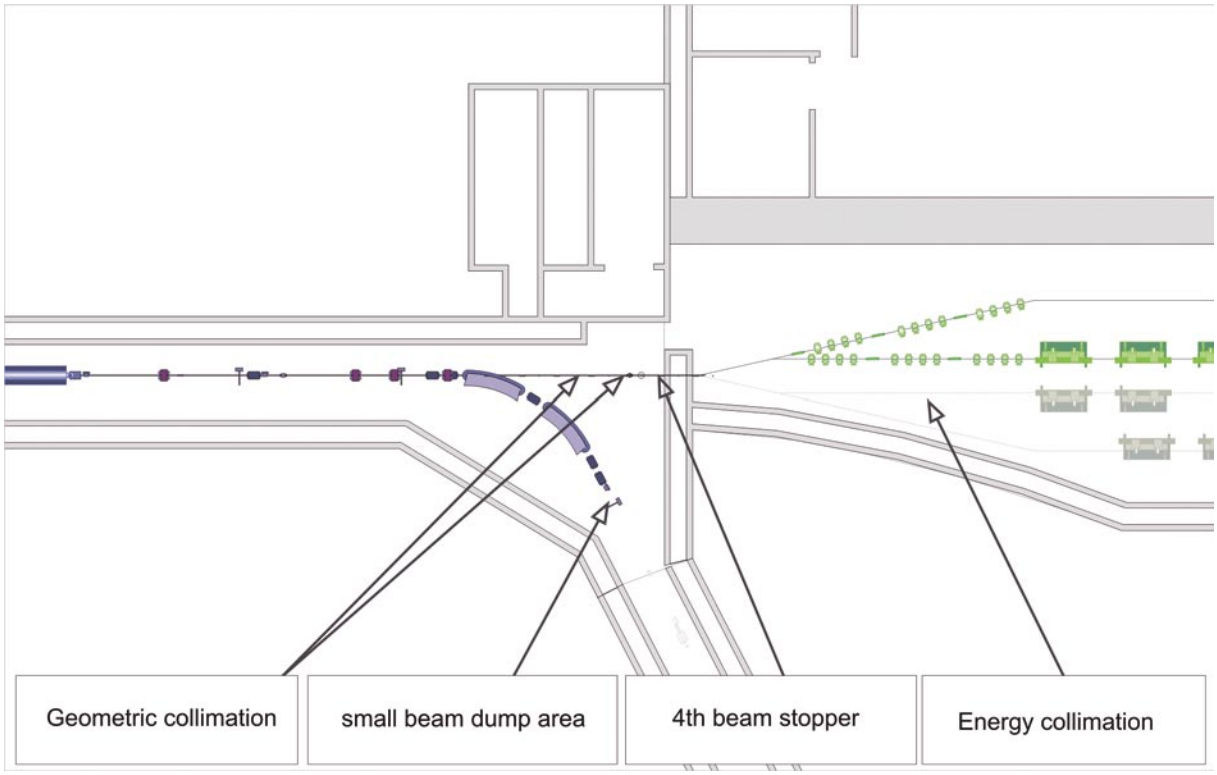

Figure 6.9.2:
End Linac and Spreader.

6.9.3.3 Main Beam Dump

A beam dump transfer line is foreseen in the beam lines at the end of each radiator. In order to be fail safe, and thus to completely eliminate the possibility of electrons propagating into the experimental stations, a permanent magnet will be used for the first deflection of 15 deg. The large angle is meant to keep the critical wavelength low so that the generated synchrotron radiation does not contaminate with the FEL light and keeps the thermal stress low. The layout is shown in Figure 6.9.3.

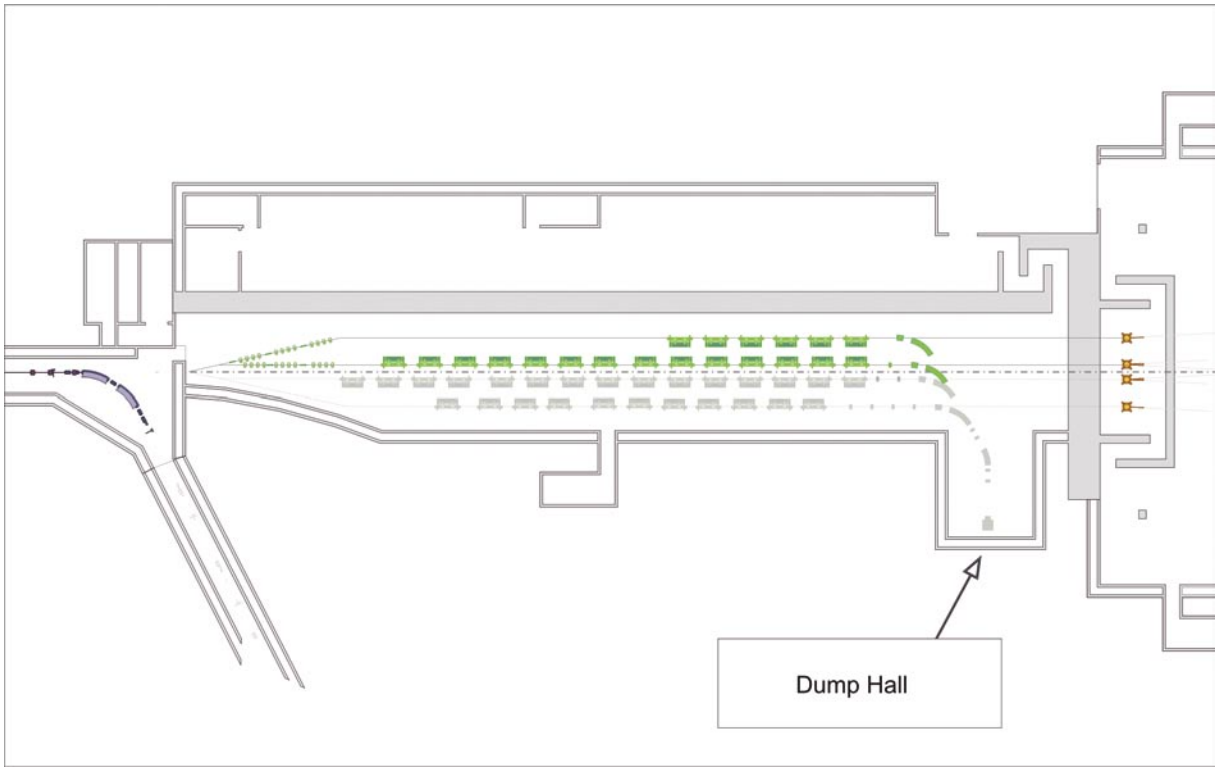

Figure 6.9.3:
A 20 m long TL leads to the dump hall.

The first bending set consists of one permanent and one electromagnetic dipole; it allows a 15+45 deg bending angle. The second bending set consists of an electromagnet of 30 deg bending angle (see, Figure 6.9.3). Using appropriate bypasses the FEL radiator lines can be connected to a unique chamber that eventually will transport the beams to the dump. Beam current toroids and loss monitors will be installed before and after the bends to control any losses (e.g. if beam has the wrong energy) and send a beam inhibiting signal to the photoinjector.

6.9.3.4 Dump Hall

An inadvertent loss of beam towards the ground will be intercepted by the underground rock, acting as dumper. Great care will be used to avoid that the dump be exposed to rain water, with possible contamination of underground waters with radioactive isotopes. A dedicated beam dump hall will be constructed to keep open the possibility of using the electron beam for diagnostics and experiments, and of using the light for micro-lithography and micro-mechanics, and for producing isotopes or neutrons for a future neutron source. This hall will be situated to the right of the FEL in the direction of the beam at the end of the radiator hall and will have an area of at least 50 m^2. Unlike the linac dump (which operates only during linac experiments) this dump will carry the burden of continuously dumping the electron beam.

6.9.3.5 Beam Dump Specifications

Although the single pulse mode involves low beam power, it is advisable to specify the dump with the maximum foreseen average and peak powers since, after years of operation, the dump becomes radioactive and it's preferable not to have to change the dump when the machine is upgraded.

It is foreseen to increase the transverse beam dimensions by at least a factor of 3 before the beam hits the dump. With this additional assumption, the main specifications of the FERMI dump are the following:

a. must absorb up to 4 kJoules/cm^2 / (macro) pulse;

b. must absorb an average beam power of up to 15 kW;

c. energy and radiation absorption efficiency > 99%;

d. natural production of isotopes must be minimized and isotopes must be short lived;

e. must be designed such as no maintenance will be required for a 10 year period for the absorbing core.

A standard graphite-aluminium beam dump that meets the above specifications [43] is described in Figure 6.9.4; electrons enter from left. More detailed calculations will define the details such as the cooling needed, the slow sweep system, etc.

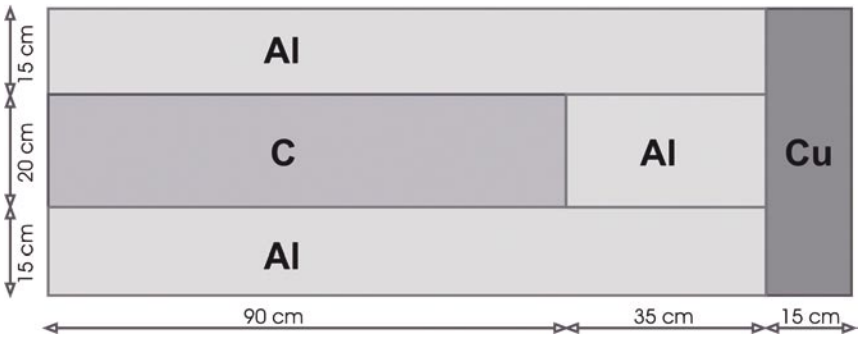

Figure 6.9.4:
Schematic of the graphite-aluminum beam dump.

6.10 Instrumentation, Diagnostics and Feedback

This paragraph addresses some aspects of the electron beam diagnostics. A more detailed treatment of the instrumentation may be found in Chapter 9. The justification for long-term feedbacks and details about their functionality and interplay with the diagnostics specifications may be found in Chapter 10.

6.10.1 Laser Heater

In addition to being a tool for the control of the microbunching instability, the laser heater is also an excellent diagnostics instrument. To exploit this fact, a FODO channel placed after the laser heater will be used for electron beam size measurements at various phases of the betatron oscillations and also for emittance diagnostics. Removable screens will be employed in the locations indicated on the plot of Figure 6.2.2. The betatron phase advances between first and second screen, second and third screen and third and fourth screen are 24°, 79°, 24° in the horizontal plane, and 72°, 23°, 57° in the vertical plane.

6.10.2 Magnetic Chicanes

The energy dispersion is at its maximum in the middle of the chicane and, therefore, this is a convenient place for collimation and energy monitoring. Since the electron bunch typically has a significant energy chirp while it propagates through the chicanes, the collimator can be used to trim electrons in the head and tail of the electron bunch, thus helping reduce the peak current spikes at the bunch edges.

6.10.3 Spreader

The FODO channel after the L4 linac sections is designed to provide approximately 135° of betatron phase advance in both planes for emittance measurements using the removable screens marked as solid circles on the plot. Downstream of the FODO channel a possible convenient place for a deflecting cavity is indicated. This cavity will be used for slice emittance and energy spread measurements at high dispersion points in the spreader.

As mentioned above the collimation section is ideal for beam measurements: beam position monitors, current transformers, loss monitors and synchrotron radiation detections windows will be installed there. In order to tune the collimators, two Optical Transition Radiation (OTR) stations are needed, one for the transverse section and one in the dispersive section for energy spread tuning.

6.10.4 Feedbacks

The high sensitivity of a seeded machine to short-term fluctuations (jitters) and long-term variations (drifts) of the electron beam quality make the presence of feedbacks a fundamental specification of the machine design. This paragraph addresses some basic thoughts on this subject.

A longitudinal feedback is dedicated to the stability of the bunch length and of the average beam energy in correspondence of each magnetic chicane and of the Spreader, where appropriate diagnostics can be located. Together with a charge feedback in the Injector, it provides information about the long-term stability of the bunch current and of the FEL resonant energy.

A trajectory feedback maintains the trajectory stability in order to minimize the perturbations to the orbit and to the compensation of the "banana" shape induced by the beam break-up instability. This is especially true for the L4 linac section, which is the most sensitive part of the machine to this kind of instability. The undulator entrance is also another critical point for the trajectory stability; in fact, the beam based alignment technique requires tight tolerances on the stability of the beam launching just before the insertion devices.

6.11 Appendix A: Method of Vlasov's Equation

The direct numerical solution of the Vlasov equation represents a complementary approach to the more prevalent method of simulating beam dynamics by macroparticle tracking. In particular, a Vlasov solver offers the advantage of being immune from the statistical fluctuations stemming from using a limited number of macroparticles, which may interfere with a correct interpretation of the results when studying the microbunching instability. Small scale structures are more easily resolved and the unfolding of instabilities more accurately characterized. Moreover, in contrast to semi-analytical studies based on the linearized Vlasov equation, numerical solutions of the full equation can be used to investigate saturation effects, which may be important.

It should be pointed out that the Vlasov solver should not be expected to substitute the macroparticle simulations since at this time only a 2D phase-space solver is available. Moreover, the physics that can be currently investigated with the existing solver is limited in practice to short-scale effects of the collective forces (microbunching).

The existing code allows one to include models of impedance describing space charge, coherent synchrotron radiation (CSR), and RF structure wake fields. CSR is evaluated in free space with the assumption that the bunch follows a trajectory with uniform radius of curvature. This excludes transition effects through the entrance and exit of bending magnets. In the study discussed here the RF structure wake fields were not included.

It was argued that it is possible in 2D to account for the particles smearing due to the transverse emittance in an approximate but meaningful way by introducing an effective low-pass filter in the evaluation of the collective force. Some confidence in the validity of the above model of emittance-induced smearing can be obtained from comparison with predictions from linear theory [24] in the regime where linear theory applies. Incidentally, such comparisons have also been successfully used to provide general validation of the coding.

Figure 6.11.1 shows the gain curves for a beam that travels through approximately 36 m of transport line (including L1) before entering the bunch compressor. The gain curves are evaluated at the exit of BC1. In this case space charge effects are significant and are included in the calculation.

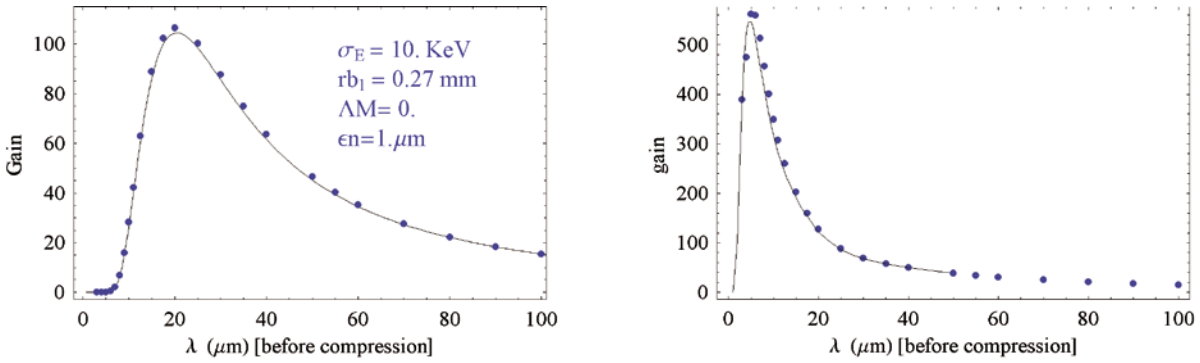

Figure 6.11.1:
Gain curves through for L1+BC1 in the presence of CSR and space charge (with space charge excluded in BC1) as determined by linear theory (solid line) and from the numerical solutions of the Vlasov equation (blue dots). σ_E*=10 KeV; smearing effect of transverse emittance is included in the left but not in the right picture.*

The gain plotted is the ratio between the amplitude of a sinusoidal charge-density modulation for a given frequency at the exit and entry of the bunch compressor. The amplitude is understood to be expressed in units of the peak current (which is different at entrance and exit because of compression). The beam is a flat-top with Gaussian energy spread.

In the Vlasov code the local value of the transverse rms size is used so that the "effective" beam radius appearing in the impedance model is taken as [8] $r_b^2 = [1.3\ (\sigma_\xi^2 + \sigma_\psi^2)]$. For the linear theory calculation a constant in z transverse size is assumed. The parameter r_b for the linear theory was adjusted to fit the gain curve against the Vlasov solver calculation. The same value, r_b =0.27 mm was then used to produce both pictures in Figure 6.11.1. The application of the Vlasov solver was then extended to include the L2 and L3 and the second bunch compressor BC2. The goal was to study the effect of shot noise in the development of the microbunching instability and determine its impact on the uncorrelated rms energy spread on the beam past BC2. Result is shown in Figure 6.11.2.

The initial beam density is a flat-top in charge density and Gaussian in the uncorrelated energy spread. The shot noise was modeled by perturbing the initial, smooth density function in phase space with random noise. The calculation indicates that most of the energy modulation induced by space charge (the dominant collective effect) takes place between BC1 and BC2. By the time the beam reaches BC2 these fluctuations are sufficiently large to cause the instability to reach saturation, as indicated by the two bottom plots. Notice that in this calculation SC and CSR are the only collective effects present.

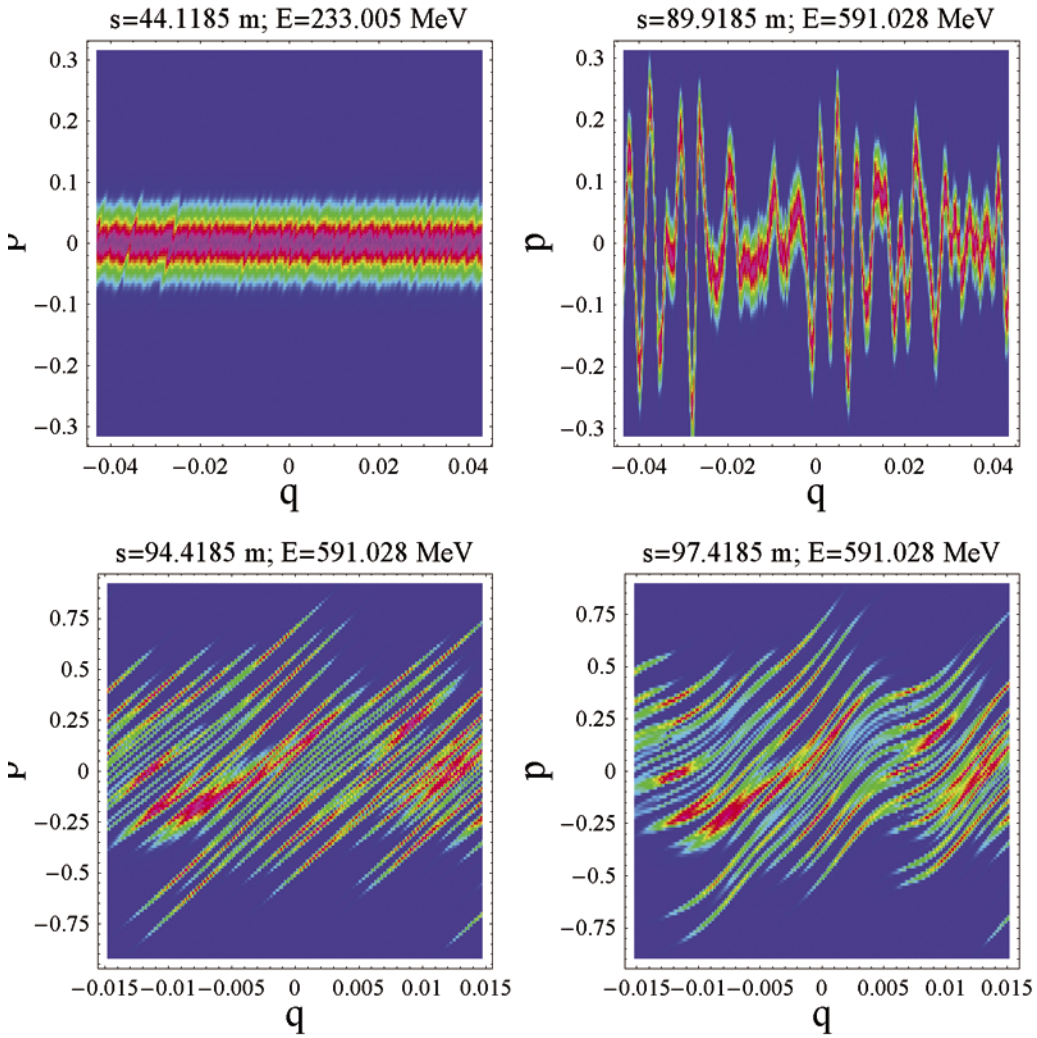

Figure 6.11.2:
Longitudinal phase space at selected locations starting from a noisy flat top bunch with Gaussian rms energy spread; s=0 is at the start of the laser-heater section. The top left pictures is at the exit of BC1; top right picture is at the entrance of BC2 and the remaining two after the BC2 3rd and 4th dipole (q is the z-coordinate in units of 1 mm, p is the uncorrelated energy in MeV).

6.12 Appendix B: 6D Parallel Tracking Code IMPACT

IMPACT is a suite of parallel particle-in-cell codes designed for modeling high intensity, high brightness beams in RF proton linacs, electron linacs and photoinjectors. It consists of two parallel particle-in-cell tracking codes (one is longitudinal position-dependent and one is time-dependent), an RF linac lattice design code, an envelope matching and analysis code, and a number of pre- and post-processing codes. The present version of IMPACT can treat intense beams propagating through drifts, magnetic quadrupoles, magnetic soleniods, magnetic dipole, and RF cavities, using map integrator and nonlinear Lorenz integrator. Recent additions include new capabilities for modeling short range longitudinal and transverse wakefields as well as 1D CSR wakes.

Both parallel particle tracking codes of the IMPACT suite assume a quasi-static model of the beam and calculate space-charge effect self-consistently at each time step together with the external acceleration and focusing fields. Typical IMPACT simulations at NERSC are run with a few millions to a few tens million particles, though smaller and larger runs are possible.

6.13 References

[1] K. Bane, Proc. of EPAC 2004, Lucerne, Switzerland.

[2] P. Tenenbaum, SLAC-TN-04-038 (2004).

[3] Y. Derbenev et al., TESLA-FEL=95-05 (1995).

[4] S. Di Mitri, proc. of FEL 2006, Berlin, Germany.

[5] E.L. Saldin, E.A. Schneidmiller, M. Yurkov, TESLA-FEL-2003-02 (2003).

[6] P. Emma, Proc. of EPAC 2004, Lucerne, Switzerland.

[7] S. Di Mitri, ST/F-TN-06/09 (June 2006).

[8] M. Cornacchia et al. ST/F-TN-06/15 (July 2006).

[9] D. Douglas, JLAB-TN-98-012 (1998).

[10] P. Craievich et al., ST/F-TN-05/01 (March 2005).

[11] G. D'Auria, A. Ratti, ST/F-TN-05/07 (March 2005).

[12] G. D'Auria et al., ST/F-TN-06/10

[13] A. Zholents et al., submitted to PRST-AB, November 2006.

[14] W. Fawley, G. Penn, ST/F-TN-06/07 (2006).

[15] K. Bane et al., SLACPUB-7862 (1998).

[16] K. Bane., SLAC-PUB-9663 (2003).

[17] P. Craievich, T. Weiland, I. Zagorodnov, NIM A, 558, 58 (2006).

[18] K. Bane, SLAC-PUB-11829 (2006).

[19] K. Bane et al., Proc. Of ICAPC, Monterey, SLAC, CA, p.137 (1998)

[20] K. Bane, A. Mosnier, A. Novokhatski, K. Yokoya, in Proc. ICAPC, Monterey, CA (1998) and SLAC-R-580, p. 137 (1998).

[21] 4GLS Conceptual Design Report, http://www.4gls.ac.uk/documents.htm, April (2006).

[22] D. H Dowell, T. D. Hayward, A. M. Vetter, Proc. of PAC 1995, New York.

[23] K. Flotmann, T. Limberg, P. Piot, TESLA-FEL-2001-06.

[24] Y. Derbenev, V. Shiltsev, SLAC-PUB-7181 (1996).

[25] J.J. Bisognano et al., PAC 1997, p.1644.

[26] A. Zholents, ST/F-TN-05/15

[27] G.Dattoli, A.Renieri. Laser handbook, Vol.4 (1985).

[28] Z. Huang et al., Phys. Rev. ST-AB, 7, 074401 (2004).

[29] E. Saldin et al. , NIM A 483 (2002).

[30] M. Borland, APS LS-287 (2000).

[31] P. Emma, TESLA 95-17 (July 1995).

[32] T.O. Raubebenheimer, P. Emma, S. Kheifets, Proc. of PAC 1993.

[33] H. Wiedemann, Particle Accelerator Physics, Vol.I, pgg. 225 – 240, ed. Springer (2003).

[34] P. Craievich, S. Di Mitri, Proc. of EPAC 2006, Edinburgh, Scotland, UK.

[35] J. Delayen, PRST-AB, **6**, 084402 (2003).

[36] J. Delayen, PRST-AB, **7**, 074402 (2004).

[37] P. Craievich and S. Di Mitri, Proc. of the FEL 2005 Conf., SLAC, CA (June 2005).

[38] G. De Ninno, B. Fawley and G. Penn, ST/F-TN-06/01 (CBP Tech Note-356).

[39] $B_y=b_0+b_1(x/R)+b_2(x/R)^2+b_3(x/R)^3+O(x^4)$ with multipolar index n=0,1,2,3 etc… for dipole, quadrupole, sextupole component, etc…

[40] K. Bane, P. Emma, Proc. of PAC 2005, Knoxville. Tennessee.

[41] M. Budiman, Matlab utility: Latin Hypercube Sampling, budiman@acss.usyd.edu.au, 2004.

[42] S. B. van der Geer et al., http://www.pulsar.nl/gpt.

[43] TESLA–FEL 99-06, DESY (December 1999).

[44] A. Zholents et al., LBNL-62345 (January 2007).

[45] F. Parmigiani (Sincrotrone Trieste), private communication.

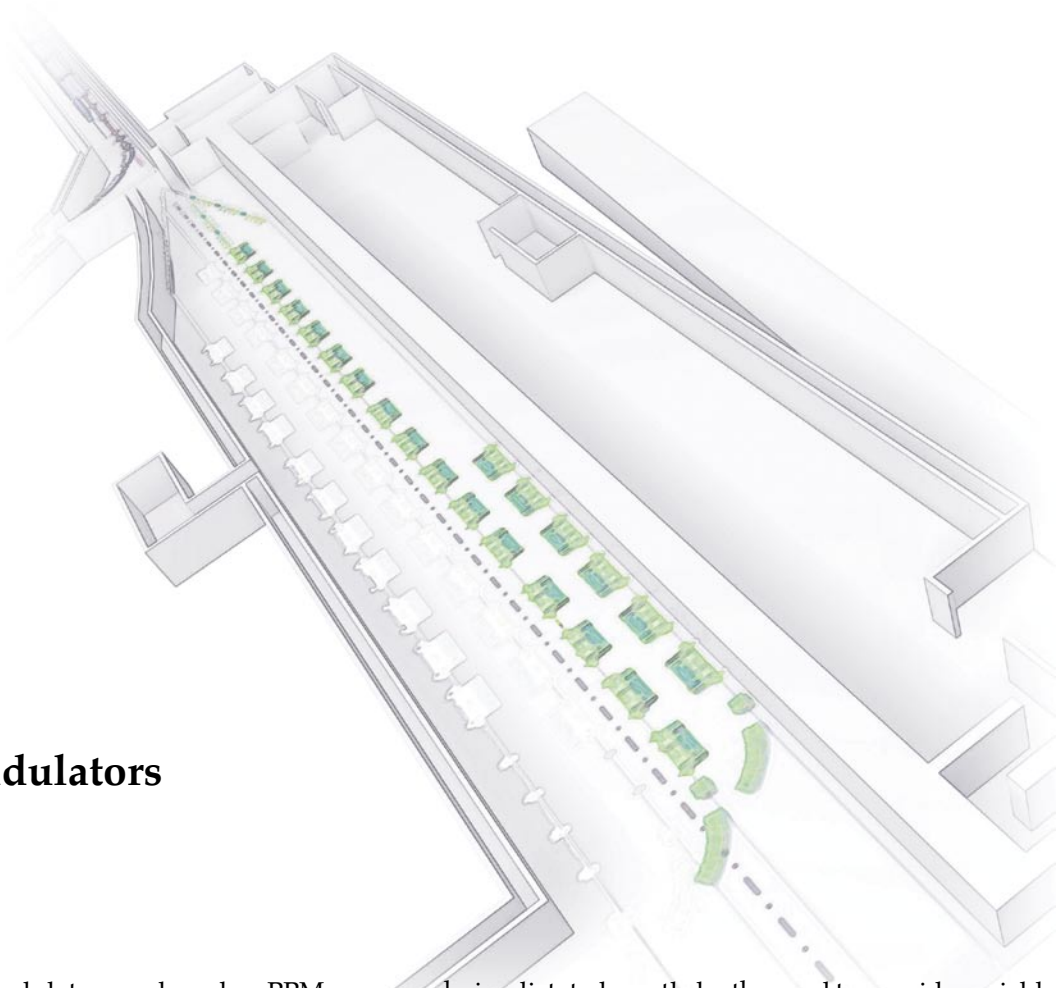

7 Undulators

Synopsis

The FERMI undulators are based on PPM arrays, a choice dictated mostly by the need to provide variable polarization. The present design is based on a remanent field Br=1.2 T, which allows to choose material grades with close to the maximum available coercitivity. High coercitivity makes the material highly resistant to radiation, a feature of paramount importance for its long lifetime. The undulator coefficient K must be greater than 1 in order to provide sufficient FEL gain. The minimum acceptable gap height is 10 mm, dictated by residual gas pressure and energy losses induced by resistive wall wakefields in the undulator vacuum chambers.

The modulators for both FEL-1 and FEL-2 have fixed, linear polarization. They must be tunable in the 240-360 nm range, a requirement that can be satisfied by a wide range of period lengths among which the shortest acceptable, ~ 10 cm, is favoured for FERMI. The first stage radiator and the second stage modulator for FEL-2 are also designed for fixed, linear polarization.

All the other undulators are of the variable polarization type, based on the widely used APPLE-II (Advanced Planar Polarized Light Emitter) configuration, the most efficient one for this application. All polarizations are tunable over the full design tuning ranges of 100 to 40 nm and 40 to 10 nm of FEL-1 and FEL-2 respectively. Because no analytical expression is known for the field amplitude as a function of the geometrical parameters of such devices, a semi-empirical formula is used derived by fitting the results of 3D magnetostatic calculations performed on a number of different special cases.

Detailed design of all undulators is in progress to include various higher order effects such as those due to the finite anisotropic permeability of the magnetic material and the precise magnet block shape and dimension.

Undulator alignment techniques have been studied in detail since misaligned individual undulator magnets can both modify the magnetic field, depending on the sign and magnitude of the roll-off coefficients, and distort the ideal trajectory, governed by the undulators focusing properties. Based on the request that, at nominal FEL performance, the relative difference in field strength between neighboring individual undulator magnets must be less than ± 0.2%, a worst case tolerance of up to ~200 μm has been set on their misalignments; this corresponds to a relative field change of less than 0.1%. Dedicated correction coils at both ends of each individual undulator magnet compensate the residual random magnetic field errors as well as the misalignment effects. Undulator focusing has been computed by 3D numerical tracking of the beam in the undulator field, and trajectory corrections, by beam-based alignment (BBA) techniques complemented by spontaneous radiation observations, have been simulated. It has been found that misalignements of up to 100 μm can be satisfactorily corrected. It can also be envisaged, given the rather comfortable tolerances on the trajectory straigthness, to correct the effects of the Earth magnetic field by ad-hoc shimming of individual undulators.

The undulator mechanical design is strongly influenced by the experience gained with the construction of the Apple II undulators installed on the ELETTRA storage ring. The undulator rests on a rigid C-shaped frame ("carriage") supported at each end by a post equipped with a vertical guide on which two (upper and lower) stainless steel backing beams can slide up and down. Each backing beam, supporting one (longitudinally) movable and one fixed aluminium beam to which the magnet arrays are attached, can be displaced vertically by two synchronized motors to adjust the undulator gap aperture. Two additional motors driving the moveable aluminium beam move the magnet array longitudinally (in "phase"). Gap height, longitudinal shifts and magnet vertical position are measured by absolute encoders with better than 1 $\mu\mu$m resolution. The carriage in turn rests on a platform remotely moveable in the horizontal plane for fine-aligning the whole structure. The main design tolerances are: 10 μm rms on planarity and parallelism of the backing beams and 5 μm rms on gap height.

As concerns the thermal stability, considering the tolerable relative difference in field strength between neighboring individual undulator magnets, the change of the undulator peak magnetic field with temperature and the thermal expansion of its support structure, one concludes that the ambient temperature, averaged over a time interval of a few hours, determined by the thermal inertia of the device, must be stable to within ± 0.7°C.

Aluminium has been chosen as the undulator vacuum chambers material because of its lightness, ease of fabrication and good electrical properties. The material specific outgassing, the most important parameter limiting the ultimate pressure, is kept low by following scrupulous cleaning and assembling procedures. A simulation of the system vacuum behaviour indicates that a maximum average pressure below 5·10-7 mbar can be easily reached provided strict construction, assembly and maintenance prescriptions are followed. Such a value is much lower than what is required to meet the conservative limits set on outgassing, bremsstrahlung production and carbon compounds deposition on the vacuum chamber inner walls. More detailed simulations will be performed following completion of detailed design of all components.

The undulator region optics is designed so that the average betatron function in each plane can range from 7 to 11 m, satisfying the design aim of a moderate focusing strength. The radiator optics uses a sequence of three standard FODO cells. The maximum quadrupole gradient is 10 T/m, including a 20%

margin. The matching of the FODO lattice, with the undulator gaps closed, was done using MAD in which the undulator is described by an uncoupled 6*6 transfer matrix, computed using Racetrack in both the 100 nm and 40 nm photon wavelength configurations and for three representative polarizations: horizontal, circular and vertical.

Special attention has been given to the problem of wakefields generated in the narrow gap undulator vacuum chamber which can increase the bunch energy spread. Since one finds that transverse wake effects can be neglected, the main concern is the longitudinal wake driven by the resistive wall (RW) of the chamber, by the impedances of cavity-like objects and by the roughness of the chamber inner surface. To minimize the effect of resistive wakefields a rectangular (or elongated elliptical) aluminium chamber is chosen. As far as surface roughness is concerned, computations were carried out in the worst case of a circular perfectly conducting chamber with diameter equal to the chamber inner gap and a sinusoidal surface corrugation with longitudinal periodicity λs and amplitude h_o. The tolerable roughness value parameter is found to be $(\lambda s/h_o)>>200$, compatible with that obtainable with careful but standard machining techniques and surface treatments. Resonant wakefields have not yet been considered; in any case, the detailed chamber design will be such as to avoid the presence of high Q resonator-like structures.

Finally, the consequences of trajectory position errors in the undulators have been studied and, in the worst case of FEL operation at the (10 nm) shortest design wavelength, a tolerance has been set of ± 10 μm rms, with respect to a straight line, over the whole undulator length. It has also been checked, as mentioned above, that beam-based alignment procedures allow reaching the specified goal. An additional bunch-to-bunch feedback system is also foreseen to keep the beam on the optimized trajectory during FEL operation.

7.1 Magnet Technology

As mentioned in Chapter 4, the final radiators are required to provide variable polarization, while for the modulators and the intermediate radiators fixed linear polarization is envisaged. Amongst the various known technologies, pure permanent magnet (PPM) structures offer a number of advantages: simpler and more accurate design, reduced interaction with external magnetic field sources (including the earth magnetic field) and more straightforward applicability of error compensation techniques based on magnet sorting, swapping and shimming.

The so called hybrid undulator uses ferromagnetic poles to channel the flux generated by the permanent magnets, and can provide a higher field in the range of parameters considered here. However, this only applies to the fixed polarization case, since no practical variably polarized hybrid undulator exists. Therefore, the advantage of this more efficient solution, namely a reduction of the total undulator length, would affect only a fraction of the total magnetic structure. For these reasons the FERMI@Elettra undulators will be based exclusively on PPM arrays.

7.2 Design Constraints

The resonance condition for FEL radiation to be produced is:

$$\lambda = \frac{\lambda_0}{2\gamma^2}\left(1 + K_{rms}^2\right), \qquad 7.2.1$$

λ being the radiation wavelength, λ_0 the undulator period length and γ the electron relativistic factor. Note that, having defined the deflection parameter K in terms of its rms value, the above relation holds for any field polarization. At 1.2 GeV electron energy the resonance condition can be written in practical units as

$$\lambda_0\left(mm\right) = \frac{11.03 \cdot \lambda\left(nm\right)}{1 + K_{rms}^2}. \qquad 7.2.2$$

The deflection parameter must be greater than 1 in order to provide sufficient FEL gain. This implies that, for the shortest FEL wavelength of 10 nm (FEL-2), the corresponding undulator period must be shorter than ~55 mm. On the other hand, the shortest acceptable period length is determined by the required tuning range (100 to 40 nm for FEL-1 and 40 to 10 nm for FEL-2) and by the smallest allowed magnetic gap. Considerations on the maximum allowable residual gas pressure in the chamber and the energy loss induced by resistive wall wakefields in undulator vacuum chambers of different shapes and materials (see Section 7.10 and 7.11) lead to an acceptable minimum gap of 10 mm.

The most widely used magnetic material for applications in insertion devices is NdFeB, a sintered alloy produced in different "grades" characterized by different remanent field (B_R) and intrinsic coercivity (H_{CI}) values. Typically the strongest grades, with the highest remanence, have a lower intrinsic coercivity and viceversa. The table below shows indicative ranges of these two quantities for commercially available materials:

Table 7.2.1: Typical remanence and intrinsic coercivity for NdFeB.

Typical B_r (T)	*Typical H_{CJ} (kOe)*
1.4 ÷ 1.5	11 ÷ 16
1.3 ÷ 1.4	12 ÷ 24
1.2 ÷ 1.3	17 ÷ 33
1.1 ÷ 1.2	22 ÷ 36

In terms of efficiency of magnetic field generation a high remanence is preferred, since the peak undulator field is proportional to this quantity (see eq. 7.3.5 below). However, in a high radiation environment like that of a linac-based FEL, resistance to radiation (scattered electrons and associated electromagnetic cascade) is of paramount importance in order to guarantee a sufficiently long lifetime of the permanent magnets. The exact mechanism of radiation damage depends on the nature of the radiation (electrons, neutrons, X-rays, γ-rays) but the result of excessive exposure is the same, namely

permanent demagnetisation. Several studies exist on the subject [1], showing that high intrinsic coercivity also implies increased hardness against demagnetization; a tradeoff therefore exists between top field and radiation resistance. The present design is based on a remanent field B_r=1.2 T, which allows choosing material grades with close to the maximum available H_{CJ}.

7.3 Linearly Polarized Undulators

In a standard vertical-field undulator the magnetic field distribution can be written (to second order in the transverse coordinates X and Y) as:

$$\begin{aligned} B_x(x,y,z) &= -B_o \cdot k_x^2 \cdot x \cdot y \cdot \cos(k \cdot z) \\ B_y(x,y,z) &= B_o\left(1 + \frac{k_x^2}{2} \cdot x^2 + \frac{k_y^2}{2} \cdot y^2\right) \cdot \cos(k \cdot z) \\ B_z(x,y,z) &= -k \cdot y \cdot B_o \cdot \sin(k \cdot z) \\ k &= \frac{2 \cdot \pi}{\lambda_0} \end{aligned} \qquad 7.3.1$$

Here k_X and k_Y, the roll-off coefficients, describe the horizontal and vertical quadratic roll-off of the main field component; *k* is related to them through Maxwell's equations which impose

$$k^2 = k_x^2 + k_y^2 \ . \qquad 7.3.2$$

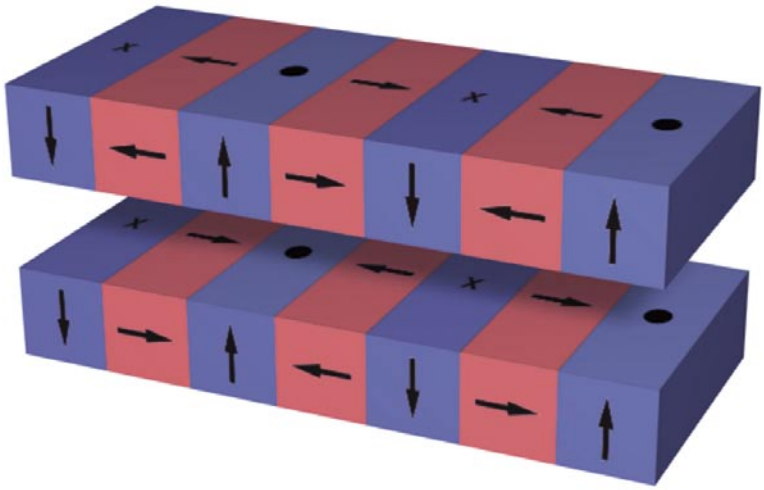

Figure 7.3.1:
Schematic of a fixed polarization PPM undulator based on two Halbach arrays: the magnetic field amplitude is adjusted by changing the vertical gap between the arrays.

A 2D approximation can be used when the magnets are wide enough in the *x* direction that one can set $k_X \to 0$, a condition easily satisfied; the field expression then reduces to

$$\begin{aligned} B_x(x,y,z) &= 0 \\ B_y(x,y,z) &= B_o\left(1+\frac{k_y^2}{2}\cdot y^2\right)\cdot\cos(k\cdot z) \\ B_z(x,y,z) &= -k\cdot y\cdot B_o\cdot\sin(k\cdot z) \end{aligned} \qquad 7.3.3$$

and

$$k_y = k = \frac{2\cdot\pi}{\lambda_0} \qquad 7.3.4$$

In a standard PPM undulator with 8 blocks per period the on-axis peak field B_0 is given by the classical relation [2]:

$$B_0 = 2\cdot B_r\cdot e^{-\pi\cdot g/\lambda_0}\cdot\frac{\sin(\pi/4)}{\pi/4}\cdot\left(1-e^{-2\pi\cdot h/\lambda_0}\right) \qquad 7.3.5$$

The block height *h* is usually chosen to be $\lambda_0/2$, producing ~96% of the maximum theoretical field with a reasonable volume of magnetic material, so that

$$B_0 = 1.723\cdot B_r\cdot e^{-\pi\cdot g/\lambda_0}\ . \qquad 7.3.6$$

Taking B_r=1.2 T (see Section 7.2) one has

$$B_0 = 2.067\cdot e^{-\pi\cdot g/\lambda_0} \qquad 7.3.7$$

and the associated rms deflection parameter is:

$$K_{rms} = \frac{e\cdot B_0\cdot\lambda_0}{2\sqrt{2}\pi\cdot m_0 c} = 0.66\cdot B_0(T)\cdot\lambda_0(cm)\ . \qquad 7.3.8$$

The previous relations can be used to determine the period length of fixed polarization undulators such as used for the first modulators of both FEL-1 and FEL-2. Such devices are specified to be tunable to the seed laser wavelengths, in the 240 nm to 360 nm range (see Chapter 4). The deflection parameter, the peak field and the field roll-off coefficient values in this range are listed in Table 7.3.1 for different period lengths.

Table 7.3.1: Main parameters of various linearly polarized undulators for the 240-360 nm range.

λ_0 (cm)	λ (nm)	K_{rms}	B_0 (T)	k_Y (m^{-1})
8	360	7.0	1.32	79
	240	5.7	1.07	79
10	360	6.2	0.94	63
	240	5.0	0.76	63
12	360	5.7	0.72	52
	240	4.6	0.58	52
14	360	5.2	0.57	45
	240	4.2	0.46	45
16	360	4.9	0.46	39
	240	3.9	0.37	39

The table shows that the tunability condition is satisfied for a wide range of periods, from which the value λ_0=16 cm, giving 19 periods per undulator, has been selected and used in the FEL simulations of Chapter 4. Additional studies are in progress to further optimize the choice of λ_0 since a shorter period would have a number of advantages, namely

- a higher deflection parameter, which increases the electron-radiation coupling,
- a shorter magnet length for a given number of periods,
- a tuning range extended towards shorter wavelengths.

The parameters of the other fixed polarization devices, the first stage radiator and the second stage modulator for FEL-2, have also been computed and are listed in Table 7.3.2.

Table 7.3.2: Main parameters of a linearly polarized undulator covering the 40-100 nm range.

λ_0 (cm)	λ (nm)	K_{rms}	B_0 (T)	k_Y (m^{-1})
6.5	100	4.0	0.93	97
	40	2.4	0.56	97

Note that equation (7.3.5) relies on the approximation that the magnetic material has unit permeability, meaning that fields produced by individual magnet blocks can be linearly superimposed. The final detailed magnetic design therefore needs further work to take into account various other effects due to the finite width and the dimensional tolerances of the magnet blocks, the actual anisotropic permeability of the magnetic material and to magnetic field harmonics affecting the emission wavelength. Based on our experience, including such effects is expected to require only slight adjustments of the period length and / or of the gap width.

7.4 Variably Polarized Undulators

The most efficient undulator structure for providing variable polarization is the so called APPLE-II (Advanced Planar Polarized Light Emitter) [3], schematically illustrated in Figure 7.4.1.

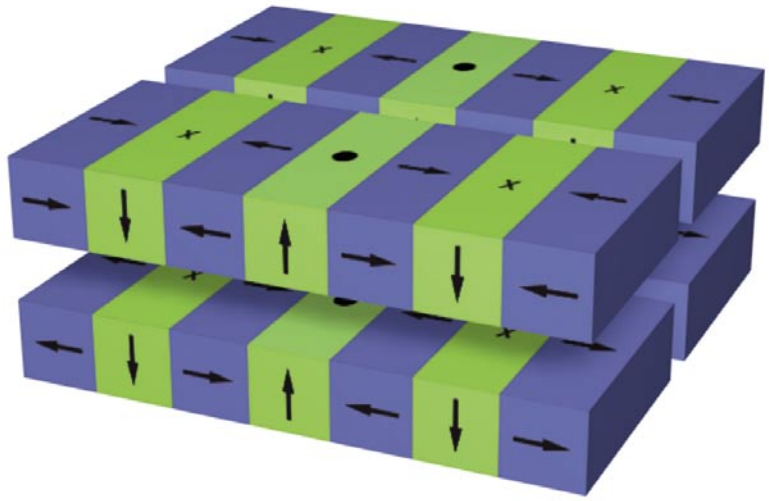

Figure 7.4.1:
Sketch of an APPLE-II undulator: magnetic field strength and polarization can be adjusted by changing the vertical gap (g) and the longitudinal position (Zs) of the arrays respectively.

Compared with alternative solutions, this device can most efficiently generate magnetic field configurations leading to horizontally, elliptically, circularly or vertically polarized radiation, while remaining accessible from the side in the mid-plane. The latter feature has a number of advantages as far as installation of the vacuum chamber and, more important, magnetic measurements are concerned. It has therefore been widely used at several synchrotron radiation facilities, including ELETTRA.

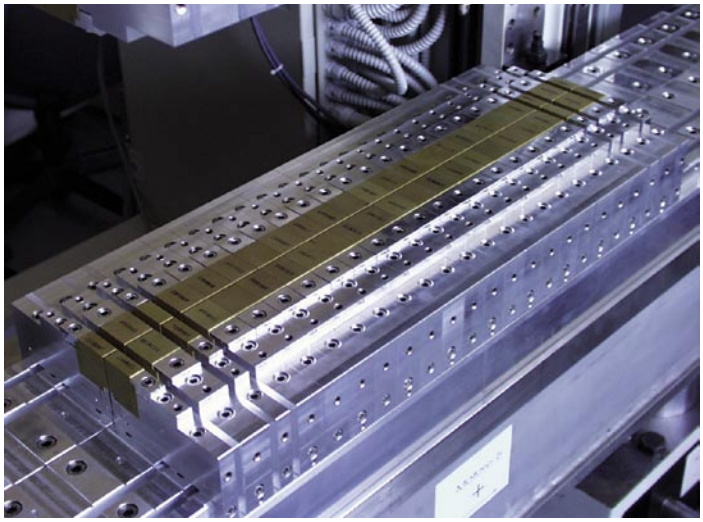

Figure 7.4.2:
An Apple-II undulator during assembly.

Like in the case of linear polarization vertical field undulators, the magnetic field can be written, to second order in the transverse coordinates X and Y, as

$$\begin{aligned} B_x(x,y,z) &= B_{x0}\cdot(1+\frac{k'^2_x}{2}\cdot x^2+\frac{k'^2_y}{2}\cdot y^2)\cdot\sin(k\cdot z)+B_{yo}\cdot k_x^2\cdot x\cdot y\cdot\cos(k\cdot z) \\ B_y(x,y,z) &= B_{x0}\cdot k'^2_y\cdot x\cdot y\cdot\sin(k\cdot z)+B_{yo}(1+\frac{k_x^2}{2}\cdot x^2+\frac{k_y^2}{2}\cdot y^2)\cdot\cos(k\cdot z) \\ B_z(x,y,z) &= k\cdot x\cdot B_{x0}\cdot\cos(k\cdot z)-k\cdot y\cdot B_{yo}\cdot\sin(k\cdot z) \end{aligned} \qquad 7.4.1$$

where:

$$k_x^2+k_y^2=k'^2_x+k'^2_y=k^2 \qquad 7.4.2$$

For APPLE type undulators there is no analytical expression of B_0 as a function of the device geometrical parameters. However, a semi-empirical formula is obtained (as suggested in Ref. [4]) fitting the results of 3D magnetostatic calculations performed on different magnet configurations; it has the following general form

$$B_0=a\cdot\exp\left[-b\cdot\left(\frac{g}{\lambda_0}\right)+c\cdot\left(\frac{g}{\lambda_0}\right)^2\right], \qquad 7.4.3$$

often used to describe the field versus gap aperture dependence and as a help in choosing a starting set of parameters for numerical calculations. An important shortcut is provided by the principle of "scale invariance", stating that, no matter what the configuration of a collection of unit-permeability magnetic blocks is, the magnetic field they generate is unchanged if their linear dimensions and their separation distances are all simultaneously scaled by the same factor [1].

This scaling procedure is applicable to FERMI, given the design and the foreseen range of parameters of the undulators. The height (h) and the width (w) of each block and the blocks horizontal separation (s) have therefore been parametrized as

$$h = \frac{\lambda_0}{2}, \quad w = \frac{\lambda_0}{2}, \quad s = \frac{\lambda_0}{60} \quad . \qquad 7.4.4$$

The resulting coefficients appearing in Eq. (7.4.3), for the three main polarization modes (horizontal, circular and vertical), are listed in Table 7.4.1.

Table 7.4.1: Coefficients to be used in eq. (7.4.3) for various polarization modes.

Polarization	*Fitting coefficients*		
Horizontal	a = 1.76	b = 2.77	c = - 0.37
Circular	a = 1.54	b = 4.46	c = 0.43
Vertical	a = 2.22	b = 5.19	c = 0.88

These coefficients are then used to determine the (approximate) period length of the final radiators so that the desired tuning range (100 to 40 nm for FEL-1 and 40 to 10 nm for FEL-2) is covered for all polarizations, namely λ_0 = ~6.5 cm for FEL-1 and λ_0 = ~5.0 cm for FEL-2. Pending more detailed calculations, and taking into account details such as the earlier mentioned non-unit permeability, the above approximate values have been used throughout this report. The corresponding sets of main undulator parameters, computed for two radiation wavelengths and three main polarization configurations, are listed in Tables 7.4.2 and 7.4.3.

Table 7.4.2: Parameters of FEL-1 radiator (λ_0 = 6.5 cm) at both extremes of its tuning range in the three main polarization modes.

λ *(nm)*	K_{rms}	B_{X0} *(T)*	B_{Y0} *(T)*	k_X *(m^{-1})*	k_Y *(m^{-1})*	k_X' *(m^{-1})*	k_Y' *(m^{-1})*
100 - H	4.0	0	0.93	55	87	-	-
100 - C	"	0.66	0.66	55	79	147 · i	177
100 - V	"	0.93	0	-	-	161 · i	189
40 - H	2.4	0	0.56	14	96	-	-
40 - C	"	0.40	0.40	27	93	116 · i	151
40 - V	"	0.56	0	-	-	124 · i	157

H = horizontal, C = circular, V = vertical polarization

Table 7.4.3: Parameters of FEL-2 radiator (λ_0 = 5 cm) at both extremes of its tuning range in the three main polarization modes.

λ (nm)	K_{rms}	B_{X0} (T)	B_{Y0} (T)	k_X (m^{-1})	k_Y (m^{-1})	k_X' (m^{-1})	k_Y' (m^{-1})
40 - H	2.8	0	0.85	58	113	-	-
40 - C	"	0.60	0.60	72	102	185 · i	225
40 - V	"	0.85	0	-	-	197 · i	235
10 - H	1.1	0	0.33	22 · i	128	-	-
10 - C	"	0.24	0.24	14	125	133 · i	183
10 - V	"	0.33	0	-	-	139 · i	187

H = horizontal, C = circular, V = vertical polarization

7.5 Alignment Tolerances

An incorrect alignment of individual undulator magnets produces two effects:

i) a field change whose strength depends on the sign and magnitude of the roll-off coefficients

ii) a trajectory distortion that depends on the focusing properties of the magnet.

In terms of field uniformity, tolerances can be derived based on the requirement that for close-to-ideal FEL performance the relative difference in integrated field strength between neighbouring magnets must be less than ± 0.2% (see Section 4.3.3). Expression 7.4.1 tells us that the relative field change due to horizontal and vertical displacements Δ_X , Δ_Y of the undulator axis, is:

$$2\left(\Delta B/B\right) = k_X^2\Delta_X^2 + k_Y^2\Delta_Y^2 \qquad 7.5.1$$

and, based on the data in Tables 7.4.2 and 7.4.3, it can be conservatively assumed that the magnitude of the roll-off coefficients, k_X and k_Y, does not exceed 250 m^{-1}. It follows that single undulator misalignments of up to ~200 μm can in principle be tolerated. This can be seen in figure 7.5.1 for the case of the FEL-2 radiator, which is the most sensitive to field imperfections. It can be seen that the relative field change is less than 0.1% when moving off-axis by 200 μm in either X or Y directions.

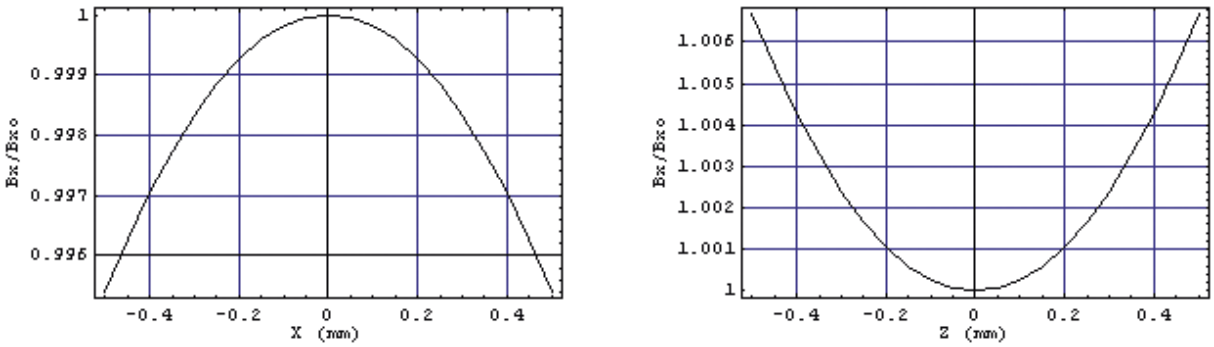

Figure 7.5.1:
FEL-2 radiator transverse field distribution with closed gap (40 nm) and vertical polarization.

The effects of the undulator focusing properties on the electron trajectory have been estimated based on numerical tracking of the beam in the 3D undulator field. As an example, Figure 7.5.2 shows that the trajectory in the FEL-2 radiator offset from the nominal position by $\Delta_X = \Delta_Y = 200$ μm, which causes the position and angle errors to reach up to 50 μm and 30 μrad respectively, values exceeding the tolerances required for FEL operation (see Section 4.3.3). Nonetheless, in this particular example, the error on the optical phase, 2° rms, stays within the specified tolerance of 0.15 rad ≈ 9° rms.

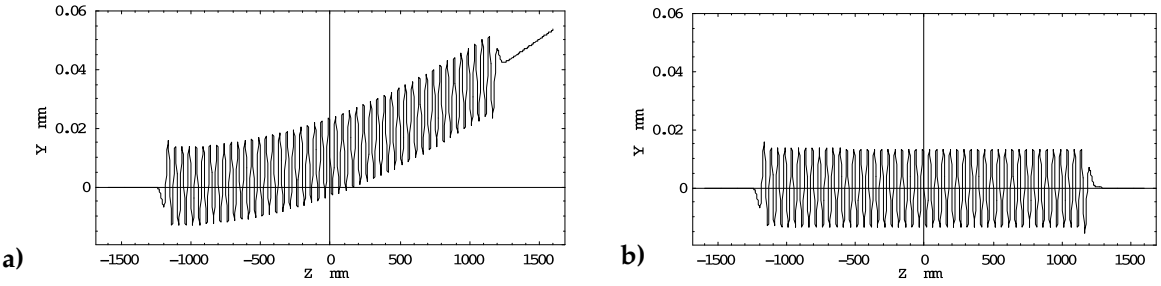

Figure 7.5.2:
Electron trajectory in presence of a misalignment of 200 μm (a) compared to the ideal case (b).

Such a large trajectory offsets must be corrected during commissioning. Dedicated correction coils, mounted at both ends of each individual undulator magnet, correct the effect of residual random magnetic field and misalignment errors. Figure 7.5.3 shows a simulation where the trajectory distortion has been corrected in this way. The maximum trajectory offset and tilt are reduced to about 10 μm and 10 μrad respectively, well below specification. The associated contribution to the phase error is also reduced to 0.8 deg.

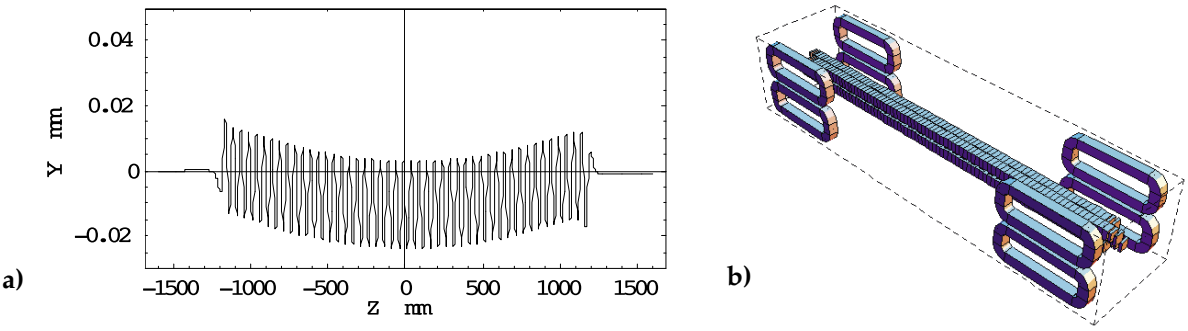

Figure 7.5.3:
Partial compensation of the trajectory distortion (a) can be obtained using correction coils, arranged as schematically sketched in (b).

In practice, undulator modules will be further fine-aligned, whenever necessary, using beam-based alignement (BBA) techniques assisted by observations of the spontaneous radiation. It can be shown that residual misalignments (before BBA) at the level of 50 μm, due to effects such as field strength errors, trajectory distortions and optical phase errors, can be corrected by BBA to meet the specified tolerances.

7.6 Effect of the Earth Field

In presence of a constant magnetic field an electron initially traveling along the z direction is deflected by an angle

$$\theta = -\frac{e}{\gamma m_0 c}\int B\,dz \ , \text{ or, in practical units,} \qquad \theta\,(\mu rad) \cong \frac{30 \cdot B[G] \cdot z(m)}{E(GeV)} \ . \qquad 7.6.1$$

For B(G) = 0.5 G, the trajectory of a 1.2 GeV electron is bent by 25 μrad and displaced by 25 μm every 2 m of travel, a value incompatible with the tolerance set on the FERMI beam average trajectory straightness in the undulator. As an example, Figure 7.7.1 shows the trajectory in one of the FERMI undulators when constant magnetic field components of 0.2 G horizontal and 0.5 G vertical (again typically observed Earth field components) are added. Note that the contribution to the phase error, 3° rms, is also non negligible.

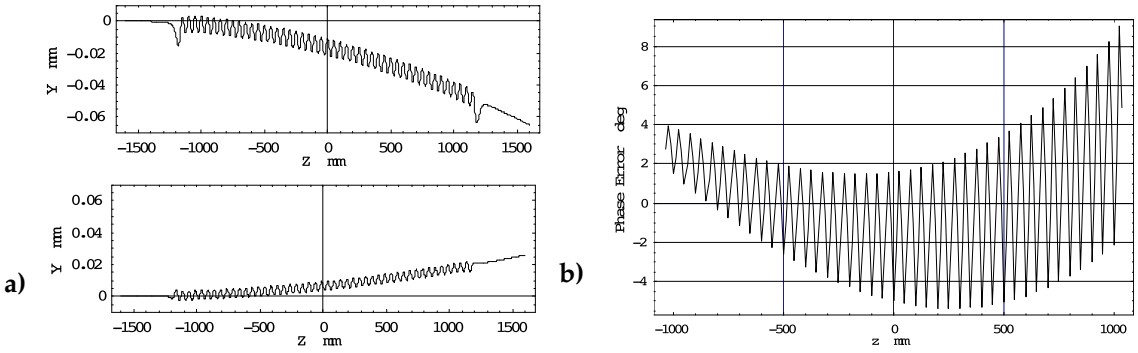

Figure 7.6.1:
(a) electron trajectory in presence of a constant environmental field of 0.2 G (horizontal) and 0.5 G (vertical). (b) corresponding phase error distribution.

Considering that the beam trajectory will be corrected during initial commissioning, so that after a first correction (see section 7.12 on beam-based alignment) it can be assumed to pass through the center of all BPMs, the earth field effect will cause it to look as shown in Fig. 7.7.2 or in more detail in Figure 7.7.3, namely as a sequence of parabolic arcs in between successive BPMs on which the oscillation inside the magnet is superimposed.

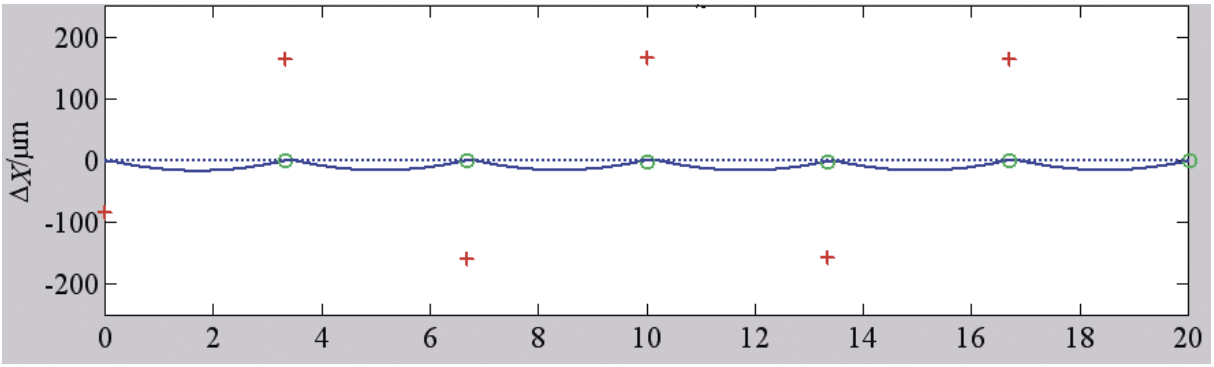

Figure 7.6.2:
Sketch of beam trajectory in the undulator in presence of the Earth magnetic field.

One sees that the corrected trajectory excursion is significantly reduced both in angle and offset, and that the residual phase error is less than *1° rms*. Still, one concludes that Earth field effects must be either compensated or shielded. Shielding is discarded as impractical due to the dimensions of the apparatus and must therefore be compensated. Compensating-out the effect by shimming, discarded by LCLS [6] because the environmental field intensity and direction in the laboratory can differ from those at the final undulator location, is still being considered for FERMI since tolerances on the trajectory straightness are less demanding than those of the LCLS.

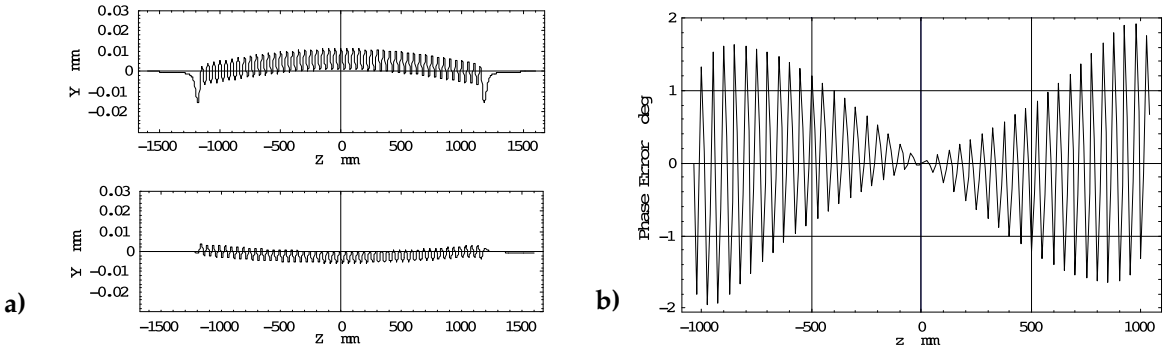

Figure 7.6.3:
Beam trajectory (a) and phase error (b) inside an undulator section, in presence of the Earth field and assuming that the corrected trajectory goes through the center of the BPMs mounted at both ends of the section itself.

7.7 Mechanical Design Considerations

The undulator mechanical design is based on the experience gained with the construction of the Apple II undulators installed in the ELETTRA storage ring [7-11]. The main differences of the present FERMI design with respect to the one implemented in ELETTRA are the magnet length (2.5 m in FERMI, against 2 m in ELETTRA) and the tighter specifications on the gap height and on the electron-photon phasing. The new requirements will be met by suitably modifying the existing design.

The magnet main supporting structure ("carriage") is made of rectangular steel tubes welded together to form a rigid C-type frame. The carriage is supported by two vertical posts, one at each end. Each of two stainless steel backing beams (upper and lower), movable up and down on rails fastened to the main support posts, carries one longitudinally movable and one fixed aluminium beam, on each of which a magnet array is fixed. The undulator gap is changed by moving the backing beams up and down, driven by a pair of synchronized motors. The relative longitudinal position of the two aluminium beams carrying the magnet arrays ("phase"), also driven by two (upper and lower) synchronized motors, determines the radiation polarization. Finally, the carriage is mounted on a horizontally movable platform for the fine alignment of the whole structure. Undulator gap height, longitudinal (phase) shifts and carriage transverse positions are all measured using absolute encoders with better than 1 μm resolution.

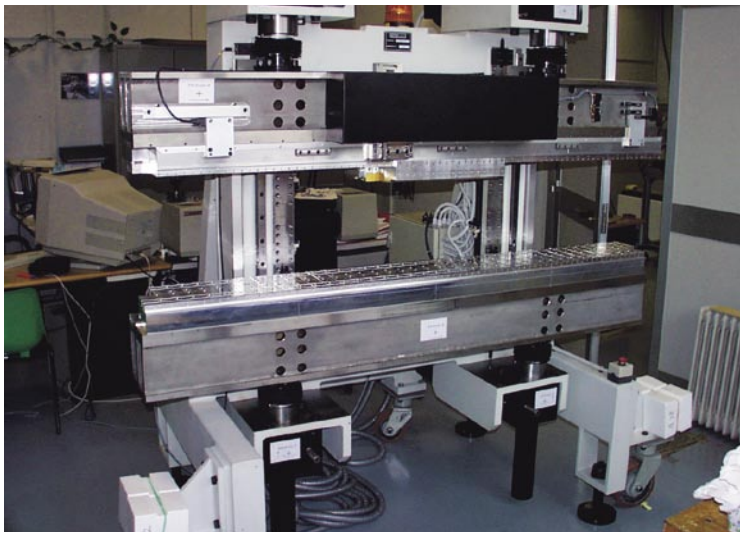

Figure 7.7.1:
Support structure of one of the ELETTRA elliptical undulators.

The permanent magnet blocks are clamped onto individual holders using the indentures cut into each of two of their opposite edges, as shown in Fig. 7.7.2. The holders are in turn fastened to four base plates by pins and bolts. Such a structure has been developed and perfected to allow adjusting the position of individual magnet blocks both horizontally and vertically (shimming), in order to compensate for random magnetization errors.

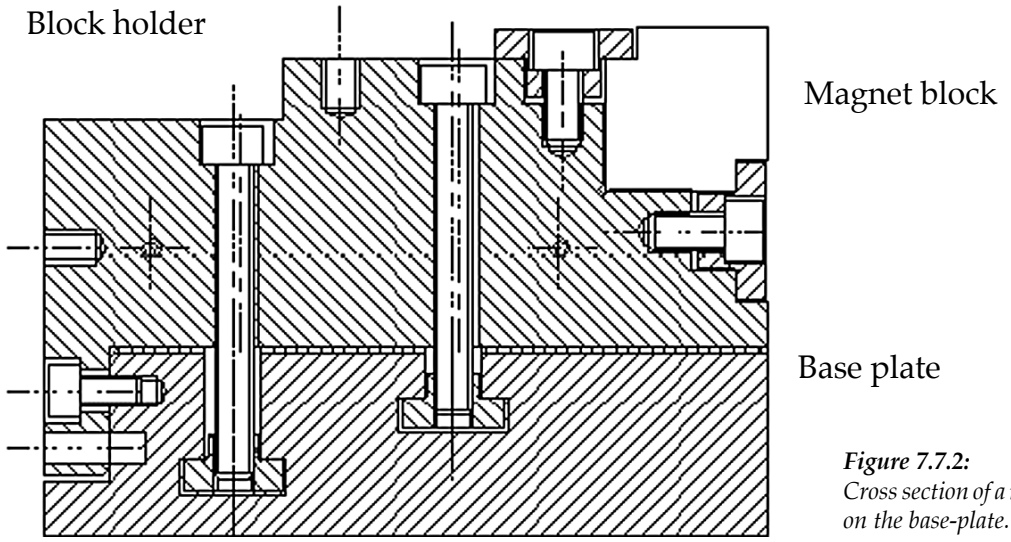

Figure 7.7.2:
Cross section of a magnet block holder on the base-plate.

A design study of the assembly is in progress, aimed at guaranteeing the following mechanical tolerances:

i) planarity and parallelism of each backing beam: 10 μ*m*

ii) maximum magnetic gap error: 30 μ*m*

iii) gap and phase positioning accuracy: 5 μ*m*

iv) beam axis adjustable in the horizontal and vertical directions to within 5 μ*m*

Such tolerances must be met at all gap and phase values in the presence of the strong magnetic forces that change in magnitude and direction as the undulator is tuned to different wavelengths or polarizations. As an example, Figure 7.7.3 shows the strength of forces acting on the individual arrays and on the backing beam of the FEL-1 radiator as functions of gap height and phase. Forces acting on the FEL-2 variable polarization device are smaller due to the smaller size of its magnetic blocks.

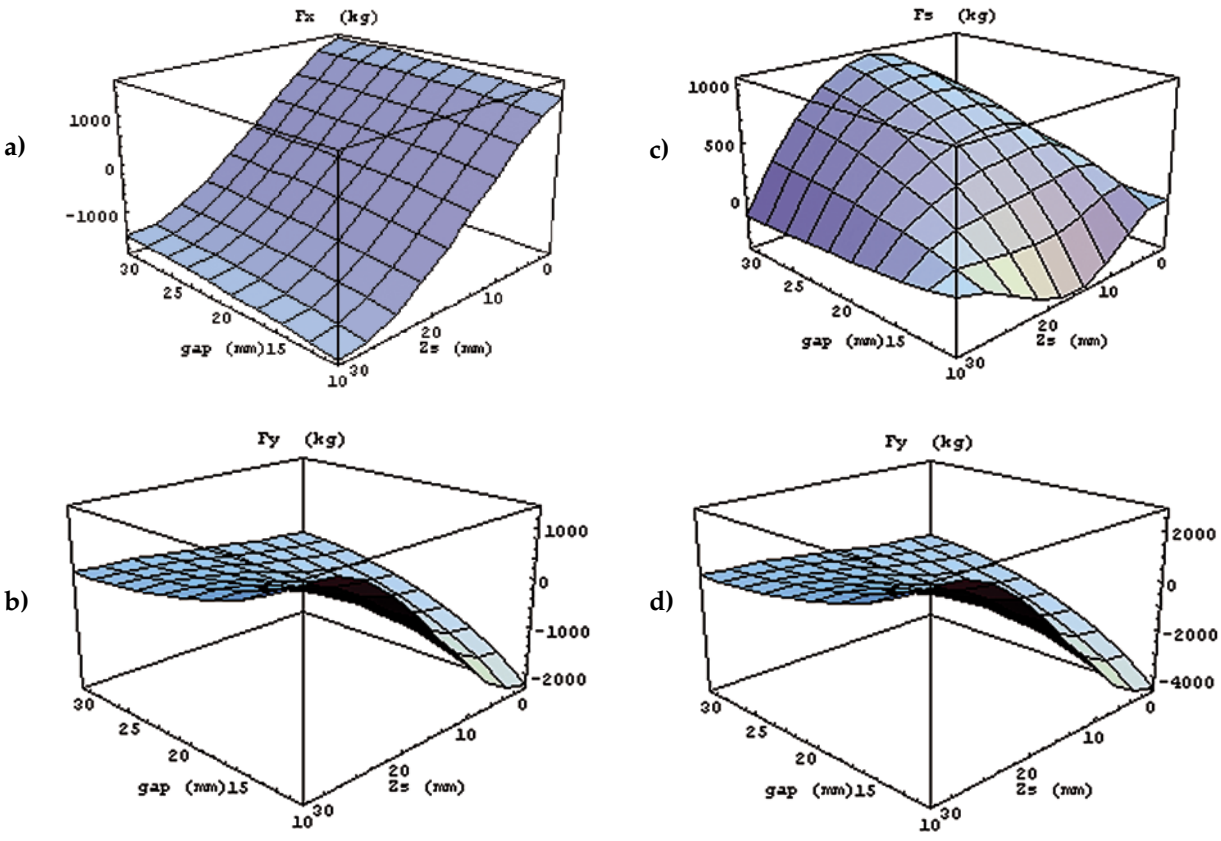

Figure 7.7.3:
Magnetic forces on the FEL-1 radiator as a function of gap and phase: horizontal (a), longitudinal (b) and vertical (c) force components on the movable array; vertical force on the upper/lower backing beam (d).

Deformations and stresses on the support structure and on its strongback have been evaluated using the finite element modeling (FEM) code ANSYS. Figure 7.7.4 shows the simplified model of the main frame and of the lower support beam used in the simulations. Models of the linear rails and the permanent magnets assemblies have also being developed and analyzed.

a) b)

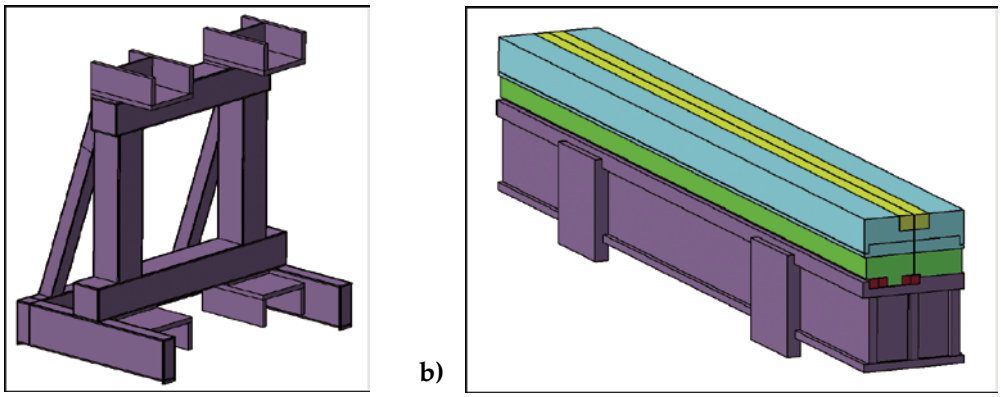

Figure 7.7.4:
Models of the steel frame (a) and of the lower beam (b).

Special attention has being given to the determination of permanent magnet arrays transverse and vertical deformations since they produce systematic field errors directly affecting the undulator performance [12]. The calculations have been benchmarked against the existing ELETTRA EU10.0 APPLE II undulator whose performance is known and whose forces per unit length are comparable to those expected in the FEL-1 radiator.

a) b)

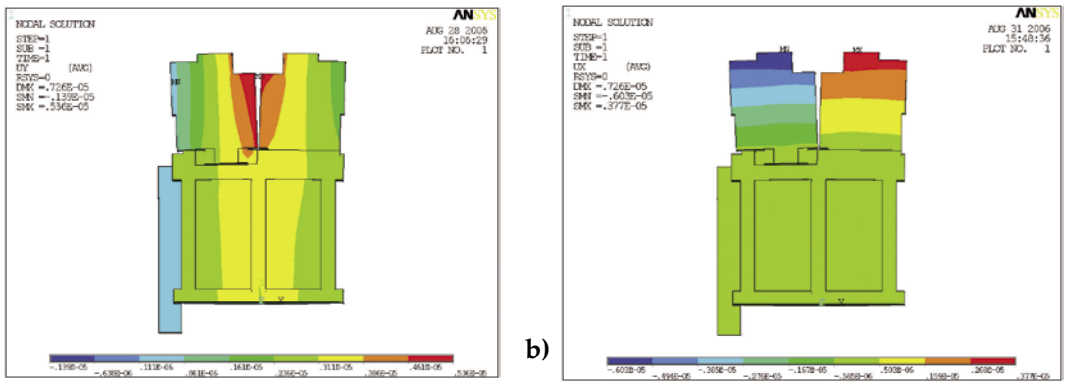

Figure 7.7.5:
FEM results showing the transverse (a) and vertical (b) deformation at the center of the EU10.0 undulator beam.

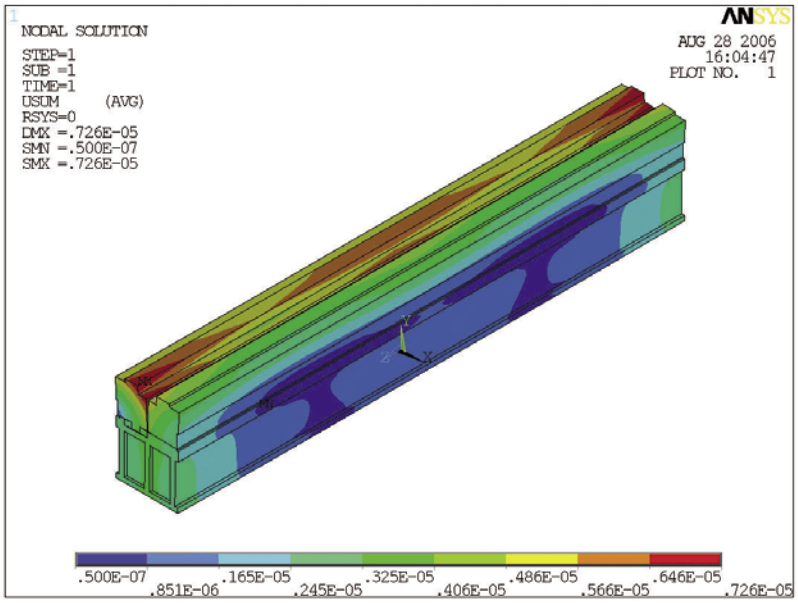

Figure 7.7.6:
Deformation of complete beam of the EU10.0 undulator.

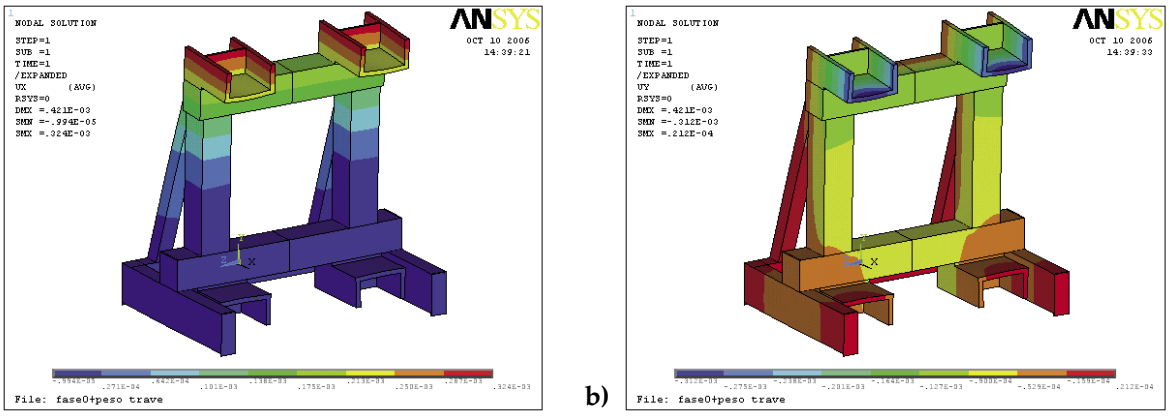

Figure 7.7.7:
Transverse (a) and vertical (b) displacements of the support frame.

The FEM calculations were carried out on EU10.0 in the minimum gap and zero phase configuration, in which the horizontal and vertical forces are both close to their maximum. The results, shown in Figures 7.7.5, 7.7.6 and 7.7.7, are in good agreement with measurements recently performed on the same device [13]. The study proved specially useful in finding the position of the gap encoders most effective in preventing carriage deformations from spoiling the accuracy of the gap height measurement. In this respect, the alternative of having the encoders supported on a separate frame is also being evaluated.

7.8 Thermal Stability Requirements

The main effect of unavoidable ambient temperature fluctuations is a change of the peak magnetic field due to reversible magnetization losses in the permanent magnet material. The corresponding temperature coefficient for NdFeB is typically $\Delta B_r/B_r = 0.15\%/^{o}C$.

For the FEL to operate (see Section 4.3.3), the relative difference in field strength between neighboring individual undulator magnets is specified to be less than ± 0.2%. Therefore, were thermal changes of the magnetic blocks the only source of field variation, the undulator average temperature would be required to stay within ± 1.3 °C.

However, there are other factors to consider. Thermal expansion of the undulator support structure changes the transverse distance between the two linear permanent magnet arrays, fastened to a common steel backing beam ("horizontal gap"), and the undulator (vertical) gap height. Sensitivity coefficients can be evaluated from basic magnetic field expressions (see Section 7.4 and 7.5) showing , as an example, that the FEL-2 radiator, having the shortest period, is the most sensitive to gap height variations when operating in the vertical polarization mode, the $\Delta B/B$ change reaching up to 10%/mm.

A similar effect is found when changing the horizontal block separation ($\Delta B/B$~8%/mm); gap height and block separation stability of the order of 20 μm are required to fulfill the ± 0.2% tolerance criterion mentioned above. A conservative estimate of the deformation of a carefully engineered support structure indicates that an average temperature change of less than 1°C is needed to keep the error on both the horizontal and the vertical gap within less than 15 μm.

Adding up the two effects and accounting for the thermal inertia of the device, one concludes that the average ambient temperature must be stable to within ± 0.7 °C, averaged over time intervals of a few hours.

7.9 Magnetic Optics in the Radiator Region

The radiator is a sequence of 3 FODO cells, with an undulator in each of the straights. Matching of the FODO lattice with the undulators gaps in their "closed" position was done with MAD, in which the undulator is introduced as an uncoupled 6x6 transfer matrix computed using RACETRACK. The calculations are done for the 100 nm and the 40 nm photon wavelength (FEL 1 covered range) configurations, and for three representative polarizations, horizontal, circular and vertical.

The constraints taken into consideration in designing the optics are:

1) average betatron functions in the 7 to 11 *m* range in both planes, with maxima less than ~13 *m* and minima not less than ~5 *m* (see Chapter 4). When varying the polarization and/or the wavelength of the FEL output, the quadrupoles must therefore compensate for variations of the transport optics due to the change in the undulator focusing properties.
2) integrated quadrupole strength small enough for quadrupole misalignments and magnetic errors not to dominate trajectory errors ;
3) a maximum quadrupole field gradient small enough for hysteresis effects not to significantly affect reproducibility of the various different optics needed in operation;
6) quadrupole physical dimensions compatible with the straight section space reserved for diagnostics devices, corrector magnets, and other needed instrumentation.

A matched FODO lattice with phase advances in the range of 40° to 60° in either plane has been shown to nicely meet all requirements, in particular that of rather low beta excursions along the channel, combined with sufficiently low maximum beta values.

Table 7.9.1 lists the strengths and phase advances of the 0.15 *m* long, FODO cell quadrupoles, called QR1 and QR2, in the fully open undulator gaps configuration and for three different polarizations (see also Section 7.7). The quadrupole specified top gradient of 10 *T/m* includes a 20% margin. The maximum betatron function stays within 12.5 m. The open gap optics has the highest and closest to each other phase advances compared to all other operational configurations; this because as gaps are closed and undulator effects become stronger, the lattice behaves less and less like a pure FODO and the phase advance difference between the two planes tends to grow. The effect is most evident for the circular and vertical polarizations at a photon wavelength of 100 *nm*, where the defocusing quadrupoles change to focusing.

Table 7.9.1: Radiator quadrupole strengths [m^{-2}] – magnetic length 0.15 m.

Polarization	*QR1*	*QR2*	*Beta phases*	*Racetrack & Mad phases*
Open und.	*defocussing*	*focussing*	$\Phi_x = 58^o$	$\Phi_x = 58^o$
	-1. 964	1. 964	$\Phi_y = 58^o$	$\Phi_y = 58^o$
H – 40nm	*defocussing*	*focussing*	$\Phi_x = 48^o$	$\Phi_x = 48^o$
	-1.381	1.524	$\Phi_y = 47.8^o$	$\Phi_y = 48^o$
C – 40nm	*defocussing*	*focussing*	$\Phi_x = 48.2^o$	$\Phi_x = 48^o$
	-1.274	1.625	$\Phi_y = 47.6^o$	$\Phi_y = 48^o$
V – 40nm	*defocussing*	*focussing*	$\Phi_x = 49.7^o$	$\Phi_x = 49.2^o$
	-1.161	1.798	$\Phi_y = 48.5^o$	$\Phi_y = 49.2^o$
H – 100nm	*defocussing*	*focussing*	$\Phi_x = 41.5^o$	$\Phi_x = 42^o$
	-0.457	0.717	$\Phi_y = 42.4^o$	$\Phi_y = 42.2^o$
C – 100nm	*focussing*	*focussing*	$\Phi_x = 46^o$	$\Phi_x = 45.7^o$
	0.013	1.317	$\Phi_y = 42.6^o$	$\Phi_y = 41.9^o$
V – 100nm	*focussing*	*focussing*	$\Phi_x = 52.9^o$	$\Phi_x = 49.9^o$
	1.448	1.474	$\Phi_y = 44^o$	$\Phi_y = 46.5^o$

H = horizontal, C = circular, V = vertical polarization

As an example, Figures 7.9.1 and 7.9.2 show the behaviour of the Twiss functions in the undulator region for the last two configurations of Table 7.9.1, namely, circular and vertical polarization and 100 nm wavelength.

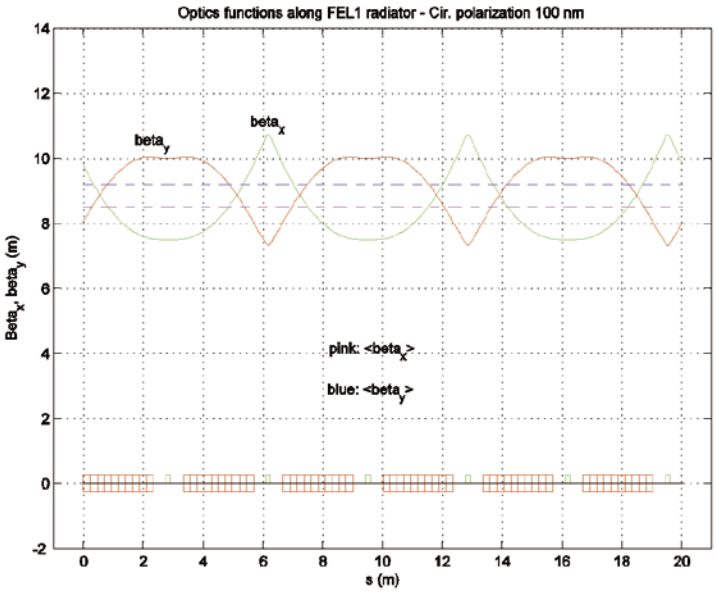

Figure 7.9.1:
Twiss functions in the undulator region for circular polarization at 100 ***nm****; FODO cell phase advances* $\phi_x = 45.7^o$, $\phi_y = 41.9^o$

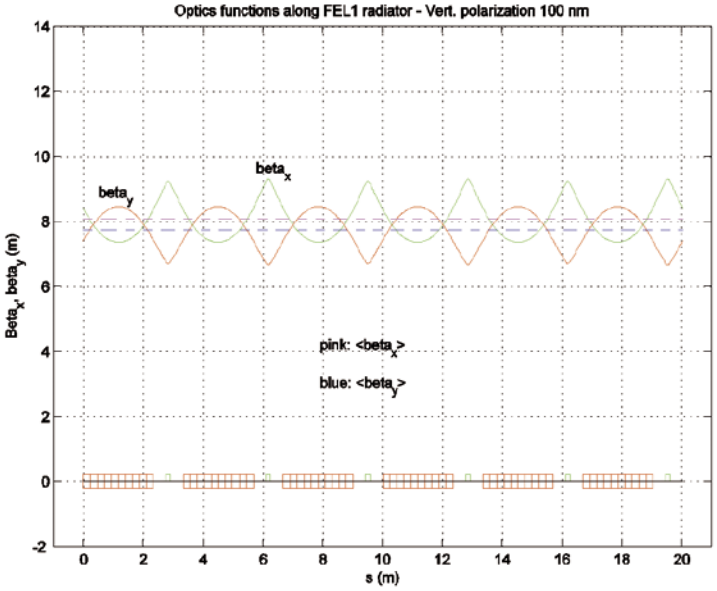

Figure 7.9.2:
Twiss functions in the undulator region for vertical polarization at 100 ***nm****; FODO cell phase advances* $\phi_x = 49.9^o$, $\phi_y = 46.5^o$

7.10 Undulator Vacuum System

The undulator vacuum system is designed to fit the minimum undulator gap (10 mm); it is built in modules, each consisting of a diagnostics section followed by an undulator vacuum chamber. The diagnostics section hosts all instrumentation for beam diagnostics and alignment as well as the vacuum diagnostics and pumping system instrumentation.

The design complies with the following general guidelines.

- The chamber material electrical resistivity and roughness must be low enough for the resistive wall and the roughness impedance to be kept within specified, acceptable limits (see below) [14].
- The material atomic number must be low and the vacuum chamber capable of surviving at least one direct hit by the full current, full energy, accidentally mis-steered bunch [14].
- Cost and ease of fabrication must be taken into account.

While the mechanical properties of copper, aluminium, titanium, and stainless steel are all suitable for HV vacuum chamber applications, copper and aluminium are preferred because of their superior electrical characteristics. For FERMI, aluminium has been chosen because of its lightness and ease of fabrication combined with good, if not best, electrical properties [15-18].

The average pressure in the undulator vacuum chamber is specified not to exceed $5 \cdot 10^{-7}$ mbar.

7.10.1 Description

The undulator vacuum chamber is made of extruded aluminum; the inner profile is as shown in Figure 7.10.1. The minimum allowed internal gap is 6 mm, the wall thickness is 1.5 mm. No lateral pumping is foreseen.

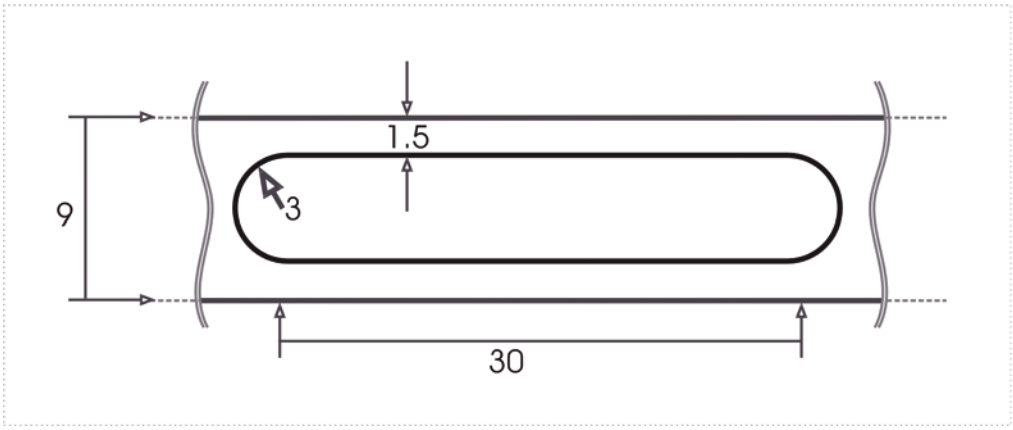

Figure 7.10.1:
Transversal profile of the undulator vacuum chamber. Values in mm.

The surface roughness is specified to be < 0.5 μm rms [16], a conservative value considering what is achieved using state of the art extrusion and surface polishing processes [21]. Preliminary calculations of the effects of the roughness impedance predict, assuming the vacuum chamber cross section is circular with 3 mm radius, a maximum tolerable roughness of <~ 250 nm; this is not too far from the above specification given the worst case assumption made on the chamber shape. Further R&D, both to validate the applied theory and to improve the surface properties, is in progress.

The transition vacuum chamber between two undulator modules is built of the same material and has the same internal shape as that of the undulator in order to avoid wakefield producing discontinuities. A bellow allows to easily connect two adjacent modules and to compensate small length variations due to thermal excursions, particularly during bakeout. The bellow is directly welded to the vacuum chamber in order to save space for diagnostics instrumentation. Its detailed design will be defined so as to minimize geometrical wakefield effects.

A box (Figure 7.10.2), surrounding a vacuum chamber section with pumping slots, carries four flanges to which pumps and auxiliary vacuum instrumentation or other components such as pressure gauges, residual gas analyzer, vacuum valves or beam diagnostics instrumentation can be connected. Care is taken to ensure that the pumping slots do not significantly contribute to wakefield amplitudes.

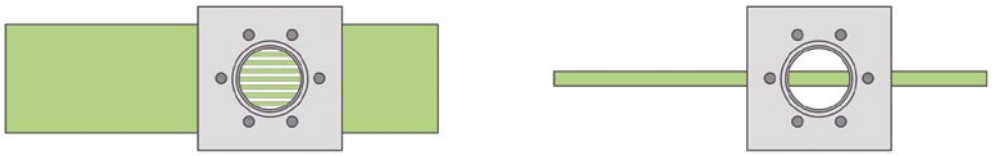

Figure 7.10.2:
Sketch of top view and side view of the pumping box.

Each chamber is equipped with at least a 20 l/s sputter ion pump (SIP) in order to ensure the design operating vacuum pressure also in presence of possible small leaks. Because of the relatively high starting and working pressures, triode pumps are foreseen. Note that the obtainable final pressure is conductance limited, as discussed in Section 7.10.2.

In order to minimize discontinuities occurring between each pair of coupled vacuum chambers, flat flanges and VAT-like seals are specified.

The general undulator vacuum layout is presented in figure 7.10.3. Only two all-metal gate valves are used, one at the beginning and one at the end of the undulator chain vacuum system. They are equipped with RF contacts and with a side flange to connect the system to the pumping station used during

bakeout and pump-down. An additional pumping station can be connected if needed to an all-metal angle-valve mounted on a pumping box placed half way in between the two end gate valves, in order to lower the average pressure at which the ion pumps are switched on.

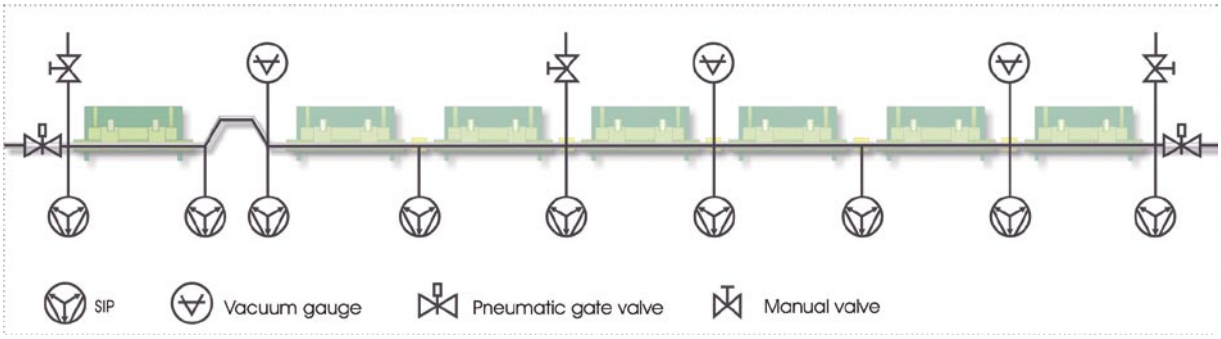

Figure 7.10.3:
General undulator vacuum layout.

At least three pressure gauges (two "Penning" and one "Pirani") and, where needed, a residual gas analyzer are installed to monitor the system both during pump-down and during normal operation.

In case either the foreseen vacuum level or the chamber wall roughness should turn out to limit the beam performance, other vacuum chamber shapes or technical solutions are being considered, such as: extruded aluminium vacuum chamber with ante-chamber to achieve lower average pressures; a stainless steel chamber with a better surface finishing to reduce roughness and with a thinner chamber wall so as to bring the internal gap up to 7 or 8 mm. The latter solution would require aluminium coating to ensure the required electrical properties of the inner surface.

7.10.2 Vacuum Performance

The maximum average pressure allowed in the system during operation is specified not to exceed $5{\cdot}10^{-7}$ mbar in order to keep bremsstrahlung below the specified safety thresholds [18]. A first indication on the tolerable amount of bremsstrahlung during machine operation can be obtained comparing the FERMI expected working parameters with the experimental data from ELETTRA under typical operating conditions (See Table below).

Table 7.10.1: Typical operating conditions of FERMI and ELETTRA.

	P (mbar)	*E (GeV)*	*I (A)*	*L(m)*
FERMI	$5{\cdot}10^{-7}$	1.2	$8{\cdot}10^{-9}$	50
ELETTRA	$1{\cdot}10^{-8}$	2	0.3	11

The ratio of the total dose rate at a conventional reference distance of ten meters from the end of the straight sections was calculated using the following formula [25]:

$$\dot{D}[Gy/h]_{at10m} = 1.7 \cdot 10^{-16} \cdot E^{2.43} \cdot \frac{p}{p_{atm}} \cdot I \cdot L \qquad 7.10.1$$

where E is the electron energy [MeV], I the average electron current [e^-/s], L the straight section length [m], p the average pressure ,p_{atm} the atmospheric pressure (1013 mbar).

The result is:

$$\frac{\dot{D}_F}{\dot{D}_E} \approx 1.8 \cdot 10^{-6} \quad . \qquad 7.10.2$$

The very low ratio is due to the fact that, while the peak currents of the two accelerators are comparable, the FERMI repetition rate and consequently its average current are several orders of magnitude lower than that of the LCLS. Similar results can also be drawn from experience at FLASH [23].

While more detailed calculations are in progress for radiation protection purposes, the undulator vacuum chamber design average pressure of $5x10^{-7}$ is expected to be more than adequate as far as production of bremsstrahlung is concerned.

In order to evaluate the effect of photon induced desorption due to incoherent synchrotron radiation, more detailed knowledge of the photon distribution along the undulator vacuum chamber than at present available is necessary. Nevertheless, first indications can be obtained from comparing FERMI's parameters to those of LCLS, although undulator types and chamber material and shape are different. For FERMI, the electron beam average power of ≤ 12 W at 10 Hz repetition rate is 150 times lower than the maximum average power of LCLS (1.8 kW) [14]; the FEL radiation peak power is also about 35 times lower for FERMI. On the other hand, the LCLS calculated average pressure increase due to photon induced desorption in the copper chamber is in the range of 10^{-9} mbar with a desorption yield (molecules desorbed per incident photon) of Cu about one order of magnitude lower than that of aluminium [24]. From the above data one therefore expects the desorption induced pressure rise in the FERMI undulator chamber to be lower than that computed for LCLS by at least one order of magnitude and therefore negligible compared to the design average pressure.

Concerning the possibility of carbon contamination of the surface, at FLASH - where the vacuum specification for the undulator vacuum chambers requires the residual gas pressure for masses > 45 amu to be not higher than 10^{-3} of the total pressure - no carbon contamination is observed [23]. A similar specification is also foreseen for FERMI so that no significant contamination is expected.

7.10.3 Pressure Profile

In a distributed pumping system along a pipe with uniform outgassing, the pressure profile is classically represented by a parabola [26] the maximum (P_l) and minimum (P_0) values being

$$P_l = q \cdot B \cdot l \cdot (\frac{1}{S} + \frac{1}{2 \cdot C}) \ , \qquad 7.10.3$$

respectively, with q being the specific outgassing, B the perimeter of the pipe cross-section, $2l$ the distance between two neighbouring pumps, S the pumping speed and C the pipe conductance.

Because of the vacuum chamber shape, the system is conductance limited: equation 7.10.3 therefore indicates that the ion pump speed does not significantly influence the ultimate reachable pressure but only defines the pressure at the pump location; moreover, the pressure drop P_l-P_0 is independent of the pumping speed. It is therefore rather the specific outgassing rate that must be kept as low as possible in order to reach the lowest conductance allowed pressure.

With a proper cleaning procedure, including in-situ bakeout, and paying special attention to the cleanliness of the environment during assembly [19,20], one can reach specific outgassing rates of $1 \cdot 10^{-11}$ *mbar·l/s/cm²* or lower [21].

To evaluate the average pressure in the system at room temperature, a Monte Carlo simulation of thermal outgassing was performed using the MolFlow code [22] on a modular system with periodic boundary conditions simulating the modular undulator vacuum chamber. The resulting curve (Figure 7.10.4) has been normalized to a worst case specific outgassing rate of $q=1 \cdot 10^{-10}$ *mbar·l/s/cm²*, taking also into account the contributions from in-vacuum beam diagnostics components. The lowest pressure is, of course, at the pump location while the highest one, approximately at the undulator midpoint, is about one order of magnitude higher; the average pressure in the whole chamber is $4 \cdot 10^{-7}$ mbar.

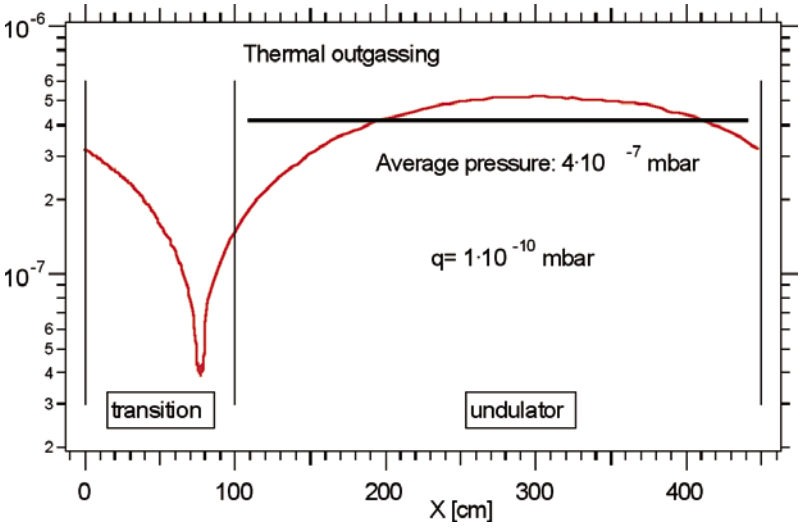

Figure 7.10.4:
Pressure behaviour inside one module (transition+undulator) of the undulator vacuum system, assuming periodic boundary conditions. The average pressure in the undulator vacuum chamber is also shown.

7.10.4 Conclusion

In conclusion, aluminium has been chosen as the undulator vacuum system material, because of its lightness, ease of fabrication and good electrical properties. The material specific outgassing, the most important parameter limiting the ultimate pressure, is kept low by following scrupulous cleaning and assembling procedures. A simulation of the system vacuum behaviour indicates that a maximum average pressure below $5 \cdot 10^{-7}$ mbar can be easily achieved provided strict construction, assembly and maintenance prescriptions are followed.

More detailed simulations will be performed following completion of the detailed design of all components.

Structural and thermal properties of the vacuum chamber including mechanical stress and consequences of possible beam losses are being studied further.

7.11 Wakefields in the Undulator Vacuum Chamber

Since the effects of transverse wakes in the undulator vacuum chambers can be neglected, the main concern is the longitudinal wakes which may blow-up the electron bunch energy spread and consequently degrade the quality of the FEL radiation. They may originate from:

- the resistive wall (RW) effect due to the finite conductivity of the chamber walls,
- the impedance of cavity-like objects,
- the roughness of the chamber inner surface.

The treatment of RW wakefields and of their effect on the FEL performance follows the approach of references [27-30]. Wake functions driven by the wall resistivity are obtained in the time dependent (AC) approximation by numerically computing the inverse Fourier transform of the AC impedance. The very high frequency components in the wake function spectrum acting back on the electron beam degrade the final FEL beam quality by blowing up the electron bunch energy spread.

The theory presented in ref. [27,29] has been applied to both round and parallel-plate geometries, and to aluminium and copper vacuum chambers. The round chambers have an inner radius of 6 mm , while the parallel plate chamber gap is 10 mm. The induced electron bunch energy spread has been evaluated for both the medium and the long bunch case, as described in Chapter 5 of this report.

The theory of surface roughness in a circular chamber, on which the calculations of this study are based, may be found in ref. [31]. The theory of parallel plates [32] is less well established; the overall wakefield is computed by adding up the various excited modes that can propagate through the chamber itself. In the limit of two infinite parallel plates there must be a continuous spectrum of modes that, when added up, tends to cancel the overall effect [7]. Consequently, the induced energy spread is expected to be no larger than for a circular chamber with a radius comparable to the parallel plate separation.

7.11.1 The Resistive Wall Wakefields

This Section provides an overview of the effects of RW induced, AC (time dependent) wakefields . More details are given in ref. [33.]

The interaction between the electron beam and the vacuum chamber is generally described by a coupling impedance and varies according to the wave number *k* of the excited electromagnetic modes that can propagate inside the chamber. The impedance is computed using an RLC parallel circuit to model the chamber response.

The key parameter is the AC conductivity of the chamber wall:

$$\tilde{\sigma} = \frac{\sigma}{1 - ik c\tau} \quad , \tag{7.11.1}$$

the DC conductivity, σ, and the electron relaxation time, τ , being given in table 7.11.1.

Table 7.11.1: DC conductivity and relaxation time for Al and Cu.

	aluminium	*copper*
σ [$\Omega^{-1}m^{-1}$]	4.22×10^{7}	6.45×10^{7}
τ [s]	8.00×10^{-15}	2.70×10^{-14}

The normalized AC longitudinal coupling impedance of a circular chamber can be written as

$$Z(k) = \frac{Z_0}{2\pi a\,[\lambda(k)/k - ika/2]} \tag{7.11.2}$$

and that of a parallel plates chamber as

$$Z(k) = \frac{Z_0}{4\pi}\int_{-\infty}^{\infty}\left[\frac{\lambda(k)}{k}\cosh^2(ax) - \frac{ik}{x}\cosh(ax)\sinh(ax)\right]^{-1} dx \tag{7.11.3}$$

where $\lambda(k)$ is a function whose inverse imaginary part gives the skin depth [30], namely

$$\lambda(k) = \sqrt{Z_0\tilde{\sigma}|k|/2}\,(i + \mathrm{sgn}(k)) \quad , \tag{7.11.4}$$

where *a* denotes the radius of the circular chamber or the half-gap of the parallel plate and $Z_0 \approx 377\ \Omega$ the vacuum impedance.

The wake functions in the time domain are obtained from the inverse Fourier transform of the impedance. They are described by the wake function excited by a point charge

$$w(s) = \frac{2c}{\pi}\int_0^{\infty}\Re(Z(k))\cos(k\,s)\,dk \tag{7.11.5}$$

where s > 0 is the distance from the point charge. The dependence on the chamber material and on the aperture *a* is shown in Fig. 7.11.1 for a circular vacuum chamber and in Fig.7.11.2 for one with parallel-plates.

The figures clearly show that an aluminium, parallel plates chamber is favoured over a circular one with same aperture since [33]

- the maximum amplitude of the wake function $w(s \to 0^+)$ is $\pi^2/16$ times lower and
- the wakefield is damped at least 1.5 times faster.

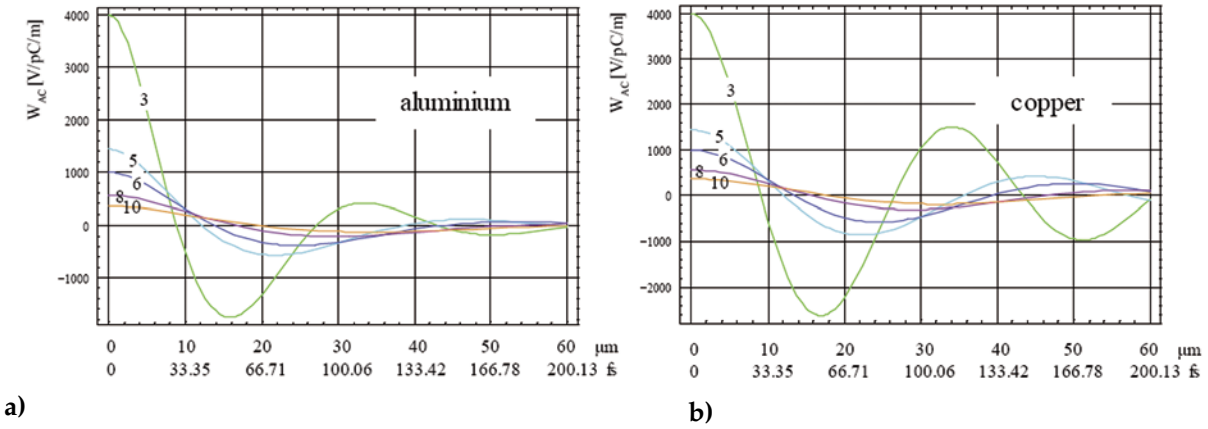

Figure 7.11.1:
Longitudinal AC wake functions for aluminium (a) and copper (b), evaluated at different radii of the circular cross-section vacuum chamber. The radius is indicated in ***mm*** *next to each curve.*

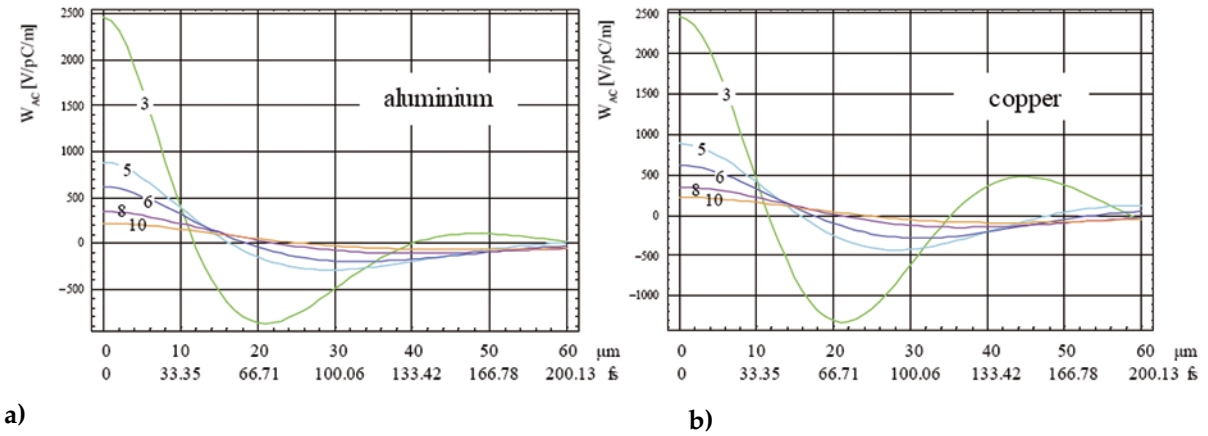

Figure 7.11.2:
Longitudinal AC wake functions for aluminium (a) and copper (b), evaluated at different half-gaps of the rectangular cross-section vacuum chamber. The half-gap height is indicated in mm next to each curve.

The effect of the longitudinal resistive wall wakefield is to induce an energy spread which is correlated with the longitudinal position inside the bunch. This correlated energy modulation follows closely the shape of the wake functions, and, consequently, the choice of the chamber aperture is crucial for the FEL efficiency.

The induced energy spread, for the medium bunch case with a total bunch charge $Q = 0.8$ nC and for the long bunch with $Q = 1$ nC have been computed; the resulting bunch profiles are shown in Chapter 5.

The first step in calculating the energy spread is to compute the wake potential, defined as the convolution of the wake function with the electron bunch linear current density distribution ρ(s), namely

$$W_b(s) = -\frac{1}{Q}\int_0^\infty w(s')\rho(s-s')ds' \quad , \qquad 7.11.6$$

with the sign convention that positive values indicate energy gain for a particle located at a distance s behind the leading point charge. With this convention, the energy spread is given by

$$\Delta E(s) = eW_bQ \qquad 7.11.7$$

The AC wake functions were convoluted by binning the charge distribution in 5 μm bins. The results for two cases (a = 3 and 5 mm), are shown in Fig. 7.11.3 for the medium bunch and in Fig. 7.11.4 for the long bunch case.

It is to be noted that, apart from rather large amplitude oscillations at the head and the tail of the bunch, in the worst case of a 3 mm radius circular chamber the residual absolute energy variation at the bunch core is - 10 keV/m for the medium bunch case and 5 kV/m for the long bunch case. The aluminium chamber clearly offers a flatter bunch core and lower amplitude oscillations near the bunch head and tail. As far as the chamber shape is concerned, the overall average energy loss suffered in a parallel plate chamber is slightly less than that in a circular cross-section with same aperture.

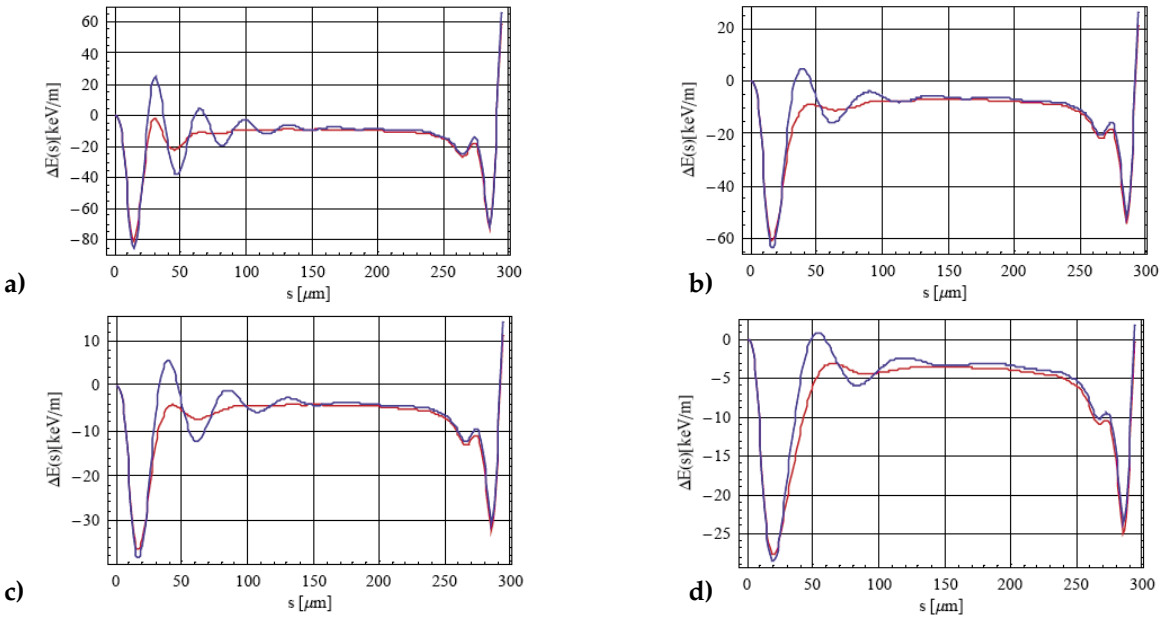

Figure 7.11.3:
Induced energy spread in the medium bunch passing through a circular (a, c) and a parallel-plates vacuum chamber (b, d), for ***a*** *= 3 (a, b) and* ***a*** *= 5 mm (c, d), taking aluminium (red) and copper (blue) for the wall material.*

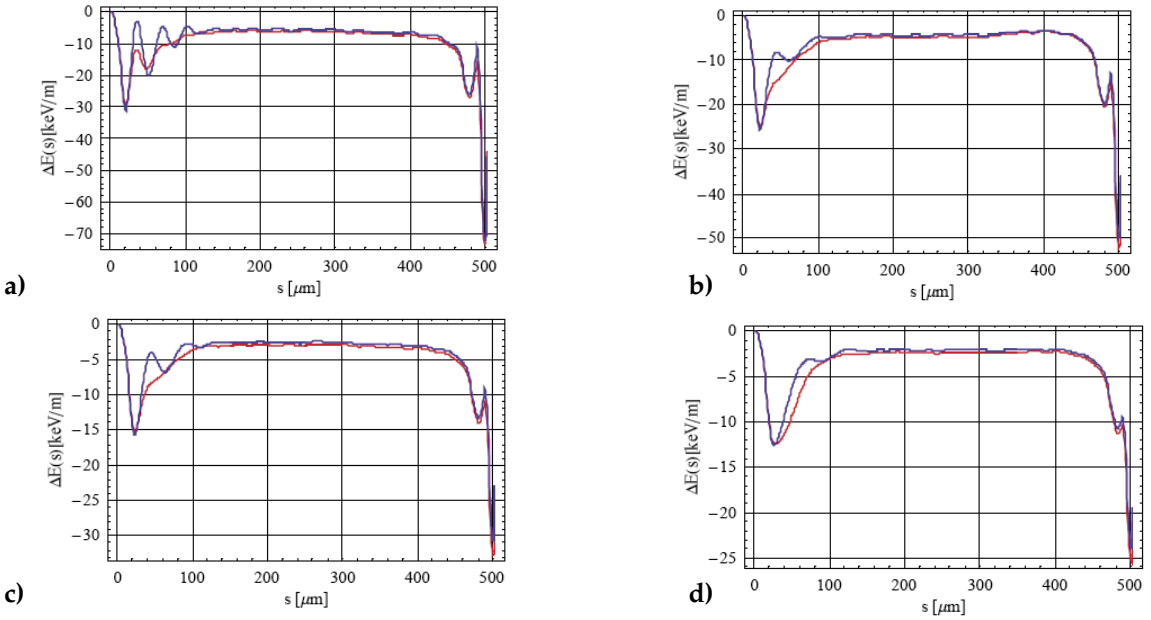

Figure 7.11.4:
Induced energy spread in the long bunch passing through a circular (a, c) and a parallel-plates vacuum chamber (b, d), for a = 3 mm (a, b) and a = 5 mm (c, d), taking aluminium (red) and copper (blue) for the wall material.

7.11.2 The Roughness Wakefields

This section addresses the effects of the wakefields that are excited by the interaction of the bunch charge with the roughness of the vacuum chamber surface. The model for the study is inspired by ref. [31], where a round perfectly conducting pipe wall, having a sinusoidal corrugation with longitudinal periodicity λ_s and amplitude $h_{0,}$ is considered. The results presented here were obtained in the small-angle approximation, assuming an amplitude h_0 which is much smaller than the period λ_s or, in terms of aspect ratio, $AR = \lambda_s / h_0 >> 1$.

The wake function for this model is:

$$w(s) = \frac{Z_0 c}{4\pi}\frac{1}{AR^2}\frac{2\sqrt{\pi^3}}{a}\frac{\partial}{\partial s}\left(\frac{\cos\left(\frac{\pi}{\lambda_s}s\right)+\sin\left(\frac{\pi}{\lambda_s}s\right)}{\sqrt{\frac{2\pi}{\lambda_s}s}}\right) \qquad 7.11.8$$

where a is the pipe radius, Z_0 the vacuum impedance and c the speed of light.

Figure 7.11.5 (a) shows the wake function of Eq. (7.11.5) for two different radii of the round pipe, 3 *mm* and 5 *mm*, with AR = 250 and λ_s = 25 μ*m*. It is worth noting that the two wake functions look very much alike. Figure 7.11.5 (b) shows a comparison between different geometries of the surface roughness of a 3 *mm* radius pipe. The figure clearly shows that wakes generated by roughness are quite sensitive to the roughness depth, h_0.

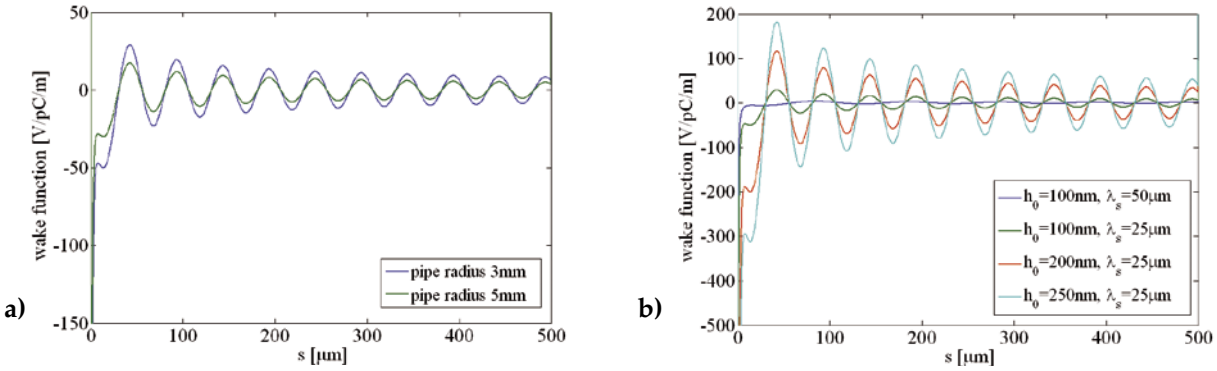

Figure 7.11.5:
Medium buch case. Surface roughness wake function in a circular cross section vacuum chambers. (a): wake functions for a = 3 mm (blue line) and a = 5mm (green line), with h_0 = 100 nm and λs = 25 μm (AR = 250). (b): wake function for a = 3mm, and AR = 500 (blue), AR = 250 (green), AR = 125 (red) and AR = 100 (cyan).

The wake potential $W_b(s)$ and the energy spread $\Delta E(s)$ are plotted in Figure 7.11.6 for the medium bunch case. Figure 7.11.6 (a) shows the results of the convolution between wake functions and current distribution, i.e. the energy deviation versus longitudinal position inside the bunch for AR = 250 and a radius of the round vacuum chamber of 3 *mm* and 5 mm respectively. Figure 7.11.6 (b) shows the energy

deviation versus *s*, for a 3 mm radius pipe and different aspect ratios *AR*. One concludes from it that aspect ratios larger than ~250 are desired.

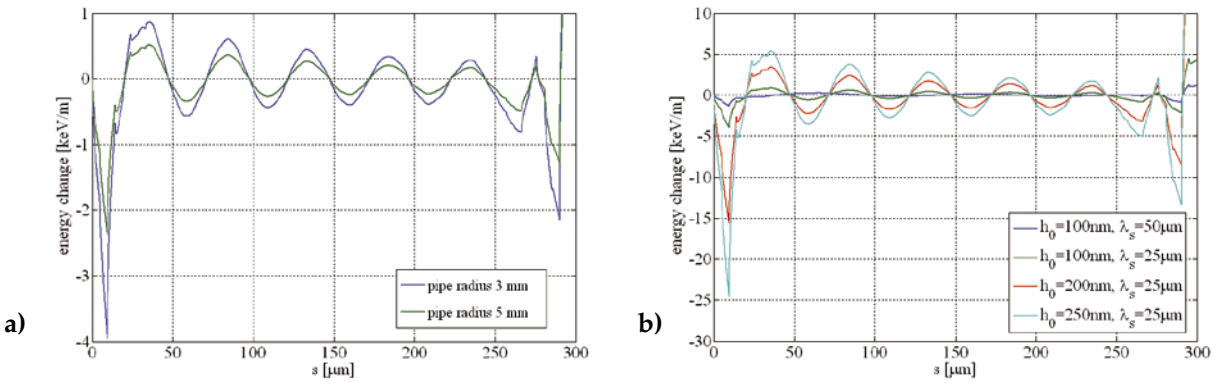

Figure 7.11.6
Medium bunch case. Energy variation induced in a circular cross-section vacuum chamber. (a): energy variation for a = 3 mm (blue) and a = 5 mm (green), with AR = 250. (b): energy variation for a = 3 mm and AR = 500 (blue), AR = 250 (green), 125 (red) and 100 (cyan).

Figure 7.11.7 shows the energy variations in the long bunch case, with the same roughness geometry. In this case wake effects are small and, in the worst case of *AR* = 100, the energy variation in the bunch core is less than 1 *keV/m*.

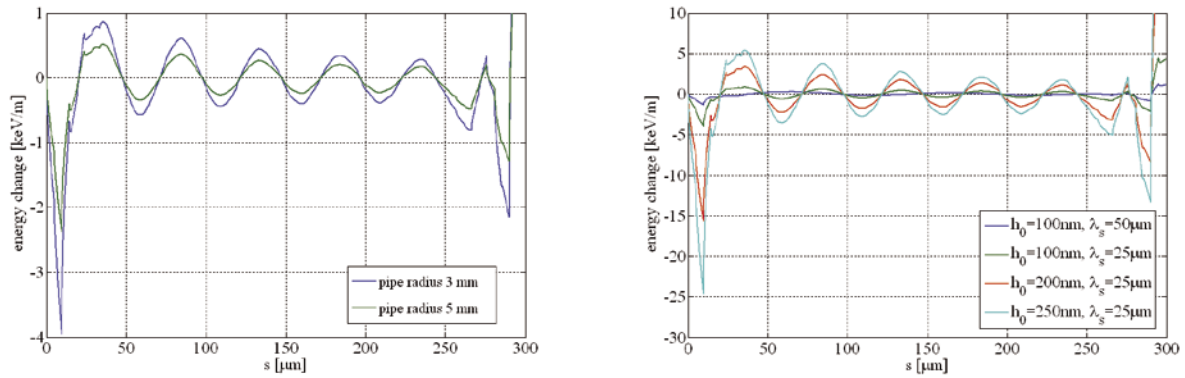

Figure 7.11.7
Long bunch case. Energy variation induced in a circular cross-section vacuum chamber. (a) Energy variation for a = 3 mm (blue) and a = 5 mm (green), with AR = 250. (b) Energy variation for a = 3 mm and AR = 500 (blue), AR = 250 (green), 125 (red) and 100 (cyan).

In addition to the effects just described an additional contribution arising from relatively low frequency synchronous modes, where surface corrugations are shallow, (i.e. those with a low AR value) must be taken into account. The effect is modelled assuming a sinusoidal wall surface modulation, like in the high frequency case [31]. The wake function for such a synchronous mode is

$$w(s) = \frac{Z_0 c}{4\pi}\frac{8}{a^2} U \cos\left(\frac{\omega_0}{c} s\right) \qquad 7.11.9$$

where the dimensionless factor U and the mode frequency ω_0 both depend on a, h_0 and λ_s. The values of these functions can be found in ref [31]. It is found that, in a 3 mm radius round pipe, the effects of the synchronous mode become significant only if AR<~ 150. The synchronous mode induced energy spread with AR = 125 and 100 are plotted in Figure 7.11.8 and Figure 7.11.9 for the medium and long bunch cases, respectively.

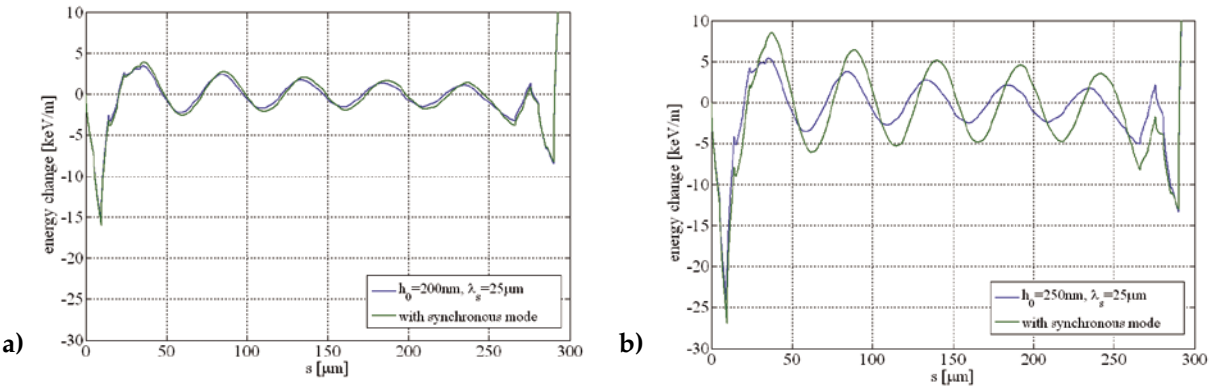

Figure 7.11.8
Medium bunch case. Effect of the synchronous mode on the energy spread in a 3mm radius pipe and aspect ratio AR = 125 (a) and AR = 100 (b).

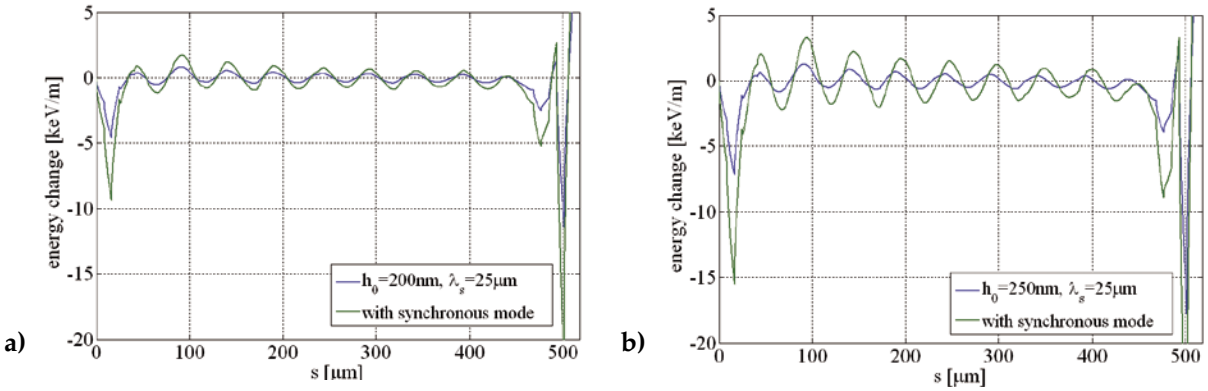

Figure 7.11.9
Long bunch case. Effect of the synchronous mode on the energy variations with a pipe of radius 3 mm and aspect ratio AR = 125 (a) and AR = 100 (b).

It is concluded that the effect of the synchronous mode is negligible if the surface roughness aspect ratio is larger > 250.

In a rectangular cross-section vacuum chamber the roughness wakefield is derived by taking into account the higher order modes of the excited field that can propagate inside the chamber. Depending on the corrugation height, these modes are more or less coupled to each other (hybrid modes). In the limit of two infinite parallel plates a continuous spectrum of modes exists whose sum tends to vanish, as shown in ref. [32]. Consequently, for any given aperture, the induced energy spread in the parallel plate (or elongated ellipse) case is expected to be lower than in a circular cross section pipe. Pending further study one can therefore assume that specifications derived for the circular pipe case also hold for a parallel plate one.

7.12 Alignment and Trajectory Control

7.12.1 Introduction

In the absence of magnetic perturbations and misalignments, the average electron beam trajectory in the undulator is a straight line on which a very small amplitude oscillation is superimposed. In this ideal situation slippage-free transverse overlap of the electron and the radiation beams is guaranteed. In a real situation, misalignment of magnetic elements, the finite resolution and misalignment of the BPMs and undulator magnetic field errors all contribute to distorting the ideal beam trajectory.

The goal of undulator magnets and quadrupoles alignment procedures is to keep the trajectory distortion in the undulator region below the tolerance specified for successful FEL operation; namely, according to simulations [34], within < 10 μm in the most critical case of FEL operation at 10 *nm* wavelength, the lowest end of the foreseen operating range.

Such a tight tolerance is mainly dictated by the phase error due to slippage between the electron bunch and FEL radiation, occurring when the electron trajectory strays from a straight line [35].

The phase error accumulated over a length l by an electron entering the undulator at an angle x' with respect to the undulator axis is

$$\Delta\Phi = k_r \cdot \Delta s = \cdot k_r \left[l \cdot \sqrt{\left(1 + \left(x'\right)^2\right)} - l \right] \approx k_r \cdot \frac{l\left(x'\right)^2}{2} \qquad 7.12.1$$

where k_r is the radiation wave vector and Δs the path length difference between FEL photons and the electron beam. In addition, a field error on the j^{th} undulator pole imparts a further angular kick to the beam that one can write

$$\theta = (2K/\gamma)(\Delta B/B) \qquad 7.12.2$$

Assuming that during the initial commissioning the beam is steered through the center of all BPMs, the residual trajectory errors are due to the BPMs finite resolution and misalignment. In a simple model in which the focusing and defocusing actions of the undulator are neglected, the average phase error per section introduced by N undulator pole magnetic errors and by the inaccuracy of the trajectory correction is [35] :

$$\left\langle \Delta\Phi \right\rangle = k_r \left[\frac{\lambda_u}{24}\left(N^2 + 5\right)\left\langle \theta^2 + \psi^2 \right\rangle + \frac{2}{N \cdot \lambda_u}\left\langle \Delta_{BPM-inac}{}^2 \right\rangle \right] \quad , \qquad (7.12.3)$$

$$\left\langle \theta_j^2 \right\rangle = \left\langle \theta^2 \right\rangle \qquad \left\langle \psi_j^2 \right\rangle = \left\langle \psi^2 \right\rangle$$

$$\Delta_{BPM-inac} = \sqrt{r_{BPM}^2 + \Delta_{BPM-pos}^2}$$

where r_{BPM} and $\Delta_{BPM-pos}$ are the corresponding BPM resolution and misalignment, k_r is the radiation wave number, λ_u the undulator period, θ the kick due to a pole error, Ψ the pole roll angle error, K the undulator parameter, γ the electron beam Lorentz factor and $\Delta_{BPM-inac}$ the overall inaccuracy of the position measurements. The mean values of magnetic pole field and roll angle errors are assumed to be independent of the pole location. The same assumption is made for the the inaccuracy of the BPMs.

To proceed, one uses the model of a N/2 periods undulator sketched in Figure 7.12.1, in which a BPM plus a corrector are placed next to both the magnet ends. Quadrupoles in between undulators are not explicitly considered because their misalignment simply changes the required initial steering corrections. Straight lengths are also not shown for simplicity.

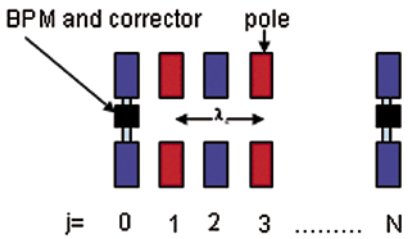

Figure 7.12.1:
Simplified model of an undulator with N/2 periods. A BPM and a corrector placed next to each of its ends are indicated.

Figure 7.12.2 shows the mean phase error in an undulator section, at 40 nm FEL wavelength, as a function of the position measurement inaccuracy due to BPMs misalignment. Pole magnetic field and roll angle random errors are conservatively assumed to be $(\Delta B/B) = 10^{-3}$ and $\psi = 10^{-3}$ rad respectively.

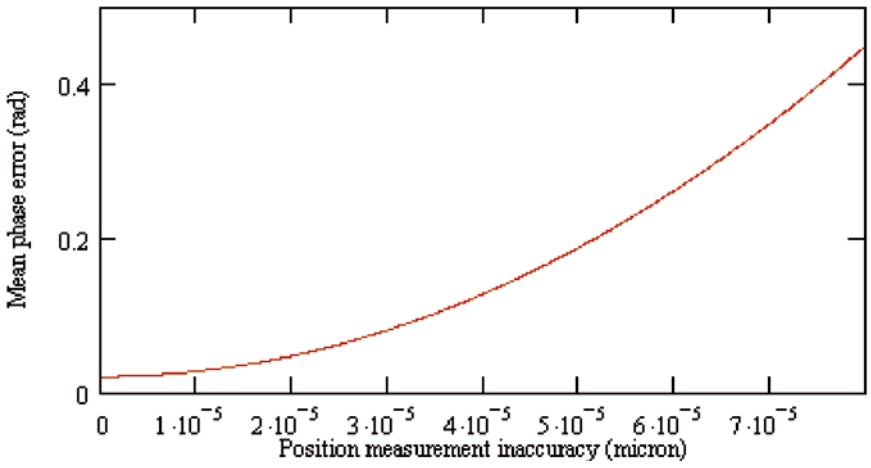

Figure 7.12.2:
Mean phase error as a function of the mean position measurement inaccuracy, specified above.

Figure 7.12.2 indicates that the tolerable absolute *rms* trajectory position error must be less than 50 μ*m* if the accumulated phase error is to be less than the 0.2 *rad* generally accepted value, verified by simulations [34].

As concerns the achievable accuracies, one notes that mechanical and electrical centers of a stripline type BPM can only be made to coincide to within ~100 μ*m*, while the achievable rms error on the position of the BPM mechanical center with respect to the ideal straight line trajectory is also of the order of 100 μ*m* (see 13.4.3), giving an overall BPM expected *rms* position error of ~140 μm. Even using cavity type BPMs, whose mechanical and electrical centers can be made to coincide to within a few μ*m*, conventional mechanical alignment errors would still be of the order of 100 μ*m*. One therefore concludes that the 50 μ*m* specification mentioned above cannot be met by conventional equipment and surveying techniques.

The FERMI alignment strategy is therefore to still use stripline beam position monitors but, in order to reduce the electron trajectory distortions to within the specified tolerance, to complement state-of-the-art mechanical alignments with the trial and error, beam-based alignment (BBA) technique pioneered at Stanford on the SLC [36], and now foreseen, in somewhat different forms, by all FEL projects under development [37, 38]. In this section it is shown that BBA meets FERMI's electron trajectory straightness specification.

The procedure foreseen for FERMI, described in more detail in the following section, is the same as for LCLS. Quadrupoles and BPMs are pre-assembled in such a way that they can be considered, alignment-wise, a single item. A set of BPM readings is taken at three different energies, numerically analyzed and used to physically correct the quadrupole magnet transverse position and to adjust the BPM position nominal calibration. By repeating the procedure several times the incoming electron beam position and angle at the undulator entrance can be adjusted to meet the desired tolerance.

7.12.2 Beam-based Alignment Procedure Details

The technique of beam based alignment is well described in [39]. The goal is to determine the position of the centers of the BPMs with respect to a straight line to better than a few μ*m* and force the electron trajectory through them.

BPMs and quadrupoles in between undulator sections are pre-assembled on a girder before installation in the tunnel and supported independently from the undulators; lattice quadrupoles are mounted on movers and equipped with dipole correctors. BPM readings being only relative, there is no need for very accurate BPM position fiducialization since their true position error, obtained through the BBA procedure and the algorithm devised for the LCLS [37], can be allowed for by software corrections of their calibration. Gross trajectory corrections are obtained by physically displacing the quadrupoles using their movers. Fine adjustments, with better than 1 μm resolution, are made using the dipole correctors instead.

It is expected that the basic procedure will need to be repeated approximately once a month with the undulator gaps wide open. Assuming the initial conditions at the undulator entrance remain the same, further perturbations of the ideal trajectory when the gaps are closed can only come from the quadrupole field errors, their residual misalignments or from the earth magnetic field.

Simulations of the whole procedure were carried out for a standard magnetic lattice, using random sets of BPM readings at 1.2 GeV, 900 MeV, and 600 MeV. All magnet settings and the electron beam

launching angle and position at the entrance of the undulator were assumed to be energy independent. Quadrupole and BPM misalignments were computed, the necessary corrections applied and the launching parameters adjusted accordingly. The process was repeated at least 3 times.

The main factors determining the ultimate quality of the procedure are the BPM resolution, the jitter in the electron beam position and angle, and, possibly, quadrupole and BPM position drifts during the time when measurements and corrections are performed. It was found that the algorithm is not very sensitive to the initial quadrupole and BPM position errors, which did allow to specify a conservative value of 100 μm for the initial mechanical misalignment of these elements. Inaccuracies in the fiducialization of the electric center of the BPMs (100 m) and of the magnetic center of quadrupoles (20 μm) were added in quadrature to the position errors. Input measurement resolutions and error values used in the simulations are listed in Table 7.12.1.

Table 7.12.1: Resolution and error values used in BBA simulations.

BPM rms resolution	1	μm
BPM offsets (uncorrelated)	100	μm
BPM offsets (uncorrelated)	50	μm
BPM mean calibration error	10%	
BPM rms calibration error	3%	
Quad offsets (correlated	100	μm
Quad offsets (uncorrelated)	50	μm
Quad fiducialization	20	μm
Quad mean gradient error	0.3%	
mover resolution	2	μm
mover mean calibration error	5%	
mover rms calibration error	3%	
beam energy mean uncertainty	1%	
beam energy rms uncertainty	0.1%	
beam position/angle initial offset	10	σ/σ′ beam
beam position/angle rms jitter	0.01	σ beam
Quadrupole and BPM drifts	±2	μm

Figure 7.12.3 shows the final beam trajectory deviation from a straight line as a function of the possible quadrupole and BPM drifts while BBA is being carried out. Seventy different simulation runs for both the horizontal and the vertical plane were done, with different seeds randomly chosen within the respective standard deviations listed in Table 7.12.2. The error bars are the one standard deviation of the 70 runs set.

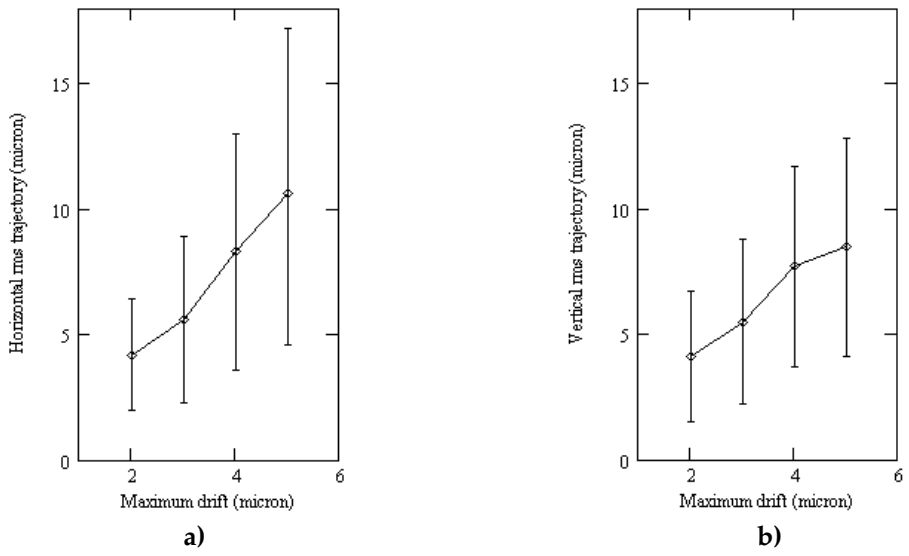

Figure 7.12.3:
Horizontal (a) and vertical (b) final trajectory deviation as a function of the maximum drifts of quadrupoles and BPMs during the BBA procedure. The probability of each drift is taken to be uniform in the range: ± (assumed maximum absolute drift value).

Figure 7.12.3 shows that, in order to meet the tolerances demanded by FEL operation at 10 *nm*, the maximum tolerable drifts should stay within ± 2 μm.

Figure 7.12.4 shows the final beam trajectory deviation at the end of the BBA procedure, as a function of the BPM resolution, the beam launching angle and position jitters during BBA operation. In order to achieve the stated goal, a BPM resolution of ≤ 1 μ*m* is needed. The resolution of a stripline BPM is 20 μm for a single measurement. Averaging the BPM readouts over a large number of pulses improves the resolution of the measurements. The beam position random error shown in the figures is the standard deviation of the mean of 400 measurements. This number of measurements reduces the statistical error on the determination of the launch angle and position to ~1% for a single shot jitter of 20% of the beam size and angular spread. This is sufficient to achieve the BBA goal. In addition, feedback systems will be implemented to bring the average of multiple beam position and angle jitter measurements within 1% of the design beam size and angular spread.

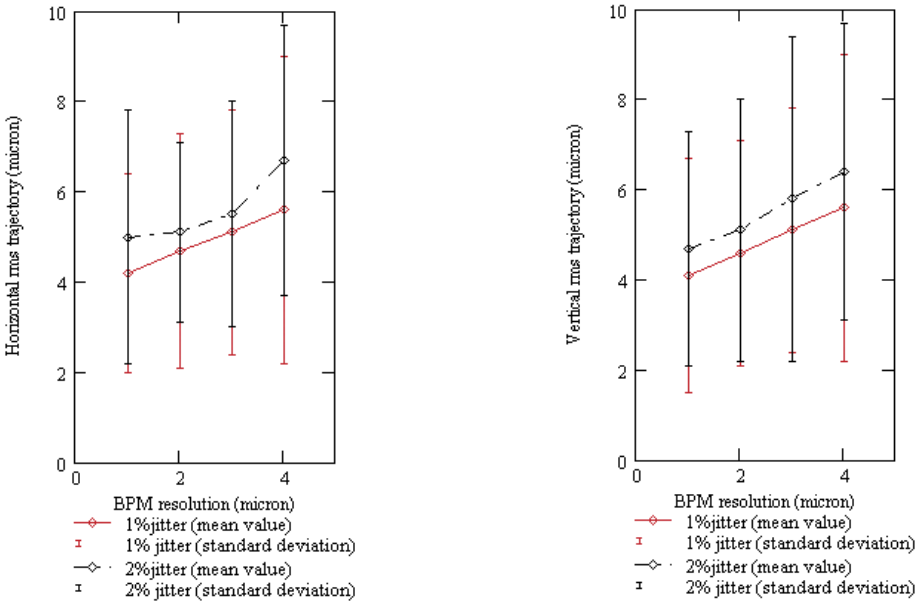

Figure 7.12.4:
Horizontal (a) and vertical (b) rms final trajectory as a function of BPM resolution. The two curves are for two different beam jitter values. The jitter is in percentage of the beam transverse dimension.

7.12.3 Earth Magnetic Field Effects

The results reported above were obtained without considering the earth's magnetic field. When the earth field is included in the simulations the trajectory is scalloped in a sequence of parabolic arcs in between quadrupoles (see Section 7.6). In order to quantify the distortions a simulation was performed, with the undulator field switched off and in the ideal case of perfect alignement. The value of the sagitta of the parabolic arcs was found to be 17 μ*m* in the horizontal plane, corresponding to an *rms* trajectory deviation in an undulator magnet of 5 μ*m*. By tuning and shimming the undulator one can reduce the distortion due to the Earth's field to the order of ~1 μ*m*; since the distortion adds in quadrature with all other effects, its contribution is negligible.

7.12.4 Conclusion

The consequences of deviations from the ideal trajectory in the undulators have been studied. It is found that FEL operation at the 10 nm shortest design wavelength, requires the electron trajectory in the undulators to be a straight line to within 10 μm rms with respect to the undulator magnetic axis and over the whole undulator length. In this section it has been shown that beam-based alignment procedures allow reaching the this goal.

7.13 References

[1] X. M. Marechal, T. Shintake, AIP Conf. Proc. 705 (2004) p. 282.

[2] K. Halbach, Physical and optical properties of rare earth cobalt magnets, Nucl. Instrum. and Methods 187 (1981) p. 109.

[3] S. Sasaki, Analyses for a planar variably-polarizing undulator, Nucl. Instrum. and Methods A347 (1994) p. 83.

[4] P. Elleaume, J. Chavanne, B. Faatz, Design considerations for a 1 A SASE undulators, Nucl. Instrum. and Methods A455 (2000) p. 503.

[5] S. Sasaki, Modeling and measurement of μ-metal shielding effect on the magnetic performanc of an LCLS undulator, proc. 28th International Free Electron Laser Conference 2006, p. 718.

[6] Z. Wolf, Introduction to the LCLS undulator tuning, Technical Note LCLS-TN-04-7.

[7] B. Diviacco et al., Construction of Elliptical Undulators for ELETTRA, Proc. 1998 European Particle Acclerator Conference, p.2216.

[8] B. Diviacco et al., Development of Elliptical Undulators for ELETTRA, Proc. 1999 Particle Acclerator Conference, p.2680.

[9] B. Diviacco et al., Development of Elliptical Undulators for ELETTRA, Proc. 2000 European Particle Acclerator Conference, p.2322.

[10] B. Diviacco et al., New insertion Devices for ELETTRA, Proc. 2001 Particle Acclerator Conference, p.2468.

[11] B. Diviacco et al., Design, Construction and Field Characterization of a Variable Polarization Undulator for SOLEIL, Proc. 2005 Particle Acclerator Conference, p.4242.

[12] M. Musardo, B. Diviacco, Magnetic field errors induced by deflection of the undulator support structure, Sincrotrone Trieste technical note, in preparation.

[13] D. La Civita et al., Misure di deformazione meccanica dell'ondulatore elicoidale EU10.0, Sincrotrone Trieste Technical Note ST/M-TN-06/08.

[14] LCLS Conceptual Design Report, SLAC–R–593, April 2002, UC-414.

[15] Dean R. Walters, LCLS Vacuum chamber review, April 20, 2006.

[16] Tesla Technical Design Report, part II, chapter 9.

[17] Soon-Hong Lee et al., Magnetic properties of undulator vacuum chamber materials for the Linac Coherent Light Source, proc. 27th International Free Electron Laser Conference 2005, p. 383.

[18] Dean R. Walters, Argonne National Laboratory, private communication.

[19] U. Hahn et al., Design and performance of the VUV FEL at the TESLA test facility at DESY, Nucl. Instr. And Meth. A 445 (2000), p. 442-447.

[20] U. Hahn, J. Pfluger, M. Ruter, P.K. den Hartog, M. Erdmann, E.M. Trakhtenberg, G. Wiemerslage, S. Xu, The vacuum chambers for the VUV SASE FEL at the TESLA test facility (TTF FEL) at DESY, proceedings of the 1999 Particle Accelerator Conference, New York, 1999.

[21] Yoshio Saito, Materials and processing of vacuum components for the high-intensity proton beam accelerator, Vacuum 73 (2004) p. 181.

[22] R. Kersevan, MolFlow User's Guide, Sincrotrone Trieste Technical Note ST/M-91/17.

[23] U. Hahn, DESY, private communication.

[24] A. Mathewson, CERN, Workshop on Vacuum for Future Synchrotron Radiation Sources, Orsay, April 1996.

[25] G. Tromba, A. Rindi, Gas Bremsstrahlung from electron storage rings: a Monte Carlo evaluation and some useful formulae, Nucl. Instrum. and Methods A 292 (1990) p. 700.

[26] A. Roth, Vacuum Technology, North-Holland.

[27] A. Wu Chao, Physics of Collective Beam Instabilities in High Energy Accelerators, 1993.

[28] H. Henke and O. Napoly, Wake Fields between two Parallel Plates, CERN/LEP-RF/89-71 CLIC Note 103, 1989.

[29] K. L.F. Bane and G. Stupakov, Resistive Wall Wakefield in the LCLS Undulator Beam Pipe, SLAC-PUB-10707.

[30] K. L.F. Bane, The Short Range Resistive Wall Wakefields, SLAC/AP-87, June 1991.

[31] G. Stupakov, Surface Roughness Impedance, SLAC-PUB-8743, December 2000.

[32] K. L.F. Bane and Gennady Stupakov, Impedance of a rectangular beam tube with small corrugations, Phys. Rev. S.T. 6, 024401 (2003).

[33] P. Craievich and C. Bontoiu, Longitudinal Resistive Wall Wakefields in the Vacuum Chamber of the FERMI FEL1 Undulator, Internal note ST/F-TN-06/17, October 2006.

[34] W.Fawley et al., FERMI@Elettra FEL Design Technical Optimization Final Report, Sincrotrone Trieste Technical Note ST/F-TN-06/16, LBNL-61333.

[35] P. Emma, Phase Slip in an Undulator with Pole and BPM Errors, Proc. 2001 Particle Acclerator Conference, p. 2742.

[36] C.E.Adolphsen, Beam Based technique for the SLC Linac, SLAC-PUB-4902 (1989).

[37] Bessy FEL Technical Design Report, March 2004.

[38] SCCS X-FEL Conceptual Design Report, May 2005.

[39] LCLS Conceptual Design Report, SLAC–R–593, April 2002, UC-414, Section 8.12.

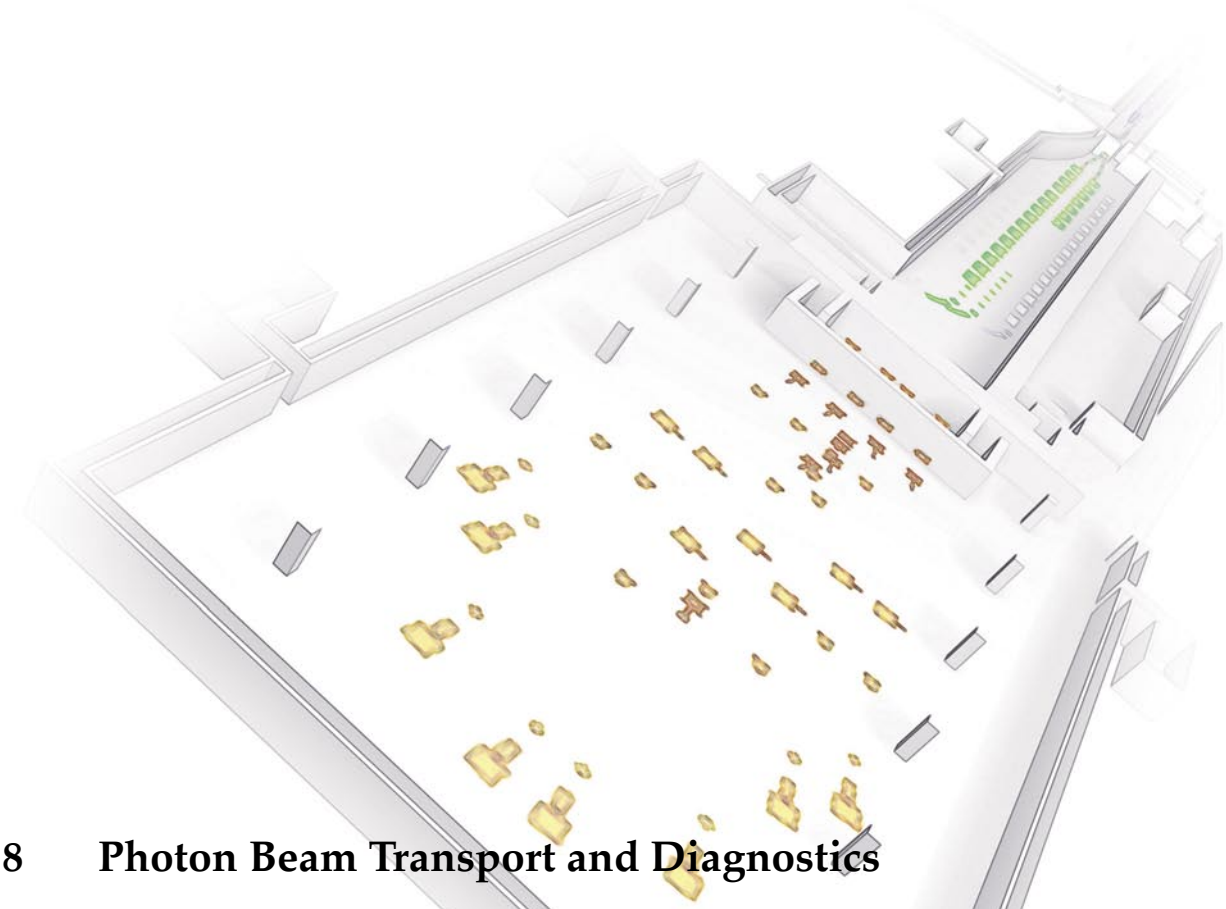

8 Photon Beam Transport and Diagnostics

Synopsis

FERMI@Elettra includes two separate undulator sections named FEL-1 and FEL-2 delivering radiation in the 100 ÷ 40 nm and 40 ÷ 10 nm ranges, respectively. For FEL-1 a 50 ÷ 100 fs pulse is delivered with a peak power of about 1-5 GW, and ~ 10^{14} photons per pulse are expected. FEL-2 is characterized by a 200 fs pulse carrying about 1 GW and 10^{12} (fresh bunch mode).

In order to characterize, select, and carry the photon beam to the experimental endstations, a set of optical systems is placed after the undulators. Characteristics such as energy, energy resolution, pulse length, intensity, arrival time, polarization, and so on, are determined by means of several diagnostics located between the undulators and the experimental hall. Gas-based systems such as absorbers and intensity monitors are mounted within window-less in-vacuum sections. The gases intercepting the radiation axis serve as natural absorbers reducing the overall photon flux. Additionally, the gas ionization signal gives information about the relative intensity of the beam. A system of slits removes unwanted off-axis radiation mainly coming from spontaneous emission. It also works as an angular collimator making possible spectral-angular filtering.

At the entrance of the experimental hall radiation coming from each FEL impinges on a plane mirror used as a power absorbing element upstream of the more delicate elements along the beamlines. Moreover, this optical element is important from the radio-protection point of view.

In order to energetically and temporally characterize the radiation, an energy spectrograph, an angular distribution detector, and a temporal pulse length-measuring device are installed. The on-line spectrograph uses a variable line spacing plane grating that passes more than 95% of the radiation in reflection (zero order) to the following beamlines, while a small fraction of the total number of photons is diffracted within the orders of diffraction. The first order, in particular, is focused and directed onto a linear spatially sensitive detector to analyze the energy spectrum of the radiation, pulse by pulse. A two-dimensional detector characterizes the quality of the emitted radiation by checking the off-axis emission to give useful feedback for the undulator tuning. A streak camera determines the pulse length with a temporal resolution tentatively below 0.5 ps.

Proper beamline designs are currently under study for the different experiments foreseen for FERMI@ Elettra. A main design goal is the possibility of serving some of the endstations with light coming from both FELs (not simultaneously). Moreover, the optics take into account the fact that the effective photon source moves longitudinally as the emission energy is varied.

Different traditional monochromator schemes are considered, and a detailed study is in progress to determine the best configuration for the needs of the different experiments. In addition, a scheme for a time preserving monochromator is described and discussed.

8.1 Introduction

Two free-electron-lasers are employed to deliver radiation from 12 to 124 eV with bandwidths of 40 and 15 meV (for FEL-1 and 2 respectively). Some experiments can work with this level of energy resolution, and keep the pulse length as short as possible. In those cases in which a higher degree of monochromatization is needed, the inevitable drawback of a lengthening the pulse length must be faced. Consequently, different designs are adopted for the two cases: high-energy resolution and short-pulses beamlines. These lines are currently being designed according to the specific users' needs. Another design takes contemplates focusing of the FEL radiation directly on the samples in the endstations.

The major design challenge is the high peak power of the FEL pulses (up to several gigawatts) that imposes severe constrains on the beamline design and on the optical coatings. Moreover, the pulsed structure of the radiation calls for proper diagnostics to characterize the pulse length, spectral profile, and intensity. These diagnostics at first serve as tools for optimizing the machine performance, and include also more specific tools as radiation angular distribution detectors.

8.2 Differences between FEL and Synchrotron Radiation

The very high peak energy arriving on the optical elements, together with the extremely short pulse length, is the main difference between FEL and synchrotron radiation (SR). This difference calls for modifications of usual synchrotron beamline designs as well as the choice of proper materials. The peak energy density from the FEL is four to five orders of magnitude higher than in undulator beams at 3rd generation synchrotron facilities. Such energy, delivered in sub-picosecond pulses, creates a large number of ionized surface atoms on the optical elements (as well as on the samples) before de-excitation processes can take place. As a consequence, desorption (ablation) of surface atoms may occur. Recent first tests carried out at 12 eV on silicon-, carbon-, and gold-coated mirrors carried on at TTF-FEL in DESY [1] can help meet this new challenge (not present at SR facilities). To provide a conservative safety

margin the FERMI@Elettra beamlines are designed with peak fluences on optical elements that are 10 times lower that the damage thresholds verified for the chosen optical materials. Furthermore, focusing of the undispersed FEL radiation onto optical elements (slits included) is avoided in favor of grazing incidence angles on the optics. Finally, surface materials with as low ionization cross sections as possible are preferred.

8.2.1 Pulsed Structure

The radiation presents a pulsed structure with frequency of 10 – 50 Hz, and a pulse length of about 50 ÷ 200 ps, with a peak power of 1 ÷ 5 GW. The product of the pulse frequency and the pulse length, for the given peak energy determines the total delivered power. To safely estimate this value it is conservative to take 100 Hz as the frequency ($T = 10^{-2}$ s) for both FELs. For FEL-1 the product is about 10^{11}, while for FEL-2 it is 2.5×10^{10} in the fresh bunch mode. Therefore, the integral power load delivered on the first optical element of each beamline is about 1 W, or even less. One must add to this value the power due to the spontaneous emission of the undulator, as well as of the radiation emitted by the bending magnet used to deflect the beam out of the photon trajectory. Also in this case the pulsed nature of the radiation guarantees very low values for the average thermal load. These values are much smaller than what expected in typical SR beamlines, and consequently standard direct side cooling (with water) is appropriate (even if operations without cooling are possible).

Another major issue related to the pulsed structure is the fact that when this kind of radiation passes through a diffraction grating its time distribution is inevitably modified. This is a consequence of the different optical paths traveled by the individual photons within the same pulse. While the path difference is close to zero in the case of mirrors, it is no longer negligible in the case of diffractive elements. In this case (Figure 8.2.1) the rays traveling at opposite edges of the pulse travel different paths, this difference increases as the footprint of the photon beam on the grating surface is larger.

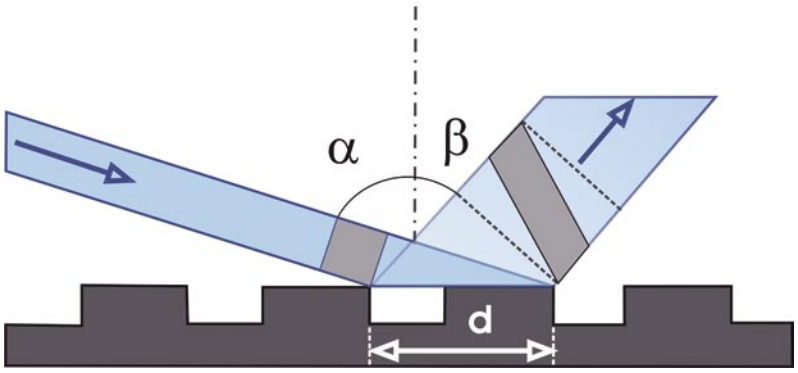

Figure 8.2.1:
Sketch of the path difference due to a single groove of a diffraction grating.

This path difference is equal to $Nd(\sin\alpha-\sin\beta)$, where N is the number of grooves lightened by the beam, d is the groove spacing, α and β are the incidence and diffraction angles, respectively. A pulse time duration enlargement Δt is determined and it can be roughly estimated to be equal to the path difference divided by the speed of light. According to the expected beam divergences and the necessary angles of incidence, Δt will range from 0.1 to 1 ps depending on the requested photon energy resolution. To be

more accurate a computer code able to simulate ray by ray the effect of this enlargement in the presence of mirrors or gratings for any source distribution has been created. An example is illustrated in Figure 8.2.2, where the effect of a high-resolution monochromator on the time profile of an incoming pulse (for two different pulse lengths) is simulated.

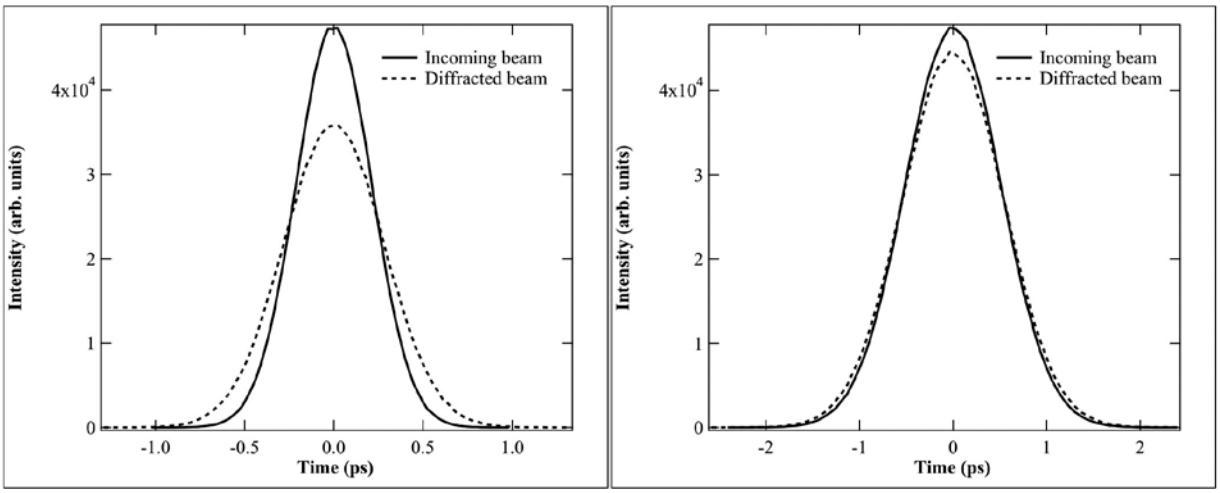

Figure 8.2.2:
Effect of a monochromator providing a bandwidth of less than 2 meV at 50 eV with a 1.2 ps pulse (right) and 0.5 ps pulse (left). The solid curves represent the incoming beam time profile, the dotted curves the diffracted beam profile.

Of course, one should always take into account the fact that a monochromatic beam can never be shorter then its transform limit, therefore, for a high resolution monochromator, thanks to the very low divergence of the beam, the effect of the enlargement due to the grating is negligible (or comparable) with respect to the natural time broadening due the lower energy bandwidth. The only case in which the grating effect is relevant is the case of low-resolution monochromators for FEL-1.

Clearly, when there is a strong demand very high-spectral purity of the photon beams in the experimental endstations, non-standard solutions must be adopted. One possibility is working with a double grating, time preserving monochromator (described in Section 8.4.3.2). This configuration uses two diffraction gratings mounted in opposite angle configurations: $\alpha \rightarrow \beta$ for the first one, $\beta \rightarrow \alpha$ for the second one (see Figure 8.2.3). In this way the longer path traveled by a photon on the first grating is compensated by traveling a shorter path on the second, and vice versa.

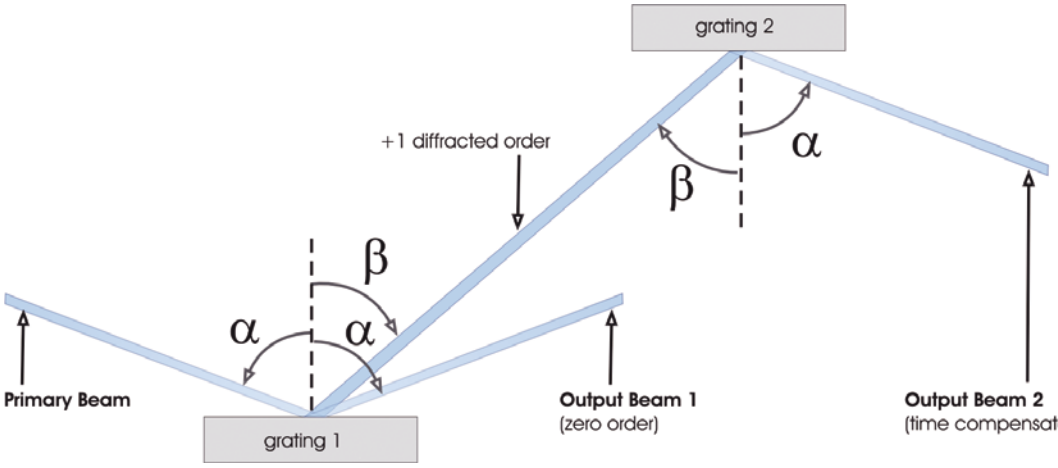

Figure 8.2.3:
Time-compensated monochromator working in α→β – β→α configuration.

8.2.2 High Powers

One of the main problems related with the very high peak brilliance is the power arriving on the optical elements in a very short temporal interval. Even if the average power is of the order of few Watts, requiring just a simple cooling system to prevent small mirror deformations, the peak power can go up to 10 GW in particular for FEL-1. To simulate the behavior of the FEL with enough margin to include variations of both pulse length and peak power, and to give a safe estimate of the behavior of the optics under such a high energy density, a box-shaped pulse has been used. In particular, for a 200 fs –pulse an energy of 2 mJ is delivered. Since the divergence of the beam is quite small, 50 μrad, it produces an energy density up to 0.2 J/cm^2 at 10 meters from the source. Such an energy density is higher than the damage threshold of several materials. Consequently grazing angles of incidence are used.

The absorbed energy density is also a key parameter, since the typical lattice disruption value of the order of 1 eV/atom must be not exceeded [2]. This quantity depends on a combination of parameters including the angle of incidence, the material attenuation length and atomic density, and the reflectivity. In particular, reducing the grazing angle of incidence introduces a competition between the reduction of the optical surface power load and the reduction of the geometrical dilution effect (due to the shorter penetration depth) leading to an increase of the load on the very first layers.

An experimental study was performed by A. Andrejczuk *et al.* [3], where the damage threshold of some materials was determined at 98 nm-wavelength and normal incidence. Shorter pulses or longer wavelength (for fixed pulse energy) determine a lower damage threshold. Moreover, the damage threshold is further reduced if the interval between two consecutive pulses is of the same order of the relaxation time of the materials [4]. Typically the ablation is a thermal process, and this means that it is expected to be lower on materials where the energy can be carried away rapidly [5].

There are some pre-process, before the ablation, which do not "destroy" the surface, but which can drastically deteriorate its optical properties. For instance, in bare silicon, the ablation threshold is 3.7 eV per atom for a 20 fs pulse at 780 nm (6.2 eV/atom for 500 fs) while the melting threshold is 2.6 and 5.4 eV/atom for 20 and 500 fs respectively [6]. In other materials (graphite or diamond) the damage threshold is from 2 to 4 times smaller than the ablation one [7].

Nevertheless, dedicated research efforts, including experiments, are required to improve understanding of the mechanisms contributing to ablation of optical surfaces, with the aim of properly defining the bulk and coating materials for the beamline elements.

Possible candidates for coating and/or bulk mirror materials are carbon and silicon, due to their sufficiently high damage thresholds and the possibility of realizing good quality optical surfaces with both materials. As a safety margin, designs with energy densities 10 times lower than the expected damage thresholds are preferred. The thresholds measured at 98 nm were redefined at different wavelengths simply by taking into account the differences in cross section at different energies. Also this assumption requires further study.

In table 8.2.1 the expected energy density 10 meters from the source and the necessary minimum angle of incidence to work within an energy density 10 times below the damage threshold are reported for an high density graphite coating. For FEL-2 there are no major constrains, while for FEL-1 great care must be used in selecting the position and angle of incidence for a mirror.

Table 8.2.1: Expected energy density and maximum angle of incidence at 10 and 20 meters from the source for different possible machine configurations, for a carbon-coated mirror.

FEL	*Pulse Length*	*Peak Power*	*Energy density @ 10m*	*Safety incidence angle C coating (1/10 damage*
1	200 fs	3 GW	180 mJ/cm^2	2°@10m / 6.3°@20m
1	1 ps	3 GW	890 mJ/cm^2	0.4°@10m / 1.3°@20m
1	200 fs	10 GW	590 mJ/cm^2	0.6°@10m / 1.9°@20m
2	400 fs	1 GW	600 mJ/cm^2	2 @10m
2	1 ps	0.3 GW	450 mJ/cm^2	2.6°@10m
2	1 ps	1 GW	1500 mJ/cm^2	0.8°@10m

To take into account also the volume dilution effect some calculations have already been made for the 4GLS source [8]. In this study the damage thresholds obtained experimentally for normal incidence 12.7 eV-photons [3] have been rescaled for different energies and 5°-grazing angle of incidence. In particular, it was found that within the 10 – 110 eV range there is a multiplying factor ranging between 20 and 100 for the damage threshold of carbon and silicon. This means that the thresholds found for normal incidence are increased going to grazing incidence, even if the reduced penetration of the photons in the material is taken into account.

Together with the issue of mirror damage, damage induced by the radiation on different optical elements like gratings, slits, multilayer coatings, transmission beam splitter should be taken into account. As an

example, the radiation impinging on a diffraction grating hits the groove walls with angles reaching very large values (see Figure 8.2.1 as a guideline), up to quasi-normal incidence. The effect on the groove shape is still to be determined and proper studies and tests must be carried out in order to determine the best groove profiles. More generally, tests on the damage threshold for different optical elements are mandatory and must be performed to help selecting the most efficient optical systems for the beam transport.

8.2.3 Coherence

The measure of the spatial coherence of the beam can be made in several ways. While all these methods are invasive, fortunately, one can reasonably assume that the transversal coherence does not vary from shot to shot. Interference effects could be used to measure the transverse coherence length, possibly in the whole beam in a single shot (like in the Fizeau or Michelson experiments). In contrast, it is very difficult to preserve the coherence along a beamline, simply because the presence of non-perfect optical elements. If an high degree of coherence is necessary, the relevant optics must have a surface profile much better then what is requested for SR beamline. Residual slope errors in the order of 0.1 μrad (rms), including the holding effect, are necessary. This implies a substantial effort in metrology, probably including "at wavelength" metrology in a dedicated facility.

8.2.4 Beam Splitters and Filters

Several experiments require the splitting of the incoming beam into two beams for a further recombination (study of interference effects), or with the purpose of their relative delay for pump-probe experiments. The easiest way to split the beam at these energies is the use of a diffraction grating (Figure 8.2.4).

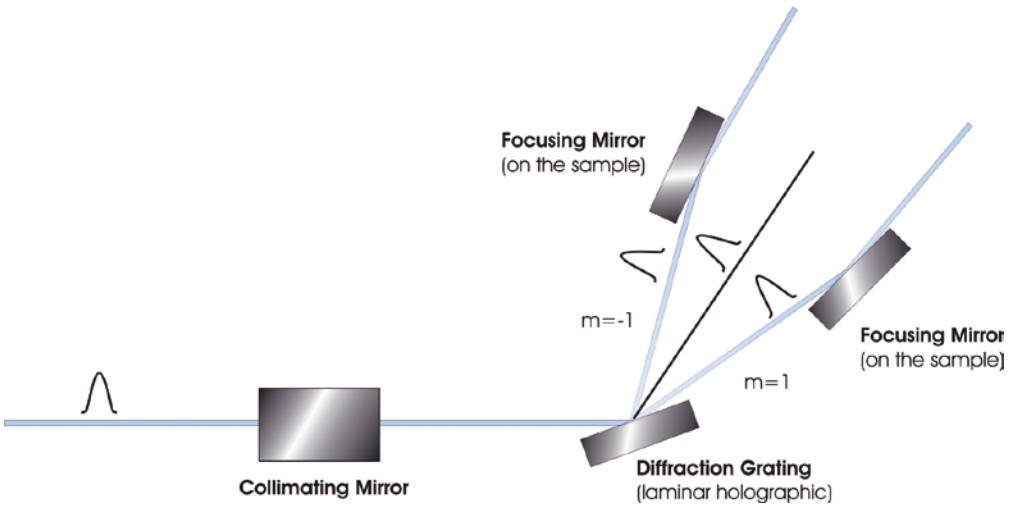

Figure 8.2.4:
Scheme of the beam splitter proposed for the time-resolved spectroscopy beamline (Masciovecchio, Ruocco, Sette, Torre).

The grating disperses the same wavelength at different diffraction orders including the zero order, which corresponds to the reflected beam. Several needs must (or could) be met: 1) splitting the beam at different directions but with almost the same intensity (if necessary), 2) avoiding temporal lengthening of the pulse (if necessary), 3) permitting the use of both beams within a wide energy range (the direction of the diffracted beam depends on the incoming wavelength). Nevertheless, optimizing case-by-case, possible solutions exist. Figure 8.2.4 presents a scheme planned for one of the beamlines proposed for FERMI@Elettra (Masciovecchio, Ruocco, Sette, Torre). In this case, the efficiencies of the +1 and –1 order are almost the same (17.5 and 17.8%).

Another option is the use of thin metallic foils that pass part of the radiation and reflect the remainder at a particular angle. This task is challenging because the metallic films, often used as filters, do not have surfaces as good as a mirrors. Moreover, they are easily damaged by the incoming peak energy. This approach as well as the use of multilayer optics requires further study. Regarding the filters, most of the work is done by the monochromators. With filters one can remove energies outside the central Gaussian peak from the optical spectrum.

Some experiments require suppressing higher harmonics or reducing their intensity. The latter task can be accomplished by using gas cells, with or without entrance and exit windows. Except for the determination of the proper gas mixture and pressure, cell design is not a significant problem (see section 8.3.1). This solution, in some cases, is also useful for suppression of higher orders, but multilayer mirrors or transmission filters are probably better. A detailed study of the filtering is foreseen during the conceptual design of the first approved beamline for FERMI@Elettra.

8.3 Optical Systems before the Beamlines

Several optical systems serve as interfaces between the FERMI@Elettra undulators and the experimental stations, performing many different functions. Besides the installation of the beamlines in the experimental hall (discussed in the next section – 8.4), other systems are inserted between the exit of the undulators and the first mirrors of the beamlines. These include differential pumping sections hosting gas I_0 monitors and absorbers, some kind of angular divergence defining systems (e.g. slits), and the very first mirrors of the beamlines acting as power absorbers and radio-protective elements.

8.3.1 Absorption Cell and I_0 Monitor

The FEL radiation is transported through a window-less system starting from the exit of the undulators. To host sections in which it is possible to perform gas absorption measurements, differentially pumped sections are inserted before the protective wall in front of the first mirrors. Here a double task can be accomplished: the attenuation of the FEL radiation intensity and the monitoring of its absolute intensity. The former is realized through the use of high-pressure noble gases that are pumped at a pressure of 0.1 mbar as an upper limit [9] into a 6-meter-long cell. Figure 8.3.1 reports the calculated transmission of this cell for different gases at pressures of 0.1 and 0.15 mbar in the spectral range 10 to 100 nm.

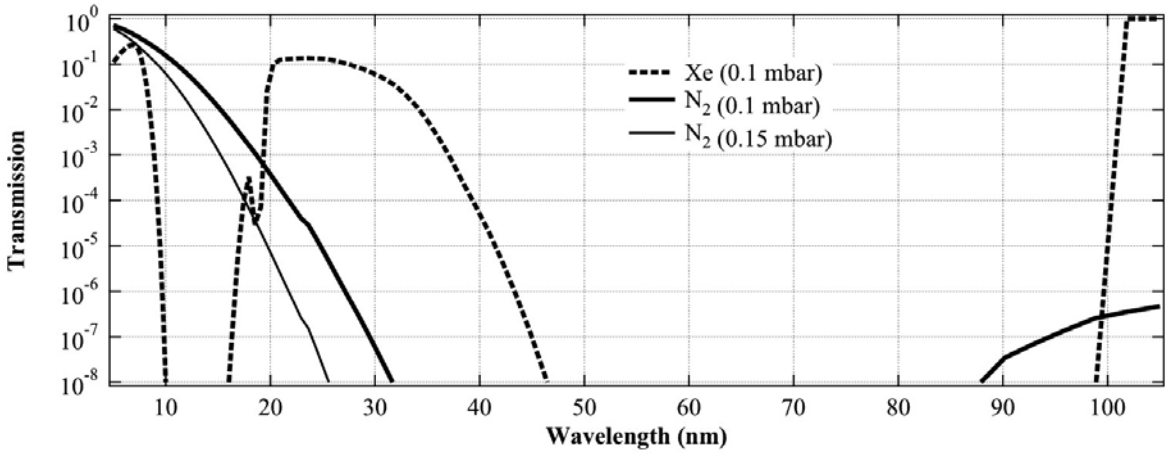

Figure 8.3.1:
Calculated transmission of the gas absorber for different gases and pressures (gas cell is 6 meters long).

It is clearly possible to attenuate the intensity of the FEL radiation by several orders of magnitude by selecting the proper gas. From about 20 to 100 nm nitrogen can be used, while between 19 and 9 nm xenon is preferred.

The second task to be accomplished within the differentially pumped section is the monitoring of the radiation intensity by a gas-monitor / detector, probably similar to that developed for the DESY FEL [10]. The monitor, based on atomic photoionization of a rare gas at low particle density ($P = 10^{-5}$ mbar), is free from degradation and almost transparent. Consequently, it is suitable for on-line measurements. Moreover it can simultaneously detect photo-ions and photo-electrons, and measure the absolute photon number per pulse.

Also within the same vacuum chamber, pairs of parallel plates are installed for beam position monitoring. This item is discussed in Section 8.6.3.

8.3.2 X-ray Slits

The FEL radiation emitted from the undulators entering the x-ray beam transport system consists of an intense coherent emission with a rms angular divergence of about 50 μrad for FEL-1, and 15 μrad for FEL-2, surrounded by a broad spontaneous distribution with a larger angular divergence. For some experiments the low energy spontaneous emission constitutes background noise that must be removed. Other experiments may require removing greater amounts of the off-axis radiation. These considerations impose the introduction of an element (collimator) to delimit angular divergence. The collimator has not yet been designed. Careful consideration and detailed calculations must be carried out to determine if it is possible to place horizontal and vertical double slits before the beamlines. These cannot be used for focused, undispersed FEL radiation due to the ablation effects on the jaws. Another possibility [1] is the

baffling of the grating, which can safely improve the pulse length without excessively deteriorating the energy resolution. Unfortunately, since baffling cannot reduce the effective source size, as an entrance slit would do, this method cannot improve the energy resolution if the beamline is limited by a large source size.

8.3.3 First Mirrors

Two plane mirrors (one for each FEL) are placed at the entrance of the experimental hall, still behind a protection wall. Their role is to deflect the FEL radiation by about 3° to prevent unwanted radiation (including bremsstrahlung, undulator x-rays and so on) passing through and traveling along the beamlines and/or in the experimental hall. As these mirrors also serve as power absorbers, much less energetic radiation is delivered to the more delicate, downstream optical elements, such as the variable line spacing (VLS) grating, located after the mirrors. As seen in Table 8.2.1, to prevent optical surface damage these mirrors are located at least 15 meters from the undulator exits, and work with an incidence angle of 1.5°. Very likely the coating material will be carbon or gold, due to their excellent optical characteristics.

8.3.4 Time Arrival Monitor

A system to monitor the arrival time of the photon pulses may be installed just after the undulator exit, close to the electron beam dump section. Here dipole radiation is emitted when the electrons are forced to bend away from the undulator axis and towards the beam dump. This radiation, in principle, can be used as a marker for the time arrival of the photon beam pulses into the optical systems (beamlines) since it is directly related to the electron bunch time arrival in the undulators. Different methods can be employed to measure the time arrival jitter. One option is to use an optical streak camera to measure the dipole radiation with resolution ~300 fs, thus giving good information about long-term drifts [11]. Another possibility is to employ electro-optical sampling of the electric field surrounding the ultra-relativistic electron bunch. This task is accomplished by monitoring the transient birifrangence of a crystal (like ZnTe) placed adjacent to the electron beam. In this way resolutions below 100 fs are achievable [12].

8.4 Beamline Design

The design of the photon beam transport system is the major task to be accomplished to fulfill the requests of the FEL users who work on the endstations. This work must take into account the various characteristics of the radiation such as pulse length preservation, monochromatization and energy resolution, source shifts compensation, focusing in the experimental chambers, beam splitting, and so on. Obviously, different beamlines will have different needs that cannot be fulfilled simultaneously, for example, short pulses and high energy resolutions. While a thorough design and description of the beamlines of FERMI@Elettra is still in progress, some conclusions about this issue may be already drawn.

8.4.1 Source Longitudinal Shift Compensation

The FEL radiation is generated in the final sections of the radiators used for FEL-1 and FEL-2, but the effective longitudinal position of the photon source is energy dependent; shifts as large as 5 meters are foreseen. If a small spot is required, it is probably necessary to employ adaptive focusing mirrors. Use of mechanical benders and piezoelectric bimorph mirrors [13] has been already made at ELETTRA with optics developed by SESO. If a homogeneous unfocused beam is required, the bimorph mirrors are preferable, although it still must be determined how close to the experimental chamber a non-bakable mirror (like this one) can be hosted.

Since the beam can move longitudinally, it is almost impossible to have a spot smaller then about 5-10 μm. In fact to have such a small spot the source would have to be de-magnified by a factor 20 or more, and the divergence would increase the same amount. A source distance change of *X* produces an image shift of *X* divided by the square of the demagnification. That means that r a demagnification of 20 and a beam movement of 2 meters produces an enlargement close to 10 μm. This demagnification cannot be compensated by adaptive optics, but it can be minimized by reducing the accepted beam divergence or by proper optical setup.

8.4.2 FEL 1-2 Switching Mirror Chamber

One of the main goals of the photon beam transport system design is the possibility of directing (not simultaneously) the radiation generated by either FEL into the same endstation(s). This requirement enables a broad range experiments without the need of moving the endstations in the experimental hall. To fulfill this requirement, a preliminary layout of the experimental hall with the beamlines has been realized (see Figure 8.4.1). The critical dimension is the distance between the two undulator sections from which the two FEL beams originate. This value, which has been set to 2 meters (Chapter 7 for details), imposes some limitations on the beamline design.

A reasonable solution is depicted in figure 8.4.1. The two parallel beams coming from the undulators are deflected by the first mirrors towards two VLS plane gratings used for diagnostics (see Section 8.6.1). The VLS gratings then send the zero order beams to the main switching mirror chamber. This chamber can re-direct each of the two incoming beams to the three following branch-lines, where the beamlines are realized. As a consequence, the chamber hosts four mirrors since in two cases the beams simply pass through it without need of deviation. Additional beam switching can be performed along the two external branch-lines following the 3-way switching chamber. In this way serving all the endstations depicted in Figure 8.4.1 with both FELs can be accomplished. A complete mechanical design must be

produced in the near future probably involving mirror exchange systems very similar to those typically used in the ELETTRA switching mirrors (see Section 8.5 for further details).

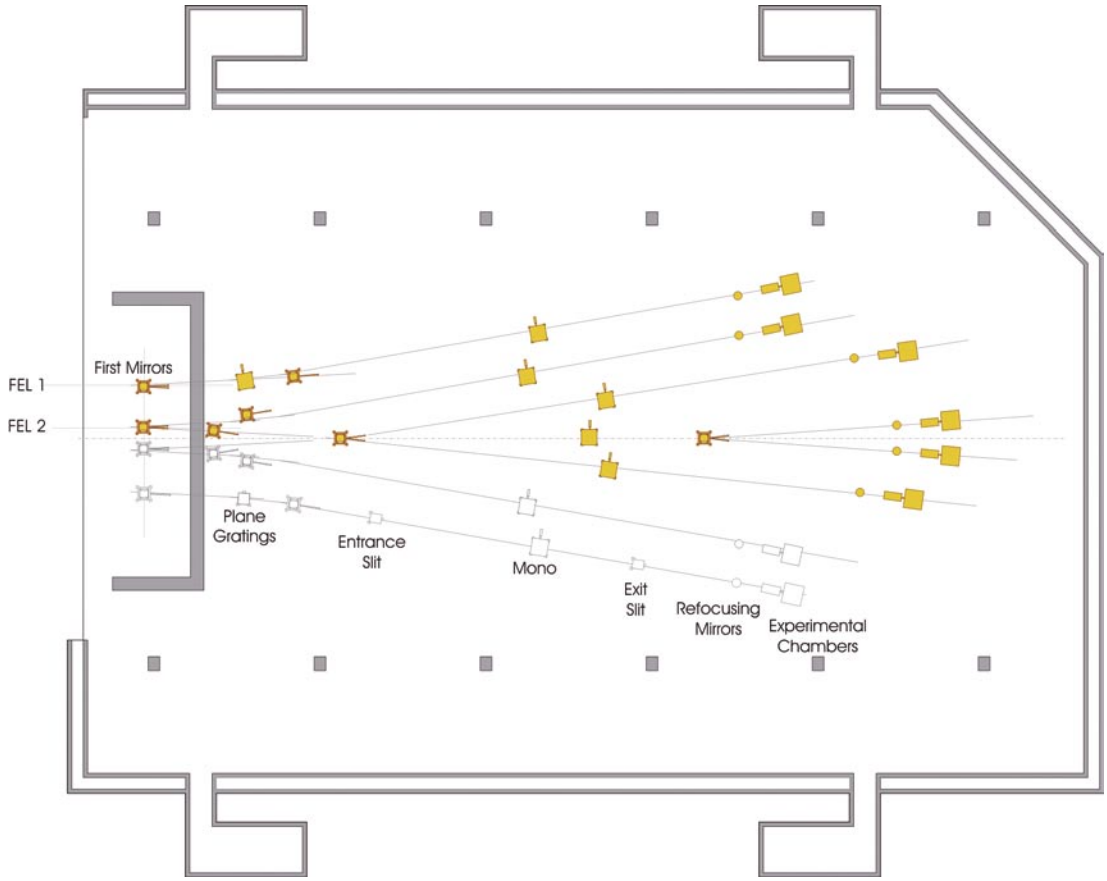

Figure 8.4.1:
Tentative layout of the experimental hall.

8.4.3 Monochromators

As already stated, some experiments/beamlines may need to stretch the bandpass delivered by the FEL at the cost of a pulse elongation. Consequently, monochromators must be installed along some beamlines to meet this requirement. They are based on diffraction gratings working at grazing angles of incidence, assuring low power densities on their optical surfaces. The use of diffraction gratings also helps in splitting the beam, when needed, due to their capability of diffracting the radiation in several orders, including the zero order (specular reflection). A comparative study of the several possible schemes has to be carried out to select the best solution for the different needs. In addition, monochromatized beams could produce without pulse elongation through the use of time preserving monochromators. These

instruments include two gratings working in opposite angle configurations to monochromatizes the pulse, while maintaining its original duration.

8.4.3.1 Traditional Schemes

In the energy range of FEL-1 the best monochromators operate at normal incidence. Unfortunately, the high energy density at FERMI@Elettra makes this solution impossible. A second design constraint is that the source distance changes for different selected energies. The ideal solution for compensating source distance variations is a variable included angle spherical grating monochromator (Padmore monochromator [14]), which gives the possibility of freely choosing the angles of incidence and diffraction, and consequently the position of the monochromator image. A plane grating with variable groove density [15] could work in a similar way and, in principle, produces less aberration in the final image, but it cannot provide a non-monochromatic focused beam. The SX700 (variable included angle plane grating monochromator [16]), with a collimating mirror before it and a focusing mirror after, could work properly but it involves four optical elements. A possible solution is the Dragon monochromator [17], for which the exit slit is movable to follow the variation of the focal distances for different energies. The beam can be refocused later on the sample by proper adaptive optics (see next paragraph). Therefore, several approaches can be used but the one least sensitive to beam instability, source movements, and that lets the beam pass through with the least disturbance must be preferred.

The major challenge is the realization of a system that cuts higher orders. In this energy range the efficiency of the second order of diffraction is still quite high as compared to the first one, even with a well-designed grating profile. It probably will be necessary to use filters, but this strongly depends on the level of higher harmonics produced by the undulators.

8.4.3.2 Time Preserving Monochromator

Most beamlines will use two monochromators, one with large band pass, used to “clean” the pulse from any photons with energy outside the central Gaussian peak, and one that selects a very narrow bandwidth.

For the first task, a coarse grating with few lines per millimeter (50 or less) is enough, considering that a bandpass of the order or 10 or more meV is expected. Such a grating has an effect only in the case of FEL-1, in which a pulse of about 100 fs is expected. Thereafter a grating with 33.3 lines/mm, suffices to select a 5-10 meV band pass, increasing the pulse length to 0.2-0.25 ps (Figure 8.4.2, left). Pulse stretching can be compensated by the use of a second grating with working angles inverted with respect the first one. In this case the rays that have traveled a longer path through the first grating will travel a shorter one in the second, and vice versa. In practice, on a case-by case basis, one must assess if it is better to “recompress” the signal, losing a factor 2 in intensity (grating efficiency in this energy range is not higher than 50%) or to use a slightly longer pulse.

In the case of FEL-2, when a 5-10 meV bandpass is required, it suffices to use a single grating, since the lengthening of pulse duration is negligible (Figure 8.4.2, right). In this case a 66.6 l/mm grating is used and an incoming pulse length of 0.5 ps is supposed.

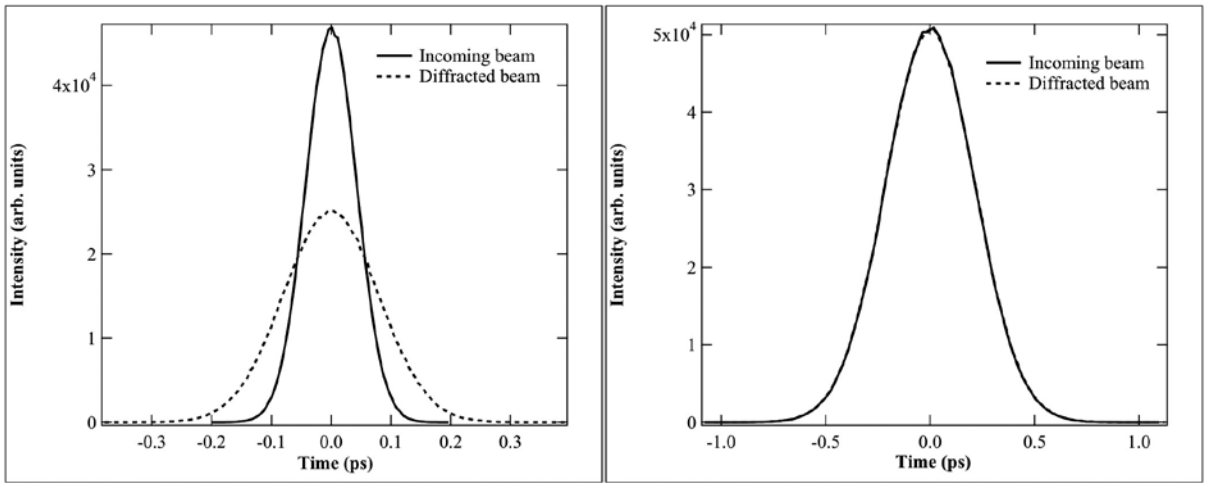

Figure 8.4.2:
Effect of the temporal lengthening of the pulse due to the monochromator to select a energy band pass of 5-10 meV in the case of FEL-1 (left side) and FEL-2 (right). The effect is similar in the whole energy range and is completely negligible for FEL-2.

When a high-resolution monochromator is needed in principle, the effect on the beam duration is more evident but it is probably possible to work below the transform-limited value (as in Figure 8.2.2). Therefore, in the design of a monochromator the temporal lengthening has to be taken into account. The proposed design should be optimized with respect to groove density and angle of incidence in such a way as to minimize this effect, avoiding stretching of the pulse beyond the transform limit.

A test of a time compensating double monochromator using commercial UV gratings made by Jobin Yvon is scheduled in the laser laboratory of ELETTRA where a 260 nm pulsed source is available. This is an almost costless test, performed to gain experience on the necessary precision, tolerances and practical problems related with the realization of a real time preserving monochromator.

8.4.4 Refocusing Optics

Refocusing sections are needed after the monochromators (when used) in order to focus the photon beam onto the samples in experimental chambers. Several optical designs may be used, depending on the spot sizes requested. These designs may include the use of single toroidal mirrors to refocus the beam in both horizontal and vertical directions, or the use of pairs of mirrors (spherical or plane elliptical) in a Kirkpatrick-Baez configuration (with the possibility to use adaptive optics if necessary). No major optical and technical problems are expected in the design and realization of these sections.

8.4.5 Experimental Stations and Related Equipment

Typically, experimental stations are placed at the end of each beamline. Independent of the details of the experiments to be performed, sufficient room is needed around each experimental station to allow the

installation of the experiment-related instrumentation such as optical tables, preparation and sources chambers, transfer lines, racks for electronics, pumping stations and so on. To achieve this goal the optical design of the beam transport system includes planar optical elements to separate the different beamlines as much as possible.

Pump-probe experiments will require a reference signal supplied to the endstations including information about the time arrival of the single pulses. For this purpose an optical signal derived from the seeding laser will transported to the endstation and used to select the optimal timing set-up.

8.5 Mechanics

This section provides an overall layout and a preliminary design of the beam transport and diagnostic system. Particular attention is paid to those elements that differ from or are more critical to experimental performance than those developed for the ELETTRA beamlines.

8.5.1 Layout

The overall layout of the beam transport and diagnostic system (Figure 8.5.1), based on the optical scheme described in paragraph 8.4 (Figure 8.4.1), accounts for the considerations described in the previous sections.

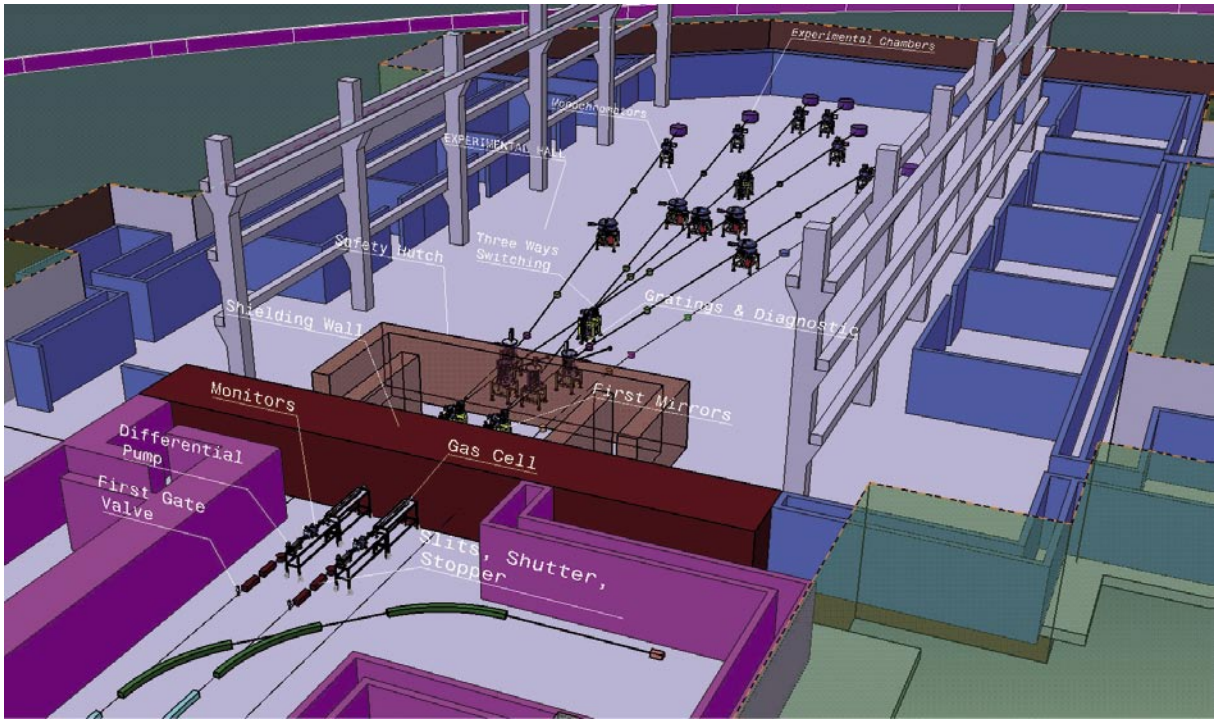

Figure 8.5.1:
Preliminary beamline layout and experimental hall.

The 3D beamline skeleton consists of a set of cylinders with a vertical axis representing the vacuum vessels containing a generic optical element (point of interaction between the photon beam and any optical surface); the cylinders are connected to each other by pipes with the horizontal axis representing the beam path with the proper angles in the point of intersection. This simple scheme is adopted for efficiency using the Sincrotrone Trieste CAD system. The choice of a relatively small number of parameters (FEL axis distances, position of the chambers along beam axis, grazing angles) makes it possible to reflect the optical layout updates (within the basic scheme) in a slim and fast model. The skeleton is then "dressed" by positioning the proper chambers substituted for the vertical cylinders and covering the "beam pipes" with the proper vacuum elements (chamber, valves, etc.) as the mechanical design proceeds.

In practice it is neither possible nor desirable to freeze the layout of the beam transport and diagnostic system at the outset. In fact during the initial commissioning of the facility not all the beamlines will be installed and or ready for use. Therefore the layout is constructed as 1) a basic tool to drive any further development of the overall system, and 2) to anticipate all the necessary space for building and plant layout from the very beginning.

In Figure 8.5.1 the optical scheme is reproduced in true dimensions, and an external beamline coming out from a possible additional undulators chain (say FEL-3) is included to account for future developments.

The layout study has proceeded by recognizing those beamline elements already working in 3rd generation synchrotron beamlines that can be customized for the new beam transport and diagnostic system. Particular attention has been dedicated to those elements that will be common for the future beamlines. These elements (Switching, Gratings and Diagnostic, etc.) are described in the next sections, and the associated models provide the mechanical schemes for the final design. In other cases the simplified CAD models (Prefocusing, Refocusing, Monochromators, Slits, etc.) are simply elements extrapolated from present applications that look "reasonable" even for future application. They are put into the layout to gain understanding of the relative position and the possible interferences between the beamlines with realistic models. Moreover, the resulting layout is useful for understanding how to develop the auxiliary systems, i.e. cooling piping, electrical cabling (both power and signals), pneumatic systems, etc., and the basic schemes for the overall vacuum system.

8.5.2 Experimental Hall

The mechanical layout of the overall beamline transport and diagnostic system scheme drives some of basic system requirements the buildings and plant installations, (see Chapter 14). The FERMI@Elettra photon source will be constructed using the existing LINAC, presently used as pre-injector of the ELETTRA storage ring. The LINAC will be modified for the new FEL application but the basic structure in the present position is preserved, i.e. the electron beam axis is -3.9 m underground (LINAC floor -4.75 m), with respect to the conventional ground zero level (Elettra experimental hall). Since maintaining high beam quality limits the electrons optics to small angles of deflection, to the FEL layout avoids vertical deflections that imply very long slopes before the undulator sections. As a consequence the experimental hall itself is constructed underground, since the photon beam has the same level. For the experimental hall the distance between the floor and the photon beam has been increased to 1.3 m (vs. 0.85 m in the LINAC tunnel), i.e. the resulting floor is -5.2 m under ground level.

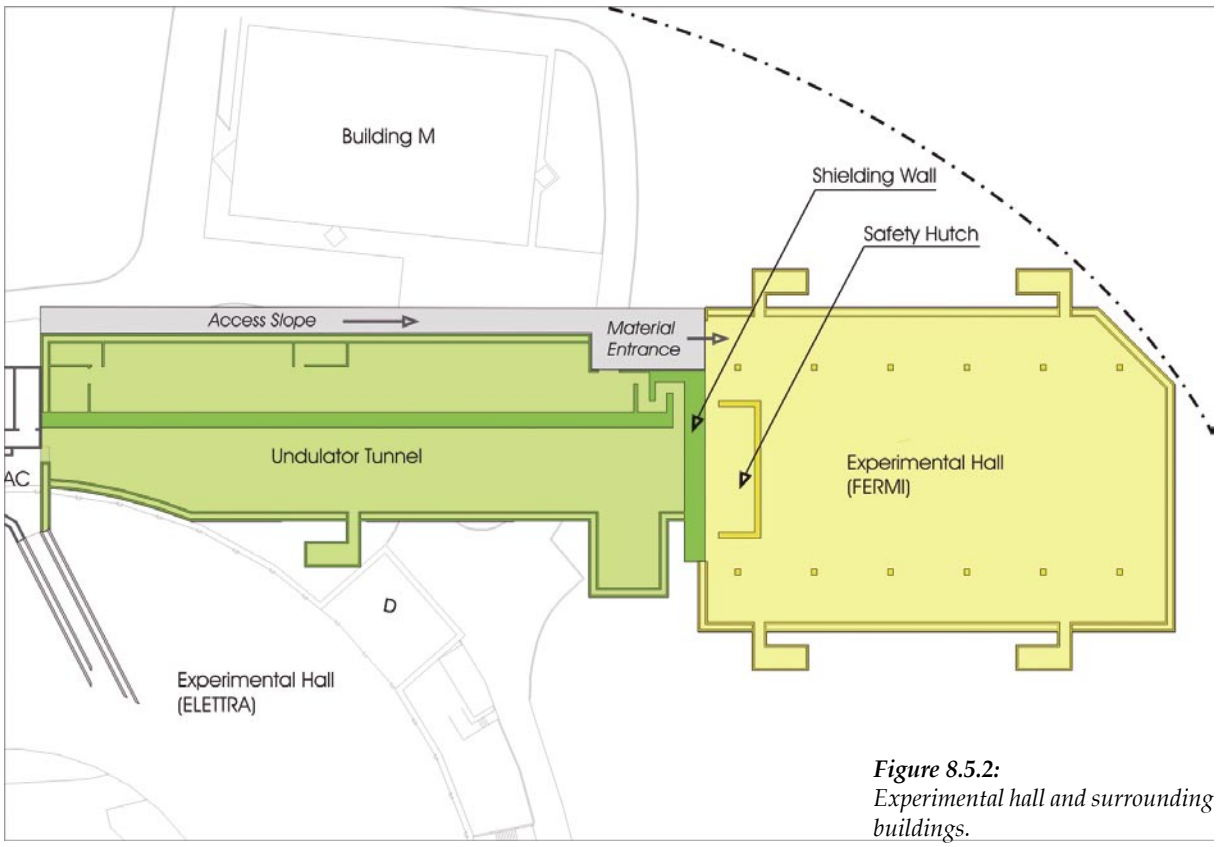

Figure 8.5.2:
Experimental hall and surrounding buildings.

The overall dimensions of the experimental hall are approximately 60×40 m (L×W), and its position with respect to the absolute axis system (origin in the ELETTRA storage ring center, x-axis parallel to LINAC direction, z vertical) is described in Figure 8.5.2. In this picture the relative position of the experimental hall with respect to the surrounding buildings is also visible. The experimental hall is separated from the undulator tunnel by a 3 m-thick concrete wall as a primary safety radiation protection element. The first-mirrors chambers (switching mirrors) are placed in the Safety Hutch since the role of these mirrors is to absorb the main heat load and to deflect the photon flux (3°) while the residual gas-bremsstrahlung (0°) is absorbed by the next concrete wall. The lateral walls of the Safety Hutch are about 800 mm-thick and the access is through a labyrinth. Therefore, to permit installation and maintenance access, the roof consists of removable blocks permitting the use of a crane for handling the devices and the roof blocks themselves.

The Experimental Hall area is divided into three parts by two rows of pillars that have the primary function of supporting the crane system for the beamline chamber installation and handling. All the beamlines are placed in the 26 m wide central zone. The width is set by the consideration that, in the present conceptual layout, the distance between the external experimental chambers is about 20 m. In analogy with the ELETTRA Experimental Hall, the height of the crane railways is about 8 m and therefore the height of the overall building is about 10-11 m (at least in the central area between the

pillars). Since the Experimental Hall floor is -5.2 m from zero level, about one half of the building will be underground.

The two external areas delimited by the rows of pillars are useful space for auxiliary beamline laboratories (mechanical and electrical pre-assembly and testing, vacuum lab, experimental chambers lab, etc.) and general systems (cooling, pneumatic and electric systems).

All of the described dimensions will be optimized in the final design drawings.

8.5.3 Switching Elements

The Switching Mirror Chamber (SMC) is a key element in the layout of the photon beam transport system since, as already outlined in paragraph 8.4.2, one of the main tasks of this system is to redirect the photons of both FELs to the maximum number of possible beamlines.

The basic switching scheme is described in Figure 8.5.3. Three SMCs feed five beamline branches (BL1 ÷ BL5). SMC1 and SMC2 are the chambers in which the first mirrors (two mirrors per each chamber) are

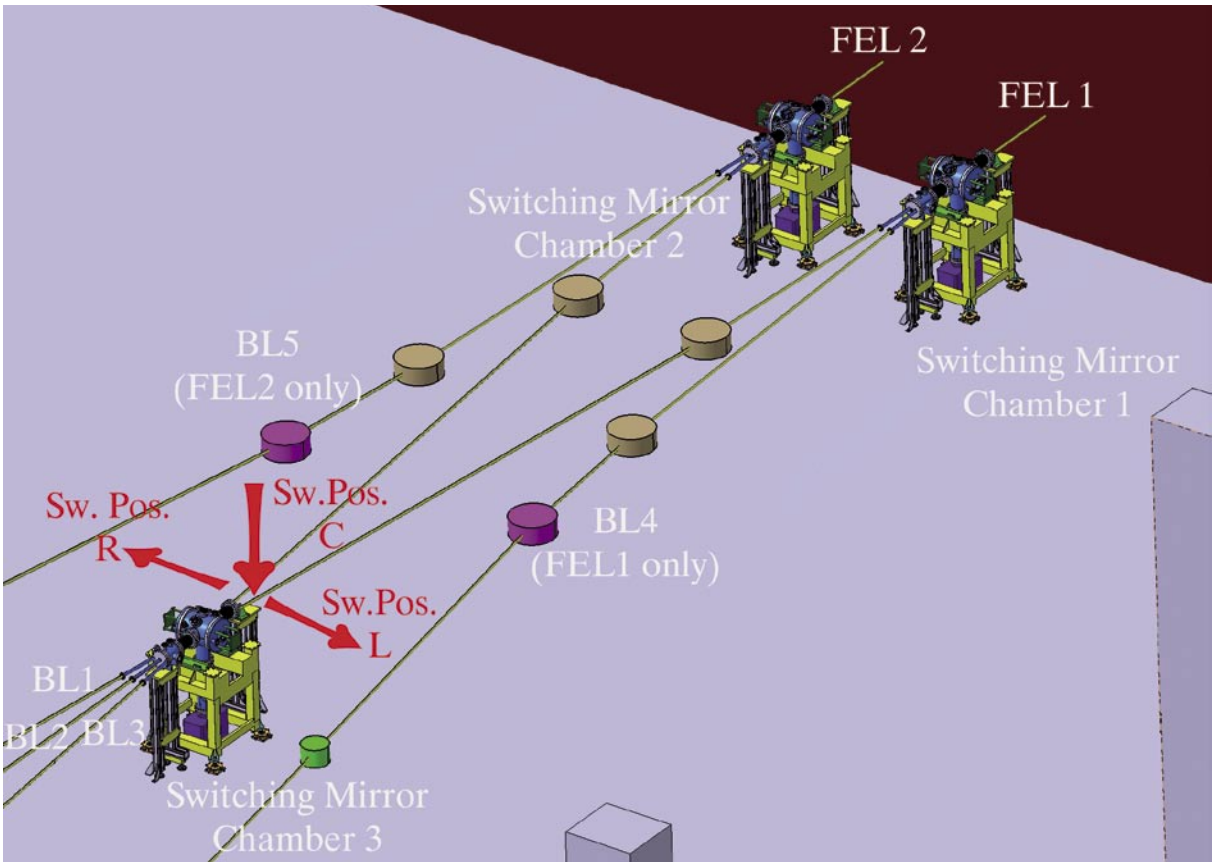

Figure 8.5.3:
Photon beam switching scheme.

placed and which receive the photons from FEL-1 and FEL-2 respectively. As the function of these two chambers is similar to that of many other switching chambers at ELETTRA beamlines, the mechanical scheme is derived from these devices. The switching function is obtained by a horizontal translation (perpendicular to the beam) of the whole chamber. In the two possible positions (left and right position) the center of the respective mirror is aligned with the photon axis.

Each mirror has two angular degrees of freedom (pitch and roll) controlled by a manipulator similar to the one described in Figure 8.5.4. The manipulator axis (and therefore the connection flange) is inclined at 90°+ α (where α is the grazing angle of the mirror) in the horizontal plane with respect to incoming beam direction. Theoretically the two translation movements are enough to obtain the $\pm 2\alpha$ beam deflection, while the pitch and roll controls are used for the fine alignment of the beam.

When the beam is deflected through the central part of the layout, photon flux distribution over three different beamline branches is required. Hence, the switching device (SMC3) must have six switching positions (three beamline output per each FEL photon input) instead of the two switching position required for SMC1 and SMC2. In SMC3 two of these six connections are simply realized by adding a central position to the chamber (neutral position). In this situation the photon beam coming from both FEL-1 and FEL-2 simply runs through the chamber and connects FEL-1 to BL1, FEL-2 to BL3. Once the SMC3 is in left or right position, two different angles of deflection are required. This second switching degree of freedom is obtained by controlling the pitch of the mirror through the manipulator. In the present layout the two required defections are $2\alpha_1 = 5°$ (FEL-1→BL2, FEL-2→BL2) and $2\alpha_2 = 10°$ (FEL-1→BL3, FEL-2→BL1).

For the manipulator to have a symmetrical behavior through the pitch angle travel, the manipulator axis must be inclined by $90+\alpha_m$ (where α_m is the average between α_1 and α_2) in the horizontal plane with respect to the incoming beam direction. The total range of the pitch control must exceed $(\alpha_2 - \alpha_1) = 2.5°$ to have some residual pitch control in the two extreme positions.

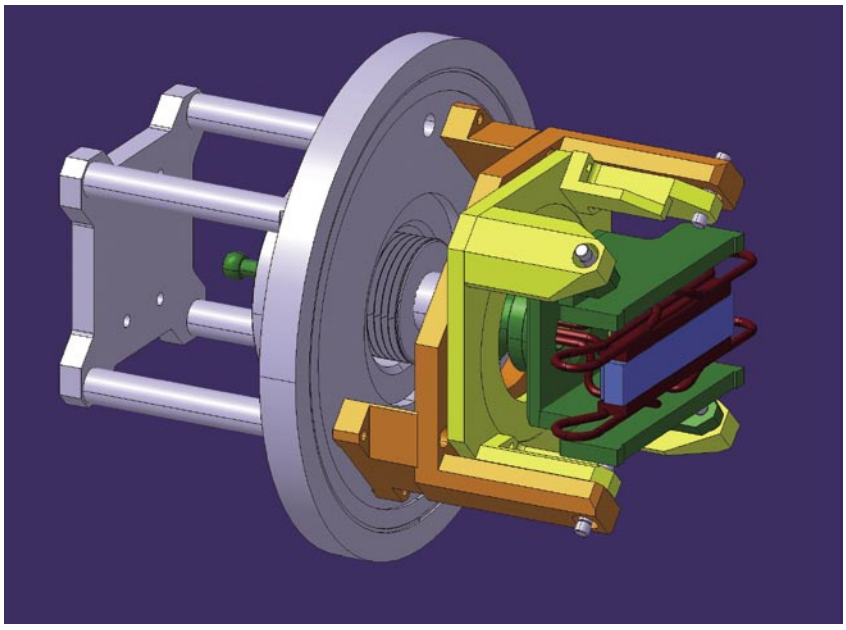

Figure 8.5.4:
Switching mirror manipulator.

In the present layout scheme each of the two FELs photon beams can feed four of the five planned beamline branches (Figure 8.5.3). Furthermore, the switching mirror scheme can be used to split again each branch line, if an increased number of beamline is required.

8.5.4 Gratings and Diagnostics Elements

One of the advantages of the present photon beam transport system layout is the possibility to concentrate the diagnostic system, common for all the beamlines, in the first part of the layout scheme, just after the first mirrors, and outside the safety hutch. The next section describes the physical principles of the diagnostic system and presents an overview of a preliminary mechanical scheme.

The gratings and diagnostic system are positioned between the first mirrors (SMC1 and SMC2) and the 3-way switching chamber (SMC3), just outside the 800 mm thick wall of the safety hutch. In Figure 8.5.3 the grating chambers are respresented as brown cylinders. In Figure 8.5.5 the cylinders are replaced by the proper vacuum vessels, in which the grating manipulator is visible in transparency.

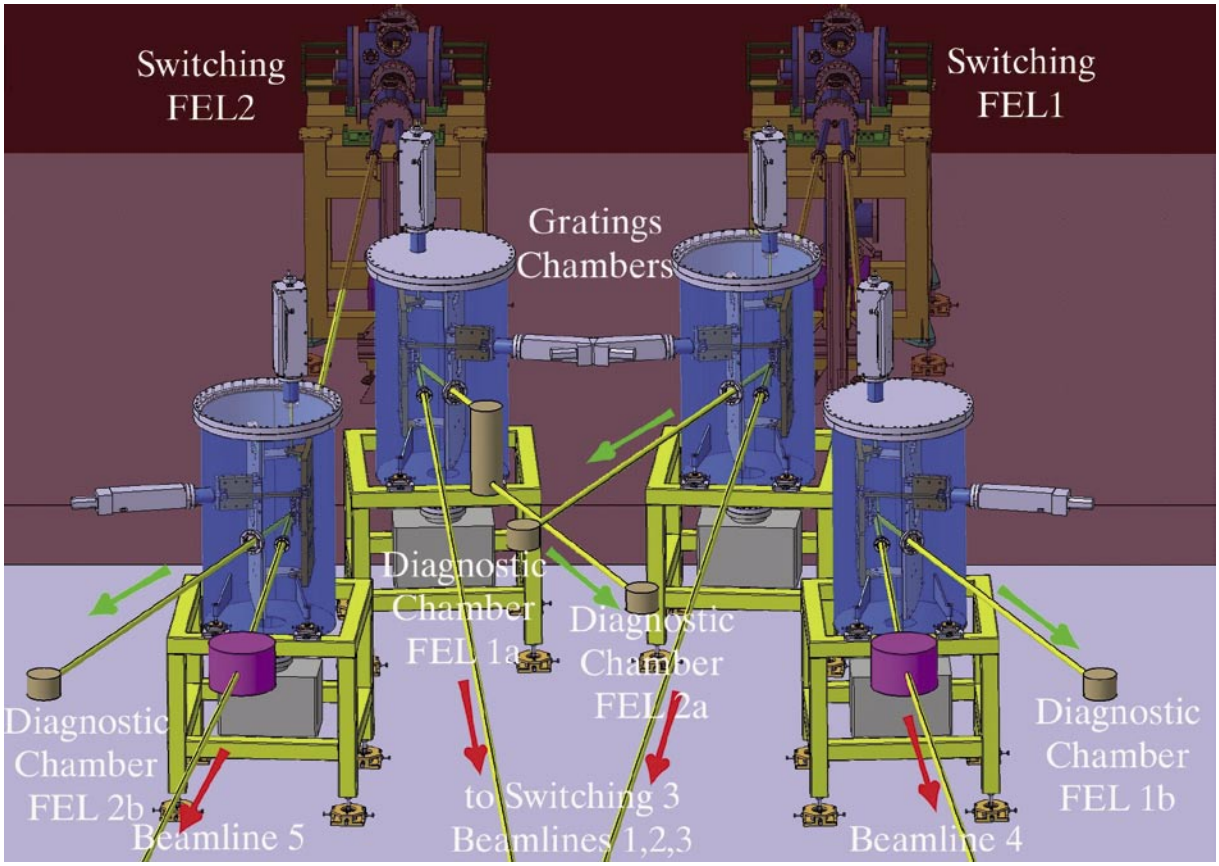

Figure 8.5.5:
Beamline diagnostics layout.

The two upstream switching chambers are also visible in transparency, otherwise hidden by the shielding wall of the safety hutch.

In each of the four chambers the proper plane grating deflects the zero order beam to the beamline branch (red arrows), while the first order (green arrows) is measured by a linear or bi-dimensional detector mounted in the small brown vacuum vessels of Figure 8.5.5. Each of these elements is connected to the grating chambers with bellows, and mounted over a motorized X-Y linear stage. These additional degrees of freedom permit positioning the detector at different angles with respect to the grating (transverse movement Y), and with different distances with respect to the grating itself (longitudinal movement X, along beam direction). A critical location for the diagnostics system is that of the two internal grating chambers where the first order beams intersect (diagnostic chamber FEL-1a and FEL-2a). To avoid the intersection of the two devices a periscopic chamber (two plane mirrors) is placed along one of the two diagnostic lines (FEL-2a in the Figure 8.5.5).

In the gratings chamber the gratings are mounted on a vertical sliding system that allows the grating selection for the proper energy range. The translating system can then rotate around the same translation axis and the rotation (pitch control) is driven by the crank gear. By moving the stage in the horizontal direction it is possible to finely control the pitch of the active grating, and therefore the beam deflection.

8.6 Photon Beam Diagnostics

Several characteristics of the emitted radiation can be measured. Some of these measurements must be highly reliable and precise, possibly shot by shot, so that the experimentalist can use the information to normalize their data. The same or similar information is useful for machine physicists to improve the performance of the FEL. The photon diagnostics are developed to satisfy the requirements of both the users and the machine physicists. Some photon beam characteristics, such as polarization degree, background to peak ratio, energy vs. time distribution (chirp) could be useful but their measurement is difficult. As they are not considered critical, the design of such diagnostics is left for the future.

The different diagnostics employ state-of-the-art instrumentation (eventually with a limited in- house modification), and maintain the option of upgrade based on internal or collaborative research and development.

8.6.1 On-line Energy Spectrograph

The photon spectrograph is an on-line device able to measure, shot-by-shot, the energy profile and consequently the relative intensity of each incoming pulse. Since each undulator can feed more than one beamline, to avoid duplication of instruments the first part of each beamline will be constructed as in Figure 8.6.1.

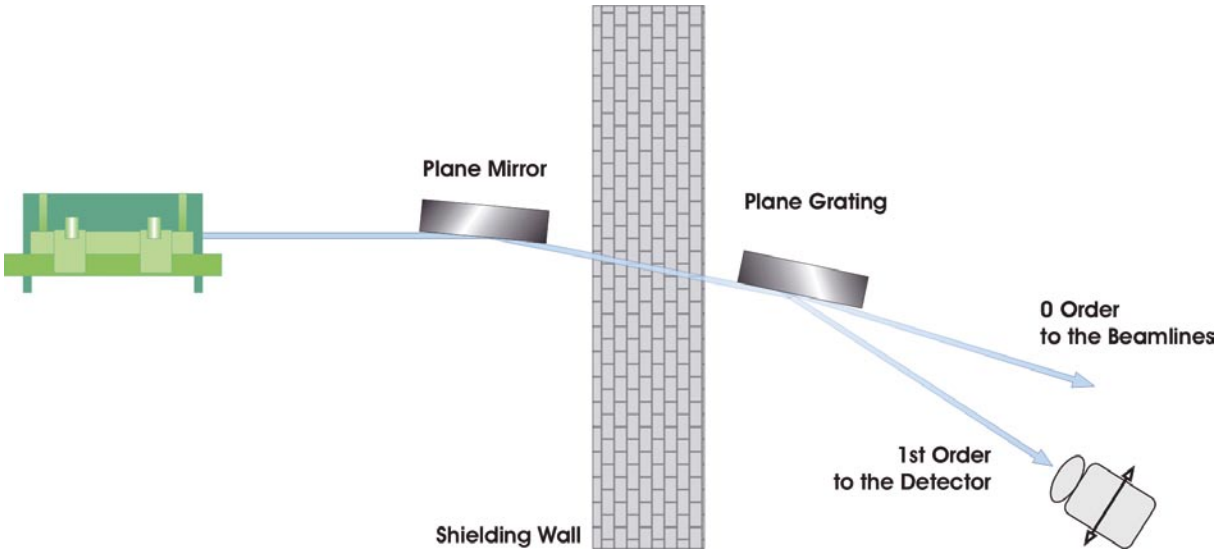

Figure 8.6.1:
Layout of the photon transport system from the undulator to the diagnostics.

A first plane mirror (used only for safety reasons) deflects the beam outside the shielding wall. Just outside the wall, a plane VLS grating deflects the zero order to the beamlines and the first order to a linear or bi-dimensional detector. The advantage of using a plane VLS grating is twofold: no further optics are needed to focus the beam on the detector, and the beam passes trough the instrument (via the zero order) without altering its divergence.

In principle the VLS grating could also be positioned before the shielding wall, but there are two major advantages of having it outside. The first is related to long-term deterioration, which is much less critical for a mirror than for a grating, from the optical point of view. Consequently it is better to place the mirror upstream of the grating. If excessive power arrives at the first element and damages it, a plane mirror is cheaper to replace than a VLS plane grating. The second advantage is the possibility to have the spectrograph (that can be about 3 meters long) completely outside the wall, with easy access for alignment, calibration, and so on. The disadvantage is the additional reflection that does not significantly alter the intensity of the beam (reflectivity > 95% is expected in the whole range) but can degrade the beam quality.

The VLS grating focuses different energies in different positions, and a position-sensitive detector collects the photons, transforming a spatial distribution into an energy distribution. Since the expected energy width of the beam can be lower than 10 meV, the spectral profile must be defined with a precision about 1 meV. This is not a problem for FEL-1, where a possible solution is the use of two gratings covering the whole energy range, providing resolution of the order of 0.2-0.5 meV, using a 13 μm-spatial resolution detector. For FEL-2, working at higher photon energies, the ultimate resolution reaches values about 5 meV. The system works with a fixed VLS plane grating and with a movable detector. Since the expected photon flux is quite high, the grating profile is optimized to deliver as much flux as possible in the zero order, and less then 1% in the diffraction orders.

Up to date it is not possible to collect a bi-dimensional detector image with enough dynamic range (16 bits) with a repetition rate of 10 or 50 Hz (value for FERMI@Elettra). In contrast a linear array detector can be read even with a higher repetition rate. The FERMI system therefore adopts a linear array detector (back illuminated or front illuminated with a proper phosphor coating) to measure the beam shot by shot, and a bi-dimensional detector placed close to the former, which measures one shot each 10-20 pulses triggered by a mechanical shutter.

8.6.2 Off-Axis Photon Beam Characterization

A second measurement of interest is determining the beam profile outside the central emission cone, to check the alignment and tuning of the undulators. This measurement is, in principle, quite easy using a standard, bi-dimensional, back illuminated CCD such as the one used for the spectrograph. In this way the radiation emitted at different angles with respect to the undulator axis is collected at different CCD rows. Moreover there is no need to collect images shot to shot, but simply to acquire averaged information over longer periods (e.g. seconds).

8.6.3 Position Sensitive Detector

To determine and control the spatial position of the photon beam along its path to the experimental stations, several position sensitive detectors are installed. These devices should provide information about both horizontal and vertical directions, monitoring spatial shifts of the beam in time. A possible design for this kind of instrument uses parallel plates in a gas atmosphere to collect the signals from gas ionization. Both electrons and ions can be collected, similar to the system successfully tested and employed in the FLASH FEL source in DESY-Hamburg [9]. This system is able to characterize the position of the beam with an accuracy of about 20 μm. The position sensitive detector can be mounted close to the gas absorbing section placed between the undulators and the first optical elements of the beamlines. Other more conventional beam position monitors can be installed and used along the beamlines themselves. They include fluorescent screens and metallic plates (both offline) for alignment, photodiodes for quantitative indications about beam shifts (off- and on-line), slit-pair systems (online) to monitor the beam alignment and eventually to correct it with a feedback procedure.

8.6.4 Photon Pulse Duration Characterization

Depending which FEL is used, different pulse lengths are delivered to the beamlines. In particular, FEL-1 delivers pulses of about 100-200 fs (FWHM), while FEL-2 delivers pulses of ~500 fs (fresh bunch mode). In order to characterize these lengths some instrumentation must be developed. The main difficulty is that to date no direct online measurements of this quantity are possible with sufficient time resolution. Streak cameras working in the EUV and soft x-ray regimes are capable, at the best, of resolutions around 500 fs [18] [19]. Other destructive (*e.g.* offline) methods exist for measuring the pulse length, such as auto- or cross-correlation techniques involving the use of ultra-fast lasers with short and well-defined pulse durations.

Initially invasive (not shot-to-shot) measurement of pulse lengths will be performed with cross-correlation techniques, with a precision of about 100 fs or less. Eventually, measuring the same quantity on-line, shot-to-shot, with a precision of the order of 200-250 fs may become possible by means of a streak camera. Experimental studies carried out at Lawrence Berkeley Laboratory (H. Padmore and co-workers) demonstrate the future feasibility of this kind of measurement. Active collaboration with this group is under way.

8.7 References

[1] BESSY FEL Technical Design Report (2004).

[2] LCLS Design Study Report (1998).

[3] HASYLAB annual report (2001).

[4] Y. Dong et al., *Appl. Surf. Sci.* **252**, 352 (2005).

[5] D. von der Linde et al., *Appl. Surf. Sci.* **154-155**, 1 (2000).

[6] H. Jeschke et al., *Appl. Surf. Sci.* **197**, 839 (2002).

[7] H. Jeschke, et al., *Appl. Surf. Sci.*, **197-198**, 107 (2002).

[8] 4GLS Conceptual Design Report (2006).

[9] K. Tiedtke et al., *AIP Conference Proceedings* **705**, 588 (2004).

[10] M. Richter et al., *Appl. Phys. Lett.* **83**, 2970 (2003).

[11] S. Düsterer et al., XFEL 2004 Workshop, Stanford (2004).

[12] H. Schlarb et al., *Proceedings of EPAC 2004*, 345 (2004).

[13] R. Signorato at al., *J. Synchrotron Rad.* **5**, 797 (1998).

[14] H.A. Padmore, *Rev. Sci. Instrum.* **60**, 1608 (1989).

[15] D. Cocco et al., *Proceedings SPIE* **3767**, 271 (1999).

[16] H. Petersen, *Opt. Commun.* **40** (1982).

[17] C.T. Chen and F. Sette, *Rev. Sci. Instrum.* **60**, 1616 (1989).

[18] J. Liu et al., *Appl. Phys. Lett.* **82**, 3553 (2003).

[19] Z. Chang et al., Univ. of Michigan, USA.

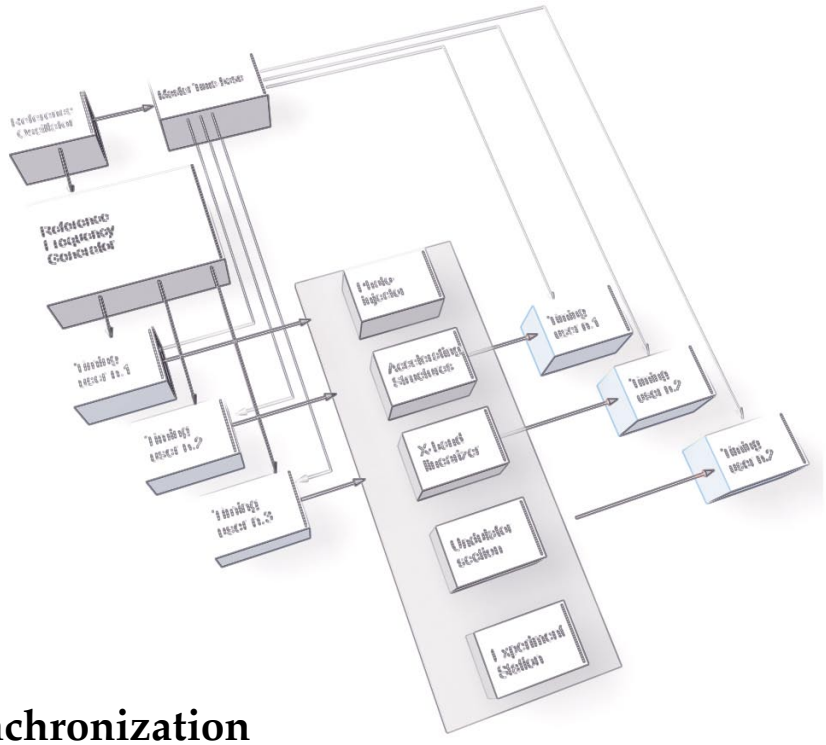

9 Timing and Synchronization

Synopsis

The FERMI timing and synchronization (T&S) scheme is based on a hybrid system utilising both "pulsed" and continuous wave (CW) timing techniques.

The "pulsed" technique has been originally developed at MIT [1]: an ultra-low phase noise pulsed laser, called optical master oscillator (OMO), is locked to the radiofrequency reference generator. Its pulses distributed over dispersion compensated fiber links (FO) give the time reference to all the "pulsed" timing clients, such as lasers and diagnostics devices

The "CW" timing technique, developed by LBNL at Berkeley [2] is based on a frequency stabilized CW laser amplitude modulated by the radio frequency (RF) of CW timing clients, such as low level RF systems. In this scheme, the FO links are stabilized using the optical mixing concept which fully exploits a carrier frequency 10^5 times higher than the repetition rate of the pulsed system.

The FERMI timing system is compatible with both the European ($f_{S\text{-}band\text{-}EU}$=2.998010 GHz) and U.S. ($f_{S\text{-}band\text{-}US}$ = 2.856 GHz) S-band frequencies, a necessary condition since the fourth harmonic (X-band) linearizer, that is part of the FEL design, will work at the US frequency. The greatest common divisor of these two frequencies is the coincidence frequency f_{COIN} (15.779 MHz) used to generate the "bunch clock" at the FEL repetition rate frequency f_{bunch}=10-50 Hz. At each period of the coincidence frequency waveform the rising slopes of the (EU) S-band and the (US) aX-band waveforms overlap, thus providing the required phase coincidence.

The reference oscillator for the whole timing system is a microwave sinusoidal oscillator, operating at the European X-band frequency of 11.992 GHZ, which provides the required, fs grade, ultra low phase noise and long term stability. The oscillator is housed in a temperature controlled "timing hutch" close to a set of ultra low phase noise dividers which generate the European S-band frequency (2,998.010 MHz), the optical master oscillator (OMO) reference frequency, $f_{REF\ OMO}$, and the greatest common divisor frequency, f_{COIN}, output signals.

The output signals are distributed to the OMO, to the CW timing and to the master time-base unit and finally, via dedicated stabilized optical channels, to the timing system end users.

FERMI's timing clients belong to two main classes: optical and electrical. Optical clients lock to the reference signal optically (by cross-correlation) or directly to the optical reference to measure phases or bunch arrival times. Electrical clients instead require electrical reference signals, provided by ultra-low phase noise optical to electrical (O/E) converters.

The timing system is completely integrated into the FERMI control system, thus allowing for remote control and monitoring of the performance and reliability of all key sub-systems.

9.1 Introduction

In its final configuration, FERMI is a two stage, harmonic generation seeded FEL providing coherent radiation at wavelengths ranging from 100 nm to 10 nm.

Being based on the seeded FEL scheme and aiming at routine operation in the "fresh bunch" configuration, FERMI requires state of art timing and synchronization systems.

Femto-second lasers, deeply integrated in the electron bunch and photon pulse generation systems, in diagnostic set-ups and in time resolved experiments require a timing stability and resolution at the level of 10% of the laser pulse duration.

Requirements on the stability of the accelerator RF system call for acceleration call for ultra-stable and ultra-low phase noise reference signals being distributed to the Low Level RF feedback loops. Such stringent requirements can only be met by optical and electro-optical (E/O) techniques.

9.2 System Requirements

The *timing system* must generate and distribute throughout the facility a timing reference signal to all sub-systems requiring it. The main function of the *synchronization system* is instead that of allowing to keep jitters and/or drifts of the relevant sub-systems (such as the electron bunch) with respect to the reference signal to within the specified tolerances (see Table 9.2.1). The *timing system* is therefore a critical machine sub-system in itself, whereas the *synchronization system*, distributed to many different sub-systems - including user experiments - is a critical function to be implemented. This conceptual distinction is mirrored in Table 9.2.1.

The main characteristics of the FERMI FEL scheme, which pose precise system requirements on the T&S system, are:

- shot to shot *energy* and *current stability* better than 0.1% and 10% respectively;

- *100s fs bunch length*, posing demanding tolerances on the timing signal fed to diagnostics components such as the "bunch arrival time" monitor;

- *extensive integration into the system of ps and fs lasers,* involved in the electron bunch generation (photo-cathode, laser heater) process, in the radiation production (seed laser) process and in the experiments. As an example, time resolved experiments call for a synchronisation precision at the level of better than 100 fs;

- *fresh bunch seeding scheme*, which requires the seed laser pulse timing with respect to the electron bunch arrival time to stay well within one half of the electron bunch duration, on a shot-to-shot basis. Since the flat, useful part of the bunch is ~ 500 fs_{FWHM} long, the electron bunch relative arrival time peak-to-peak jitter is specified to be ≤50 fs_{RMS}.

Table 9.2.1: Distribution throughout the machine of sub-systems requiring synchronization.

		accelerator sub-systems						
		LLRF	magnets & Power Supplies	undulator sections	diagnostics	timing	lasers	controls
accelerator sections	inj	x	x		x	x	x	x
	low en linac	x	x		x	x		x
	bunch compr.		x		x	x		x
	linac	x	x		X	x		x
	spread		x		X			x
	hν gen		x	x	x	x	x	x
	beam lines				x	x	X	x

9.2.1 Reference Oscillator Drift and Jitter Specifications

The time noise on the synchronization signals is divided into “drift” and “jitter” depending on the frequency band it belongs to, namely:

drift: DC to 10 Hz (FERMI initial repetition rate)

jitter: 10 Hz to one half the gun laser repetition frequency, $F_{rep\ laser}/2$.

At the sub-ps_{RMS} level, the phase noise of an oscillator is measured in the frequency domain and is quantified in dBc/Hz, indicating the strength per Hz of bandwidth of a jitter component at a given frequency offset from the carrier. The representation is very convenient as it allows to clearly identifying the *phase noise spectral components*, i.e. the frequencies, which contribute most to the overall drift and jitter of any given sub-system.

This classification leads us to the concept of *phase noise spectral components*. One must know the sensitivity to the various phase noise spectral components for each sub-system that needs to be synchronized to optimize its reference signal.

9.2.2 Reference Timing Distribution Lines

The various different lines distributing the timing reference signals are listed in Table 9.2.2.

For each timing client the following properties and parameters have been indicated:

type of reference signal continuous wave or pulsed

number of lines to be provided

physical layer electrical or optical, with duration of the pulse

frequency

maximum allowed jitter.

The latter is the sub-system total allowed jitter, defined on the basis of its net effect on the bunch.

9.2.3 Timing Jitter Budget

For each timing client, the net effect on the bunch jitter is computed as the quadratic sum of the timing line (phase reference) and the client (sub-system) contributions, since the two contributions are Gaussian and statistically independent. The resulting values for each line are listed in Table 9.2.2, under the heading "Max. allowed Jitter".

Table 9.2.2: Maximum jitter for each timing line.

Timing client	*Client jitter [fs_{RMS}]*	*Timing line jitter [fs_{RMS}]*	*Bandwidth of interest*
RF, S-band	167	118	DC-1kHz
RF, X-band	69	49	DC-1kHz
Photoinjector laser	200	141	DC - ≈1kHz
Seed laser	100	71	DC - ≈1kHz
Experiment laser	100	71	DC - ≈1kHz
Streak camera driver	500	354	DC - ≈1kHz
Streak camera fiducial	100	71	DC-50MHz
Bunch arrival monitor	100	71	DC-50MHz
E/O sampling station	100	71	DC-50MHz

Table 9.2.2 also lists, under "Bandwidth of interest", the bandwidth within which each timing client is most sensitive to jitter. The different sensitivities are explained by the intrinsic band characteristics of the sub-systems (RF accelerating structures) and the related stabilization loops (laser PLLs). This is an important issue that must be taken into consideration in the design of the timing lines to the different sub-systems.

The resulting overall client jitter specifications are listed in Table 9.2.3, for each line, under the heading "Max. allowed Jitter".

Table 9.2.3: FERMI client timing specifications.

Timing client	*Time structure of reference signal needed by the client*	*Electrical or Optical /duration* *[fs_{FWHM}]*	*Frequency* *[Hz]*	*max. allowed jitter* *[fs_{RMS}]*	*Number of lines*
RF, S-band	quasi-CW	E (t_{RF}>2 μs)	2.998010•10^9 (EU S-band)	167	12
RF, X-band	quasi-CW	E, (t_{RF}>2 μs)	11.992040•10^9 (US X-band)	69	1
Photoinjector laser	CW pulsed cross-corr seeding	E O, O,	$F_{LASER\ OSC}$ 1 to 50 Hz $F_{LASER\ AMP}$	200	1
Seed laser	CW pulsed cross-corr seeding	E, O, O,	$F_{LASER\ OSC}$ 1 to 50 Hz $F_{LASER\ AMP}$	100	1
User laser	CW pulsed cross-corr seeding	E, O, O,	$F_{LASER\ OSC}$ 1 to 50Hz $F_{LASER\ AMP}$	100	2
Streak camera driver	pulsed, elec. trigger pulsed, opt. trigger	E, 100 ps O, 1 ps	$F_{LASER\ OSC}$ 1 to 50 Hz	500	2
Streak camera fiducial	pulsed	O, 500 fs	1 to 50 Hz	100	2
Bunch arrival monitor	pulsed	O, 1 ps	$F_{LASER\ OSC}$	100	6
E/O sampling station	pulsed	O, 100 fs	$F_{LASER\ OSC}$	100	2

9.2.4 Accelerator Related Frequencies

The FERMI reference frequencies are unambiguously determined by both the European (EU) S-band frequency (*2,998 010 GHz*) for the linear accelerator and the USA (US) X-band (4•2,855 999 GHz = *11,423 996 GHz*) for the fourth harmonic linearizer which must operate synchronously up to the 50Hz maximum bunch repetition frequency.

A unique, different from 1, greatest common divisor (GCD) of the two frequencies exists only for the two exact S-band values indicated above. The GCD is f_{COIN}=15.779 MHz with the division factors shown in Table 9.2.4.

Table 9.2.4: Table of the FERMI reference frequencies.

Signal name	*Symbol*	*Value*	*Notes / division factor*
μ-wave Master reference	f_{MASTER}	11.992 040 GHz	EU X-band
FERMI radio frequency	f_{RF}	2.998 010 GHz	EU S-band
American radio frequency	$f_{US\ RF}$	2.855 998 GHz	US S-band
American X-band	$f_{US\ X\text{-}band}$	11.423 996 GHz	US X-band
G.C.D.	f_{COIN}	15.779 000 MHz	EU S-band / 190 US S-band / 181

9.3 Description of the Timing System

A schematic layout of the FERMI T&S system is shown in Figure 9.3.1, in which the main sub-systems of the accelerator complex, the gun, the accelerating sections, the x-band structure, the undulator section and a generic beam-line (labelled “experiment”) are shown as blocks.

9.3.1 T&S System Diagram

A reference oscillator synchronizes the entire machine, ensuring the specified time stability and “low frequency” jitter level.

Two main units are directly linked to the reference oscillator: the reference frequencies generator and the master time base. The former generates the S-band and X-band frequencies, the laser repetition frequency and other needed intermediate frequencies. The latter generates the machine triggers, typically “digital” signals, such as the bunch repetition rate and various gates and triggers for the laser systems and the diagnostics.

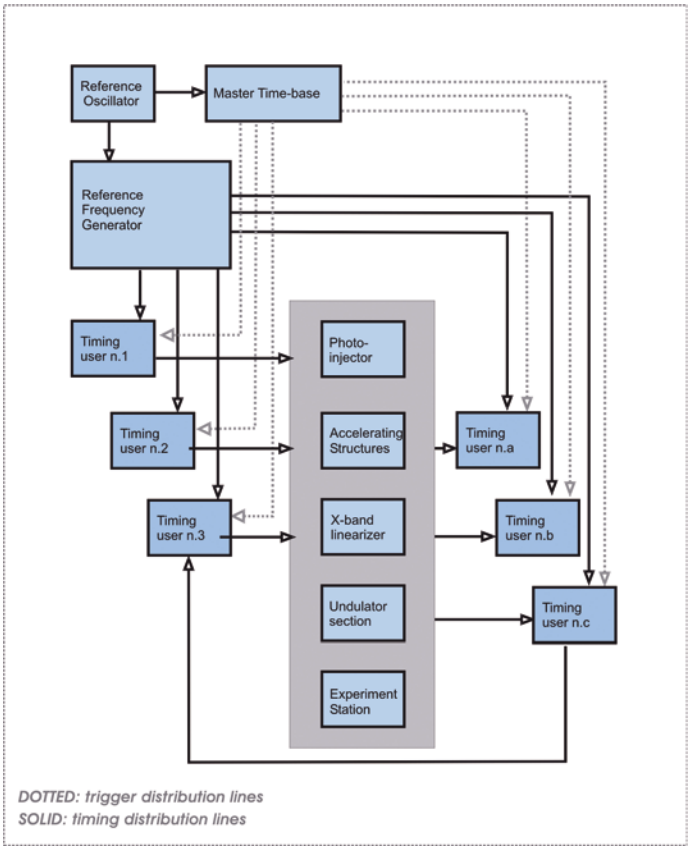

Figure 9.3.1:
Block diagram of the timing and synchronization system.

In the T&S system one distinguishes several classes of *timing clients*. A basic classification criterion is based on the physical layer of the reference signal they need be connected to: *optical* or *electrical*. Furthermore, one can also identify *timing clients* acting on accelerator sub-systems (labelled in Figure 9.3.1 as: 1, 2,...n), such as lasers, the RF system and the RF deflectors, and other *timing clients* (labelled in Figure 9.3.1 as: a, b, c) who may receive inputs from the accelerator under different forms (either electrically or optically) or who are closely interacting with the electron or photon beams. To this fourth class belong diagnostics clients such as bunch arrival monitor, streak cameras and Electro-Optical sampling stations. In some cases, the information about the relative (bunch to reference) measured time difference is fed back to one of the clients of the first (a) class, to implement a given “synchronization” task.

Two major R&D efforts are in progress related to the development of optical clock systems allowing to "synchronize" a large-scale accelerator facility, by generating the reference signal (clock) and distributing it typically over distances of several hundred meters.

Two synchronization schemes for such most demanding timing clients have in fact been recently proposed and are being developed:

- in MIT, work is in progress, in collaboration with DESY, on a pulsed optical clock whose in principle feasibility has already been demonstrated,
- a CW optical clock system is under development in LBNL.

While both schemes are expected to meet the kind of performance required of a complete femto-second, large scale timing system, each is best suited for "synching" specific classes of sub systems: the MIT/DESY "time domain" one for "pulsed" clients such as laser diagnostics ones, the LBNL "frequency domain" one to provide the reference signal to the Low Level RF "quasi CW" clients.

The FERMI timing and synchronization systems will therefore exploit the best of both schemes (sharing the Reference Oscillator) by closely integrating them into the final FERMI timing design.

9.3.2 The Reference Oscillator

The Reference oscillator provides the phase noise floor for the facility; it ensures the required ultra low phase noise at the lower end of the phase noise spectrum, and therefore stable, precise timing throughout the facility.

Single frequency off the shelf reference oscillators can be found on the market, in the (factory selectable) range of 8 to 12 GHz, with output power levels of 13 dBm ± 3 dB and phase noise values as low as:

- 108 dBc/Hz @ 100 Hz
- 138 dBc/Hz @ 1 kHz
- 156 dBc/Hz @ 10 kHz
- 166 dBc/Hz @ 100 kHz

Compatible ultra low phase noise frequency dividers can also be purchased so that, starting from the EU X-band frequency ($f_{X\text{-}band}$= 11.991 GHz), the S-band and the Master Oscillator (OMO) repetition rates can be obtained by subsequent divisions, without spoiling the reference ultra low phase noise level.

9.3.3 Pulsed Timing Section

The pulsed section of the FERMI timing system relies on the Optical Master Oscillator. The OMO is a fibre laser, typically, passively mode locked to the reference oscillator; it generates a *comb* of discrete optical pulses at λ=1550 nm which are used as synchronizing events. The duration of the optical pulse is: 100 fs< $t_{PULSE\ OMO}$< 1 ps.

The OMO provides excellent jitter performance in the upper region of the jitter spectrum (f_{OFFSET}>10 kHz). To improve the natural phase noise performance of the OMO in the lower part of the phase noise spectrum, it is phase locked to the ultra low phase noise reference frequency, $f_{REF\ OMO}$.

The fibre laser repetition rate, f_{OMO}, must be a sub-multiple, with dividing factor N, of the accelerator S-band frequency (2.997 GHz). Possible values are listed in Table 9.4.1.

N=1 is currently under investigation for an actively mode locked fibre laser. This specific case is shown in Figure 9.3.2. The stream of optical pulses generated by the OMO is distributed to the end clients by means of individually stabilized FO links, the group velocity being stabilized by an active loop. When required, optical pulses can be provided at a lower repetition rate.

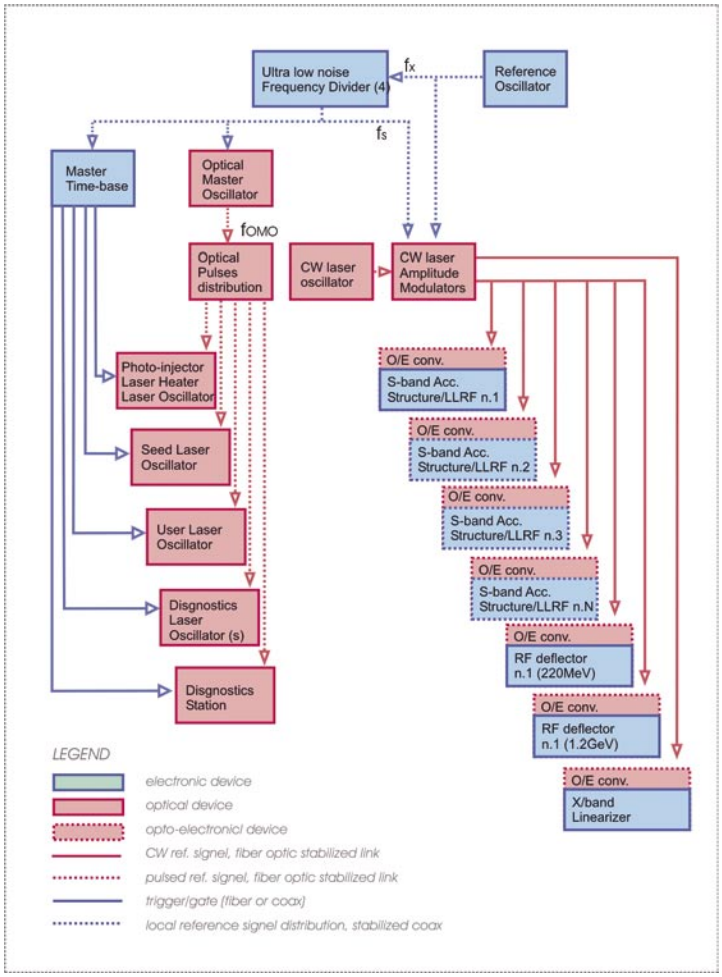

Figure 9.3.2:
Block diagram of the FERMI timing system, with $f_{REF}=f_{X\text{-}band}$ *and* $f_{OMO}=f_{S\text{-}band}$.

9.3.4 Continuous Wave Timing Section

In the CW timing section, an optical carrier signal is generated by a long coherence length, CW laser, at λ=1530 nm. The optical carrier is amplitude modulated by a radio frequency signal using an electro-optical modulator and transmitted over a "phase velocity" stabilized fiber optics link. On the transmitter side a fiber amplifier and a splitter create multiple lines, one for each client. The signal carried by the fiber is detected by a photodiode at the receiver side and the radio frequency signal extracted. All fiber paths not part of a stabilization loop are housed in temperature controlled racks, in order not to generate additional phase noise.

9.3.5 Reference and Triggers

Two classes of signals can be identified, *reference frequencies* and *triggers*, that can be distributed using different techniques since they have different requirements in terms of tolerable jitter:

- the Reference Distribution System distributes the reference frequencies around the machine keeping their phase noise at the level of the reference oscillator (i.e. < 20 fs_{RMS});

- a less performing (less expensive) distribution system can be adopted for triggers and gates on which a ≤ 10 ps_{RMS} jitter is tolerated.

9.4 Machine Frequencies and Trigger Generators

The machine frequencies and trigger generators are asked to:

- provide ultra-low phase noise references to all sub-systems to be synchronized
- provide the bunch repetition frequency
- generate the G. C. D. frequency

In the following paragraphs the solutions proposed for the different sub-systems are presented.

9.4.1 Machine Frequencies Generator

As previously said, a set of reference frequencies have to be generated and distributed to synchronize all the different FERMI sub-systems. The basic idea is to obtain all (but one) reference frequencies using low phase noise frequency dividers fed by an ultra low phase noise oscillator, the Reference oscillator (see Par. 9.3.2). The expected jitter from this configuration is at the 5 fs_{RMS} level.

The only exception is the US X-band frequency, obtained by up conversion of a frequency synthesizer.

9.4.2 Laser Frequencies

FERMI makes massive use of lasers, including both oscillators and amplifiers: in the following, “laser” refers to laser oscillators.

The adoption of an hybrid scheme for the optical timing allows, in principle, to operate the whole facility using a single laser (oscillator). This single laser could serve both as optical reference and as seed to the various amplifiers operating in the facility. This solution leads to an intrinsically synchronized facility, the only sources of jitter/drift being the stabilized fibre optics links for which sub-5 fs_{RMS} jitter has been already demonstrated.

On the day-zero though FERMI will start to operate in a multi laser configuration where the Optical Master Oscillator (OMO) synchronizes the remote lasers by providing them the ultra stable optical reference. The optical reference can either be converted into an electrical one to be used as reference input to the timing stabilizer units controlling the repetition rate of the remote lasers (jitter ≈ 100 fs_{RMS}) or can be used directly in a cross correlator scheme for remote laser synchronization (jitter ≈ 5 fs_{RMS}).

When dealing with pulsed laser synchronization two frequencies can be identified:

the reference frequency, $f_{REF\ LASER}$

the repetition rate of the laser pulses, f_{LASER}

These two signals need not to be necessarily the same: depending on the laser synchronization architecture; what is generally true is:

$f_{LASER} = m \bullet f_{REF\ LASER}$, m integer

For the OMO we define:

the OMO reference frequency, $f_{REF\ OMO}$

the OMO repetition rate, f_{OMO}

For the OMOs currently under evaluation, $f_{REF\ OMO} = f_{OMO}$.

The $f_{REF\ OMO}$ has to be an integer sub-multiple of the microwave master reference f_{MASTER}, since any relative jitter between these two signals is directly seen as jitter of the OMO output.

The available values of the reference frequencies for the Optical Master Oscillator and for the other facility lasers (photo-cathode laser, seeding laser and user's lasers) can be obtained from those listed in Table 9.2.4 and are shown in Table 9.4.1 with the respective microwave master frequency division factors.

Table 9.4.1: Table of the FERMI sub-multiple reference frequencies.

Signal name	*Symbol*	*Value [MHz]*	*Notes*
FERMI radio frequency	f_{RF}	2,998.010	EU S-band
OMO reference frequency	$f_{REF\ OMO}$	599.602	possible OMO ref
OMO reference frequency	$f_{REF\ OMO}$	299.801	possible OMO ref
OMO reference frequency	$f_{REF\ OMO}$	157.790	possible OMO ref
LASER ref. frequency	$f_{REF\ LASER}$	78.895	possible LASER ref
LASER ref. frequency	$f_{REF\ LASER}$	31.558	possible LASER ref
LASER ref. frequency	f_{COIN}	15.779	possible LASER ref

Note that the Master Time base frequency is 50 HZ.

9.5 Timing Channels

As shown in the block diagram (Figure 9.3.2) the FERMI timing system adopts two media for the generation and the distribution of the timing signals in the facility. Fiber optics and coaxial lines have been adopted to suit the physical layer of the different adopted device (μ-wave Reference generator, fiber laser or LLRF controller).

In the following paragraphs the characteristics of the different media are outlined.

9.5.1 Local Reference Distribution Coaxial Channel

As shown in Figure 9.3.2, the Reference signal generated by the Reference oscillator (via the low noise divider) needs to be locally routed to the different devices users (OMO, CW laser amplitude modulators). The length of the links must preferably be shorter than 1m, so that units to be connected should be located in a same rack. Phase stable cables with low temperature coefficient (< 5 ppm/°C) will be used.

9.5.2 Optical Timing Channel

Optical reference signals will be distributed through single mode fibers (SMF28).

Depending to the type of signal transmitted (pulsed or CW) either "group velocity" or "phase velocity" stabilization schemes will been adopted, both solutions having showed jitter performances well below 10 fs_{RMS} during both laboratory and field tests.

Maximum attention has to be paid to short fiber links not within a stabilization loop: such these links will be housed in a temperature and vibration controlled ambient.

9.5.3 Coaxial Timing Channel

Coaxial, double shield wideband cables will be used for the various trigger and gate signals with more relaxed jitter specifications. The cables will be run in the machine tunnel on radiation safe cable trays, the expected temperature excursion being less than ±1°C.

9.6 Synchronization of Electrical Clients

Most of the FERMI sub-systems to be synchronized, the largest number of which are diagnostics LLRF controllers, need electrical reference signals, f_{REF}, at (RF) power levels to be defined item by item.

9.6.1 Low Level Radio Frequency

Because of the synchronization scheme selected for the Low Level RF controllers, the S-band reference signal has to be brought to each LLRF box. As of today, this reference signal is obtained by envelope detection of the CW, amplitude modulated optical signal at 1550nm wavelength. All the electronics located downstream from this E/O converter must be designed in such a way as to preserve the fs grade jitter at the end location.

The most appropriate configuration for the reference distribution is a “star” one, since it prevents jitters from adding up; the jitter is thus the same at all remote stations, independently from their distance.

On the contrary, spilling optical power from a single phase-stabilized optical link does not ensure the required fs-level jitter everywhere.

9.6.2 Diagnostics

Diagnostics equipment also requires both electrical and optical reference signals for synchronous operation.

There are two different equipment categories, requiring synchronization

- at the pick up level or
- at the level of the acquisition electronics

respectively.

Bunch Phase Monitors (BPhM), Electro Optical Sampling (EOS) stations and Streak Cameras belong to the first category whereas all other diagnostics belong to the second one which, because FERMI operates at low repetition rate, needs a bunch clock for acquisition.

Both the BPhM and the EOS scheme rely on the pulsed optical reference signal to output the measurement. The Streak Camera needs a low phase-noise trigger, which can even be a high energy optical pulse, to initiate the "streaking ramp".

A fiducial light pulse (the optical reference itself) may be provided as well to compensate for the residual jitter on the sweep start since, when the camera operates in the optical trigger mode, the ramp would still exhibit some jitter (at the few hundred fs level) even were the trigger ideally jitter-free.

9.7 Synchronization of Optical Clients

Other important optical timing clients are the lasers. Basically, lasers can be synchronized either electrically, to ~ 100 fs, or optically to achieve jitters below 10fs and even down to sub-fs performance in carrier envelope stabilization schemes.

On "day zero", the FERMI lasers (mainly the photo-cathode and the laser heater ones) will be synchronized electrically, by providing an electrical reference signal to the laser timing stabilizer box.

The scheme has been already successfully tested at ELETTRA in 2004 by locking the Storage Ring synchrotron radiation pulses to an external synchronized fs laser oscillator [ref]. The minimum achievable jitter has been measured to be in the 100s fs $_{RMS}$ range.

Eventually it is foreseen to synchronize the lasers electrically during coarse alignment and to switch to optical for fine adjustments.

Optical synchronization is based on cross-correlating the laser oscillator pulses to the reference optical clock ones; the jitter measured in the laboratory has been shown to be as low as 5 fs_{RMS}.

A further option, being considered for the longer term, is direct seeding of the remote laser amplifiers directly using the optical clock pulses, thus obtaining an intrinsically synchronized machine.

9.8 Integration of Synchronisation with Controls

Full integration into the accelerator and experiments control system is foreseen, to provide full remote control of all devices and equipment, including real-time monitoring of the sub-systems timing, to allow for efficient and fault free operation of the whole facility.

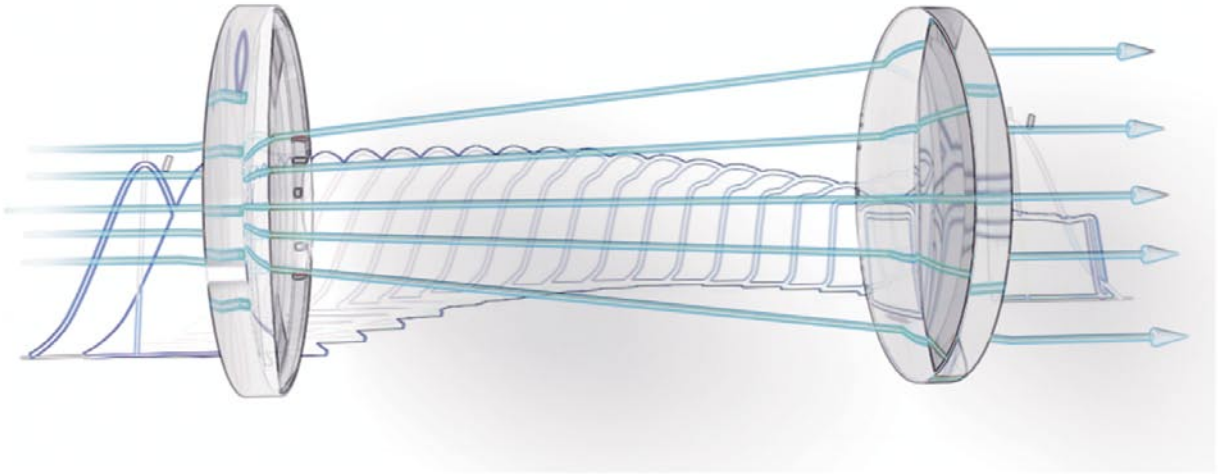

10 Laser Systems

Synopsis

Laser systems will undoubtedly be crucial to determining the overall performance of FERMI. As can be seen from the previous chapters, the laser systems will include the photoinjector laser (PIL), laser heater (LH), seed laser (SL) and beam-line lasers (BLL). In addition, the timing and synchronization system will contain a mode-locked optical master oscillator (OMO). This chapter emphasizes the PIL and SL, as the technology for the other two systems will be very similar; the OMO has already been considered in Chapter 9. The main issues related to the FERMI laser systems have been thoroughly studied during the last year, some of the important points and preliminary data have been summarized and presented in [1]. We note that nearly all the features required of the laser systems by the FERMI FEL design are within reach of readily available laser technology. In contrast, a few characteristics, such as pulse/beam shaping for the photoinjector laser as well as wavelength stability and pulse quality for the seed laser are challenging and will require additional R&D. As it will be shown later, the comparison of the existing laser technologies for obtaining the required parameters indicated the basic unit in all cases to be a Ti: Sapphire chirped pulse amplifier pumped by diode pumped solid state lasers.

The photoinjector laser includes two amplifier stages – a regenerative stage followed by a multipass stage – to reach a pulse energy of 20 mJ in the IR. Pulse shaping is done partially in the IR, by an acousto-optic dispersive filter (DAZZLER), and is completed in UV in a transmission grating-based stretcher or Fourier-system. Beam shaping is done either in the IR or in the UV by an aspheric shaper. A small part (~400 μJ) of the IR beam is split away and transported for use by the laser heater.

The seed laser needs to provide tunable radiation in the UV in two pulse duration regimes: 100 fs and 1 ps. This is flexibility is obtained by using a dual-pulse duration regenerative amplifier. In the 100 fs regime, the regenerative amplifier directly pumps a traveling-wave parametric amplifier (TOPAS) followed by harmonic conversion stages. In the 1 ps regime, output of the output of the regenerative amplifier is further amplified in a two pass stage to ~10 mJ, and then pumps a ~1 ps TOPAS. Beam-line lasers will be based on the same technology, with final pulse energy and wavelength ranges remaining to be specified.

All systems will be synchronized to the timing and synchronization signals by phase-locking loops in the local mode-locked seed lasers. The possibility to use direct seeding by locally amplifying and frequency doubling the fibre distributed 1550 nm sync pulses is under study.

10.1 Photoinjector Laser

The Photoinjector laser (PIL) is a fundamental element in all FEL designs. The pulse and beam quality of this system is crucial to the overall FEL performance, as it is directly imprinted on the emittance of the generated electron bunch. It is now well accepted that both temporal and spatial shaping of the drive laser radiation will be needed for obtaining good photoinjector performance. In addition, for guns based on copper photocathode, ~0.5 mJ pulse energy in the UV is required, which implies at least one multipass amplifier, followed by two harmonic generation stages.

The rationale for the gun laser specifications presented in Table 10.1.1 were discussed in Chapter 5. Most importantly, the reliable generation of ~ 1 nC of charge with low thermal emittance (i.e. wavelength range 260-270 nm) requires UV pulses with energy~0.5 mJ. Assuming a third harmonic generation conversion efficiency of 10 % and losses associated with the temporal and spatial shaping of up to 70 %, we conclude that one needs to start with >18 mJ per pulse. The present technology available for reaching reliable operation in this energy range is a combination regenerative-multipass amplifier system.

Table 10.1.1: Summary of the required PIL parameters.

Repetition rate	10-50 Hz
Pulse duration	3-10 ps (FWHM)
Pulse shape	flat-top or increasing ramp
Rise-time	0.5-1 ps (10-90%)
Spatial profile	top-hat, ~ 1 mm (up to 2 mm) $1/e^2$ radius
Fundamental wavelength	780-800 nm
UV wavelength (third harmonic)	260-267 nm
UV Pulse energy on the photocathode	~0.4 mJ
Timing stability with respect to RF	< 0.2 ps rms (0.3 ps rms producer spec)
Energy stability in UV	< 3% rms
Stability of the beam position on the photocathode	< 1.5% rms

In addition, the relatively large bandwidth required for pulse shaping leads to the need of initial pulse duration in the 100-150 fs range. The only mature, commercially available lasers that deliver pulses of such energy and duration are Ti: Sapphire-based systems. Relatively new solid state media with direct diode pumping, such as Yb:KYW are very attractive in some respects and are to be considered for future projects; however, at present they do not reach some of the essential parameters required (i.e. pulse energy). Consequently we have selected Ti:Sapphire as the active medium for the FERMI photoinjector laser.

10.1.1 Laser System Layout

A block diagram of the Ti:Sapphire based femtosecond amplifier system is shown on Figure 10.1.1. It consists of a mode-locked femtosecond oscillator, a regenerative amplifier and a multipass amplifier stage.

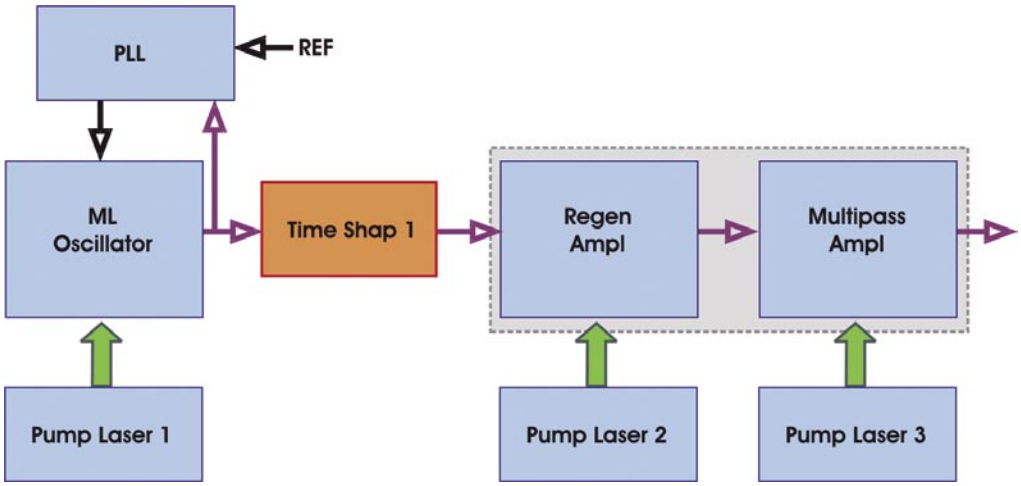

Figure 10.1.1:
Laser system configuration.

10.1.1.1 Mode-Locked Oscillator

The mode-locked oscillator generates the seed pulses for the system; hence its quality is crucial for the overall system performance. The first version of the FERMI system is based on a Kerr-lens mode-locked Ti:Sapphire laser, however a fibre laser based solution will also be tested.

The principal characteristics of this system are as follows:

Pulse duration/bandwidth: to account for 1) the requirements of temporal shaping, 2) bandwidth limitations coming from group-velocity mismatch effects, and 3) the problems in manufacturing very thin large cross-section BBO crystals, we have chosen the oscillator bandwidth in the range 12-15 nm.

Central wavelength: 770-780 nm represents a good compromise between the gain of the active medium and the photocathode efficiency corresponding to the third harmonic.

Repetition rate: 78.893 MHz.

Phase locking loop: this critical sub-system determines the fidelity of locking to an external reference signal. Details on the techniques used and expected performance were already given in Chapter 9. The initial photoinjector laser configuration is based the Synchro-lock PLL™ of Coherent, which was specified to guarantee better than 300 fs rms jitter in the 10 Hz-10 MHz range.

10.1.1.2 Amplifiers

The laser oscillator pulse energy is typically in the few nJ range and has to be boosted to ~20 mJ by the amplifier chain. A proven approach is to use a regenerative amplifier (1-2 mJ) followed by a multipass stage. Schemes that rely on an entirely multipass design while possible, often suffer from problems with beam quality and alignment sensitivity. Indeed, most commercial products are now based on regenerative amplifier technology for energies up to 2-3 mJ and employ one or more multipass stages when higher energies are needed. In all cases, chirped pulse amplification scheme is used [2].

The main decision concerning the FERMI photoinjector laser was the choice of pumping technology. In fact, the required repetition rate and energy level place the photoinjector laser system on the border between flash lamp and diode pumping. Lamp-pumped Nd:YAG/YLF, frequency doubled lasers are best suited for 10 Hz operation. At 50 Hz they become less stable and display lower beam quality. Moreover, for a system with 24 h/day operation, flash lamps would need to be changed every 5-6 days assuming lifetime of 3.10^7 shots. In contrast, diode pumping is much more expensive and may involve higher running costs. To reach the 20 mJ, energy range requires several pump lasers if CW pumping is used. Alternatively, using a quasi-CW-pumped, diode-based system in general reduces diode lifetime and raises operating costs. Balancing all these considerations and giving highest priority to laser system stability, repeatability and beam quality, we chose the CW diode-based pumping scheme shown in Figure 10.1.2. The pump beams in the green come from one Evolution 15™ and two Evolution HE™ lasers, delivering 10 mJ and 2x40 mJ, respectively.

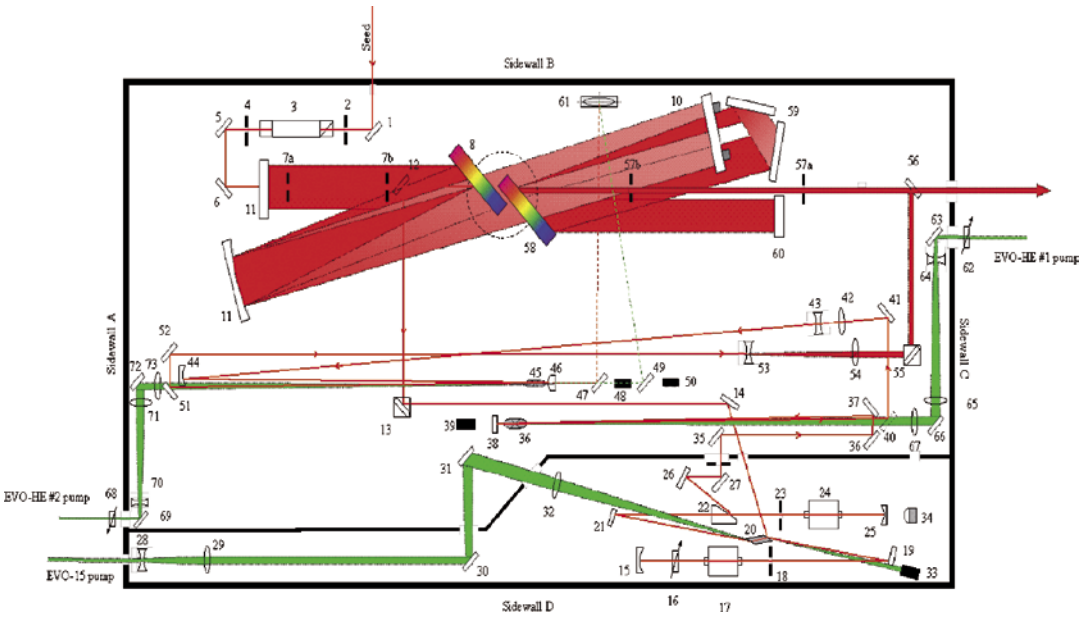

Figure 10.1.2:
Optical scheme of the amplifiers.

10.1.2 Pulse Shaping

The laser system described above can deliver pulses of different duration and shape, determined by the bandwidth of the seed laser and the alignment of the amplifiers, compressor, etc. Generally, the master laser oscillator delivers nearly transform limited, $sech^2$ – type pulses, which can be fitted by a Gaussian function as well. Due to uncompensated, high order dispersion in the amplifier, the 100 fs system would typically produce near Gaussian pulses with a time-bandwidth product 1.2-1.4 times the transform limit. The pulse shaping converts this pulse into one with rise- and fall times of 0.5-1 ps and duration in the 5-10 ps range. The shape requested at present is an increasing ramp; however the system design would also allow the generation of more complex shapes, as well as a flat-top according to the original specifications. Detailed considerations about the different solutions and schemes that were studied are given in [1]. Here we will only briefly recall that there are two main approaches. The first one, furthermore referred to as Fourier-shaping , is based on a spatial displacement of the spectral components of the incoming pulse, modulation of their amplitude and/or phase distribution and then recollimation of these components into a modulated light pulse [3]. The basic optical setup implementing this idea is a dispersive 4-f system consisting of two gratings and a unit magnification telescope [3,4]. The spectral modulation is performed by a spatial light modulator positioned in the common focal plane of the lenses.

The second technique is based on a device called DAZZLER [5]. It also works in the frequency domain, however without spatial separation of the pulse frequency components. The laser pulse is sent trough an acousto-optic modulator where a properly shaped acoustic wave is present. The pulse spectral components are diffracted only by acoustic wave regions that match their wavelength and therefore can be manipulated both in amplitude and phase by the amplitude and positions of these regions [6].

Analyzing the advantages and limitations of the two above mentioned techniques, it can be seen that a hybrid two-stage pulse shaping incorporating the two main shaping techniques is needed in order to satisfy the PIL shaping requirements [1,4] The foreseen system layout is shown schematically on Figure 10.1.3. Initial shaping of the seed 100 fs pulse from the laser oscillator is provided by an acousto-optic dispersive filter (DAZZLER) [2,3] upstream of the regenerative amplifier. The DAZZLER is programmed for both amplitude and phase modulation, where the first shapes the spectral amplitude to the desired shape, and the latter inserts the desired phase delay function.

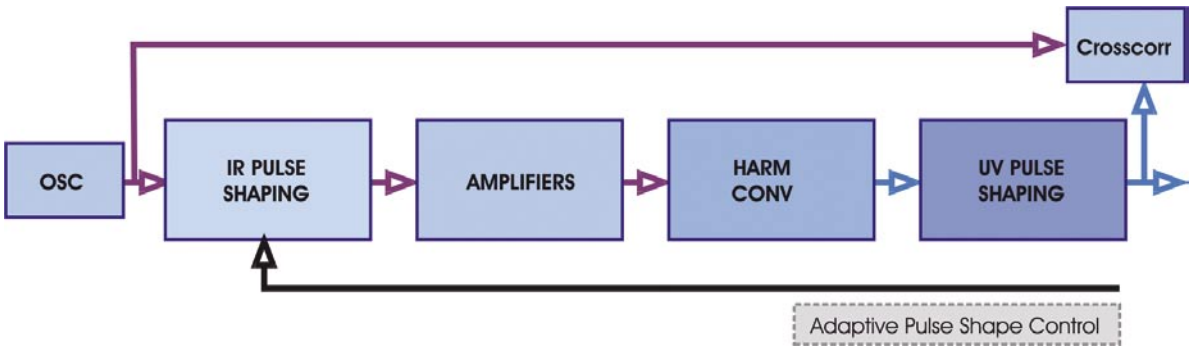

Figure 10.1.3:
Pulse shaping sequence.

The phase modulation at this stage is not yet sufficient to produce the final pulse. We adjust the pulse duration at the amplifier exit (mainly by adding a second order phase term by the grating compressor) to yield a best compromise between a) high conversion efficiency and b) minimum pulse distortion due to high order nonlinear effects (e.g. self-phase modulation). After the harmonic conversion, we then use a UV shaping unit to obtain the final pulse duration and shape.

Two alternative configurations are under still investigation. The simpler one is a two pass grating stretcher that permits expanding the pulse to the desired length by adding second-order dispersion. If a more complex phase function is needed, we will implement 4-f type Fourier shaping, based on a deformable-mirror modulator. In both cases the setup will employ high-efficiency, transmission diffraction gratings, now being tested at ELETTRA.

In order to illustrate better the described scheme, on Figure 10.1.4 we present the results of a simplified simulation of pulse shaping which generates the increasing ramp requested for the FERMI 'long bunch case'. The simulation is done starting with a transform-limited Gaussian pulse at 800 nm having 12 nm of FWHM bandwidth (dashed blue line on the left graph). The spectrum shown in red line is obtained after amplitude modulation by the Dazzler. In addition, it is assumed that the latter completely compensates the residual high-order dispersion of the system. The pulse shape shown by red line on the right graph corresponds to the amplifier output, where a second order dispersion of about 60000 fs^2 has been introduced by detuning the compressor. Assuming that the third harmonic generation is performed in sufficiently thin BBO crystals, so GVM and spectral acceptance effects can be neglected, the UV pulse shape (dashed blue line) is proportional to the third power of the IR one. The final shape and duration, shown by solid blue line are obtained by adding only second order dispersion from the UV grating stretcher. We note that this stretcher will inevitably add also a third order dispersion term on the order of 100 000 fs^3 , which is in principle possible to compensate in advance by the Dazzler, so it has not been taken into account into the above presented simulation. As mentioned above, in case the DAZZLER compensation is not sufficient the odd dispersion terms will be cancelled by the use of deformable mirror.

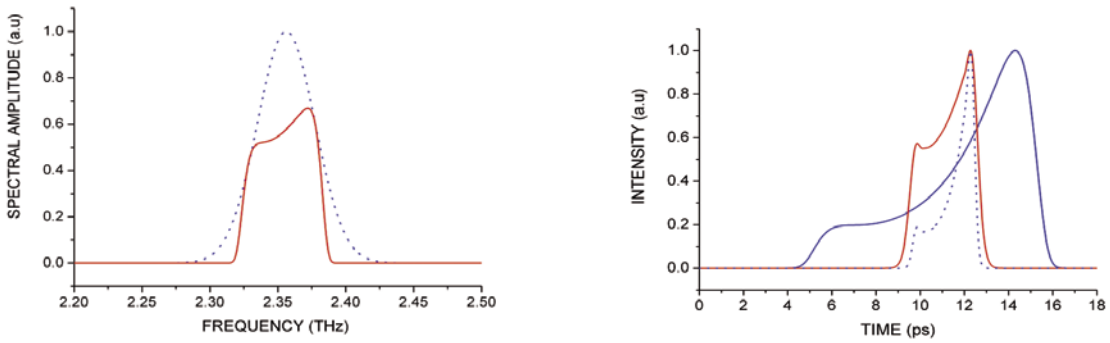

Figure 10.1.4:
Pulse shaping simulation. Left: Input optical spectrum (dashed blue) and amplitude modulated DAZZLER output (red solid); Right: IR pulse shape after amplifier (red), initial UV pulse (dashed blue), stretched UV pulse (solid blue).

10.1.3 Beam Shaping

The ideal spatial (transverse) beam distribution is close to flat-top. Therefore, we need an optical system that transforms the original (nearly Gaussian) shape of the laser beam into a uniform profile.

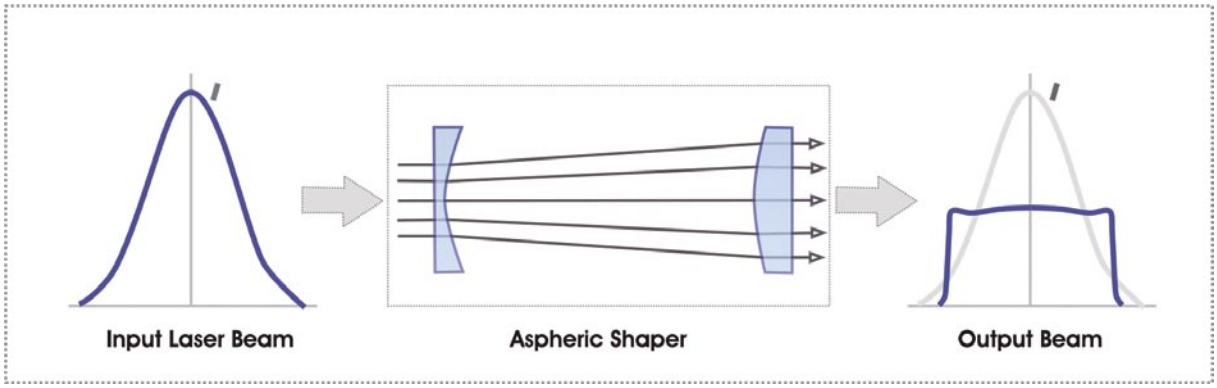

Figure 10.1.5:
Sketch of beam shaping.

Laser technologists have attacked this challenge for many years and have proposed numerous approaches (see [4,5] and Refs therein). Our preliminary analyses and our experiments at ELETTRA (and also at LCLS, see [6]) indicated that aspheric shapers [5] with the modification using a Galilean telescope (See Figure 10.1.5), can meet the specifications for the photoinjector laser system. The main advantages are low insertion loss, high damage threshold and the possibility to work directly in UV. Such shapers are commercially available from two suppliers. Figure 10.1.6 presents an experimental result obtained at ELETTRA using MolTech aspheric shaper in the infrared. Similar profiles have been obtained in the UV by using the Newport version of the shaper [6].

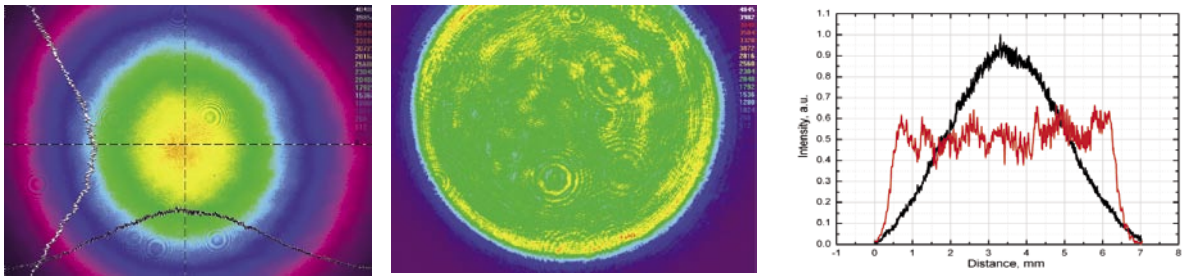

Figure 10.1.6:
Experimental results using a MolTech pi- shaper: images of input Gaussian (left) and output flat-top (center) beams; cross-section of both beams (right).

The figure shows that, while on average the shape is close to flat-top, the ripple is higher then 10%. Most of the ripple likely originates from imperfections in the aspheric lenses. Additional beam deterioration may come from the non-perfectly Gaussian shape and asymmetry of the laser beam after amplification and harmonic conversion. We plan further R&D to improve the performance of the beam shaper.

10.1.4 Harmonic Generation

Figure 10.1.7 displays the main features of the setup implemented for third harmonic generation (THG). The principal features of the design are as follows:

Short, type I BBO crystals for both stages. Our analysis, done using in-house codes plus the freeware SNLO [7] shows that this combination yields the best combination of efficiency and accepted bandwidth.

The "time-plate" design used is more compact and robust than the more common interferometer-like designs, in which the fundamental and SH light are separated after the SHG crystal and recollimated after the polarization rotation.

Beam-size and pulse duration will be adjusted in order to work at peak power level yet avoiding high order non-linear effects in order to keep pulse phase clean.

~15% efficiency has been demonstrated with IR pulses in the 1 mJ range.

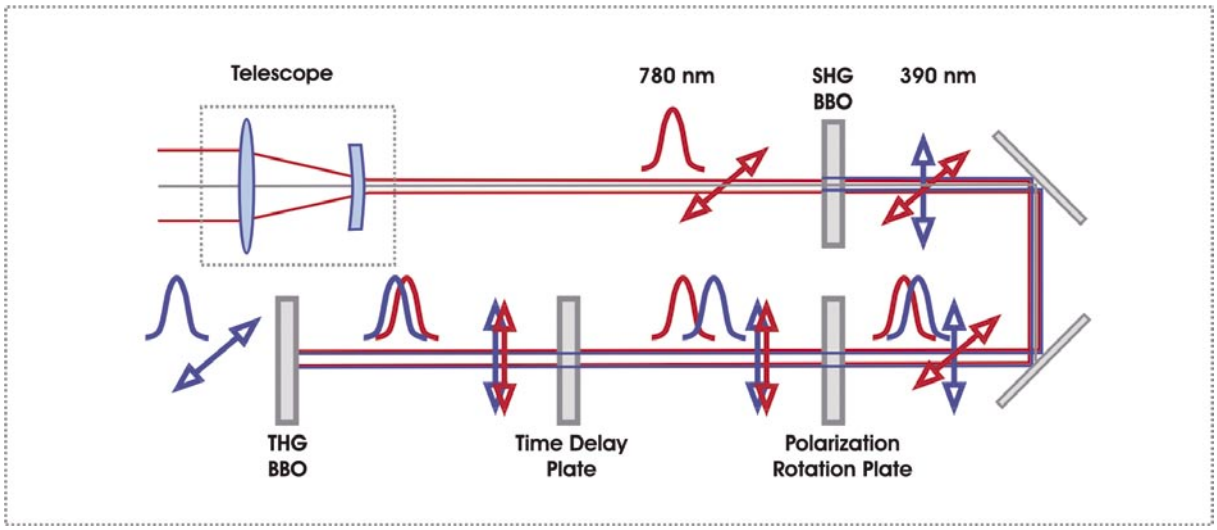

Figure 10.1.7:
Harmonic generation setup.

10.1.5 Beam Transport and Imaging

The beam transport system must propagate the beam from the PIL laser room to the photocathode without distorting its spatial and temporal shape; it also must provide zooming capability. We will optimize the complete engineering design of the optical system using ray tracing software. The main features of the PIL beam transport system (see Figure 10.1.8) are as follows:

Flat-top beams with steep edges tend to develop sharp diffraction peaks and rings upon propagation; therefore, the optical system is based on consecutive imaging with the photocathode plane coinciding with the end image plane of the relay imaging.

The required zoom can be obtained using a commercial motorized UV zoom lens.

The longest propagation distance is the straight section between the laser room and photoinjector in which the beam propagates in a low vacuum enclosure.

Nearly normal incidence geometry is chosen for the photocathode, thus eliminating the need for elements for pulse /beam tilt compensation.

Beam position is monitored on several position sensitive detectors (or CCDs) and controlled by steering mirrors.

Pulse arrival time on the photocathode can be adjusted by variable optical delay line.

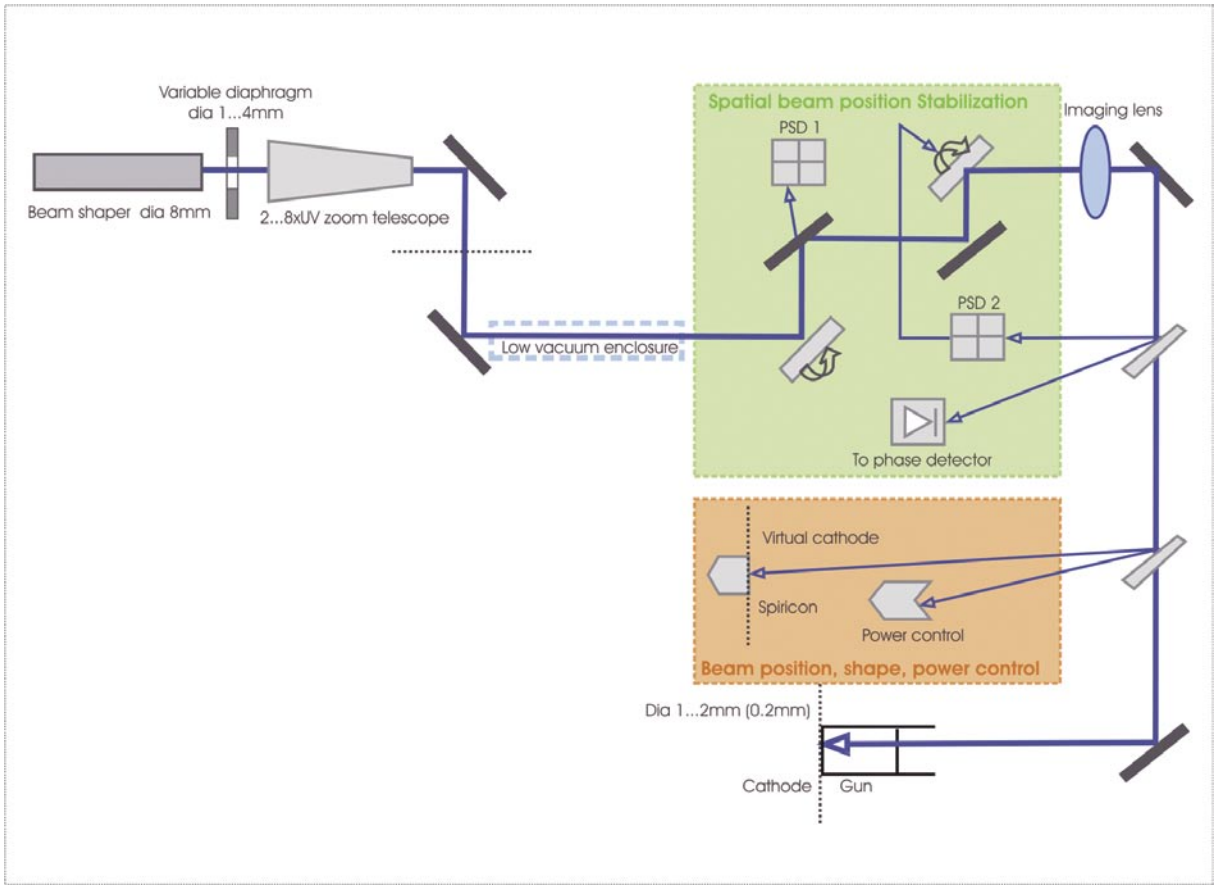

Figure 10.1.8:
Optical beam transport system of the PIL.

10.2 Seed Laser System

10.2.1 Main Requirements

The main requirement for the this laser source is to deliver sufficiently high peak power (~100 MW) in the UV, at wavelengths tunable in a rather large range 240-360 nm and in two pulse durations regimes, namely 100 fs and 1 ps. Obviously, maximum obtainable stability of all parameters is also requested, in particular central wavelength stability and low jitter. The main parameters are summarized in the table below.

Table 10.2.1: Seed Laser parameters.

Parameter	*Specification*	*Note*
Pulse duration	100 fs; 1 ps	Switchable, not real time
Wavelength range, nm	240-360	Real time tuning in sub-ranges
Jitter, rms	< 100 fs	
Wavelength stability	< 0.1%	
Energy stability, rms	< 5%	
Pulse/beam shape	Gaussian	Low residual phase modulation
Spot-size at input, μm	200-300	

10.2.2 Seed Laser Configuration

At present the requirement of such a broad tuning in the UV can only be met by using optical parametric amplification (OPA) in the visible or near infrared followed by consecutive harmonic generation. Moreover, the high UV pulse energy needed (~100 μJ with 1 ps long pulses) requires pumping the parametric amplifier with IR pulses of 10-15 mJ. These considerations lead to our design of a system configured as shown in Figure 10.2.1.

A single Ti:Sapphire based pump source for both the short and long pulse regimes provides a pulse energy of 2.5 mJ and 10 mJ, respectively. Two options remain under consideration for the short pulse regime. In the first one (a on Figure 10.2.1) a white-light, continuum based, non-collinear OPA (NOPA) pumped by the SH of the Ti: Sapphire at 390 nm, is used [8]. This scheme has the advantage that a single SHG stage suffices to cover the full UV range needed. Also, it gives some flexibility in varying the duration of the generated pulse, because the NOPA process can yield substantial shortening of the pump pulses. However, this scheme has some points that need further study:

No commercial product provides the required energy per pulse in the UV; the available literature describes systems that are about a factor of 2 to 5 lower in energy. Scaling the pump energy by parallel scaling of spot size in the NL crystals should allow us to reach the required values.

Wavelength stability is of crucial importance for the FEL seed laser. At present there is no experimental data on NOPA performance in this respect. We expect that by adding an accurate system for wavelength control of the white-light-seeded stage, the NOPA output wavelength stability will be limited by the pump laser one.

The second option is the use of a traveling wave OPA scheme (TOPAS), schematically shown in the lower box (**b**) of the figure. In this case the pump is directly at 780 nm, and tunable IR signal and idler wavelengths are produced. These signals are subsequently frequency doubled and mixed in different stages to produce tunable UV radiation in three slightly overlapping ranges that allow us to cover the full required range.

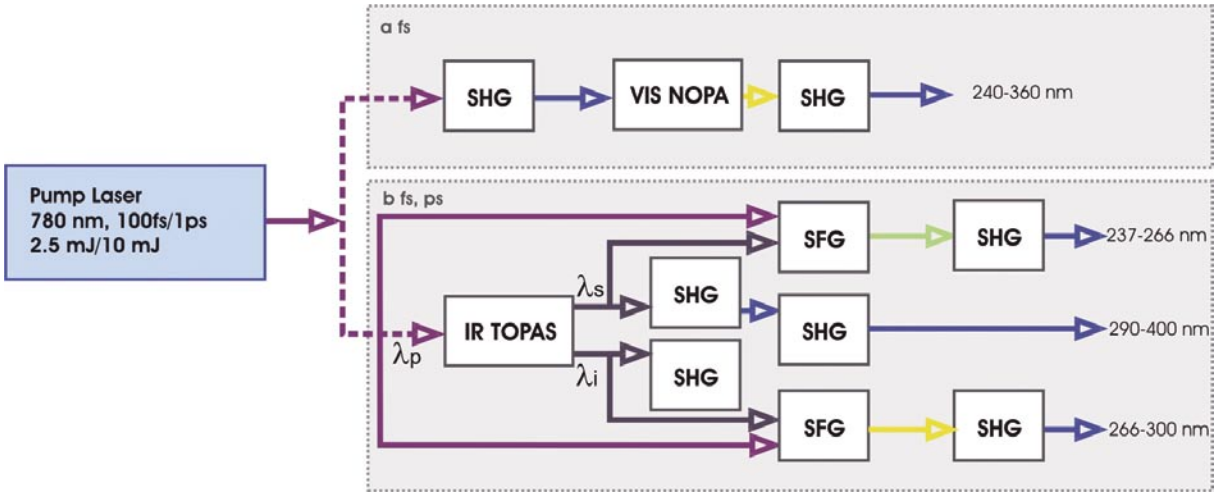

Figure 10.2.1:
Possible Seed Laser configurations: a. NOPA based scheme (fs regime only) b. TOPAS based schemes, both fs and ps version available.

While this scheme is more complicated than the NOPA, its advantage is the availability of a commercial version produced by Light Conversion (www.lightconversion.com). This company can built both 100 fs and 1 ps models with specifications similar to the ones presented in Table 10.2.1. An example of a tuning curve measured on an installed fs system is shown below.

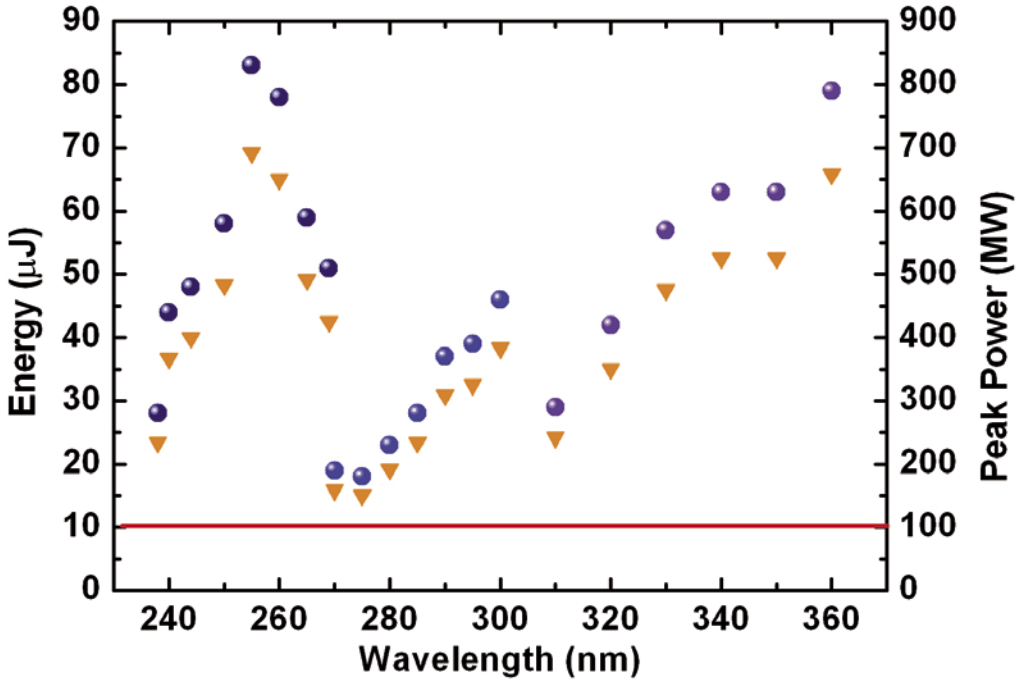

Figure 10.2.2:
Tuning curve of a fs TOPAS by Light Conversion. Circles: measured data in 3 mJ pumped system; triangles: data scaled to 2.5 mJ pump energy.

At all wavelengths of interest this commercial system provides well above the requirement of 100 MW peak power even with 2.5 mJ pump energy. Consequently, only a regenerative amplifier is needed in this case. In 1 ps operation the required minimum pulse energy is 10 times higher, i.e. 100 μJ. Fortunately, the conversion efficiency both in the TOPAS and in the nonlinear mixing stages will also be higher due to strongly reduced group velocity mismatch (GVM) effects. We estimate that ~ 10 mJ of pump energy at 780 nm should be sufficient for reaching ~100 μJ per pulse. The system layout is therefore correspondingly determined: a single pump system contains both the 100 fs and 1 ps sub-systems (see Figure 10.2.3). In short pulse option, the pulse is extracted after the regenerative amplifier and, after compression, pumps a fs-TOPAS. Alternatively, the same seed pulse can be fed into the long pulse optical chain, where it enters a ps stretcher with spectral filtering to reduce the bandwidth; it then passes through the same regenerative amplifier followed by an additional two-pass amplifier.

The pump laser system is now available at ELETTRA. We plan a series of experiments to measure and improve both wavelength stability and beam quality in the near future. In addition to the required dual pulse duration, an important difference with respect to the photoinjector laser is the more stringent jitter requirement (<100 fs rms). A possible way to tackle this need is to replace the Ti:Sapphire seed oscillator with a frequency doubled fibre laser which has intrinsically smaller phase noise. In addition to jitter reduction, the use of fibre laser opens up the possibility to consider the 'direct seeding' approach

(see Chapter 9) which offers additional advantages in terms of system reliability, integration, etc. We have recently started experimental studies on the optimization of the frequency doubling efficiency of a femtosecond fibre oscillator, which is one of the key points which will determine the applicability of the above mentioned approach.

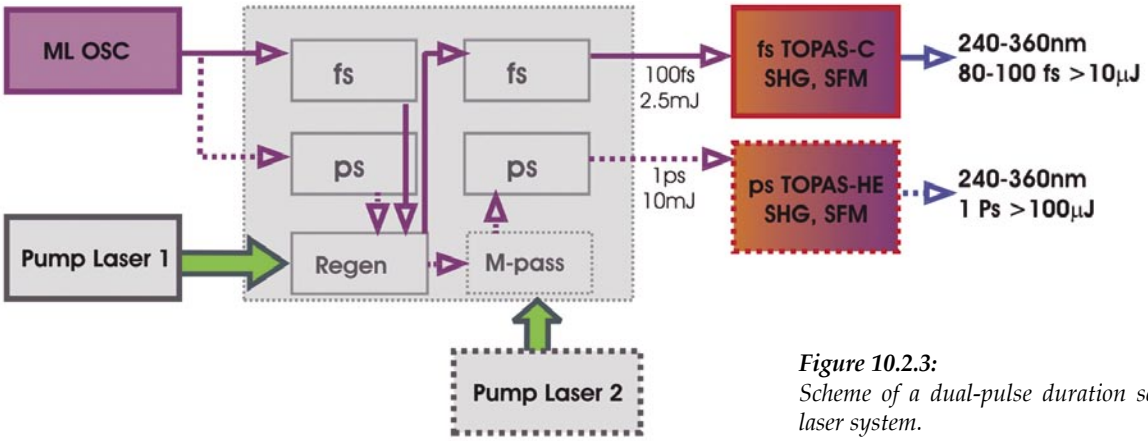

Figure 10.2.3:
Scheme of a dual-pulse duration seed laser system.

10.3 Other Laser Systems

10.3.1 Laser Heater

The functional requirements of the laser heater were introduced in Chapter 6. This laser heater is positioned at about 8 m from the photoinjector. There is some freedom in choosing its exact wavelength; however with respect to diagnostics, a near infrared wavelength is better. Pulse duration and peak power should be in the 15 ps and 10 MW ranges, respectively; the bandwidth of the pulse can be ~10 nm or more. A straightforward means of meeting these requirements is to use a small part of the IR (780 nm) output of the photoinjector laser (PIL) by inserting a 2-4 % beam sampler after the compressor of the PIL. The pulse will then be stretched to about 15 ps by a compact grating stretcher placed on the PIL laser table, and then transported to laser heater position. The requisite optical beam transport and imaging system is very similar to that used for the gun. The available pulse energy provides sufficient margin for spatial and temporal expansion of the beam in order to guarantee good overlap with the bunch at the heater.

10.3.2 Beam-Line Lasers

As already outlined in Chapter 4, a large fraction of the experiments on FERMI will be of 'pump-probe' variety. Therefore, all experimental beam-lines will be eventually equipped with an ultrafast

laser system. Detailed description of the requirements for these systems goes beyond the scope of this CDR. However, for the sake of completeness, a few general observations are useful. A typical source for pump-probe measurements at FERMI would have the following features:

- Lockable with high accuracy to the timing and synchronization signals of the machine, ideally the jitter should be a few times smaller than the pulse duration
- Pulse duration/bandwidth that corresponds to the FEL pulse duration. Ideally, each system should support both short pulse (<100 fs) and long pulse (narrow bandwidth) operation with >1 ps pulse length
- Pulse energy in the few μJ range
- Wavelength – tuneable in bands from UV (>200nm) to IR (2-10 μm).

The ideal beam-line laser is thus very similar to the seed laser described in Ch.10.2. The optimum technology of building it is a fixed-wavelength, amplified, ultrafast laser followed by an OPA with properly chosen harmonic generation and mixing stages. To meet the stringent jitter requirements, this system also must contain a phase-locking loop scheme to allow sub-100 fs jitter values.

10.4 References

[1] FERMI Technical Note Lasers.

[2] D. Strickland and G. Mourou, Opt.Comm. 56 (1985), 219.

[3] A.M. Weiner, J.P. Heritage, E.M. Kirschner, J. Opt. Soc. Am. B 5, (1988) 1563.

[4] M.B. Danailov, A. Demidovich and R. Ivanov, Proc.FEL 2006 , paper THPP026.

[5] P. Tournois, Opt. Comm. **140** (1997), p.245.

[6] D. Kaplan, P. Tournois, Ultrafast Optics IV p.105-118 By F. Krausz, G. Korn, P. Corkum, I.A. Walmsley (Eds), 2004 Springer - Verlag Series in Optical Sciences.

[7] F.M. Dickey and S.C. Holswade (eds), Laser Beam Shaping- Theory and Techniques (Marcel Decker Inc, 2000).

[8] J.A. Hoffnagle and C.M. Johnson, Appl.Opt. 39 (2000), 5488.

[9] S. Gilevich, W. White, private communication.

[10] SNLO is a nonlinear optics software by Arlee Smith, can be downloaded from www.sandia.gov.

[11] E. Riedle,M. Beutter, S. Lochbrunner, J. Piel, S. Schenkl, S. Sporlein, W. Zinth, Appl.Phys.B 71 (2000), 457.

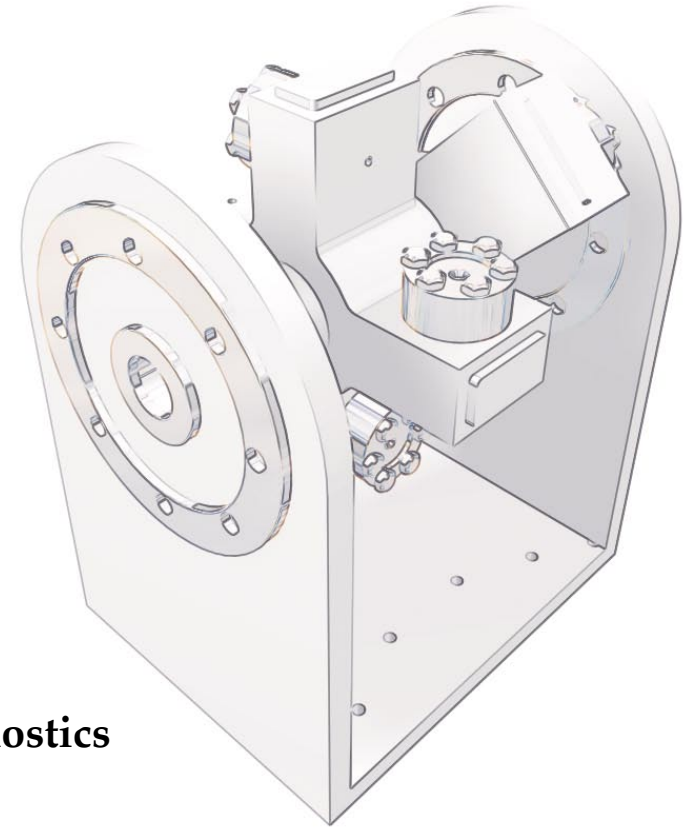

11 Electron Beam Diagnostics

Synopsis

The FERMI beam diagnostics includes a complete set of instruments specifically designed to completely characterize the FERMI free electron beams. Measurements to be performed at different machine sections are presented, starting from the photo-injector and moving downstream, through the linac and the FEL.

The characterization of the photo-injector, given the electron bunch physical properties, is based on a set of traditional instruments. The bunch charge and the transverse and longitudinal profiles are measured by means of a current transformer, movable Faraday cups, Yttrium Aluminium Garnet Cerium crystal (YAG:Ce) screens and a Cherenkov radiator coupled to a single sweep streak camera respectively. This set-up ensures a detailed characterization of the bunch non-gaussian longitudinal profile, one of the new features of the FERMI photo-injector. A movable slit plus screen assembly measures the emittance of the space charge dominated, low energy bunch, while a dispersive beamline is foreseen for energy, energy spread and longitudinal phase space measurements. The uncorrelated energy spread can also be measured exploiting the bunch correlation between energy and longitudinal position.

The following linac sections are equipped with standard intra-section diagnostics stations (X-Y position, profile and charge). Two cavity beam position monitors (BPMs) with micrometer resolution measure the bunch transverse position at the entrance of the first ELETTRA type accelerating section (S1) for beam centering.

Two four-screens stations separated in betatron phase by $\pi/4$ are located downstream from BC1 and at the end of the linac respectively, and used to accurately measure the beam emittance.

Dedicated diagnostic stations also equip both bunch compressors (BC1 and BC2): the bunch length, arrival time (i.e. jitter) with respect to the reference, energy and energy spread are measured non-destructively enabling on-line monitoring of the beam. Measurements of the coherent radiation (CSR, CDR) generated by short bunches in the compressors provide relative bunch length information. A newly developed bunch arrival time monitor based on an electro-optical technique performs bunch arrival time measurements.

Finally a dedicated "energy BPM" is located in the dispersive section of each chicane to monitor the beam energy. The beam energy spread is crosschecked (destructively) either using a wire scanner or a screen. Two radio frequency deflectors, located downstream from BC1 and at the end of the linac respectively, are needed to accurately measure bunch length and, coupled to a downstream dipole, to measure slice emittances and slice energy spread.

A set of three cavity BPMs is placed in a drift space, in front of both the FEL1 and the FEL2 modulator undulators, to measure the beam transverse position with micron accuracy in the single shot mode and to check the beam alignment in the transverse (X-Y) coordinate plane. An electro-optical sampling station provides single shot measurements of the bunch arrival time and of the longitudinal profile non-destructively.

Finally, intra-undulator diagnostics stations, measuring the transverse beam position and the FEL photon beam intensity, are used to optimize the FEL process.

11.1 Introduction

The chapter has two parts: in the first (Paragraphs: 11.1 to 11.2.11) the beam parameters to be measured are listed following the machine topology, from the photo injector down to the FEL sections. The second part (Paragraph: 11.3) covers the instruments foreseen to meet the diagnostics specifications.

Some instruments, such as those to measure the bunch length and arrival time with < 100 fs resolution, require a significant development effort. In particular, the bunch arrival time is measured at several locations using a novel electro-optical technique that has demonstrated sub-100 fs resolution.

On-line energy and energy spread monitoring is another demanding task; in the bunch compressor region a single instrument able to cover the full operating range while preserving state of art performance is still being developed.

For the radio frequency deflectors, innovative approaches are under investigation to add additional features to those of the basic set-up. In particular, a two-plane RF deflector is foreseen, able to handle full energy beams.

The quality of the photoinjector high brightness electron beam plays a crucial role for the performance of the FERMI seeded FEL. Optimization of the gun is made possible by a complete set of beam monitors for an extensive characterization of the 5 MeV electron beam longitudinal and transverse phase space.

A set of standard instruments for measuring the transverse position and the charge per bunch is installed in each gap between linac sections to ensure non intercepting, on-line beam monitoring. Both the BC1

and the BC2 bunch compressors (*see par.* 11.2.5) are completely instrumented to provide signals to beam energy and bunch length stabilization feed-back systems.

In a seeded FEL like FERMI the temporal and spatial overlap between the electron beam and the seed laser pulse has to be checked, particularly at the input of the modulator; this is obtained using a pair of dedicated cavity BPMs associated with an electro-optical sampling station. The onset of laser induced bunching is checked downstream from the modulator chicane by coherent transition radiation based diagnostics. The FEL radiation intensity is monitored along the radiator chain, by means of suitable optical detectors, all the way through saturation. Finally, the complete spectral-angular distribution is measured by dedicated spectrometers, one for each FEL chain.

Standard beam line diagnostics is presented briefly, while state-of-the-art diagnostics is discussed in more detail.

11.2 Measurements to be Performed

11.2.1 Injector Diagnostics

The injector is equipped with a full complement of instruments to measure the electron beam properties, in order to produce input signals for the machine protection system and information vital for understanding the FEL lasing process. Considerations about the photoinjector beam instrumentation and diagnostics are also found in section 5.5.

The key electron beam parameters monitored along the injector section are discussed below. Of these, only the bunch charge and the transverse beam position can be measured with non-intercepting devices.

The primary purpose of beam position and profile monitors is to help align the beam on axis through the first accelerating cavity. The beam rms diameter ranges from 0.5 to 2 mm and is measured with an accuracy of 10 – 100 μm, depending on the type of monitor used and on beamline parameters at the monitor. Position and profile measurements also provide information on the laser beam stability.

At low energies, where the beam dynamics is strongly dominated by space charge effects, accurate emittance measurements are performed using either a 2D pepper-pot device or a 1D slit array, as described in Section 11.3.7. The thermal emittance, whose expected value is ~0.6 mm mrad, is measured at low bunch charge (~ 50 pC) using the solenoid plus scintillation screen technique [1]. Beam charge measurements aimed at providing information on possible drifts of the photocathode quantum efficiency and at helping to adjust the laser settings, in particular the correct phase between the laser and RF gun, are performed using Faraday cups (see par. 11.3.10.1) and/or a current transformer (see par. 11.3.10.2).

The nominal bunch charge varies between 0.3 nC and 1.0 nC and is measured with 10 - 50 pC resolution depending on the type of monitor used and on the beam parameters at the monitor.

In order to check the beam proper alignment and to optimize the collimation efficiency, additional measurements are implemented on the photoinjector laser beam.

The electron beam longitudinal current distribution and the bunch length are measured using an aerogel Cherenkov emitter coupled to a streak camera (see Par. 11.3.16). The expected bunch length of about 10 ps is measured with 200 fs resolution.

A magnetic spectrometer is a crucial diagnostics element for establishing the proper RF gun tune and overall performance. The dispersive beamline provides information on the beam energy, energy spread and longitudinal phase space. The expected rms energy spread varies in the range 100 – 300 keV depending on the phase between the laser pulse and the gun peak field. The design goal is to measure it with 1 % resolution.

A compact optical bench, located in the tunnel close to the gun, is dedicated to the photocathode laser diagnostics and used to monitor the laser performance on-line, based on the "*virtual cathode*" scheme (see Par. 5.5.2.1).

11.2.2 Laser Heater Diagnostics

The laser heater design is based on a four magnet chicane with a short undulator in between the second and the third dipole (see Par. 6.2.1). The laser heater diagnostics will be mainly dedicated to the alignment of the electron beam in the undulator and to guaranteeing the transverse overlap of the electron beam with the laser beam. Two stripline BPM (section 11.3.3) plus YAG:Ce screen pairs (Section 11.3.5) are installed upstream and downstream from the undulator respectively. The BPM will measure the electron beam position with a resolution of ~50 microns while the YAG:Ce will be used to measure the electron beam and laser beam profiles.

11.2.3 Linac1, Linac2, Linac3 and Linac4

The accelerating structures of the linacs (1, 2, 3 and 4) are equipped with intra section diagnostics, where transverse position and profile along with the bunch integrated charge are measured. The main purpose of the intra section diagnostics is to ensure the correct steering of the beam on the axis of the accelerating structures while monitoring the efficiency of the charge transport process. BPMs and current transformers provide this functionality, non destructively. Screens have been adopted for "first trajectory" steering and for beam profile measurements. Due to longitudinal space constraints ad-hoc instruments have been conceived, deeply integrated in the machine layout. Precise initial alignment is of fundamental importance to provide the beam position relative to the accelerating structures.

11.2.4 X-Band Linearizer

The X-band linearizer is necessary to longitudinally manipulate the electron bunch. It is operated at 11.423996 GHz, the 4th harmonic of the accelerating S-band frequency. Two dedicated BPMs are used to monitor the bunch trajectory in order to keep it aligned on the cavity axis. A wide band (BW > 10 GHz) electromagnetic pick-up, connected to a multi channel, wide band (BW = 15 GHz), real-time (not sampling) oscilloscope, will provide information on the relative bunch phase with respect to the X-band frequency.

11.2.5 BC1 and BC2 Compressors Diagnostics

Bunch compressors (BC) are key components of the seeded FEL. A complete set of non intercepting diagnostics is foreseen to produce error signals for the feedback loops used to stabilize the electron bunch energy and peak current [2]. The different operation regimes foreseen for FERMI call for a flexible set-up of both the bunch compressors and the associated diagnostics. To this end beam position monitors in dispersive regions (called "energy BPMs" or EBPMs, see Section 11.3.4) and diagnostics

stations containing an optical transition radiation (OTR) screen (Section 11.3.6) and a wire scanner (Section 11.3.9) are mounted inside the bunch compressors to measure the beam position, energy and energy spread. In particular EBPMs will be used for the on–line, non-intercepting energy measurements driving the energy feedback. A relative bunch length monitor is needed to find the optimum compression value and to stabilize the bunch peak current. It will be based on the detection of coherent synchrotron radiation (CSR) from the last bend of the BCs and of coherent diffraction radiation (CDR) generated from a downstream the same bend. The system allows non-intercepting measurement of the relative bunch length. The bunch arrival time at the entrance and at the exit of the compressor will be measured shot by shot using a bunch phase monitor (Section 11.3.15).

A schematic layout of the full complement of bunch compressor diagnostics is shown in Figure 11.2.1.

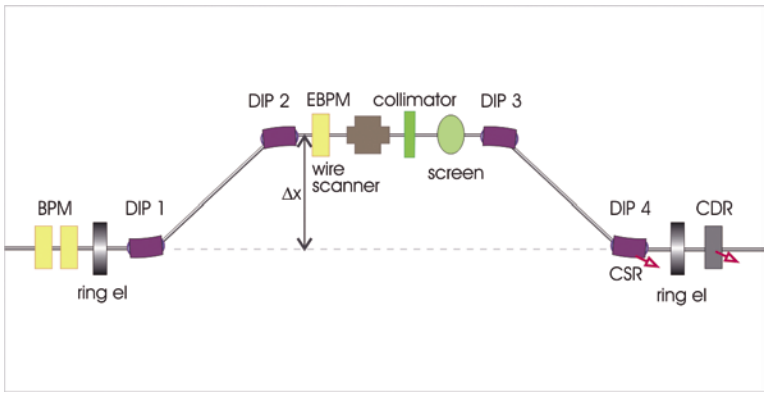

Figure 11.2.1:
Bunch Compressor Diagnostics layout.

11.2.6 Front-end Last Diagnostics Station

A diagnostics station will be located immediately downstream from the second bunch compressor (BC1), just before the beam dump. It will mainly consist of two sub-systems: a RF deflector, called "low energy deflector", plus a multi-screen emittance measurement station. The RF deflector (described in 11.3.12) is a vertically deflecting, compact (~1 m), 5 cell standing wave structure used to measure both the longitudinal profile and the horizontal slice emittance.

The multi-screen station is used to measure the beam transverse emittance and investigate the effects of CSR induced emittance dilution.

The energy and energy spread will be measured by a YAG:Ce screen located after the beam dump bending magnet.

11.2.7 End of Linac and Spreader Diagnostics

The linac end has been identified as another key location for beam diagnostics. A high energy RF deflector, a multi-screen emittance station and a spectrometer will be located in this area.

The RF deflector (described in 11.3.12) is a traveling wave structure, ~ 2 m long, powered by a dedicated modulator. It does allow for both vertical and horizontal deflections. This feature will make it a unique instrument that allows measuring both the vertical and the horizontal slice emittance using a YAG:Ce screen placed 10 m downstream from the deflector. Furthermore, on a second screen downstream from the electron beam dump bending magnet, the correlated slice energy spread can be measured.

Four screens properly spaced in phase are also mounted in the same area to measure the beam emittance. Both the vertical and the horizontal beta function values at the screens are 5 m, producing a 56 μm *rms* beam size for a *1 mm mrad* normalized emittance. The optical detection system resolution is specified to be 10 μm. Screens behind the dump bending magnet allow it to function as a spectrometer.

A collimator, located in a high dispersion region of the spreader, will provide energy collimation to meet undulator radiation protection and beam dynamics requirements. A BPM and a screen are foreseen both in front and behind the collimator for transverse profile and position measurements. Collimator blades with micrometer positioning resolution are expected to be sufficient for both betatron space and energy cleaning. Energy and energy spread measurement systems will also be provided downstream from the collimator.

11.2.8 FEL Modulator Diagnostics

Because the interaction of the seed laser with the electron beam takes place in the FEL modulator, the beam position and angle at the modulator entrance is highly critical. A pair of high resolution cavity BPMs is therefore installed in front of it (see Par. 11).

The superposition in space of the seed laser beam and the electron beam will be checked by means of YAG:Ce screens (Section 11.3.5) placed both upstream and downstream from the modulator while their superposition in time will be checked by an Electro-Optical Sampling station (EOS) (see Par. 11.13.9) located upstream. The EOS will provide single shot, non-intercepting measurements of the bunch longitudinal profile, its arrival time and its jitter.

11.2.9 FEL Radiator Diagnostics

The FEL modulator is followed by a chicane which converts beam energy modulation into current modulation. The desired laser induced microbunching will be measured by detecting the coherent transition radiation (CTR) produced by the beam in traversing a thin pop-in screen. A pop-in diagnostic station similar to the ones installed in between undulator sections (see Par. 1.13.3), is located immediately downstream from the chicane and just in front of the first undulator section, and serves the purpose. The intensity of the CTR will be measured by a silicon photodiode. For FEL-1, the radiation can be transported out of the vacuum chamber and its spectrum measured using a UV spectrometer since it is mainly emitted at the seed laser wavelength in the near UV. For FEL-2, because the CTR wavelength is shorter than ~ 100 nm (vacuum UV), transport in air is not possible and an in-vacuum solution is foreseen.

Another crucial parameter to be measured at the modulator location is the beam position: a cavity BPM placed downstream from the pop-in station is provided for this purpose. The beam profile will be measured using either a YAG:Ce or an OTR screen. Multipurpose diagnostics stations are also foreseen along the FEL undulator chain, one at each straight section in between undulator sections; their configuration and working principle are described in Paragraph 11.3.8.

Additional parameters to be measured along the beam trajectory are: the electron and photon beam relative position, their profile, their intensity and the induced bunching evolution. This set of measurements will be done using the same kind of tools described above but, because the photon and the electron beams now overlap, in a more complex configuration.

11.2.10 Beam Dump and FEL Downstream End Diagnostics

Both the FEL and the spontaneous radiation produced in the radiator must be characterised in terms of energy per pulse, transverse profile and divergence, pointing stability and spectral distribution.

The FEL radiation beam transverse profile and pointing stability will be measured by ad hoc developed screens since the beam energy density could cause damage. Information on the spontaneous radiation spectral distribution, important for the undulator final tuning procedure, as well as on FEL radiation will be obtained by measuring the radiation spectral distribution on-axis and its angular distribution. As an example, the K factor of each undulator section can be tuned by optimizing the frequency of the on axis first harmonic. Most of these measurements, including the spectral distribution, will be done in single shot, using the diffracted beam from monochromators in the experimental hall (see Par. 8.4.3). The FEL energy and intensity stability will be measured in a gas cell system (see Par. 8.3.1).

In order to measure the electron beam final timing jitter a station equipped with a synchro-scan streak camera detects the visible radiation extracted from the last beam dump magnet. The device is illuminated simultaneously by SR and by a reference optical pulse from the ultra stable timing system or by the user laser. In spite of a nominal resolution of less than 2 ps_{FWHM} this technique provides the relative time stability of the electron bunch with respect to an optical reference pulse (or a user laser pulse) with a sensitivity of the order of 400 *fs*.

11.3 Instrumentation

11.3.1 Beam Position Monitors

Three different kinds of beam position monitors will be used. Matched stripline BPMs are foreseen where high resolution is not required while cavity BPMs are used where high resolution is needed, like at the entrance of the FEL modulator.

11.3.2 Cavity Beam Position Monitor

Cavity beam position monitors (TM_{110} cavity type) are foreseen where resolution of the order of 1 μm is required (not achievable with matched stripline BPMs). Beam based alignment will heavily rely on their performance. In particular, cavity BPMs are used in front of the modulator (2 cavity BPMs in a drift) to accurately measure the transverse position and angle of the beam entering the modulator. Accurate measurements of the beam transverse position are also needed in between undulator sections.

The present design is, conceptually, a scaling from X-band to C-band of the cavity BPM developed for NLC [3]. The complete design study is reported in ref. [4], while in Figure 11.3.1 are summarized the parameters and a 3D model of the BPM is shown. Analytical and numerical models show that the resolution at C-band remains below 1 μm. Furthermore, common mode losses of the scaled object are at the same level as those of the original X-band device.

Careful mechanical implementation and integration with other intra-section diagnostics is needed to guarantee not only resolution and long term stability but also accurate and reproducible alignment.

C-band cavity BPM	
Cavity gap	$10mm$
Cavity radius	$26.4mm$
Beam pipe radius	$10mm$
Coupling WG	$34.85 \times 6mm^2$
Distance WG to beam axis	$12mm$
WG standard	WR137
Resonant frequency	$6.5GHz$
Unloaded Q factor	8530
External Q	10500
Coupling coefficient	0.1
Reference cavity	
Cavity gap	$10mm$
Cavity radius	$17.6mm$

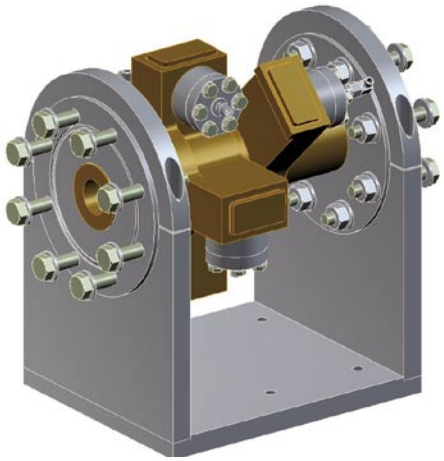

Figure 11.3.1:
Dimensional and RF parameters of the C-band cavity BPM and the reference cavity (left). C-band cavity BPM 3D model with its four coupling waveguides and reference cavity (right).

11.3.3 Stripline Beam Position Monitors

Most of FERMI BPMs located where space is not a stringent constraint, like in between linac sections, are matched stripline BPMs. The strips are 150 mm long and signal detection is based on commercial, 500 MHz electronics. Sum signals also provide fast beam loss information during tune up. The strips are fixed to and aligned with respect to flanges which are, in turn, fixed to the BPM body. The mechanical uncertainty on the centre of the assembly position is specified to be less than 20 μm. The readout electronics is designed so that, after careful initial alignment to 50 μm rms absolute accuracy, the long term (8 hours) single shot absolute position peak to peak fluctuation remains smaller than ~ 70 μm.

For locations where longitudinal space is an issue, like in the photoinjector, resonant striplines [5], [6], less bulky than matched ones, are being considered; preliminary tests indicate that they provide a resolution approaching that of cavity beam position monitors. The dedicated electronics needs further developing.

11.3.4 Energy Beam Position Monitors

The beam centroid transversal displacement in the BC1 and BC2 bunch compressors, Δx, spans over ~100 mm. A vacuum chamber at least 150 mm wide would therefore needed to accommodate the electron beam (±3 σ = 35 mm) plus the closed orbit allowance. On the other hand, the rms energy stability required by the FEL (ΔE/E=0.1%) does translate, in terms of rms displacement variations, into 200 μm under nominal BC1 operating conditions. To correctly operate the feedback system the resolution of the position measurement must be at least four times better. A single shot resolution of ~50 μm is needed, a specification that can not be met with a chamber much wider than 60 mm. In order to accommodate the up to 100 mm beam displacement in the bunch compressor, the central (2^{nd} and 3^{rd}) dipoles and the BPMs will therefore be mounted on high reproducibility translators and moved, to follow the beam displacement, which allows reducing the chamber width to 60 mm only. Further design studies and simulations are in progress.

Other position diagnostics options, such as the one proposed at DESY [7], based on the measurement of the relative time difference between two pulses generated in a transverse strip-line arrangement, are also under consideration.

11.3.5 Scintillation Screens

Screens, either scintillators or the optical transition radiators (OTR, described in section 11.3.6), are used to measure the electron beam transverse profile. In particular, YAG:Ce screens with thickness of about 100 μm are used in the photoinjector. Thin YAG:Ce is a fast scintillator with excellent mechanical and chemical resistance. YAG:Ce screens are made from selected inorganic crystal materials with cubic structure; the grain size and transparency ensure a spatial resolution better than 10 μm, compatible with 10 μm limit of the CCD sensor and optical setup. The material mechanical properties allow producing thin screens, down to 0.005 mm thick. The wavelength of maximum emission is 550 nm, the decay constant 70 ns and the photon yield at 300 K 35000 photons/MeV [8]. Screen positions along the beamline are chosen to avoid saturation effects at high charge densities (~0.1pC/μm^2). YAG:Ce screens can also be used to detect photon beams, from VUV to gamma rays.

YAG:Ce screens are the preferred solution at low energy because of their higher photon yield compared to OTR screens. Standard ceramic scintillating materials such as Aluminium Oxide doped with Cr_2O_3 (commercially called Chromox) have been discarded because of their poorer performance in terms of spatial resolution, decay time and afterglow. Screens will also be used during laser alignment of accelerator components.

11.3.6 Optical Transition Radiation (OTR) Screens

OTR screens are usually thin metal foils or metal coated substrates. The choice of the metal depends on the application but most often Ti, Al and Ag are used. The substrates can be mylar Teflon or Si. Because OTR is a local, surface, instantaneous effect and since very thin foils can be used, it provides spatial resolutions down to ~1 μ*m*, high linearity and high radiation resistance. The instantaneous OTR emission can thus be used to measure the longitudinal beam profile. Such screens are also used as CTR emitters for micro bunching detection, as previously discussed. At present we are considering to use 0.3 mm Si substrates coated with 200 nm of Al. The photon yield becomes comparable to that of the YAG:Ce screen one only at a few hundred MeV.

11.3.7 Emittance Measuring Devices

The emittance measurement at low energy (5 MeV) will be based on single slit and multi-slit (pepper-pot) devices which slice-up the beam into well separated sampling beamlets by means of an intercepting mask. The slits convert the space charge dominated incoming beam into several emittance dominated beamlets which then drift to a detection screen. Slit spacing has to be larger than the slit width and smaller than the beam size to ensure that the image can be resolved [9]. The drift space in between the mask and the screen must be long enough in order to have high resolution for low emittance beams and short enough to prevent overlapping of beamlet profiles on the screen. Evaluation of the rms emittance only depends on the slit mask geometry, the beamlets size and the intensity distribution on the screen [10], the resolution being mainly limited by jitters of the beam transverse position or profile.

11.3.8 Intra-Undulator Pop-in Station

Multipurpose pop-in stations are compact devices equipped with several screens. (see Figure 11.3.2). They are meant to provide information on the electron and photon beam transverse position. Each pop-in will consist of a remotely movable holder mounted at 45° with respect to the accelerator axis and holding at least three elements: a YAG:Ce screen, an OTR screen and a UV mirror. The system is interceptive and therefore only used during commissioning and for periodic checks.

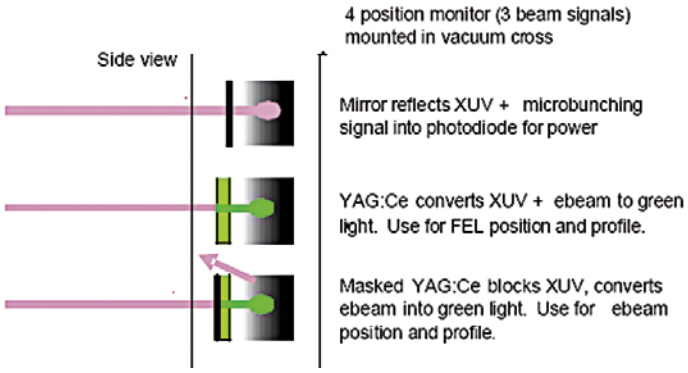

Figure 11.3.2:
Multi screen functional scheme.

Visible light from the YAG:Ce screen will be used to image both the XUV photon beam and the electron beam with a CCD camera. It provides information about both the electron and the XUV beams position and profile. A mask can also be used to block the XUV radiation and allow only the electron beam to reach the YAG:Ce screen.

The OTR screen is used to image the electron beam only, since FEL radiation reflected by the screen is stopped by the vacuum viewport. XUV radiation can be detected by a Si photodiode, to provide an absolute energy measurement and thus reconstruct the gain curve of the FEL along the undulator chain.

The CTR signal due to laser induced bunching can also be measured on the same detector. To discriminate between the two signals a filter can be used, since the CTR signal does appear at the seed laser wavelength. This part of the equipment needs to be in ultra high vacuum, to avoid XUV radiation absorption in air. Possible screen radiation damage problems by the high peak power XUV beam need further investigation.

11.3.9 Wire-Scanners

Compared to screens, wire scanners can provide resolution down to 1 μm level, dominated by the wire diameter. On the other hand they are delicate, comparatively slow and therefore able to reconstruct a beam profile only on a multi shot basis.

11.3.10 Bunch Charge Measurement

11.3.10.1 Faraday Cup

A Faraday cup with better than 10 pC accuracy is used to measure the absolute bunch charge and to calibrate non-intercepting charge measuring instruments such as BPMs or integrating current transformers. It also serves as beam dump for the injector beam.

11.3.10.2 Integrating Current Transformers

Integrating Current Transformers (ICT) are used to measure non-destructively the beam charge with high relative accuracy. Commercial ICTs will be used that integrate the signal with a time constant of the order of 10 nsec, depending on the model. They are embedded in conflat flanges for direct mounting on the beam pipe [11]. The latter feature is crucial when space is limited, like in the photoinjector.

11.3.11 Energy Spectrometers

11.3.11.1 Photo-injector Energy Spectrometer

A first design based on a 90º bending magnet followed by a YAG:Ce screen has been studied and is described in Chapter 5. The intrinsic relative energy resolution is $\delta_{min} \geq 2/D \sim 2$ keV, where D is the dispersion value at the screen. Alternative solutions with smaller bending angles are being evaluated both in terms of energy resolution and of mechanical constraints.

11.3.11.2 BC1 Energy Spectrometer

A bending magnet will be located downstream from BC1 and used as an energy spectrometer. An energy resolution of the order of 60 KeV is the design value.

11.3.11.3 Linac-end Energy Spectrometer

An energy and energy spread measurement will be performed at the end of the linac. It will make use of the existing linac transfer line bending magnets that will be used for FERMI as beam dump magnets. The energy stability requirements of FEL are of $\delta E/E=(\pm 0.5 \times 10^{-4})$. The design relative resolution of the spectrometer has been chosen to be 2.5×10^{-5} which means at 1.2 GeV, an absolute resolution of 30 keV. The dispersion provided by the two bending magnets and the drift space between them is D_{tot}=1.85 m. The energy resolution translates directly into a space resolution of 46 μm. The relative energy spread,

expected to be 0.01%-0.1%, will be measured with a resolution of 5%. The energy spread in combination with the dispersion (D_{tot}=1.85 m) will induce a transverse broadening of the beam, whose expected rms beam size is 185 μm. The 5% resolution requirement translates then to 9 μm spatial resolution. The resolution requirements for both beam energy and energy spread measurements should be met using OTR screen and high resolution optics systems of the same kind of those used for emittance measurements.

11.3.12 Radio Frequency Deflectors

Two radiofrequency deflectors are foreseen as diagnostic tools, one after BC1 (DEF1) at 220 MeV and one at the end of the linac, in front of the spreader (DEF2), at 1.2 GeV. They are used, in conjunction with appropriate monitors, to measure the bunch length σ_z and the slice vertical and/or horizontal emittance in a dispersive free region. The betatron phase advance between the RF deflecting cavity and the monitor shall be $\pi/2$. The intrinsic resolution is ~15 μm for DEF1 and ~5 μm for DEF2.

The deflectors will operate in the S-band at a frequency of 2998.010 MHz. DEF1 is a rather short (~0.5 m) standing wave structure fed 5 MV by spilling RF power from an accelerating section modulator; it deflects the beam in the vertical direction only. DEF2 is a traveling wave structure, ~2 m long, capable of 20 MV; it can deflect the beam in both the vertical and the horizontal direction.

The beta function at the deflectors, β_d, is 10 m at DEF1 and 20 m at DEF2.

11.3.13 Radiation Detectors

Radiation detectors ranging from diodes to pyrodetectors will be used, depending on the spectral distribution and intensity of the radiation, since the shorter the bunch the farther the emission spectrum extends towards high frequencies.

11.3.14 Bunch Arrival Time, Electro-Optical Sampling Station

The electro-optical effect exploits the birefringence induced in a suitable crystal by the transverse electric field produced by the beam relativistic electrons. For bunch charges of the order of 1 nC and at distances of a few millimetres the field can be of the order of tens of MV/m. Such a strong ultra fast changing electric field can be probed by a linearly polarized femtosecond laser pulse by detecting the laser phase delay induced by the birifringence in the crystal. The phase delay measurement is obtained by splitting the beam spatially in two opposite circular polarization components using a $\lambda/4$ plate followed by a Wollaston prism; a balanced photo detector is then used to detect the difference of the two intensities, ΔEO, proportional to sin(Γ), where Γ is the phase delay given by:

$$\Gamma = \left(\pi d/\lambda_o\right) n_o^3 \, r_{41} \, E_a \sqrt{1 + 3\cos^2\alpha} \quad ,$$

and where λ_0 is the laser central wavelength, d and n_0 the EO crystal thickness and reflective index, r_{41} the electro-optical coefficient, E_a the electric field amplitude and α the angle between the main crystallographic axes and the electric field.

Electro-optical sampling (EOS) has been used worldwide (FELIX, SPPS, TTF2) in recent years to non-

interceptingly measure the bunch arrival time in a single shot [12]. Furthermore, the technique is used to provide information on the electron bunch profile and the FEL pulse generation timing.

Each FERMI undulator chain will be equipped with an EOS station. The electron bunch duration at the end of the linac ranges from 700 to 1800 fs FWHM and the jitter of the bunch arrival time is 150 fs (rms) [13].

Using a time-to-space conversion scheme developed at SPPS [14] and probing the electro-optical crystal with sub-100 fs laser pulses the specified time resolution of ~100 fs is reached, in a time window of ~10 ps. A block diagram of an EOS station is shown in Figure 11.3.3; the station has four main components: laser, polarization diagnostics and delay line, in-vacuum setup, detection system.

All components, including the vacuum pipe, will be mounted on an optical table. To prevent vibrations the vacuum pipe will be connected to the rest of the machine through bellows.

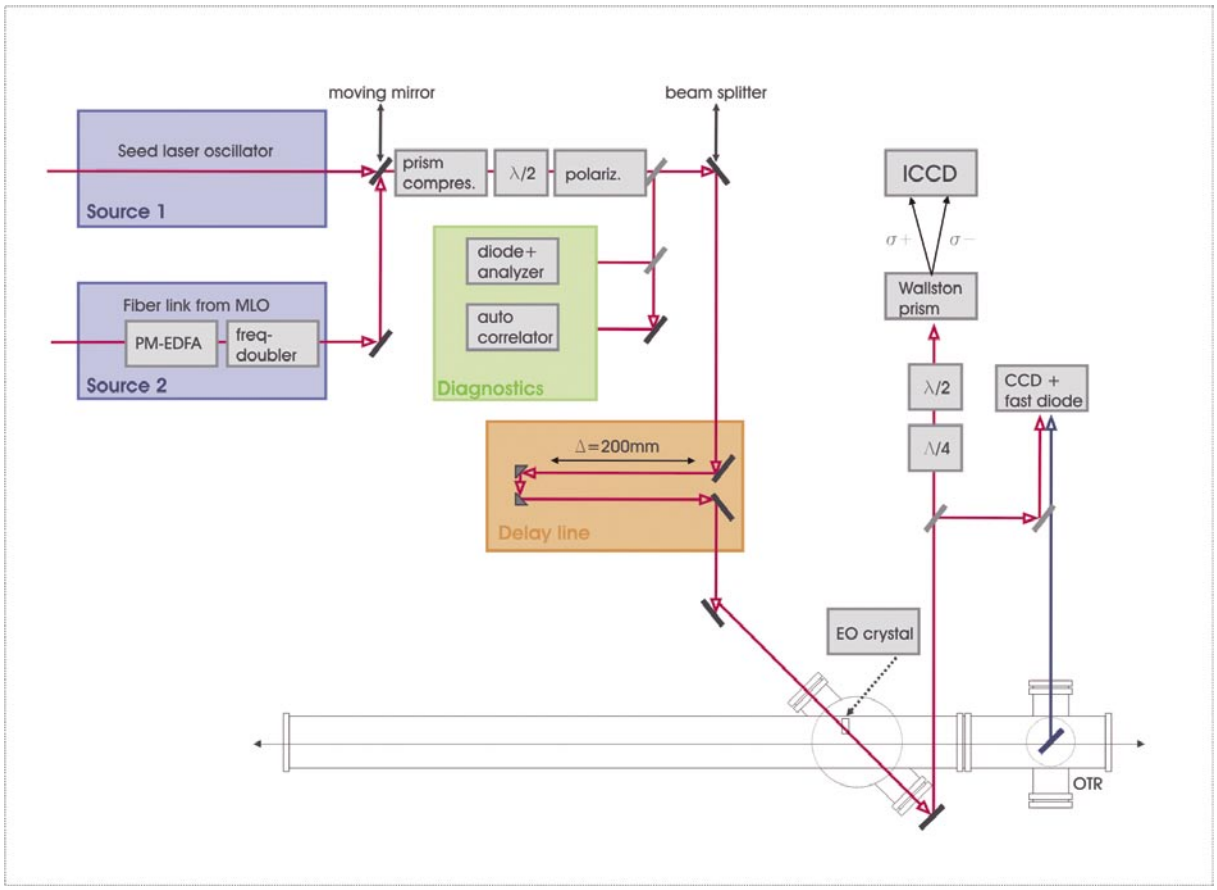

Figure 11.3.3:
Electro Optical Sampling Station layout.

11.3.15 Bunch Phase Monitor

A non-intercepting, shot-to-shot bunch phase monitor (BPhM), first developed at DESY [15], is used to monitor the bunch arrival time. A compact and simple device, suited to be installed anywhere in the tunnel, it is based on an inductive, wide band (>10 GHz) RF ring pickup. It allows detecting the bunch centroid arrival time with respect to the *optical clock* pulse (see par. 9.3.2), but does not give information on bunch length. The measured bunch arrival time is obtained from the "average" phase of the pickup pulse response when excited by the electron bunch. The bandwidth of the pickup is in the GHz range.

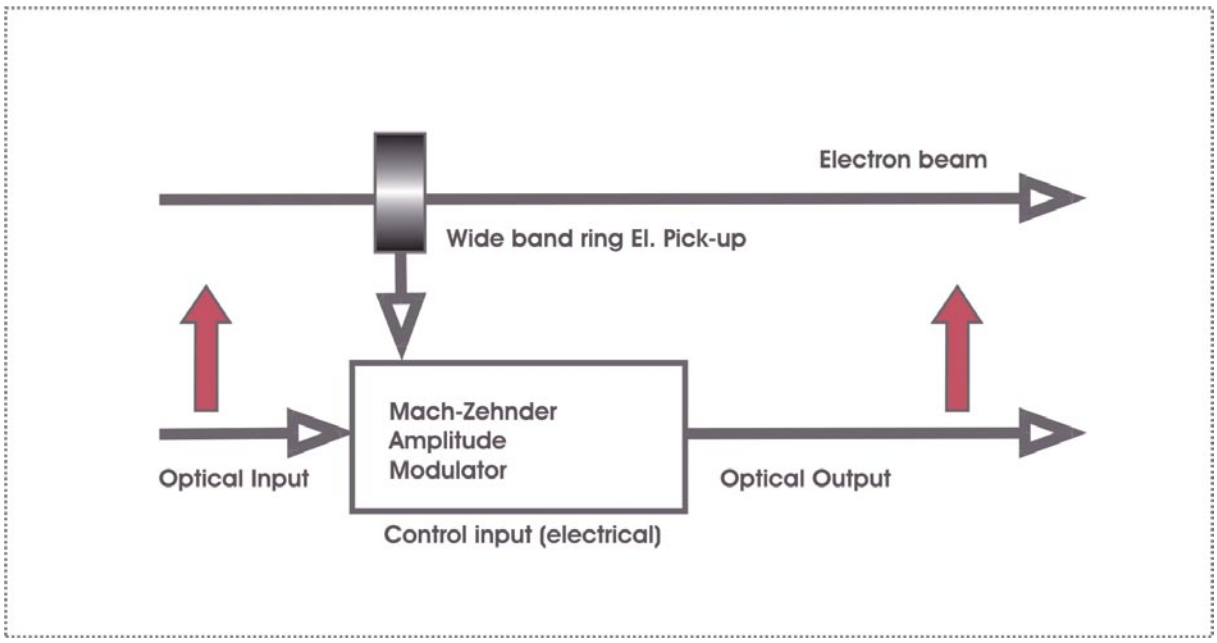

Figure 11.3.4:
Bunch phase monitor block diagram.

The pickup RF signal zero-crossing, having a 0.5V/ps slope, is sampled by a sub-ps laser pulse using a broadband electro-optical modulator (Mach-Zehnder interferometer). The modulator converts the bunch arrival time jitter into an amplitude modulation of the laser pulse which is then detected by a photo diode. Recent preliminary measurements show a time resolution of < 50 fs_{RMS}. In FERMI the laser pulse is provided via the ultra stable fibre timing distribution system whose time jitter is < 10 fs. A BPhM will be installed in front and behind both BC1 and BC2.

11.3.16 Bunch Length Monitor

To guarantee the performance of FEL1 and FEL2 in terms of output power long term stability, both the final average electron beam energy and the bunch peak current have to be stable. According to simulations, in order to guarantee the FEL beam specifications (see Par. 4.4 and 4.5), the current should be stable to within (±5%) and (±7%) for FEL1 and FEL2 respectively. From jitter studies - including

energy, R_{56} and X–band lineariser amplitude jitters, and (±2%) bunch charge fluctuation - the relative bunch length variation needed to achieve a (±5%) current stability is $\delta\sigma_z/\sigma_z$=(±4.5%).

To meet the energy stability specification, given that the RF amplitude and phase seen by the beam cannot be measured accurately enough, energy and current have to be measured along the linac and the error signals fed back to the RF plant.

Error signals to stabilize the bunch current must be derived from both bunch charge and bunch length measurements. The charge is measured in the photoinjector using a toroid monitor and the bunch length using the monitors installed behind bunch compressor BC1 and BC2. Bunch length monitors, periodically calibrated using the RF deflectors installed downstream from BC1 and BC2, provide shot to shot, absolute bunch lengths.

Relative bunch length monitors are based on the detection of coherent synchrotron radiation (CSR) emitted in the last two bending magnets of the bunch compressor and coherent diffraction radiation (CDR) from two slits, one upstream and one downstream from each bunch compressor. Computations predict an energy per pulse of ~ 1 μJ for CSR and of ~ 10 μJ for CDR. The relative bunch length sensitivity is estimated of the order of 2% for both CSR and CDR. The use of two sources provides low cost redundancy and increased flexibility. Moreover, by normalizing the signal from the downstream CDR detector to that of the upstream one the measurement is made insensitive to charge fluctuations. Being both measurements non-intercepting, the bunch length can be measured in a single shot. For commissioning purposes only, CDR screen can also be used to produce CTR, allowing for easier, albeit intercepting, measurements. During commissioning, the RF phase of the upstream linac accelerating sections will be optimised for maximum compression using the CDR/CSR ratio. Once this is done, CSR and CDR signals will be used as error signal for the current stabilizing feedback loop.

11.3.17 Streak Camera

The streak camera provides single shot bunch length and bunch longitudinal profile measurements. The fastest commercially available streak camera (Hamamatsu FESCA 200) provides a time resolutions down to 200 fs rms (@ λ=800 nm). This value deteriorates at shorter wavelengths (800 fs rms @ λ =250 nm) due to the higher energy of the photons incident on the photo-cathode surface, leading to higher charge photo-electron bunches inside the streak tube. Furthermore, the streak camera is often used for measuring the relative time position of two optical pulses (up to a maximum of 10-20 ps separation). The camera time resolution is highest in the single sweep mode or at a low repetition rate (f_{REP}< 100 Hz). This because, the time jitter of successive streaks being typically as high as 20 $ps_{pk\text{-}pk}$, accumulation of several events rapidly spoils the resolution.

To achieve high repetition rate sweeps with sub ps jitter between them, a FESCA 200 single-sweep camera capable of operating in the synchro-scan dual sweep mode has been chosen, as the powerful diagnostic tool for the complete characterization of the photo-injector beam longitudinal characteristics. The bunch longitudinal profile is obtained illuminating the camera with the Cherenkov radiation produced by the beam in an aerogel cell [16]. The system can also be used to provide an accurate characterization of the 6-10 ps FWHM photo-cathode laser pulse.

11.3.18 Beam Loss Position Monitor Using Optical Fibres

To avoid vacuum breakdown and high radiation levels caused by electron losses a machine protection system is required. Beam loss issues for radioprotection and conventional radiation sensor systems are detailed in Chapter 15. An attractive alternative solution [17, 18] that allows real time monitoring of loss location and intensity is described in this Section.

Lost electrons, due to dark current, emittance growth or malfunction of the accelerator active components, hitting the vacuum chamber create a shower of secondary particles. A three dimensional reconstruction of the particle loss position can thus be obtained, within a few *ns*, using four radially arranged optical fibers, equidistant from the vacuum chamber axis: the shower hitting the fibers generates fast Cherenkov radiation signals detected by photomultipliers at the fiber ends, from which the shower position is reconstructed.

11.4 References

[1] W. Graves et al., PAC 2001, 2227 (2001).

[2] J. Wu *et al.,* PAC2005, 1156 (2005).

[3] R. Johnson *et al.*, PT13, DIPAC 2003, 193 (2003).

[4] P. Craievich *et al.,* THPPH025, FEL '06 (2006).

[5] M. Dehler, DIPAC 2005, 208 (2005).

[6] V. Schlott *et al.*, EPAC 06, 3017 (2006).

[7] K. Hacker *et al.*, EPAC 06, 1043 (2006).

[8] http://www.crytur.cz/main.php?id=11.

[9] H. Wiedemann, Particle Accelerator Physics, Vol. 1, Springer, 1999.

[10] M. Zhang, Fermilab-TM-1988 (1996).

[11] http://www.bergoz.com/products/In-Flange.CT/In-Flange.CT.html

[12] A. Cavalieri *et al.* PRL, **94**, 114801 (2005).

[13] P. Craievich, S. Di Mitri, Fermi Tech. Note ST/F-TN-05/26 (2005).

[14] A. Cavalieri *et al.,* PRL **94**, 114801 (2005).

[15] F. Loehl *et al.*, FLS 2006 ICFA workshop, May 2006, Desy.

[16] J. Bähr *et al.*, DIPAC 2003 (2003).

[17] M. Korfer *et al.*, DIPAC 2005, 299 (2005).

[18] M. Korfer *et al.*, Nucl. Instr. and Methods A526, 537 (2004).

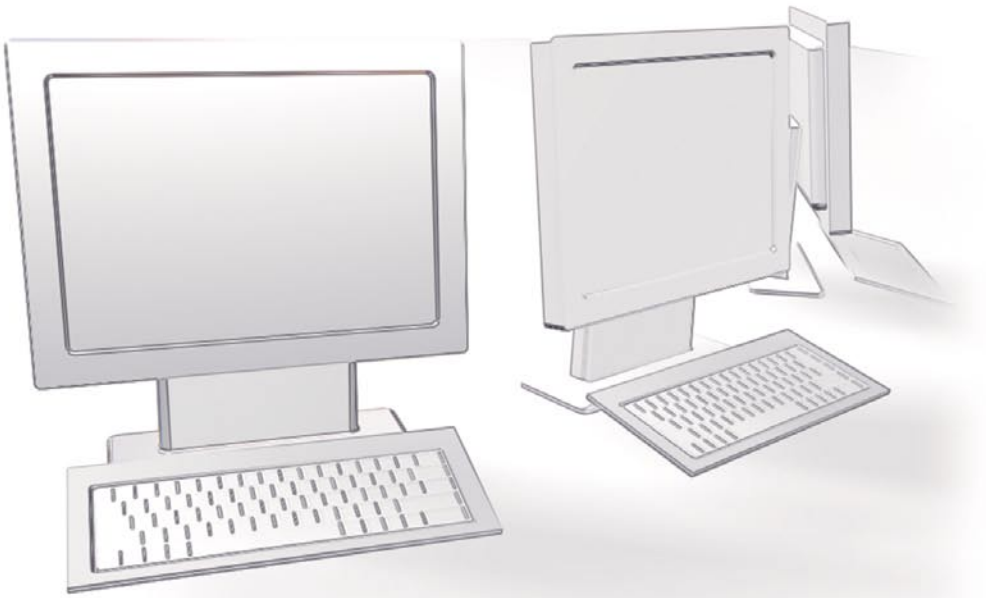

12 Controls

Synopsis

The control system provides operators, machine physicists and scientists with a comprehensive and easy-to-use set of tools to control machine components and experimental beam lines. It is designed to be robust and reliable in order to insure long periods of operation without failures or malfunctions. Diagnosis and possibly repair capabilities are implemented in order to allow for remote recovery from malfunctions of both the equipment and the control system itself, with minimum impact on the facility operation. In general, the control system design is flexible enough to accommodate the specific requirements of a large variety of both conventional and highly specialized devices that are installed and controlled on the accelerator, the beamlines and the experimental stations.

The control system consists of several computers distributed around the facility that interface with the different equipment and acquire data. A number of PC-based consoles allow to remotely operate the machine from the control room. Similar consoles in the experimental hall are used to control the experiments. A switched Ethernet network connects all the control system computers.

State-of-art software technologies are employed, based on open standards and free open-source packages. A uniform and homogeneous software environment using the GNU/Linux operating system and the Tango control system software is adopted for the whole control system. A high level software framework supports model based design of machine physics applications. General purpose control room applications (graphical panels, synoptics, alarms, archiving, logging, etc.) are implemented using the Tango package software tools.

Special attention is given to fast feedback loops, which are crucial to achieve the desired beam parameter accuracy and stability. They read sensors and set actuators on a shot-by-shot basis and are integrated in the general control system infrastructure.

Equipment protection systems, based on PLCs and on a number of distributed I/O peripherals connected via fieldbus, are designed to efficiently and reliably protect machine and beamline components.

The architecture of the access control system is similar to that of the equipment protection but, given the high degree of safety required, stricter procedures are adopted in its design, in conformity with the IEC 61508 European standard. Fail-safe versions of PLCs, fieldbus and I/O peripherals are utilized. Component redundancy and diversification are implemented whenever possible.

12.1 Introduction

The control system architecture and main hardware components are discussed in Section 12.2. Several computers are interfaced to the different pieces of equipment and perform data acquisition and control tasks. Personal computers are used as consoles in the machine control room and on the beamlines. A high speed data network connects all the control system computers.

The software framework is discussed in Section 12.3. Open standards and open-source software are adopted. A software environment based on Linux and the Tango control system is deployed on all computers.

The control system provides shot-by-shot synchronized acquisition and recording of accelerator and photon beams data for tuning and optimization purposes as well as for collection of user experiments data. Real-time processing capabilities and synchronized setting of the controlled variables are also required to implement feedback and feed-forward loops for the stabilization of beam parameters.

In Section 12.4 the main controlled devices are listed and briefly described.

A short description of the equipment protection system designed to automatically prevent accelerator and beamlines equipment from being damaged is given in Section 12.5. The system designed to implement regulations for controlled access of people to areas where radiation hazard exists, including active safety measures, is discussed in Section 12.6.

12.2 Control System Architecture

The control system architecture provides easy access to the equipment in a reliable and efficient way. It facilitates the development and maintenance of distributed applications, and the implementation of the required control schemes. It is designed to be modular and scalable in order to accommodate future changes and expansions.

The resulting system architecture, shown in Figure 12.2.1, includes various types of computers, distributed along the machine and the beamlines, all connected to the data network.

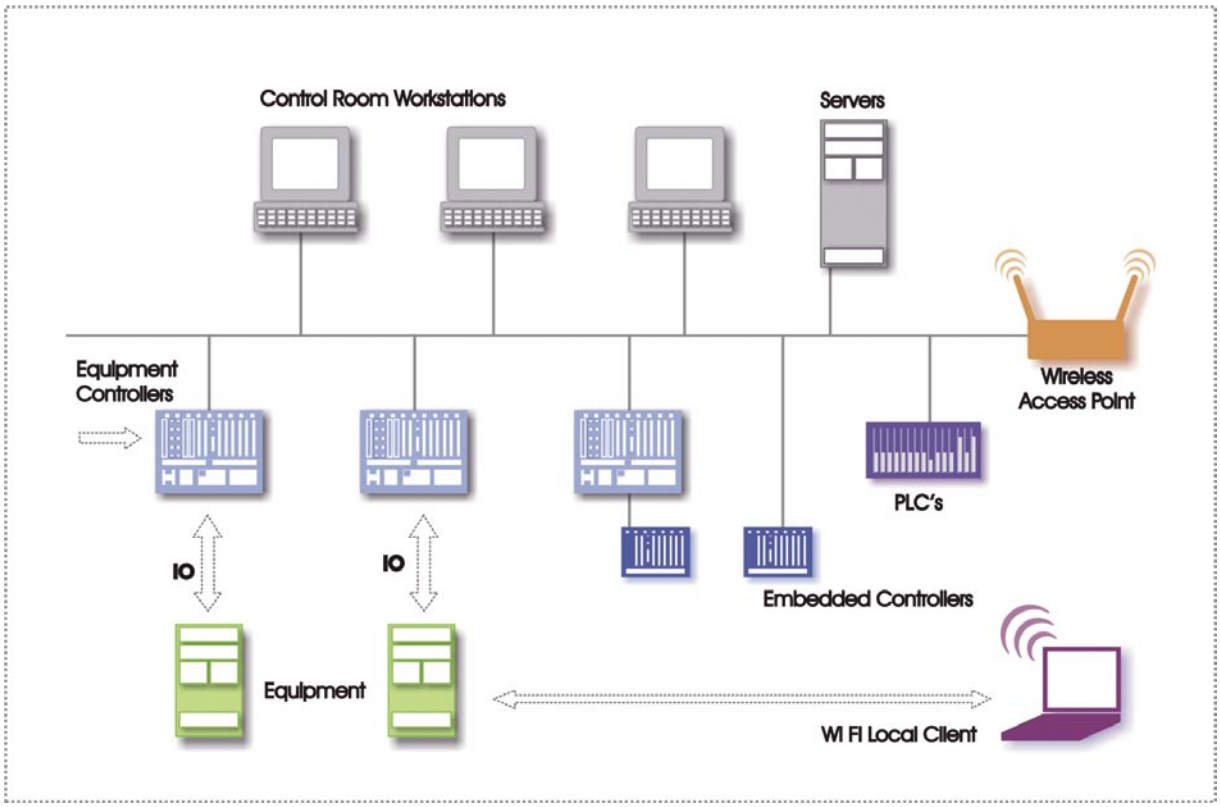

Figure 12.2.1:
Control system architecture.

12.2.1 Equipment Controllers

The Equipment Controllers (EC) are diskless computers interfaced to the controlled equipment. They acquire and process data from the field and execute control actions. Modular VME systems are adopted in order to tailor to any specific control requirements. Several Input/Outputs (I/O) types are used: analogue and digital signals, RS 232/422/485 serial lines, GPIB, fieldbuses, etc. The CPU boards have to provide good performance level together with excellent reliability and long life span.

12.2.2 Network Attached Controllers

Equipment embedded controllers featuring an Ethernet port as well as Programmable Logic Controllers (PLC), like those employed for the equipment protection and access control systems, are connected to the data network. A socket TCP/IP interface is normally used for the communication.

12.2.3 Servers

The servers are Linux computers providing common services for the control system such as remote boot, Network File System (NFS), database, alarms, historical archiving, experimental data storage, web servers, etc.

12.2.4 Consoles

The control room consoles consist of PCs (Personal Computer) running the Linux operating system. They execute client applications including graphical panels, machine physics programs, automatic procedures in support of the operations and data analysis software. Similar consoles in the experimental hall are used to control the experiments.

12.2.5 Data Network

The data network is based on Ethernet technology. A number of distributed switches connected via fiber optics up-links to the master switch provide Gigabit Ethernet connections to the control system computers. The control system data network is decoupled from the general on-site data network by means of a firewall to protect it from external intrusions or harmful traffic. The technical galleries are equipped with wireless networks to facilitate temporary connections of portable computers or electronic devices.

12.3 Software Framework

A uniform and homogeneous software environment based on the GNU/Linux operating system and the Tango control system software has been adopted for the whole control system. It is deployed on both PC and VME platforms and possibly also on the embedded computers.

12.3.1 Operating System

The open source GNU/Linux operating system is efficient, reliable, free of charge and runs on nearly all hardware platforms. Most of I/O hardware manufacturers support Linux and the device driver source code is usually available. Since the standard Linux kernel does not offer real-time characteristics, the real-time extension RTAI (Real-time Application Interface) [1] has been adopted and is used whenever a deterministic behavior of the control system is required.

12.3.2 Tango Control System Software

Tango is a fully object oriented CORBA-based control system software [2]. Born in the late '90s, Tango is now a well-established and mature project, used by a wide community of users especially in the field of synchrotron light sources. The ELETTRA controls group has first adopted Tango in 2004 for the controls of the ELETTRA injector booster and is currently a member of the international collaboration that is further developing it.

The “object model”, which is the fundamental paradigm of Tango, together with a set of useful tools

allows developing clear, efficient and maintainable code with reduced programming effort and facilitates re-using and sharing of software among different laboratories.

12.3.3 Control Room Applications

A number of generic applications are deployed such as alarm systems, historical archiving, databases, web servers, etc. Client control room applications including graphical panels, machine physics programs, applications for routine operations and specific data acquisition and analysis programs can be developed in C++, Python or Java, taking advantage of the graphical toolkits available in Tango. Commercial software packages for data analysis and presentation are also supported.

12.3.4 High Level Framework

A new High Level software Framework (HLF) [3] is being developed at ELETTRA to support model based design of machine physics applications. HLF is a set of software libraries, databases, configuration files and simulators that allow machine physics programs to control the machine through its model. HLF is fully object-oriented and uses a modular approach. A number of modules provide a set of different views or abstractions of the underlying machine.

12.3.5 Real-time Infrastructure for Feedback Systems

The stability of the electron and photon beam parameters is a crucial issue for FEL machines. Feedback loops are developed to stabilize charge, trajectory, length and energy of the electron bunches during long periods of operations. These loops operate on a shot-by-shot basis reading sensors and setting actuators at the linac repetition rate. Feedback loops are also foreseen for the laser systems to stabilize the beam trajectory and shape.

The control system provides the infrastructure necessary to synchronize the computers involved in the feedback and to exchange data in real-time. The computers use a separate port to connect to a dedicated Ethernet network that is set-up for this purpose. Specialized real-time drivers and tasks running in the RTAI kernel space provide communication and data processing with latency jitter of the order of a few micro seconds [4]. If necessary, dedicated centralized processing units can be added to execute and manage the feedback loops.

12.4 Controlled Devices and Equipment

12.4.1 Vacuum System Equipment

Vacuum equipment managed by the control system includes vacuum pumps with their high voltage power supplies, vacuum gauges and residual gas analyzers. These are interfaced to the control system through serial lines and Ethernet connections.

Vacuum valves and beam stoppers are controlled by the PLCs of the equipment protection and access control systems: status requests and open/close commands are sent to the PLCs via Ethernet TCP/IP interface.

12.4.2 Magnet Power Supplies

A large number of magnet power supplies are interfaced to the control system. They power solenoids, bending magnets, steerers, quadrupoles, phase shifters and undulator correction coils. Digital interfaces through high-speed serial links or Ethernet are privileged over direct analog/digital I/Os. High-speed low-latency interfaces are required to control the power supplies of the steerer magnets involved in trajectory feedbacks.

12.4.3 Diagnostics and Instrumentation

The control system interfaces several types of diagnostic equipment and instrumentation. It provides acquisition, processing and presentation of data, which can be immediately interpreted by machine operators and scientists. Real-time acquisition capabilities and fast data transfer allow for shot-by-shot measurements of the electron bunch characteristics, which can be displayed in real-time in the control room and on beamline consoles. Diagnostic systems include, among others, beam position monitors, current monitors, CSR diagnostics, electro optical sampling stations, profile monitors, YAG screens, collimators, beam loss monitors and various beamline diagnostics.

12.4.4 Timing and Synchronization

The timing and synchronization system generates and distributes optical and electrical signals to synchronize the machine operations and the beamline experiments.

One EC is dedicated to the timing central station, which is located close to the photoinjector laser room. It is in charge of hot swapping between a working Optical Master Oscillator (OMO) and a redundant one in case of fault of the former, to insure high availability of the timing system. Other controlled instrumentation includes oscilloscopes and an optical spectrum analyzer.

In the periphery of the timing system, standalone local units distribute timing signals with programmable delays to the end users. They are controlled via serial lines or Ethernet.

12.4.5 Linac

The existing ELETTRA linac control system will be completely replaced. The electro magnetically noisy environment and grounding issues in the linac klystron room require particular care in connecting the EC electronics to the linac equipment. Insulated I/O signals, shielded cables, fiber optics and digital interfaces are employed to reduce interferences and ground loops. RF shielded VME crates protect the I/O electronics from electromagnetic fields, while connections to the data network are done through fiber optics.

Each of the fifteen linac plants is controlled by a dedicated EC. Devices to be controlled include RF amplifiers, high voltage power supplies, thyratrons, klystrons and other auxiliary equipment and components.

The low level RF (LLRF) digital controllers feature an embedded computer connected to the control system through an Ethernet port.

12.4.6 Undulators

The FEL undulators (radiators and modulators of FEL-1 and FEL-2) variable gap segments allow for individual tuning to specific photon wavelengths. Elliptical undulators with variable polarization need additional phase control. Gap and phase of the segments of undulator are controlled with micrometric accuracy and reproducibility by a local control unit interfaced to the control system.

Feed-forward systems based on lookup tables correct trajectory and optics distortions due to the undulators by acting on correction coils and quadrupole magnets.

12.4.7 Quadrupole Movers

Mechanical movers remotely operated through the control system are foreseen for quadrupole magnets, both for initial alignment and for periodic beam based alignment procedures compensating for long term drifts. Quadrupoles are moved transversally along both the x and y axes with micrometric resolution.

12.4.8 Laser Systems

A number of laser systems are foreseen: photoinjector, laser heater, seed and pump lasers.
They include various pieces of equipment such as power meters, autocorrelators, oscilloscopes, photodiodes, shaping systems, mirrors and parametric amplifiers to measure and optimize beam parameters. They are interfaced to the control system through serial lines, Ethernet or direct I/O. Analysis and optimization software tools help the setting up of the laser systems, while feedback loops are foreseen to stabilize all relevant laser beam parameters.

12.4.9 Beamlines Optics

The beamline optics systems transport the photon beam from the FEL undulators to the experimental stations and shape it by means of a set of in-vacuum optical components such as mirrors and collimators [5]. Stepper motor movers, coupled with piezo ones, are used for mirror selection, translation and angular positioning, as well as for collimator slits adjustment.

Operations involving different “physical devices” that must be positioned and set–up according to complex rules (e.g. monochromators) are performed by higher level “logical devices”.

Hardware control parameters, photon beam parameters and data produced by different diagnostic elements are controlled, processed and displayed via the control system.

12.4.10 Experimental Stations

The control system software provides an efficient framework to develop photon beam optics and experimental station controls and to integrate them into the experiment application programs. Among others, it allows for shot-by-shot synchronized acquisition of both experimental data and photon beam pulse parameters for data normalization.

While the instrumentation set of a given experimental station is ever changing and growing in accordance with the experiment needs, basic systems to be controlled such as vacuum equipment (pumps, pressure

gauges), sample sources (pulsed supersonic jet source, pulsed plasma cluster source, vapor sources) and detection systems (time of flight, mass spectrometers, wavelength resolved visible/UV fluorescence detectors, time resolving channel plate fluorescence detectors, hemispherical electron energy analyzers) can be considered as "standard" items of the set. The control system design is flexible enough to allow for a particular subset of such devices to be installed and controlled on any given experimental station according to the experiment specific requirements.

12.5 Equipment Protection System

12.5.1 Requirements and Architecture

The equipment protection system is designed to efficiently and reliably protect machine and beamline components from damage. It is based on PLCs, in charge of executing control programs, and on a number of distributed I/O peripherals connected via fieldbus. Interlock actions implying simple logic rules but involving severe risks are implemented as hard-wired circuits.

Control room applications for the operator consoles (graphical panels, synoptics, alarms, archiving, logging, etc.) are implemented using the Tango package software tools. PLCs communicate with the control system through their Ethernet interface using the TCP/IP protocol. In addition, small consoles equipped with keyboard and LCD display for local control are installed in the machine technical gallery and in the experimental hall, wherever necessary.

12.5.2 Interlocks Description

12.5.2.1 Cooling Systems

Several sensors measuring temperatures, cooling water fluxes and pressures monitor the machine and beamline components and their cooling systems in order to prevent temperatures from drifting outside the specified ranges.

12.5.2.2 Vacuum

The gas pressure in the vacuum chamber is continuously monitored by vacuum gauges and by measuring the ion pump high-voltage power supplies current. An interlock closes the proper vacuum valves in case of anomalous pressure rises.

12.5.2.3 Linac RF Transmitter Plants

A series of interlocks are implemented on all RF plants to ensure safe operation of the linac. They inhibit switching on or switch-off the various subsystems in case of anomalous situations. Signals from cooling water and oil systems, from thyratron grid and filament, from the klystron vacuum, filament, pulse transformer, focalization system and from the sulfur hexafluoride gas system are continuously monitored at each plant. A number of additional plant parameters, such as klystron anodic current, modulator inverse current and reflected RF power at the klystron output are measured on a pulse-to-pulse basis. Additional checks related to personnel safety are also performed.

The accelerating sections vacuum level is also continuously monitored so that the RF and the photoinjector are switched-off in case of pressure increases above a given threshold. Other photoinjector protections,

continuously monitoring the gun vacuum pressure as well as the grid filaments voltage and current, enable/disable operation of the photoinjector sub-systems.

12.5.2.4 Beam Trajectory

A protection interlock based on continuous monitoring of the electron beam position in the FEL undulators prevents the beam from accidentally hitting the vacuum chamber and damage the undulator permanent magnets. Radiation beam loss monitors and additional monitors measuring bunch current differentials at several locations are also deployed and integrated into the protection system. In case of alarm the interlock trips the photoinjector.

12.6 Access Control System

The access control system protects personnel from radiation hazards by controlling access to potentially dangerous areas. Whenever an anomalous or dangerous situation is detected it switches off the electron beam and prevents it from being restarted until the danger has been removed.

The access control system architecture is similar to that of the equipment protection system but, given the extremely high degree of safety required, stricter procedures are adopted in its design in conformity with the IEC 61508 European standard [6]. Fail-safe versions of PLCs, fieldbus and I/O peripherals are utilized. Component redundancy and diversification is implemented whenever possible.

The access control system monitors the linac gallery, the undulator hall and the hutch containing the beamlines switching and deflecting mirrors.

From the access control point of view the linac gallery and the undulator hall are considered as a single area. A door between them facilitates the search procedure prior to switching on the accelerator. Both the photoinjector and the linac RF drive must be inhibited to access the linac gallery and the undulator hall. The two doors and six emergency exits of the controlled area are all interlocked. Individual access through the doors for temporary internal activities is only allowed using personal badges and safety keys, after having been granted permission by a control room operator.

Bending magnets located downstream of the FEL undulators deflect the spent electron beams into an appropriate beam dump. The bending magnet currents are continuously monitored to guarantee a correct electron beam deflection. Moreover, in order to ensure that all electrons are correctly dumped, current monitors are installed to check that no significant particle loss occurs in between the magnets and the dump.

The beamline hutch has two controlled doors that can be opened only with special keys. As done for the ELETTRA beamlines, the access policy foresees searching the hutch before the beam is turned on. Beam stoppers located at the end of the linac and behind each FEL undulator chain must be closed before access into the hutch can be granted.

The experimental hall is equipped with several radiation monitors that are part of the access control system.

Further details concerning the logics and working modalities of the access control system are given in Chapter 15 - Radiation Protection.

12.7 References

[1] http://www.aero.polimi.it/~rtai/index.html

[2] A. Goetz et al., "TANGO a CORBA Based Control System", ICALEPCS2003, Gyeongju, October 2003.

[3] C. Scafuri et al., "ELETTRA New Full Energy Injector High Level Software", EPAC2006, Edinburgh, June 2006.

[4] M. Lonza et. al., "Design of a Fast Global Orbit Feedback System for the ELETTRA Storage Ring", ICALEPCS 2005, Geneva, October 2005.

[5] "ULiSSE – Ultrabright Light Source Spectroscopy Experiments – project", http://www.elettra.trieste.it/FERMI/index.php?n=Main.UliSse

[6] http://www.iec.ch/zone/fsafety/fsafety_entry.htm

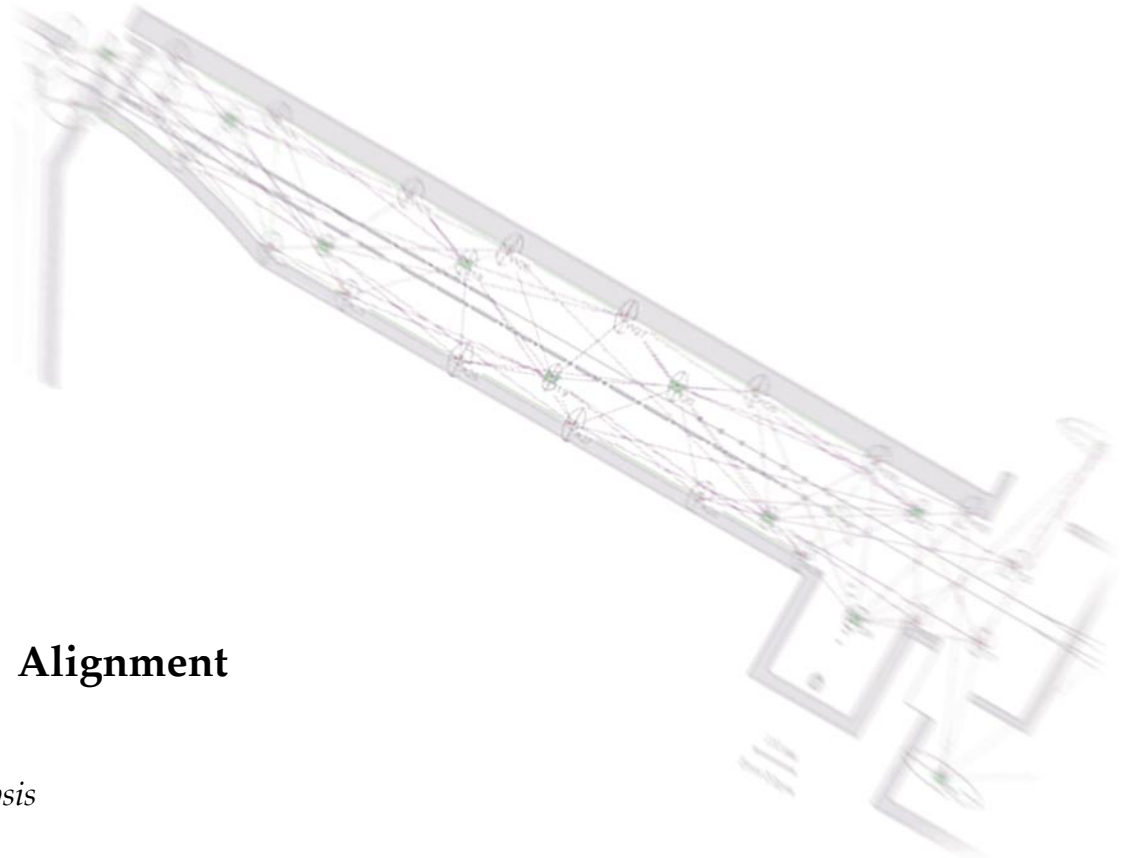

13 Alignment

Synopsis

In order to ensure that the machine components are placed according to the physics requirements, FERMI needs well defined survey and alignment procedures and techniques. Surveys are necessary for placement of components and for support of conventional facilities. ELETTRA has a solid history of quality surveying and engineering. The needs of FERMI will be well served by building on the available infrastructure of reference points and the current observation techniques. All surveys will be based on a single coordinate system integrating the existing surface network and storage ring surveys. Components that have been carefully fiducialized can then be installed and aligned using a series of steps from the ground up and later checked with a survey map. The linac area needs special attention, both for the quality control of the accelerator sections and for the alignment methods to be applied in the field.

The alignment coordinate system is a Cartesian right-handed system, with the origin placed at a particular point in the beamline. A three-dimensional network methodology is proposed, with the FERMI network integrated with that of the existing ELETTRA storage ring. The instrumentation will include theodolites, total stations, laser trackers and precise levels.

The areas to be aligned are the injector, linac, undulator, photon beamlines and experimental hall. The tolerances for the injector, linac and undulator components, 100 μm rms, are achievable with established techniques. The fine adjustment to the BPM and quadrupole positions in the undulator will be done via the beam-based alignment technique described in Chapter 7. The components of the experimental hall have relatively loose alignment requirements, and traditional measuring techniques like those currently in practice at ELETTRA can be used for the placement of components.

13.1 Introduction

Survey and alignment related tasks are found at all stages of a project like FERMI and the purpose of this chapter is to present them in a concise manner. There are often several approaches for solving a particular alignment request and it is important at the design stage to allow provision for flexibility in instrumentation and tooling. For example, in the paragraphs for the specific sections of the project, one observation scheme is presented in depth and alternative methods are mentioned in reference. Where possible, the method reusing existing ELETTRA data or techniques was preferred.

The primary purpose of alignment is to ensure the placement of all machine components within the tolerances set by the physics requirements. The procedure is split into well defined tasks: component fiducialization, assembly control, tunnel survey, floor marking, alignment and the final adjustments based on the results of Beam Based Alignment (BBA) computations. The other purpose of alignment is of a more general nature for the surveyor community and can be considered as support for conventional facilities. It starts by providing accessible and well understood references on site for all construction purposes. Often it also encompasses control measurements for building acceptance.

It is proposed to achieve both goals by designing a geodetic network that is based on the machine layout and to build references with flexible instrument and target mounts. This is presented in the next two sections.

13.2 Geodetic Network

One single coordinate system will be used for the FERMI project. The size of the project is large enough that an understanding of some basic geodetic principles is needed. Conversely, it is small enough that common approximations are possible. This section gives its formal definition and describes the principles to be used in order to first realize it and then subsequently to use it. A technical note [1] states the specific details and presents the numbers to be used.

The FERMI coordinate system will be a three dimensional Cartesian system (O, x, y, z). Its origin O will be chosen at one particular point in the beamline, such as the center of a quadrupole. Its x-axis will follow the beam-direction. Its z-axis will be opposite to the gravity vector at the origin. The y-axis will complete the triad and make it right-handed. This definition implicitly assumes that the beam direction is normal to the gravity vector at the origin which is a factor to be taken into account at the time of the construction. It is completely sufficient to represent the machine layout and also to model all geometric measurements. To take care of gravity based measurements it is also necessary to add a model of the gravity field for the area.

Because the knowledge of the Earth's density distribution is not sufficiently well known, it is not possible to compute the gravity field directly from its defining formula. Recently, with the development of satellite observations, there have been major advances at the global level and in the handling of the temporal fluctuations. For local studies, the common procedure to determine the gravity field is carried out in three steps. First, a global geo-potential model (such as EGM96) is used for the long-wavelength contribution. Secondly, the medium wavelength component is derived from all the available field observations (such as free-air gravity anomalies and differences between GPS and leveling data). Finally, the short-wavelength is inferred from a digital terrain model [2]; this part, which deals with the topographic effects, is a limiting factor for accurate and high-resolution models. For the alignment of an

accelerator one must ask if such a specialized procedure is necessary and possible or if a simplified model is sufficient. In fact, what is really important for the alignment of a machine is just the understanding of the variations of the gravity vector within the site and with respect to the value at the origin. Placing the origin in the middle of the machine limits the range for possible variations. For all these reasons, a simpler spherical model can be chosen. This sphere will act as a local approximation of the geoid (the equipotential surface of the gravity field which coincides on average with mean sea level). In practice, this means selecting a radius (R) and a distance from the origin along the z-axis (the height of the origin H_O) [3].

The realization of the coordinate system is the process of building reference marks and assigning coordinates to them. In turn, it is this set of coordinates that implicitly define the coordinate system. This process has occurred during the construction of the storage ring [4]. The ELETTRA surface network can be integrated into the FERMI network. It was designed with a two-dimensional approach and a forced-centering technology. It consisted of five monuments embedded in the rock and one monument M9 placed on top of a building near the linac entrance. M1 marked the center of the Storage Ring. The Y-axis was materialized with M1 and M0. The two markers M3 and M6 indicated the direction of the accelerator, which is parallel to the X axis. With the construction of the new booster, one point M2 had to be destroyed. Monument M3 is at the current limit of the construction for the linac extension. In the eventuality of an extension, a replacement needs to be installed and a local survey performed before removal. This network was observed by a combination of theodolite and distance measurements. A re-iteration of the observation scheme is not directly possible because most of the original lines of sight

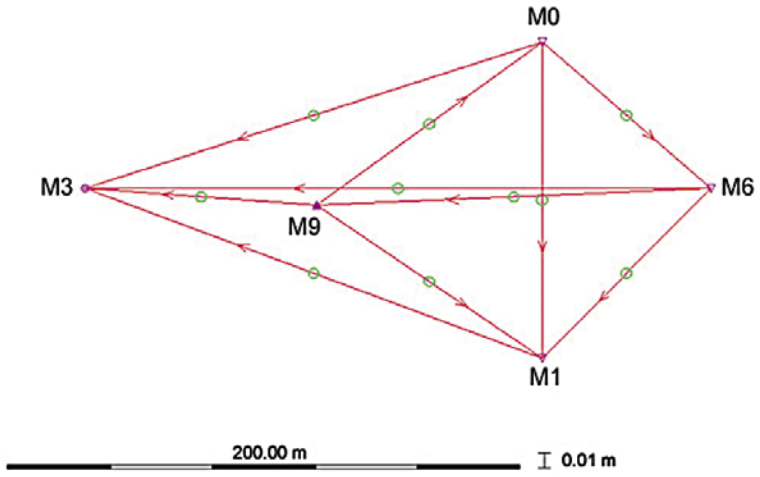

Figure 13.2.1:
GPS Network Simulation using Ski-Pro Software.

were lost with time and development. Fortunately a simple GPS network could easily be surveyed and computed within the Italian GPS Fiducial Network (IGFN) [5]. Figure 13.2.1 shows one possible baseline arrangement over the remaining pillars.

By adding a couple of points during the construction, this process accomplishes several goals at the same time. It ties the site to a known global coordinate system, provides references to the tunnel and enables a transformation formula to the Storage Ring system if needed.

13.3 Method and Instrumentation

Within the accelerator alignment community there are two different philosophies for surveying positions of monuments and machine components. They are known as the two-dimensional plus one-dimensional approach (2D+1D) and the three-dimensional approach (3D). The 3D methodology is often associated with the free-stationing of the instrumentation, such as laser trackers. On the other hand, the 2D+1D methodology is associated to the forced-centering of instruments and targets. Just as in any

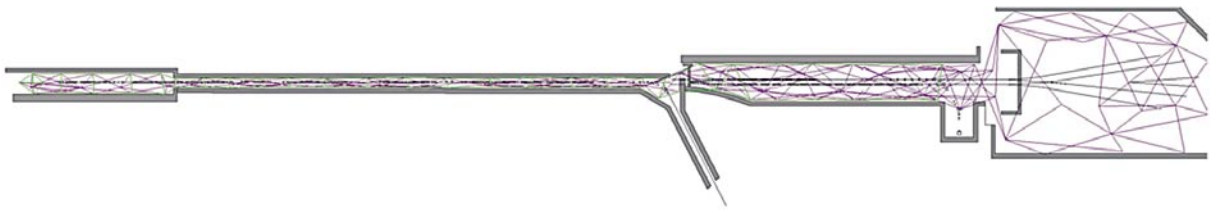

Figure 13.3.1:
Tunnel Network Simulation using SIMS Software.

classification, it is somewhat arbitrary and a practical approach is to be able to use a combination of both scenarios when needed. To achieve this, it is necessary to adopt a versatile mounting system for targets and references. It is also important to verify that the data processing software selected for the reduction and adjustment of the observations is based on a general mathematical model [6].

This versatility already exists at ELETTRA. The surface network and the original alignment of the storage ring were realized around forced-centering techniques. The Taylor-Hobson system was adopted for both the surface network and the component fiducialization of the whole machine. In this method, good mechanical fit and proper use of the instrument tribrach guarantee that the center of any 3.5" diameter sphere-target lies on the local vertical used for the instrument set-up. The net advantage of such a scenario is the reduced number of unknowns in the adjustment while its major drawback is the dependence on hardware arrangement and repeatability. It is also worth noting that, because the positions of the instruments (theodolites and total stations) are linked to the positions of the targets, lines of sight need to be preserved, otherwise the network has to be modified. The latest surveys of the storage ring magnets were performed with laser trackers. New references were installed and special adapters were used in order to place the 1.5" SMR (Sphere Mounted Retroreflector) in the 3.5" receptacles.

13.4 Component Placement

Once the monument network is processed, the placement of components in the tunnel can start. All critical components need to be fiducialized in advance. Fiducialization is the process of defining a local

coordinate system specific to the component and assigning coordinates to external references that will be used later for the alignment process. The coordinate system can either be built from geometrical features or from a materialization of the magnetic field. In all cases, it is important to evaluate the quality of the fiducialization step, as this is the first contribution in the tolerance budget. Next, the decision has to be made as to whether to place the components on a girder outside the tunnel or in an assembly area in order to ensure the relative alignment and to speed up the installation process. In either case, the alignment of individual components or the pre-assembled girders, the placement process in the tunnel follows the same successive steps.

The position of the anchors securing the supports needs to be marked on the floor. This step can be carried out with the help of templates in the case of repetitive patterns. The templates need to be surveyed for control and marked clearly to identify their position and orientation. The quality of the marking should be consistent with the chosen drilling technique: a reasonable goal is between 0.5 and 1 mm. After the installation of the supports, another round of alignment checks is advisable. The specifics of this survey depend on the mechanical arrangement of the interface between support and component. This may be as simple as reading some identified features on the support to confirm the installation or, when movers are used, an opportunity to set the movers to preserve the maximum range of movement. The quality of this survey should match the type of hardware involved at this stage. In case of mechanical registration for the component set-up, a reasonable goal is 0.25 mm; otherwise it can remain at 0.5 mm.

Next, the components are installed; this can be done without the help of a surveyor in the first case, otherwise a local set-up will be needed with a reasonable goal of 0.25 mm. All these installation surveys can be performed by local set-ups of total stations. The recommended procedure is a free stationing approach based on a solid resection. A minimum of four monuments (preferably more) are observed in both faces of the instrument and with two iterations. The quality of the position and orientation of the instrument is verified in the field, after which the observations controlling the placement can be made in one face only. The final position is recorded after two iterations per instrument face.

At this point, it is time to perform a global survey of the monuments and of all the installed components. This process is generally referred to as the mapping stage and the recommended procedure is a combination of laser tracker and precise leveling observations. The laser tracker set-ups are performed in both faces and two iterations. All the component points have at least double coverage. A double run of leveling observations connects all the floor monuments. Depending on the size and shape of the area, height differences between components and reference points are observed with precision levels. These leveling data are reduced first to correct any naming or rod calibration mistakes. Then the set of cleaned height differences is entered in the adjustment of the laser tracker data. A free datum approach based on the monument coordinates is recommended and can provide an indication of the stability of new construction. After a statistical analysis of all the residuals and a verification of the a-posteriori standard deviation of all the unknowns, the coordinates of all the points are available.

For further analysis, depending on the location of the fiducials with respect to the component, an additional step may be necessary to estimate the position and the orientation of the component. Graphical outputs are welcome at this stage to verify that the adjustment results are within the required tolerances. Then a list of the required moves is established and local set-ups are performed. Unless there are very few moves to be made and they are well distributed, it is necessary to repeat the mapping process before publishing the observed positions of the components.

The next four sections discuss the alignment of the major sections of the FERMI system.

13.4.1 Injector

This is the first part of the machine that reaches to the end of the accelerating section SØB. It is about 5 meters long and is presented in Chapter 5 of this CDR. There are two distinct tasks as far as alignment is concerned: the control of the assembly on the common table and the placement of individual components.

On the table, the critical parts are the RF gun and its solenoid with their tight relative alignment. To achieve this, the two are mounted on a common plate after independent fiducialization steps. The placement of the table and the other components such as the two accelerating sections, the spectrometer and quadrupole magnets will be completed by traditional survey techniques as described above.

13.4.2 Linac

The linac section starts at the end of the accelerator section SØB and extends to the end of the spreader. It is about 150 meters long and is presented in chapter 6 of this CDR. Two types of components need special attention as far as alignment is concerned: the accelerating sections and the quadrupoles. The BPMs will be secured to the quads.

There are two types of accelerating sections but there is no real conceptual difference in the alignment procedure. The transversal alignment requirement is identical: 100 μm rms (horizontal and vertical). The existing ELETTRA sections, S1 to S7, are $3\pi/4$ BTW units. They are 6.15 meters long and the iris radius is 5 mm. They have three fiducials distributed along the length of the vacuum vessel. They were used to set the sections at the time of their installation and have not been re-observed since. Because of the alignment requirement, it is recommended to perform a map of the seven sections as they are currently in the tunnel. This will confirm the inner relationships of the fiducials. It is also recommended to plan a fiducialization check for the sections that will be displaced [7]. This will ensure the quality level of the nominal values of the fiducials. The new accelerating sections coming from CERN are $2\pi/3$ TW units. They are 4.5 meters long and the iris diameter is 10.75 mm. They have two fiducials, one at each end. These fiducials were set to a nominal position (-25.00 cm off axis horizontally and 40.00 cm up) at the time of their first evaluation. Because most of these sections have been displaced and recently transported, it is recommended to perform a new fiducialization of all the CERN sections [8]. After all the quality inspections of the sections are completed, it will be possible to evaluate the contributions of the fiducialization to the global error budget and to derive the necessary placement tolerances.

Most of the quadrupoles in the linac have an alignment tolerance of 100 μm rms transversally. Eight magnets in the BC1 region have a tighter tolerance: 50 μm rms. All the quadrupoles have a longitudinal position tolerance of 150 μm rms. It is recommended to perform the fiducialization of these magnets in close conjunction with the magnetic field map in order to produce ideal values referenced to the magnetic axis and to minimize the contribution of the fiducialization step to the error budget.

Given the geometry of the linac tunnel, long and narrow, it is difficult to build a network more accurate than 100 μm rms in all directions with total stations, laser trackers and precision levels. Because of the limited width of the tunnel, the most difficult direction to be determined is the one transverse to the beam. The relatively large spacing between components prevents an efficient use of optical tooling methods to derive horizontal offsets. A possible solution to improve the initial placement is to introduce a combination of portable HLS (Hydrostatic Level System) and portable wire measurements. This is the concept that is being applied to the alignment of the LCLS undulator “loose end” [9]. Another alternative is to set up a straightness interferometer along the beam.

13.4.3 Undulator

The 60 meter long undulator section starts at the end of the spreader and goes up to the beginning of the beamlines and the experimental stations. It contains the beam dumps and is presented in Chapter 7 of this CDR. Three types of components need special attention as far as alignment is concerned: the undulators, the quadrupoles and the BPMs. The transversal alignment requirement for the quadrupoles and the undulators is 100 μm rms (horizontal and vertical). The BPMs will be set relative to the quadrupoles before the installation in the tunnel. Assuming an error budget of 50 μm rms for the fiducialization of the quadrupoles and the undulators, the fiducials need to be aligned to 85 μm rms to meet the required placement tolerance. This can be achieved by a combination of laser trackers and digital level observations. Figure 13.4.1 shows a plan view of a network simulation for a monument network scheme across the undulator hall. Points on the wall and aisle are laid out regularly (10 meter spacing). The approach chosen is a free net (no parameters are fixed or weighted), and the adjustment solves for the datum parameters. The a-priori standard deviations are given in the table below.

Table 13.4.1: Input to the Simulation.

Distance (D)	40 μm
Horizontal Angle	60 μm / D
Vertical Angle	70 μm / D
Height Difference	80 μm

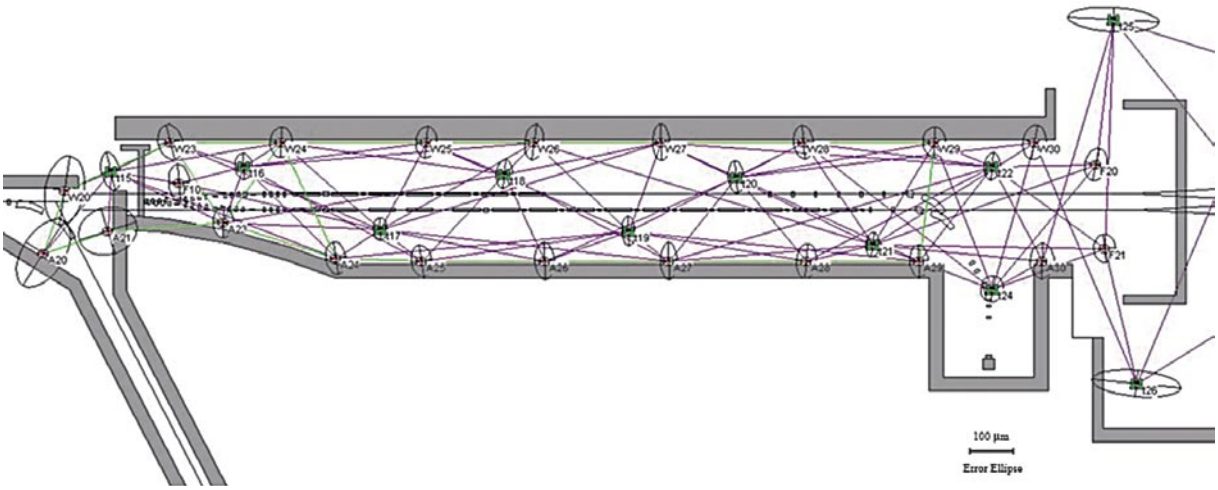

Figure 13.4.1:
Undulator Hall Network Simulation using SIMS Software.

The a posteriori standard deviations for the monuments are under the required 85 μm limit. For example, the characteristics of point W28 in the middle of the tunnel are given in the table below.

Table 13.4.2 Output Example of the Simulation.

Name	σ_x *(μm)*	σ_y *(μm)*	σ_z *(μm)*
W28	22	32	55

This network can serve as a basis for component placement. The mapping of the components will produce a denser network and the addition of level observations between components and monuments will produce an even stronger network.

13.4.4 Experimental Hall

This is the last part of the machine, starting at the end of the undulator. It is presented in chapter 8 of this CDR. There are two favorable factors that contribute to the relative ease of alignment for the Experimental Hall. Firstly, the components have relatively loose tolerance requirements for their initial positioning. Secondly, the overall wider dimensions of the building allow greater flexibility in the design of the network. For these reasons combined, traditional measuring techniques such as the ones currently in practice at ELETTRA can be used for component placement.

13.6 References

[1] Technical Note on the FERMI Coordinate System.

[2] "The GeoAdria project – the geoid of the Adratic See" by A. Borghi found at:

http://bgi.cnes.fr:8110/The-GeoAdria-project.pdf

[3] ibid [1].

[4] "Alignment for the Synchrotron Light Source ELETTRA" by F. Wei, A. Bergamo, P. Furlan Radivo, J. Grgic, D. Vivoda and A. Wrulich presented at EPAC 94.

[5] "The Italian GPS Fiducial Network: Services and Products" by F. Vespe, G. Bianco, M. Fermi, C. Ferraro, A. Nardi and C. Sciarretta found at: http://geodaf.mt.asi.it/html_old/gps/product_services.pdf

[6] "LEGO: A Modular Approach to Accelerator Alignment Data Analysis" by C. LeCocq presented at IWAA97.

[7] Technical Note on the Metrology of the ELETTRA Accelerator Sections.

[8] Technical Note on the Metrology of the CERN Accelerator Sections.

[9] "Proposal for the Alignment of the Loose End" by G. Gassner (LCLS-TN-06-11).

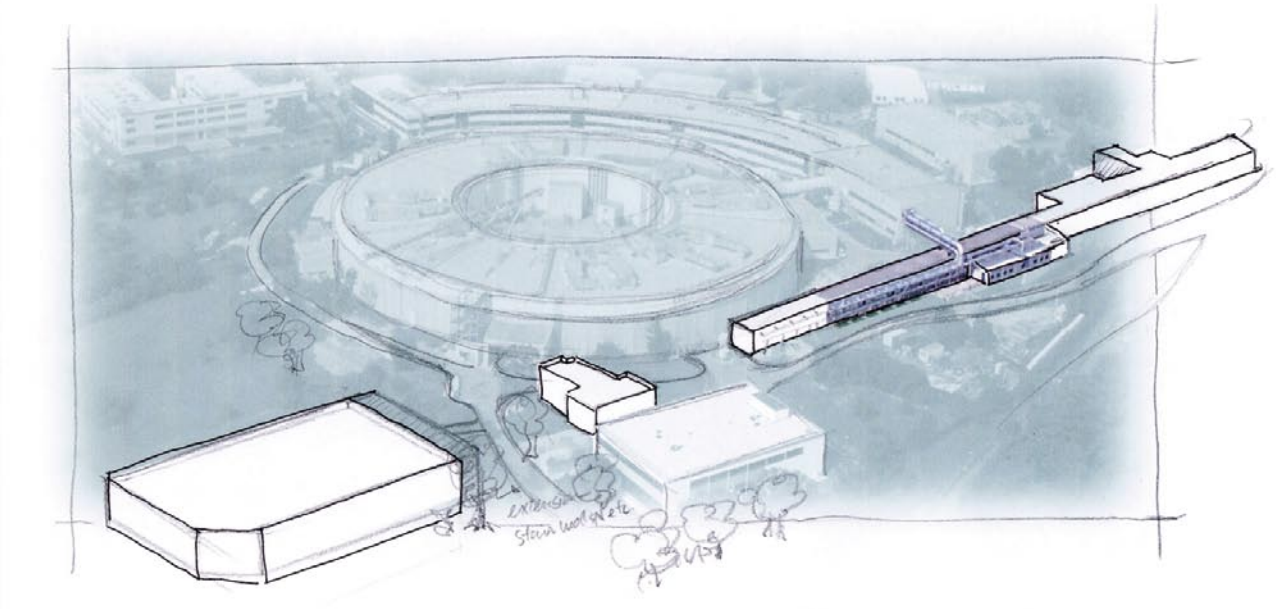

14 Civil Engineering

Synopsis

The FERMI@Elettra project requires the excavation and construction of several new buildings to house the accelerator, FEL's, Experimental area and associated offices and laboratories. These new infra-structures will be furnished and supplied with conventional systems. Furthermore the project will use most of the existing well-established infrastructures at ELETTRA as a development platform. The project will evolve from the existing infra-structure that houses the storage ring linac injector. This will require a physical extension of the present linac tunnel in both upstream and downstream directions, excavation and construction of the FEL and experimental hall. New conventional systems will be provided as will upgrading of the existing ones.

The linac is situated below ground at a depth of ~5 m in a tunnel 110 m long. The linac tunnel will be extended backwards by an additional ~80 m for a total length of 195 m and a surface area of ~750 m^2. The tunnel will conform to health physics regulations. Adjacent to this backward extension a laboratory area will be built up that will serve for the laser systems used by the Linac. This area, at the same depth as the linac, will also house support laboratories and storage rooms. The control room for the FEL will be situated at ground level approximately midway along the accelerator. The surface building (Klystron gallery) housing the RF power sources and ancillary equipment for the linac will also be extended above the tunnel to the same length.

A large hall, the FEL hall, shielded against the escaping ionizing radiation, will be built below ground as a forward extension of the Linac tunnel and house the beam transport system, diagnostics and undulators with space for future upgrades and additions. It will also house the beam dumps and photon take-off optics leading to the user hall. The FEL hall has an approximate area of 11 by 110 m^2. Adjacent to the FEL hall and protected by a shielding wall a service gallery will be built that will house equipment for the FELs In this same location a zone will be dedicated to the seed lasers and another to the pit giving access from ground level to the FEL hall. At the end of the FEL hall the experimental area will be situated, also partially below ground. The experimental zone will be separated from the FEL hall by a 3 m thick shield wall and have a footprint of 60 by 27 m^2. The land where both the FEL and the experimental hall reside will be excavated and prepared, including modification and upgrade to existing conventional systems. The experimental hall will have two or more floors and surrounding laboratories, including meeting rooms and a small conference centre. This building will have a foot-print of approximately 60 m by 40 m. Careful attention will be paid to building foundations, support structures and the placement of equipment to minimize vibrational disturbance from cultural noise.

The facility requires an upgrade of conventional facilities and the construction of new ones, including a new uninterruptible power supply rated for 600 kW. The uninterruptible unit will guarantee continuous operation of essential main systems, personnel and machine protection systems, accelerator and beamline control systems and vacuum systems. Cooling, heating ventilation and air conditioning will be built to the stringent specifications required for operation. Additional electrical power to a total of ~ 7 MW will be required beyond the present ELETTRA needs. New roads will be built taking into account access to existing infra-structures. Modifications to conventional systems include the re-routing of power cables, gas and water piping and sewage works. Construction and landscaping will conform to all environmental regulations for the protection of local flora and fauna.

14.1 Introduction

The FERMI@Elettra facility will be built inside the ELETTRA Laboratory in the Area Science Park and located in the T8 site situated about one kilometer south-west of the town of Basovizza (Trieste). The site is on the Carso highland near the highway to the Trieste harbour at about 12 kilometers (fifteen minutes by car) from the city of Trieste and thirty kilometers (45 min by car) from the Ronchi dei Legionari Friuli Venezia Giulia international airport. The site has excellent geological characteristics for synchrotron light sources, having a limestone bedrock, that guarantees stability against settling and vibrations.

The main building of the FERMI facility will be developed in a north-west/south-east direction as an extension of the present ELETTRA linac. The FERMI infra-structures will be built both below and above ground. The facility itself is composed of a linac and klystron building, an undulator hall and the experimental hall. A general layout of FERMI infrastructures is shown in site map figure 14.1.1. The site map also shows the location of the storage ring building, within which a new full energy injector is being placed. This new complex composed of a pre-injector linac and booster synchrotron will substitute the linac as main injector.

Buildings for auxiliary plant will also be constructed to house a new electrical station and relative peripheral substations, primary refrigerating plants (cooling towers, refrigerators and fluids) secondary cooling circuit distribution systems (heat exchangers, pumps, demineralising plants), heating system and air conditioning plants (refrigerators, HVACs).

New buildings for offices and laboratories will be constructed, both around the experimental hall and either side of the klystron gallery (ES1 & ES2, see Figure 14.1.1). During the construction phase temporary offices, in the form of pre-fabricated buildings, will be made available (see Figure 14.1.1 for the location) to the project team.

A new road network will also be required that will be optimized for the movement of people, vehicles and equipment around and to the new infra-structure, taking into account access to existing infra-structures (notably the TASC building MM) and construction site limits. The new road consists mainly of an extension of the present network and consists of access, loading areas and parking, as shown in Figure 14.1.1. The new road will avoid the destruction of local flora and fauna and in particular of the trees present inside the Laboratory.

The site of the ELETTRA laboratory is situated near an area that is a type C Site IT3340006 (close to a Community Important Site (CIS) and a Special Protection Zone (SPZ)), as accorded by European

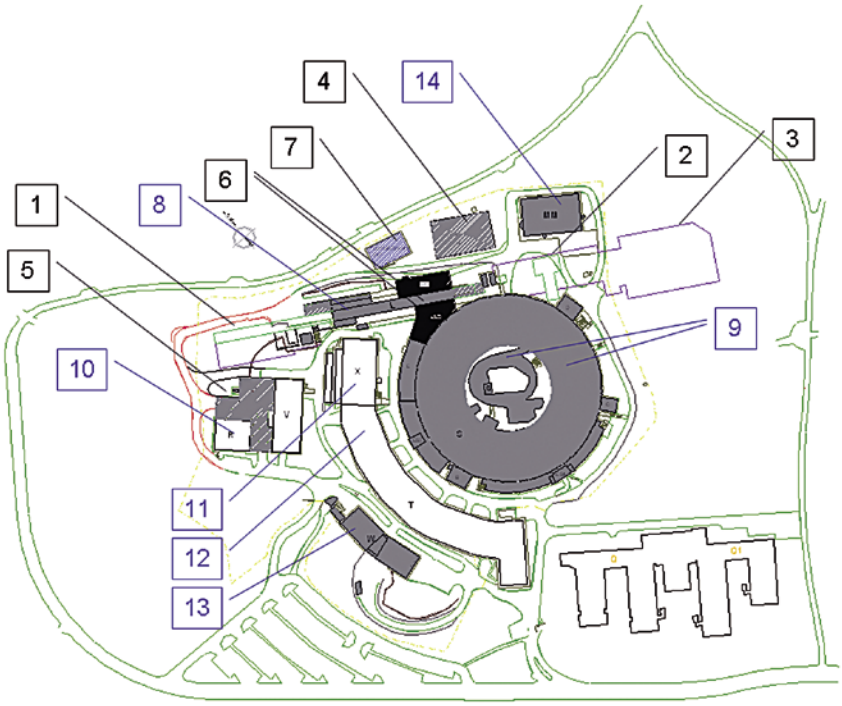

Figure 14.1.1:
General layout of the ELETTRA site showing the footprints of the synchrotron light source and FERMI infrastructures. NEW FERMI BUILDINGS: 1) Backward extension of the linac building, 2) FEL Hall, 3) Experimental Hall and associated laboratories, offices and meeting rooms, 4) Electrical Plants, 5) Plants Building (cooling towers, refrigerators and chillers, auxiliary plants, etc…), 6) Office and Laboratory Buildings ES1 ed ES2, 7) Temporary Office Building. EXISTING ELETTRA LABORATORY BUILDINGS: 8) Linac Building, 9) ELETTRA Storage Ring and Booster, 10) Plants Building (Buildings R (cooling towers, hydrants) e V (refrigerators, boilers, UPS, cogeneration and auxillary plants), 11) Building X (Electrical Plants), 12) Building T1 e T2 (Offices, Laboratories, Meeting Roms, General Services), 13) Building W (Workshop, Stores, Laboratories), 14) Building MM (TASC CNR-INFM Laboratory).

Directives 79/409/CEE and 92/43/CEE, NATURE 2000 NET. Although the the border of the FERMI laboratory is not within Site IT334006, a study of environmental impact has been performed for the project that takes into consideration the geology and the geomorphology of the area, in addition to aspects of impact to local flora, fauna and vegetation. FERMI will be developed taking into account all external factors and will minimize the effects on the environment.

14.2 Buildings

This section describes the principal characteristics of the FERMI@Elettra facility buildings. The FERMI main buildings are a series of structures that will house the main FEL components, notably the linac, FEL's and experimental hall. Buildings for auxiliary and conventional plants are structures in which the electrical, water and HVAC systems will be installed. Buildings will also be provided for support and sample preparation laboratories, office and meeting rooms. An artists impression of the surface buildings is shown in figure Figure 14.2.1. The underground layout of the buildings is shown in Figure 14.2.2.

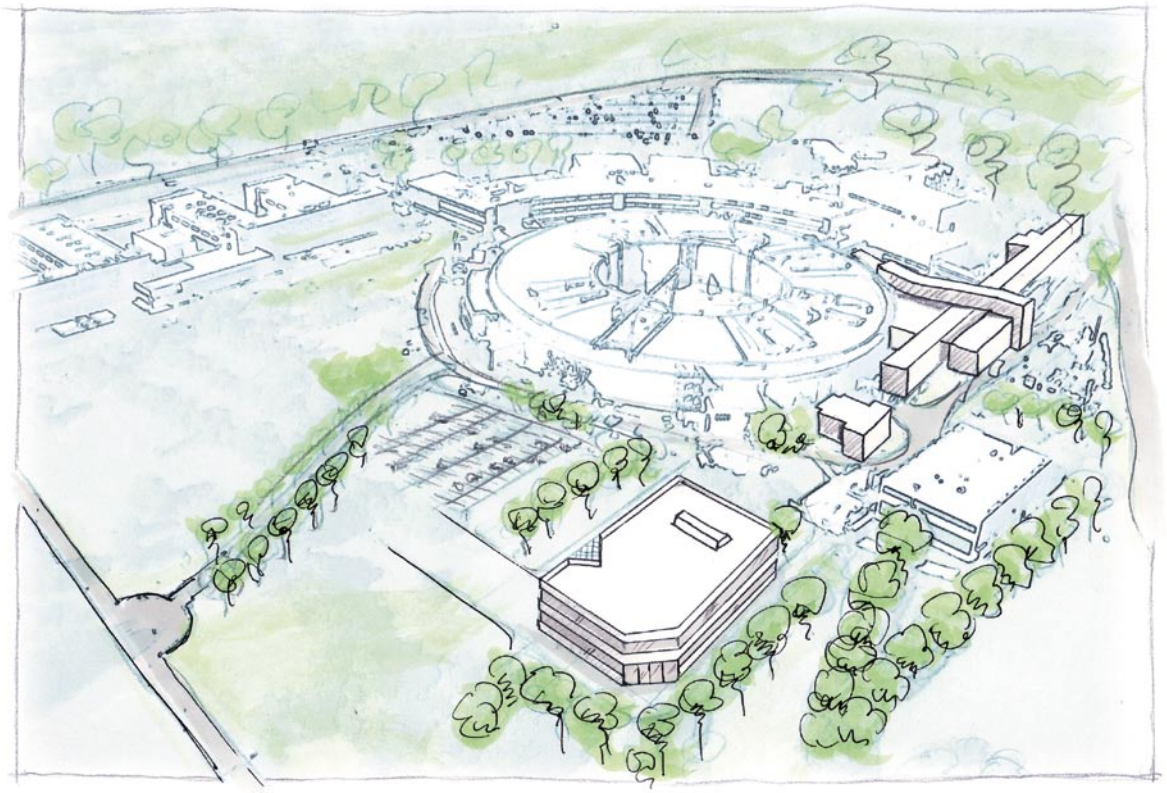

Figure 14.2.1:
Artists impression of FERMI surface buildings. From right to left the backward and forward extension of the linac klystron gallery, access building for the FEL hall and the experimental hall.

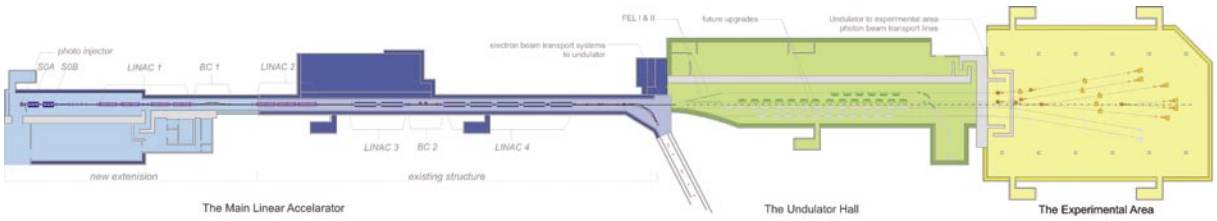

Figure 14.2.2:
Overall underground layout of FERMI showing the backward extension of the linac tunnel, the existing linac tunnel, the FEL hall and the Experimental Hall.

14.2.1 Linac Building

A schematic of the Linac building is shown in figure Figure 14.2.3. This building is composed of an underground tunnel containing the linac and a surface klystron gallery housing power sources for the linear accelerator and support equipment. The present klystron gallery will be extended both in the backward and forward direction and will house the new plants for the new linac injector and the relocated RF plants (Figure 14.2.3(a)). The linac tunnel will be extended in the backward direction by ~80 m to accommodate the photo-injector, the laser heater and the first bunch compressor. Adjacent to the new tunnel extension an underground hall will also be built that is laterally shielded and will house the photocathode laser, test and assembly rooms. The complete tunnel and surface building will have a length of approximately 195 m.

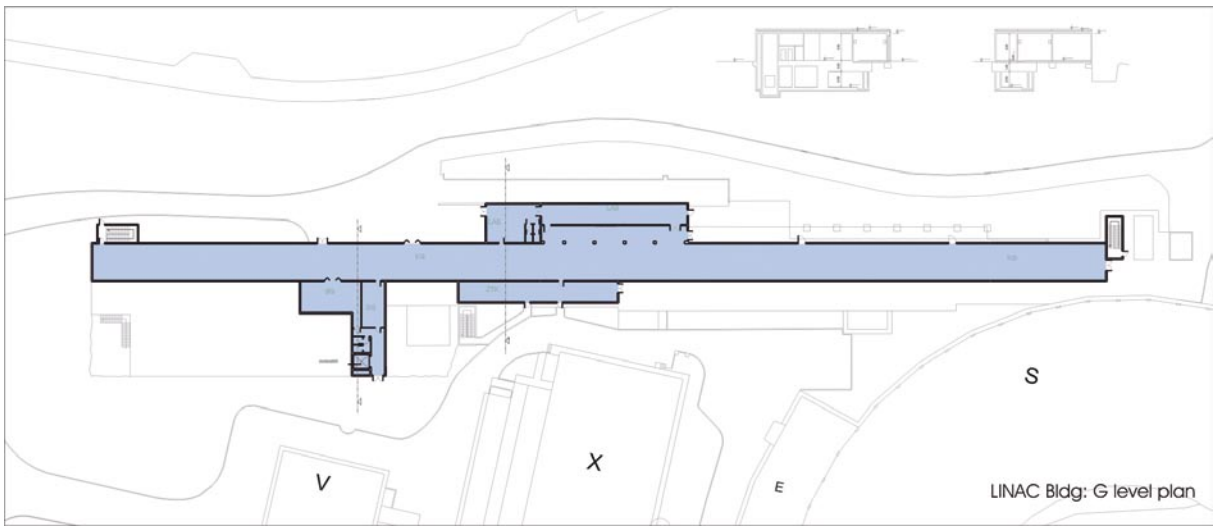

Figure 14.2.3(a):
LINAC Building. Linac surface buildings. Klystron gallery, Control room and support laboratories.

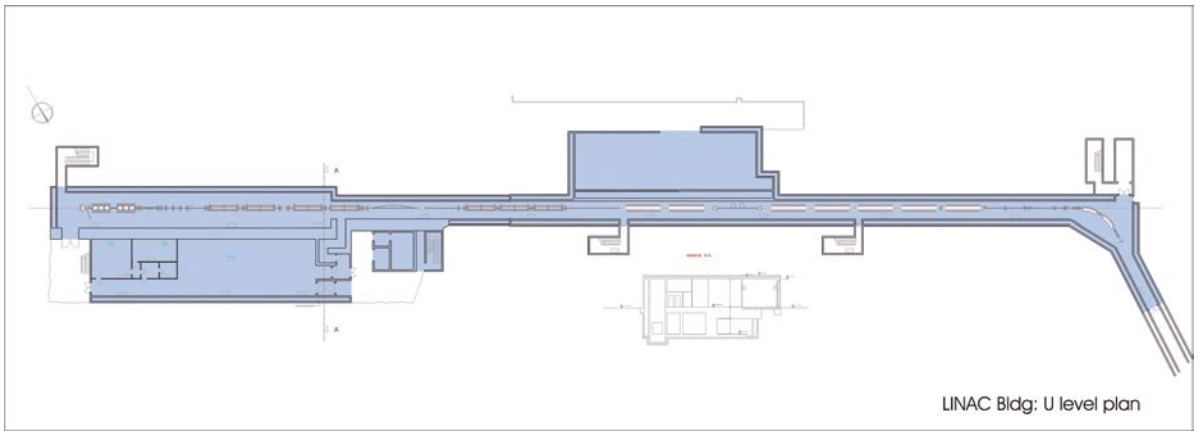

Figure 14.2.3(b):
LINAC Building.
Underground tunnels and halls. Linac tunnel, photocathode laser hall, assembly and support rooms.

In a manner similar to the existing linac building, the new building will be divided into different functional zones:

a) An underground gallery, extending to the FEL hall, will house the photoinjector, injector and main linear accelerator including diagnostics and safety systems.

b) Adjacent to the tunnel housing the linac injector a service gallery will contain the laser room for the photocathode laser, an optical laboratory, assembly rooms and store rooms. The temperature of the laser room will be regulated to +/- 0.5°C. Ventilation and air conditioning of the hall will have specifications guaranteeing low dust contamination. The room will also be isolated from vibrations.

c) Surface buildings (co-linear to the tunnel) will house the high power RF plants and electrical auxiliary systems for the linac sections and photocathode electron gun. These buildings will be an extension of the present klystron gallery and will be similarly off-set with respect to the linac tunnel, permitting correct access of the waveguides feeding the linac sections with power. The klystron gallery will be extended backwards by ~80 m and forwards by ~20m to an overall length of ~195 m. An extension will also be made of the crane that has a capacity of 5000 kg.

d) A surface building will be dedicated to the control room, laboratories and a store room. The control room will be positioned in proximity of the present one.

e) The existing water substation building attached to the klystron gallery, that houses part of the cooling system, will be doubled to room the new cooling plants.

The sides (not flanking bed-rock) and ceiling of the linac tunnel will be constructed to shield against the escape of ionizing radiation and will conform to European radiation protection regulations. A sufficient number of emergency exits will be provided conforming to safety regulations. Access to the tunnel will be through chicanes dimensioned to inhibit propagation of scattered radiation and conforming to emergency service specifications.

At the upstream end of the linac tunnel an access pit will be used for the transportation of heavy machine components, such as accelerating sections and magnets. These will be lowered into the pit and moved into the linac tunnel through a shield door. A monorail crane will be used to transport equipment in the tunnel. The existing crane with a capacity of 3000 kg will be extended into the new tunnel.

14.2.2 Undulator Hall

At the downstream end of the linac building, at the same level as the linac tunnel, the FEL hall will be built. The hall will house the beam transport system from the linac to the undulator chains composing the FELs, the beam dump systems and the take off optics. The dimensions of this hall are approximately 110 by 11 m^2 with a height of 3.5 m (see Figure 14.2.4). Parallel to the FEL hall a service gallery will house ancillary equipment. The tunnel will have a roof of concrete 2 m thick to stop ionizing radiation reaching the outside. Similarly the wall separating the FEL hall from its adjacent service gallery will have a 2 m thick wall. This will permit access to the service gallery during operation for maintenance and control. The possibility of placing the service gallery on the surface above the FEL hall will also be evaluated during the detailed design phase.

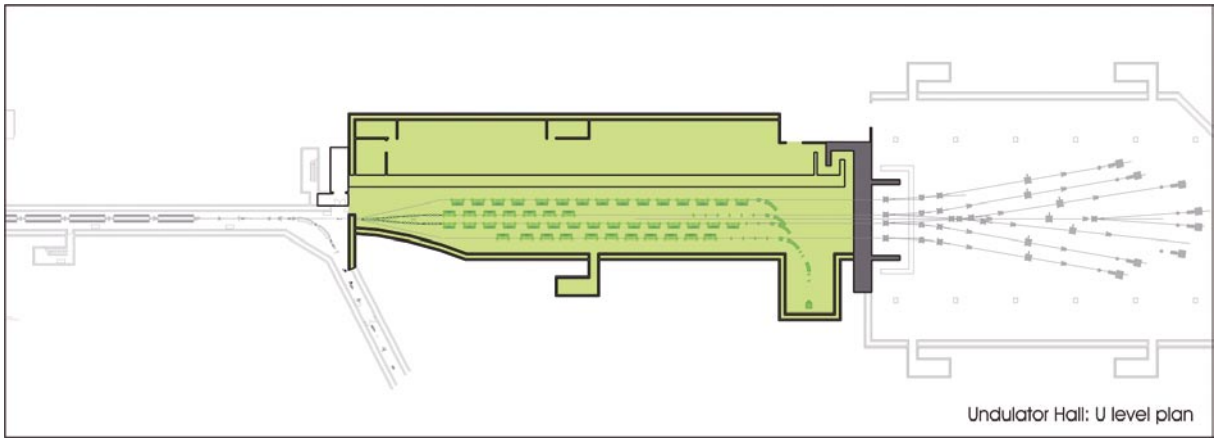

Figure 14.2.4:
Plan view of the FEL Hall.

In the tunnel two chains of undulators and associated equipment will be installed constituting FEL-1 and FEL-2. Leading to the undulators from the end of the linac, a beam transfer line, composed of magnets, vacuum chamber and diagnostic equipment will be assembled. In parallel to the two foreseen undulator chains, space will be left for additional undulators for future developments and upgrades

(Figure 14.2.4 shows space for four undulator chains). The "spent" electron beam exiting the FELs will be deflected to a side enclosure and channeled into a beam dump. This area will be shielded against the escape of ionizing radiation by the surrounding rocks and a 2 m thick concrete roof.

At the end of the FEL hall a 3 m thick concrete wall will separate it from the experimental hall. The photon beams generated in the undulator chains will pass through holes in this wall and impinge onto deflecting mirrors. The electron beam will never reach this wall, having been deflected to the beam dump in the side enclosure. Both passive and active fail-safe systems will be used to guarantee the impossibility of the electron beam ever reaching the end wall. The front ends, composed of gas chambers and delay lines and diagnostics, will be situated within the FEL hall, just prior to reaching the end wall.

At the start of the FEL service gallery, a clean room isolated against vibrations will house the Seed Laser. This room will be thermally controlled to better than +/- 0.5 °C. Along the rest of the service area gallery, electrical equipment and control racks will be installed. A sufficient number of emergency exits conforming to safety regulations will be provided, both to the FEL hall and away from the service gallery to the open. Access to the FEL hall will be through chicanes that will satisfy safety regulations for space and access. The option of placing the seed laser room on the surface at the end of the klystron gallery will be evaluated during the detailed design phase.

At surface level an access building will be constructed above an opening to the FEL hall. This building will be sufficiently large to allow the access of a transportation truck and will mount a crane used to lower equipment into the FEL hall. During operation of the facility the opening to the FEL hall will be closed with shield blocks conforming to radiation safety requirements.

14.2.3 Experimental Hall

The experimental hall will be situated at the end of the FEL hall, see Figure 14.2.6. Separating the two halls will be a 3 m shield wall. Just after the shield wall, and within the experimental hall, a mirror room

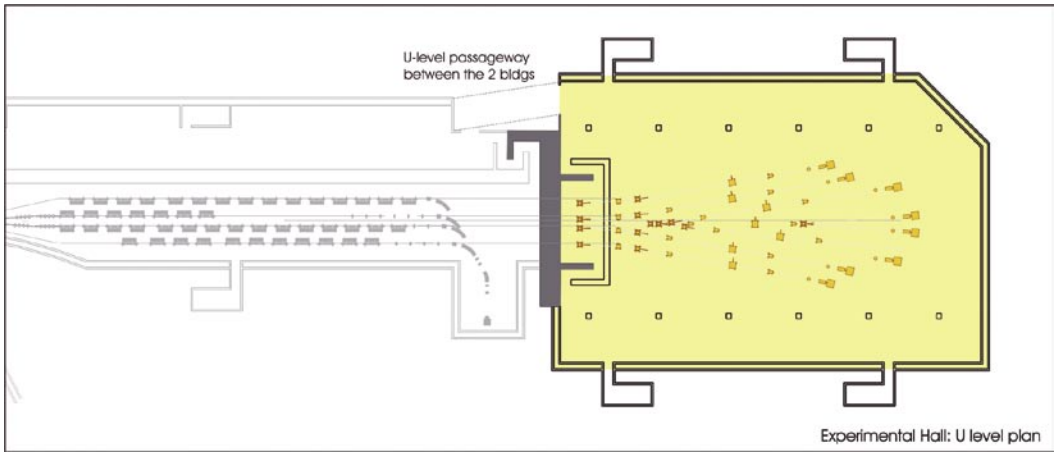

Figure 14.2.5:
Plan view of the Experimental Hall.

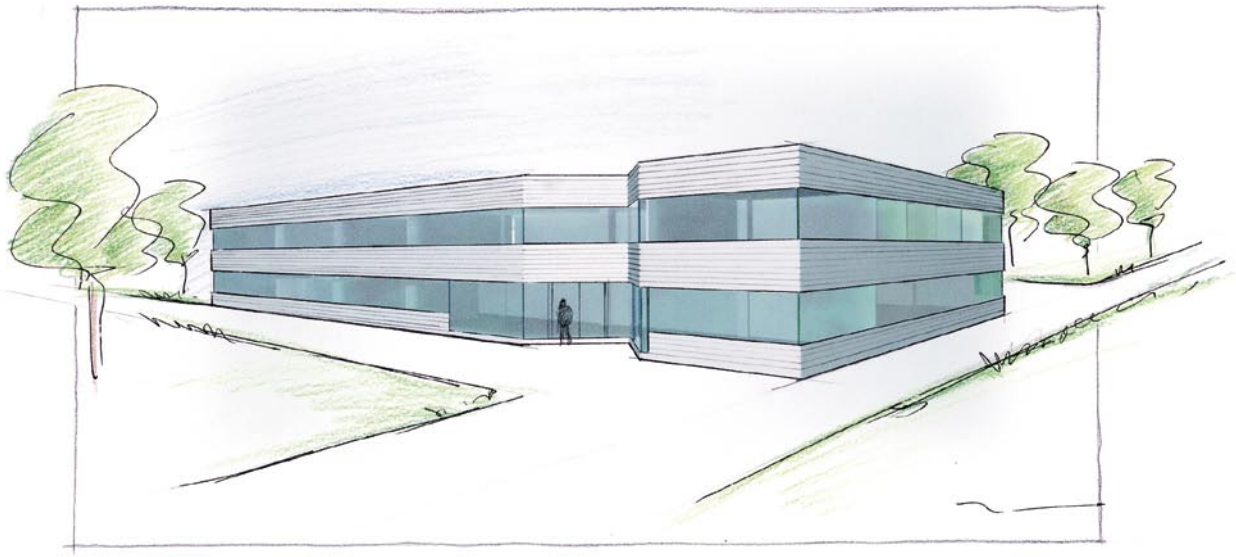

Figure 14.2.6:
The Experimental Hall.

will be built. This room will be separated from the Experimental hall proper by a 0.8 m thick wall. The mirror room will house the first deflecting mirrors. The roof of the mirror room will be sufficiently thick to shield against the escape of ionizing radiation. The FEL photon beams, after being deflected by the mirrors, will be transported through beamlines by additional optics to experimental end stations. The beamlines are approximately 50 m in length and are positioned 1.3 m from floor level.

The Experimental hall will be dimensioned to allow installation of up to 10 beamlines and accompanying end stations (60 m by 27 m wide, a height of 8 m and a floor area of roughly 1620 m^2). A 7000 kg bridge crane will access the experimental floor area at a height of 6 m.

Support laboratories will be built on either side of the Experimental hall. The Experimental building will have three floors, including the beamline area and will be approximately 60 m long by 40 m wide. The upper floors will be used for offices, meeting rooms and storage space. An artists view of the building above ground is shown in Figure 14.2.6.

Transportation of equipment to the Experimental hall will be via a sloping road accessing the lower level of the building. This road will permit the movement of heavy or bulky components to a loading area. The Experimental hall bridge crane will then be used to transport this material into and around the hall. A sufficient number of emergency exits conforming to regulations will be provided.

14.2.4 Conventional Installations

The principal infrastructures necessary for conventional installations and auxiliary plants are an electric main station, a cooling tower facility and a water plant building housing pumps and piping, as indicated in the general layout Figure 14.1.1.

14.2.4.1 Main Electric Station

On the north-east side of the site, a building on two floors housing the main electric station will be constructed with a foot-print of 25 m by 40 m. A new electric cabinet will take power from the main electric line of the local electrical supplier ACEGAS-APS. The principal distribution system for Sincrotrone Trieste will be housed in this building. A metal clad switching system will be used to supply medium voltage power to peripheries and transformers. Uninterruptible power supplies will have their own room. The building will also house all subsystems to power the storage ring, linac, FEL hall, Experimental hall and laboratories of the AREA di Ricerca.

14.2.4.2 Cooling and Water Facilities

In the area between the present cooling tower facility and the heating/refrigeration plant, as shown in the general layout Figure 14.1.1, a new building (900 m^2) will be erected containing conventional installations, heating and cooling plants, the compressed air station and other technological plants. The FERMI facility requires a cooling system that is described in detail below. The existing cooling tower will be upgraded and new plants installed. Peripheral local substations will provide heating and ventilation.

14.2.4.3 Office and Laboratory Buildings

Two buildings either side of the klystron gallery (ES1, ES2 and temporary pre-fabricated buildings, see Figure 14.1.1), will provide office, laboratory and storage space for FERMI project personnel.

14.2.4.4 Prefabricated Building

This will be a provisional prefabricated building installed in the north-east area as shown in Figure 14.1.1. The building will permit 50 work places with meeting rooms.

14.2.4.5 ES1 and ES2 Building

On either side of the klystron gallery and close to the storage ring building two new office and laboratory buildings (ES1 and ES2) will be erected having two floors. The ground floor will be arranged and serviced to house laboratories. The area on the first floors will be mainly reserved for offices.

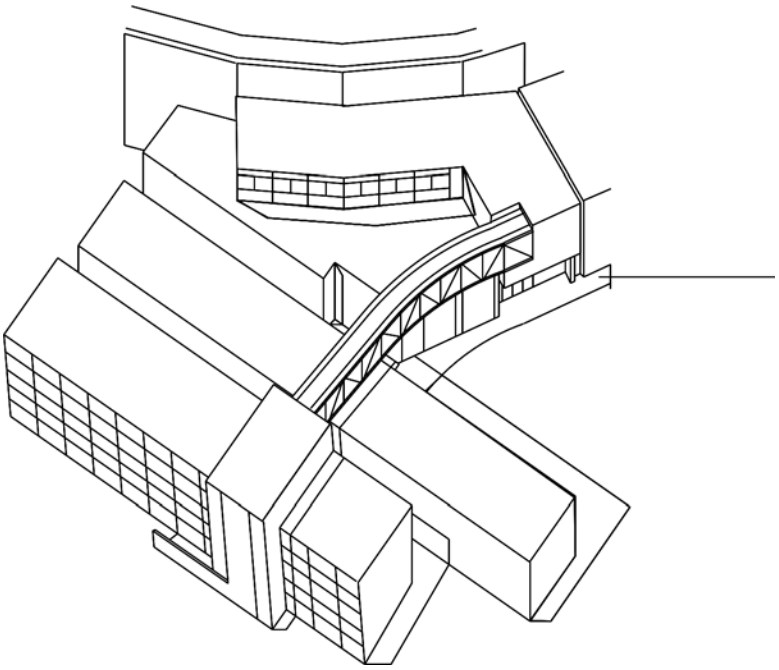

a) Schematic view of buildings ES1 and ES2 either side of the klystron gallery. An access bridge crossing the klystron gallery will connect the two buildings. ES2 is located between the storage ring building and the klystron gallery.

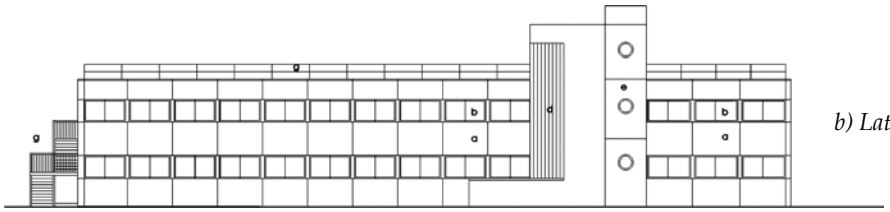

b) Lateral view of building ES1

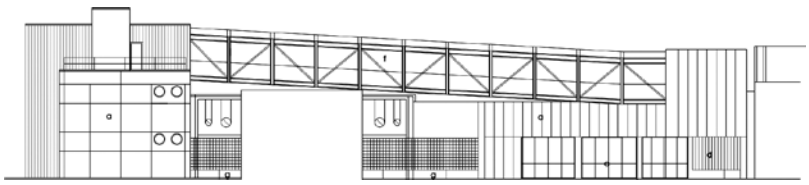

c) Cross-sectional view of buildings ES1 and ES2.

Figure 14.2.7:
Schematic views of office and laboratory buildings ES1 and ES2.

14.3 Auxiliary Plants

14.3.1 Electrical Power System

The FERMI electrical power system is outlined in Figure 14.3.1 and its main parameters are summarized in Table 14.3.1.

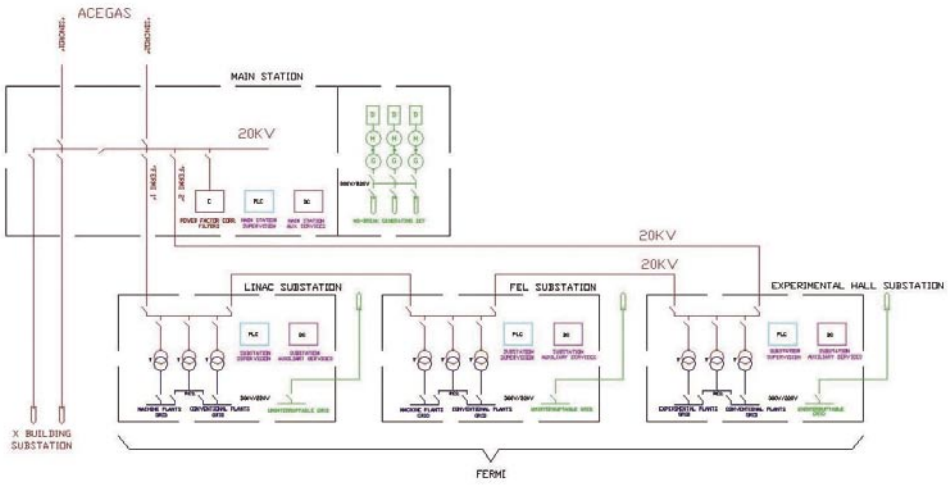

Figure 14.3.1
Electrical Power System scheme.

The electric plant is composed of a new electrical station taking power from the main line of the supplier ACEGAS-AS. The station will be powered from existing 20 kV cables. The total power used will be 12 MW. Parameters of the medium voltage systems are given in the following table.

Table 14.3.1: Electrical Power System Parameters.

Nominal Voltage	20 kV	± 10%
Nominal Frequency	50 Hz	± 1% (95% year) [+4% – 6%] 100% year
Three phase current	11.5 kA	
Neutral		Isolated
Medium Voltage System		IT
Fault current towards earth	32A	
Reaction time towards an earth fault	< 0.6s	

14.3.1.1 Main Distribution

From the ACEGAS electrical station the two existing 20 kV incoming lines will be connected to the new metal clad cabinet in the main electrical building. This building also houses harmonic filters and re-phasing systems. From the metal clad cabinet new 20 kV electrical lines will supply the existing ELETTRA metal clad cabinet, situated in building X (see site map Figure 14.1.1), that is connected to the Sincrotrone Trieste and Area di Ricerca Facilities. This will handle the present total power of 5 MW and that of the FERMI systems (linac, FEL, Experimental building and auxiliary plants) for a total power of 7 MW. The drop in voltage will be compensated since an excessive drop will have an adverse effect on the functioning of plants. The systems will be powered via a low voltage line, the parameters of which are given in Table 14.3.2 below.

Table 14.3.2: Electrical Parameters of the Medium Voltage plant.

Nominal Voltage:	400 V / 230V
Nominal Frequency	50 Hz
Neutral	Earthed
Low Voltage System	TN-s
Reaction time towards an earth fault	< 0.4s
Voltage Drop	< 4%

14.3.1.2 Electric Substations

The FERMI Substation will be installed in a central position with respect to the principal FERMI facility buildings to optimize the low voltage supply of power. The substation will have room for 20 kV/0.4 kV transformers and the relative power centres that will supply the various electrical racks of the linac, FELs, beamlines and experimental stations and associated conventional systems. All main and secondary electrical stations will be connected via a cabled network using underground or suspended conduits.

14.3.1.3 Emergency and Uninterruptible Power System

An emergency and uninterruptible power supply will be housed in the main electric building. The system is presently composed of three 400 kVA rotating electric groups each connected through a flywheel/friction system to a diesel engine that starts when the main external supply is interrupted. A fourth group will be installed to cover the uninterruptible power needs of the FERMI facility.

A dedicated distribution circuit will start from the power center supplied by these groups. The electrical parameters of this circuit are given in table 14.3.3. The drop in voltage will be compensated since an excessive drop will have an adverse effect on the functioning of systems.

Table 14.3.3: Electrical Parameters of the low voltage uninterruptible plant.

Nominal Voltage	400 V / 230V
Nominal Frequency	50 Hz
Neutral	Earthed
Low Voltage System	TN-s
Reaction time towards an earth fault	< 0.4s
Continuity	Absolute
Voltage Drop	< 4%

14.3.1.4 Normal and Emergency Illumination Plants

All new buildings will be equipped with normal and emergency lighting. Particular attention will be given to energy saving strategies that adopt presently available technologies as foreseen in the European project GreenLight with which Sincrotrone Trieste is associated.

Emergency lights will conform to safety regulations; they will be of the self-powered type and will guarantee illumination of escape exits. Luminous panels will indicate the shortest access routes to emergency exits.

14.3.1.5 Energy Saving Policy

According to the energy saving policy of Sincrotrone Trieste electrical equipment will be preferentially chosen that is energy efficient. A complementary electrical plant producing a limited quantity of electrical power will also be used. The design of the complete electrical system will be optimized to maximize energy savings.

14.3.1.6 Earthing and Protection against Lightning

A new electrical grounding network will be constructed for FERMI that will take into account the existing system. The present system is not homogeneous and is composed of connected electro-welded webs, rods and dispersion plates. The composition of the terrain is Carsic rock (limestone) with a average electrical resistence of 3 kOhms/m. The equivalent dimensions of the grounding network is 350 m and provides a low earth resistence of 4.29 Ohms and a worst case voltage drop of 2 Volts.

All buildings will adopt lightning rods or arrays for protection against atmospheric electrical discharges that conform to safety regulations.

14.3.2 Cooling Systems

Cooling circuits and chiller plants for the facility are schematically outlined in Figure 14.3.2 and main parameters given in Table 14.3.2.

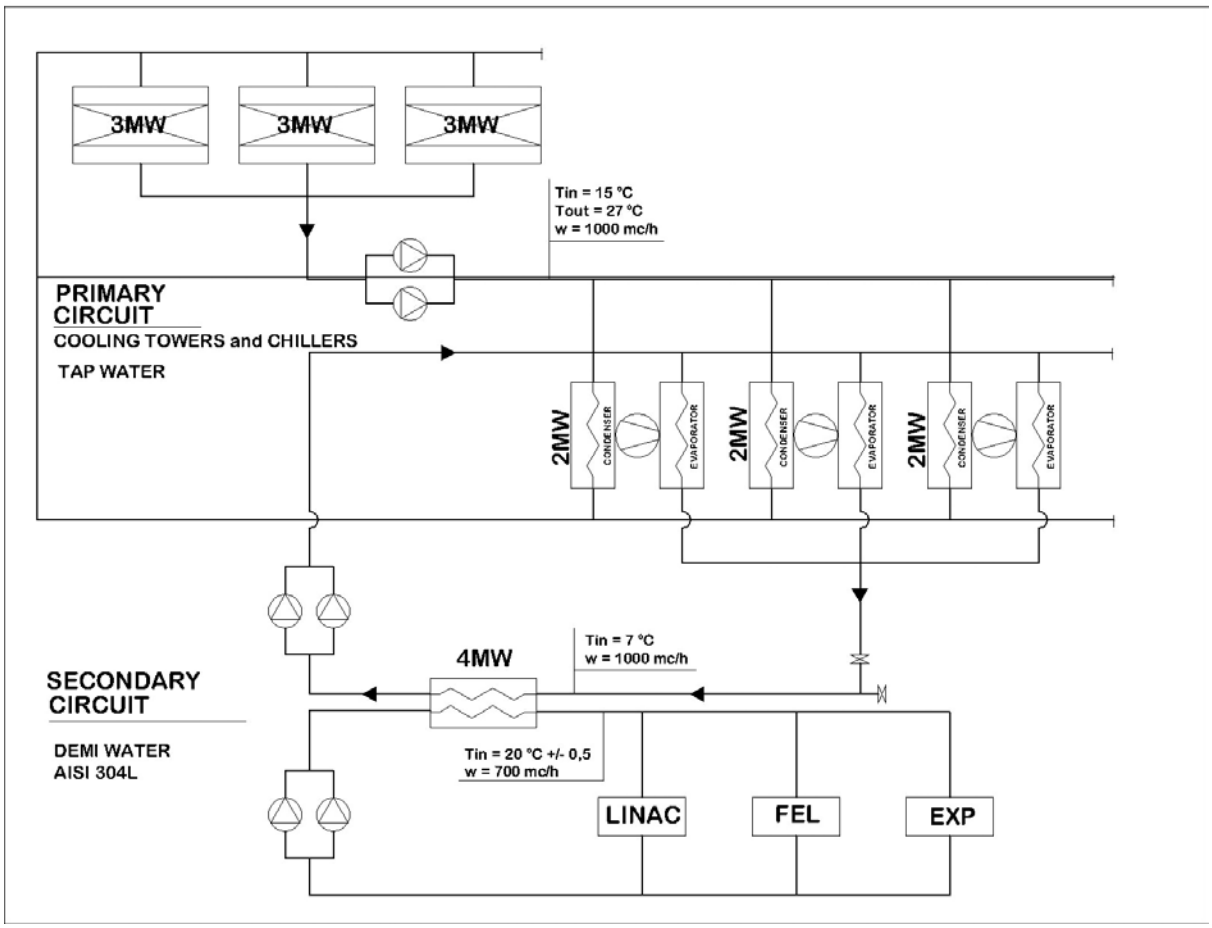

Figure 14.3.2:
Schematic of the systems cooling circuit.

Table 14.3.2: System Parameters for the cooling circuits.

Circuit	*t in [°C]*	*t out [°C]*	*Stab. [°C]*	*Q [m3/h]*	*P [bar]*
Primary	15	27	+/- 2	1000	6
Secondary	20		+/- 5	1000	10-20
Tertiary	Tertiary circuits will be fully specified during the technical design stage of conventional systems.				

FERMI equipment will be cooled by a system having primary, secondary and optionally tertiary circuits. The primary circuit will use domestic water and will have cooling towers and chillers. The main-secondary circuit will use demineralised water that may be connected to several tertiary circuits (used when more stringent temperature stability is requested).

14.3.2.1 Primary Cooling System

The primary cooling system (shown in Figure 14.3.2) will cool the demineralised water of the secondary circuit via refrigerated water and heat exchangers. The refrigerators will use cooling tower condensers that may be by-passed during winter months. After passing through the cooling towers, the water is sent either directly to the heat exchanger or the secondary circuit. Water will be treated to avoid contamination by bacteria.

Redundancy will be built into primary components to guarantee continuity of operation. Equipment and piping will be built using carbon steel.

14.3.2.2 Secondary Cooling Circuit

Only one main secondary cooling circuit using demineralised water will be installed for all the FERMI facilities (i.e, linac, undulators and experimental beamlines and end stations). The technical specification of the circuit is given in Table 14.3.2.

The secondary circuit essentially consists of one pumping group, one heat exchanger, one closed expansion vessel, piping, regulation valves and control instruments.

The water temperature will be regulated using a mixing valve mounted on the primary circuit at the exit of the heat exchanger actuated via a feedback system that monitors and controls the cooling process (usually based on the inlet temperature of the circuit).

A ion-resin exchange unit will produce demineralised water (1 μS/cm) from the city mains supply and will also treat the circulating water in order to keep the electrical conductivity within the required design limits.

Redundancy has been built into the principal machinery to guarantee continuity of operation. Equipment and piping will be built in AISI 304 L stainless steel.

14.3.2.3 Tertiary Cooling Circuits (for the Linac Building, Undulator Hall and Experimental Hall)

Whenever operational specifications are beyond those provided by the secondary cooling circuit local tertiary circuits will be used. Several such systems are foreseen for special components of the linac, FELs and beamlines, See Figure 14.3.3.

The tertiary cooling circuit will be a skid-mounted cooling plant designed to assure the temperature of strictly regulated systems (to better than +- 0.1°C). Each plant essentially consists in one pumping group, one heat exchanger, one close expansion vessel, piping, regulation valves and instruments.

Redundancy has been built into the principal machinery to guarantee continuity of operation. Equipment and piping will be built in AISI 304 L stainless steel.

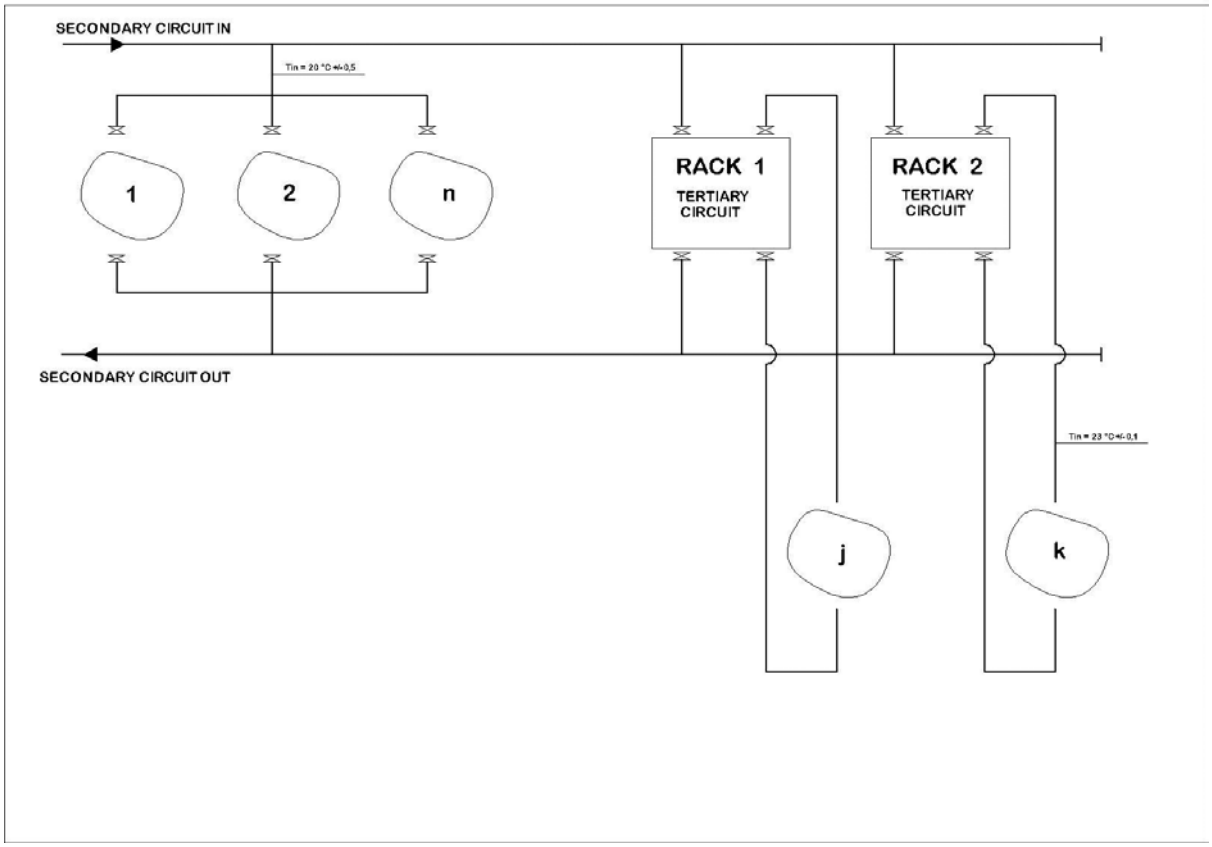

Figure 14.3.3:
Schematic of the tertiary cooling system.

14.3.3 Air Conditioning Systems

All FERMI buildings will be air conditioned. The HVAC system is particularly important for the linac, FEL and experimental halls, including service galleries and specific areas housing electronic equipment. Office and laboratory buildings will be conditioned according to regulations. The HVAC plants are placed in a central position with respect to FERMI infra-structures to minimize the length and quantity of ducts and conduits and the consequent thermal losses.

Each building will be served by a dedicated refrigerant cooling system (chillers, pumps, etc.) and a thermal station (methane boiler, pumps, etc.).

Redundancy has been built into the principal systems to guarantee continuity of operation. Parameters for the HVAC system are given in Table 14.3.4.

Table 14.3.4: Air Conditioning System Design Parameters.

Building	*t [°C] Winter*	*t [°C] Summer*	*Humidity*
Linac tunnel	27°C +/-1°C	27°C +/-1°C	50% +/-10%
Klystron Gallery	20°C +/-1.5°C	23°C +/-1.5°C	50% +/-10%
FEL Hall	22°C +/-0.5°C	22°C +/-0.5°C	50% +/-10%
FEL Service Gallery	20°C +/-2°C	25°C +/-2°C	50% +/-10%
Experimental Hall	20°C +/-0.5°C	25°C +/-0.5°C	50% +/-10%
Laser Rooms	20°C +/-0.5°C	25°C +/-0.5°C	50% +/-10%
Laboratories	20°C +/-2°C	25°C +/-2°C	50% +/-10%
Offices	20°C +/-2°C	25°C +/-2°C	50% +/-10%
Meeting Rooms (*)	20°C +/-2°C	25°C +/-2°C	50% +/-10%
Conference Room (*)	20°C +/-2°C	25°C +/-2°C	50% +/-10%

(*) For these locations the system will maintain specification only if the the number of people in the room does not exceed the design one.

14.3.3.1 Linac Building

For the extension of the existing buildings an upgrade of the existing HVAC plants is foreseen using new air treatment units in closed air circuits. Existing conduits will be used for the extension.

14.3.3.2 Undulator Hall

The FEL hall housing the beam transport system and undulators requires stringent air conditioning. The average ambient temperature must be stable to within +/- 0.7 °C over time intervals of a few hours to minimize mis-alignments, mechanical deformations and changes in the magnetic properties. Specifications will be better defined during the detailed technical design of the systems.

14.3.3.3 Experimental Hall

The experimental hall will house advanced electronics and optics that will need a thermally stabilized environment for proper performance. Ambient conditions will be subject to perturbations resulting from normal activities around the beamlines and experimental end stations (normal operation, installations and vacuum bakeouts). The environment will be thermally stabilized to +/- 1°C and critical areas, for example laser installations to +/- 0.5°C. Air temperature and humidity in the Experimental hall will be kept under strict control by closed circuit air units. Fresh air will be assured via a primary air unit.

14.3.3.4 Offices and Laboratories

As a general rule, fan coils will be installed in offices and laboratories and, when required, fresh air will be assured using a primary air unit. Special requirements for laboratories, the FEL control room and computer server locations will be met using dedicated systems.

14.3.4 Conventional Fluids and Gas Systems

Laboratories will be provided with compressed air, gaseous and liquid nitrogen and when required other gases or cryogenic liquids.

14.3.4.1 Compressed Air

A new centralized plant will supply compressed air to both technological and scientific areas. It will provide compressed air with a pressure of 7.5 bar. The plant is composed of three rotary compressors, dryers, oil removal filters and peripheral storage tanks. The tanks will guarantee pressure stability and reserve capacity against failure.

14.3.4.2 Nitrogen

Nitrogen will be stored in liquid form in a single tank centrally located. Three liquid nitrogen delivery taps will be installed: in the linac, FEL and experimental halls. A gaseous nitrogen line from the evaporation equipment of the tank will also be provided.

14.3.4.3 Water Plant Supports & Building Foundations

FEL systems and components are particularly sensitive to cultural noise and vibrations. This is especially true of low frequency ground vibrations caused by equipment such as rotary pumps and piping. The location and type of foundation for mechanical systems such equipment will be carefully evaluated and designed to minimise unwanted disturbance.

14.3.5 Control System for Auxiliary Plants

All the auxiliary plants will be locally controlled by PLCs that perform the control, regulation, signal acquisition and alarm functions. The PLCs will be connected via a data network to a supervising system composed of two servers, working in hot backup mode, and of a series of slave machines necessary for local plant management. The overall system will be similar to the existing one for reasons of operational compatibility and ease of maintenance.

14.3.6 Safety Systems

14.3.6.1 Fire-Protection System

The fire-protection system, designed in accordance with national fire-protection laws and regulations, includes a fixed water plant, a passive protection sub-system, a fixed inert gas extinguishing plant, distributed fire extinguishers, the fire detection system and the smoke extraction system.

14.3.6.2 Fixed Water Plant

This will be an up-grade of the existing plant. The system consists of a closed ring piping system connected to water hydrants and distribution panels. The FERMI plant will be an extension of the ELETTRA one.

14.3.6.3 Passive Protection Subsystem

All buildings will be passively protected by delimiting specific high-risk areas within each building.

The subsystem is designed to limit the propagation of a fire, in the event of a fire developing in spite of the application of active protection measures (detecting/extinguishing). Each area consists of one or more rooms that are identified and marked by physical fire-break boundaries, e.g.: fire proof doors (of the REI 120 type), etc.

14.3.6.4 Fixed Inert Gas Extinguishing Plant

The fixed inert-gas extinguishing plant (CO_2, N_2, etc.) consists in several cylinders located near high risk areas, specifically close to server and computer control centres. It will be activated by smoke detection units.

14.3.6.5 Fire-Extinguishers

Fire extinguishers will be portable or trolley types, loaded with CO_2 gas or powder. They will be installed in all buildings, in high-risk areas, in stairways, corridors and near access points to high fire-risk rooms.

14.3.6.6 Fire Detection System

The fire detection, warning and control system will consist of a series of local building panel boards and of main panel boards installed in the FEL control room and in the main entrance control room.

A network of automatic fire detection sensors (single units or linear sets) and alarm actuators will be installed in the rooms of protected buildings. Signals for this system will be sent to both central and local control units and activate several optical and acoustic alarm panels installed in corridors and stairways. The system will also actuate the closure of fire doors.

14.3.6.7 Smoke Extraction System

Smoke produced in the linac tunnel and in the FEL and experimental halls will be removed by the extraction fans of the air-conditioning system. The system will automatically inhibit re-circulation of air.

Smoke gathering in the experimental hall will be removed by automatic and/or manual opening of a series of smoke-extractors positioned close to the ceiling.

14.3.6.8 Information System

All buildings will be equipped with a speaker system connected to the main security centre or control room that will provide information to personnel. The system will be an extension of the existing ELETTRA one.

14.3.6.9 Special Plants

Areas of specific high risk to personnel, such as inert gas plants, will have safety systems conforming to safety regulations.

14.4 Modifications to Existing Systems

14.4.1 Drainage

A network of drainage pipes will collect all wastewater and channel it to the main sewer system. A separate draining system will dispose of rainwater. Dangerous fluids from laboratories, workshops and technological rooms will be collected and disposed of according to applicable regulations.

14.4.2 Sewage

All waste water will be channeled to a lift station where pumps will proceed to discharge the waste through a pressure line to the municipal disposal system of Basovizza located 500 m from the station and 12 m higher.

14.4.3 Liquid Nitrogen Distribution

The Liquid Nitrogen tank now located next to the ELETTRA storage ring building will be moved to another location adjoining the Experimental hall. The relative piping for distributing the nitrogen gas will also be modified. The Liquid Nitrogen tanks close by the MM building will require modification in case of interference with the new road network.

14.4.4 TASC CNR-INFM Infrastructures (Building MM)

The conventional infrastracture of the TASC CNR-INFM building MM including normal water, both hot and refrigerated, compressed air, demineralised water, electrical power, telephone and data links and the fire alarm connection are all connected to central plants via an underground conduit. The conduit is directly affected by the new FERMI constructions, in particular by the FEL hall and associated service gallery. Modifications to the conduit, re-piping and re-cabling will be performed. In addition, local plants will be set up to provide hot and chilled water.

14.4.5 The ELETTRA Facility

The external lines supplying the ELETTRA facility with water, gas and electrical power will be modified to additionally supply the FERMI facility. As earlier mentioned, the liquid nitrogen tanks located in proximity to the FEL hall will be relocated to a central area. Sewage pipes will also be upgraded and relocated.

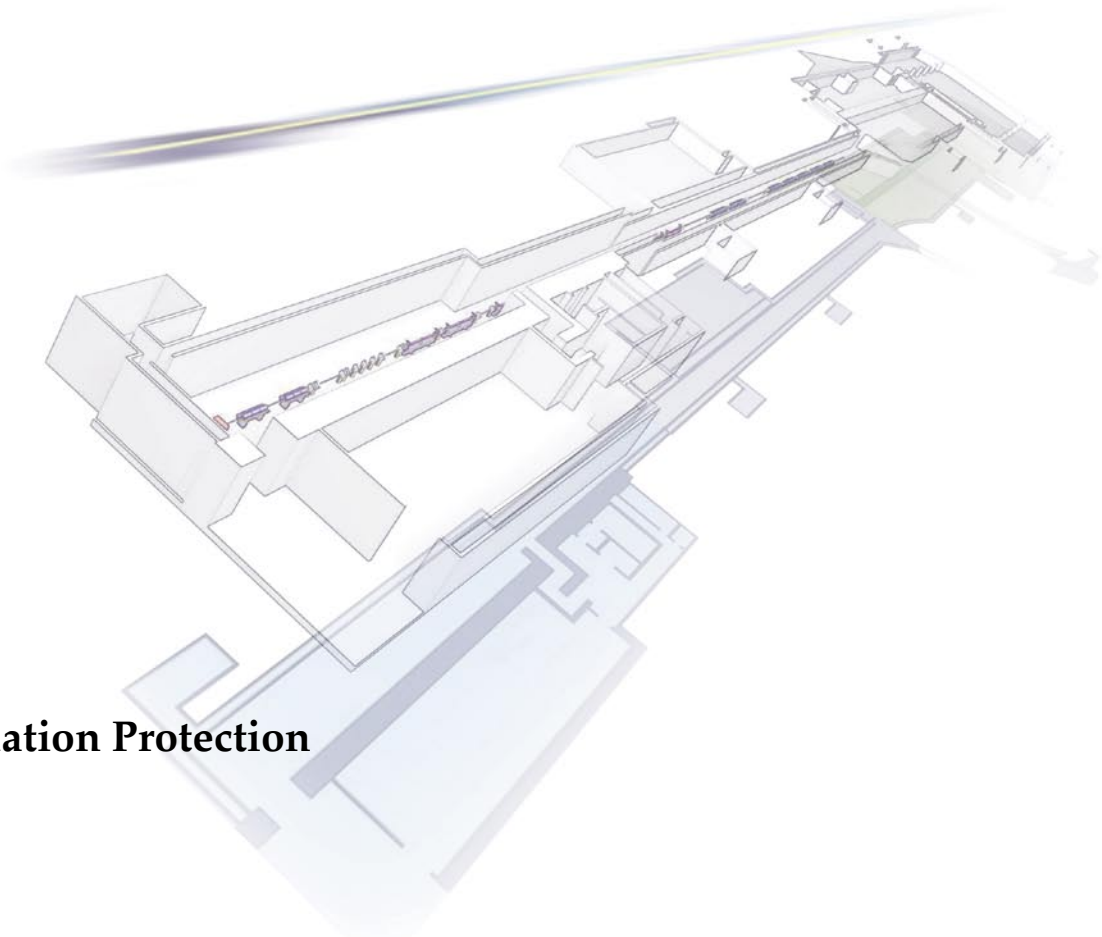

15 Radiation Protection

Synopsis

The main goals of Radiation Protection are to evaluate the ionizing radiation sources produced in the linac and undulator tunnel and in the beamline hutches, to estimate the needed biological shielding barriers and to adopt appropriate safety systems for personnel protection.

In the design of the shielding for FERMI, the different sources of ionizing radiation produced inside the accelerator tunnel have been considered. The radiation intensity depends strongly on the electron beam energy and current and is related to the beam loss frequency and distribution inside the machine.

The evaluation of the shielding thickness has been performed on the basis of semi-empirical expressions available from the literature and that have been validated by experimental measurements performed at ELETTRA during radiation protection surveys.

The goals of dose limits for the various areas around the facility (*free*, *supervised*, and *controlled* areas) are lower than those established by Italian regulations in compliance with the European/Euratom directives.

According to our project goals, only the linac and undulator tunnel will be classified as *controlled area*. The undulator Service Area and seeding laser room will be considered *supervised areas* while the experimental hall outside the beamline hutch will be a *free access area*. Only personnel involved in machine operation will be classified as *radiation workers* and will be monitored using personal dosimeters. The experimental users will be *not classified* from the radiation protection point of view.

Radiation monitoring outside the tunnels will be based on passive dosimeters and on a network of active gamma and neutron detectors located at various points of the experimental hall and of the undulator Service Area. Similarly to the ELETTRA storage ring, radiation monitors will be connected to the radiation safety system and beamlines operation will be prevented if predetermined gamma dose-rate thresholds is exceeded.

15.1 Ionising Radiation Sources

During normal operation of the accelerator, gamma and neutron radiation fields are produced where all or a fraction of the beam is lost, i.e. around beam-stoppers, beam dumps or collimators. In case of malfunctions, beam losses can also be distributed elsewhere, such as along the accelerating sections, around the spreader, or inside magnets.

In addition, high energy gamma rays (the so-called "gas bremsstrahlung") are generated in the interaction of the electron beam with the residual gas inside the vacuum chamber: its intensity is proportional to the vacuum pressure but it is much lower than the radiation intensity produced by beam losses, therefore it does not determine the accelerator shielding thickness.

Gas Bremsstrahlung is produced mainly in the forward direction and is transported through the beam pipe outside the shielding, together with FEL radiation. Since this radiation is very penetrating, it must be taken into account in the shielding evaluation of the beamlines hutch, together with high energy scattered radiation produced by beam losses inside the accelerator tunnel.

Synchrotron radiation generated in the bending magnets along the transfer line towards the beam dump can be partially extracted from the accelerator tunnel through the beampipe but it is peaked at lower energies (X-rays) and it does not determine the shielding requirements for the beamline hutches.

The interaction of high energy electrons with matter gives rise to large amounts of secondary particles (gamma rays, electrons, positrons, neutrons) which represent, from the health physics point of view, the effective radiation sources to consider in the shielding calculation.

The products of the electromagnetic cascade generated by the electron beam can be divided into four components:

i) High energy gamma rays (up to the energy of the primary electrons) generated in the electromagnetic cascade initiated by the electrons. The cascade at high energy is peaked mainly in the forward direction; however, lateral and backward components must also be considered.

ii) Medium energy neutrons (up to a few MeV) generated by giant resonance reactions of gamma rays with matter. These neutrons are emitted isotropically from the interaction region.

iii) High energy neutrons (up to a few hundred MeV) produced by gamma ray interactions with nucleus components (quasi-deuteron interactions, photo-pion production). They have a low forward preference; their intensity is much lower than the intensity of medium energy neutrons, but they may determine the shielding thickness in the forward direction as they are far more penetrating.

iv) Muon pairs ($\mu+/\mu-$) are produced by gamma rays whose energy is higher than 212 MeV, with a cross section much lower than the e+/e- production. Compared with the gamma component, in the

FERMI energy range the muon intensity is absolutely negligible once the shielding thickness in the forward direction is higher than 1.5 m of ordinary concrete [1].

The interaction of the primary electron beam and of the cascade products with machine components produces radioactive isotopes. The induced radioactivity at FERMI will affect mainly the beam dumps and, in much lower measure, beam-stoppers, collimators, vacuum chamber and IDs. Particular attention will be devoted to the design and fabrication of the beam dumps. They will be limited in number, positioned in areas remote from the machine and shielded locally, in order to reduce as much as possible exposure to personnel accessing the machine tunnel during maintenance periods. The composition and layout of the beam dump targets will be optimized to reduce long-lived radioisotope production and to contain as much as possible the secondary cascade.

15.2 Radiation Shielding

15.2.1 Methods for Shielding Evaluation

The most commonly used method for the evaluation of shielding thickness for an accelerator facility is based on semi-empirical expressions obtained from experimental data of shower production and development. These formulas correlate the beam energy and power with equivalent radiation sources of given intensities produced during the beam losses. Monte Carlo simulation techniques can also be used to simulate beam losses in very simple geometrical configurations and to calculate the consequent dose distribution and propagation.

The shielding for the FERMI facility has been evaluated using some semi-empirical expressions proposed by several authors [1, 7]. Furthermore, radiation measurements performed at ELETTRA during radiation protection surveys have been used as benchmarks.

15.2.2 Accelerator Parameters, Working Factors and Dose Limits

The intensities of radiation sources produced during beam losses depend on the following factors:

- beam characteristics (energy, current, repetition rates),

- beam loss scenarios (acceleration efficiency, faults and malfunctions frequencies, expected duration of beam losses),

- machine use factors and operation modes.

The dose limits for personnel and population established by Italian regulations in compliance with the European/ Euratom instructions, foresee the definition of three areas: **free access areas** (“aree non classificate” or “zone libere”), **supervised areas** ("zone sorvegliate") and **controlled areas** ("zone controllate"). In Table 1.3.1 the dose limits foreseen according to the above regulations, together with our goals for the commissioning and normal operation of the facility, are reported.

Table 1.3.1: Dose limits foreseen fo,r different areas of the FERMI facility.

	Free access areas	Supervised areas	Controlled areas
Italian/European Regulation Dose limits (mSv/year)	1	6	20
Our goals during commissioning (mSv/year)	0.5	4	10
Our goals during normal operations (mSv/year)	0.5	2	5

15.2.3 Shielding Requirements for the Accelerator

The shielding for the roof of the linac was originally designed for a 2 GeV machine with maximum average current of 0.1 μA. With these parameters, assuming operation of the machine as injector of the storage ring, i.e. about 1 hour/day, and producing beam losses at full power into one of the beam-stoppers located along the linac-to-storage ring transfer line, the shielding thickness adopted for the roof was 1.5 m of heavy concrete plus 0.5 m of ordinary concrete. During operation of the FERMI FELs, the beam energy will not exceed 1.2 GeV; however, the machine is foreseen to run continuously with beam losses into the beam dumps. Calculations show that the present shielding thickness for the roof can be maintained provided local shielding is installed around beam dumps, beam-stoppers, collimators and close to other points where part or fraction of beam can be preferably lost. The shielding of the wall at the end of the undulators hall will be fabricated from ordinary concrete with a thickness of 3 m.

15.2.4 Shielding Requirements for the Beamlines

The main source to consider in designing the shielding for the beamline hutches is gas bremsstrahlung. A further contribution could be due to the channeling through the beamline vacuum chamber of the secondary particles (i.e. gammas, electrons and neutrons) produced in unwanted partial beam losses occurring in the undulator hall.

These two radiation components will interact with the first optics elements of the beamlines and further develop downstream. Therefore, the first mirror must produce a deviation of the FEL beam of not less than three degrees so as to intercept most of the high energy radiation. The shielding of the beamline hutches will be realized in ordinary concrete, the thickness of which will be finalized on the basis of Monte Carlo simulations once the technical designs of the beamlines is finalized. Additional lead shielding will be positioned around those elements more affected by the high energy products of the gamma component.

15.3 Areas and Personnel Classification

15.3.1 Areas and Personnel Classification

In accordance with the above considerations, the following areas classification is foreseen:

Controlled areas ("zone controllate") including:

- the entire linac tunnel and undulator hall with machine in stand-by status,
- the delimited areas adjacent to each klystron in the klystron hall,
- the delimited areas around beam-stoppers and beam dumps with machine in *shutdown status*.

Supervised areas ("zone sorvegliate") concerning:

- the undulator Service Area and seeding laser room during the commissioning of the facility.

Free access areas ("zone libere") include:

- the laser room, adjacent to the linac front-end,
- the undulator Service Area and seeding laser room at the end of the facility commissioning,
- the experimental hall and all the areas outside the linac and undulator tunnels.

Personnel involved in machine operation will be classified as radiation workers (Cat. B).

15.4 Radiation Safety System

The access control system for FERMI must guarantee that access to the machine tunnel and to the beamline hutches is allowed when safe conditions for personnel are fulfilled. The system is based on low level computers, the Programmable Logic Controllers (PLCs). The access to accelerator tunnel is also supervised by PCs located in the control room. The system fulfills three basic requirements: fail safe logic, redundancy and less than complete automation. The fail safe logic guarantees that if a fault condition occurs in one of the safety components, the machine or the beamline is stopped in a safe status. The redundancy assures that the permission to enter the accelerator tunnel or the hutch is given only if at least two independent conditions are fulfilled at the same time.

Direct operator intervention is requested to give the final assent during the access procedure (to unlock the entrance door) to enter the machine tunnel or to guarantee that nobody remains inside the accelerator after a period of shutdown (*patrol* inspection). For the beamline hutch, an inspection (search procedure) is required to have assent to open the beamline's beam stoppers.

15.4.1 Elements Controlled by Radiation Safety System

The Radiation Safety System will relay the access conditions to the machine tunnel and to beamlines hutch based on a certain number of signals coming from different devices. These signals are mainly:

- the photoinjector HV power supply and klystron modulator (HV_photoin, RF_ photoin),
- the klystron modulator feeding the different accelerating sections and X-band section (RF_ linac, RF_ Xband),
- the beam-stopper positioned at the end of the linac tunnel (BST_linac),
- the beam-stopper located at the end of the undulator hall (BST_linac).

Other elements are controlled by the safety system to guarantee a correct transport of the beam towards the beam dump. These are:

- the HV power supply of the bending magnets, at the end of the undulator hall, that allow the beam transport into the beam dump;
- the toroids for measuring the beam current along the transfer line to the beam dump.

15.4.2 Access Procedures

15.4.2.1 Access to Accelerator Tunnel and *Patrol* Inspection

Similar to the present safety philosophy for the ELETTRA storage ring, the procedure to enter the injector tunnel during a *stand-by* period of machine is based on the following operations:

- the person presents his/her personal card at the automatic badge reader. If the accelerator is switched off and the person is authorized to enter, the system gives the first assent to open the door;
- in the panel positioned near the badge reader, one of the keys is automatically unlocked by the system; the person takes the key out of the panel;
- the control room operator, after recognizing the person through a TV camera, gives the third and final assent for the entrance and unlocks the door;
- the person enters, closes the door and deposits his key in the inner panel.

The exit procedure consists of the same steps in the reverse sequence, excluding the operator consent: one must take the key out of the internal panel, open the door, deposit the key in the external panel and have the card read.

During the machine shutdown, free access is given to the tunnel and all the doors remain unlocked. At the end of a shutdown period the operator is required by the system to perform a *patrol* inspection in order to verify that nobody remains inside the machine enclosure. This procedure requires that the operator enters the accelerator tunnel using a special badge and executes a complete inspection pushing patrol buttons during the search.

15.4.2.2 Conditions for Entrance Inside the Accelerator Tunnel

Access to the accelerator tunnel is allowed if the following conditions are together fulfilled:

- the photoinjector is OFF;
- no radiofrequency is applied to the linac accelerating sections;
- a delay time has passed from the photoinjector switching off. This will permit to minimize radiation exposure risk due to the induced radioactivity.

Special rules and procedures will be established to access the area around the beam dump.

15.4.2.3 Access to the Beamline Hutches and "Search Inspection"

The first part of the beamlines, called "front-end hutch", will be enclosed inside shielding walls It will be accessible through two doors.

Similarly to the ELETTRA beamlines, the access to the hutch is performed using two keys, called the "B" and "C" keys that must be inserted into the apposite locks on the key panel positioned near the door.

The procedure foresees the following operations:

- the user inserts the "B" key in the key panel and rotates it (this operation will unlock the "C" key);
- the user extracts the "C" key and uses it to open the hutch door (the extraction of the "C" key will lock the "B" key in the panel).

Once finished the work inside the hutch, an inspection ("search") must be performed to verify that no one is still inside before starting the operation with the FEL beam. The search inspection corresponds to the exit procedure from the hutch.

The inspection will be performed as follows:

- after asking everybody to exit the hutch, the user enters the hutch keeping the "C" key with him,
- he/she closes all the hutch doors,
- he/she inserts the "C" key in the search panel and rotates it, pushing at the same time the search button,
- he/she exits the hutch, closes the door and insert the "C" key in the key panel within 30 seconds from pushing the button,
- he/she rotates the "C" key and extracts the "B" key within 10 seconds.

If the inspection is not correctly executed, the safety system will generate an emergency status. Two additional safety devices (optical barriers) will help the search execution and permit to detect the presence of other persons inside the hutch during the inspection.

15.4.2.4 Conditions for Entrance Inside the Beamline Hutches

Access to a beamline hutch is allowed if the following conditions are fulfilled simultaneously:

- the beam-stopper placed at the end of the linac tunnel is closed,
- all the beam-stoppers placed at the end of the Undulator Hall after the electron beam extraction towards the beam dump are closed,
- the radiation levels measured by the radiation monitors placed around the Experimental Hall beamlines do not exceed a pre-established threshold.

15.4.2.5 Alarms and Emergencies

An emergency status will be generated in one of the following conditions:

- one of the hutch or machine doors is forced open;
- one of the emergency button placed inside the machine or the hutch is pushed;
- one of the two optical barriers detects the presence of somebody inside the hutch
- a search inspection is not correctly executed;
- the radiation monitors do not work properly or one of the alarm thresholds has been exceeded.

For any alarm status the machine or the beamline is stopped in a safe status.

The machine is stopped by switching off, at the same time, the HV and RF systems of the photoinjector and the HV and RF systems of all the accelerating sections.

The FEL beam in the beamlines hutch is switched off closing the beam-stopper placed at the end of the linac tunnel and all the beamstoppers placed at the end of the Undulator Hall after the electron beam extraction towards the beam dump.

15.5 Laser Radiation

All main laser systems, described in Chapter 10, emit light with parameters corresponding to Class IV, as defined by the international laser safety standard IEC 825-1. Both eye and skin exposure to emission by these lasers is potentially hazardous and therefore all safety precautions, prescribed by the above safety standard, will be adopted. In particular, all laser rooms and laser entrance ports (e.g. at photoinjector) will be signed and equipped according to the above standard. It has to be noted that very high attention has to be given to the safety aspects of the user lasers, because the nature of the experiments may require frequent changes of geometry, wavelength, etc, and access to them is granted to higher number of people and also during FEL operation (contrary to machine lasers).

15.6 Radiation Monitoring System

15.6.1 Internal Beam Loss Monitors

A network of gamma detectors is installed inside the linac tunnel to localize the dose distribution due to beam losses occurring along the different accelerating sections. The existing system will be integrated with new modules to cover the entire tunnel and upgraded with higher dynamic range electronics in case a higher sensitivity is required.

15.6.2 Radiation Monitoring Outside the Shielding

Radiation monitoring system must be designed to be able to detect radiation pulses of very short duration. Environmental monitoring outside the tunnels will be based on passive dosimeters such as TLD, films, imaging plate and bubble detectors. In addition, a network of active gamma and neutron detectors will be located at various points of the experimental hall and in the undulator Service Area. Similarly to the monitoring system in the ELETTRA experimental hall, these detectors will be connected to a PC and will provide measurements of instantaneous doserates and integrated doses over pre-determined periods.

Each unit consists of an environmental ionisation chamber for measuring the gamma dose, a BF3 counter for the neutron component and a micro-processor for communications with the PC. Measurements of instantaneous dose-rates and integrated doses over pre- determined periods are communicated to the PC every minute.

As explained in the previous section, in addition to the environmental stations, some gamma monitors located in the vicinities of the beamlines exits will be connected with the beamline personnel safety system.

Each monitor provides three signals whose meanings are:

1) no failure status

2) pre-alarm status

3) alarm status.

The beamlines PLC acquires these signals generating the following actions:

1. **no failure status OFF** (malfunction) causes: no entry allowed in the beamlines hutch, the closure of all the beamstoppers of the beamlines front-end, closure of the linac beamstopper,
2. **pre-alarm status ON** (pre-alarm) causes: no entry allowed in the beamlines hutch, the closure of all the beamstoppers of the beamlines front-end,
3. **alarm status ON** (alarm) causes the same actions produced for the malfunction.

15.7 Radiation Safety Rules and Procedures

Personnel entering radiation areas are required to record their entrance in a register. Access to radiation areas is allowed to radiation workers holding personal dosimeters. Occasional access to radiation areas is allowed to authorised personnel (not classified as radiation worker) that have been assigned a guest dosimeter with real time reading.

15.8 Radiation Safety Training

The personnel involved in machine and beamlines operations will be trained in radiation safety issues. Three main training levels are foreseen, according to the different personnel tasks. These will be oriented to: radiation workers, machine operators and beamlines users. Procedures, manuals and training materials are available at the web site of ELETTRA ([10]-[12]).

Radiation workers will be trained on the risks of exposure to ionizing radiation, in the Radiation Protection rules to access classified areas and in the procedures to access the accelerator and undulator tunnel. In addition, operators will also be trained in the logic and philosophy of the machine and beamlines safety systems.

Beamlines users will be trained in the procedures to access the beamlines hutch and in the logic and philosophy of the beamlines safety systems.

15.9 References

[1] W.P. Swanson, "Radiological safety aspects of the operation of electron linear accelerators", Technical Reports Series N. 188, IAEA, 1979.

[2] M.Fabretto, P.Michelini, A.Rindi, G.Tromba:, "Shieldings and safeties for the ELETTRA Facility - Status Report", Sincrotrone Trieste Internal Report ST/M-89/7, 1989.

[3] H. Dinter et al, "Calculations of doses due to electron-photon stray radiation from a high-energy electron beam behind lateral shielding", Internal report DESY 88-117, 1988.

[4] K. Tesch, "Data for simple estimates of shielding against neutrons at electron accelerators", Part. Accelerators 9, 201 (1979).

[5] F. Lucci, M. Pelliccioni and M. Roccella, "Measurements on 1 GeV electromagnetic cascade and cascade-produced neutrons in shielding materials", Internal Report CNEN LNF-69/27, 1969.

[6] H. Dinter and K. Tesch, "Dose and shielding parameters of electron-photon stray radiation from a high-energy electron beam" Nucl. Instr. Meth. 143, 349 (1977).

[7] Proceedings of the specialists' Meeting on "Shielding Aspects of Accelerators, Targets and Irradiation Facilities", Nuclear Energy Agency (1994).

[8] V. Vylet and J.C. Liu, "Radiation protection at high energy electron accelerators", Rad. Prot. Dosim. 96, 333 (2001).

[9] NCRP. "Radiation Protection for Particle Accelerator Facilities", NCRP Report No. 144 (2005)

[10] "Radiation Protection at the accelerators": collection of internal reports available in the intranet web at: http://www.elettra.trieste.it/organisation/genserv/health/index.phtml. (It includes: Radiation protection handbooks and rules concerning the accelerators, Radiation emergency procedures, etc.).

[11] "Radiation Protection at the beamlines": collection of internal reports available at http://www.elettra.trieste.it/organisation/genserv/health/index.html. (It includes: Radiation Protection Handbooks for the beamline users, Radiation emergency procedures for beamlines, etc.).

[12] Videotape "Radiation and General Safety" for users, ELETTRA staff and suppliers. It can be watched at: http://www.elettra.trieste.it/organisation/genserv/health/video/index.html.

Appendix

A. Parameter List

A.1 Photoinjector

A.1.1 Photo-Cathode

Parameter	*Value*	*Units*
Cathode material	Metal (Cu)	-
Active diameter of cathode	12	mm
Quantum efficiency (@ 266 nm)	$\sim 2 \cdot 10^{-5}$	-

A.1.2 RF Cavity

Parameter	*Value*	*Units*
Number of cells	1.6	-
RF frequency	2.998	GHz
RF pulse duration	3	µs
Peak power	15	MV
Maximum extraction field	110	MV/m

A.1.3 S0B Output Electron Beam

Parameter	*Medium bunch*	*Long bunch*	*Units*
Electron beam energy	95	95	MeV
Bunch charge	0.8	1	nC
Current	30-80	30-100	A
Bunch length (FWHM)	10	11	ps
Correlated energy spread	0.3	0.4	%
Uncorrelated energy spread	< 3	~ 2	KeV
Normalized emittance	1.2	1.3	mm·mrad
Normalized emittance – slice (RMS)	< 1.2	< 1.2	mm·mrad
β_x, β_y	18	21	m
α_x, α_y	-0.1	0.3	-

A.1.4 Jitter of Input Parameters (expected variations)

Parameter	*RMS tolerance value*	*Units*
Laser time jitter	200	fs
Laser pulse length (FWHM)	5	%
Laser spot size	4	%
Laser pulse centering	0.1	mm
Charge	4	%
Gun field	0.25	%
Gun RF phase	0.1	Deg
SØA/B field	0.25	%
SØA/B RF phase	0.1	deg

A.1.5 Output Jitter Sensitivity

Parameter	*Medium bunch*	*Long bunch*	*Units*
Arrival time	351	266	fs
Peak current	2.4	3.3	%
Energy	0.17	0.17	%
Correlated energy spread	42	24	KeV
Emittance	13.1	6.3	%
β_x	2.1	6.3	m
α_x	0.15	0.26	-

A.2 Linac

A.2.1 Energy Budget

Cavity type	*Energy gain*	*Units*
Gun	5	MeV
S0A/B	45	MeV
C1-C7	47	MeV
S1-S7	120	MeV
X-band	18	MeV

A.2.2 Electron Beam

Parameter	*Medium bunch*	*Long bunch*	*Units*
Output energy	1.141	1.171	GeV
Bunch charge	0.8	1	nC
Peak current	850	500	A
Bunch length (FWHM)	0.6	1.4	ps
Energy spread – slice (RMS)	150 – 250	100 – 150	keV
Energy spread – projected (RMS)	0.06	0.07	%
Norm. horiz. emittance – slice (RMS)	0.8 – 1.2	1.0 – 2.0	mm·mrad
Norm. vert. emittance – slice (RMS)	0.7 – 1.1	0.9 – 1.9	mm·mrad
Norm. horiz. emittance – projected(*) (RMS)	2.0	3.2	mm·mrad
Norm. vert. emittance – projected(*) (RMS)	1.4	1.9	mm·mrad

(*)*projected along longitudinal direction*

A.2.3 Focusing

Parameter	*RMS tolerance value*	*Units*
Number of quadrupoles	44	-
Quadrupole gradient (integrated)	< 2.7	T
Phase advance (Main Linac)	4.2	deg/m

A.2.4 First Bunch Compressor

Parameter	*Medium bunch*	*Long bunch*	*Units*
Compressor	chicane	chicane	-
Number of dipoles	4	4	-
Bending angle per dipole	0.07	0.07	rad
Dipole magnetic length	0.5	0.5	m
Total length	8.0	8.0	m
R_{56}	- 28.0	- 28.0	mm
Electron energy	230.2	243.7	MeV
Norm. horiz. emittance – projected (RMS) (*)	1.43	1.90	mm·mrad
Norm. vert. emittance – projected (RMS) (*)	1.35	1.93	mm·mrad
Energy spread – slice (RMS) (*)	65 – 80	50 – 80	keV
Bunch length (RMS) (*)	1040	1150	μm
Peak current(*)	80	90	A
Norm. horiz. emittance – projected (**)	1.43	1.93	mm·mrad
Norm. vert. emittance – projected (**)	1.35	1.93	mm·mrad
Energy spread – slice (RMS) (**)	70 – 100	80 – 100	keV
Bunch length (RMS) (**)	280	560	μm
Peak current(**)	270	180	A

(*)at compressor entrance; (**)at compressor exit

A.2.5 Second Bunch Compressor

Parameter	*Medium bunch*	*Long bunch*	*Units*
Compressor type	chicane	chicane	-
Number of dipoles	4	4	-
Bend angle of chicane dipoles	0.053470	0.074500	rad
Magnet length	0.5	0.5	m
Total length	8.0	8.0	m
R_{56}	- 16.2	- 31.5	mm
Electron energy	584.2	602.2	MeV
Norm. horiz. emittance – projected (RMS) (*)	1.44	1.93	mm·mrad
Norm. vert. emittance – projected (RMS) (*)	1.35	1.93	mm·mrad
Energy spread – slice (RMS) (*)	70 – 100	80 – 100	keV
Bunch length (RMS) (*)	275	560	μm
Peak current(*)	270	180	A
Norm. horiz. emittance – projected (**)	1.90	3.22	mm·mrad
Norm. vert. emittance – projected (**)	1.35	1.93	mm·mrad
Energy spread – slice (RMS) (**)	150 – 250	100 – 150	keV
Bunch length (RMS) (**)	90	160	μm
Peak current(**)	750 – 850	500	A

(*)at compressor entrance; (**)at compressor exit

A.2.6 Jitter of Input Parameters (expected variations)

Parameter	*RMS tolerance value*	*Units*
C1-C4 RF phase	0.1	deg
X-band phase	0.5	deg
C5-C7 RF phase	0.2	deg
S1-S2 RF phase	0.2	deg
S3-S7 RF phase	0.15	deg
C1-C4 RF voltage	0.1	%
X-band voltage	0.25	%
C5-C7 RF voltage	0.2	%
S1-S2 RF voltage	0.1	%
S3-S7 RF voltage	0.1	%
BC1 magnetic field	0.05	%
BC1 magnetic field	0.2	%

A.2.7 Beam Dump

Parameter	*Value*	*Units*
Number of dipoles	2	-
Dipole magnetic length	0.5	m
Max deflection angle	90	deg
Total length	15	m
Electron energy	1.2	GeV
Norm. horiz. emittance – projected (RMS)	2.0 – 3.2	mm·mrad
Norm. vert. emittance – projected (RMS)	1.4 – 1.9	mm·mrad
Energy spread – projected (RMS)	0.07	%
Bunch length (RMS)	90 – 160	mm
Peak current	< 1 kA	A

A.3 Laser Systems

A.3.1 Photoinjector Laser

Parameter	*Value*	*Units*
Laser medium	Ti:Sa	-
Repetition rate	10-50	Hz
Pulse duration (FWHM)	4-6/10	ps
Longitudinal shape	flat-top	-
Ripple on flat top	10	%
Longitudinal homogeneity on cathode	10	%
Transverse homogeneity on cathode	10	%
Transverse beam shape	flat top	%
Rise-time (10-90 %)	0.5-1.0	ps
Spatial profile radius (flat top)	~ 1	mm
Fundamental wavelength	~ 780	nm
Operating wavelength	~ 260	nm
Pulse energy (at 780 nm)	18	mJ
Maximum micro-pulse energy on cathode	0.4	mJ
Timing stability (RMS)	< 0.3	ps
Energy stability (RMS)	< 4	%
Spot diameter jitter (peak-to-peak)	4	%
Spatial stability (RMS)	<	%
Timing jitter (RMS)	200	fs

A.3.2 Seed Laser

Parameter	*Value*	*Units*
Laser medium	Ti:Sa	-
Tuning range	360-240	nm
Power	~ 100	MW
Pulse duration (FWHM)	100/1000	fs
Longitudinal micro-pulse form	Gaussian	-
Short-term stability (RMS)	5	%
Wavelength stability (RMS)	0.1	%
Spatial homogeneity	< 10	%
Spot size	200-300	µm
Spot size jitter	3	%
Pulse shape	Gaussian	

A.4 Undulators

A.4.1 FEL-1

A.4.1.1 Modulator

Parameter	*Value*	*Units*
Magnet material	Nd Fe B	-
Type	Planar	-
Period	16	cm
Number of periods	19	-
Segment length	3	m
Number of segments	1	-
K at 360 nm	4.9	-
K at 240 nm	3.9	-

A.4.1.2 Dispersive Section

Parameter	*Value*	*Units*
Length	1	m
R56 at 100 nm	~ 30	μm
R56 at 40 nm	~ 30	μm

A.4.1.3 Radiator

Parameter	*Value*	*Units*
Magnet material	Nd Fe B	-
Type	Apple II	-
Period	6.5	cm
Number of periods	36	-
Segment length	2.3	m
Number of segments	6	-
Active length	13.8	m
K at 360 nm	4	-
K at 240 nm	2.4	-
Break length	1	m
Total length FEL-1	**22.8**	**m**

A.4.1.4 Radiator Optics

Parameter	*Value*	*Units*
Focusing scheme	FODO	-
Quadrupole number	6	
Max quadrupole gradient (integrated)	1.5	T
Average β′s	9	
Max β′s	12	m
Phase advance per cell	~ 50	deg

A.4.2 FEL-2

A.4.2.1 First-stage Modulator

Parameter	*Value*	*Units*
Magnet material	Nd Fe B	-
Type	Planar	-
Period	16	cm
Number of periods	19	-
Segment length	3	m
Number of segments	1	-
K at 360 nm	4.9	-
K at 240 nm	3.9	-

A.4.2.2 First-stage Dispersive Section

Parameter	*Value*	*Units*
Length	1	m
R56 at 100 nm	~ 30	μm
R56 at 40 nm	~ 30	μm

A.4.2.3 First-Stage Radiator

Parameter	*Value*	*Units*
Magnet material	Nd Fe B	-
Type	Planar	-
Period	6.5	cm
Number of periods	36	-
Segment length	2.3	m
Number of segments	3	-
Active length	6.9	m
K at 100 nm	4	-
K at 40 nm	2.4	-
Break length	1	m

A.4.2.4 Delay Section

Parameter	*Value*	*Units*
Length	1.8	m

A.4.2.5 Second-Stage Modulator

Parameter	*Value*	*Units*
Magnet material	Nd Fe B	-
Type	Planar	-
Period	6.5	cm
Number of periods	36	-
Segment length	2.3	m
Number of segments	1	-
K at 360 nm	4	-
K at 240 nm	2.4	-

A.4.2.6 Second-Stage Dispersive Section

Parameter	*Value*	*Units*
Length	1	m
R56 at 40 nm	~ 30	μm
R56 at 10 nm	~ 8	μm

A.4.2.7 Second-Stage Radiator

Parameter	*Value*	*Units*
Magnet material	Nd Fe B	-
Type	Apple II	-
Period	5	cm
Number of periods	48	-
Segment length	2.4	m
Number of segments	6	-
Active length	14	m
K at 40 nm	2.8	-
K at 10 nm	1.1	-
Break length	1	m
Total length FEL-2	**37.5**	**m**

A.5 Photon Output

A.5.1 FEL-1

Parameter	*Value*	*Units*
Photon energy range	12 ÷ 31	eV
Wavelength range	100 ÷ 40	nm
Pulse length	50 ÷ 100	fs
Bandwidth	~ 20	meV
Polarization	Variable	-
Repetition rate	10 ÷ 50	Hz
Peak power	1 ÷ 5	GW
Photons per pulse (at 31 eV)	$\sim 4 \cdot 10^{13}$	-
Photons per pulse (at 12 eV)	$\sim 2 \cdot 10^{14}$	-
Peak brightness (at 31 eV)	$\sim 6 \cdot 10^{32}$	Ph/s/mm^2/mrad^2/0.1 % bw
Power fluctuation	~ 25 %	%
Central wavelength fluctuation	Within bandwidth	-
Output transverse position fluctuation	50	μm
Pointing flactuation	< 5	μrad
Output spot size radius (intensity, RMS)	300	μm
Divergence at 31 eV (intensity, RMS)	50	μrad
ρ parameter radiator (at 31 eV)	$2.9\ 10^{-3}$	-

A.5.2 FEL-2

Parameter	*Value*	*Units*
Photon energy range	31 ÷ 124	eV
Wavelength range	40 ÷ 10	nm
Pulse length	100 ÷ 200	fs
Bandwidth	5	meV
Polarization	Variable	-
Repetition rate	50	Hz
Peak power (at 124 eV)	~ 0.4 GW	GW
Photons per pulse (at 124 eV)	~ $1 \cdot 10^{13}$	-
Peak brightness (at 124 eV)	~ 10^{32}	Ph/s/mm^2/mrad^2/0.1 % bw
Power fluctuation	> 50	%
Central wavelength fluctuation	Within bandwidth	-
Output transverse position fluctuation	50	μm
Pointing fluctuation	< 5	μrad
Output spot size radius (intensity, RMS)	210	μm
Divergence at 124 eV (intensity, RMS)	15	μrad
ρ parameter last radiator (at 124 eV)	$1.2\ 10^{-3}$	-

B. Glossary

4GLS	Fourth Generation Light Source
ADC	Analog to Digital Converter
ALS	Advanced Light Source (LBNL)
ANL	Argonne National Laboratory
APS	Advanced Photon Source (ANL)
APPLE	Advanced Planar Polarised Light Emitter
ASTRA	A Space Charge Tracking Algorithm, particle tracking code
BBO	BaB2O4 , Beta barium Borate
BBU	Beam Break-Up
BC1	Bunch Compressor 1
BC2	Bunch Compressor 2
BLL	Beam-line Laser system
BPM	Beam Position Monitor
BTW	Backward Traveling Wave accelerating structure
BW	Band Width
CCD	Charge Coupled Device
CERN	Organisation Europeenne pour la Recherche Nucleaire
CPU	Central Processing Unit
CSR	Coherent Synchrotron Radiation
CTR	Coherent Transition Radiation
CW	Continuous Wave
DAZZLER	Acousto-optic Dispersive Filter
DC	Direct Current
DESY	Deutsches Elektronen-Synchrotron, Hamburg, Germany
ELETTRA	Synchrotron Radiation User Facility (Trieste, Italy)
ESRF	European Synchrotron Radiation Facility
EU	European Union
FEL	Free Electron Laser
FEM	Finite Element Modeling
FFXM	full-field X-ray microscope
FIFO	First In First Out
FODO	Focus-Drift-Defocus-Drift lattice type
FPGA	Field Programmable Gate Array
FROG	Frequency Resolved Optical Gating
FWHM	Full Width at Half Maximum

GENESIS	An FEL Simulation Code
GINGER	An FEL Simulation Code
GPT	General Particle Tracer, particle tracking code
GTL	gun-to-linac drift
HGHG	High Gain Harmonic Generation
HOM	Higher Order Mode
HV	High Voltage
ID	Insertion Device
IEEE	Institute of Electrical and Electronic Engineers
INFN	Istituto Nazionale di Fisica Nucleare
I/O	Input/Output
IR	Infra-Red
ISR	Incoherent Synchrotron Radiation
LB	Long Bunch
LBNL	Lawrence Berkeley National Laboratory
LCLS	Linac Coherent Light Source
LED	Light Emitting Diode
LIL	LEP Injector Linac
LITRACK	Linac Tracking, particle tracking code
LLRF	Low Level RF
LSC	Longitudinal Space Charge
MATLAB	Mathematical Laboratory – A mathematical software packege
MIT	Massachusetts Institute of Technology
MLB	Medium Length Bunch
MKS	Meter-Kilogram-Second (units)
OMO	Optical Master Oscillator
OPA	Optical Parametric Amplifier
OTR	Optical Transition Radiation
PFN	Pulse Forming Network
PIL	Photoinjector Laser system
PLC	Programmable Logic Controller
PLL	Phase-Locked Loop
PPM	Pure Permanent Magnet
QE	Quantum Efficiency
RF	Radio Frequency
R&D	Research and Development
RMS	Root Mean Square
ROC	Radius Of Curvature

RW	Resistive Wall
SASE	Self Amplified Spontaneous Emission
SL	Seed Laser system
SLAC	Stanford Linear Accelerator Center
SLS	Swiss Light Source
SR	Synchrotron Radiation
T&S	Timing and Synchronization
TFW	Traveling Forward Wave accelerating structure
TOF	Time Of Flight
UCLA	University of California, Los Angeles
UHV	Ultra High Vacuum
UV	Ultra-Violet
VLS	Variable Line Spacing grating
VUV	Vacuum Ultra Violet
XUV	Extreme Ultraviolet
YAG	Ytterium-Aluminum-Garnet

SINCROTRONE TRIESTE S.C.P.A.
Società di interesse nazionale ai sensi della Legge 370/99

S.S. 14 km 163,5 in AREA Science Park
34012 Basovizza, Trieste ITALIA
tel. +39 040 37581 – fax +39 040 9380902

www.elettra.trieste.it/fermi

Conceptual Design Report

Stampa
Graphart
Trieste

Sincrotrone Trieste S.C.p.A.
S.S. 14 km 163,5 in AREA Science Park
34012 Trieste ITALY
www.elettra.trieste.it - info@elettra.trieste.it